

AN ELECTROCHEMICAL STUDY OF THE
OXIDATIVE DISSOLUTION OF SYNTHETIC COPPER-SILVER-
SELENIDE MINERALS IN AQUEOUS MEDIA

BY

RONG LUO, B.Sc.

*Submitted in accordance with the requirements
for the degree of Doctor of Philosophy*

The University of Leeds,
Department of Mining and Mineral Engineering

October 1990

紛吾既有此內美兮又重之以脩能

芘江離與辟芷兮紉秋蘭以爲佩

離騷

Abstract

The electrochemical behaviour of synthetic components of copper refinery anode slimes e.g. silver selenide (naumannite) & copper silver selenide (eucairite) in aqueous media, e.g. 1M HNO₃ & 1M HClO₄ solutions, have been investigated using a variety of techniques including linear sweep cyclic voltammetry, chronoamperometry, chronopotentiometry, intermittent galvanostatic polarisation & stripping voltammetry. The electrochemically treated mineral electrodes have been subjected to a series of solid state analysis e.g. X-ray diffraction, scanning electron microscopy, energy dispersive X-ray analysis & electron microprobe analysis to identify possible phase transitions on the surface, while the aqueous solutions were analysed by atomic absorption spectroscopy. Considerable attention was also paid to the synthesis of Ag₂Se, Cu₂Se & CuAgSe by hydrochemical & solid state (vapour transmission) methods. The characterisation of the synthetic minerals was accomplished by the above analytical methods.

Under anodic conditions, silver selenide is oxidised directly to elemental selenium via the reaction $\text{Ag}_2\text{Se} = 2\text{Ag}^+ + \text{Se} + 2\text{e}$. No evidence for the formation of any intermediate phases, e.g. AgSe, was found by surface analysis, though CV & IGP experiments suggest the possible presence of an intermediate. The formation of a metastable elemental selenium product was proved by both EDXA & electrochemical techniques e.g. cathodic stripping (including cathodic excursions in CV & IGP) in which the reduction of the elemental selenium to H₂Se was observed. The elemental selenium product is porous & does not impose restriction on the diffusion of product or reactant across the silver selenide/electrolyte interface. Instead, the slow heterogeneous charge transfer process plays an important role in determining the rate. Silver selenide was reduced at potentials more negative than 0.2V to elemental silver & H₂Se gas.

Copper was found to be preferentially "leached" into solution during the

anodic polarisation of copper silver selenide (Cu:Ag \approx 30:1 in the solution at initial stages), forming a silver-rich product layer which was subsequently oxidised to elemental selenium. This is probably due to the catalytic effect of silver ions released instantaneously at the imposition of polarisation. EMPA reveals positive evidence for formation of Ag₂Se on the electrode surface, which is similar to a mechanism proposed to explain the catalytic effect of Ag⁺ (aq) on sulphides e.g. chalcopyrite, heazlewoodite & pyrite.

The Fe³⁺/Fe²⁺ couple was studied with a newly-developed technique to obtain the kinetic parameters diffusion coefficient, charge transfer coefficient, half wave potential $E_{1/2}$ & standard heterogeneous rate constant. These results were comparable to literature values.

Furthermore, this work also included an extensive study of the theoretical aspects of fundamental electrochemistry & led to the development of a set of powerful & accurate software routines for digital simulation of electrochemical data. This included provision for a wide variety of electrochemical mechanisms & for the techniques of cyclic voltammetry, chronoamperometry & chronopotentiometry. The digitally simulated data were extensively assessed using numerical & analytical methods, including where applicable convolution & allied techniques. A new numerical technique was developed to analyse complicated electrochemical reactions e.g. simple electron transfer process coupled with a catalytic reaction. In this independent variation of homogeneous chemical kinetic & diffusional parameters was possible. The implications of the above simulation routines to the study of electrode processes involving solid phase(s) e.g. minerals were also considered. However, due to the complexities arising from the involvement of solid phase(s), more work is needed so that these systems can be theoretically treated.

Acknowledgement

I would like to thank my supervisors, Dr. Norman Taylor of the School of Chemistry, Dr. Robert Gee of the School of Materials & Dr. Nevill M. Rice, of the Department of Mining & Mineral Engineering, for their advice, help & encouragement throughout the course of this work. Thanks are also due to Professor P. Gray, Professor J. Nutting & Professor P.A. Young, for the provision of joint laboratory facilities, & in particular for their inter-departmental cooperation which created the opportunities for much of this work.

Particular acknowledgement is made here to the following:

Dr. P.D. Battle & Mr. C. Jones, of the School of Chemistry, for conducting some of the powder X-ray diffraction analysis.

Dr. T. Boddington, of the School of Chemistry, for advice & discussion over theoretical aspects of this work.

Dr. E. Condliffe, of the Department of Earth Sciences, for operational & analytical assistance with electron microprobe analysis.

Mr. C.J. Gascoigne & Mr. M. Holmes, of the School of Chemistry, for their glass blowing services.

Mr. P.A. Halford-Maw & Mr. D.G. Mills, of the School of Chemistry, for assistance with instrumentation etc.. Their help & critical advice regarding the construction of the simulation software etc. is also gratefully acknowledged.

Mr. A. Hanusch, of the Department of Mining & Mineral Engineering, for practical assistance in operating the powder XRD instruments.

Mr. J.P. Harrington & Mr. A. Nichells, of the School of Materials, for assistance with scanning electron microscopy.

Mr. A. Hedley & other members of the Microanalysis Section of the School of Chemistry, for conducting atomic absorption spectroscopy analysis.

Mr. D. Horner, of the School of Materials, for assistance in photographic aspects & especially for his careful preparation of the photos for this thesis.

Mr. S.R. Lloyd, of the Department of Mining & Mineral Engineering, for practical assistance during the synthesis of the copper selenide.

Mr. M. Pegden & Mr. P. Townhill-Rewston, of the Department of Mining & Mineral Engineering, for assistance during preparation of selenide pellets.

Mr. C. Reyner & other members of the Mechanical Workshop of the School of Chemistry, for the fabrication of experimental equipment.

It would be imprudent to use the 8-character phrase, 'T-H-A-N-K Y-O-U', to express my grateful appreciation to Dr. Pamela V. Taylor & Dr. Norman Taylor. As a result, I have never said that phrase, trying to avoid hearing the reply 'NEVER MENTION IT' !

I would like to take this opportunity to thank my colleagues; Mark Baxby, Ibrahim S. EL-Hallag, Chris Jones, Youssef Moharram, David Rose, Dr. Steve Wallace, Dr. Terry E. Warner & Lordwell K. Witika; for the many informal discussions relevant or irrelevant to this work.

I also wish to thank my friends, especially Meigui & Ming, & my wife, Linghua, for their encouragement & without whom, many memorable events, ranging from dinner parties to country walking, could not have taken place. I also wish to thank my daughter, Yi, for the happiness & joy she has brought into my life. Similarly, life could be much more difficult for me without the constant support & encouragement of my parents & my friends back in China - the land of my birth.

Finally, I wish to acknowledge the State Higher Education Commission of the People's Republic of China & the British Council for the provision of a TC Scholarship Award.

Contents

Abstract		PAGE	i
Acknowledgements			iii
Contents			v
Preface			x
Abbreviations			xiii
List of Tables			xiv
List of Figures			xv
1	Introduction		1
1.1	Extractive Metallurgy of Copper Anode Slimes		1
1.1.1	Nature of Copper Anode Slimes		1
1.1.2	Conventional Processes for the Treatment of Copper Anode Slimes		4
1.1.3	Hydrometallurgical Treatment of Copper Anode Slimes		7
1.1.3.1	Oxygen Pressure - Sulphuric Acid Leaching		9
1.1.3.2	Sulphuric Acid Leaching		12
1.1.3.3	Oxygen Pressure - Alkaline Leaching		13
1.1.3.4	Saline Leaching		15
1.1.3.5	Hydrochlorination of Copper Anode Slimes		17
1.1.3.6	Nitric Acid Leaching		18
1.1.3.7	Electrochemical Leaching		23
1.2	Crystal Structure of Selenides of Copper and Silver		26
1.3	Thermodynamics of the Metal(s) - Selenium - Water Systems		31
1.4	Oxidative Dissolution of Copper Anode Slimes and Synthetic Anode Slimes Components		38
2	Experimental		43
2.1	Synthesis & Characterization of CuAgSe, Ag₂Se, & Cu₂Se		43
2.1.1	Introduction		43
2.1.2	Synthesis of CuAgSe, Ag ₂ Se, & Cu ₂ Se		45

2.1.3	Characterization of the Synthetic Compounds	51
2.2	Analytical Techniques	58
2.2.1	Powder X-ray Diffractometry (XRD)	58
2.2.2	Scanning Electron Microscopy (SEM) & Energy Dispersive X-ray Analysis (EDXA)	59
2.2.3	Electron Microprobe Analysis (EMPA)	61
2.2.4	DC Arc Spectrographic Analysis	62
2.2.5	Atomic Absorption Spectroscopy (AAS)	62
2.3	Electrochemical Techniques	63
2.3.1	Instrumentation	63
2.3.1.1	Electrode Fabrication & Cell Design	63
2.3.1.2	Electrochemical Apparatus	66
2.3.1.3	Experimental Procedures	68
2.3.2	Electrochemical methods	69
2.3.2.1	Open Circuit Potential Measurement	69
2.3.2.2	Cyclic Voltammetry (CV)	70
2.3.2.3	Stripping Voltammetry	72
2.3.2.4	Chronoamperometry (CA)	72
2.3.2.5	Chronopotentiometry (CP)	74
2.3.2.6	Intermittent Galvanostatic Polarization (IGP)	75
2.4	Purity of Materials	77
3	Electrochemical Study of the Dissolution of Synthetic Copper-Silver-Selenide Minerals in Aqueous Media	79
3.1	Potentiometric Measurement	79
3.2	Cyclic Voltammetry (CV)	84
3.2.1	Introduction	84
3.2.2	Silver Selenide (Ag_2Se)	84

3.2.3	Copper Silver Selenide (CuAgSe)	92
3.3	Stripping Voltammetry	120
3.4	Chronoamperometry (CA)	126
3.4.1	Introduction	126
3.4.2	Chronoamperometric Study on Silver Selenide	126
3.4.3	Chronoamperometric Study on Copper Silver Selenide	129
3.5	Chronopotentiometry (CP)	145
3.5.1	Introduction	145
3.5.2	Chronopotentiometric Study on Synthetic Silver Selenide and Copper Silver Selenide	149
3.6	Intermittent Galvanic Polarization (IGP)	156
3.6.1	Silver Selenide	156
3.6.2	Copper Silver Selenide	161
3.7	Chronoamperometric Studies on the Fe³⁺/Fe²⁺ Couple in Acid Media	174
4	Digital Simulation in Electrochemistry	184
4.1	Introduction	184
4.2	Mass Transport Phenomena in Cells	186
4.2.1	Diffusion	187
4.2.1.1	The Diffusional Process	187
4.2.1.2	The Nernstian Diffusion Layer	189
4.2.2	Migration	191
4.2.3	Convection	192
4.2.4	Total Mass Transport Equation	193
4.3	Homogeneous kinetics	194
4.4	Digital Simulation of A Diffusional Process - the Implicit Crank-Nicolson Technique	197

4.4.1	Digitisation of the Semi-finite Diffusional Equation	197
4.4.2	The Implicit Crank-Nicolson Technique	200
4.4.3	Implementation of the Crank-Nicolson Technique	204
4.5	Simulation of a Simple Electron Transfer Process	206
4.5.1	Initial & Boundary Conditions	207
4.5.2	Simulation of E-t & i-t Profiles Generated by a Potentiostat in the Controlled Potential/Current Techniques (DC)	210
4.5.3	Simulation of a Simple Electron Transfer Process under Controlled Potential Conditions	213
4.5.4	Controlled Current (Chronopotentiometry) Technique	219
4.6	Digital Simulation of Electrochemical Mechanisms with Homogeneous Chemical Kinetics e.g. Following and/or Preceding Chemical Reactions	225
4.7	Digital Simulation of Multistep Charge Transfer Processes	234
4.7.1	Simple Multiple Charge Transfers (EE)	234
4.7.2	Successive Charge Transfers with Coupled Chemical Reaction(s) e.g. the ECE, ECE ₂ & ECEC Mechanisms	242
4.7.3	The SQUARE Mechanism - Four Sided Reaction	246
4.8	Assessment of Results	251
4.8.1	Convolution Transform of Current	251
4.8.2	Analysis of Simulated Data for Cyclic Voltammetry	257
4.8.2.1	Simple Electron Transfer Reactions	257
4.8.2.1.1	Nernstian i.e. Reversible Electron Transfer Reactions	258
4.8.2.1.2	Irreversible Electron Transfer Reactions	266
4.8.2.1.3	Quasi-reversible Electron Transfer Reactions	269
4.8.2.2	Electron Transfer with Coupled Homogeneous Chemical Reaction	273
4.8.2.2.1	Electron Transfer with Following Homogeneous Chemical Kinetics – The EC Mechanism	273

4.8.2.2.2	Electron Transfer with Preceding Homogeneous Chemical Kinetics – The CE Mechanism	284
4.8.2.2.3	The EC Catalytic Mechanism	292
4.8.3	Analysis of Simulated Data for Chronoamperometry	312
4.8.3.1	The Butler-Volmer Equation & the Tafel Behaviour	312
4.8.3.2	The Cottrell Behaviour - A Test for Diffusion Control	317
4.8.3.3	Test of Digital Simulation Using the Convolution Technique	320
4.8.3.4	Analysis of Digital Simulation Results Using e.g. the $\Delta Q/\Delta i$ vs $\Delta t^{1/2}/\Delta i$ & $\Delta i/\Delta t^{1/2}$ vs $\Delta Q/\Delta t^{1/2}$ Relationships	325
4.8.3.5	Analysis of Digital Simulation of Coupled Homogeneous Reactions	334
5	Conclusions	338
	Bibliography	342
	Reference	343
	Appendix	
A-1	Thermodynamic Data & Equilibria Equations for Construction of Eh-pH Diagrams	356

Preface

Ever since the electrolytic refining technique for copper purification was patented in the late nineteenth century [1], great advances have been made in such aspects as the efficiency & scale of refinery plants [1,3,37], cell designs [3,9,37], quality of products [1,3,37,57], working conditions & treatments of the electrolyte [5,56] & the by-product - the anode slimes or sludges [1,2,9,15]. As a consequence, the electrolytic refining of copper is now so widely employed that nearly 95% [3] of the world's production of copper is obtained by electro-refining, which in turn leads to the production of a large amount of the valuable anode slimes (about 0.3 - 1.0% by weight of total production [2]). With the increase in the complexities of the raw copper-bearing ores being treated, the recovery^{of} associated metals such as nickel, lead, silver, gold, selenium, tellurium, tin, & platinum group metals, is of increasing economic attraction to the copper refiners, presumably due to the fact that the overall commercial value of the anode slimes is about twice that of the copper collected at the cathodes [5,6,38], regardless of the extremely low production of the anode slimes as compared with that of the cathode copper [5,7]. For this reason, various attempts have been made to work out a more effective process, by which the metals can be extracted as completely as possible, in association with reasonable costs of production, purer products, & less environmental pollution. In recent years, especially, many papers dealing with the extraction of metals from the slimes have been documented & patents have been issued. In particular, several hydrometallurgical processes [7-15], among which are oxygen pressure leaching in sulphuric acid media, pressure leaching with soda or sodium hydroxide solutions, leaching with salts such as FeCl_3 , CuCl_2 & $\text{Fe}_2(\text{SO}_4)_3$, leaching with sulphuric acid or nitric acid solution, have been extensively examined with considerable success. Although most of the investigations were undertaken under

laboratory or pilot scale conditions, the results showed potentials for the application of these hydrometallurgical methods to the comprehensive utilisation of copper electrorefining anode slimes, because those processes do have, if not exaggerated, several advantages over the conventional pyrometallurgical or combined pyro-hydro-metallurgical (mainly pyro-) processes. In addition, some special processes, e.g. flotation [16,17,50] which aimed at the recovery of silver & gold & electrochemical leaching processes [19,39-43,70,121-2,124], were reported with encouraging results. It is almost certain that some of those hydrometallurgical processes will come into production sooner or later.

While new techniques were being developed, theoretical investigations have also been carried out. Azerbaeva & coworkers [18-29] have studied the leaching behaviour of selenides & tellurides of alkaline metals systematically by leaching of pure compounds, construction of metastable Eh-pH diagrams etc. Most recently, Montoya-Jurado [15] has carried out a series of kinetic studies on the leaching of synthetic selenides of silver & copper in nitric acid media, trying to explain the observed two-stage leaching behaviour of copper & silver during the nitric acid leaching of raw anode slimes [14]. However, progress is insufficient for the mechanism of nitric acid leaching of the anode slimes to be understood well enough for the commercial application of this technique.

In view of the fact that every oxidative or reductive leaching process proceeds electrochemically (i.e. electron transfer processes between leaching reagent & the minerals are always involved in part of the overall leaching process) e.g. the leaching of sulphides of alkaline metals [32-6], it would be most worthwhile doing a systematical electrochemical investigation on the selenide-nitric acid systems so that a close approach to the understanding to the nitric acid leaching process of anode slimes could be achieved. As we can see later, a combination of the majority of the existing electrochemical techniques, e.g. potentiometry, linear sweep cyclic voltammetry (LSCV OR CV), stripping

voltammetry, chronoamperometry (CA), intermittent galvanostatic polarisation (IGP) & chronopotentiometry (CP), has been employed to study the electrochemical behaviour of several synthetic components of anode slimes from different aspects, & several kinetic properties have been qualitatively discussed.

A majority of electrochemical investigations involve the elucidation of reaction mechanisms. This necessitates the understanding of the basic theoretical aspects of an electrochemical system. In this work, a considerable attention has been directed towards systems of macro planar electrodes in un-stirred electrochemical cells. The diffusional problems of the above systems are defined by Fick's second law & are much simpler as compared to those involving for example dissolution of solid phase(s) such as mineral electrodes. The latter involves diffusion in BOTH the solid phase & the aqueous electrolyte & forms an important basis for suggested work in the future.

Abbreviations / Acronyms

XRD	X-ray Diffractometry
EMPA	Electron Microprobe Analysis
SEM	Scanning Electron Microscopy
EDXA	Energy Dispersive X-ray Analysis
ESCA	Electron Spectroscopy for Chemical Analysis
AAS	Atomic Absorption Spectroscopy
emf	Electromotive Force
IGP	Intermittent Galvanostatic Polarization
CV	Cyclic Voltammetry
CA	Chronoamperometry
CP	Chronopotentiometry
RE	Reference Electrode
WE	Working Electrode
CE	Counter Electrode
RDE	Rotating Disk Electrode
SCE	Saturated Calomel Electrode
ET	Electron Transfer
CN	Crank-Nicolson Technique
E	Simple Electron Transfer
EC	Electron Transfer with Following Chemical Reaction
EC _{dimer}	Electron Transfer with Following Dimerisation
EC _{cat}	Electron Transfer with Following Catalytic Reaction
CE	Electron Transfer with Prece-ding Chemical Reaction
CEC	Electron Transfer with Prece-ding & Following Chemical Reaction
EE	Multi-step Electron Transfer (Successive)
EE _{disp}	Successive Electron Transfer with Disproportionation
ECE	Successive Electron Transfer with Chemical Reaction
ECE _{disp}	ECE reaction with Disproportionation
ECEC	Successive Electron Transfer with Chemical Reactions
SQUARE	Four Sided Reaction with Two ET & Two Chemical Reactions
ECE2	Chemically Coupled Electron Transfer Reactions
CROSS	SQUARE Reaction with Disproportionation

Tables

	PAGE
1.1 Range of Composition of copper anode slimes	2
1.2 Common compounds in copper anode slimes	2
1.3 Phase composition of selenium & tellurium in slimes	2
2.1 Conditions for synthesis of copper silver selenides	50
2.2 EMPA results for Ag ₂ Se & CuAgSe	53
3.1-2 Open-circuit potentials of Ag ₂ Se	82
3.3 EMPA analysis for CuAgSe samples	131
3.4 $i\tau^{1/2}$ data for Ag ₂ Se	151
3.5-6 Aqueous analysis data for Ag ₂ Se & CuAgSe	152
3.7 Processes denoted on the IGP traces	164
3.8 Results from chronoamperometric data of the Fe ³⁺ /Fe ²⁺ couple	180
4.1 Differential equations for simple electron transfer process with coupled homogeneous chemical kinetics	227
4.2 Initial & boundary conditions for the EC, EC _{dimer} , EC _{cat} , CE & CEC mechanisms	228
4.3 Differential equations for multistep electron transfer process with/without coupled homogeneous chemical kinetics	235
4.4 Initial & boundary conditions for the EE, ECE, ECEC & SQUARE (four-sided) mechanisms	236
4.5 Results from the plots i vs I_1 (eqn. 4.98a) & $\ln k$ vs ΔE	322
4.6 Results from the plots $\Delta Q/\Delta i$ vs $\Delta t^{1/2}/\Delta i$ & $\ln k$ vs ΔE	333

Figures

		PAGE
1.1	Canadian Copper Refiners Ltd. silver refinery flowsheet	8
1.2	Phase equilibria for the Ag-Se system	26
1.3-4	Crystal structure of Ag ₂ Se	28
1.5	Phase equilibria for the Cu-Se system	30
1.6-8	Eh-pH diagrams of Ag-Se-H ₂ O, Cu-Se-H ₂ O & Cu-Ag-Se-H ₂ O systems	35-7
2.1	Schematic diagram of the vessel for preparation of selenides	46
2.2	XRD for CuAgSe	47
2.3-4	XRD for CuAgSe	49
2.5-6	XRD for Ag ₂ Se & CuAgSe	54
2.7-8	SEM images of Ag ₂ Se & CuAgSe	55-6
2.9-10	EDXA for CuAgSe	57
2.11	Illustration of sample press & mould	60
2.12	Schematic diagram of the working electrode	64
2.13-4	Metrohm cell & experimental set-up	67
3.1-2	Open-circuit potential measurements	83
3.3-4	Cyclic voltammograms of 1M HNO ₃ & 1M HClO ₄ solutions	83
3.5-28	Cyclic voltammograms for Ag ₂ Se	96-108
3.29	Concentration profiles with an alloy	109
3.30	Cyclic voltammogram for Ag ₂ S	109
3.31	SEM images for CV samples	110
3.32-3	EDXA analysis for CV samples	111
3.34-48	Cyclic voltammograms for CuAgSe	112-9
3.49-51	Stripping voltammograms for Ag ₂ Se	123-4
3.52	EDXA result for a silver selenide (Ag ₂ Se) sample	124
3.43-54	Stripping voltammograms for CuAgSe	125
3.55	Chronoamperograms for 1M HNO ₃ & 1M HClO ₄ solutions	132

3.56-61	Chronoamperograms for Ag ₂ Se	133-6
3.62 & 64	XRD & EDXA results for Ag ₂ Se samples	137
3.63	SEM images for Ag ₂ Se samples	138
3.65-70	Chronoamperograms for CuAgSe	139-42
3.71-2	EMPA analysis for CuAgSe samples	143-4
3.73-6	Chronopotentiograms for Ag ₂ Se	153-4
3.77-8	Chronopotentiograms for CuAgSe	155
3.79-86	IGP traces for Ag ₂ Se	165-8
3.87	SEM images for Ag ₂ Se samples	169
3.88-9	EDXA analysis for Ag ₂ Se samples	170
3.90-94	IGP traces for Ag ₂ Se	171-3
3.95-8	Treatment of chronoamperometric data for the Fe ³⁺ /Fe ²⁺ couple	181-2
3.99-100	Cyclic voltammograms for the Fe ³⁺ /Fe ²⁺ couple	183
4.1	Concentration profile defined by Fick's law	189
4.2	Plot of concentration against distance at a given time	193
4.3	Principles for the sampling of the (x,t) plane	198
4.4-5	Concentration-space-time surface & cross-section	201
4.6	Illustration of the "δx/2 shift" method	203
4.7	Illustration of the signals & responses for CV, CA & CP	212
4.8	Geometrical illustration of <i>the method of false position</i>	221
4.9	Geometrical illustration of <i>Newton's method</i>	223
4.10	Graphic illustration of the function $F(p) = C_A e^{-\alpha p} - C_B e^{(1-\alpha)p} - M$	223
4.11	Schematic illustration of evaluation of the convolution integrals	255
4.12	Comparison of I ₁ convolution data evaluated with various methods	255
4.13-4	Test of FAST ET using traditional methods	259
4.15-7	Test of FAST ET using convolution techniques	264-5
4.18-21	Test of irreversible ET using convolution techniques	267-8
4.22-5	Test of quasi-reversible ET using convolution techniques	271-2

4.26-35	Test of EC_{rev} reactions using convolution techniques	276-80
4.36-9	Test of EC_{irrev} reactions using convolution techniques	282-3
4.40-9	Test of CE_{rev} reactions using convolution techniques	287-91
4.50-55	Test of EC_{cat} reactions (EQUAL diffusion coefficients) using convolution techniques	300-2
4.56-68	Test of EC_{cat} reactions (UNEQUAL diffusion coefficients) using convolution techniques	305-11
4.69-71	Tafel plots for simple ET	314-5
4.72-3	Cottrell test for diffusion control	319
4.74-77	Assessment of CA data using $i - I_1$ plots	323-4
4.78-81	Assessment of CA data using $\Delta Q/\Delta i$ vs $\Delta t^{1/2}/\Delta i$ plots	331-2
4.82-4	Assessment of CA data for the EC_{cat} reactions	336-7

1 Introduction

1.1 Extractive metallurgy of copper anode slimes

1.1.1 Nature of copper anode slimes

The grey powdery anode slimes collected from copper electrolytic refining tankhouses contain varying amounts of copper, nickel, silver, gold, lead, arsenic, selenium, tellurium, antimony, tin, platinum group metals, etc., depending on the anode composition. This depends primarily on the mineralogical and chemical composition of the raw copper-bearing materials, the extraction methods, and the conditions under which electrolytic purification of blister copper (anode) is performed. As a result, the behaviour of the impurities during the electrolytic refining of copper [1-3,16,59] and the characteristics of the anode slimes [9,45-6, 15] have been widely studied, so as to get a better understanding to the refining process and the subsequent treatment of the anode slimes. Analytical techniques involved are: X-ray diffractometry [6,14,45,47,58], scanning electron microscopy [14,45-6], electron microprobe [16], energy dispersive X-ray analysis [14,55], polarography [46], spectrography [14,45], X-ray fluorescence [45] and atomic absorption spectroscopy [14]. Generally, most of the anode slimes contain sufficient amounts of copper, silver, gold, selenium and tellurium for economic extraction except for some cases where tin and silver are the main components [5,49]. *Table 1.1* shows the common elemental composition of raw copper anode slimes [9]. A summary of the possible compounds in the anode slimes is presented in *Table 1.2* [5,45-7,49-55,58-9] and the possible phase composition of selenium and tellurium components in *Table 1.3* [42].

It is worth noting that these compounds do not necessarily exist as single-compound phases. They might, instead, mechanically agglomerate together or form a kind of homogeneous phase, namely the solid state solution. An example

Table 1.1 Range of composition of anode slimes [9]

Component	Content(%)	Component	Content(%)
Copper	3 - 40	Selenium	0.5 - 58
Silver	6 - 30	Tellurium	0.5 - 10
Lead	0.3 - 35	Arsenic	0.3 - 10
Nickel	0.1 - 45	Antimony	0.1 - 16
Iron	0.1 - 2	Bismuth	Trace - 1.0
Gold	0.0 - 2.0	Insoluble	0.3 - 16
Platinum metals	0.0 - 1.0		

Table 1.2 Common compounds in copper anode slimes [1,3,5,11,14,45,49,55]

Element	Ag, Au, Cu, Se, Te, platinum group metals
Selenide	β -Ag ₂ Se, Cu ₂ Se, CuAgSe, PbSe
Telluride	Ag ₂ Te, Cu ₂ Te, CuAgTe, (Ag,Au)Te ₂ , PbTe
Sulphide	Ag ₂ S, Cu ₂ S, PbS·Ag ₂ S·Sb ₂ S ₃ , Ag-Pb-Bi sulphides
Oxide	CuO, Cu ₂ O, NiO, ZnO, SnO ₂ , SiO ₂ , As ₂ O ₃ , Fe ₂ O ₃ , Bi ₂ O ₃ , 3 Cu ₂ O·NiO·Sb ₂ O ₅ , As-Sb binary oxides
Chloride	Cu ₂ Cl ₂ , AgCl
Sulphate	NiSO ₄ , CuSO ₄ , PbSO ₄ , CaSO ₄ , Sn(OH) ₂ SO ₄
Arsenate	BiAsO ₄ , SbAsO ₄ , Cu ₈ Al ₂ (AsO ₄) ₃ (OH) ₂₇ ·33 H ₂ O, PbHAsO ₄ , Cu ₃ (AsO ₄) ₂ , 8 PbO·As ₂ O ₃ , 3 PbO·As ₂ O ₅
Silicate	CaSiO ₃ , PbSiO ₃
Antimonate	Sb ₂ O ₅ ·x H ₂ O, Pb ₂ Sb ₂ O ₆ , Pb ₂ Sb ₂ O ₇ , CuSbO ₄
Others	Arsenide, solid state solutions, etc.

Table 1.3 Phase composition of selenium & tellurium [52]

Phase	Se	Cu ₂ Se	Ag ₂ Se	PbSe	CuAgSe
Assay (%)	2.51	4.84	0.47	0.0044	0.73
Phase	Te	Cu ₂ Te	Ag ₂ Te	PbTe	Insoluble
Assay (%)	1.16	0.73	0.26	0.069	0.004

of the former case are the "nodule-structured" particles [16]. These particles were suggested to be composed of a spherical core of lead sulphate, 4-15 μ m in diameter & an outer layer of the agglomerate of copper selenides, silver selenide, gold telluride, lead sulphate & cuprite. While the latter can be illustrated by the presence of a solid state solution of metallic gold & silver in the metallic copper & the so-called "Tailiite" [14] - a newly identified solid state solution of zinc, tin, nickel & iron oxide which is chemically and electrochemically stable in relatively strong oxidative atmosphere such as 1-4M HNO₄ solutions.

Although the behaviour of the impurities during the anodic dissolution of copper and the nature of the anode slimes have been studied intensively over the past few decades, the formation of the anode slimes is still not fully understood due to the complexity of the system. Generally, the components of the anode slimes fall into three categories - primary, secondary & tertiary products [9,46].

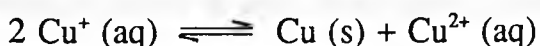
(1) Primary products

Principally, compounds in this category are electrochemically "insoluble" in the electrolyte (more precisely, slightly or partially soluble, although the solubilities may differ from component to component), and precipitate at the bottom of the tanks, with copper and some less "inert" components being slowly leached from the anodes. Examples are Cu₂Se, Ag₂Se, Cu₂S, Cu₂Te, CuAgSe, AuAgTe, Ag₂S, NiO, Cu₂O, Ag, Au, platinum group metals [1,3,5,11,14,45,49, 55], and some solid state solution phases e.g. "Tailiite" [14].

(2) Secondary products

This type of products result from reactions between the dissolving impurities or between these impurities and the electrolyte, during the anodic dissolution of copper. Substances eg Cu₂Cl₂, AgCl, PbSO₄, Sn(OH)₂SO₄, CaSO₄, Cu & complex Sn-As-Pb-Sb compounds, are examples. It is suggested that the formation of Cu₂Cl₂ & AgCl is caused by the Cl-containing electrolytes e.g. NaCl

& HCl which are used to prevent electropositive elements e.g. Ag from plating onto the cathode. While elemental copper is partially formed via the following reactions [1]:



On the other hand, Makarov [61] concluded that the presence of metallic copper in the electrolytic slimes was only due to mechanical crumbling of copper anodes rather than the above disproportionation reactions. This conclusion was reached by carrying out a series of experiments in electrolyte with or without monovalent copper species (Cu^+) and subsequently determining the concentrations of the cupric and cuprous aqueous species and thus the ratio of $[\text{Cu}^+]/[\text{Cu}^{2+}]$. In addition, part of the Ag_2Se and AgCuSe were reported [58] to be formed via the interaction between Cu_2Se and silver during the anodic dissolution. Ag_2Se and Ag_2Te were also reported to be formed via reactions between silver and selenium or tellurium during the anodic corrosion [5,57].

(3) Tertiary products

These products are basically some undissolved or partially dissolved debris which has been mechanically detached from the dissolving anodes. Thus, the constitution of this product is similar to that of the copper anodes.

1.1.2 Conventional processes for the treatment of copper electrolytic slimes

The recovery of precious metals from copper refinery slimes dates back to the end of the 19th century [2], when the electrolytic refining of copper became economically acceptable & gradually took the place of pyro-refining processes. From then on, a number of attempts have been made to develop more effective processes by which various valuable elements are separated and recovered as

completely as possible. At the early stages, most attention was paid to the separation and recovery of silver and gold [6,38,46,81], by means of relatively simple processes e.g. direct smelting and cupelling, with the unwanted elements being "slagged off". In practice, these treatments are not very effective in the separation of silver & gold from other elements, which leads to a low recovery & poor purity of these products. With the development of extractive metallurgy, the recovery of the appreciable amount of selenium, tellurium and platinum group metals, became economically attractive. As a consequence, various pyrometallurgical and combined pyro-hydro-metallurgical processes for the recovery of silver, gold, as well as platinum group metals and the relatively less valuable elements e.g. selenium and tellurium, have been developed in several copper refineries so as to make the anode slimes treatment more efficient and profitable.

Although the slimes treatments may differ from case to case, the processes are basically composed of some if not all of the following steps, depending on the nature of the sample treated [2,5,6,11,38]:

(1) Copper and nickel are removed as completely as possible by oxidation processes followed by leaching in dilute sulphuric acid solution. The oxidation is usually accomplished either by aeration in dilute sulphuric acid or by high temperature treatments such as oxidative roasting, sulphatizing roasting. The leaching liquor is then purified for the production of copper sulphate.

(2) Selenium is volatilized & collected as SeO_2 from the fume by oxidative or sulphatizing roast, with some elemental selenium being collected via a dust precipitator. An exception to this is the soda ash oxidising roasting process in which selenium is converted into water soluble compounds e.g. sodium selenite or selenate and recovered via leaching, reduction with SO_2 and similar reagents.

(3) Gold & silver are recovered as an alloy (Doré Bullion) via melting & slagging treatment in a reverberatory furnace (Doré furnace). Most of the other precious metals e.g. platinum group metals, are also accumulated into the alloy.

(4) After the separation of silver from gold in a Moebius Cells, the gold (in the electrolyte) is subsequently refined in the Wohlwill Cells. An alternative method for gold and silver separation consists of three stages, i.e. sulphatizing with concentrated H_2SO_4 , leaching with water to extract silver, followed by precipitation of silver with copper, while the gold is enriched in the mud.

(5) Platinum group metals are recovered by precipitation from the electrolyte of gold electrolytic purification.

Generally, the conventional operations for copper anode slimes treatment can be categorised into several groups, i.e. oxidative roasting [64,66], direct smelting [2,6,38,46,66,81], sulphatizing roasting [5,46-7,62], soda ash smelting [112], soda ash roasting [63], and chlorination [102], according to methods used in the copper and selenium removal stages. The main objective of the oxidative roast and the sulphatizing roast processes is to transfer the copper, nickel and probably part of other non-ferrous impurities into water- or acid- (normally dilute sulphuric acid) soluble compounds because they are harmful to the subsequent processes for the recovery of gold and silver, with the selenium being volatilized as SeO_2 . Exceptionally, a low-temperature roasting process (250-450°C) was also reported [82], in which all the Se- and the Te-bearing compounds were oxidised to selenite and tellurite, respectively. To accelerate the oxidation of silver selenide, catalysts, such as cupric oxide (CuO), were added. The roasted slimes were subsequently leached in a sodium hydroxide solution (20%) at 70-100°C, whereupon the Se and Te dissolved. The tellurium was then precipitated from the filtrate as TeO_2 by adjusting the acidity of the solution to neutral, and the selenium was recovered from the Te-free solution by reduction with SO_2 . The soda ash roasting and smelting, on the other hand, are usually restricted to the treatment of low copper content or decopperized slimes. After smelting or roasting, the Se- and Te-bearing compounds are converted into the water soluble selenite and tellurite for the recovery of selenium and tellurium. Nonetheless, the

methods for the recovery and separation of silver and gold are almost identical.

Comprehensive details of the above processes are given in the literature [2,5,6,11,45-6,58,81], whilst a brief description of a typical industrial process is given below. *Figure 1.1* illustrates the flowsheet of the conventional sulphatizing roasting process employed by the Canadian Copper Refiners Ltd. to treat slimes characterised by high selenium (18-20%) and tellurium (3.4%) contents [2].

The conventional routes have been the major methods for treatment of anode slimes for a long period of time, probably owing to the fact that these operations are reliable and hydrometallurgical processes were not economically competitive at the same period. However, several serious disadvantages have been associated with those processes ever since they came into production. These include pollution, high energy consumption, complicated procedures, low recovery of metals (the recoveries for selenium and tellurium are usually around 70% [5,6,38,46,81]) & poor qualities of products. Furthermore, large amount of by-products produced in those processes must be recycled to the refining process to achieve higher recovery of metals. This in turn makes the treatment of the slimes even more difficult and complicated. As a result, the application of conventional processes for anode slimes treatment are restricted to cases where the composition of the anode slimes is relatively simple.

1.1.3 Hydrometallurgical methods for the treatment of copper anode slimes

As mentioned before, the applications of conventional processes for copper anode slimes treatment have been severely limited in the past decades, owing to various weaknesses over several aspects. Most recently, especially, with the increasing social concern about the environment, the increasing complexity of the composition of the raw copper-bearing ores and thus that of the anode slimes, & the rise of the cost of fuel & energy, the recovery of associated elements from

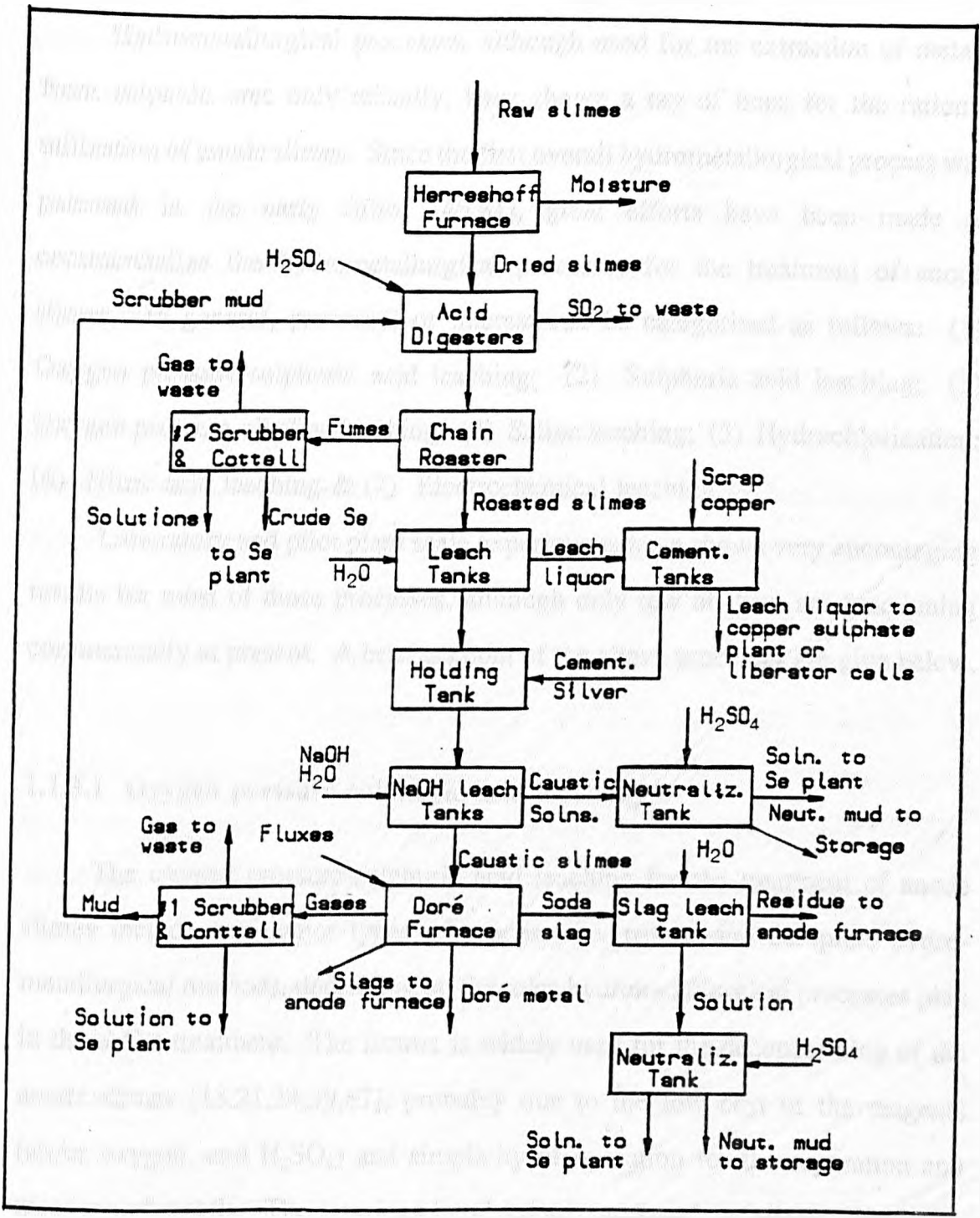


Figure 1.1 Canadian Copper Refiners Ltd. Silver Refinery Flowsheet

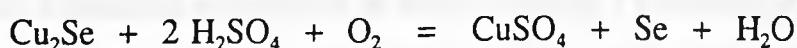
the anode slimes has become ever-increasingly important.

Hydrometallurgical processes, although used for the extraction of metals from sulphide ores only recently, have shown a ray of hope for the rational utilization of anode slimes. Since the first overall hydrometallurgical process was patented in the early fifties [46,81], great efforts have been made to commercialize the hydrometallurgical processes for the treatment of anode slimes. In general, processes of interest can be categorised as follows: (1) Oxygen pressure-sulphuric acid leaching; (2) Sulphuric acid leaching; (3) Oxygen pressure-alkaline leaching; (4) Saline leaching; (5) Hydrochlorination; (6) Nitric acid leaching & (7) Electrochemical leaching.

Laboratory and pilot plant scale experiments have shown very encouraging results for most of those processes, although only few of them are functioning commercially at present. A brief account of the above processes are give below.

1.1.3.1 Oxygen pressure-sulphuric acid leaching

The oxygen pressure-sulphuric acid leaching for the treatment of anode slimes include two major types of process, i.e. partial and complete hydro-metallurgical methods, depending on the roles hydrometallurgical processes play in the entire treatment. The former is widely used for the decopperizing of the anode slimes [13,21,24,39,67], probably due to the low cost of the reagents (air/or oxygen, and H₂SO₄) and simplicity of operation for the separation and recovery of metals. The reactions involved are proposed as follows [9]:



After treatment with dilute sulphuric acid solution in an autoclave in the presence of oxygen (or air), most of the copper and nickel in the slimes can be leached into solution which is subsequently separated from the residue for the production of CuSO_4 , while the residue is treated by the conventional processes described in Section 1.1.2 for recovery of selenium, tellurium and precious metals. Occasionally, a large proportion of the tellurium (more than 85%) also goes into the solution. To recover the dissolved tellurium species (tellurite and tellurate), copper scrubbers are added to the leach liquor to precipitate the tellurium as copper telluride, which is subsequently separated from the solution, redissolved in a NaOH solution to eliminate impurities and then reduced with SO_2 to precipitate elemental tellurium. Additionally, sparging with air [81] or SO_2 [6,38,77,81] serves as alternatives for the reduction of tellurium in solutions containing low selenium. Zinc powder is also used occasionally [6,38,81].

The removal of copper & nickel in the early stages facilitates the subsequent separation of silver & gold. However, the separation & recovery of selenium, tellurium & precious metals are still dependent on the conventional processes. Therefore, those partial hydro-metallurgical processes suffer from similar weak points to the conventional ones.

To solve these problems, several completely or mainly hydrometallurgical processes have been invented & tested at laboratory & bench scale. In these processes, most of the target metals e.g. Cu, Ni, Te, and probably Ag & Se, are converted into soluble compounds which are subsequently leached into solution & recovered. These processes possess several advantages over conventional methods. These include improved recovery of selenium, tellurium & precious metals, simplified procedures & better working conditions [8,9,68,71,73].

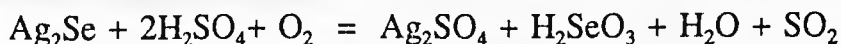
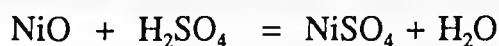
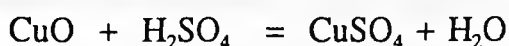
A typical process is illustrated in reference [68], where copper anode slimes containing 11.8% Cu, 12.7% Se, 2.8% Te, 12.2% Ag & 10.6% Pb were leached with dilute H_2SO_4 (15-20%, solids/liquid ratio = 1:20 to 1:25), with simultaneous

introduction of air and/or oxygen gas containing NO, NO₂, or NO₂/NO-generating compounds to the system (in an autoclave under pressure up to 5 atm) to oxidize the metals e.g. Cu, Ni, Se, Te & Ag. The oxidation products were dissolved in H₂SO₄ to obtain a leach liquor containing most of the Cu, Ni, Te, Se & Ag, leaving the gold in the residue. The recoveries of copper & selenium were 96% & 95.6%, respectively. In addition, other oxidants e.g. KMnO₄ [71], K₂Cr₂O₇ [74], ozone [73] & Fe₂(SO₄)₃ were also reported as supplementary oxidants to accelerate and enhance the oxidation of the metals.

Although the separation & recovery of metals from anode slimes has been improved remarkably & operations simplified in the oxygen pressure-acid leaching processes, there is still room for improvement. For example, the separation of selenium and tellurium were unsatisfactory in some cases [46], and the dissolution of precious metals such as silver was usually poor. Thus, residue from this process needs to be further processed for the recovery of precious metals. This in turn leads to complicated procedures and high treatment costs. In addition, when anode slimes contain an appreciable amount of nickel (up to 40%), which usually occurs in the anode slimes as refractory nickel oxide, aeration in dilute sulphuric acid solution is not powerful enough to dissolve and transfer all the nickel content into solution. Hence the subsequent smelting process for production of Doré metals is affected to some extent by the nickel remaining in the sulphuric acid treated slimes. Furthermore, high pressure operations are very expensive. Consequently, the oxygen pressure-sulphuric acid leaching is usually used to decopperize anode slimes prior to other hydro-metallurgical processes, such as sulphuric acid leaching [13,77,83], nitric acid leaching [84] and caustic pressure leaching [11,79], so that the separation and recovery of metals can be significantly improved and operations simplified.

1.1.3.2 Sulphuric acid leaching

Results of pilot plant & laboratory scale tests have indicated that most of the valuable metals e.g. Cu, Ni, Se, Te & Ag can be transformed by concentrated sulphuric acid (at elevated temperatures) into water soluble compounds, leaving most of the gold (96-99.9%) in the residue [13,39,46,68,72,76-8,80,83,114]. The mixture is subsequently treated by filtration to obtain a solution for further treatment to recover each of the metals. The reactions involved can be summarized as follows [2,5,49]:



For example, in a patented process described by Heimala [72] most of the silver as well as selenium and tellurium were converted into soluble compounds by treatment in alum or strong sulphuric acid solution (98% H_2SO_4) at 160-300°C (preferably 160-200°C), for three hours with continuous introduction of air into the system. The loaded leaching liquor was subsequently separated from the residue, and electrolysed to separate and recover the silver, selenium and tellurium in the aqueous solution.

Occasionally, a pre-decopperizing treatment by aeration in dilute sulphuric acid solution was employed to improve the sulphatization of selenium, tellurium and silver, and to simplify the operations for metal separation and recovery [13,

77,83]. The selective extraction of silver & selenium from a decopperized anode slime [77] was achieved by a two-stage leach with concentrated H_2SO_4 at 250-270°C & under anhydrous conditions. The tellurium (as tellurates), was extracted by leaching the residue from H_2SO_4 treatment with deionised water. It was reported that the filtrate from concentrated sulphuric acid leaching accounted for 99.8% Se, 2.2% Te & 99.2% Ag originally present in the slimes, compared with 0.2% Se, 97.8% Te & 0.2% Ag, respectively, from the water leach filtrate, while the residue from the water leaching contained 99.99% of the gold in the slimes.

Compared with conventional & sulphuric acid pressure leaching, the concentrated H_2SO_4 leaching process is much more powerful & effective because the majority of the silver, copper, nickel, selenium & tellurium content can be transferred to solution rather than the incomplete dissolution of the former processes. Accordingly, recovery of metals is apparently improved. However, this process is not without problems associated with SO_2 and SO_3 emissions, and corrosion of reaction vessels.

1.1.3.3 Oxygen pressure-alkaline leaching

Chalcogens and chalcogenides can not only react with strong acids e.g. sulphuric acid and nitric acid, but also with strong alkalis [6,38,22-4,90-2]. The products of both types of reaction are various soluble compounds containing selenious ions or tellurous ions, although selenates & tellurates were observed on occasion. As a result, a variety of approaches have been made to verify the feasibility of oxygen pressure-caustic leaching processes for the treatment of copper anode slimes because, theoretically, caustic solutions can selectively dissolve selenium & tellurium, leaving the gold & silver in the residue.

A simple procedure was proposed by Goldstein [82], based on calcination of the anode slimes in an oxidising atmosphere at 270-320°C & digestion with 20% NaOH solution at 50% solids & at 80-100°C. However, the extraction of

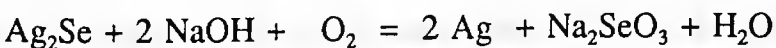
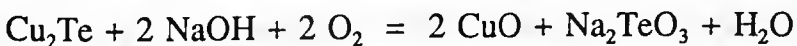
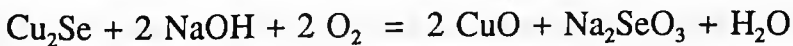
selenium & tellurium was unsatisfactory. In another process [11,79,86-7], selenium & tellurium was easily transferred to solution by leaching with NaOH in an autoclave under a pressure of 1.5 to 6 atm or higher & in the presence of commercial oxygen gas. In some cases, selenium & tellurium could even be selectively leached out by carefully controlling the oxygen partial pressure at different stages [46]. In addition, air or oxygen-enriched air could also be used as substitute for oxygen gas, although higher total pressures were needed to maintain an appropriate oxygen partial pressure [11] & longer leaching times required to achieve high extraction of Se & Te. To accelerate the dissolution selenium & tellurium, catalysts e.g. CuO, were added in some cases [21].

In a typical industrial process employed in the Canadian Copper Refiners Ltd., Montreal [11], a two-stage counter-current leaching with intermediate liquid-solids separation was used to achieve a high extraction rate for selenium. After the two-stage leaching, copper, selenium and tellurium were oxidised and more than 90% of the selenium was extracted as sodium selenite. The residue was then leached with sulphuric acid to extract more than 80% of the tellurium which appeared in the residue as sodium tellurate.

In practice, a decopperizing treatment by e.g. acid pressure leaching is usually employed to improve the extraction of selenium & tellurium [79]. After decopperizing and detellurizing, the slimes were treated with caustic solution to recover selenium at high efficiency [79]. Both laboratory and mini-plant scale experimental results indicated that under optimum conditions, i.e. 5-7 atm oxygen pressure, 180-200°C, solids/liquid ratio=1:4, large excess amount of NaOH & 3-4 hours retention time, the extraction of selenium could be close to 99%.

Possessing quite a few advantages, such as ease of conversion of Se & Te into solution, high efficiencies of separation of Se & Te from other elements & relatively lower consumption of energy, the caustic leaching process has shown a promising potential for the treatment of copper anode slimes. However,

conditions for leaching e.g. temperature & oxygen pressure must be carefully controlled to avoid the oxidation of selenium from tetravalent state to the undesirable hexavalent state [11,46,79,88-90], which cannot be readily recovered from solution by conventional methods e.g. reduction with SO₂ gas. On the other hand, the oxidation of tellurium from tetravalent state (tellurite) to the hexavalent state (tellurate), favours the separation of selenium from tellurium, because sodium tellurate is insoluble in alkaline solution and thus can be precipitated from the leach liquor. The precipitate is subsequently dissolved with dilute H₂SO₄ solution & recovered by electrolysis [75,93] or conventional methods. Nonetheless, controlling the conditions is not easy. Over-oxidation of selenium species or under-oxidation of tellurium species results in incomplete separation of Se & Te, and thus low recovery of these elements & poor qualities of the two final products. Furthermore, the oxidation of selenium from selenite to selenate is always inevitable in caustic pressure leaching, as the reaction proceeds concurrently with the oxidation of Se²⁻ to Se⁴⁺, and it is even more serious when the platinum group metals content is relatively high because of the catalytic effects of these metals [85]. The oxidation occurs as follows [11]:



1.1.3.4 Saline leaching

Acidified solutions of salts of some transition metals, e.g. chlorides & sulphates of Cu²⁺ & Fe³⁺, has found widespread application in the extractive

hydrometallurgy of sulphide ores in the past decades [94-7]. Similarly, it has been found that various Cu^{2+} & Fe^{3+} salts, e.g. cupric (ferric) chloride & sulphate, are capable of oxidising selenium and tellurium to tetravalent states [46]. Fortunately, these oxidants are not powerful enough to further oxidise selenium & tellurium to the undesirable hexavalent states, which are difficult to reduce to the elemental forms for the recovery of Se & Te by conventional methods e.g. sparging with SO_2 . Hence, the problem of loss of selenium & probably tellurium via formation of hexavalent species encountered in the caustic pressure leaching can be avoided to some extent. Recently, the oxidative leaching of chalcogenides in acidified solutions of ferric or cupric salts, particularly FeCl_3 , has attracted considerable attention [25-9,98] and promising results have been reported. However, this method is still in the stage of laboratory development. Furthermore, these reagents (e.g. cupric & ferric chlorides & sulphates) appear not to be selective. Thus the separation of Se & Te was always conducted in aqueous solutions, which made the overall operations rather complex.

Chalcogenides of Bi, Sb, Cu, Ag & Pb could also be oxidised to metal ions & elemental chalcogens in acidified (H_2SO_4 or HCl) solution of Cu^{2+} (eg CuSO_4) & optionally Fe^{3+} (eg FeCl_3) in association with continuous injection of oxygen gas [4]. It was reported that 100% decomposition was achieved for Bi_2S_3 at optimum conditions. In some cases, ferric chloride, in association with HNO_3 , Cl_2 & air, was used to treat a decopperized & deselenized slime for the separation of silver & gold [8]. The silver remained in the residue as AgCl , whilst the gold went into the solution as AuCl_3 complexes. In a process described by Whitney [99], a Zn-rich cementation precipitate or electrolytic sludge was leached with acidified hot ferric chloride solution to convert the silver to saturated AgCl solution from which silver was subsequently recovered via precipitation of AgCl . The gold remained undissolved & thus could easily be separated from the silver species. It was reported that the operations were

simplified & the required time shortened in comparison with the conventional process in which both the gold & silver were leached out either by concentrated HNO_3 or by the "aqua regia" solution. To recover the gold from the leaching solution, activated carbon or sodium cyanide are usually added, followed by several operations to separate & subsequently reduce the gold to elemental form.

1.1.3.5 Hydrochlorination of copper anode slimes

With respect to the significant solubilities of chlorides of most metals in aqueous solutions, hydrochlorination treatment of the copper anode slimes has been the subject of a number of investigations [42,100-1], simply because it can facilitate the complete separation of silver content from most of the impurities, e.g. Cu, Ni, Sb, Zn, Bi & Fe, presented in the slimes. After hydrochlorination treatment, most of the impurities went into the solution, leaving the silver in the residue as AgCl . However, the hydrochlorination treatment has no apparent effect on dissolution of selenium, tellurium, gold & platinum group metals. Thus a further treatment was required to recover these elements.

In an attempt to produce super-pure silver from copper anode slimes, James [100] employed a comprehensive hydrometallurgical process, using hydrochloric acid (up to 12N) in combination with continuous injection of chlorine gas to convert a large majority of the non-ferrous & ferrous metals to corresponding chlorides. The soluble chlorides were subsequently separated from the residue containing AgCl precipitate by filtration. However, most of the lead content also remained in the residue due to the low solubility of PbCl_2 . The filtered residue was then washed with acidified hot water (containing 1g/l HCl) to selectively remove PbCl_2 . The washed cake containing AgCl was subsequently redissolved in ammonia solution (2-12N) followed by NaOH precipitation & reduction with dextrose, for the recovery of Ag (99.999%). Alternatively, silver could be recovered straightforwardly from the ammonia solution by reduction with copper.

Furthermore, in an attempt to reveal the mechanism of hydrochlorination of copper electrolytic slimes, Laikin [42] systematically studied the electrochemical behaviour of synthetic compounds of anode slimes by determining the polarisation curves. It was also reported [113] that tellurium could be selectively dissolved from a mud containing Te, Se & S by treating the mud with a solution containing 96.7 g/l H_2SO_4 , 59.1 g/l HCl 59.1 & 5 g/l Cu^{2+} (as CuSO_4) with oxygen blown in at a rate of 20l/h and at 65°C. A solution containing more than 90% of the tellurium but almost free of selenium & sulphur was obtained.

Hydrochlorination offers an easy way for separation of silver from gold selenium, tellurium & most of the non-ferrous metals in the anode slimes. However, it cannot completely eliminate the contamination of the silver products caused by Pb, owing to the low solubility of PbCl_2 which co-precipitates with AgCl during leaching with HCl. In addition, Se, Te & Au cannot be transferred into solution in this process. Therefore, further treatment of the residue is required for the recovery of Se, Te & Au. This in turn makes the overall treatment complicated & costly. As a result, this process is normally used for treatment of silver-rich slimes or as an alternative for Ag-Au separation.

1.1.3.6 Nitric acid leaching

It can be seen that almost all the above stated hydrometallurgical processes, i.e. acid pressure leaching, alkaline pressure leaching, sulphuric acid leaching & hydrochloric acid leaching, are performed either under high pressure conditions (up to 20 atm) or at high temperatures (110-300°C). This leads to several severe disadvantages e.g. high energy consumption, complicated operations, relatively poor working environment & high cost of capital investment. To meet with the stringent requirements for the treatment of anode slimes, two special processes, i.e. electrochemical & nitric acid leaching, have attracted considerable attention

over past decades. Compared with those described above, these processes can operate at relatively low temperatures (below 100°C) & under ambient pressure. In addition, they can easily dissolve almost all the valuable components in the copper anode slimes. Recently, most of the approaches along these lines have been carried out at both laboratory & pilot plant scale. Several patents have been issued based on satisfactory results. However, the mechanism of the dissolution of the components is not well established at present, owing to the complexity of these systems. Hence, a lot of work must be done before the commercialization of these processes can be brought into reality.

As one of the most powerful inorganic solvents, nitric acid has found a broad application in many fields. In the minerals industry, for instance, it is widely used in the separation of several noble or rare elements e.g. Ag, Au, Zr, Mo & platinum group metals from metallurgical by-products e.g. slimes & slag and secondary or recycling materials e.g. used high temperature alloys, ceramics & electronic or electrical components. However, it was not until the mid 1970's that the investigation of the feasibility of the nitric acid leaching processes for copper anode slimes treatment aroused general interests [7,19,84,104-9].

The earliest attempts were those of Gendolla [104] who described a comprehensive hydrometallurgical process for recovery of selenium, tellurium, silver & gold from copper anode slimes by nitric acid elution. Leaching of slimes containing 10-50% Cu, 3-25% Ag, 0.2-2% Au, 2-15% Se, 0.5-8% Te & traces of platinum at 70-90°C in a solution of 1:1 HNO₃ resulted in the dissolution of nearly all the selenium, tellurium & silver contents. The silver was then precipitated from the leach liquor with NaOH or HCl solution. The AgCl precipitate was subsequently treated in a similar fashion as stated earlier. While the Se & Te were recovered by known methods, i.e. neutralization (with NaOH or NH₃·H₂O) of the solution to pH 5-7 to obtain a Se-Te concentrate. The copper(II)/selenium ratio in the solution was reported to be one of the crucial

parameters for the precipitation. This Se-Te concentrate was then re-dissolved in dilute H_2SO_4 solution, followed by reduction with SO_2 gas under different conditions (acidities) to separate & recover the two elements. The final yields of selenium & tellurium in this process were 88.9% & 87.6%, respectively.

In a similar approach made by Charewicz [105,108], a two-stage counter-current nitric acid leaching process (25% HNO_3 , at 80°C) was employed to achieve complete conversion of the selenium, tellurium and silver into solution. The techniques for recovery of silver, selenium and tellurium from the leaching liquor were similar to those stated above [104]. The residual copper is then recovered from the Se & Te-free solution by cementation with iron scrubbers. On the other hand, the residue after the dissolution of AgCl in ammonia solution was treated by 1% KCN at 50°C for 5 hours to transfer the gold & the residual silver into solution. The aqueous silver- & gold-cyanide complexes were then reduced with aluminum powder to produce a concentrate of silver & gold, which was subsequently treated electrolytically to separate & recover silver & gold. The recovery for Se, Te, Ag & Au were 90, 88, 99.74 & 95%, respectively. In addition, elution of gold from the residue after the removal of Ag, Se & Te could also be conducted in an "aqua regia" solution [84,119]. The gold-loaded leach solution was subsequently extracted in 5 stages with diethylene glycol di-butyl ether, followed by reduction with oxalic acid to precipitate and recover up to 99.46% of the gold originally existing in the slimes [84]. Furthermore, leaching with HNO_3 (4M) & FeCl_3 in association with the injection of Cl_2 gas was also used to selectively remove gold & silver from slimes free of Cu & Se [8].

Another process for the treatment of copper anode slimes with HNO_3 in association with oxygen at 120°C was used to obtain a solution of selenium & silver, with other elements being concentrated in the residue [110]. The leach solution was subsequently treated with HCl & passed over a strong acidic cation exchanger. Then, the solution was treated with SO_2 to precipitate the selenium

as SeO_2 . The removal of the selenium from the slimes was 95% for treatment of a sample containing 7.04% Se, 1.5% Te, 19.73% Ag, 23.65% Pb & 2.85% Sn.

To recover the silver from the nitric acid leaching solution, several other methods have been tested. These include electrodeposition (or electrowinning) [13,19,72,107] & solvent extraction [111]. Organic solvents used were hydroxylamine (LIX 63), D2EHPA, with kerosene as a diluent. The recovery of selenium & tellurium, on the other hand, can also be accomplished by several alternative methods e.g. reduction with thiourea [106], electrowinning [13,72] & solvent extraction [84,119-120]. In a recently patented process [84], the filtrate from AgCl precipitation was pre-treated by two operations, i.e. denitration (with tributyl phosphate [84,115]) & chlorination (with HCl solution). Then, the HNO_3 -free solution was extracted with $(\text{BuO})_3\text{PO}$ (TBP) in kerosene in six stages. The Se-containing liquor was subsequently stripped, concentrated & reduced with a stream of sulphur dioxide to recover Se, whilst, the Te-containing solution was treated with SO_2 to recover tellurium. The recoveries of selenium & tellurium were 74.4% & 71% respectively. Furthermore, the selective extraction of copper & selenium from a solution containing Se, Te, Cu, etc., was also achieved.

For processing of samples containing large amounts of copper & nickel, a decopperizing treatment by sulphuric acid pressure leaching was found to be very useful [7,13-14,69,84]. Most recently, a comprehensive investigation of the nitric acid leaching for treatment of anode slimes was carried out by Zhou [14]. In this process, the anode slimes were treated in several operations, e.g. removal of copper & nickel by H_2SO_4 in the presence of air, leaching of selenium, silver & tellurium with dilute HNO_3 (2-8N) at 50-90°C, denitration (by TBP) of the HNO_3 leaching filtrate & recycling of HNO_3 , selective solvent extraction of silver from solution with di-n-octyl sulphide, and finally separation & recovery of selenium & tellurium from the Ag-free solution by reduction with SO_2 under different conditions (acidities). The residues from the nitric acid leaching were collected

for further processing to recover gold and other noble metals. Promising results were obtained from laboratory scale tests. A parallel investigation was carried out to study the leaching behaviour of copper & silver chalcogenides in HNO_3 solution [15]. However, due to the complexity of the system, the leaching behaviour of components in the anode slimes is still not well established.

Although satisfactory results have been claimed for the above processes, most of them cannot be used to verify the feasibility for the commercialization of these processes. This is because these results are mainly obtained from laboratory or batch tests. Since the late 1970's, several approaches have been made by Hoh & coworkers [7,69,84,118]. Successful laboratory & pilot plant scale results have already resulted in the commercial investigations on the so-called "INER process" [7,69,118], which consists of three major operations, i.e. HNO_3 leaching, solvent extraction & reduction. Raw anode slime (with less than 10% H_2O) was firstly treated with dilute H_2SO_4 solution in the presence of air (1 atm) to remove most of the copper & nickel contents. The decopperized slime was leached with NH_4Ac at 40-60°C to convert the lead content into solution as $\text{Pb}(\text{Ac})_2$, which was subsequently crystallized to recover lead acetate. The residue from lead removal was then leached with nitric acid solution at four stages to achieve 'complete' conversion of Ag, Se & Te into solution. Solid/liquid separation was conducted after each leaching stage, followed by solvent extraction with TBP to selectively extract & separate various elements in the mother liquor. The metal-loaded organic phase was collected and stripped to obtain an aqueous solution & an organic solvent for recycling. The Se & Te were recovered by reduction with SO_2 . The silver was precipitated from the selenium stripping aqueous solution by addition of NaCl or HCl, whilst the gold was extracted from the residue of HNO_3 leaching by elution with "aqua regia". Recoveries for Pb, Ag, Se, Au & Sn in a pilot plant test (10% production plant capacity) test were 95%, 96%, 95%, 99% & 95%, respectively. Based on

reproducible pilot plant tests, a production plant with a capacity of 300 tons of anode slimes per year has been built and run successfully since 1984.

In conclusion, nitric acid leaching processes for treatment of anode slimes have shown promising potential for commercialization, according to laboratory, pilot & commercial plant scale tests. However, great efforts must be made to lower the cost & to minimise the problems of pollution from NO evolution.

1.1.3.7 Electrochemical leaching

Electrochemical leaching of anode slimes has been subjected to intensive investigations ever since it was developed. Like the nitric acid leaching process, electrochemical leaching also offers an easy way for the transfer of various valuable elements in the slimes into solution. In addition, the separation of elements from the leaching solution by electrolysis or solvent extraction in association with electrolysis is relatively simple & effective [19,39-43,92,121-5].

The simplest processes were those developed by Takei [121] and Takahashi [39], in which only copper or nickel were recovered. In the former, the copper in the slimes produced during the electrorefining of copper was immediately recovered by electrolysis of the suspension (in dilute H_2SO_4) of the slime in a compartment (using a diaphragm) consisting of a non-consumable anode (Pb) & a copper cathode. In the latter, the anode slimes were initially cast as anodes which were electrolysed in dilute H_2SO_4 to remove copper. The nickel solution was subsequently concentrated to produce $NiSO_4$ by crystallization.

The first approaches to the leaching of selenium & tellurium were based on studies of synthetic anode slimes components in various electrolytes [41,122-5], to try to understand the electrochemical behaviour of these components in simple systems. Erdenbaeva [122-3] investigated the electrochemical behaviour of some synthetic selenide & telluride suspensions on mercury electrodes or on

a sodium amalgam in such electrolytes as LiCl (1N), Na₂SO₄ (1N) & HCl (1N). He revealed that the reactions proceed via a direct interaction between a suspension of solid particles with the amalgam [122]. It was found [123] that no reaction occurred in the above system over the temperature range 25-80°C.

In order to assess the feasibility of cathodic stripping of selenium and tellurium from copper anode slimes, Ugorets [41,124] studied the chalcogenides-NaOH system by determining the cathodic polarisation curves. It was observed [41] that the powdered tellurium & copper(I) telluride were reduced to soluble Te²⁻ species during the cathodic processes in NaOH solution, which could be subsequently oxidised or electrolysed for recovery of tellurium. In addition, it was found that increases in the alkaline concentration, temperature & current density would favour the extraction of selenium & tellurium from the slimes.

Most recently, several papers dealing with the electrochemical leaching of selenium and tellurium from anode slimes have been documented [42,18,40,70]. In a process reported by Semina [40], anode slimes were electrochemically leached in a NaOH solution containing 1M Na₂SO₃ (to improve the extraction of selenium & tellurium). Optimum conditions were NaOH 120 g/l, current density <400 Am⁻² & duration 5-5.5 hours. However, the results were disappointing, due to the formation of alkali metal mono-selenides or tellurides rather than poly-selenides or tellurides. The maximum extraction was 60% for selenium & 25% for tellurium. Improved results were reported by Pivovarova [70] in a study on the electrochemical leaching of selenium from flue dust from roasting electrolyte slurries, presumably due to the simplicity of the constituents. Under optimum conditions (obtained by experimental design methods), i.e. temperature 50°C, duration 90 minutes, concentration of NaOH 100g/l, particle size 0.16-1.6mm & cathode current density 200Am⁻², up to 95% of the selenium could be recovered.

Anodic stripping of selenium was also studied. Nugumanov [18] has used an experimental planning method to select optimum conditions for the oxidising

electrochemical leaching of selenium from anode slimes containing 10.4% Se & 12.9% Pb. It was observed that the recovery of selenium increased with increase of NaOH concentration (19.2-88.0 g/l), temperature (35-75°C), current density (100-500 Am²) & liquid/solid ratio (6-8), while the oxidation of tetra-valent selenium species to the undesirable hexavalent species decreased to 5% with increasing current density, leaching time & liquid/solids ratio. Under optimum conditions (60 g/l NaOH, current density 100Am², temperature 65°C), the oxidising electrochemical leaching of the anode slimes resulted in the recovery of 96-98% selenium. The concentration of the Se⁴⁺ species in the leaching solution was limited to 0.2-0.3g/l. Pilot plant results showed a great potential for the commercial application of this process.

In addition to NaOH, solutions e.g. HCl was also used as electrolyte for the electrochemical leaching of anode slimes. In an attempt to investigate the hydrochlorination of anode slimes, Laikin [42] carried out a series of studies on the electrochemical behaviour of components of anode slimes in HCl solutions. Based on experimental results for pure compounds, the leaching of anodic sludge was carried out under the following conditions: cathode current density 12000-15000Am², anode current density 1000Am², HCl concentration 1-4M & at 50°C. The gold & rarer elements were almost entirely (97-99%) converted into solution, leaving most of the silver (98-99%) in the sediment as silver chloride. Thus, clean separation of silver from gold and other rare elements could be achieved without the production of Doré-metal.

To summarise, the electrochemical leaching treatment of copper anode slimes has several advantages (e.g. simplified operations, improved metals recovery & qualities of products) over the conventional processes. However, this process is still under laboratory development in most cases. In addition, the cost of energy con-sumption & capital investment ^{is} relatively high as compared with nitric acid leaching.

1.2 Crystal Structure of Selenides of Copper & Silver

The understanding of the mineralogical properties of copper silver selenide & silver selenide is of great importance to the elucidation of the electrochemical behaviour of these minerals. However, due to their rare occurrence in the natural environment, there is ONLY limited information on these aspects for selenide minerals of copper and silver or the corresponding synthetic compounds. A brief account of the available information of crystal structure etc. is given below.

The phase equilibria of the Ag-Se system (cf. *Figure 1.2*) shows that the

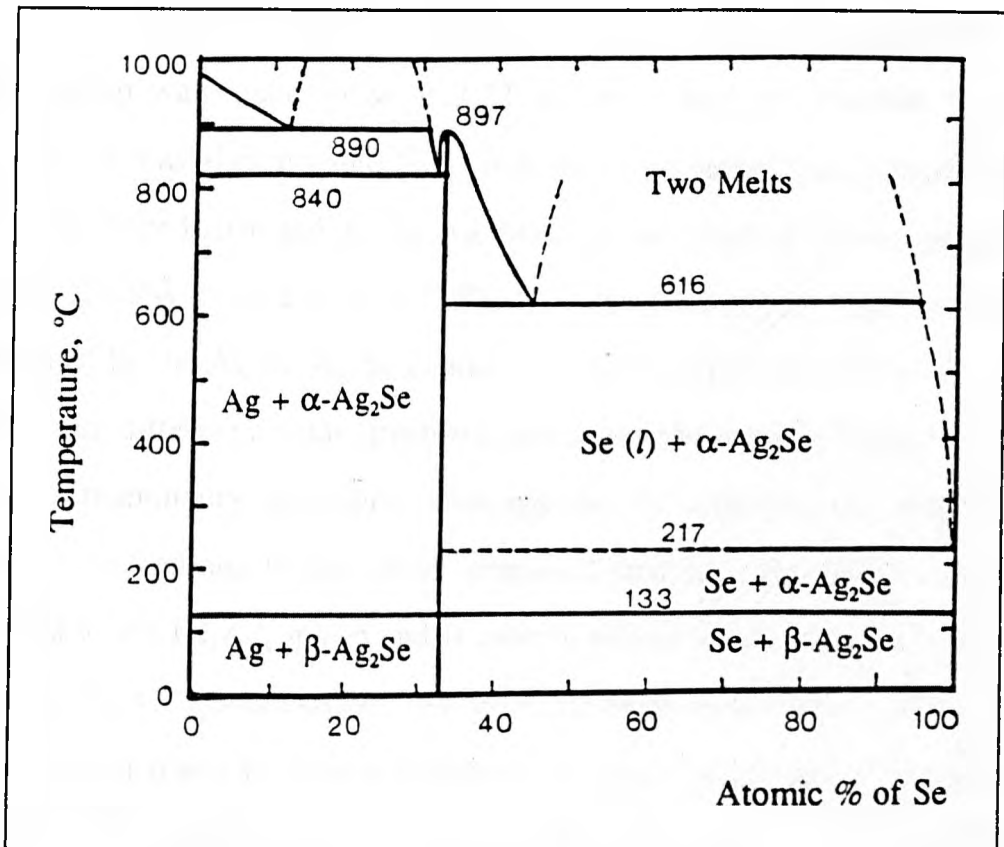


Figure 1.2 Phase equilibria for the Ag-Se system. (After Hansen [151]).

ONLY stable compound is Ag_2Se , though non-stoichiometric silver selenide compounds have been reported on occasions (e.g. $\text{Ag}_{16}\text{Se}_7$ [152]). The compound Ag_2Se appears at atmospheric pressure in two polymorphic forms. The low-temperature phase, $\beta\text{-Ag}_2\text{Se}$, is stable at temperatures below $128 \pm 5^\circ\text{C}$. Above

this temperature it undergoes an allotropic transformation (cf. *Figure 1.2*) to form the α -Ag₂Se phase [151]. X-ray diffractometric studies revealed that the natural silver selenide mineral (naumannite) [128] & the silver selenide component of the copper anode slimes [14] are present as the β -phase. It was also proved in this work that the synthetic silver selenide (cf. Section 2.1) is also β -Ag₂Se by comparison of X-ray patterns with those of the natural mineral.

X-ray diffractometric analysis [152] revealed that the β -Ag₂Se phase had an orthorhombic crystal structure with unit-cell dimensions $a = 4.3444 \text{ \AA}$, $b = 7.111 \text{ \AA}$ & $c = 7.790 \text{ \AA}$. Similar lattice parameters have also been obtained [131] by electron diffraction investigation on thin sublimed β -Ag₂Se films. The space group was found to be $P 2_122$ and each unit-cell contains four units 'Ag₂Se'. It was also reported [131] that the silver atoms form a framework of a diamond-type lattice and the Ag-Ag distances are relatively short, ranging from 2.61 to 2.82 \AA compared with 2.89 \AA in metallic silver. This structure is penetrated by the Ag-Se-Ag-Se chains with Ag-Se distances of 2.54 \AA . On the other hand, different crystal structures have been obtained by Wiegers [132] via X-ray diffractometry techniques, although the cell constants are comparable in general. In contrast to the above proposed structure, the lattice structure is assigned to the $P2_12_12_1$ group and is closely related to the monoclinic structure displayed by γ -Ag₂S (acanthite). All atoms lie on the four-fold general positions. The selenium atoms are almost distributed in a plane perpendicular to the b axis and the silver atoms occupy two entirely different structural sites. The first type of silver atoms occupy sites near the 'planes' of selenium atoms and are coordinated tetrahedrally by selenium at distances of 2.62, 2.76, 2.79 & 2.86 \AA whilst the others take positions halfway between the planes of selenium. The coordination of the second type of silver atoms by the selenium atoms at the distances (Ag-Se) of 2.72, 2.76 & 2.81 \AA is virtually triangular. In addition, the selenium atoms are found to be arranged essentially in a body-centred cubic

structure. *Figure 1.3* shows a typical (100) projection of β - Ag_2Se lattice.

The high temperature phase i.e. α - Ag_2Se has the structure of CaF_2 (Cl) type with $a = 4.993 \text{ \AA}$ at $170^\circ\text{C} - 190^\circ\text{C}$ [151]. The unit cell in the lattice contains two units of ' Ag_2Se ' and the selenium atoms are also

packed in a body-centred cubic lattice structure. The silver atoms are distributed with various probabilities over several types of interstitial sites (cf. *Figure 1.4*).

The compound CuAgSe is stable at temperatures below 190°C . The phase equilibria of the Cu-Ag-Se ternary system have not been established yet. Single crystal measurement results (e.g. rotation & Weissenberg photographs) revealed that the natural eucairite mineral

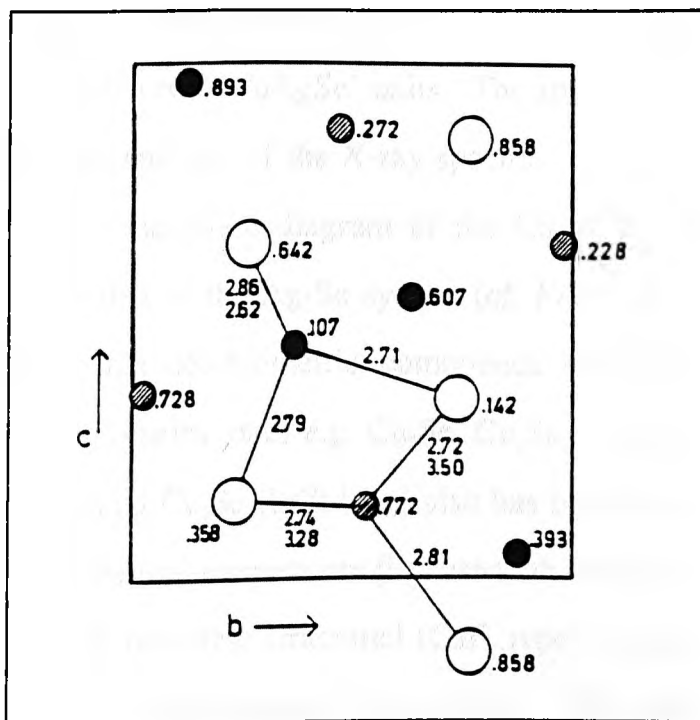


Figure 1.3 (100) projection of β - Ag_2Se . The x coordinates of the atoms & distances are given in \AA . \circ - Se \bullet/\circ - Ag (type I/II)

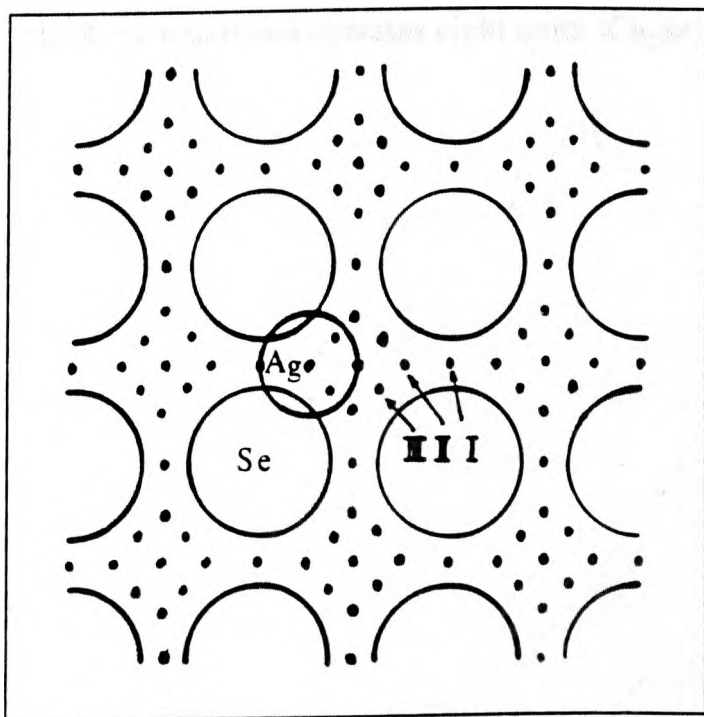


Figure 1.4 The interstitial sites on (100) plane available to Ag^+ ions in α - Ag_2Se . (After Okazaki [154]).

has a tetragonal lattice structure with cell dimensions of $a = 4.075 \text{ \AA}$ & $c = 6.29 \text{ \AA}$ respectively & each unit-cell contains two 'CuAgSe' units. The space group is assigned to P4/nmm via systematic analysis of the X-ray spectra.

As can be seen in *Figure 1.5*, the phase diagram of the Cu-Se binary system is much more complex than that of the Ag-Se system (cf. *Figure 1.2*). There are eventually a family of non-stoichiometric compounds of copper selenides, besides the reported stoichiometric ones e.g. Cu_2Se , Cu_3Se_2 , CuSe & CuSe_2 . Similar to Ag_2Se , the compound Cu_2Se (bellidoite) also has two phases under atmospheric pressure, namely the low-temperature β -phase with tetragonal or deformed cubic crystal structure & the cubic structured (CaF_2 type) α -phase which is stable at elevated ($>110^\circ\text{C}$ ¹) temperatures [127-8,151-3]. The high-temperature α - Cu_2Se phase has a cubic lattice structure with cell constant $a = 5.81 \text{ \AA}$ & each unit cell has four units 'Cu₂Se', whilst the low-temperature phase β - Cu_2Se is found to have a tetragonal lattice structure with cell constants $a = 11.52\text{\AA}$ & $c = 11.74\text{\AA}$ respectively & each unit cell contains eight units 'Cu₂Se'.

¹ Cubic crystal structure has been observed for Cu_{2-x}Se at temperatures as low as 55°C [128]. This is attributed to the 'excess' Se which lowers the transformation temperature.

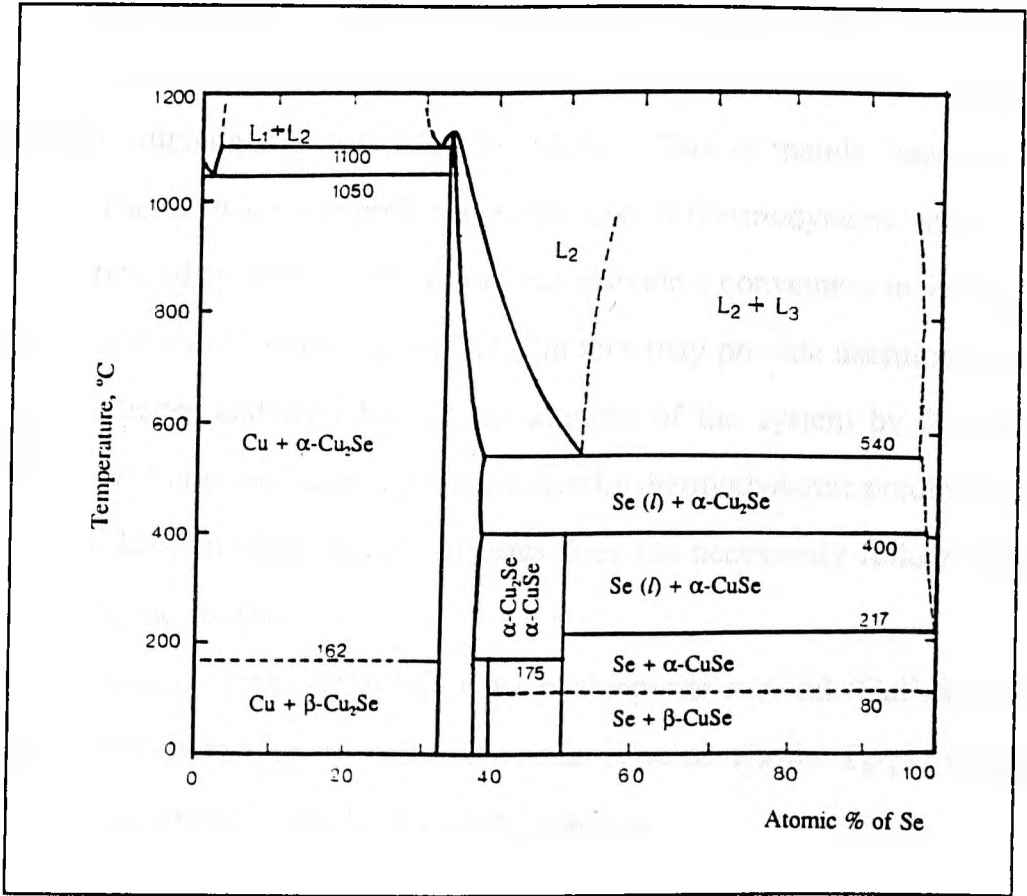


Figure 1.5 Phase equilibria for the Cu-Se system. (After Hansen [151]).

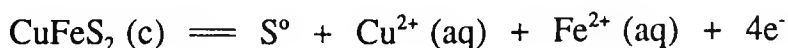
1.3 Thermodynamics of the Metal(s) - Selenium - Water System

E_h -pH (Pourbaix) diagrams have found wide applications in areas ranging from corrosion of metals to more complex systems e.g. the leaching of minerals especially sulphide minerals [20,155,160-3]. This is mainly because E_h -pH diagrams encompass a comprehensive selection of thermodynamic stability data of the portrayed systems and therefore can provide a convenient insight into the thermodynamics of these systems. This in turn may provide useful information towards a better understanding of the kinetics of the system by for example comparison of observed kinetic phenomena with thermodynamic predictions. But one has to keep in mind that the kinetics does not necessarily follow the exact thermodynamic routes.

For example, the oxidation of the chalcopyrite mineral (CuFeS_2) in acid media should, according to thermodynamic (viewed via the E_h -pH diagrams) speculations, proceed via the following reaction:

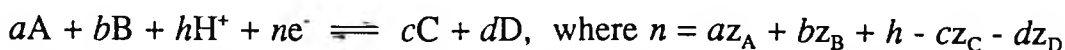


In fact the intermediate product covellite (CuS) has never been identified [162]. Instead, chalcopyrite (CuFeS_2) is oxidised, in acid media, directly to elemental sulphur & the aqueous species of copper & iron (in the form of Cu^{2+} & Fe^{2+}) via the following scheme:



One possible explanation is that the first proposed scheme involves a reaction between three solid state substances (phases) & therefore fails to proceed at a sufficient rate for its observation. The latter, on the other hand, involves only two solid phases & it is accordingly easier to overcome the energy barriers associated with formation of new phases.

The construction of E_h -pH diagrams for any system is ultimately based on systematic considerations of the possible equilibria involved & their preference under various particular circumstances. As a general approach, consider an equilibrium of the form:

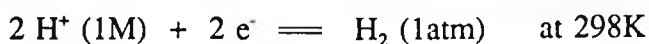


At equilibrium, the electrode potential² of any redox system is uniquely defined by the Nernstian equation. According to this equation, the electrode potential is defined here by:

$$E = E_T - \frac{2.303RT \cdot h}{nF} \text{pH} - \frac{2.303RT}{nF} \log \frac{[C]^c [D]^d}{[A]^a [B]^b} \quad (1.1)$$

where $[]$ represents activity of the corresponding species enclosed and $E_T = -\Delta G_T/(nF)$. Thus, in complex situations, the electrode potential is a function of several variables e.g. the activities of various species including H^+ (aq). To construct a E_h -pH diagram, the other variables (e.g. activities) apart from $[H^+]$ MUST be assigned such that the electrode potential (E) is ultimately a single

² Strictly speaking, the electrode potential is always a 'relative' quantity with respect to certain COMMONLY recognised standards or reference electrodes e.g. the standard hydrogen electrode (SHE) Pt/H_2 (1atm)/ H^+ (1M). The electrode potential of SHE is artificially defined as 0V. It is worth mentioning that an anomaly arises from the above definition. Considering the redox reaction involved in the SHE half cell



the free energy change of the above reaction should be zero by definition because it is related to the electrode potential via $\Delta G_{298} = -2FE_{IL/H^+}$. On the other hand, as the above redox reaction is at equilibrium, the free energy change of the above reaction can also be obtained via $\Delta G_{298} = \Delta H_{298} - (298K)\Delta S_{298}$. The standard enthalpies of formation & absolute entropies of H_2 , H^+ & e^- are zero except for $S_{298}(H_2)$ which is $65.3J \text{ mol}^{-1}$. Thus, an inconsistency is ultimately envisaged.

Nonetheless, this DOES not cause any practical problems because the electrode potential is viewed as a 'relative' quantity in any case. Thus, any incompatibility may cause in the construction of E_h -pH diagrams is ruled out. ^{that}

variable of the pH. The E_h -pH line thus gives a slope of $2.303RT \cdot h/nF$ & an intercept on the E_h axis (at pH=0) of:

$$E_T = \frac{2.303RT}{nF} \log \frac{[C]^c [D]^d}{[A]^a [B]^b}$$

If the ratio of activities is unity, the last term of the above expression becomes zero and therefore the intercept gives the value of the standard potential.

Obviously, several particular cases can be isolated from the above equation. For example, when there is no involvement of H^+ (aq) in the equilibrium ($h=0$), the electrode potential is maintained at a CONSTANT value as pH varies & thus displays a horizontal line on the E_h -pH diagram. On the other hand, when the above equilibrium does not involve any electron transfer ($n=0$), equation 1.1 becomes meaningless & a vertical line is observed. The location of this line (pH value) is defined by the thermodynamic properties of the participating species via:

$$pH = - \frac{1}{h} \left[\frac{\Delta G_T}{2.303RT} + \log \frac{[C]^c [D]^d}{[A]^a [B]^b} \right] \quad (1.2)$$

The above discussion applies to any temperature. For a majority of substances, the thermodynamic data at 298K are usually available, while data at other temperatures (T) have to be evaluated by making use of those of some well defined state. For convenience, the reference temperature is usually chosen to be 298K rather than the absolute zero temperature (0K) state. Generally, the evaluation of ΔG° for a particular temperature necessitates the initial evaluation of two other important parameters e.g. ΔS° & ΔH° ;

$$\Delta S_T = \Delta S_{298} + \int_{298K}^T (\Delta C_p/T) dT \quad (1.3)$$

and

$$\Delta H_T = \Delta H_{298} + \int_{298K}^T \Delta C_p dT \quad (1.4)$$

Hence, the free energy change can be finally obtained from

$$\Delta G_T = \Delta H_T - T \Delta S_T \quad (1.5)$$

During construction of E_h -pH diagrams at other temperatures apart from 298K, a practical difficulty arises when ionic species are involved in the equilibrium, due to the unavailability of the heat capacities for most species of this type. In this case, the empirical 'Criss & Cobble entropy correspondence principle'³ [164] is normally employed to estimate the entropies and heat capacities of ionic species at various temperature, using the known thermodynamic data at the reference temperature e.g. 298K. Based on this principle, E_h -pH (Pourbaix) diagrams at elevated temperatures have already been constructed for metal-water & metal-sulphur-water systems [160,161,165].

In the present study of the Cu-Se-H₂O, Ag-Se-H₂O & Cu-Ag-Se-H₂O systems (cf. *Figures 1.6-8*), E_h -pH diagrams have been constructed for the temperature 298K ONLY due to the unavailability of a large selection of heat

³ The entropy correspondence principle states that by fixing a standard state (usually the zero for ionic entropies at each temperature is defined by the value of hydrogen ion), the partial molar entropies of one class of ions are linearly related to the corresponding entropies at some reference temperature (normally 298K, which gives an entropy of H⁺ as -20.92 J·mol⁻¹·K⁻¹)

$$\bar{\bar{S}}_T = a_T + b_T \bar{\bar{S}}_{298}$$

where $\bar{\bar{S}}_T$ & $\bar{\bar{S}}_{298}$ are the 'absolute' ionic partial molar entropies, a_T & b_T are coefficients dependent on the class of ions (cations, anions, oxy-anions & acid oxy-anions) & temperature. It was observed that the above coefficients varied approximately linearly with temperature at temperatures up to 423K

$$a_T = a_1 + a_2 T \quad \& \quad b_T = b_1 + b_2 T$$

where a_1 , a_2 , b_1 & b_2 are temperature independent. Hence, this gives rise to the evaluation of the average heat capacity between 298K & T

$$\bar{C}_p = [a_2 + b_2 \bar{\bar{S}}_{298}] T$$

The conversion of entropies on the 'conventional' scale ($\bar{S}_H(T) \equiv 0$) to the 'absolute' scale at any temperature is achieved via

$$\bar{\bar{S}}_T = \bar{S}_T + z \bar{\bar{S}}_T(H^+), \quad \text{where } z \text{ is the charge of the ion.}$$

capacity values of various substances. The thermodynamic data used in this work are mainly extracted from published data of the National Bureau of Standards [157] while those for the selenides are based on Mills' [158] (cf. *Appendix 3* for a full list of data. Calculations & speculations of some data are also provided.).

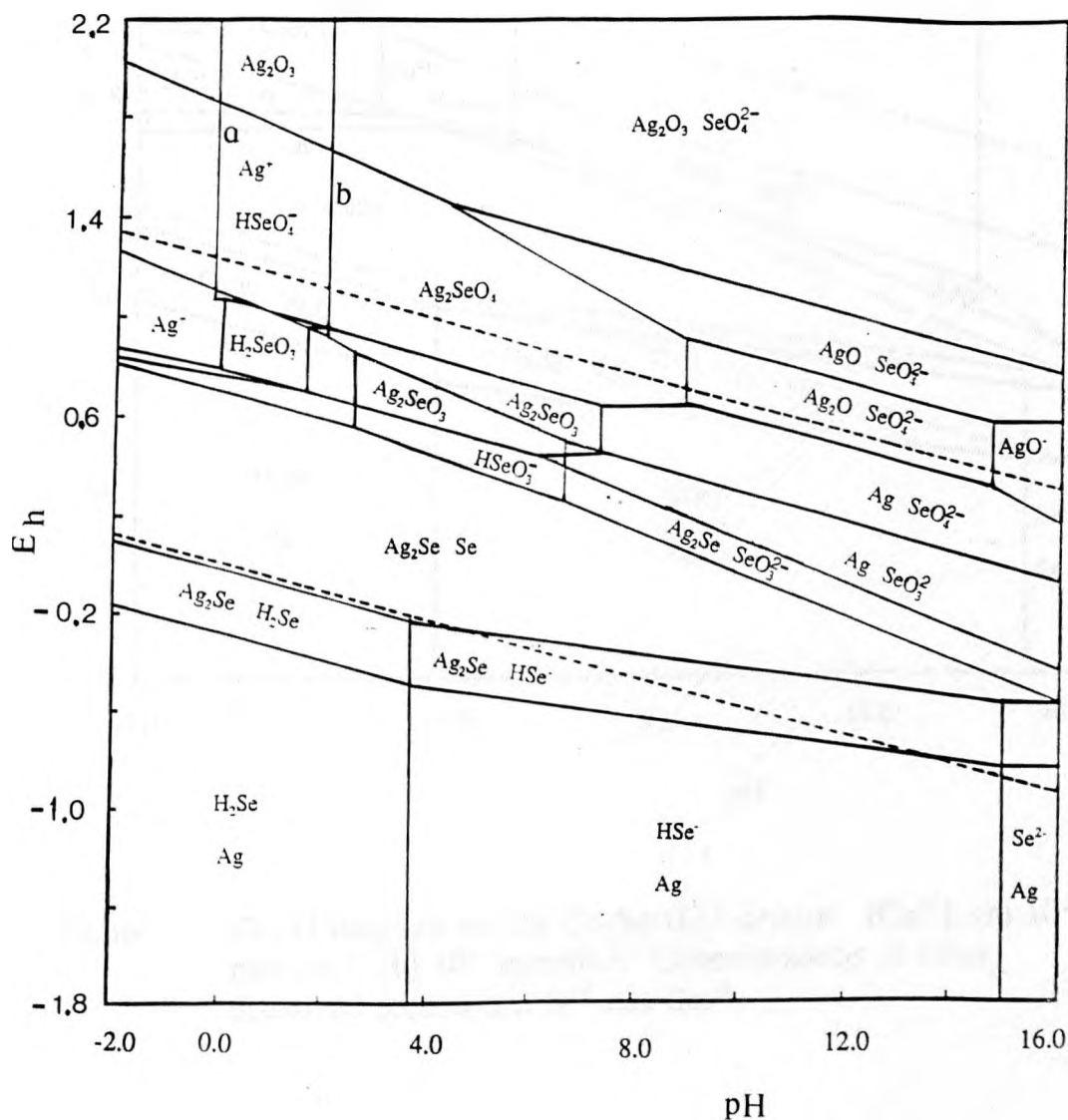


Figure 1.6 Eh-pH diagram for the Ag-Se-H₂O system. [Ag⁺]: (a) 10⁻² mol·dm⁻³ (b) 10⁻⁴ mol·dm⁻³. Concentrations of other dissolved species are 10⁻⁴ mol·dm⁻³.

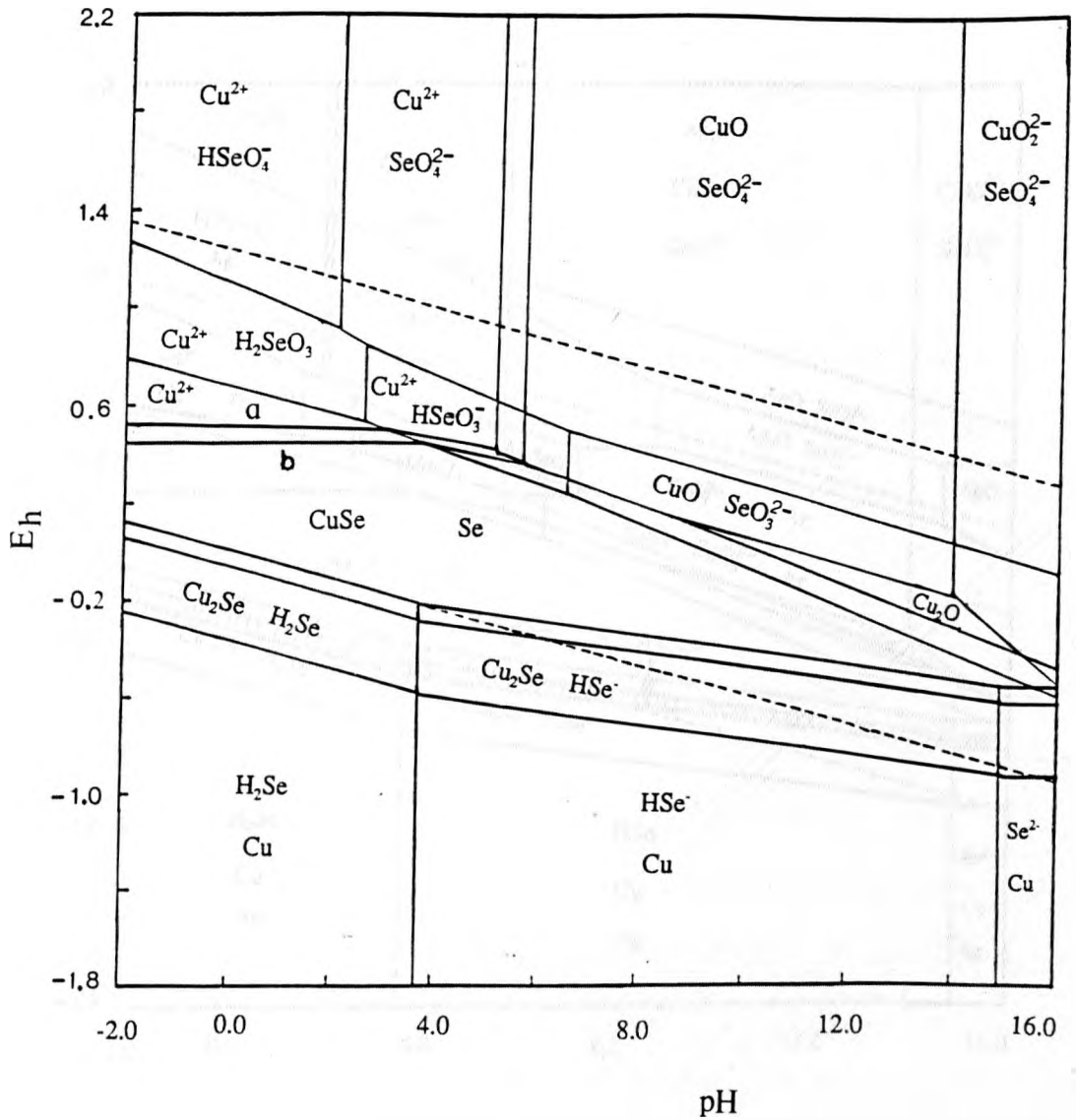


Figure 1.7 Eh-pH diagram for the Cu-Se-H₂O system. [Cu²⁺]: (a) 10⁻² mol·dm⁻³ (b) 10⁻⁴ mol·dm⁻³. Concentrations of other dissolved species are 10⁻⁴ mol·dm⁻³.

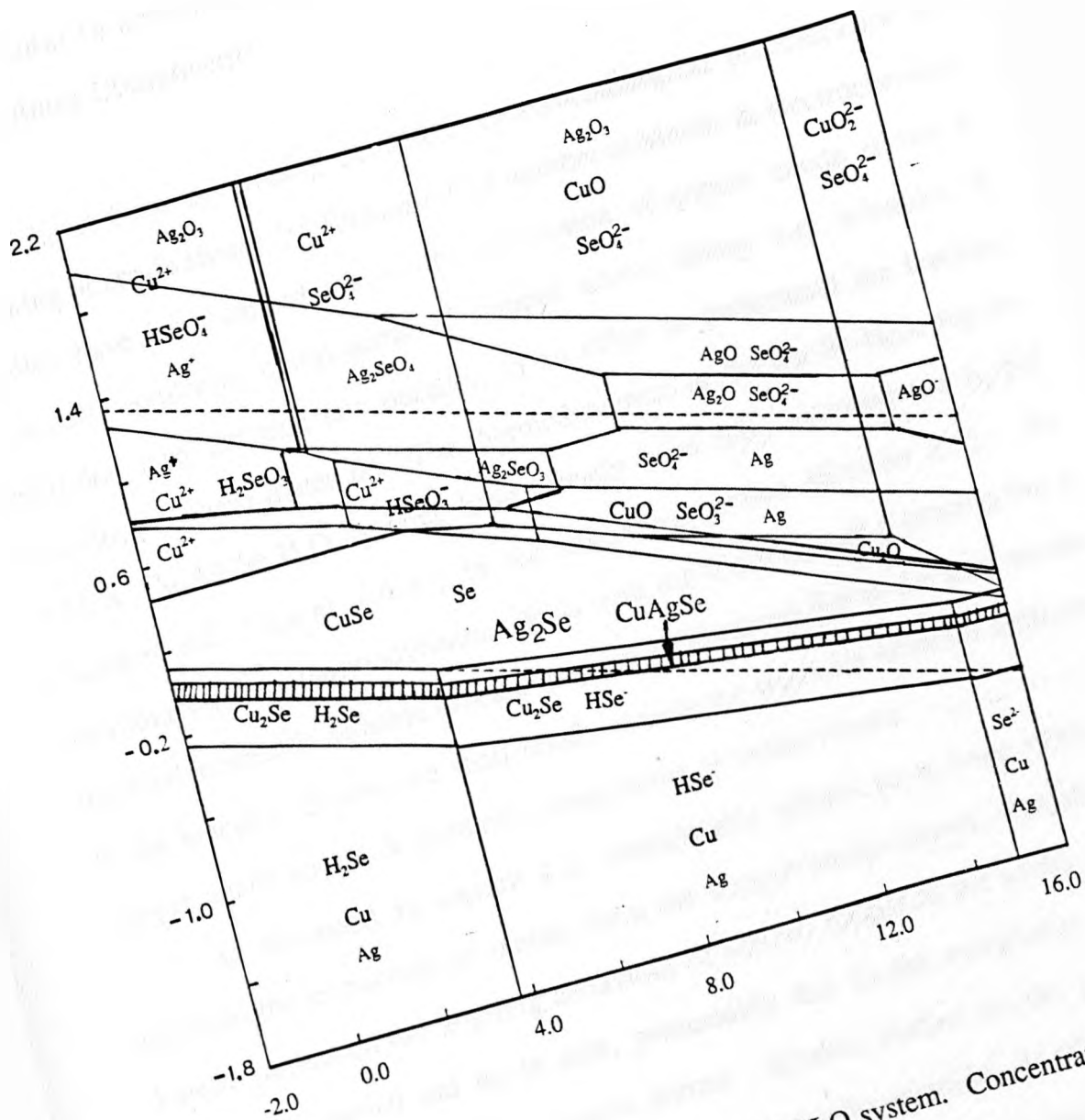


Figure 1.8 Eh-pH diagram for the Cu-Ag-Se-H₂O system. Concentration of dissolved species are 10⁻⁴ mol dm³.

1.4 Oxidative dissolution of Copper Anode Slimes and Synthetic Anode Slimes Components

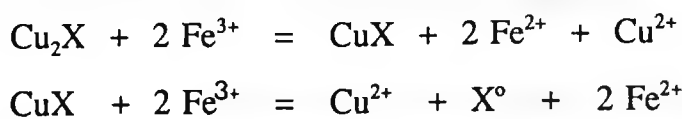
Apart from developing extractive hydrometallurgical processes for the leaching of anode slimes (*cf. Section 1.1*), a number of kinetic & electrochemical studies have been carried out on the dissolution of copper anode slimes & especially synthetic components of copper anode slimes e.g. selenides & tellurides, over the past few decades, in an effort to understand the leaching behaviour of these materials. The thermodynamics of the Cu-Se-H₂O, Ag-Se-H₂O & Cu-Ag-Se-H₂O systems have already been fully assessed via E_h-pH diagrams (*cf. Figures 1.6-8*) in the preceding section (*Section 1.3*). As mentioned above, thermodynamics deals with the feasibility of a process but a thermodynamically feasible process may not be observed due to the slow nature of the kinetics. Below, we shall briefly review the previous work on both raw copper anode slimes & synthetic components of anode slimes.

As discussed in section 1.2, considerable efforts have been made to improve the extraction of metals from the copper anode slimes, though few kinetic studies on the leaching behaviour of various metals in the anode slimes have been carried out up to date, presumably due to the complexity of the composition of raw copper anode slimes. Kinetic studies on the oxidative dissolution of pure synthetic components especially selenides & tellurides of copper anode slimes proved to be useful to provide better understanding of the complex leaching of raw copper anode slimes.

Having carried out calculations of the thermodynamic parameters (e.g. entropies, free energies of formation, solubility products & equilibrium constants) & systematic experiments on the chalcogenide-saline (typically cupric or ferric chloride) solution systems, Azerbaeva [25-9] established that leaching in acidified solutions of ferric and cupric salts, permitted selenides & tellurides to be

decomposed to elemental forms & intermediate products, at temperatures just below the boiling points of the solutions. There is no evidence of further oxidation of elemental selenium & tellurium to tetravalent states, presumably because the concentrations of the higher valence species were too low to be detected. Also, the leaching behaviour of the selenides & tellurides were quite different under experimental conditions. The major differences lay in that tellurides dissolved faster and more completely in all the solutions studied than the selenides, probably due to the physical and chemical differences between the two types of compounds. Leachants used were mainly FeCl_3 , CuCl_2 , mixtures of $\text{Fe}^{3+}/\text{Fe}^{2+}$ or $\text{Fe}^{3+}/\text{Cu}^{2+}$ solutions & occasionally $\text{Fe}_2(\text{SO}_4)_3$. Among these oxidants, the mixture of $\text{FeCl}_3/\text{CuCl}_2$ solutions was the most effective, while $\text{Fe}_2(\text{SO}_4)_3$ the least. To avoid the precipitation of AgCl in the case of chloride leaching of silver chalcogenides, NH_4Cl or NaCl , were added to the leaching solution. By controlling the amount of oxidant (ferric/cupric chloride), tellurium could be selectively leached into the solution in the form of soluble tellurite while the selenium remains in the residue as elemental selenium. However, the mechanism of dissolution of these selenides in ferric & cupric chloride solutions was not available.

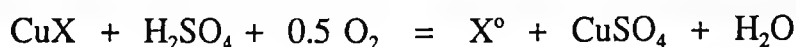
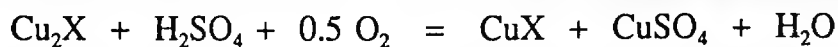
The kinetics of oxidative dissolution of copper chalcogenides in acidified solution (HCl) of ferric chloride was also studied by Kholmanskikh using the rotating disc method [181]. The dissolution was proposed to proceed according to the following reaction sequence:



where $\text{X} = \text{Se} \ \& \ \text{Te}$. It was observed that the dissolution of copper selenide & telluride was limited by the transportation of Fe^{3+} through the chalcogen product layer. The activation energy of the dissolution was found to be dependent

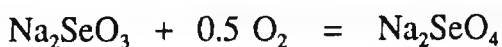
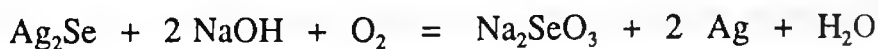
on the speed of the rotation of the disc. At a stirring speed of 800 rpm, these were determined to be 21.8 & 23.0 kJ·mol⁻¹ for copper selenide & copper telluride, respectively.

The kinetics of oxidation of metallic copper & chalcogenides of copper & silver (selenides & tellurides) in the oxygen - pressure sulphuric acid leaching process were also studied [21]. It was reported that the speed of copper dissolution increased with the rate of mixing & aeration but was independent of the concentration of sulphuric acid. The latter was assumed to be due to the decrease in concentration of dissolved oxygen in H₂SO₄ solution of relatively high concentration [21]. The dissolution sequence for the chalcogenides was very similar to that observed for chloride leaching [181]:



Experimental evidence revealed that the dissolution process eventually ceased after reaching a certain degree of decomposition. This was attributed to the formation of a film rich in the corresponding chalcogen on the reacting surface [21].

Under autoclave conditions, silver selenide was found, in a sodium hydroxide solution, to be oxidised rapidly to metallic silver & the water soluble salt sodium selenite [86]. The latter was gradually further oxidised to the undesired sodium selenate which caused the loss of a small amount of selenium. The proposed reaction sequences were as follows:



Kinetic studies revealed that the dissolution process was not limited by diffusion through the liquid film on the selenide particles.

Sheridan [185] studied the oxidative leaching of stromeyerite ($\text{Cu}_{1.07}\text{Ag}_{0.93}\text{S}$) with acidified $\text{Fe}_2(\text{SO}_4)_3$ solution. It was observed that the mineral dissolved in two stages. In the first stage, nearly 50% of the copper was preferentially leached into the solution. The above process was very fast & the extraction rate of copper was limited by a diffusion process. Based on solid state analysis using e.g. XRD & EMPA, the following phase transition was proposed:



The second stage of copper dissolution was accompanied by the formation of sulphur & the process was very slow presumably due to the retardation effect of the silver sulphide product layer [185]. This seems to disagree with observations of the catalytic effect of silver ions on some sulphide minerals [166-170]. On the other hand, different dissolution behaviour for stromeyerite was observed by Potashnikov [186]. It was observed that copper & silver dissolved in HNO_3 at equal amount (atomic ratio) with an activation energy of $34.3 \text{ kJ}\cdot\text{mol}^{-1}$.

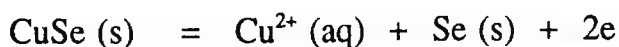
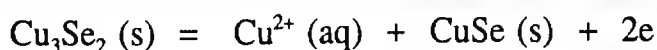
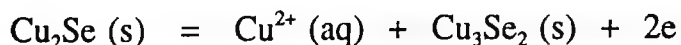
During recent studies of leaching behaviour of copper & silver from raw copper anode slimes, Zhou [14] observed that the dissolution of copper is extremely fast & in a single stage whilst the dissolution of silver showed two distinct stages. Subsequent kinetic studies via mathematical modelling revealed that the dissolution of copper & silver in 2-4M HNO_3 solutions fit fairly well to the shrinking core models. This in turn leads to the evaluation of several kinetic parameters such as activation energy. The activation energy for copper dissolution was found to be $4.78 \pm 0.014 \text{ kJ}\cdot\text{mol}^{-1}$, indicating that the rate was controlled by a diffusional process. The activation energy for the silver dissolution was determined to be 58.6 ± 0.82 & $93.1 \pm 1.7 \text{ kJ}\cdot\text{mol}^{-1}$ for the first & second stage, respectively. The mechanism for the dissolution of silver was proposed as follows [15]:



However, the possible intermediate product i.e. AgSe was not confirmed via analysis of the leaching residue using XRD.

In a parallel study carried out on synthetic selenide minerals, Montoya-Jurado [15] observed that silver selenide decomposed in HNO_3 (2-4M) in a single stage to form elemental selenium. No positive evidence was found for the formation of an intermediate product namely AgSe via analysis of residues & samples collected from "interrupted" leaching experiments. It was reported that the dissolution rate of copper was apparently enhanced in situations where copper was mixed with silver selenide, probably due to the catalytic effect of dissolved silver ions on the copper selenide minerals.

The only detailed electrochemical study on anode slimes components was carried out by Sagindykova & coworkers [163], using the anodic polarisation method. The results were interpreted mainly based on thermodynamic grounds (Eh-pH diagrams). By correlating the polarisation curves to the Eh-pH diagrams, the anodic dissolution of Cu_2Se was proposed to proceed according to the following sequences:



However, due to the complexity of the system, results obtained via the above technique alone were inadequate for the elucidation of the electrochemical behaviour of copper selenide (Cu_2Se). In addition, no analytical work was conducted on the electrochemical sample. Thus the above proposed mechanism remains conjectural.

2 Experimental

2.1 Synthesis and characterisation of CuAgSe, Ag₂Se and Cu₂Se

2.1.1 Introduction

With the increasing use of selenides and tellurides in fields such as infra-red components [126], electronics (semiconductors), reference electrodes [140] and photoelectrochemical sensors [142], the synthesis of selenides and tellurides has attracted considerable attention for decades. Generally, methods for the preparation of selenides and tellurides fall into four categories: thermal synthesis, hydrochemical synthesis, hydrothermal synthesis and electrochemical deposition. Brief descriptions of these synthetic techniques are given below.

(1) Thermal synthesis

This is one of the most common techniques for laboratory preparation of several categories of inorganic compounds e.g. sulphides & chlorides, on a large scale. The first attempt to synthesise selenides e.g. cupric selenide (CuSe) and silver selenide (Ag₂Se) using this technique was made by Early [127-8] in the later 1950's. A mixture of stoichiometric amounts of the elements (powder) was smelted at 1100-1200°C in an evacuated silica glass tube (sealed with inert gas). Perfectly crystallised compounds were obtained either by quenching the products in cold water or by cooling slowly to room temperature, although finer crystals are more likely to be produced in the latter. X-ray diffractometry analysis showed that the X-ray patterns of synthetic compounds were identical to the corresponding natural minerals. Similarly, multi-needle crystals of copper silver selenides (eucairite, CuAgSe) were prepared by fusing a stoichiometric mixture of Cu₂Se and Ag₂Se at 1250°C for one hour. The product was then cooled to 600°C and maintained at this temperature for one hour prior to further cooling

[47]. Occasionally, gentle vibration [6,38,129-130] was used to improve the chemical reactions, and therefore improve the properties of the products. Copper & silver selenides (Cu_2Se , Ag_2Se) were also prepared by passing Se vapour and N_2 over copper or silver powder at 400°C in an atmosphere free of oxygen [133].

It was reported [134] that copper and silver selenides were prepared by fusing compacted pellets (1-2 cm in diameter) of stoichiometric amount of the corresponding elements at 200°C in an evacuated silica ampoule for 75 hours. Copper(I) selenide could also be obtained by hot pressing the mixture of the elements in a certain ratio [135]. Higher qualities of products were achieved, and the temperature and pressure were remarkably reduced compared with the method described in reference [134].

(2) Hydrochemical methods

Since the late 1950's, a number of efforts have been made to synthesize selenides & tellurides in solution [126,153-5]. Benzing [136] systematically studied the feasibility of preparation of selenides & tellurides of a number of metals by reducing the corresponding metal selenite in ammoniacal hydrazine solution. Based on this work, Kulifay [137-8] developed a novel process for the preparation of intermetallics, selenides, tellurides, antimonides & arsenides. Montoya-Jurado [15] achieved similar results in the preparation of silver selenide, copper silver selenide & cupric selenide (CuSe) by following this technique. However, nonstoichiometry was observed in the case cuprous selenide [15].

Other methods, such as preparation of lead selenide by reducing lead selenite solution with streams of hydrogen gas [126], passing H_2Se through copper chloride solution in the presence of HCl & high temperature reduction of copper selenate solution with carbon, were also reported [6,38]. Most recently, Korczynski [143] developed a method for preparation of heavy metal selenides via the interactions between heavy metal salts & potassium selenide in aqueous

media. The synthetic Ag_2Se , CdSe , Sb_2Se_3 , SnSe & SnSe_2 were found to be stoichiometric by X-ray diffractometry analysis, whilst Cu_2Se , CuSe , ZnSe , HgSe , PbSe , As_2Se_3 & Bi_2Se_3 showed deviation from their theoretical compositions.

(3) Hydrothermal synthesis

In order to compare the physical and chemical properties of the synthetic copper and silver selenides with the nature minerals, Ugorets [139] developed a process for producing silver selenide under hydrothermal conditions similar to the geological conditions for the formation of this mineral. In this process Ag_2Se was prepared by heating a suspension of Ag & Se powder in alkaline solution. Further investigation showed that the oxidation of the Ag_2Se prepared under hydrothermal conditions was different from that prepared via thermal methods.

(4) Electrochemical synthesis

Recently, with the increasing use of selenides and tellurides in such fields as electroanalytical chemistry and photoelectrochemistry, many attempts have been made to produce these compounds electrochemically [140-2]. However, in most cases, selenides were prepared as thin layers or coatings according to different uses. Alekperov [144] described a methods for electrodeposition of copper selenide from a non-aqueous solution. It was reported that high quality copper selenide coatings on metal surfaces were obtained by electrolysis of a formic acid solution of Cu(I) chloride, selenium dioxide, and LiCl. X-ray and chemical analysis revealed that the composition of the copper selenide coating could be changed by controlling the deposition conditions e.g. temperature, Cu/Se ratio in the solution and total concentration of these two elements.

2.1.2 Synthesis of CuAgSe , Ag_2Se , and CuSe

It seems that the hydrochemical synthesis technique is more suitable for the

preparation of copper & silver selenides samples for the present study since the environment of the formation of the compounds in this case is more analogous to that of the electrorefining of copper. Therefore, results obtained from samples prepared via this technique are expected to be more representative.

The synthesis was carried out according to the following procedures:

- (i) Preparation of solution of stoichiometric amount of metals;
- (ii) Preparation of reducing solutions (hydrazine in $\text{NH}_3 \cdot \text{H}_2\text{O}$). Sometimes, phosphoric acid (in combination with HCl) was used as an alternative.
- (iii) Addition of the starting solutions to the boiling reducing solution. The mixture is stirred and maintained boiling for 90-120 minutes;
- (iv) After filtration, the solids were washed with deionised water and organic solvent e.g. methanol prior to air-drying at a temperature preferably around 60-80°C because Ag_2Se can be oxidised at temperature over 140°C.

A set of preliminary experiments was carried out to determine the optimum conditions for the synthesis. The parameters include starting acidity of the solution (the amount of ammonium hydroxide), temperature, intensity of stirring, reaction time, concentrations of metal ions & reducing reagent (hydrazinium).

The synthesis was carried out in a one litre pyrex vessel with

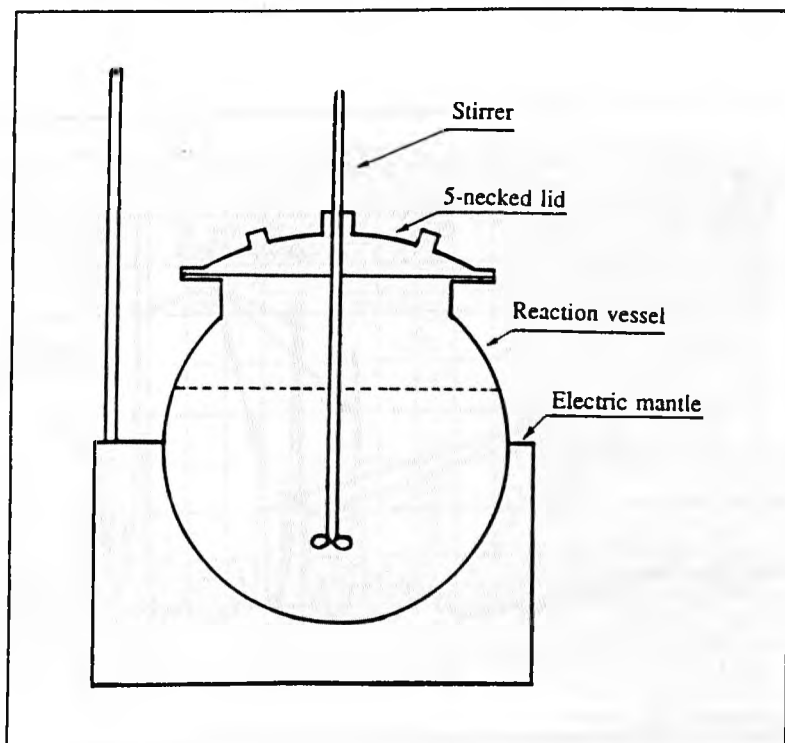


Figure 2.1 Schematic illustration of the reaction vessel for synthesis of Ag_2Se & CuAgSe

a 5-necked lid (*Figure 2.1*). A stainless steel stirrer was immersed half the depth of the solution via the central neck, & the gap between the shaft & the neck was sealed as complete as possible to prevent ammonia escaping. The temperature of the system was controlled by adjusting the power supply of the electric mantle.

(1) Effect of acidity of the solution

A set of experiments was carried out to study the effects of acidity of the reducing solution on the synthesis of copper silver selenide (CuAgSe). The pH values were measured by a Pye model 291 pH meter. It was found that the synthesis of CuAgSe was favoured in weak alkaline (notably 7.5-8.5) solutions, presumably due to the activation of Se^{2-} by hydroxyl ions [138]. Appreciable amounts of Ag_2Se were detected in the product when the starting pH values was greater than 9.5, based on X-ray diffractometric analysis (*Figure 2.2*).

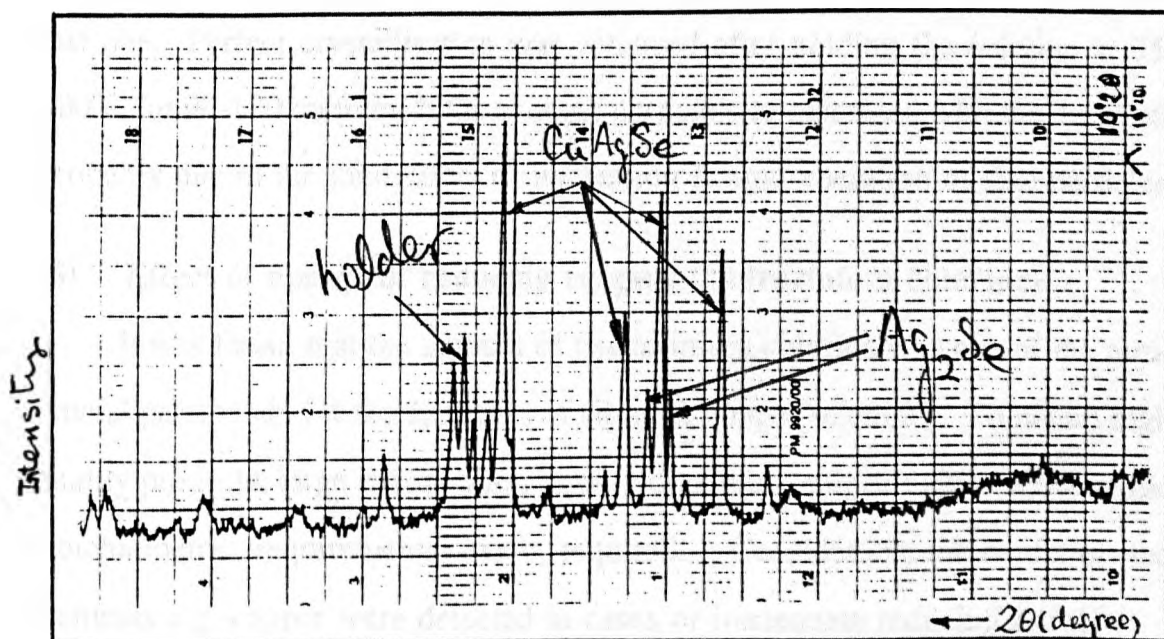


Figure 2.2 Effect of pH. Conditions: pH = 9.2, T = $97 \pm 2^\circ\text{C}$, mild stirring, $[\text{Ag}^+] = [\text{Cu}^{2+}] = [\text{H}_2\text{SeO}_3] = 0.01\text{M}$, $[\text{N}_2\text{H}_4 \cdot \text{HCl}] = 0.05\text{M}$, duration 125 minutes.

(2) Effect of temperature

Temperature is very important for most reactions. It was found that perfectly crystallized CuAgSe was obtained when the temperature was maintained at 90-110°C. When temperature was higher than 120°C,^a a small amount of silver selenide was found in the CuAgSe product (*Figure 2.3*). Temperatures in the range 85-120°C had no apparent effect on the synthesis of silver selenide.

(3) Effect of intensity of stirring

The effect of the intensity of stirring was studied qualitatively. The speed of stirring (50-160 r.p.m.) had no apparent effect on the quality of the product except for the particle size. However, a small amount of silver selenide was observed (*Figure 2.4*) in the product if the solution was not stirred.

(4) Effect of duration of the reaction

The synthesis reaction proceeds in three stages [137-8], i.e. the reduction of metal ions to the active elemental state, the combination of the elements & the nucleation of the compound. The first two stages proceed much faster than the last one. Perfect crystallisation was achieved after holding the solution at 95-100°C for 90-120 minutes & the average particle size increased with the duration, probably due to the joint effect of nucleation & agglomeration of fine particles.

(5) Effect of dosage of reducing reagent (hydrazinium chloride)

It was found that the amount of hydrazinium chloride was one of the most crucial parameters for the synthesis of silver & copper selenides. To obtain high quality products, large excess dosages of hydrazinium chloride (250-500% of the stoichiometric requirements) were required. Considerable amounts of the elements e.g. copper were detected in cases of inadequate reducing agent.

(6) Effect of concentration of metal ions

Attempts were made to scale up the production by increasing concentrations

of the metal ions (in stoichiometric ratio), but these did not give satisfactory results. In the case of synthesis of CuAgSe, a certain amount of silver selenide was observed by XRD when the concentration of copper or silver exceeded a certain limit (0.05 mol-dm^{-3} for both copper and silver).

Based on the above preliminary experiments, the key parameters for the synthesis were set up, i.e. mild stirring, duration 120 minutes, temperature 95-105°C, starting pH value 8.0-8.5, and the dosage of various reagents as *Table 2.1*. The synthesis was carried in batches to obtain the required quantity.

Table 2.1 Reagents for the synthesis of CuAgSe & Ag₂Se

Substances	Starting Solutions of Reactants	
Silver Selenide β -Ag ₂ Se	(A) Silver	13.5902g AgNO ₃ in 60ml H ₂ O + 75ml NH ₃ H ₂ O
	(B) Selenium	3.1584g Se dissolved in 25ml 2:1 HNO ₃
	(C) Reductant	60g N ₂ H ₄ 2HCl in 550ml H ₂ O + 200ml NH ₃ H ₂ O
Copper Silver Selenide (CuAgSe)	(A) Copper	2.5418g Cu dissolved in 25ml 1:1 HNO ₃
	(B) Silver	6.7951g AgNO ₃ in 30ml H ₂ O + 40ml NH ₃ H ₂ O
	(C) Selenium	3.1584g Se dissolved in 25ml 2:1 HNO ₃
	(D) Reductant	75g N ₂ H ₄ 2HCl in 600ml H ₂ O + 200ml NH ₃ H ₂ O

In the case of the synthesis of Cu₂Se, considerable amounts of metallic copper powder were found in the product presumably due to the incomplete reaction between copper & selenium to form CuSe rather than Cu₂Se. As an alternative, the "vapour transmission" technique used for the preparation of nickel-iron-sulphide minerals e.g. pentlandite & violarite [146-7] was employed.

The stoichiometric amount of copper (30.8398g) and selenium (19.1602g) were initially placed separately in the two chambers of the reaction vessel (double bulbed "96%" silica glass tube, 39mm I.D., 43mm O.D.). After loading,

the vessel was evacuated¹, using a rotary-pump & two mercury diffusion pumps with two liquid air traps, to a pressure < 0.0006 torr & then sealed in an oxygen-natural gas flame. The vessel was then placed horizontally in the mullite liner (which is continuously purged with argon gas at a rate of 2ml·s⁻¹ to serve as a precaution in case of leakage of the silica tube) of a Kanthal wound tube furnace (Carbolite CTF2 1200). The bulb containing copper was located in the hottest region (centre) of the furnace & the selenium in the relatively cooler region. The temperature was monitored by a Gallenkamp QPL 397 HJ temperature control unit via a NiCr/NiAl thermocouple placed in the central zone of the furnace.

The furnace was heated up slowly at a speed of 1K/minute to 1073K at the central zone to allow the temperature of the selenium "zone" to be raised to just over the boiling point of selenium (958K for crystalline Se). The furnace was held at this temperature for at least two days to allow complete reaction of copper with the selenium vapour. Then it was heated slowly (2K/minute) to slightly over the melting point of Cu₂Se (1380K) and subsequently maintained at this temperature for another 2 days to fuse the product so that homogeneity within the final product can be obtained. Crystals of sizes up to several millimetres were obtained by cooling the product slowly to room temperature.

2.1.3 Characterization of synthetic compounds

Product from each batch was subjected to X-ray diffractometry & scanning electron microscopy analysis and the final product of each compound was investigated by a series of analyses. These included X-ray diffractometry, scanning electron microscopy, energy dispersive analysis, electron microprobe and chemical analyses. Technical details are briefly given in Section 2.2.

¹ Acknowledgements are given to Mr. M. Holmes & C.J. Gascoigne for discussion about the problems and practical assistance.

X-ray diffraction results indicated that the X-ray patterns (*Figure 2.5*) of synthetic silver selenide were identical with those documented in the standard data file & those observed by Early [127-8] for the natural mineral (naumannite). The X-ray patterns (*Figure 2.6*) of copper silver selenide (CuAgSe, eucairite) were also found to be consistent with those in the standard data file. However, in the case of synthesis of copper silver selenide (CuAgSe), additional peaks for β -Ag₂Se could be observed occasionally. It was estimated that the silver selenide content in the copper silver selenide product was less than 3% by comparison of the peak areas with those of the corresponding pure compounds. In addition, there was no evidence for the existence of other impurities in these two products.

Scanning electron microscopy analysis showed that the particle sizes of the synthetic silver selenide were much coarser than those of the copper silver selenide, possibly due to the lower activation energy of nucleation of silver selenide. On the other hand, the particle sizes of the synthetic compounds (normally from less than 1 μm to 20 μm) were much finer than the commercial anodic slimes [14]. However, the morphologies of these two materials were very similar. Copper selenide was found [14] to be agglomerated with lead sulphate to form "rings" of different sizes (several μm in diameter). In the case of synthetic copper silver selenide, a large number of "rings" (normally less than 1 μm in diameter) were also found (*Figure 2.7 (a)*). Further SEM studies using high magnification revealed that these "rings" were actually agglomerates of even finer crystals (*Figure 2.7 (b)*) & the structure of the crystals was found to be deformed cubic rather than ring. This conclusion is further confirmed by the bonding theory of chalcogenides, which cat g rised the crystal structure of ccopper silver selenide into a 'tetragonal' type lattice [128,145]. The possible explanation to the "ring" agglomeration of crystals of CuAgSe is that the surface energies of the particles can be maintained at the lowest level by constructingring agglomerates. Thus, the particles become chemically and mechanically more

stable. It was also observed that the silver selenide had a deformed cubic structure (*Figure 2.8*).

In order to detect contamination of the synthetic products caused by stray reagents, energy dispersive X-ray analysis (EDXA) was employed. Analysis results showed no additional peaks for other elements except for a small peak for chlorine (Cl), which resulted probably from the involvement of small amount of AgCl (Cl was contributed by the reducing agent N_2H_4HCl) precipitate in the selenides agglomerates (*Figures 2.9 & 2.10*).

Electron microprobe analysis (EMPA) reveals that the synthetic copper silver selenide & silver selenide were found to be homogeneous & stoichiometric. The atomic ratio of silver selenide was Ag:Se=1.991:1 & that of copper silver selenide was Cu:Ag:Se=1.017:1.020:1 (*cf. Table 2.2*).

Table 2.2 Results of EMPA analysis

Element	k i.x./i.std.	k. ratio	(wt %) concen.	mole fraction atom. c
<hr/>				
Ag_2Se :	(Ag:Se \approx 1.991:1)			
Ag :	0.6750	0.6750	72.948	66.51
Se :	0.1543	0.1543	26.781	33.40
Total :		0.8293	99.729	
<hr/>				
$CuAgSe$:	(Cu:Ag:Se \approx 1.017:1.020:1)			
Cu :	0.2759	0.2759	25.939	33.49
Ag :	0.3821	0.3821	44.176	33.59
Se :	0.1594	0.1594	31.689	32.92
Total :		0.7174	101.804	
<hr/>				

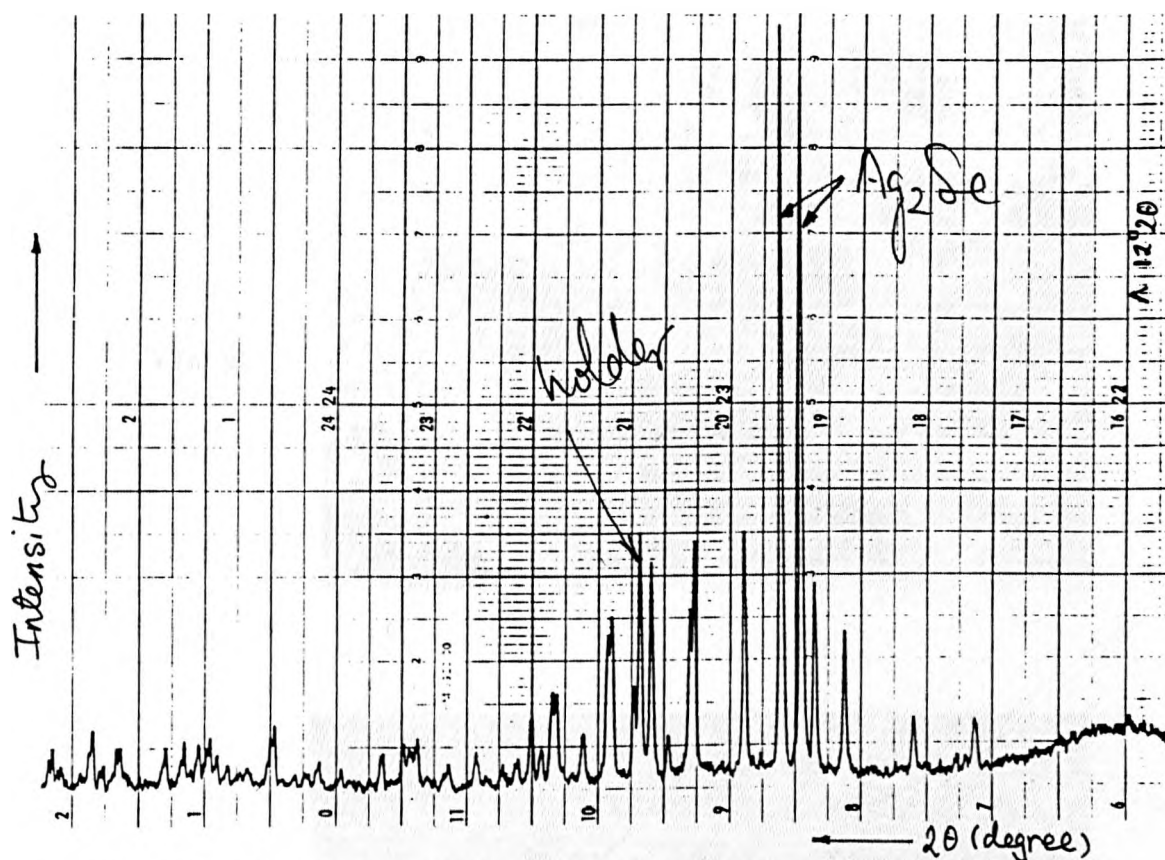


Figure 2.5 XRD for synthetic Ag₂Se. Conditions as stated in Table 2.1.

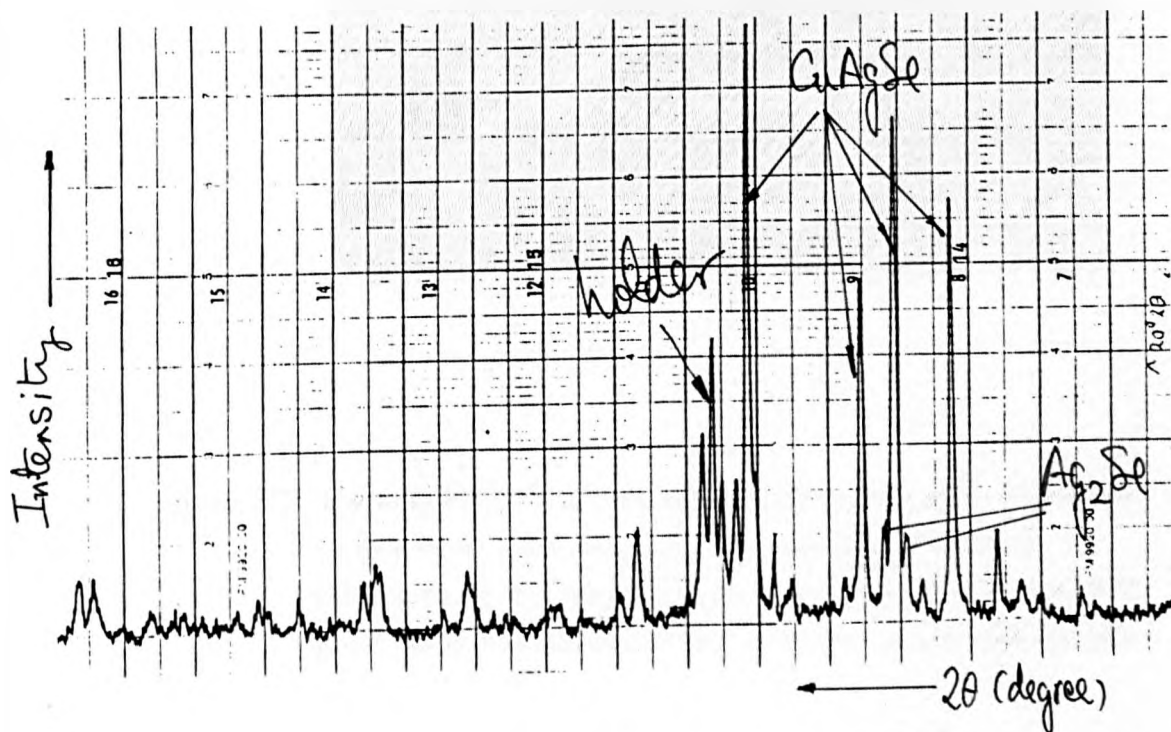
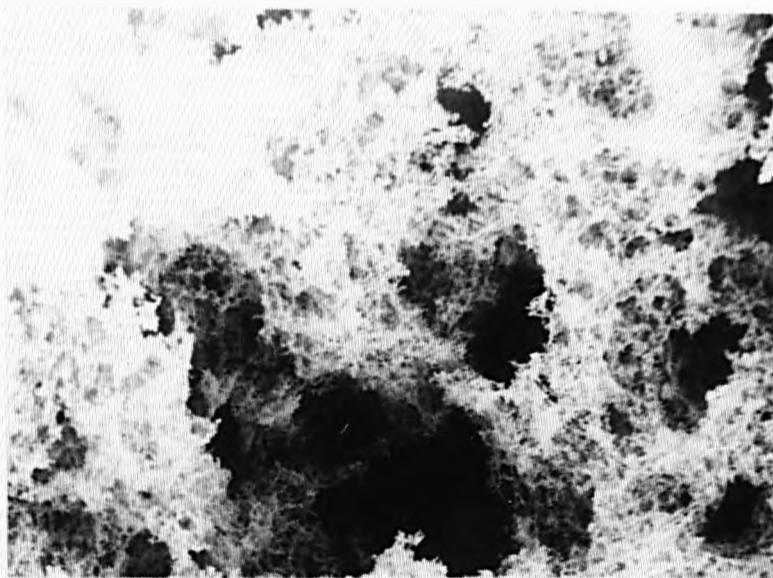


Figure 2.6 XRD for synthetic CuAgSe. Conditions as stated in Table 2.1.

(a)

2000 x



(b)

40000 x

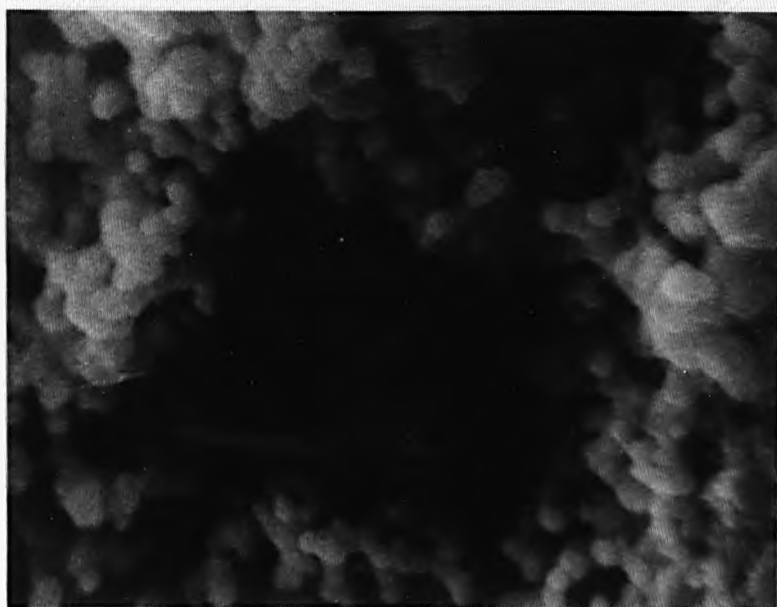


Figure 2.7 Scanning electron microscope (SEM) photographs of synthetic copper silver selenide (CuAgSe). (a) Ring morphology is evident under low magnification. (b) High magnification SEM graph shows the deformed cubic structures of CuAgSe crystals.

(a)

6500 x



(b)

15000 x



Figure 2.8 Scanning electron microscope (SEM) photographs of synthetic silver selenide (Ag_2Se). Silver selenide crystals can be observed at relatively low magnifications. Magnifications: (a) 6500 x (b) 15000 x

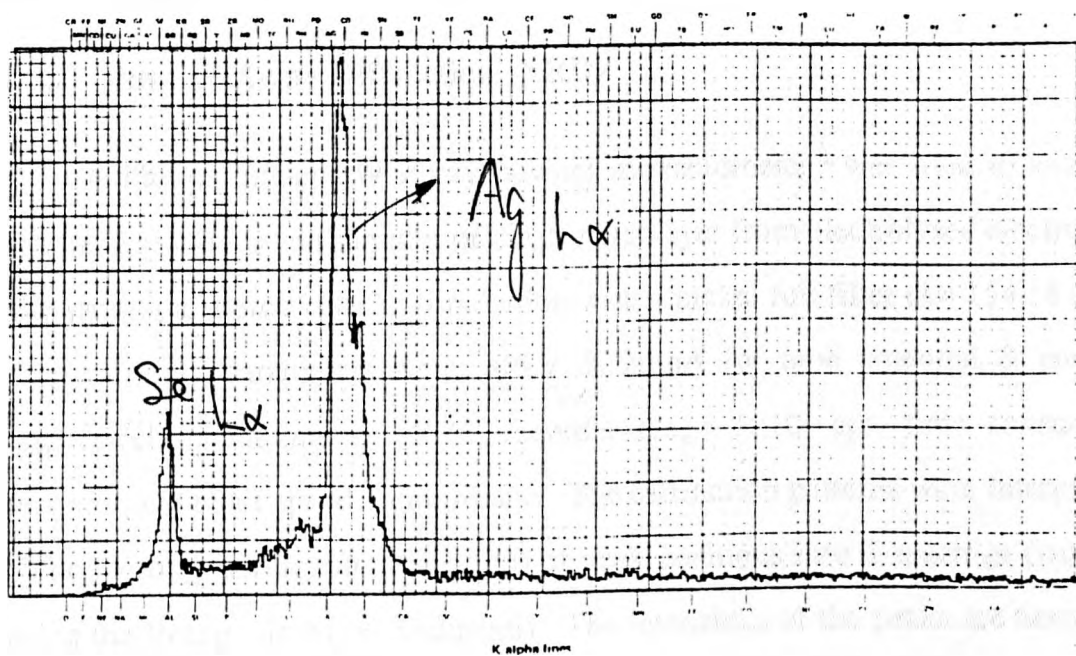


Figure 2.9 EDXA for synthetic Ag_2Se . Conditions as stated in *Table 2.1*.

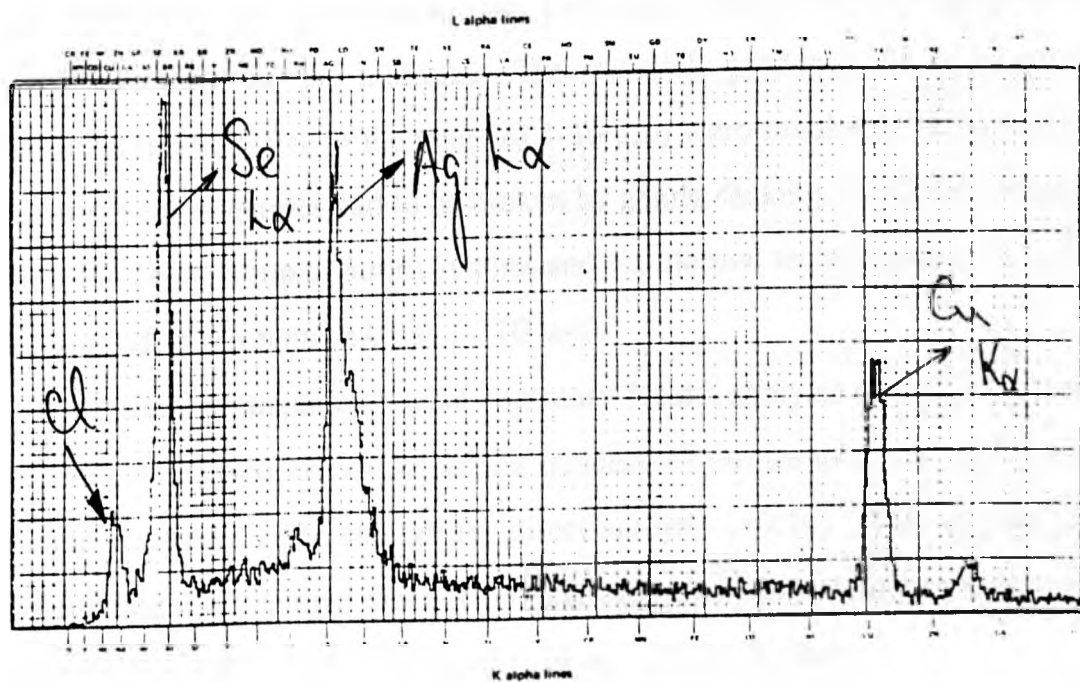


Figure 2.10 EDXA for synthetic CuAgSe . Conditions as stated in *Table 2.1*.

2.2 Analytical Techniques

2.2.1 Powder X-ray Diffraction (XRD)

A Philips model PW X-ray powder diffractometer² was used to analyze synthetic selenides and samples of the product layer from electrolysed electrodes. The radiation source is a $\text{Cu}_K\alpha$ radiation with a nickel foil filter ($\lambda = 154.18 \text{ pm}$). The operating parameters were: 40kV & 20mA for tube potential & current respectively, scanning rate $2^\circ/\text{minute}$ (2θ), recorder range 1×10^3 cps, time constant 2 seconds, and chart speed 1 cm/minute. The diffraction patterns were interpreted by converting diffraction angles (2θ) of peak positions into d-spacings (lattice), using the Bragg law (i.e. $\lambda = 2d\sin\theta$). The intensities of the peaks are normally expressed as the relative terms (I) with the highest peak intensity being 1 standard unit. Small peaks ($I < 5\%$) were regarded as 'background'.

The sample was prepared by placing the materials (approximately 0.5g) into a clean dry aluminum specimen holder, followed by flattening with a piece of glass and removal of extra materials. Generally, there is a strict requirement for the particle size of the material. The materials produced via hydrochemical methods (particle size in the range of 1-10 μm) were suitable for direct analysis, although agglomerates had to be broken by gentle shaking. However, the copper selenide crystals (up to 5mm) synthesised via thermal techniques (cf. 2.1) had to be ground to the required size ($< 10 \mu\text{m}$).

Special arrangements were necessary for the analysis of the product layers of the electrolysed electrodes as the quantity of the sample collected from one single electrode is not enough for direct analysis ($< 0.1\text{g}$). This is done jointly by running 2-3 identical electrochemical experiments to collect as much sample as possible and by reducing the size of the sample holder.

² Acknowledgement is given to (i) Mr. A. Hanush of the Dept. of Mining and Mineral Engineering for guidance in operation of the equipment. (ii) Mr. C. Jones of the Dept. of Inorganic Chemistry, for conducting some of the analysis.

2.2.2 Scanning Electron Microscopy (SEM) & Energy Dispersive X-ray Analysis (EDXA)

The morphology of the synthetic materials (Cu_2Se , Ag_2Se and CuAgSe) and electrochemically treated electrodes were examined by electron microscopic analysis³, using a Camscan Series 3-30BM scanning electron microscope. A Link system 860 series 2 energy dispersive X-ray analysis (EDXA) facility was connected to this unit for qualitative analysis of elemental composition of the specimens (a specific part). The operating parameters were: beam energy 20kV, beam current 0.15mA, working distance 23mm (for morphology analysis) or 26mm (for EDXA), and resolution 5-7 (for morphology analysis) or 3-4 (for EDXA). Spectrum lifetime was 100 seconds for the energy dispersive analysis. Special attention was given to lens aperture alignment & astigmatism adjustments (e.g. the area of interest is not flat) so that high quality photos could be obtained. The magnification of the Camscan microscope ranges effectively from 100 up to 15000 times. It was found that selenides synthesised via hydrochemical methods (cf. 2.1) were principally agglomerates of fine particles ($< 5\mu\text{m}$). To investigate the morphology of these materials, the more powerful Hitachi S700 scanning electron microscope ($\times 50000$) was employed.

The particle specimens were glued with electrical conducting material (e.g. colloidal carbon) onto aluminium stubs specially designed to fit onto the sample holder of the SEM. Alternatively, disk specimens were prepared by compressing a certain amount of synthetic material using a specially designed sample press (6mm in diameter, *Figure 2.11(a)*). The pellet was then placed in a polyethylene mould (*Figure 2.11(b)*) with its interior walls being evenly lubricated with a thin layer of grease. A previously prepared resin was subsequently poured into the mould to set the sample. Special care was taken to make sure the surface of

³ Acknowledgement is given to Mr. J. Harrington of the School of Material Science, for initial assistance in the operation of the instruments.

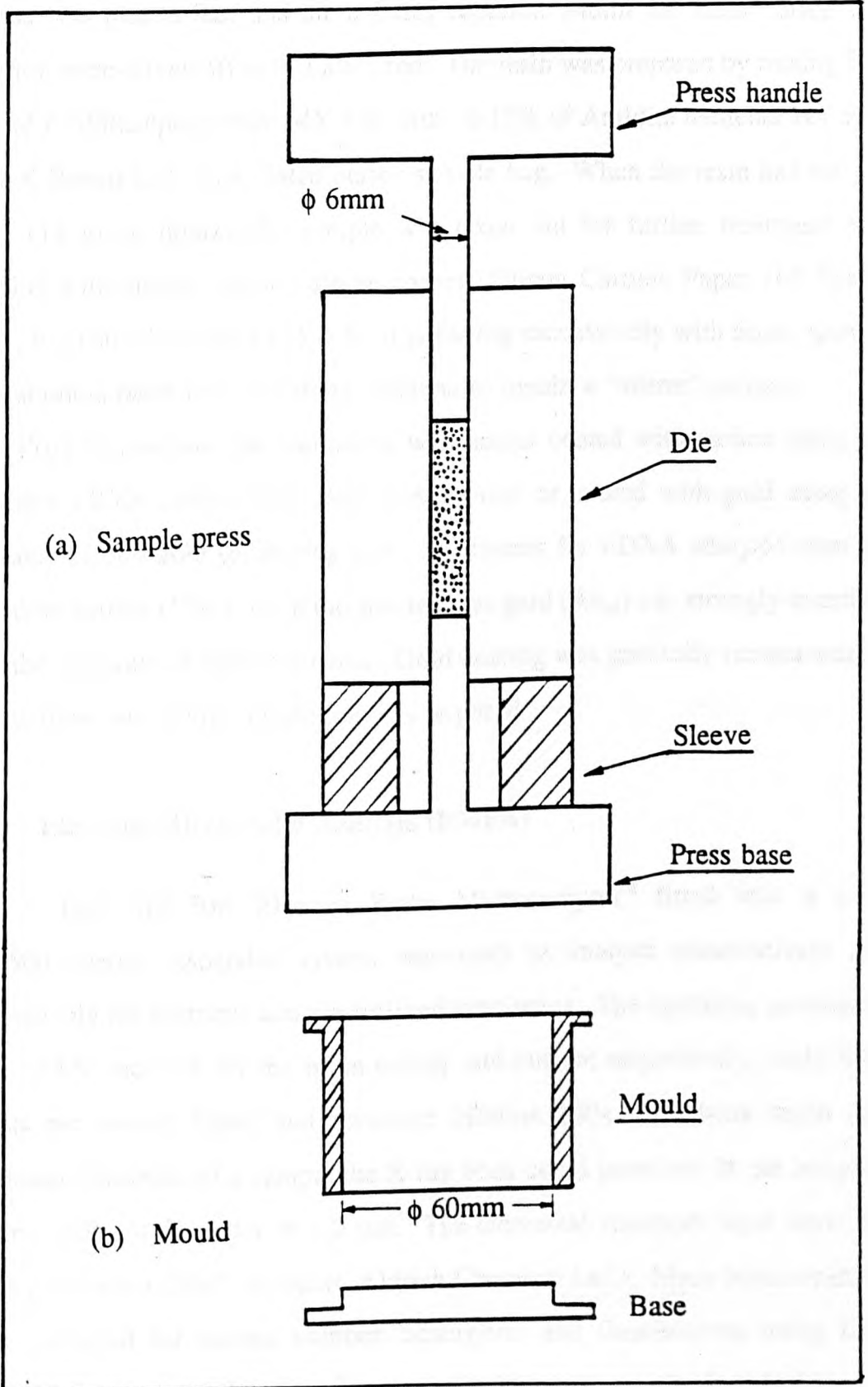


Figure 2.11 Schematic illustration of sample press & mould for preparation of electrodes & etc.

interest was placed flat, and air bubbles captured within the resin during the injection were driven off with a glass rod. The resin was prepared by mixing 85-90% of Araldite epoxy resin MY 778 with 10-15% of Araldite hardener HY 951 (B & K Resins Ltd.) in a sealed plastic sample bag. When the resin had set

(18 to 24 hours), the sample was taken out for further treatment e.g. grinding with coarse silicon carbide papers (Silicon Carbide Paper 165 Grade 400A, English Abrasives Ltd.) & final polishing successively with 6 μ m, 3 μ m & 1 μ m alumina paste on a polishing machine to obtain a 'mirror' surface.

Prior to analysis, the specimens were either coated with carbon using an Emscope TB500 carbon fibre flash coating unit or coated with gold using an Emscope SC500 gold spluttering unit. Specimens for EDXA analysis must be coated by carbon ONLY since the spectrum of gold (Au_M) can strongly interfere with the spectrum of other elements. Gold coating was generally recommended in situations where high resolution was required.

2.2.3 Electron Microprobe Analysis (EMPA)

A Joel JXA-50A Electron Probe Microanalyser⁴ fitted with a Link 860-500 energy dispersive system was used to analyse quantitatively and qualitatively the synthetic and electrolysed specimens. The operating parameters were: 20kV and 1nA for the beam energy and current respectively, scale 3000 counts per second (cps), and spectrum lifetime 100s. Analysis depth (the maximum thickness of a sample the X-ray beam could penetrate in the samples) was normally of the order of 1-2 μ m. The elemental standards used were: Se, Cu, Ag ("Golden Label" products, Aldrich Chemical Ltd.). Mean concentrations were corrected for atomic number, absorption and fluorescence using Link ZAF4/FLS software, while the elemental distributions was obtained in forms of

⁴ Acknowledgement is given to Dr. E. Condliffe of the Department of Earth Sciences for assistance in the use of this instrument.

"Digimap" (dotted maps) by means of the digitised EDS mapping technique.

The specimens were principally prepared in similar procedures as described in Section 2.2.2. Prior to analysis, all specimens were coated with carbon using an Emscope carbon fibre flash coating unit.

2.2.4 DC Arc Spectrographic Analysis

Direct current arc spectrographic analysis⁵ was employed to check the quality of the copper rods⁶ used in synthesis of copper selenide, using a Hilger & Watts DC Arc spectrophotometer (Servomex Controls Ltd.). The copper rod is used as counter electrode and a 6.5mm graphite electrode as the cathode. The operating parameters were : 260V for the working potential, 10A for the DC current while sparking (i.e. when the arc was on), with an exposure time of 20 seconds. The spectrum of the copper rod was found to be identical with that of the "specpure" copper. No additional spectrum, except for those characterising copper (3273.9 and 3247.51 Å), were found.

2.2.5 Atomic Absorption Spectroscopy (AAS)

A Perkin Elmer model 272 atomic absorption spectrophotometer⁷ was used in the determination of copper and silver concentrations in aqueous solution. The characteristic wavelengths were 218.2 & 338.2nm for Cu & Ag respectively. In the case of solid samples, a known mass of the solid was digested in oxidising acid media (e.g. H₂O₂ & aqua-regia) prior to analysis.

⁵ Acknowledgement is given to Mr. S. Lloyd of the Dept. of Mining and Mineral Engineering for conducting the analysis.

⁶ Acknowledgement is given to the BICC Prescott Copper Refinery (U.K.), for generous donation of these samples.

⁷ Acknowledgement is given to Mr.A.Hedley of the School of Chemistry for conducting these analyses.

2.3 Design of Electrochemical Experiments

2.3.1 Instrumentation and Experimental Procedures

2.3.1.1 Electrodes Fabrication and Cell Design

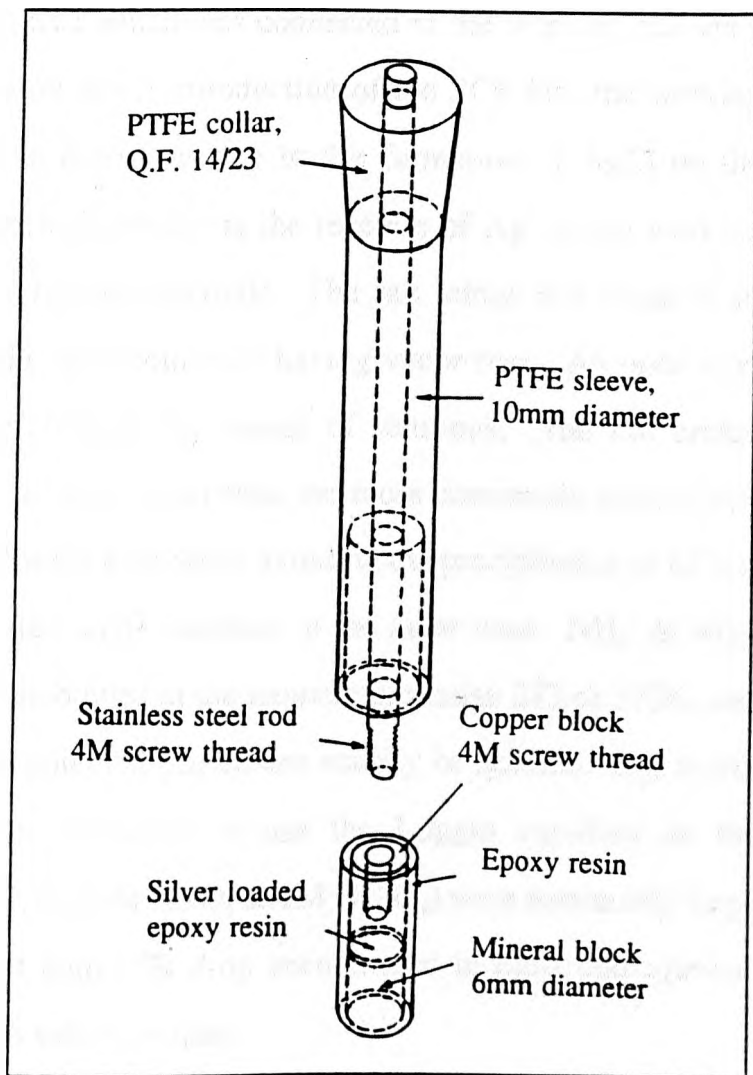
(1) Working Electrode

All the electrochemical experiments were performed on cylindrical (disk) electrodes with a diameter of 6mm. The platinum & graphite electrodes for the study of the $\text{Fe}^{3+}/\text{Fe}^{2+}$ & $\text{Cu}^{2+}/\text{Cu}^+$ couples were standard Metrohm electrodes. The mineral electrodes were compact pellets of synthetic silver selenide & copper silver selenide minerals. The synthetic minerals were very fine particles ($< 10\mu\text{m}$) and thus they were not suitable for direct electrochemical measurements. Instead, those powdery materials were initially compressed, under a pressure of $700\text{kg}\cdot\text{cm}^{-2}$ (240MPa), in a specially designed sample press using a Denison 500kN Hydraulic Testing Machine⁸. The synthetic copper selenide (cf. 2.1.3) was principally small crystals of the size up to several millimetres. Therefore, this material must be finely ground prior to compressing to achieve reasonable homogeneity in the pellet. The pellet was subsequently glued onto a copper cylinder with low resistivity silver loaded epoxy adhesive (RS components Ltd.). The copper cylinder was 18mm long & 6mm in diameter and it had a female M4 screw on the other end allowing good electrical connection to external circuit via a stainless steel rod. When the adhesive solidified, the mineral-copper rod was set in insulating epoxy resin in a similar fashion as stated in *section 2.2.2*. Thus, ONLY the circular cross-section of the electrode was exposed to the electrolyte. Once set the resin was machined to desired size (7-8mm in diameter) so that the resin coated electrode could be fitted into a PTFE tube which,

⁸ Grateful thanks are given to Mr. M. Pegden & P. Townhill-Rewston of the Dept. of Mining and Mineral Engineering for assistance in operation of the instruments.

together with a PTFE supporter, supported the electrode material. A typical design of the working electrode is illustrated in *Figure 2.12*.

The above electrode configuration was suitable for both stationary electrode and rotating disk electrode (RDE) experiments. The latter were made using a Metrohm model 628 RDE system. The RDE was used to provide an alternative experimental



approach by enhancing the mass transport of electroactive species in the aqueous phase.

(2) Reference Electrode

The reference electrode used for potential measurements was a Metrohm saturated calomel electrode⁹ (SCE) model 6.0702.100. The SCE was placed in

⁹ The term "electrode potential" always refers to the cell emf encompassing the particular electrode & a convenient standard e.g. standard hydrogen electrode (SHE, $P_{H_2} = 1\text{atm}$). The potential of the SHE is artificially defined as 0V. In most cases, electrodes e.g. SCE & Ag/AgCl are used due to the convenience of operation. The electrode potential for the saturated calomel electrode with respect to SHE at 298.15K is 0.242V and it varies with temperature.

a separate cell of saturated KCl which was connected to the working cell via a salt-bridge. This was because direct introduction of the SCE into the working electrolyte had proved to be disastrous due to the formation of AgCl on the ceramic plug of the reference electrode via the reaction of Ag^+ in the working electrolyte with Cl^- in the reference electrode. The salt-bridge was made of an inverted U-shaped glass tube with both ends having vycor frits. An open inlet tube on the top of the arc allowed the change of solutions. The salt bridge solution was 1M NH_4NO_3 solution rather than the more commonly used KNO_3 solution. This was mainly for the purpose of avoiding the precipitation of KClO_4 at the salt bridge/working electrolyte interface in the latter case. NH_4^+ & NO_3^- ions also have very similar mobilities in the temperature range 273 to 373K, and therefore the liquid junction potential caused can usually be ignored. It is worth mentioning that it was not necessary to use the Luggin capillary as the conductivities of the electrolytes (1M HNO_3 & 1M HClO_4) were reasonably large and therefore the significant ohmic IR drop encountered in most non-aqueous electrolyte systems could be safely avoided.

(3) Counter Electrode

In the three-electrode system, an auxiliary (counter) electrode is always employed to supply the current required by the working electrode without limiting or interfering with the measured response of the cell. The counter electrode used in this work was made by spot-welding a Specpure platinum sheet of dimension 10x10x0.1mm to a platinum wire (approximately 8cm in length & 0.1mm in diameter) which was in turn spot-welded to copper wire for connection to external circuit. This wire was then enclosed in a glass tube by fusing the lower end, leaving a length (4cm) of platinum wire exposed to electrolyte. The upper end of the glass tube was designed in accordance with the female joints on the vessel lid so that it could conveniently suspend the auxiliary electrode in

the electrolyte.

(4) Cell Design

There are various types of electrochemical cells catering for different applications. In this work, it was found that the complete Metrohm cell kit could be conveniently used for conducting most of the electrochemical experiments. The cell included a container (cat. 6 1418 220) with a maximum capacity of 0.07-0.08 dm³ and a lid (cat. 6.1414.010) to isolate the cell from the surroundings (inert atmosphere is required in most of the experiments) and accommodate the working, reference & counter electrodes, salt-bridge & a gas-purging system for introduction of gas to deoxygenate the solution (*Figure 2.13*). Thermal equilibrium was achieved by circulating water through the specially designed water jackets of the working and the "reference" cells from a thermostatically conditioned water bath. The temperature of the electrolyte could be maintained to within 0.5K in the range from 273.15K (addition of ice) to 373.15K.

2.3.1.2 Electrochemical Apparatus

All the electrochemical experiments were made using an EG&G model 362 scanning potentiostat modified to receive a TTL trigger input and to provide a chronoamperometric mode via a switch on the rear panel. The potential range was -9.999 to 9.999V and sweep rates 0.0001 to 5Vs⁻¹. In the controlled-current experiments (galvanostatic mode), applied current was in the range from 10⁻¹⁰A to 20A. For the intermittent galvanostatic polarisation (IGP) experiments an EG&G parc model 175 universal programmer was used to trigger the galvanostat for generation of a square current wave form. By modifying the output of the programmer, various desired current wave forms could be obtained. A small offset in the "zero" current was commonly encountered in galvanostatic mode. This was overcome by applying small external potentials via a Eurotherm milli-

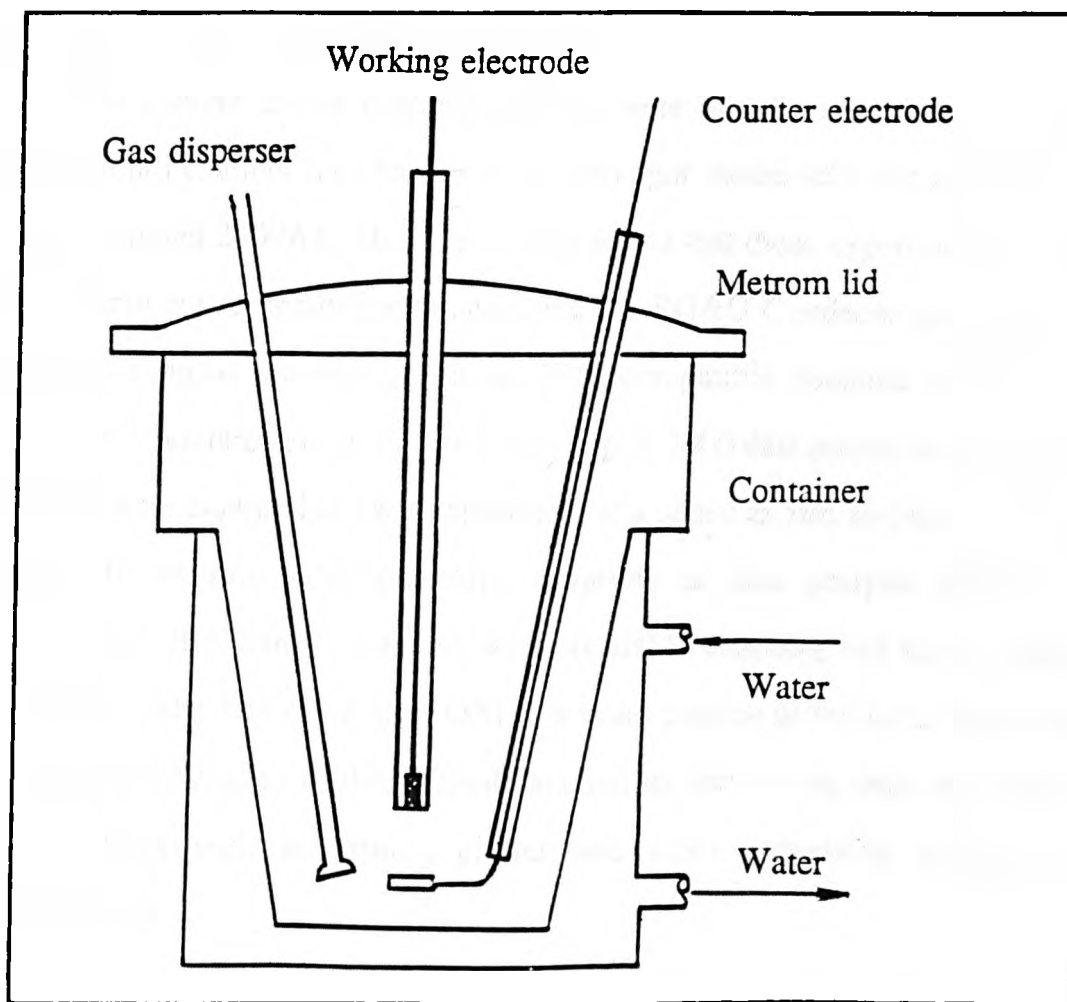


Figure 2.13 Schematic illustration of a Metrohm cell.

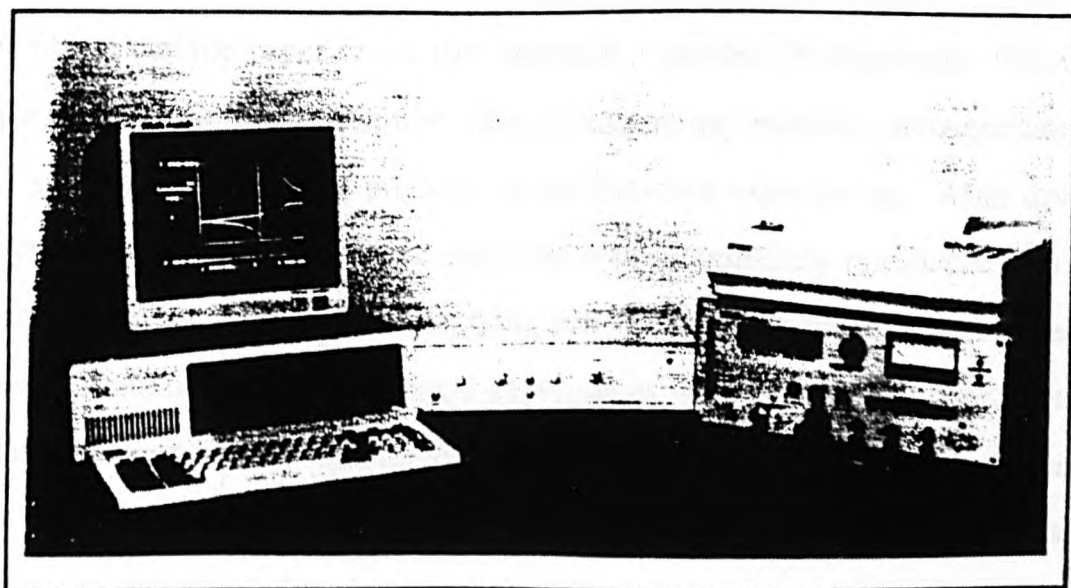


Figure 2.14 Schematic illustration of a typical experimental set-up.

volt source to the model 362 potentiostat.

The current and/or potential profiles were initially recorded on a Brown Boveri multi channel X-t chart recorder Servogor model 460, and a Bryans X-Y recorder model 2600A4. However, it was found that those experiments could be much more conveniently performed using the EG&G Condecon package which included a signal processing unit, an IBM compatible personal computer & a model 362 potentiostat (*cf. Figure 2.14*). Up to 2000 data points (equally spaced in time) were captured in each experiment at a speed as fast as below 100 μ s per point. In addition to data capture, a variety of data analysis facilities e.g. convolution & deconvolution etc. were available enabling full kinetic analysis based on all the data rather than ONLY a small portion of the data. Hard copies of the graphic display of the original data and its derivatives were accomplished via facilities such as printer, plotter and word processing packages e.g. Wordperfect.

2.3.1.3 Experimental Procedures

Prior to any experiments, the working electrode was cleaned by grinding on silicon carbide paper or on 1 μ m alumina powder (Pt electrode), followed by a thorough rinse with distilled water to remove any possible contamination of the surface e.g. remaining products of the previous experiments. After drying with a clean tissue, the working electrode was subsequently introduced into the thermostatic pre-deoxygenated working cell for electrochemical measurements. The majority of the electrochemical experiments were carried out under thermostatic conditions and in an inert atmosphere. This was possible by the choice of the particular cell design stated in *section 2.3.1.1*. In practice, prior to the start of any experiments, the electrolyte was first deoxygenated with "white-spot" nitrogen while the water bath was heated up to the required temperature. This

usually took 5-40 minutes. In stationary experiments, the gas dispenser was pulled back above the electrolyte level before experiments commenced.

2.3.2 Electrochemical Techniques

A variety of electrochemical techniques e.g. potentiometry, cyclic voltammetry (CV, triangular wave form), chronoamperometry (CA), chronopotentiometry (CP), intermittent galvanostatic polarisation (IGP) and stripping voltammetry, were employed in this work. These experiments reflect essentially different aspects of the electrochemical behaviour of a specific electrochemical process under various particularly designed conditions. In other words, they represent merely different approaches to the solution of the classical diffusional problems described by the Fick's second law which integrate time, distance, and concentration (reflecting the relationship between time, potential and current) into one unique equation (*cf. Section 4.2.1* for more details).

2.3.2.1 Open Circuit Potential Measurement

Commonly described as an equilibrium technique, open circuit potential measurement is used to study the thermodynamic properties of a system. In these experiments, the potential of the system (voltage drop across the working and the reference electrode e.g. SCE is measured while the system is maintained at 'equilibrium'. In other words, there is no net faradaic current flowing in the system during the measurement. This is conveniently done by incorporating a sufficiently large impedance in the reference electrode circuit.

Ideally, in simple systems with ONLY one pair of redox species present in the electrolyte, the open circuit potential is uniquely defined by the Nernstian equation describing electrochemical equilibrium, i.e. the forward current and

backward current are equal in magnitude (cf. 4.5.1). In this equation, electrode potential is a function of the thermodynamic properties and the activities of the participant electroactive species. For example, in the Pt/Fe³⁺/Fe²⁺ system, the equilibrium potential (E) is simply defined as

$$E = E^{\circ} + (RT/F) \ln \left([Fe^{3+}] / [Fe^{2+}] \right) \quad (2.1)$$

where [Fe³⁺] & [Fe²⁺] are the activities of ferric and ferrous species respectively, and E^o is the standard potential of the above redox couple.

However, if there are more than one pair of redox species in the electrolyte, the Nernstian equation is not suitable for the determination of the open circuit potential of the entire system. This is commonly encountered in corrosion of metals and oxidative leaching (dissolution) of minerals e.g. sulphide. Instead, a kinetically important term "mixed-potential" is generally proposed to explain such complex systems.

2.3.2.2 Cyclic Voltammetry (Linear Sweep)

A majority of the electrochemical investigations involve the elucidation of the reaction mechanism and possibly qualitative & quantitative assessment of appropriate kinetic parameters e.g. standard rate constant of electron transfer, diffusion coefficients & charge transfer coefficients (α). Polarography is probably amongst the earliest & most successful approaches. However, over the past several decades, potential sweep techniques particularly cyclic voltammetry have found ever increasing applications in studies ranging from inorganic transition metal complexes to oxidative dissolution of minerals, metals & alloys (corrosion). This is mainly owing to the fact that voltammetric techniques have a number of advantages such as ease of operation and data acquisition, and more importantly with the development of a variety of numerical techniques notably

convolution the analysis of the majority of the data and the determination of a wide range of kinetic parameters becomes applicable.

The most commonly used voltammetric technique is the linear sweep cyclic voltammetry at stationary or rotating electrodes in which the resulting faradaic current from a system is recorded as a function of the imposed potential which is itself a linear function of time. In such a typical cyclic voltammetry experiment (linear sweep), the potential always sweeps from the open circuit (equilibrium) potential, where the current flow is initially zero, at a constant rate v up to a preset limit where the sweep diverts towards the second potential limit. Obviously, a great many variations e.g. alteration of potential limits of anodic or cathodic excursion between different cycles are available in this technique. The changes in potential make possible changes of the forward & backward rates of the charge transfer reaction which in turn induce a change in the resulting faradaic current of entire system (*cf. Section 4.5.1*). With rotating electrodes, the response is akin to polarographic experiments whereas at stationary electrodes peak shaped voltammograms are obtained. The latter are due to the diffusion profiles progressively invading the bulk medium. In general, comparable information is available from both experiments. Comparing the voltammograms with theoretical features of various mechanisms, one can easily obtain certain qualitative information by "first impression". These include the potential region at which the charge transfer process(es) occur & reversibility of these process(es), possibility of involvement of additional non-electrochemical processes e.g. adsorption & decomposition of reactants/products, catalytic reactions, etc.. The above information is of great importance to the design of chronoamperometric and chronopotentiometric experiments.

Generally, the choice of sweep rate in cyclic voltammetry is sometimes influenced by the double layer capacitance and thus the ensuing charging current (unless operating in microelectrode system where the capacitive currents are

diminished.). This is particularly true in the systems where the electrode is dissolving (mineral electrodes, for example) and there is a fear of formation of thick transient layers. Bearing this in mind, a slow sweep rate ($10\text{mV}\cdot\text{s}^{-1}$) was employed in this work as 'precaution'.

2.3.2.3 Stripping Voltammetry

Stripping voltammetry finds its applications mainly in quantitative analysis. In this work, it was mainly used to identify the products of the pre-electrolysis step & thus to provide supplementary information for the elucidation of the mechanisms of the dissolution of copper silver chalcogenide electrode. It consists generally of two major steps. These include a pre-electrolysis step (frequently under constant potential) to induce a ~~an~~ electrochemical reaction on the electrode, followed by instantaneously stripping the solution using voltammetric techniques (usually linear sweep voltammetry) to identify at least some the products of the pre-electrolysis. The amount of charge passed to the system during the pre-electrolysis step can be calculated by numerically integrating the current-time (i-t) response.

2.3.2.4 Chronoamperometry

Unlike potential sweep techniques e.g. voltammetry, potential step techniques (chronoamperometry) focus on the transient behaviour of a system by applying a constant potential (in the case of double step chronoamperometry, the potential steps back, after a certain period, to another value e.g. at an over-potential of the same magnitude but opposite in sign) to the system which is initially at open circuit conditions (zero current) and then monitoring the resulting faradaic current as a function of time.

Generally, the i - t behaviour falls into three categories, i.e. mass transport controlled, kinetic controlled & mixed controlled regimes, depending on the relative magnitudes of rates of charge transfer & mass transport processes. In the first case, the heterogeneous electron transfer step is so fast that the progress of the entire process depends ultimately on the speed of arrival of electroactive species at the electrode/electrolyte interface (i.e. the depletion of either the reducing or the oxidising species occurs as soon as the potential stepping is triggered). In experiments based on planar stationary electrodes, a simple numerical transform of the Fick's second law of diffusion leads to the Cottrell relationship ($t^{1/2}$ transient)

$$i = \frac{(z_B - z_A)FA D^{1/2} C^{\text{Bulk}}}{(\pi t)^{1/2}} \quad (2.2)$$

where i , A , D & C^{Bulk} are the current, area of the electrode, diffusion coefficient (equality between D_A & D_B is assumed) and bulk concentration (assuming ONLY species A is initially present) respectively, while z_A & z_B are the charges of species A & B. At rotating electrodes a steady state current is observed which depends on the above parameters & also the rotation speed via

$$i_L = 0.62 (z_B - z_A)FAD^{2/3} \nu^{-1/6} C^{\text{BULK}} \omega^{1/2} \quad (2.3)$$

where ν is the kinematic viscosity & ω the rotation speed respectively.

Another extreme arises in situations where the charge transfer step is so slow that the electrochemical perturbations at the interface does not cause any significant alteration of the surface concentration. As a consequence, the charge transfer step rather than the mass transport step plays the most significant role in determining the rate of the overall process. The resulting faradaic current of this regime is virtually flat and the behaviour can be analyzed in a similar fashion to the steady state experiments.

i-t behaviour is often different from the above extremes. In this case, the rates of heterogeneous charge transfer & diffusion are comparable. Therefore, neither of them plays a dominant role in controlling the pace of the reaction. This transitional regime is generally called the mixed control regime & its analytical solution requires considerable mathematical manipulations.

2.3.2.5 Chronopotentiometry

Chronopotentiometric experiments are normally carried out at stationary electrodes under galvanostatic conditions where a pre-set current wave is superimposed on the working-counter electrode circuit. The potential of the working electrode required to support the external current (induce an electrochemical reaction at the working electrode) is then measured as a function of time. The most useful techniques of this kind are constant current & current reversal chronopotentiometry. In the former, the current flowing across the working-counter electrode circuit is instantaneously stepped from zero (correction of a small offset is necessary in most cases, *cf. Section 2.3.1.2*) to a certain value so that the system is forced to proceed at a CONSTANT rate (if ONLY one electrode process is occurring) throughout the lifetime of the experiment. The latter is actually a continuation of the former. Instead of terminating the experiment at the end of the electrolysis under the first CONSTANT current, a second CONSTANT current of the same magnitude but opposite in direction is instantaneously applied to the system.

For a simple electron transfer reaction of Nernstian type (k^0 very large), the mathematical manipulation of the Fick's second law of diffusion leads to the classical Sand equation at planar stationary electrodes

$$i\tau^{1/2} = (\pi^{1/2}/2) (z_B - z_A) FA D^{1/2} C^{\text{Bulk}} \quad (2.4)$$

where τ is defined as the transition time which spans the beginning of the polarisation to the moment where drastic change in potential is evident.

Kinetic parameters e.g. diffusion coefficients can theoretically be extracted via the above relationship. However, in practice, it is very difficult to obtain transition time (τ) to high precision. For example, at the very beginning of the polarisation, the current contributes mostly to the charging of the double-layer capacitance rather than inducing a faradaic reaction. This charging effect is especially significant in situations where the capacitance or the polarisation current is relatively large. As a consequence, chronopotentiometry is not frequently used for quantitative measurements.

It is worthwhile mentioning that care must be taken in choosing sensitive experimental conditions e.g. duration and intensity (current) of the polarisation such that all the details can be observed (e.g. in the case of multi-component system some characteristic potential-time behaviour may be missed) and the system is not "over-polarised" (huge rise in potential due to depletion of electroactive species at the electrode surface).

2.3.2.6 Intermittent Galvanostatic Polarisation (IGP)

The intermittent galvanostatic polarisation (IGP) is not a common technique in electrochemical investigations. It was initially used to study the thermodynamic properties e.g. equilibrium potentials of electrode processes in metal-water binary systems so that better understanding to the Eh-pH diagrams of those systems and their applications to the study of corrosion of metals can be obtained. This technique was later employed by Horvath and coworkers [148-50] to study more complex systems e.g. metal-sulphur-water tertiary systems in various environments e.g. H_2S (aq) solution. In addition, satisfactory results were obtained [146] by employing this technique to study the supergene weathering

of primary nickel iron sulphide assemblages.

The IGP technique can be considered as a special case of the cyclic chronopotentiometry technique. The difference is that in the former the system is successively maintained at open circuit conditions after periods of polarisation under constant current while in the latter the system is successively polarised under a second constant current eg with the same magnitude but opposite in direction. Similar to the chronopotentiometry technique, the experimental conditions e.g. duration (per cycle) and current of polarisation must be carefully chosen (*cf. Section 2.3.2.5*), especially when several electrode processes are involved & double layer capacity is not very small (i.e. charging time is considerably long). The response i.e. potential from the inducing electrode process is recorded as function of time.

After a sufficiently long period (total) of polarisation, the system is treated in a similar way to stripping voltammetry by altering the polarity of the polarisation current. This was found to be very efficient in this work in identifying, by comparison with results from cyclic voltammetry & stripping voltammetry, the species produced during the previous polarisation stage.

The transient behaviour of the system during the open-circuit period is of considerable importance in assessing e.g. the reaction mechanisms of the polarisation. This is because this behaviour always reflects the approach towards equilibrium & can thus be used to interpret the reaction mechanism during the polarisation.

2.4 Purities of materials

Copper Granules (-10 to +40 mesh), Batch No. 31140-5, Analytically pure (>99.9%), Aldrich Chemical Co. Ltd., Gillingham, Dorset, England.

Spectroscopic Analysis:

Iron (Fe)	< 5 ppm	Lead (Pb)	< 1 ppm
Silver (Ag)	< 2 ppm	Sodium (Na)	< 3 ppm

Copper Rod "Superquality", BICC Prescott Copper Refinery, Prescott, England.

Copper content > 99.99%. Metallic impurities less than 15 ppm (DC ARC graph identical to the Aldrich "Specpure" samples)

Silver Crystalline Pieces, Batch No. S. 90996, "JMC 54 Specpure", Johnson Mathey Chemicals Ltd. Royston, Hertfordshire, England

Spectroscopic Analysis:

Iron (Fe)	1 ppm	Magnesium (Mn)	< 1 ppm
Sodium (Na)	< 1 ppm		

Platinum sheet, Batch No. W 29986, "Puratronic" Johnson Mathey Chemicals Ltd., Royston, Hertfordshire, England

Spectroscopic Analysis:

Palladium (Pd)	6 ppm	Iron (Fe)	4 ppm
Copper (Cu)	2 ppm	Silver (Ag)	2 ppm
Silicon (Si)	1 ppm		

Platinum wire (0.1mm diam.) Batch No. 07125, "Puratronic" Johnson Mathey Chemicals Ltd., Royston, Hertfordshire, England

Spectroscopic Analysis:

Palladium (Pd)	3 ppm	Rhodium (Rd)	3 ppm
Nickel (Ni)	2 ppm	Copper (Cu)	1 ppm

Selenium powder (-100 mesh), Batch No. 22986-5, "Golden Label" (>99.99%), Aldrich Chemical Co. Ltd., Gillingham, Dorset, England

Spectroscopic Analysis:

Sulphur (S)	< 0.1 ppm	Arsenic (As)	< 0.5 ppm
Tellurium (Te)	< 1 ppm	Metallic matter	< 5 ppm

Ammonia Solution, BDH Analytical Reagent, BDH Chemicals Ltd., Poole, England

Ammonia (NH₃) 33.5%

Silver Nitrate Crystals, Batch No. 20913-9, A.C.S. Reagent (>99.9%),

Aldrich Chemical Co. Ltd., Gillingham, Dorset, England

Spectroscopic Analysis:

Chloride (Cl)	< 0.0002%	Sulphate (SO ₄)	< 0.001%
Copper (Cu)	< 0.0001%		

Silver Nitrate Crystals, Batch No. 20505-2 "GOLDEN LABEL" (99.998%),

Aldrich Chemical Co. Ltd., Gillingham, Dorset, England

Spectroscopic Analysis:

Chloride (Cl)	< 0.00003%	Sulphate (SO ₄)	< 0.0001%
Copper (Cu)	< 0.00001%		

Hydrazinium Chloride Crystals, Batch No. 28501, BDH "Analar" reagent,

BDH Chemicals LTd., Poole, England

Spectroscopic Analysis

Sulphate (SO ₄)	< 0.01%	Sulphated Ash	< 0.1%
Lead (Pb)	< 0.005%	Iron (Fe)	< 0.005%

Nitric Acid Batch No. 15954, Analytical Reagent, Vickers laboratories Ltd.,

Burley-In-Wharfedale, West Yorkshire, England

Nitric Acid (HNO ₃)	69.71%	Chloride (Cl)	< 0.00005%
Sulphate (SO ₄)	< 0.0002%	Arsenic (As)	< 0.000002%
Lead (Pb)	< 0.00002%	Non-volatile	< 0.001%

Perchloric Acid Batch No. 1873, Analytical Reagent, FSA Laboratory Supplies,

Loughborough, England

Perchloric Acid (HClO ₄)	69.5%	Ammonia (NH ₃)	< 5	ppm
Arsenic (As)	< 0.05	Chlorate (ClO ₃)	< 0.001	ppm
Chloride (Cl)	< 1	Copper (Cu)	< 0.1	ppm
Iron (Fe)	< 1	Lead (Pb)	< 0.1	ppm
Silver (Ag)	< 5	Sulphate (SO ₄)	< 5	ppm

Potassium Chloride Crystals Batch No. 10198, BDH "Analar" reagent,

BDH Chemicals LTd., Poole, England

Potassium Chloride	> 99.5%	Bromide (Br)	< 0.01%
Iodide (I)	< 0.002%	Sulphate (SO ₄)	< 0.003%
Lead (Pb)	< 0.0002%	Iron (Fe)	< 0.0002%

Ammonium Nitrate Crystals, Batch No. 10030, BDH "Analar" reagent,

BDH Chemicals LTd., Poole, England

Ammonium nitrate	> 99.5%	Chloride (Cl)	< 0.0002%
Nitrite (NO ₂)	< 0.0005%	Lead (Pb)	< 0.0002%
Sulphate (SO ₄)	< 0.005%	Copper (Cu)	< 0.0002%
Iron (Fe)	< 0.0001%		

3. Electrochemical Study of the Dissolution of Synthetic Copper-Silver-Selenide Minerals in Aqueous Media

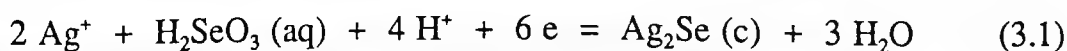
3.1 Potentiometric measurement

Potentiometric measurement at open circuit is generally described as an equilibrium technique & thus commonly used to study the thermodynamic properties of a system. For example, this technique can be used to verify thermodynamic predictions (usually based on the construction of the Pourbaix or Eh-pH diagrams. *cf. Section 1.3* for more details) of the possible reactions which may occur under certain conditions. During study of the dissolution of metal sulphide minerals, Sato [171] suggested that measurements of the 'single' electrode potential of sulphide minerals together with basic understanding of the electrode behaviour might help to clarify the oxidation or reduction mechanisms. As a result, the determination of electrode potential in oxidising or reducing solutions remained an essential tool for the elucidation of the 'first-step' heterogeneous reaction mechanism in the 1960's. The technique is relatively simple. It is ultimately based on the measurement of 'single' electrode potentials of sulphide minerals in various solutions containing the corresponding products. Thus by studying the relationship between the electrode potentials & the composition of the solution & by comparison with thermodynamic speculations, the equilibrium determining the electrode potential can thus be established.

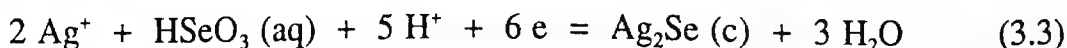
The open-circuit potentials of silver selenide electrodes in solutions containing varying amount of silver & aqueous species of selenium have been measured. The solutions of aqueous species of selenium were prepared by dissolving the required amounts of selenium powder in 1:1 HNO₃ solution. It is also worth mentioning that the open circuit potential drifts slightly towards more 'negative' values & therefore the system must be allowed to have a sufficiently

long period (normally 10 to 30 minutes) to approach equilibrium before ANY measurement is taken. As can be seen from *Figure 3.1*, the electrode potential of silver selenide depends approximately linearly on the logarithm of the concentration of silver ions. Statistical treatment using unweighed† least mean square methods on such a plot of yields a slope of 0.0522. In other words, the electrode potential of silver selenide in 1M HNO₃ solution shows a dependence of 52.2mV per decade change in the concentration of silver ions. The last point (at [Ag⁺] = 10⁻⁵ mol·dm⁻³) was excluded in the statistical treatment due to the difficulty of obtaining sensible measurements of the potential at low levels of concentration of silver ions in the solution. This helps to explain the observation that silver selenide adopts a ‘random’ rest-potential of approximately 0.3V to 0.45V in BOTH 1M HNO₃ & 1M HClO₄ solutions & in the absence of Ag⁺ at temperatures ranging from 295K to 335K.

An attempt was made initially to try to explain the above observed dependence of the open circuit potential of silver selenide on the concentration of Ag⁺ via thermodynamic considerations on the Ag-Se-H₂O system discussed in *section 1.3*. As is indicated in the Eh-pH diagrams (*cf. Figure 1.6*) the following reactions may be proposed as the potential determining processes in acid media:



$$E_{\text{V}} = 0.846 - 0.0394 \text{pH} + 0.00985 \log[\text{H}_2\text{SeO}_3] + 0.0197 \log[\text{Ag}^+] \quad (3.2)$$

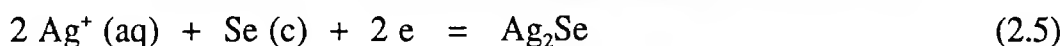


$$E_{\text{V}} = 0.846 - 0.0394 \text{pH} + 0.00985 \log[\text{HSeO}_3] + 0.0197 \log[\text{Ag}^+] \quad (3.4)$$

where [Ag⁺] = [Ag⁺]/mol·dm⁻³ etc.

However, neither of the above reactions agree with the observed potential dependence on the concentration of Ag⁺, because BOTH the reactions predict a much smaller slope for the E - log[Ag⁺] plot (theoretical value is 0.0197). A

better agreement was achieved by assuming the following reaction to be the potential determining equilibrium in acid medium:



The equilibrium potential of the above reaction can be expressed as a function of the concentration of aqueous silver ions via

$$E_{\text{V}} = 1.061 + 0.059 \log[\text{Ag}^+] \quad (2.6)$$

As can be seen from *Figure 3.2*, the pH independence of the electrode potential in moderately strong acid media (pH = 0 to 2) provides further support for the above proposal.

Similar observations have also reported for potentiometric studies on sulphide minerals e.g. galena (PbS) [162] & acanthite (Ag₂S) [148,150,161]. The equilibria determining the electrode potential in these cases are reported to be:



&



respectively. In addition, the formation of elemental sulphur rather the higher valence state namely HSO₄⁻ or SO₄²⁻ as the oxidation product from many sulphide systems gives further evidence for the above observation.

In contrast to silver selenide, there is no simple dependence of the electrode potential of synthetic copper silver selenide on the concentration of the possible oxidation product ions e.g. Cu²⁺ (aq) & Ag⁺ (aq). This is presumably due to the complexity of the ternary system. In general, copper silver selenide adopts a relatively 'definite' open circuit potential of approximately 0.3V in BOTH 1M HNO₃ & 1M HClO₄ solutions & in the absence of Ag⁺ (aq) at temperatures ranging from 295K to 335K.

Table 3.1 Open-circuit potentials of silver selenide electrodes in nitric acid solutions containing varying amounts of Ag^+ (aq).

$\text{[Ag}^+]$ mol·dm ⁻³	10^{-5}	10^{-4}	10^{-3}	10^{-2}	5×10^{-2}	10^{-1}
E (V vs. SCE)	0.435	0.574	0.624	0.662	0.701	0.743

Temperature = 295K, $[\text{HNO}_3] = 1\text{M}$, $[\text{SeO}_3^{2-}] = 10^{-3} \text{ mol}\cdot\text{dm}^{-3}$.

Table 3.2 Influence of the acidity of the electrolyte on the open-circuit potentials of silver selenide electrodes.

pH	0.155	0.553	0.986	1.383	1.696	1.988
E (V vs. SCE)	0.695	0.700	0.711	0.702	0.693	0.688

Temperature = 295K, $[\text{Ag}^+] = 5 \times 10^{-2} \text{ mol}\cdot\text{dm}^{-3}$, $[\text{SeO}_3^{2-}] = 10^{-3} \text{ mol}\cdot\text{dm}^{-3}$.

Ionic strength 'compensated' by addition of required amount of KNO_3 .

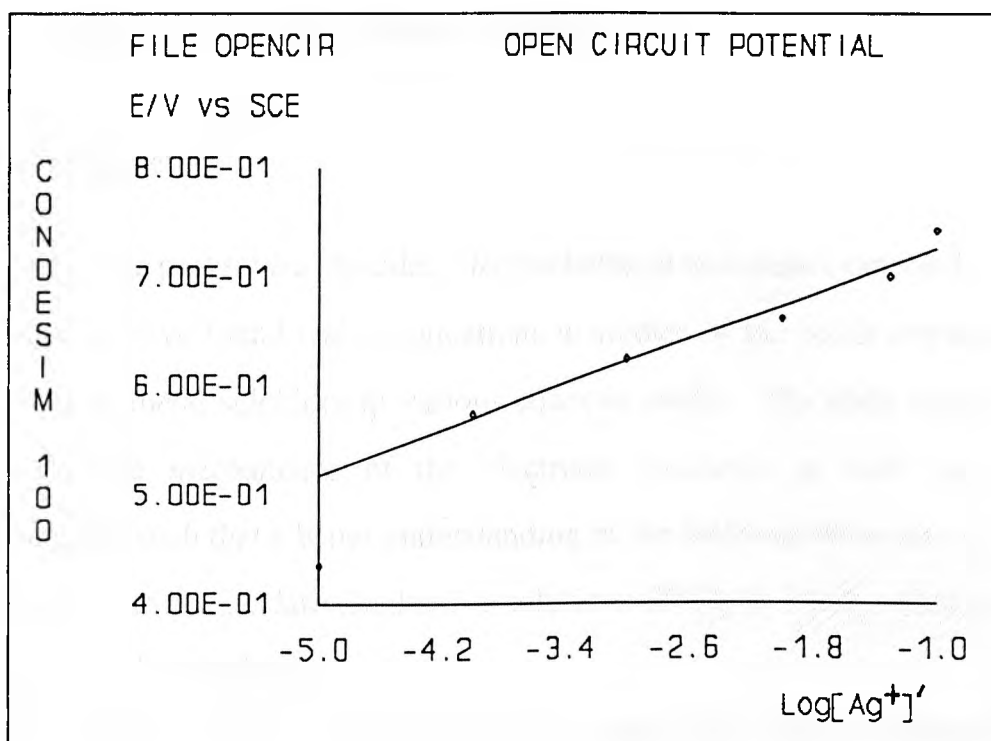


Figure 3.1 Plot of open circuit potential of Ag_2Se as a function of logarithmic concentration of silver ions. Data is listed in *Table 3.1*.

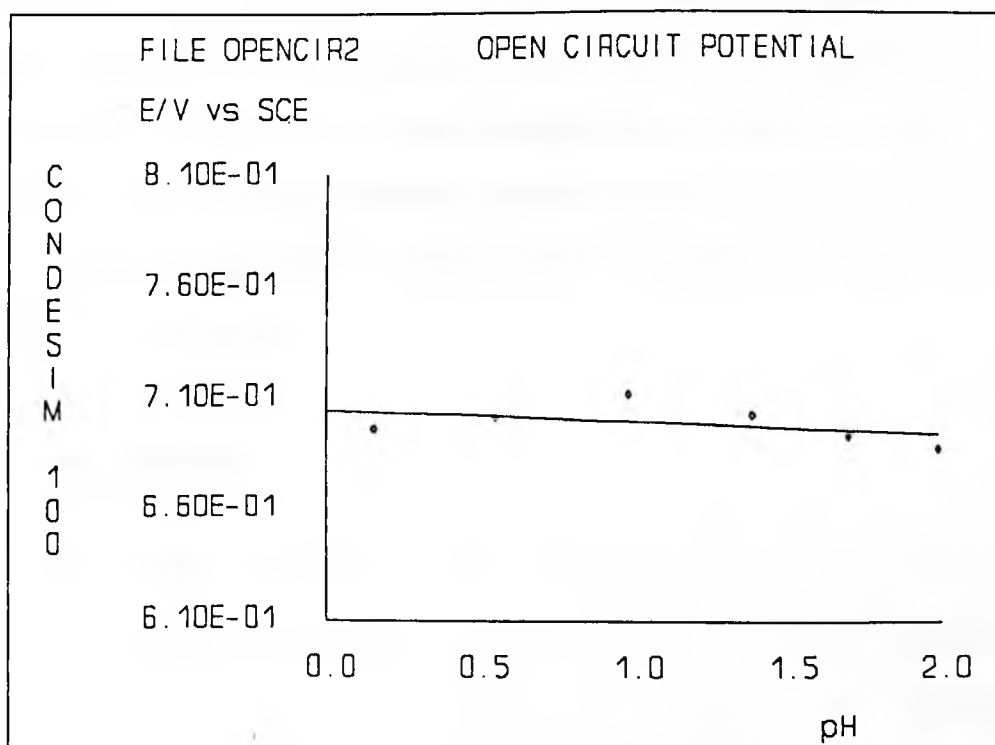


Figure 3.2 Plot of open circuit potential of Ag_2Se versus the pH value of the solution. Data is listed in *Table 3.2*.

3.2 Cyclic Voltammetry (Linear Sweep)

3.2.1 Introduction

Over the past several decades, electrochemical techniques especially cyclic voltammetry have found wide applications in studies of the oxidation/reduction behaviour of metal sulphides in various aqueous media. The main objective is to clarify the mechanisms of the electrode processes in well controlled environments such that a better understanding of the leaching behaviour of these minerals in various oxidative/reductive solutions (FeCl_3 & CuCl_2 solutions, for example) can be obtained.

In general, cyclic voltammetry can be used for BOTH quantitative & qualitative studies of a variety of electrochemical processes. However, due to the complexity caused by the involvement of a solid phase in the oxidation/reduction of mineral electrodes, quantitative evaluation of electrochemical parameters e.g. standard heterogeneous rate constant (k^0) etc. seems to be inapplicable. As a consequence, in this section we shall mainly discuss the employment of cyclic voltammetry (linear sweep) technique for the mechanistic studies of the synthetic silver selenide & copper silver selenide electrodes in acid media e.g. 1M HNO_3 & 1M HClO_4 solutions.

3.2.2 Silver Selenide

Voltammetric responses resulting from the supporting electrolytes e.g. 1M HNO_3 & 1M HClO_4 solutions are briefly studied as a precaution because the "voltammetric window" of the 'background' electrolyte is of considerable importance in choosing anodic & cathodic limits of the potential scan. Typical cyclic voltammograms for 1M HNO_3 & 1M HClO_4 solutions at 305K on a platinum electrode of similar geometry to the mineral electrodes are shown in

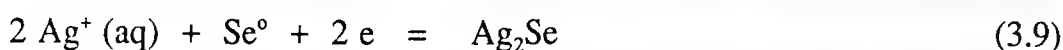
Figures 3.3 & 3.4. As can be seen, the responses from both electrolyte media are very similar. The sharp increase of current at around 1.5V vs. SCE is due to the discharge of OH^- (aq) ions to produce O_2 while that at - 0.3V vs. SCE is caused by evolution of hydrogen gas via reduction of H^+ (aq). In practice, the reduction of hydrogen on selenide mineral electrodes occurs at potentials much more negative than that on platinum due to the appreciable overpotential for hydrogen evolution. This in turn allows a much wider 'voltage window' to be used with 'safety'. The current peak at around 0.4V vs. SCE on the returning wave is probably caused by the adsorption of H^+ (aq) ions onto the platinum electrode surface. Basically, within potential regions of practical interest for leaching of selenide minerals (i.e. lower than 1.0V vs. SCE for most oxidants), the 'background current' is negligible compared to the 'massive' current resulting from the oxidation or reduction of the selenide mineral electrodes.

Voltammetric studies of silver selenide electrodes were carried out mainly in 1M HNO_3 & sometimes in 1M HClO_4 solutions at temperatures mainly 295K, 305K & 325K. The latter corresponds to the leaching practice for anode slimes recommended by Zhou [14]. *Figures 3.5-3.10* show cyclic voltammograms for silver selenide in 1M HNO_3 & 1M HClO_4 solutions at a temperature of 305K with or without rotating the electrodes. As can be seen, the rotation of the electrodes did not cause noticeable changes to the current-potential responses, which suggests that mass transport processes in the aqueous phase does not play a significant role in determining the rate. This is consistent with the observations by Parker [31,35] during leaching of chalcopyrite that the extraction rate of copper is almost independent of the speed of stirring (agitation).

On the other hand, appreciable anodic currents or 'oxidative dissolution rates' for silver selenide were obtained ONLY in relatively high potential regions (e.g. > 0.8V vs. SCE), which substantially departed from the "rest" potential. In other words, a sufficiently large overpotential is required to obtain a reasonable

rate of anodic dissolution of the silver selenide electrodes. This type of behaviour was observed even in the first cycle of the potential scan & thus the influences of elemental selenium or other possible product layers were ruled out. The considerable departure of the current peak from the thermodynamic standard potential for oxidation of silver selenide to silver ions & elemental selenium implies that, in the absence of other processes generating a mixed potential, the oxidation process involves a relatively slow electron transfer, which possibly plays an important role in determining the pace of the entire process.

Potentiometric measurements on silver selenide electrode conducted earlier in this work (*cf. Section 3.1*) indicate that the potential determining step in strong acid (1M HNO₃) is indeed the equilibrium between Ag⁺ (aq), Se⁰ & Ag₂Se via:



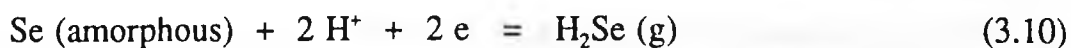
This is further confirmed by cyclic voltammetry results as shown in *Figures 3.5-3.10*. In the first cycle, as the potential initially scanned anodically (*Figures 3.5-3.7*), single peak shaped current-potential responses were observed. On the other hand, if the electrode was subjected to an initial cathodic excursion, an additional current on the subsequent anodic scan was observed due to the dissolution of metallic silver produced via the reduction of silver selenide during the cathodic excursion (*cf. Figures 3.8-10*).

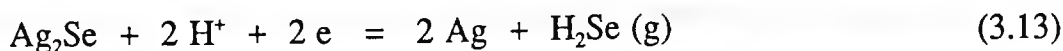
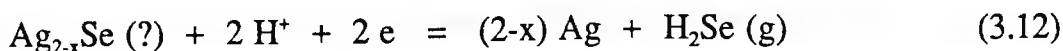
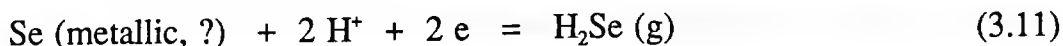
Thermodynamically, the current peak at large anodic potentials (1.0V vs. SCE) may be attributed to the oxidation of silver selenide via several routes as is indicated in the Eh-pH diagrams (*cf. Figure 2.6*). However, the appearance of the reduction peaks of Ag⁺ (at 0.5V to 0.6V vs. SCE) & selenium (at 0.1 to 0.3V vs. SCE) on the returning wave gave strong support for the proposal that silver selenide is at least partly oxidised to Ag⁺ & elemental selenium by forcing the above equilibrium (*equation 3.9*) towards the left hand direction at large anodic potentials. In addition, the lack of selenium species in the solution

sampled in the high potential region ($> 0.7V$) via AAS analysis gave further evidence for the assumption that a majority of the oxidation product of the selenium in silver selenide is elemental selenium (or intermediate product of silver-selenium compounds ?) rather than high valence species e.g. $HSeO_3$ or SeO_4^{2-} . The surface of the silver selenide, immediately retrieved from the electrolyte after an anodic excursion from the rest potential to $0.9V$ vs. SCE, showed a very thin brown/red tarnish (film ?) which was considerably different from the oxidation of sulphide minerals. In the latter case, relatively thick layer of sticky (glassy ?) sulphur was observed [147].

The deposition of silver ions, liberated during the oxidation, at $0.5V - 0.6V$ vs. SCE on the returning potential scan was further confirmed by a series of cyclic voltammetry experiments (*cf. Figures 3.23-3.24*). The peak at the above potential region gradually built up with the increase of the anodic potential limit. This gave a clear evidence of the dependence of this peak on the degree of the oxidation of the silver selenide electrode. However, when the electrode was rotated, this peak became less apparent probably due to the enhanced mass transport of silver ions to the bulk of the electrolyte (*cf. Figure 3.19-20 & 25-26*). The deposition of silver in this potential region is further proved by the observation of silver crystals on the silver selenide electrode surface via SEM & EDXA analysis (*cf. Figures 3.31 & 3.32*). The samples for analysis were the selenide electrodes which were removed from the electrolyte immediately after passing the potential region for silver deposition on the returning sweep.

As the potential scanned further cathodically, TWO other distinctive peaks appeared. These were due to the reduction of the product of the oxidation of silver selenide at higher anodic potentials or the reduction of the silver selenide electrode itself via the following possible reactions:





Figures 3.11-22 shows the dependence of the cathodic peaks on the degree of anodic oxidation of silver selenide electrode by progressively increasing the anodic potential limits. As the anodic limits increase the cathodic peaks become more & more apparent. This gives further evidence for the assumption that the above observed peaks on the cathodic excursion are caused by the reduction of a product formed via oxidation of silver selenide electrodes during the preceding anodic treatment.

As is shown in *Figures 3.25-26*, by slightly increasing the cathodic limits to just past the first peak but before the second one, a relatively large peak is obtained, at the potential region of silver dissolution, on the following anodic excursion. The increase in the peak current is apparently due to the increased amount of elemental silver produced via the reduction of either an intermediate silver selenium compound which was produced during the previous anodic scan or the reduction of silver selenide electrodes. The reduction of elemental selenium at this stage is ruled out because it cannot increase the amount of elemental silver on the electrode surface!

The current peak immediately adjacent to the first one is likely to be caused at least partly by the reduction of elemental selenium produced from anodic dissolution of silver selenide. An important feature at the TWO adjacent cathodic peaks is that gas bubbles developed gradually on the electrode surface, followed by a dramatic colour change of the aqueous solution from colourless to brown-red. This provides further evidence for the evolution of hydrogen selenide because the reduction of hydrogen ions in the solution is unlikely to occur at such a high potential region ($> 0.1\text{V}$ vs. SCE, which is equivalent to $> 0.34\text{V}$ vs.

SHE). Furthermore, the high overpotential of hydrogen evolution on silver (product layer) surfaces causes further difficulty for the reduction of aqueous hydrogen ions. The assumption that metallic silver is produced during the cathodic excursion was further confirmed via EDXA analysis of silver selenide electrodes immediately after cathodic treatment (*cf. Figure 3.33*). Comparable results have also been obtained via stripping voltammetry & intermittent galvanostatic polarisation (IGP) experiments.

However, due to the insensitivity of XRD for detecting the intermediate product (which is probably caused by the difficulty of collecting a sufficient amount of representative samples. *cf. Section 3.4*), the mechanism of the anodic dissolution of silver selenide is still unclear. For example, it is uncertain whether one of the cathodic peaks on the cathodic excursion is contributed by the direct reduction of silver selenide or the reduction of a possible intermediate product formed during the preceding anodic excursion. The lack of apparent reductive current peaks in the first cycle of an initially cathodic excursion might suggest that the reduction of silver selenide did not occur in the above potential regions. Nonetheless, this may be due to the low activity of a freshly polished surface. Besides, the reduction of silver selenide in these potential regions is thermodynamically feasible. Previous studies on some sulphide minerals, such as silver sulphide [148,161,171,172], also suggest that direct reduction of mineral electrodes to metallic silver & hydrogen sulphide is possible.

Cyclic voltammograms of silver selenide in 2M HNO₃ & 2M HClO₄ solutions at 325K are shown in *Figures 3.27-28*. Note that, in contrast to the 'incomplete' voltammograms illustrated in *Figures 3.5-10*, the entire anodic peaks are recorded in *Figures 3.27-28*. The former might lead to false conclusion that the silver selenide electrodes dissolve at 'unlimited' rate at larger overpotentials.

In fact, the faradaic current resulting from MOST simple electrode

processes conforms to peak-shaped behaviour. Current gradually approaches a limiting value as the diffusion field of the reactant builds up steadily within a layer immediately adjacent to the electrode surface. See *Figure 3.29* for an illustration of the concentration profile of a system involving the corrosion of an alloy [173]. In other words, the 'surface' concentration of the reactant decreases until the depletion of this species at the reaction 'front' is complete. In stationary experiments, the magnitude of the peak current reflects several parameters associated with the reactant, e.g. the BULK concentration & diffusion coefficient of the reactant, & heterogeneous & possibly homogeneous chemical kinetics. When the potential is well past the wave, the transport of the reactant from the BULK solution (or solid) to the electrode surface gradually becomes the dominant step over electron transfer in determining the overall rate.

The above discussion applies to aqueous & non-aqueous solvent systems (*cf. Section 4* for more detail about theoretical development for systems where BOTH the reactant & product are ONLY present in aqueous medium) as well as systems involving solid phase(s) [173]. Failure to understand this might lead to inappropriate interpretation of the cyclic voltammograms. During electrochemical studies of acanthite (Ag_2S) in sulphuric acid solution (*cf. Figure 3.30*), Price [161,172] concluded that "the decrease in current observed at potentials higher than about 1.2V" is caused by "a covering of the electrode surface with Ag_2SO_4 ". The formation of the protective Ag_2SO_4 film may have a retardation effect on the mass transport of Ag^+ (aq) ions from the $\text{Ag}_2\text{S}/\text{Ag}_2\text{SO}_4$ (& possibly elemental sulphur) boundary to the BULK of the electrolyte. This in turn affects the observed "extraction rate" of silver. However, this is, obviously, not the determining factor for the current.

In an attempt to explain the electrochemical behaviour of pentlandite, Warner [147] observes that the low leaching rate is due to the retardation effect of amorphous sulphur which decreases the effective area of the electrode and/or

produces a passive film which hinders ionic mass transport in the aqueous phase adjacent to the pentlandite surface. However, there are only slight differences between the resulting faradaic currents from successive scans & the formation of the sulphur layer on the pentlandite electrode surface does not seem to have the anticipated progressive effect [147]. In addition, though the sulphur layer may have some retardation effect on the mass transport of the liberated metal ions to the bulk of the electrolyte, it apparently cannot impose any restrictions to the discharge of the metal atoms in the pentlandite lattice. Similar mechanisms have also been proposed by Parker [31,35] & MacMillan [36] to explain the leaching behaviour of sulphide minerals such as chalcopyrite (CuFeS_2). The retardation of the dissolution of copper is attributed to electron transfer & ionic mass transport through either an intermediate metastable film of "semi-conductor metal deficient polysulphide" [31,35] or "solid electrolyte interface" [36], instead of sulphur layer.

During studies of leaching of CuFeS_2 with CuCl_2 solution at 343K, Hirato [174] observed that the leaching rate of copper is proportional to the ratio $[\text{CuCl}_2]^{1/2}/[\text{CuCl}]^{1/2}$. This can be readily explained on purely thermodynamic grounds. The increase in the ratio $[\text{CuCl}_2]/[\text{CuCl}]$ produces a higher equilibrium potential for the above redox couple & thus it is equivalent to increasing polarisation potentials in potentiostatic experiments (*cf. Section 3.4* for more detail about chronoamperometry experiments). The general trend would be an initial increase in resulting faradaic current which decreases with time in a similar fashion to the $i-t^{1/2}$ transient as the electrode process gradually approaches the 'DIFFUSION-controlled' regime. This is comparable with the observation of the parabolic kinetics for extraction rate of copper [174].

To summarise, the anodic dissolution of silver selenide involves a slow electron transfer process, which probably plays an important role in determining the rate of the oxidative leaching of silver selenide. Cyclic voltammetry

experiments also indicate that a large anodic potential is required in order to obtain a reasonable rate for silver extraction. This also indicates that at relatively higher potentials & longer times the dissolution of silver selenide is ultimately limited by the 'self-diffusion' of silver atoms within the solid phase.

3.2.3 Copper Silver Selenide

In general, the voltammetric (linear sweep) behaviour of the ternary compound copper silver selenide (CuAgSe) is very similar to that of silver selenide. Typical cyclic voltammograms for copper silver selenide in 1M HNO₃ solution & occasionally in 1M HClO₄ solution at a temperature of 303K are shown in *Figures 3.34-3.37*. Again, an important feature of the cyclic voltammograms is that the speed of rotation of the electrodes did not cause noticeable changes to the current-potential responses. This again suggests that mass transport processes in the aqueous phase do not play a significant role in determining the rate.

As the potential scans anodically from the rest ('open-circuit') potential, the resulting faradaic current from the system increases steadily until the relatively high potential region (e.g. > 0.8V vs. SCE) is reached, where a large anodic peak is observed. In other words, a sufficiently large overpotential is required to obtain a reasonable rate of anodic dissolution of the copper silver selenide electrodes. Similarly to the synthetic silver selenide, the current-potential responses resulting from successive scans are almost identical. This suggests that the formation of product layer (e.g. selenium & possibly intermediate silver-selenium product) does not significantly retard the dissolution of the copper silver selenide electrodes. This is consistent with the results obtained by Montoya-Jurado [15] during the kinetic studies of the nitric leaching of copper silver selenide. He concludes that the formation of selenium does not slow the dissolution of copper. The considerable departure of the current peak from the

thermodynamic standard potential implies that the oxidation of the copper silver selenide also involves a relatively slow electron transfer, which possibly plays an important role in determining the rate.

The resulting faradaic currents from the copper silver selenide - 1M HNO₃ or 1M HClO₄ electrolyte systems are slightly greater than those obtained in the corresponding silver selenide systems. This suggests a higher reactivity for the copper silver selenide which is probably caused by the interaction (catalytic) between the silver ions, released from the oxidation of copper silver selenide itself, & the solid phase. Similar behaviour has also been observed during the kinetic studies of nitric leaching of synthetic components of copper anode slimes, e.g. copper selenide, silver selenide, copper silver selenide & mixtures of some of these pure materials [15]. Preferential leaching of copper has also been observed for commercial anode slimes during leaching with nitric acid (2-4M) solution [14]. The large ratio of copper to silver in the aqueous solution (AAS reveals that Cu:Ag ratio is greater than 30:1 in the solution) in the higher potential region & the lack of apparent reduction of silver ions Ag⁺ on the reverse scan give a further indication of the above assumption. Attempts have been made at this stage to identify possible products which might be present in the selenide electrode. Analytical techniques used include SEM, EDXA & XRD. However, due to the insensitivity of XRD etc., no positive evidence has been found for the formation of intermediate products, though the appearance of reduction peaks on the reverse (cathodic) scans may suggest the possible presence of an intermediate or transitional layer between the bulk of the copper silver selenide & the electrode surface. The sample for XRD was collected from several copper silver selenide electrodes under identical experimental conditions. On the other hand, the lack of selenium species in the solution via AAS analysis suggests that the oxidation product of selenium is at least partly elemental selenium. The observed colour change of the electrode from metallic 'shiny'

state to brown (red ?) & the appearance of the current peak on the cathodic excursion in the potential region characterised by selenium reduction (*cf. Eh-pH diagrams in Section 1.3*) give further evidence of the proposal for formation of elemental selenium.

The above observed results seems to be in good agreement with those obtained from other electrochemical techniques e.g. stripping voltammetry (linear sweep), chronoamperometry, intermittent galvanostatic polarisation (*cf. Sections 3.3, 3.4 & 3.6*). Especially, it is worthwhile mentioning that the observation (via EMPA, *cf. Section 3.4*) of Ag_2Se on the copper silver selenide electrode surface under potentiostatic conditions confirms the assumption of the catalytic effect displayed by silver ions.

Similar to cyclic voltammograms for synthetic silver selenide, current-potential responses from copper silver selenide electrodes on the cathodic excursions also display several reduction peaks which are likely to be caused by the successive reduction of the products of oxidation of copper silver selenide during the preceding anodic scan. The dependence of the magnitudes of these reduction peaks on the degree of anodic oxidation as illustrated via a series cyclic voltammetry experiments with progressively increasing anodic potential limits (*cf. Figures 3.38-42*) gives further evidence for the above proposal. As mentioned previously, the characteristic reduction peak for aqueous silver ions becomes much less apparent due to the low concentration of Ag^+ in the solution (especially near the electrode surface). The two adjacent peaks observed for silver selenide are also observed for copper silver selenide in a similar potential region (0.1V to 0.3V vs SCE) on the cathodic excursions, although a slight 'overlapping' of the two peaks is evident. This is possibly caused by the reduction of Cu^{2+} to Cu^+ (elemental copper was not observed by EDXA) in that potential region. Attempts to 'isolate' these peaks proved to be unsuccessful. Another feature of the copper silver selenide electrodes is that the second of the

adjacent peaks is much broader than that for silver selenide. This is probably due to the complexity of the oxidation products or the reduction of copper silver selenide. A change in colour of the solution from colourless to brown-red is also observed while gas bubbles gradually develops on the electrode surface. This indicates that hydrogen selenide gas is produced from the reduction of materials on the copper silver selenide electrode since the reduction of hydrogen ions in the electrolyte on copper silver selenide electrode does not occur until a large negative potential ($<-0.5V$ vs. SCE) is applied. The appearance of a relatively large anodic peak (which is initially absent in the first anodic excursion) in similar potential region as that observed for the dissolution of elemental silver in the voltammetric studies of silver selenide indicates that elemental silver is produced via the reduction of copper silver selenide and/or intermediate products e.g. Ag_2Se & silver rich product layer. This peak is, to a certain degree, dependent on the first of the two adjacent peaks as is demonstrated in *Figures 4.43-44*). By progressively increasing the cathodic limits, the magnitudes of the anodic peak, corresponding to silver dissolution, on the following anodic excursions increases accordingly. This gives a strong indication of the formation of elemental silver in this potential region since the magnitudes of the peak for deposition of silver ions remain virtually 'unchanged'.

Cyclic voltammograms for copper silver selenide in 2M HNO_3 & 2M $HClO_4$ solutions at 330K & various sweep rate are shown in *Figures 3.45-49*. Generally, these voltammograms are very similar to those observed at relatively lower temperatures (303K, *cf.* 3.34-37). The general trend of slight increase in resulting faradaic currents is consistent with the observation of increasing leaching rate for copper in nitric acid leaching of copper silver selenide [14,15]. The increase in the resulting faradaic currents from the copper silver selenide electrodes - electrolyte systems on successive scans gives further evidence for the proposal of catalytic effect of silver ions.

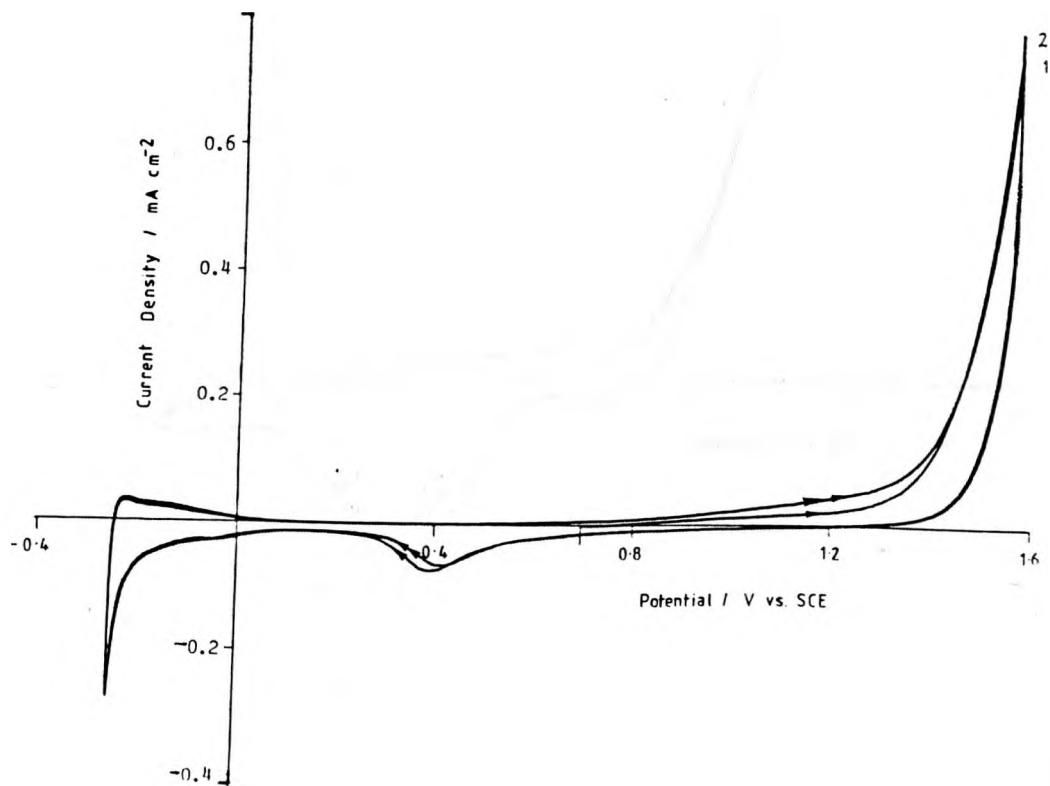


Figure 3.3 Cyclic voltammogram for platinum in 1M HNO_3 solution (stationary, N_2 saturated) at $305 \pm 0.5\text{K}$. Successive scans: initially anodic of rest potential (0.566V vs SCE), followed by cathodic excursions.

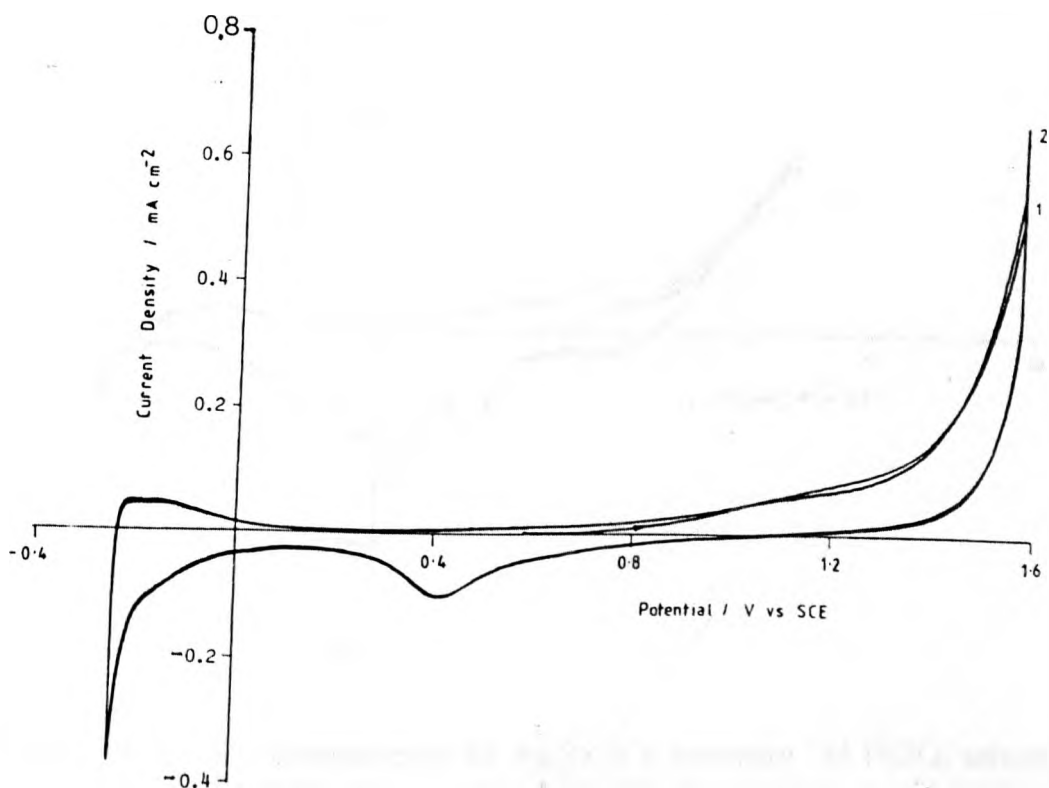


Figure 3.4 Cyclic voltammogram for platinum in 1M HClO_4 solution (stationary, N_2 saturated) at $305 \pm 0.5\text{K}$. Successive scans: initially anodic of rest potential (0.620V vs SCE), followed by cathodic excursions.

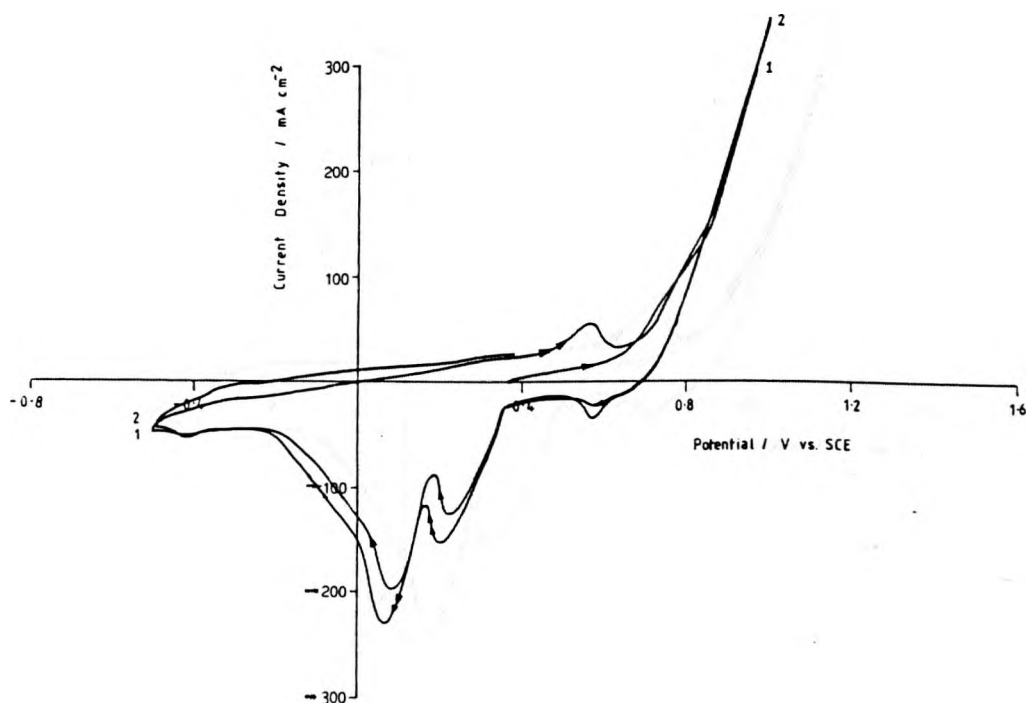


Figure 3.5 Cyclic voltammogram for Ag_2Se in a stationary 1M HNO_3 solution at $305 \pm 0.5\text{K}$. Sweep rate : 0.01 Vs^{-1} . Successive scans: initially anodic of E_{rest} (0.387 V vs. SCE), followed by cathodic excursions.

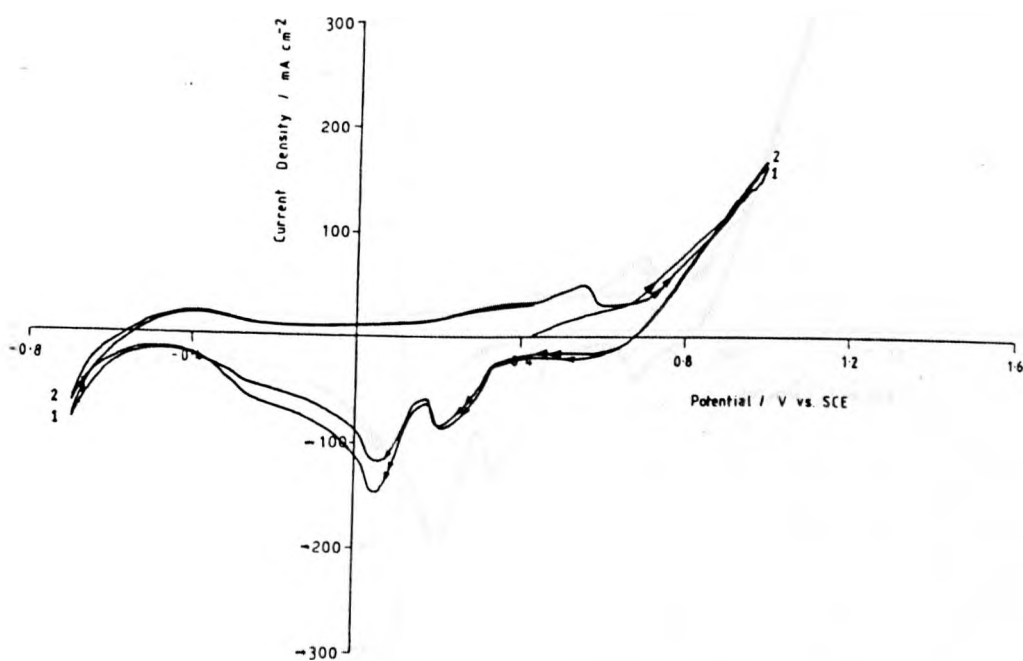


Figure 3.6 Cyclic voltammogram for Ag_2Se in a stationary 1M HClO_4 solution at $305 \pm 0.5\text{K}$. Sweep rate : 0.01 Vs^{-1} . Successive scans: initially anodic of E_{rest} (0.405 V vs. SCE), followed by cathodic excursions.

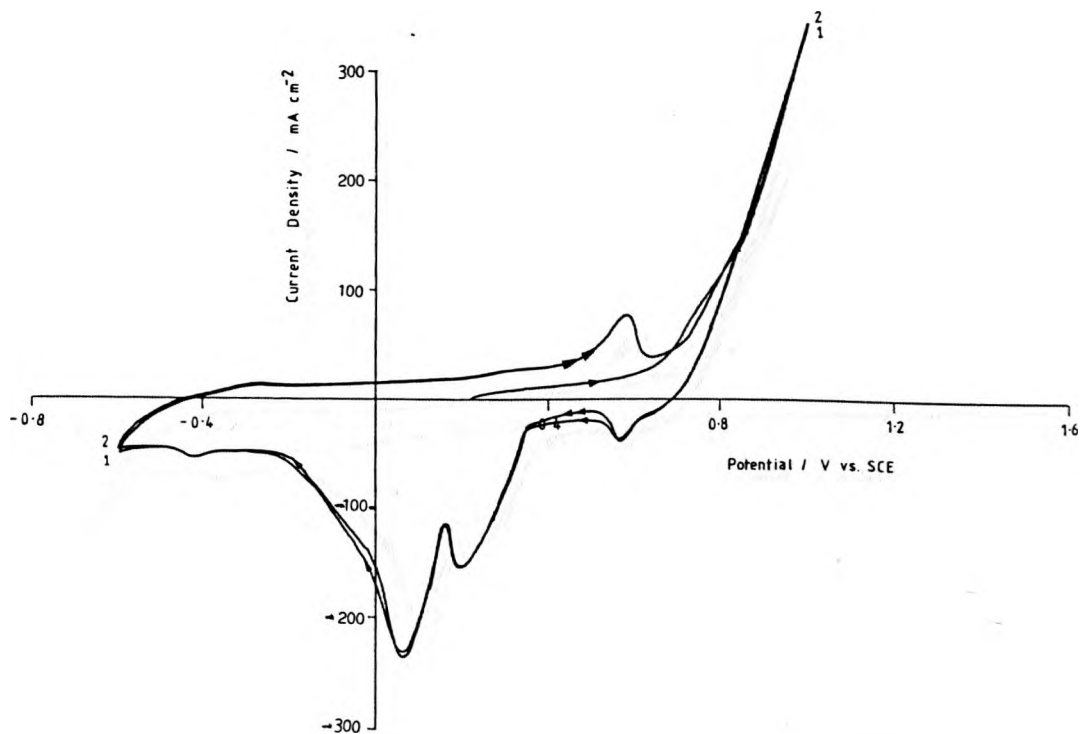


Figure 3.7 Cyclic voltammogram for Ag_2Se in 1M HNO_3 solution at $305 \pm 0.5\text{K}$. RDE : 1200rpm. Sweep rate : 0.005 Vs^{-1} . Successive scans: initially anodic of E_{rest} (0.321 V vs. SCE), followed by cathodic excursions.

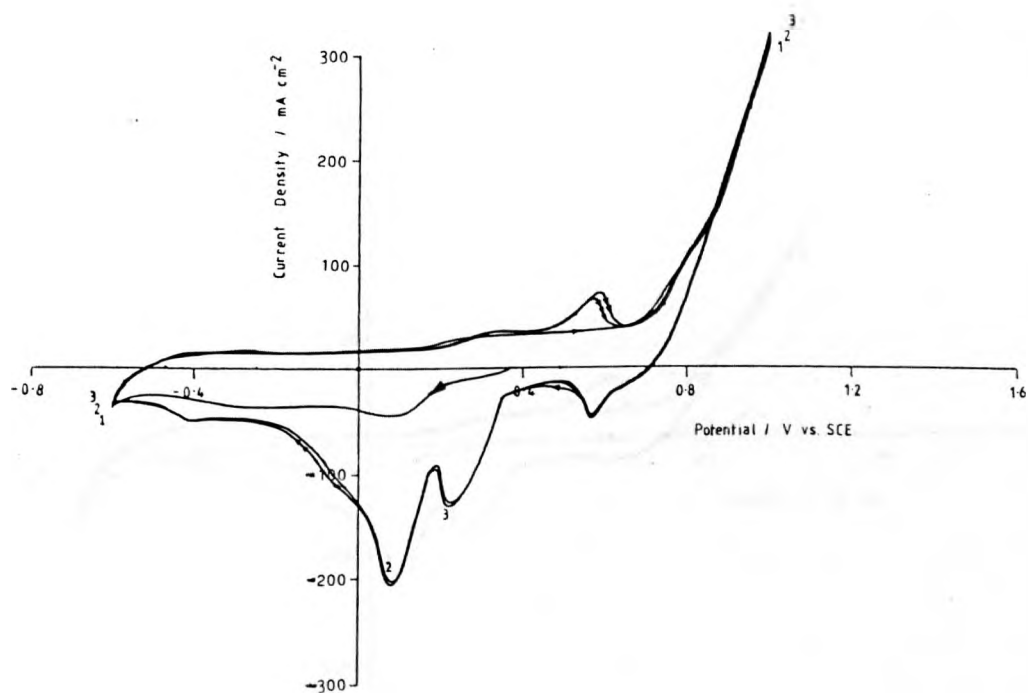


Figure 3.8 Cyclic voltammogram for Ag_2Se in a stationary 1M HNO_3 solution at $305 \pm 0.5\text{K}$. Sweep rate : 0.01 Vs^{-1} . Successive scans: initially cathodic of E_{rest} (0.392 V vs. SCE), followed by anodic excursions.

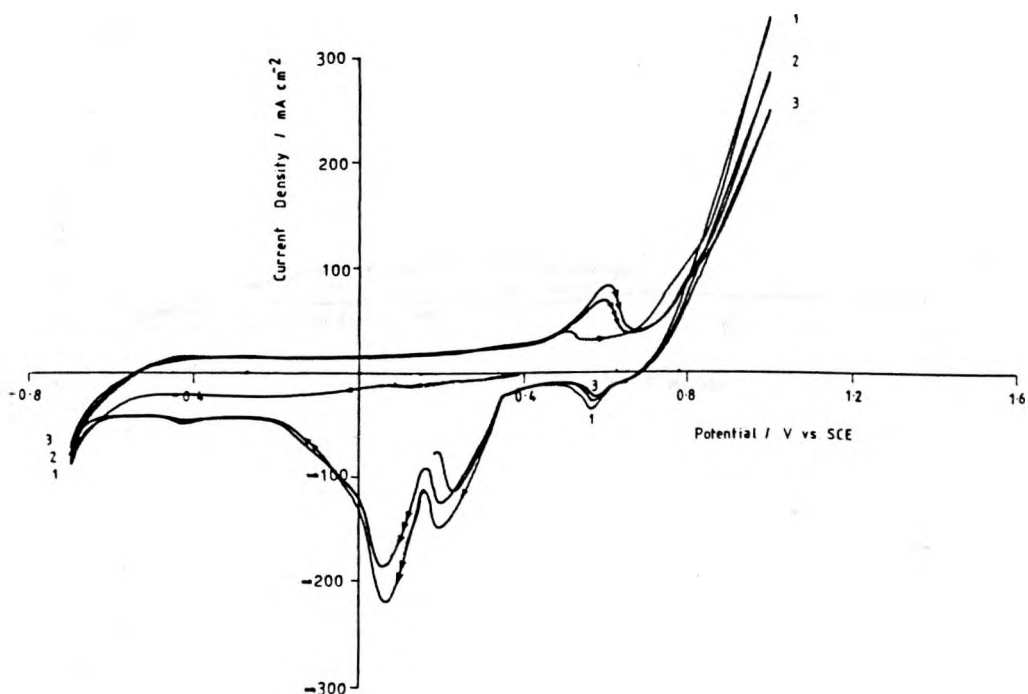


Figure 3.9 Cyclic voltammogram for Ag_2Se in a stationary 1M HClO_4 solution at $305 \pm 0.5\text{K}$. Sweep rate : 0.01 Vs^{-1} . Successive scans: initially cathodic of E_{rest} (0.395 V vs SCE), followed by anodic excursions.

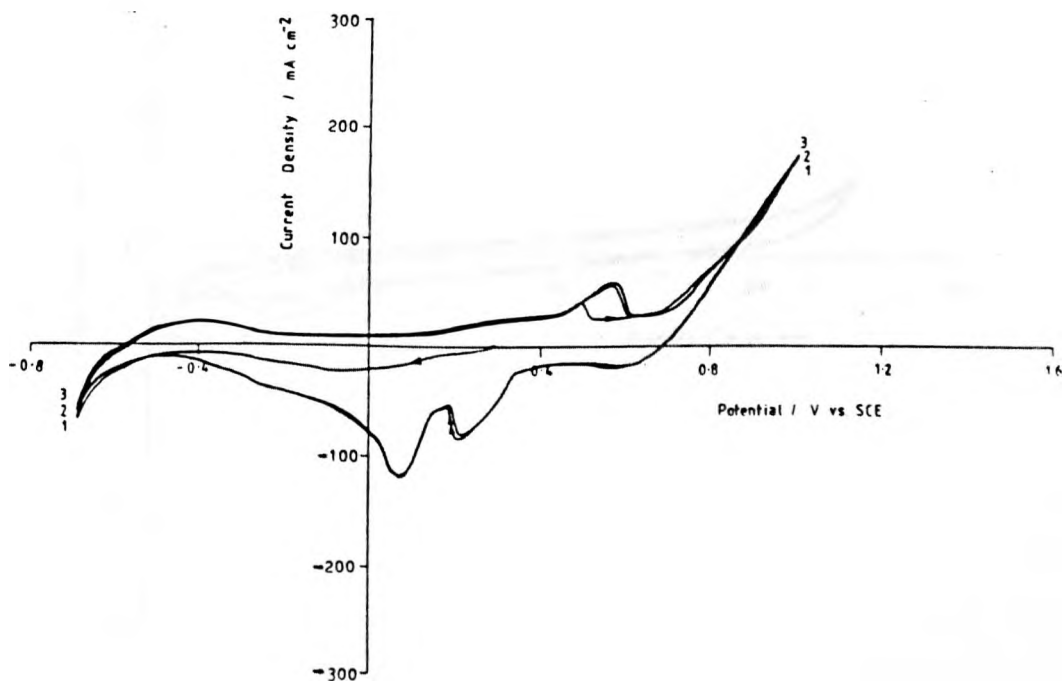


Figure 3.10 Cyclic voltammogram for Ag_2Se in 1M HNO_3 solution at $305 \pm 0.5\text{K}$. RDE : 1200rpm. Sweep rate : 0.01 Vs^{-1} . Successive scans: initially cathodic of E_{rest} (0.316 V vs SCE), followed by anodic excursions.

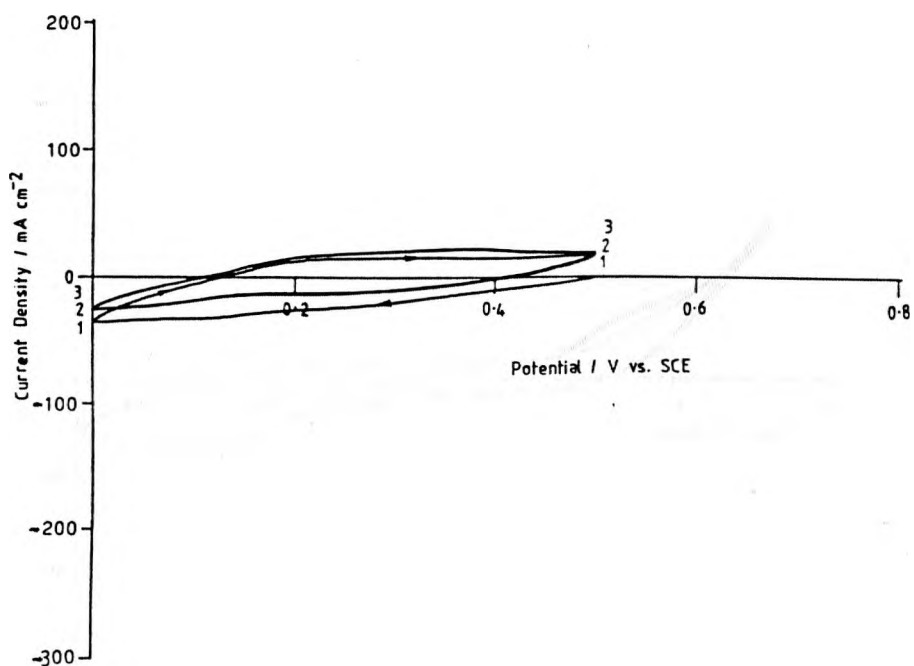


Figure 3.11 Cyclic voltammogram for Ag_2Se in a stationary 1M HNO_3 solution at $295 \pm 0.5\text{K}$. Sweep rate : 0.01 Vs^{-1} . Successive scans: initially cathodic of E_{rest} (0.393 V vs. SCE), followed by anodic excursions.

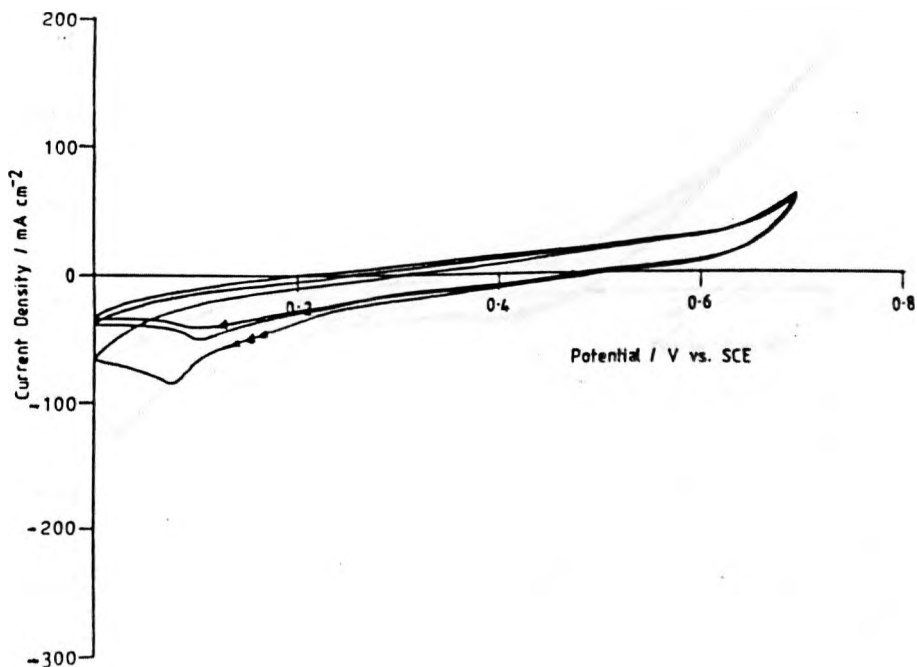


Figure 3.12 Cyclic voltammogram for Ag_2Se in a stationary 1M HNO_3 solution at $295 \pm 0.5\text{K}$. Sweep rate : 0.01 Vs^{-1} . Successive scans: initially cathodic of E_{rest} (0.461 V vs. SCE), followed by anodic excursions.

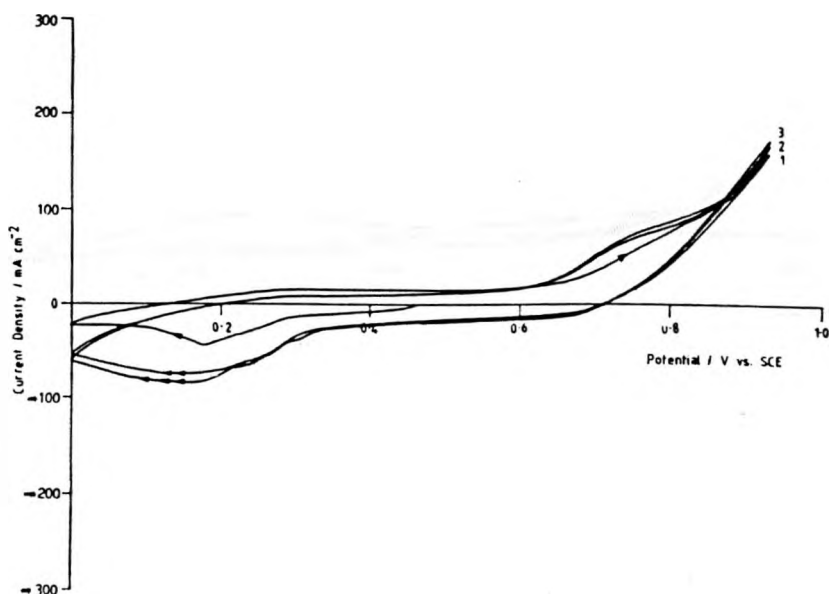


Figure 3.13 Cyclic voltammogram for Ag_2Se in a stationary 1M HNO_3 solution at $295 \pm 0.5\text{K}$. Sweep rate : 0.01 Vs^{-1} . Successive scans: initially cathodic of E_{rest} (0.466 V vs. SCE), followed by anodic excursions.

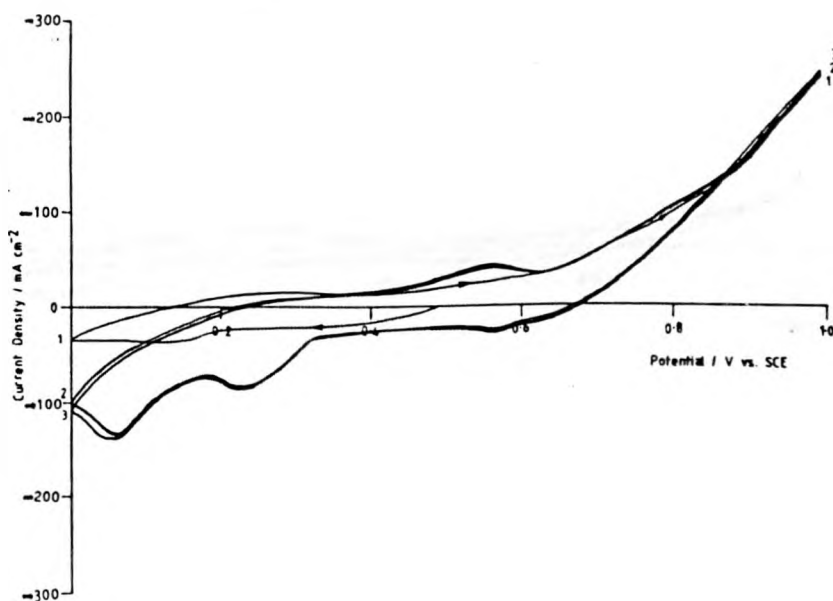


Figure 3.14 Cyclic voltammogram for Ag_2Se in a stationary 1M HNO_3 solution at $295 \pm 0.5\text{K}$. Sweep rate : 0.01 Vs^{-1} . Successive scans: initially cathodic of E_{rest} (0.489 V vs. SCE), followed by anodic excursions.

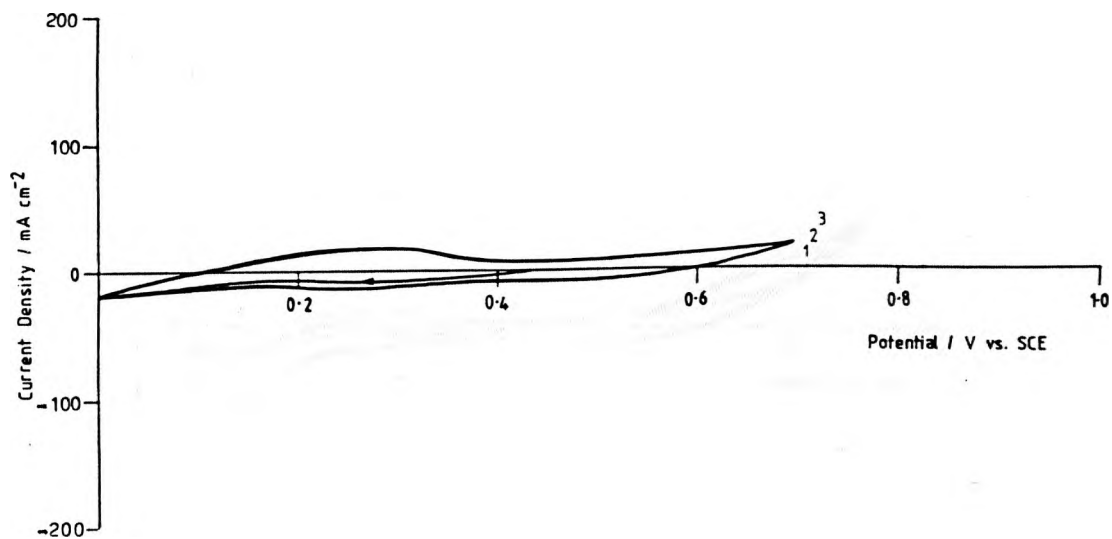


Figure 3.15 Cyclic voltammogram for Ag_2Se in a stationary 1M HClO_4 solution at $295 \pm 0.5\text{K}$. Sweep rate : 0.01 Vs^{-1} . Successive scans: initially cathodic of E_{rest} (0.433 V vs. SCE), followed by anodic excursions.

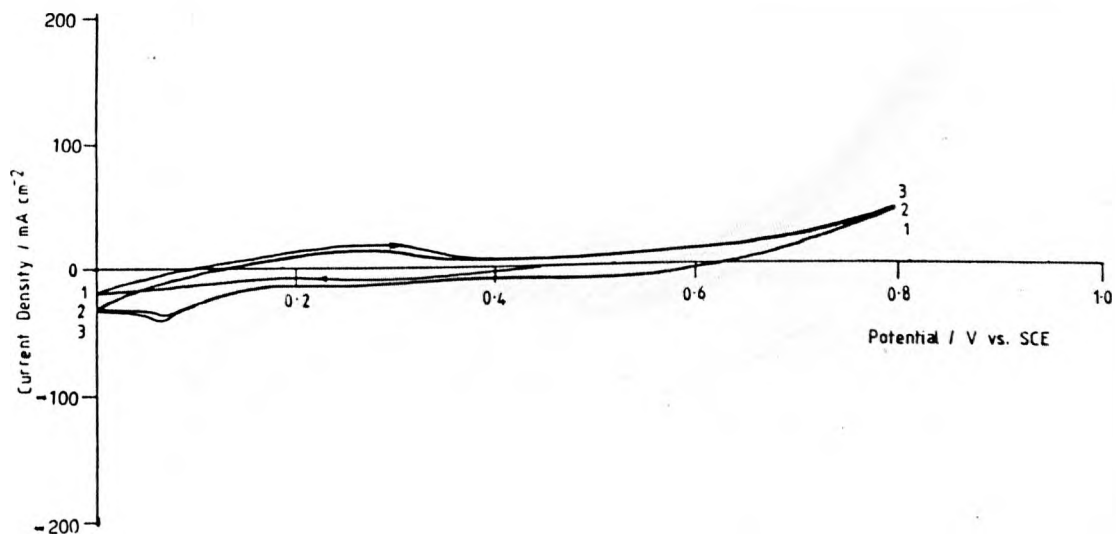


Figure 3.16 Cyclic voltammogram for Ag_2Se in a stationary 1M HClO_4 solution at $295 \pm 0.5\text{K}$. Sweep rate : 0.01 Vs^{-1} . Successive scans: initially cathodic of E_{rest} (0.445 V vs. SCE), followed by anodic excursions.

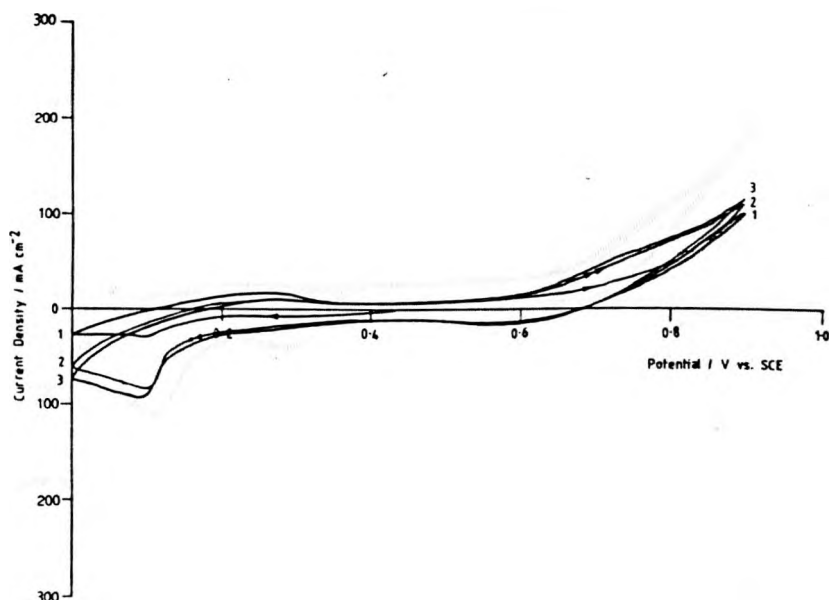


Figure 3.17 Cyclic voltammogram for Ag_2Se in a stationary 1M HClO_4 solution at $295 \pm 0.5\text{K}$. Sweep rate : 0.01 Vs^{-1} . Successive scans: initially cathodic of E_{rest} (0.435 V vs. SCE), followed by anodic excursions.

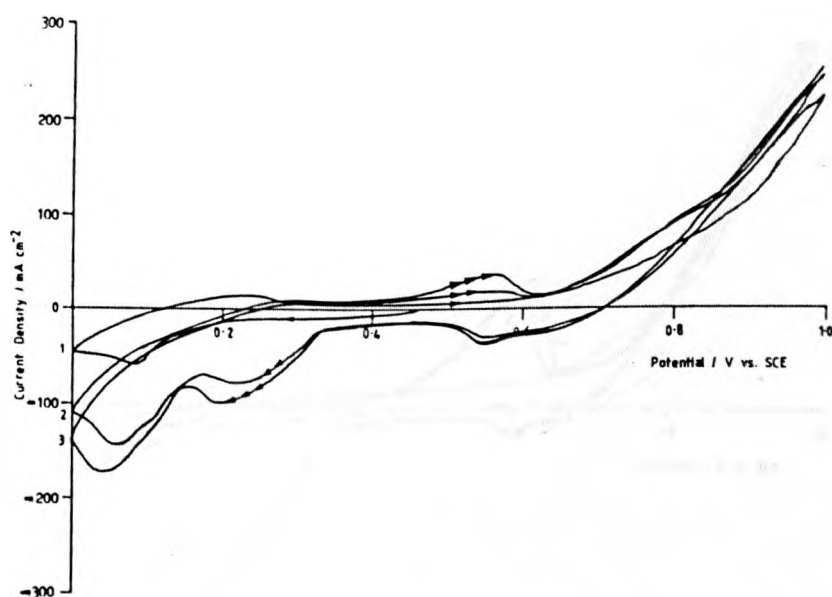


Figure 3.18 Cyclic voltammogram for Ag_2Se in a stationary 1M HClO_4 solution at $295 \pm 0.5\text{K}$. Sweep rate : 0.01 Vs^{-1} . Successive scans: initially cathodic of E_{rest} (0.456 V vs. SCE), followed by anodic excursions.

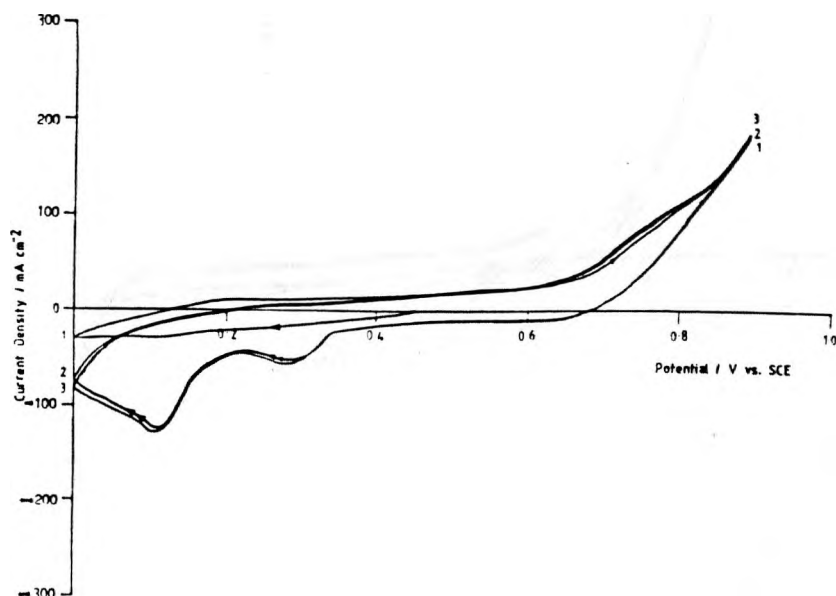


Figure 3.19 Cyclic voltammogram for Ag_2Se in 1M HNO_3 solution at $305 \pm 0.5\text{K}$. RDE : 1200rpm. Sweep rate : 0.01 Vs^{-1} . Successive scans: initially anodic of E_{rest} (0.445V vs. SCE), followed by cathodic excursions.

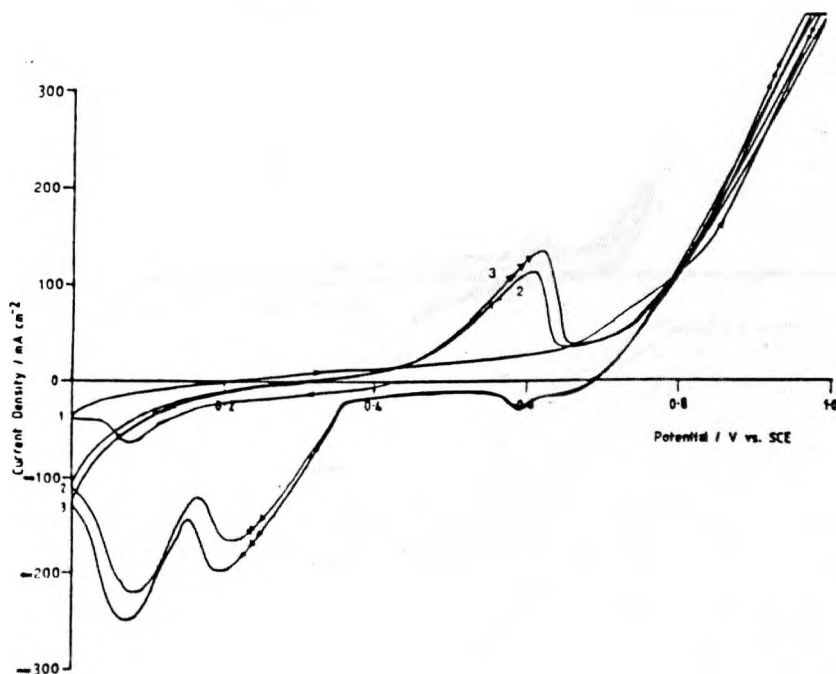


Figure 3.20 Cyclic voltammogram for Ag_2Se in 1M HNO_3 solution at $305 \pm 0.5\text{K}$. RDE : 1200rpm. Sweep rate : 0.01 Vs^{-1} . Successive scans: initially cathodic of E_{rest} (0.445V vs. SCE), followed by anodic excursions.

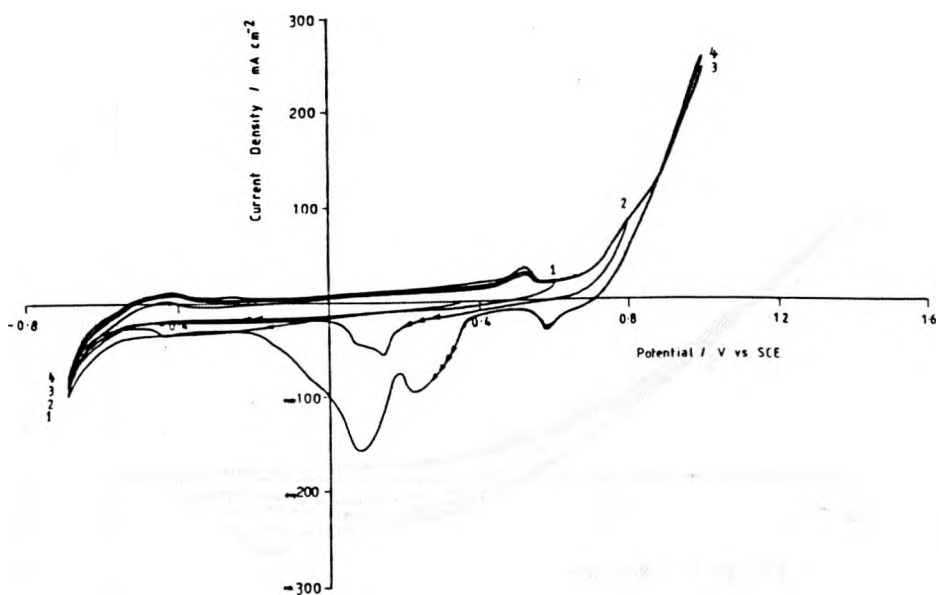


Figure 3.21 Cyclic voltammogram for Ag_2Se in 1M HNO_3 solution at $295 \pm 0.5\text{K}$. Sweep rate : 0.01 Vs^{-1} . Successive scans: initially cathodic of E_{test} , followed by anodic excursions with increasing anodic limiting potentials.

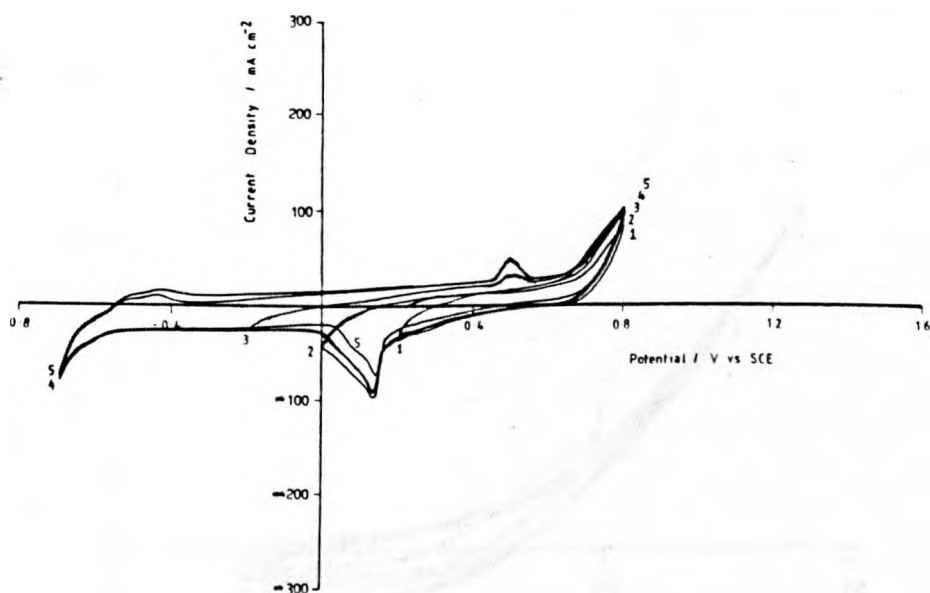


Figure 3.22 Cyclic voltammogram for Ag_2Se in 1M HNO_3 solution at $295 \pm 0.5\text{K}$. Sweep rate : 0.01 Vs^{-1} . Successive scans: initially anodic of E_{test} , followed by cathodic excursions with increasing cathodic potential limit.

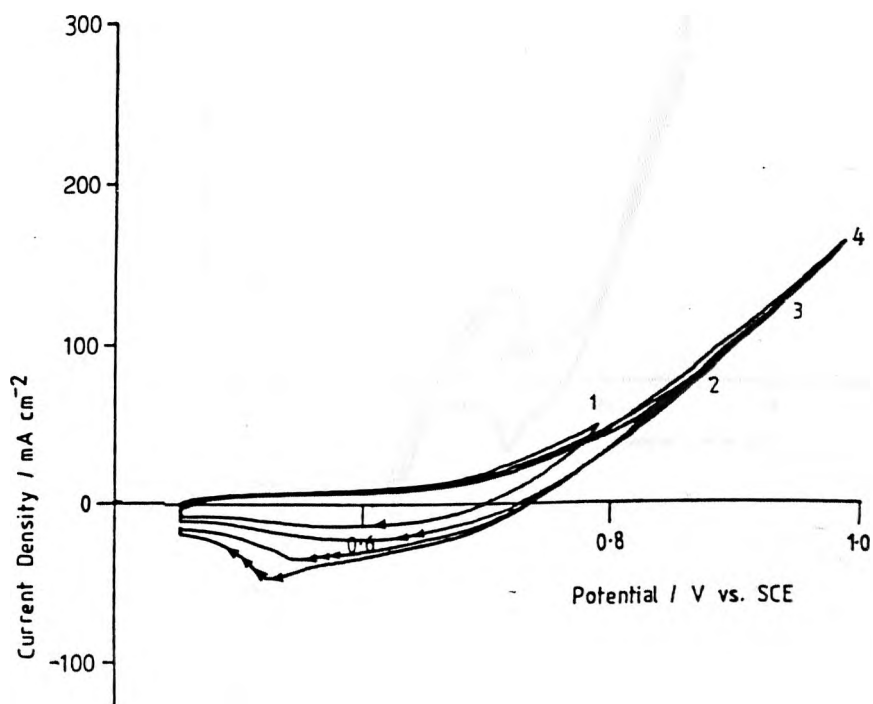


Figure 3.23 Cyclic voltammogram for Ag_2Se in 1M HNO_3 solution at $295 \pm 0.5\text{K}$. Sweep rate : 0.005Vs^{-1} . Successive scans with increasing cathodic limiting potentials.

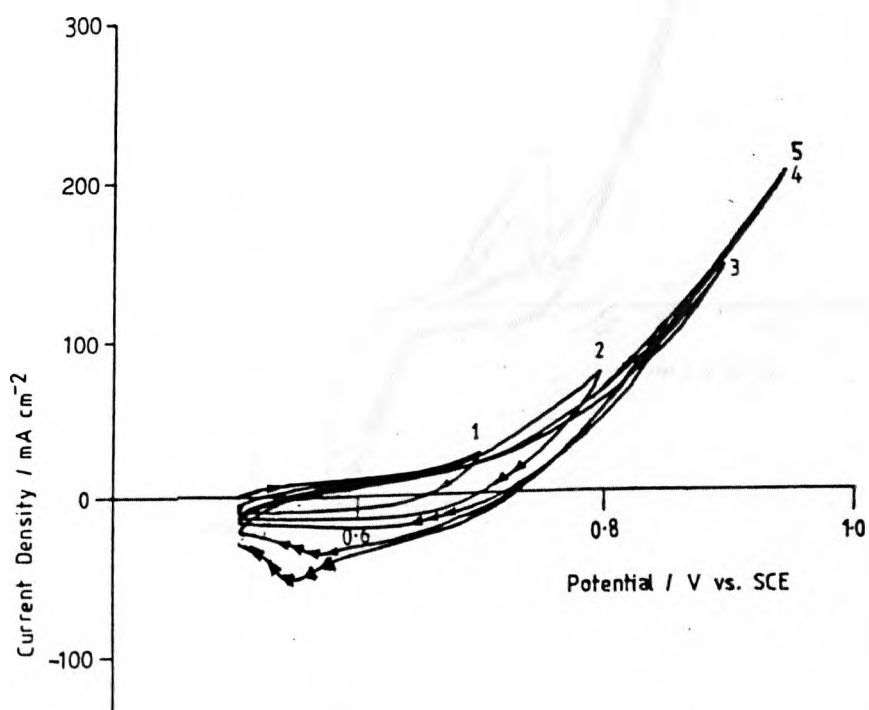


Figure 3.24 Cyclic voltammogram for Ag_2Se in 1M HNO_3 solution at $305 \pm 0.5\text{K}$. Sweep rate : 0.005Vs^{-1} . Successive scans with increasing cathodic limiting potentials.

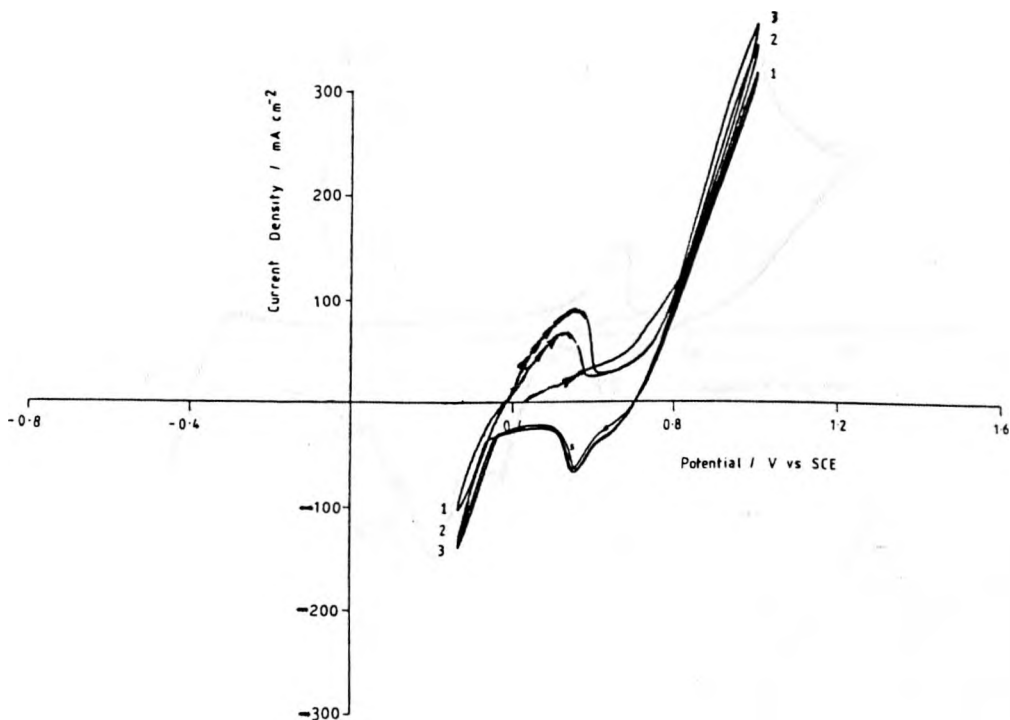


Figure 3.25 Cyclic voltammogram for Ag_2Se in 1M HNO_3 solution at $325 \pm 0.5\text{K}$. Sweep rate : 0.01 Vs^{-1} . Successive scans: initially anodic of E_{rest} , followed by cathodic excursions.

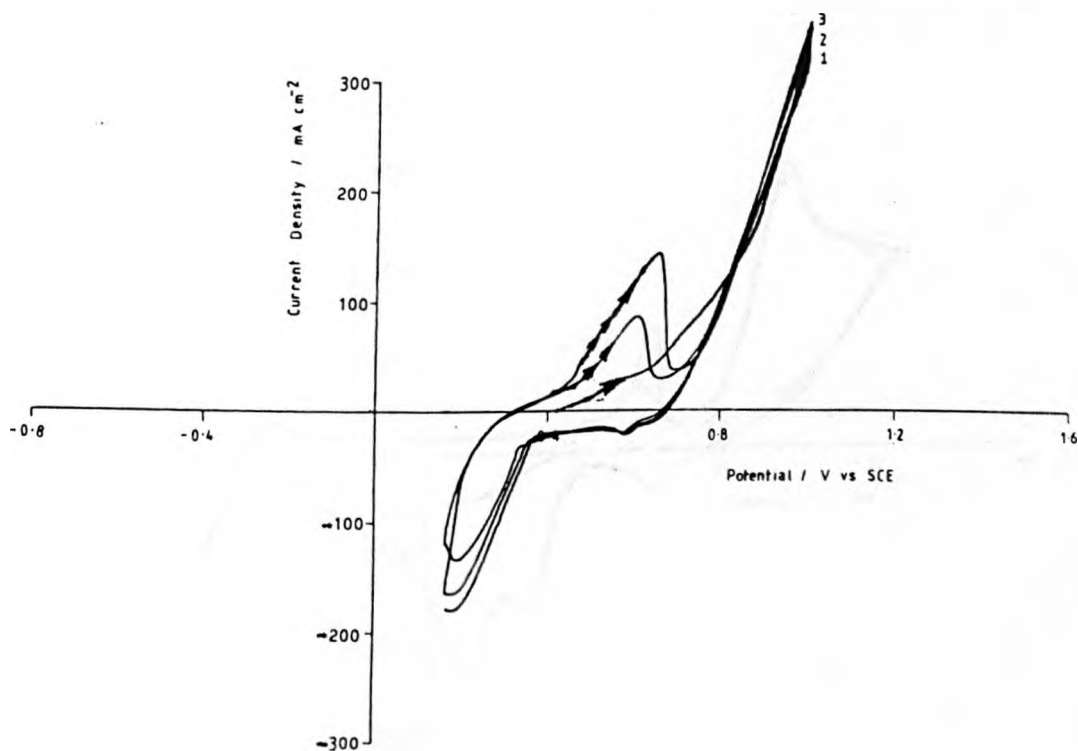


Figure 3.26 Cyclic voltammogram for Ag_2Se in 1M HNO_3 solution at $325 \pm 0.5\text{K}$. RDE: 1200rpm. Sweep rate : 0.01 Vs^{-1} . Successive scans: initially anodic of E_{rest} , followed by cathodic excursions.

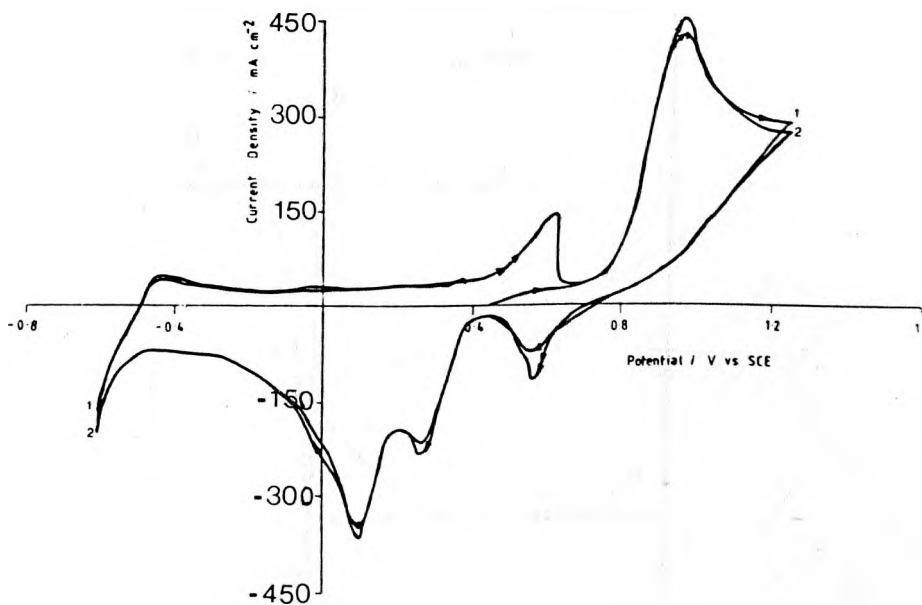


Figure 3.27 Cyclic voltammogram for Ag_2Se in 1M HNO_3 solution at $325 \pm 0.5\text{K}$. Sweep rate : 0.01 Vs^{-1} . Successive scans: initially anodic of E_{Test} , followed by cathodic excursions.

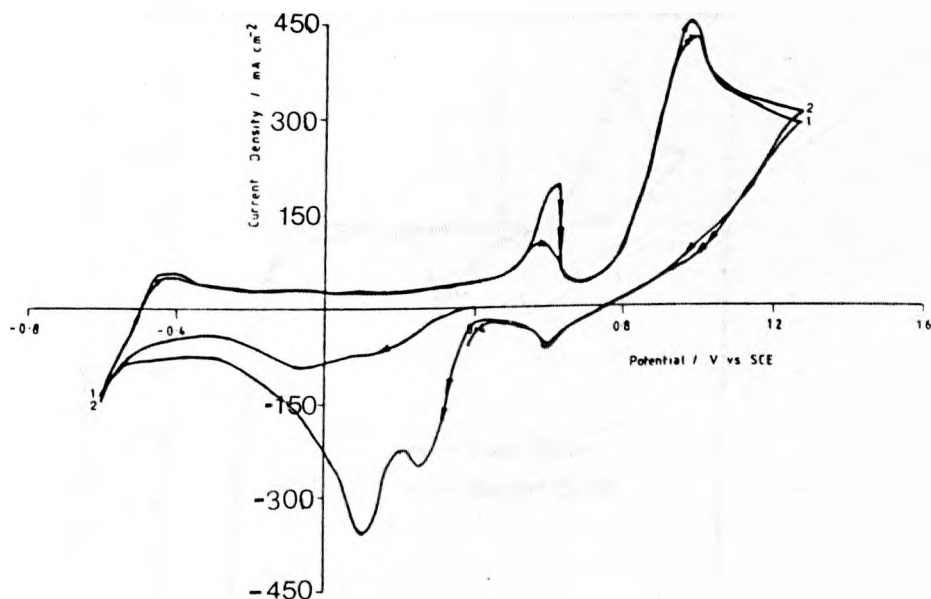


Figure 3.28 Cyclic voltammogram for Ag_2Se in 1M HNO_3 solution at $325 \pm 0.5\text{K}$. RDE: 1200rpm. Sweep rate : 0.01 Vs^{-1} . Successive scans: initially cathodic of E_{Test} , followed by anodic excursions.

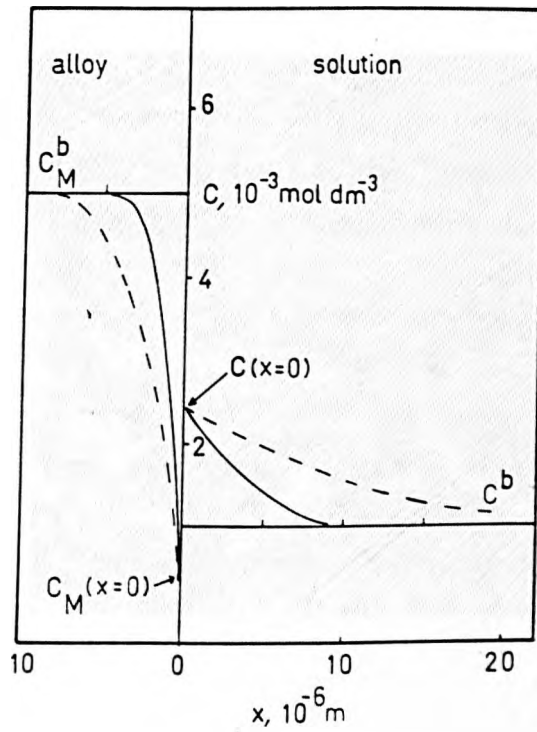


Figure 3.29 Variation of the concentration of the active metal in an alloy phase & metal ion in solution as a function of distance after imposition of a potential step perturbation. After MacDonald [173].

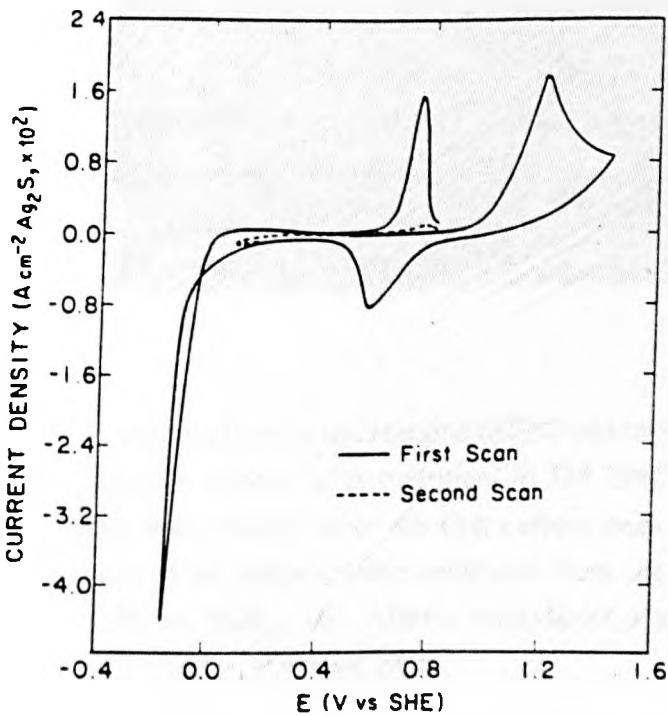
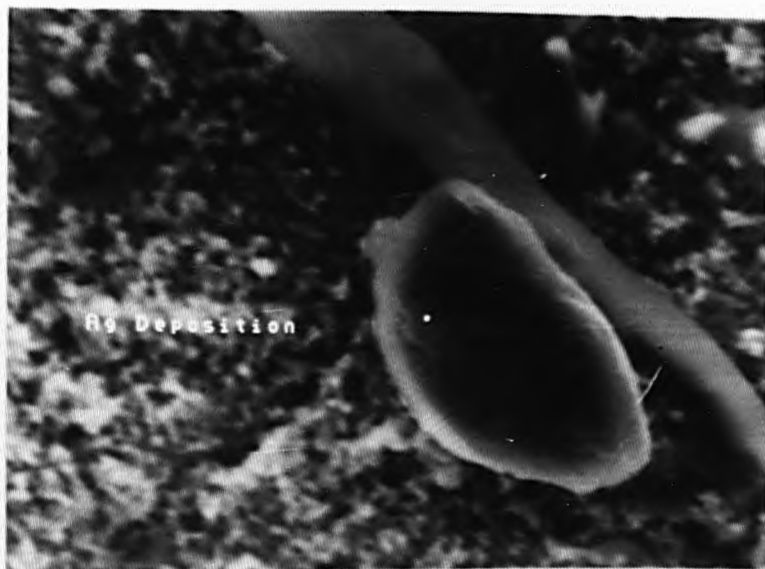


Figure 3.30 Cyclic voltammogram for a pressed pellet of Ag_2S in $1\text{M H}_2\text{SO}_4$ solution. Sweep rate : 0.01 Vs^{-1} . After Price [172].

(a)

1500 x



(b)

1800 x

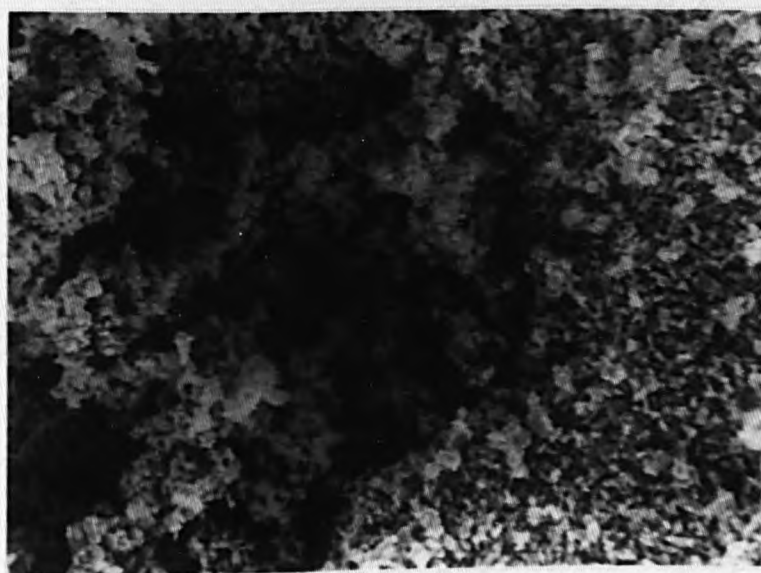


Figure 3.31 Scanning electron microscope (SEM) photographs of the silver selenide surface after treatment in 1M HNO₃ at 315K. (a) Immediately after the first current peak on the returning scan of an initial anodic excursion from the rest potential to 1.2V vs. SCE. (b) After a cathodic excursion from the rest potential to -0.4V vs. SCE.

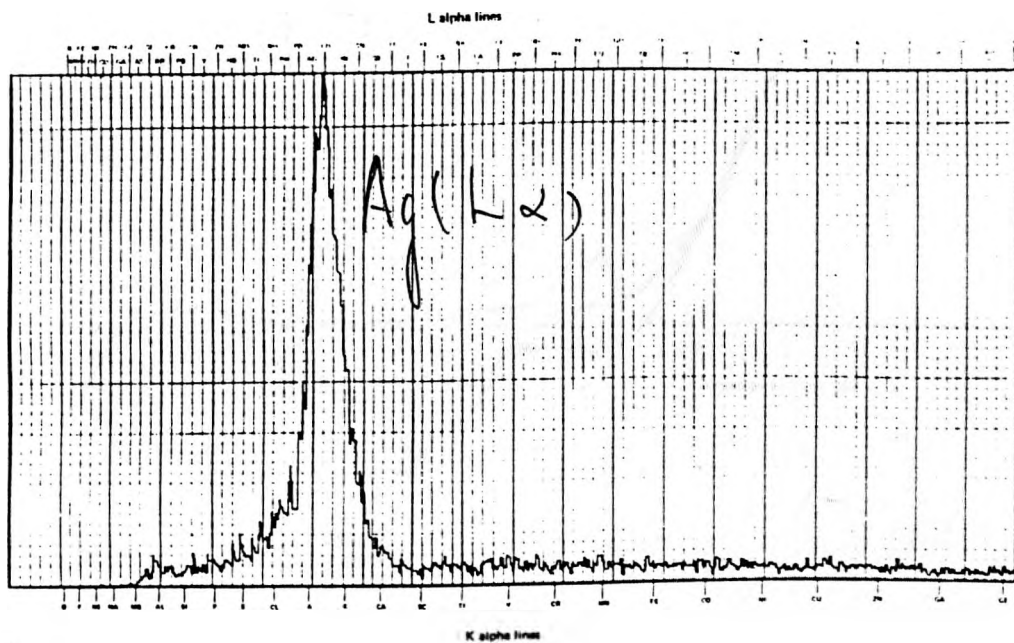


Figure 3.32 EDXA reveals that the crystals shown in *Figure 3.31(a)* are silver crystals.

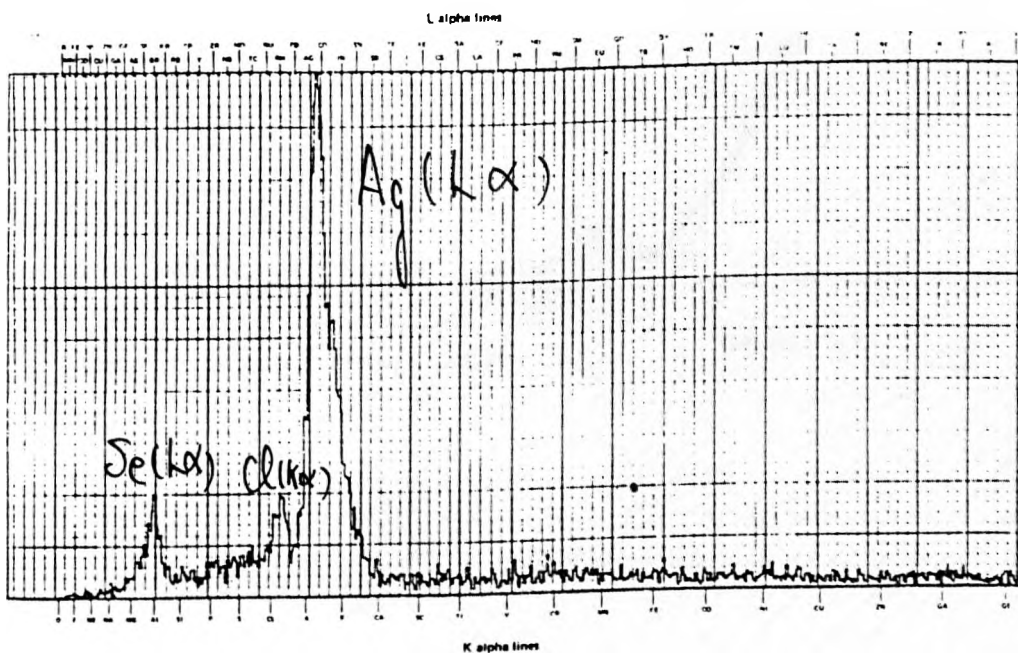


Figure 3.33 EDXA reveals the formation of silver on Ag_2Se electrodes after a cathodic excursion from the rest potential to -0.4V vs. SCE. (Surface is shown in *Figure 3.31(b)*).

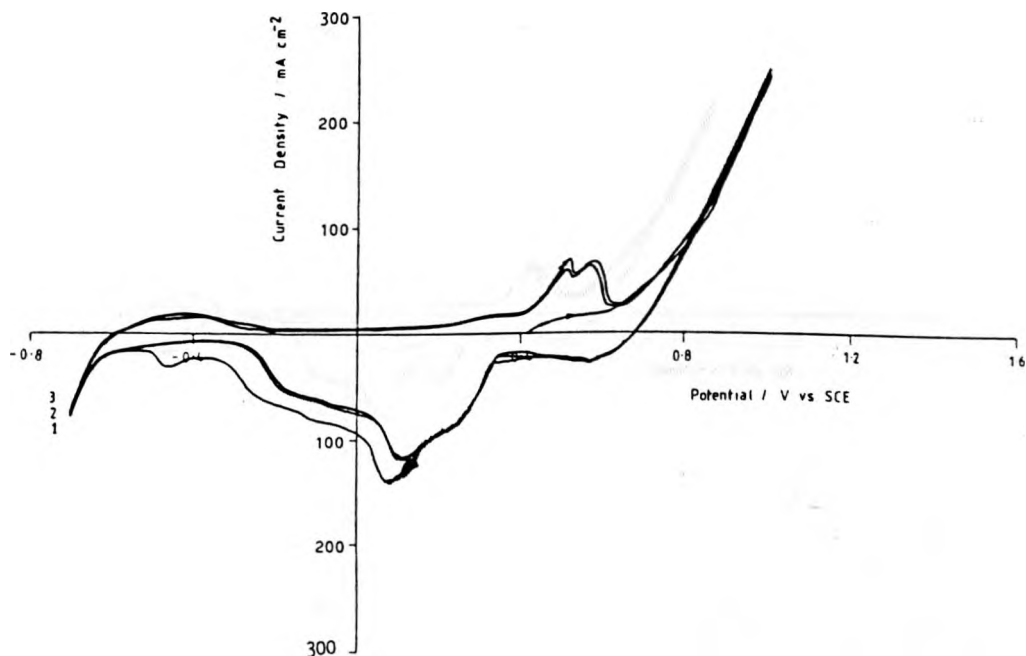


Figure 3.34 Cyclic voltammogram for CuAgSe in a stationary 1M HNO₃ solution at 303±0.5K. Sweep rate : 0.01 Vs⁻¹. Successive scans: initially anodic of E_{rest} (0.378 V vs. SCE), followed by cathodic excursions.

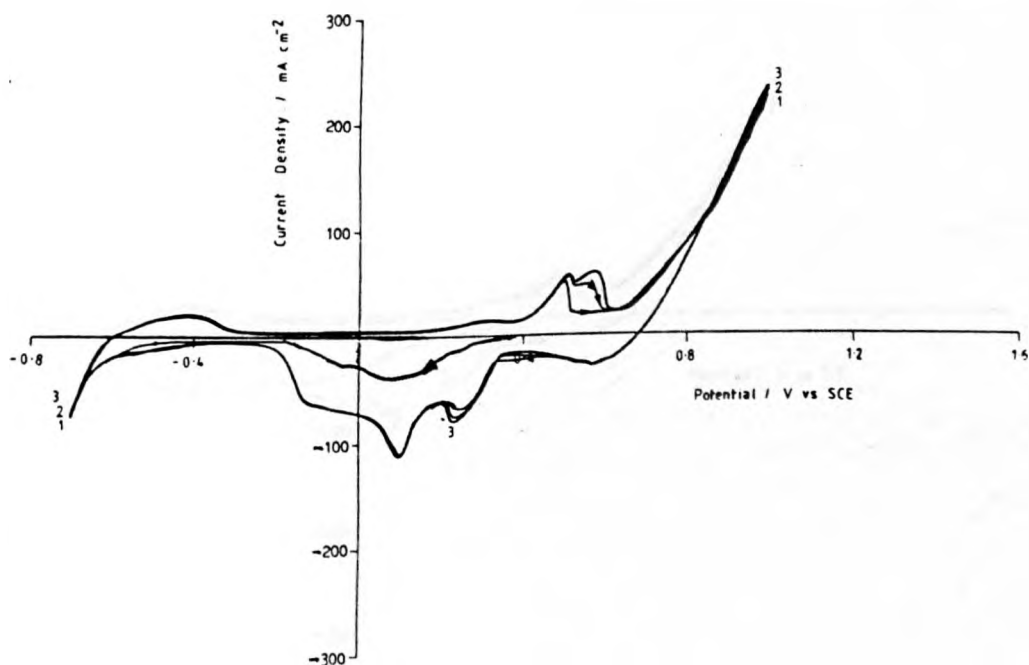


Figure 3.35 Cyclic voltammogram for CuAgSe in a stationary 1M HNO₃ solution at 303±0.5K. Sweep rate : 0.01 Vs⁻¹. Successive scans: initially cathodic of E_{rest} (0.392 V vs. SCE), followed by anodic excursions.

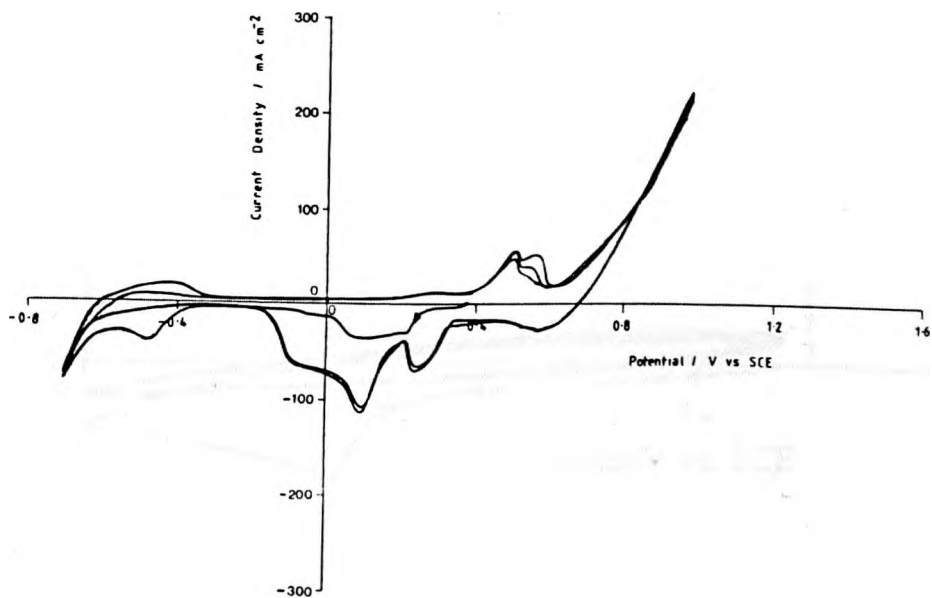


Figure 3.36 Cyclic voltammogram for CuAgSe in 1M HNO₃ solution at 303±0.5K. RDE : 1200rpm. Sweep rate : 0.01 Vs⁻¹. Successive scans: initially cathodic of E_{rest} (0.388 V vs. SCE), followed by anodic excursions.

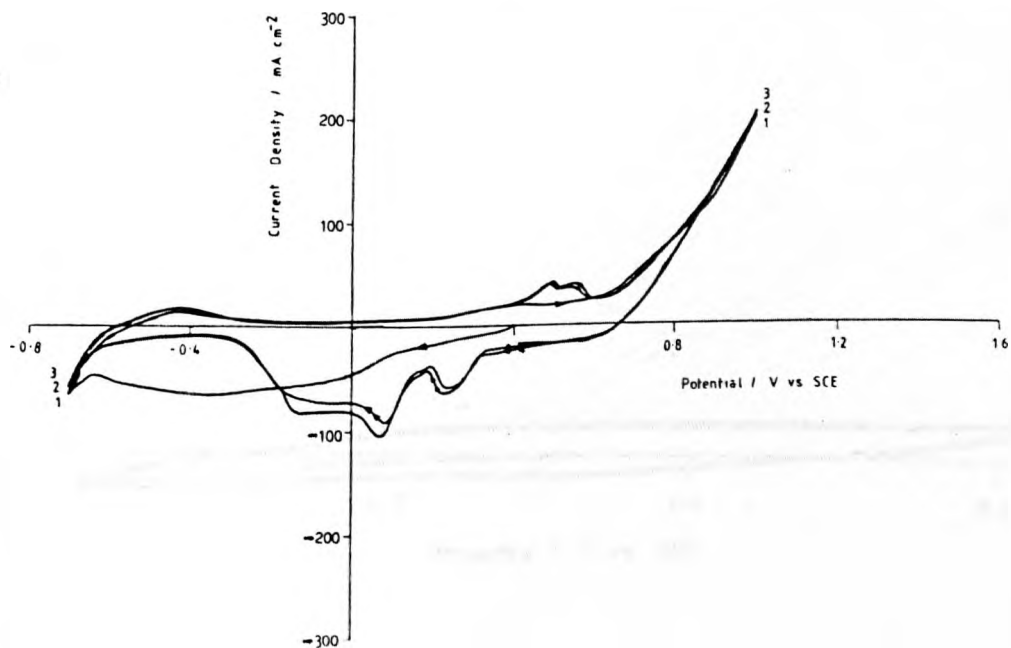


Figure 3.37 Cyclic voltammogram for CuAgSe in a stationary 1M HClO₄ solution at 303±0.5K. Sweep rate : 0.01 Vs⁻¹. Successive scans: initially cathodic of E_{rest} (0.400 V vs. SCE), followed by anodic excursions.

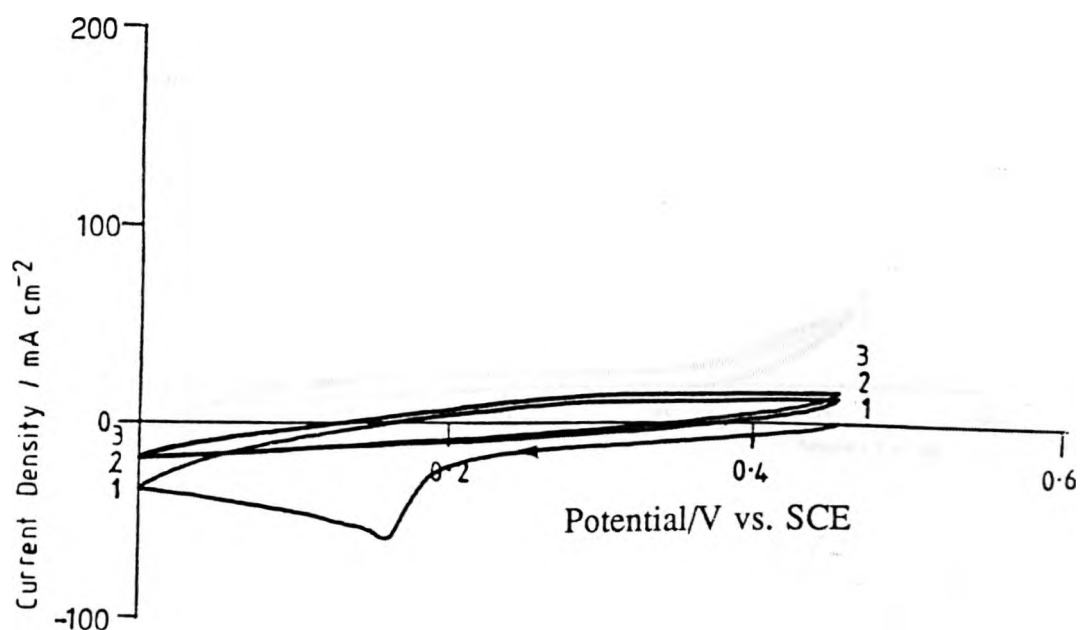


Figure 3.38 Cyclic voltammogram for CuAgSe in a stationary 1M HNO₃ solution at 292±0.5K. Sweep rate : 0.01 Vs⁻¹. Successive scans: initially cathodic of E_{rest} (0.387 V vs. SCE), followed by anodic excursions.

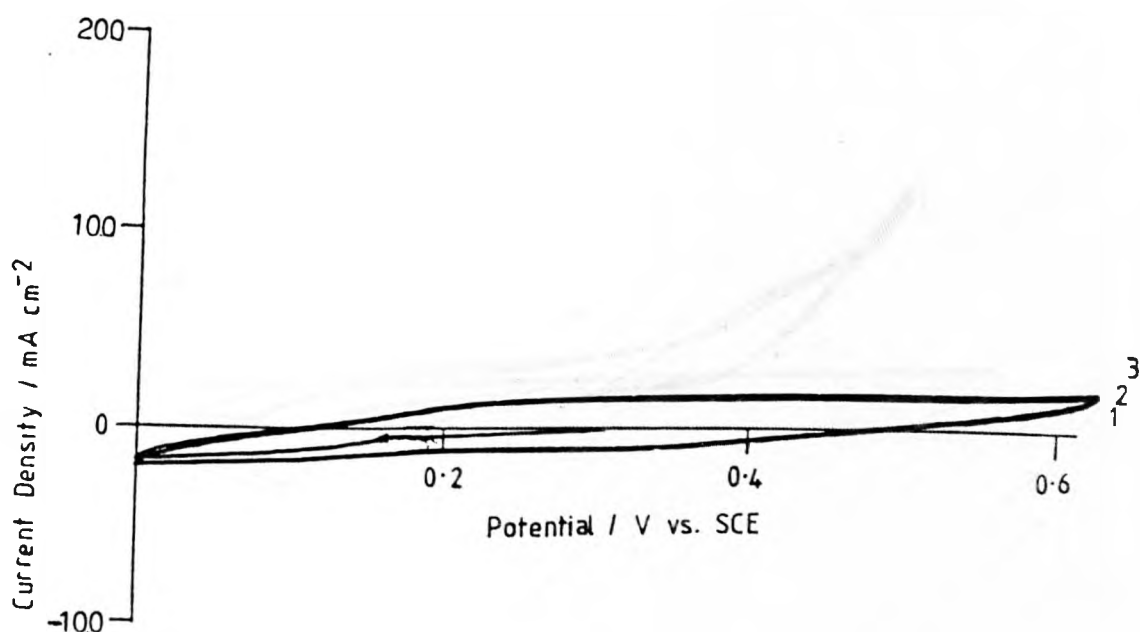


Figure 3.39 Cyclic voltammogram for CuAgSe in a stationary 1M HNO₃ solution at 292±0.5K. Sweep rate : 0.01 Vs⁻¹. Successive scans: initially cathodic of E_{rest} (0.316 V vs. SCE), followed by anodic excursions.

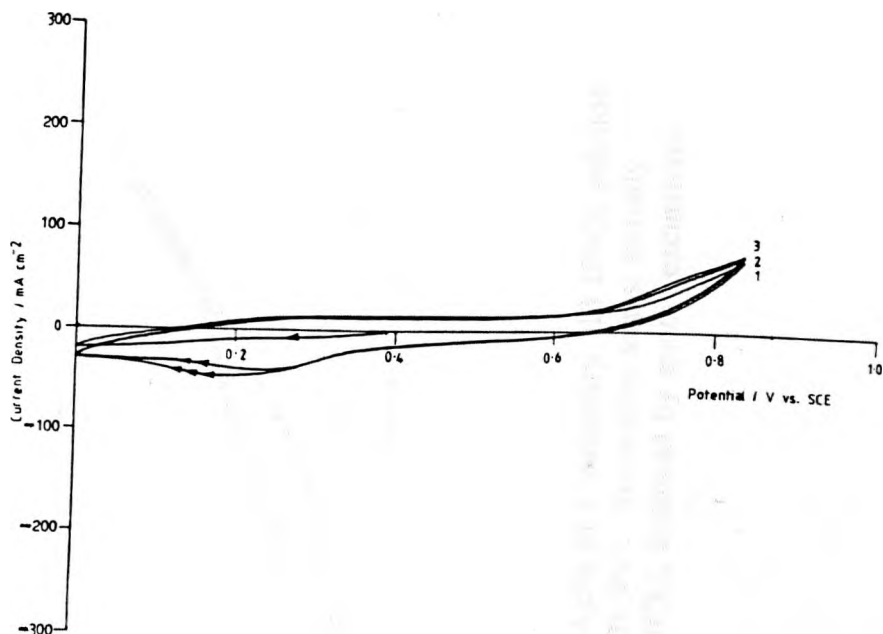


Figure 3.40 Cyclic voltammogram for CuAgSe in a stationary 1M HNO₃ solution at 292±0.5K. Sweep rate : 0.01 Vs⁻¹. Successive scans: initially cathodic of E_{rest} (0.382 V vs. SCE), followed by anodic excursions.

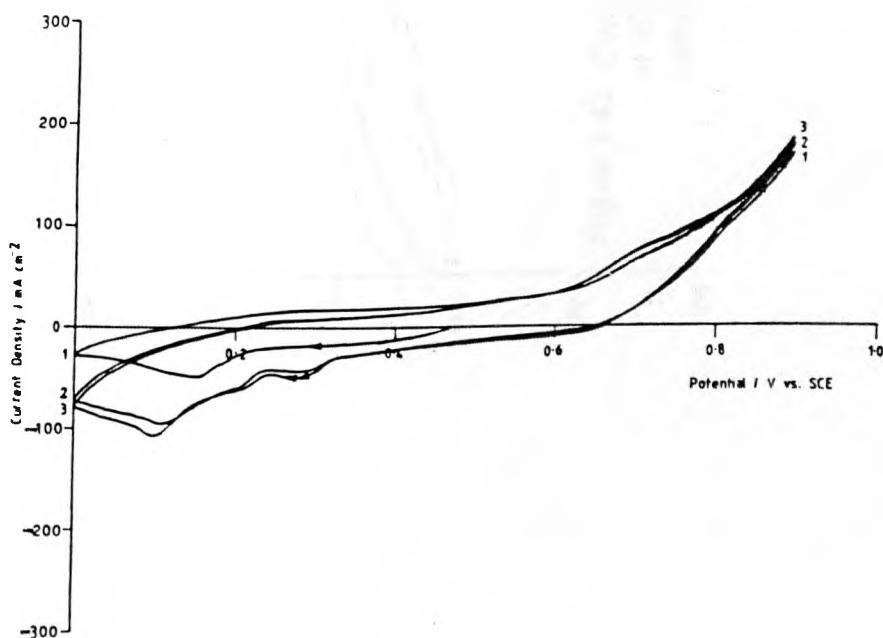
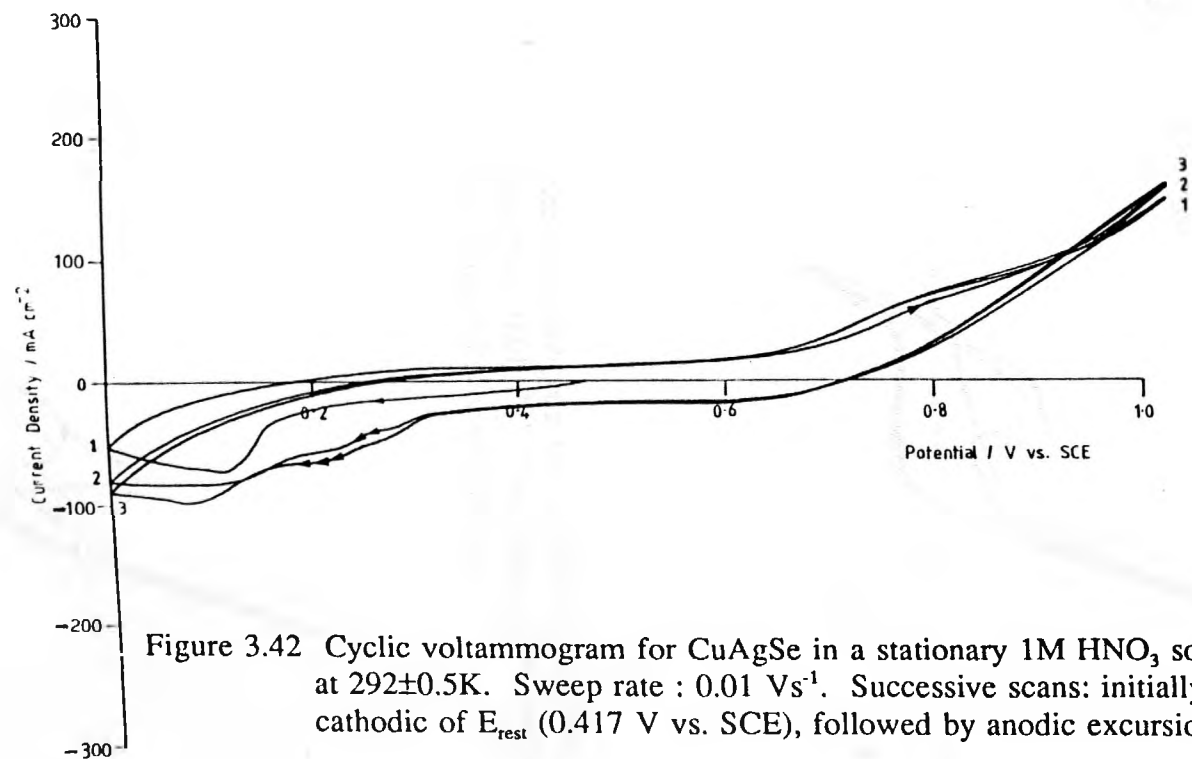


Figure 3.41 Cyclic voltammogram for CuAgSe in a stationary 1M HNO₃ solution at 292±0.5K. Sweep rate : 0.01 Vs⁻¹. Successive scans: initially cathodic of E_{rest} (0.429 V vs. SCE), followed by anodic excursions.



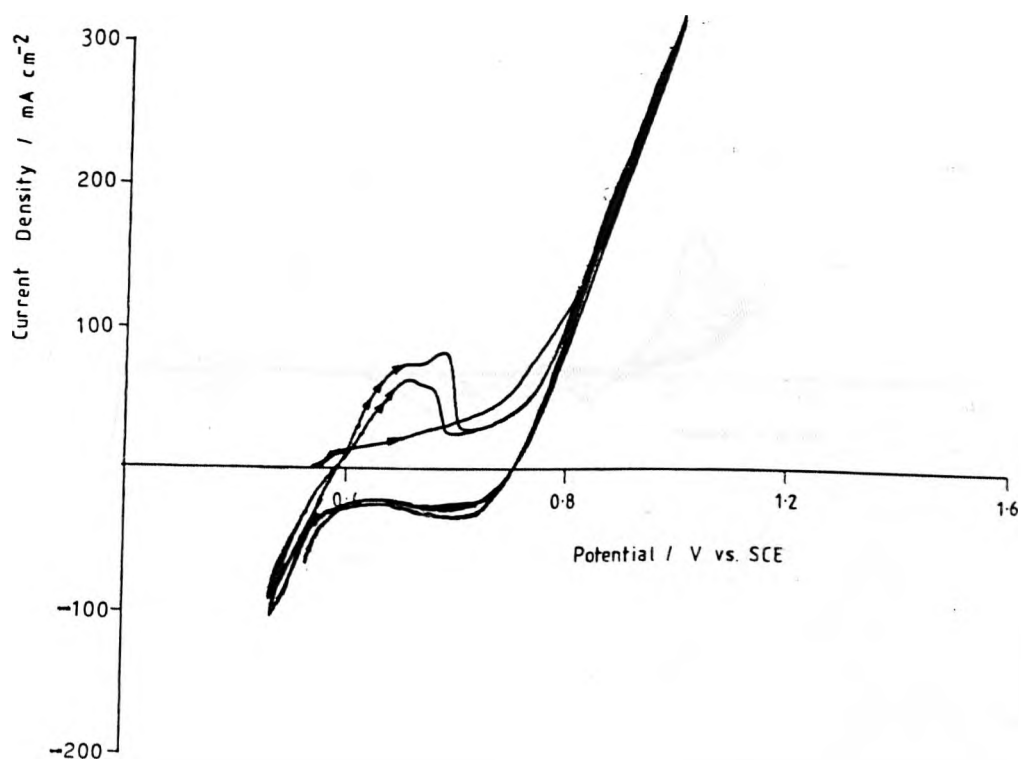


Figure 3.43 Cyclic voltammogram for CuAgSe in 1M HNO₃ solution at 315±0.5K. Sweep rate : 0.01 Vs⁻¹. Successive scans: initially anodic of E_{rest}, followed by cathodic excursions.

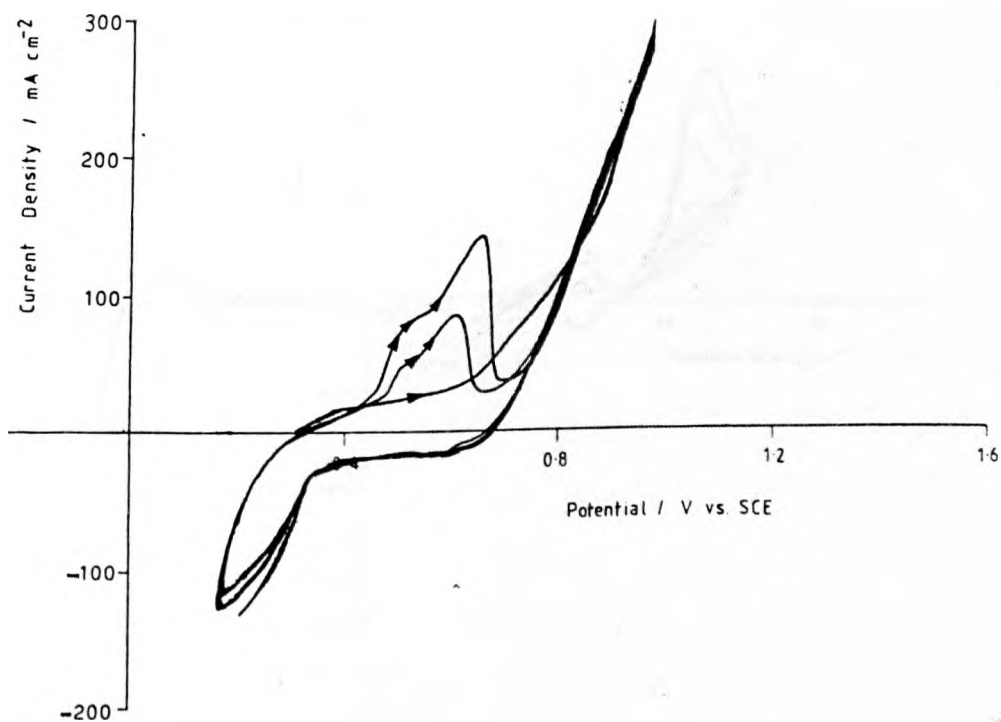


Figure 3.44 Cyclic voltammogram for CuAgSe in 1M HNO₃ solution at 320±0.5K. Sweep rate : 0.01 Vs⁻¹. Successive scans: initially anodic of E_{rest}, followed by cathodic excursions.

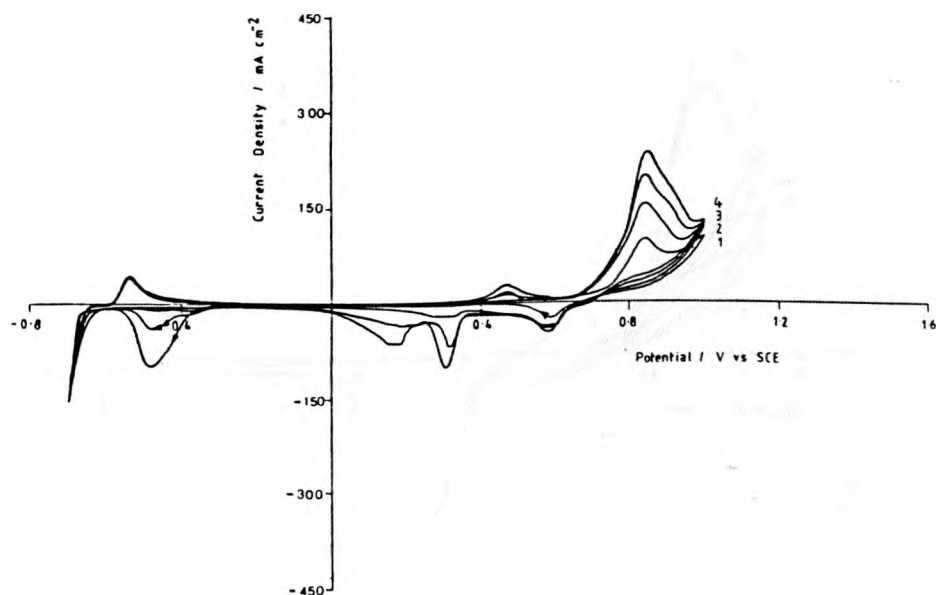


Figure 3.45 Cyclic voltammogram for CuAgSe in a stationary 2M HNO₃ solution at 330±0.5K. Sweep rate : 0.005 Vs⁻¹. Successive scans: initially anodic of E_{rest} (0.306 V vs. SCE), followed by cathodic excursions.

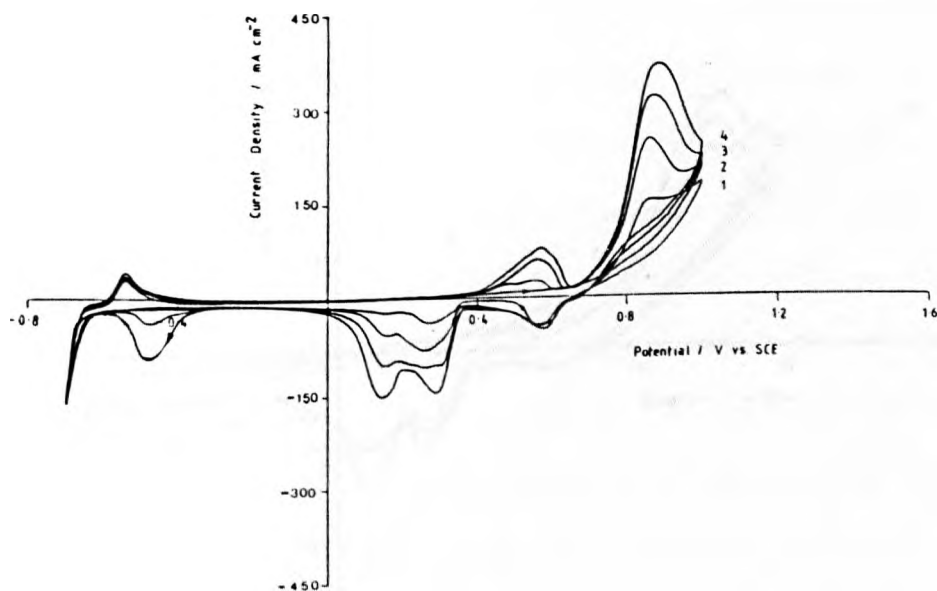


Figure 3.46 Cyclic voltammogram for CuAgSe in a stationary 2M HNO₃ solution at 330±0.5K. Sweep rate : 0.01 Vs⁻¹. Successive scans: initially anodic of E_{rest} (0.315 V vs. SCE), followed by cathodic excursions.

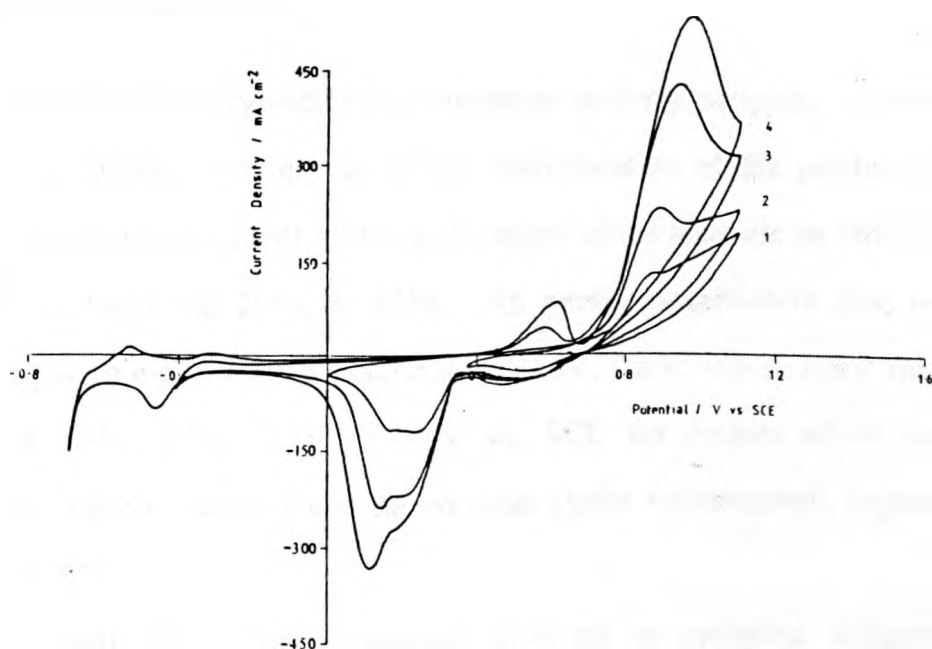


Figure 3.47 Cyclic voltammogram for CuAgSe in a stationary 2M HNO_3 solution at $330 \pm 0.5\text{K}$. Sweep rate : 0.02 Vs^{-1} . Successive scans: initially anodic of E_{rest} (0.368 V vs. SCE), followed by cathodic excursions.

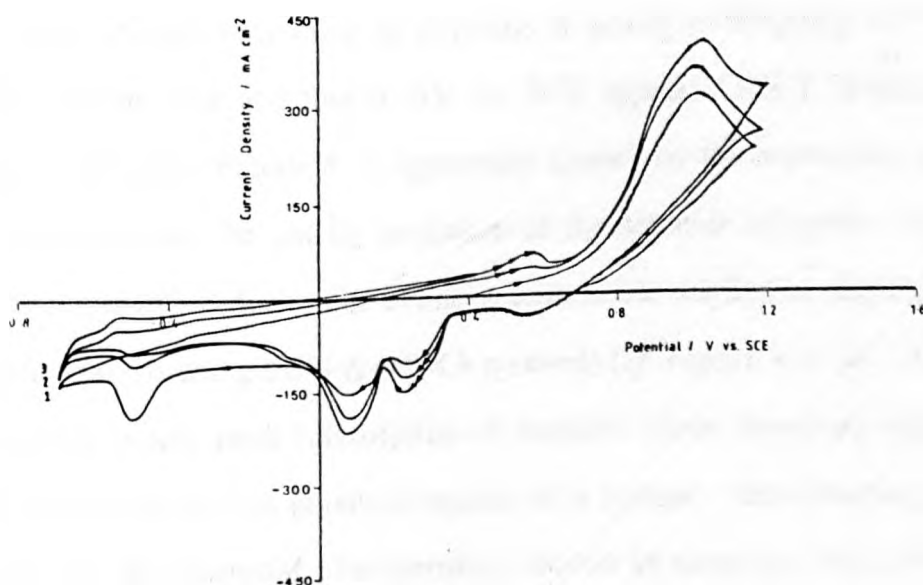


Figure 3.48 Cyclic voltammogram for CuAgSe in a stationary 2M HClO_4 solution at $330 \pm 0.5\text{K}$. Sweep rate : 0.015 Vs^{-1} . Successive scans: initially anodic of E_{rest} (0.402 V vs. SCE), followed by cathodic excursions.

3.3 Stripping Voltammetry

Though traditionally used for quantitative analysis, stripping voltammetry (cathodic) is found to be very useful for identification of the products of the oxidative dissolution of silver selenide & copper silver selenide in 1M HNO₃ & 1M HClO₄ solutions at 295K & 325K. An anodic polarisation time of 8-12 minutes & the pre-electrolysis potentials of 0.5V, 0.6V, 0.8 & 0.9V for silver selenide & 0.4V, 0.5V, 0.7V & 0.9V vs. SCE for copper silver selenide respectively were indicated from the previous cyclic voltammetric experiments (*cf. Section 3.2*).

In general, the cathodic currents observed in stripping voltammetric treatment increase with increasing polarisation potential & temperature. As can be seen from *Figures 3.49-51 & 53-4*, stripping voltammograms for BOTH silver selenide & copper silver selenide display three characteristic peaks in the potential regions 0.45V, 0.2 to 0.3V & 0.1V vs. SCE, though in the case of copper silver selenide, the current peak at 0.45V is almost undistinguishable & an extra peak appears very close in potential & nearly overlapping the second.

The current peak at about 0.45V vs. SCE appears ONLY at sufficiently higher polarisation potentials & is apparently caused by the deposition of silver ions produced during the anodic oxidation of the selenide minerals. This had already been identified during the cyclic voltammetric studies on these minerals via surface analysis using SEM & EDXA methods (*cf. Figure 4.31 & 4.33*). The corresponding anodic peak (dissolution of metallic silver deposited during the cathodic excursion) in this potential region on a typical voltammogram is also consistent with this proposal. Furthermore, as can be seen in a later section of this work (*cf. Section 3.6*), comparable results have also been obtained via intermittent galvanostatic polarisation (IGP) methods.

The second peak occurs in the potential region between 0.2V to 0.3V vs.

SCE. The involvement of the metallic silver at this stage seems to be unlikely because at relatively lower polarisation potentials this peak still appears while the peak for silver deposition is not observed (at least not apparent). The reduction of elemental selenium, produced during the preceding anodic excursion, is unlikely to happen here on a relatively large scale. This is because, as is shown in the cyclic voltammograms (*cf. Figures 3.25 & 3.26*), the magnitude of the dissolution peak of metallic silver on the subsequent anodic excursion is directly influenced by the events which take place in the above potential region (i.e. 0.2V vs. to 0.3V vs. SCE on the cathodic scan). A possible explanation is that this peak may be caused either by the reduction of an intermediate Ag-Se phase (AgSe ?) or the silver selenide electrode itself, i.e.



Ascribing this peak to the direct reduction of Ag₂Se is in good agreement with observations during the reduction of silver sulphide [148,161,171-2] in acid media. EDXA analysis results gives further evidence for the formation of silver via reduction of selenide minerals. As is shown in *Figure 3.52* the surface of the electrode is virtually silver. Furthermore, gradual growth of gas-like bubbles on the electrode surface followed by a dramatic colour change of the aqueous solution from colourless to brown-red is observed when the potential is lower than 0.3V vs. SCE. This provides further evidence for the evolution of hydrogen selenide in the potential region of the above peaks.

Immediately adjacent to the second peak, the third apparent current peak is rapidly developed at potential around 0.1V vs. SCE. This is possibly due to the reduction of the elemental selenium produced during the anodic oxidation though as is anticipated from the Eh-pH diagrams the reduction of crystalline

selenium should occur at a much more NEGATIVE potential. This may be due to the fact that the majority of the elemental selenium formed during the anodic oxidation is in an amorphous phase rather than well crystallised metallic selenium. This can be deduced from the brown (red?) colour of the electrode surface after polarisation at sufficiently high potentials. Furthermore, gradual growth of gas-like bubbles on the electrode surface is still observed in this potential region. This provides further evidence for the evolution of hydrogen selenide in the potential region because the evolution of hydrogen gas seems unlikely to occur at such a high potential region. Thus, this peak can be ascribed to the reduction of at least part of the elemental selenium produced during the anodic polarisation.

However, due to the insensitivity of XRD technique for detecting possible intermediate Ag-Se compounds (AgSe ?), the mechanism remains unresolved. It is hoped that *in-situ* analysis using for example the ESCA & XPS techniques might help to identify the chemical changes on the electrode surface & thus help to understand the mechanism of the reduction process.

The reduction of hydrogen ions in the solution is not observed at potential more positive than - 0.5V vs. SCE, presumably due to the high overpotential of hydrogen evolution on selenide electrode & silver surfaces formed via reduction of the selenides.

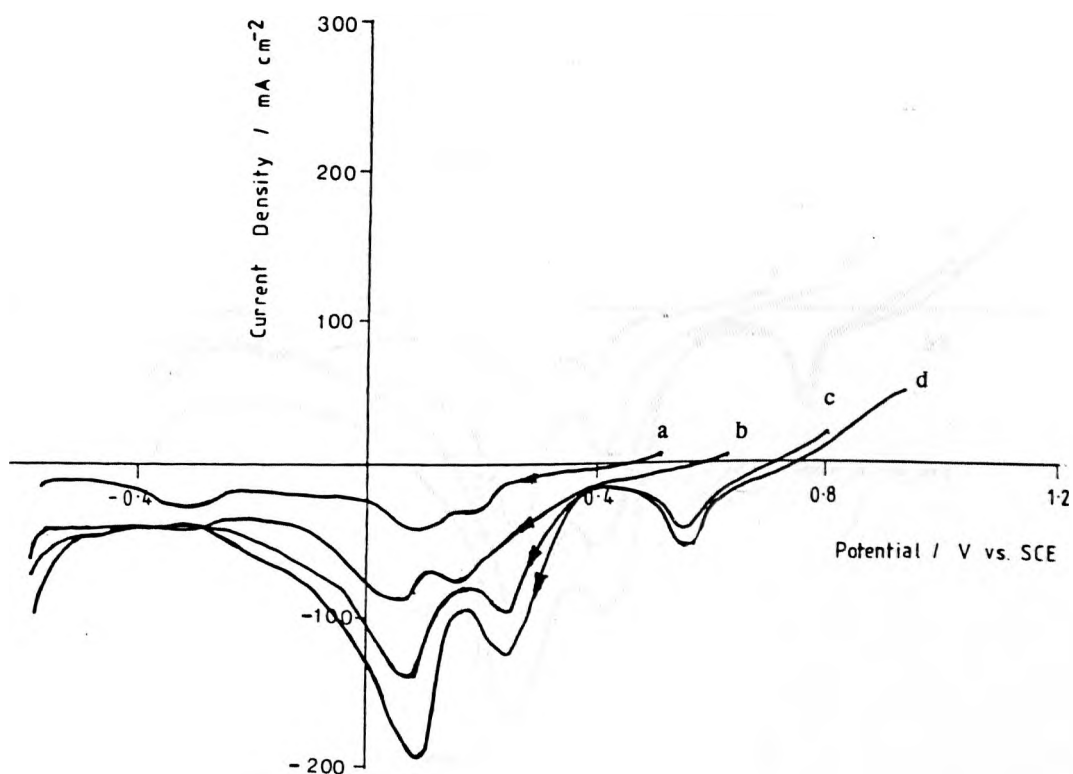


Figure 3.49 Stripping voltammograms for Ag_2Se in a stationary 1M HNO_3 solution at $295 \pm 0.5\text{K}$. Sweep rate : 0.01Vs^{-1} . Previous anodic polarisation for 600s at applied potentials: (a) 0.5V (b) 0.6V (c) 0.8V (d) 0.9V.

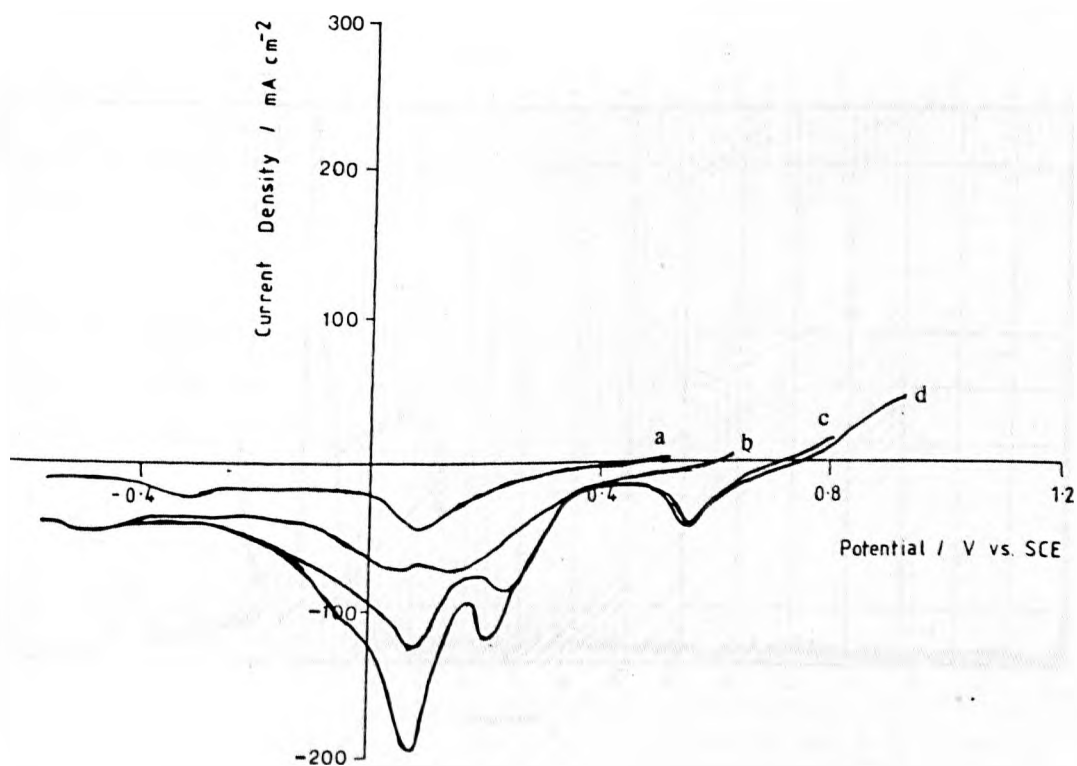


Figure 3.50 Stripping voltammograms for Ag_2Se in a stationary 1M HClO_4 solution at $295 \pm 0.5\text{K}$. Sweep rate : 0.01Vs^{-1} . Previous anodic polarisation for 600s at applied potentials: (a) 0.5V (b) 0.6V (c) 0.8V (d) 0.9V.

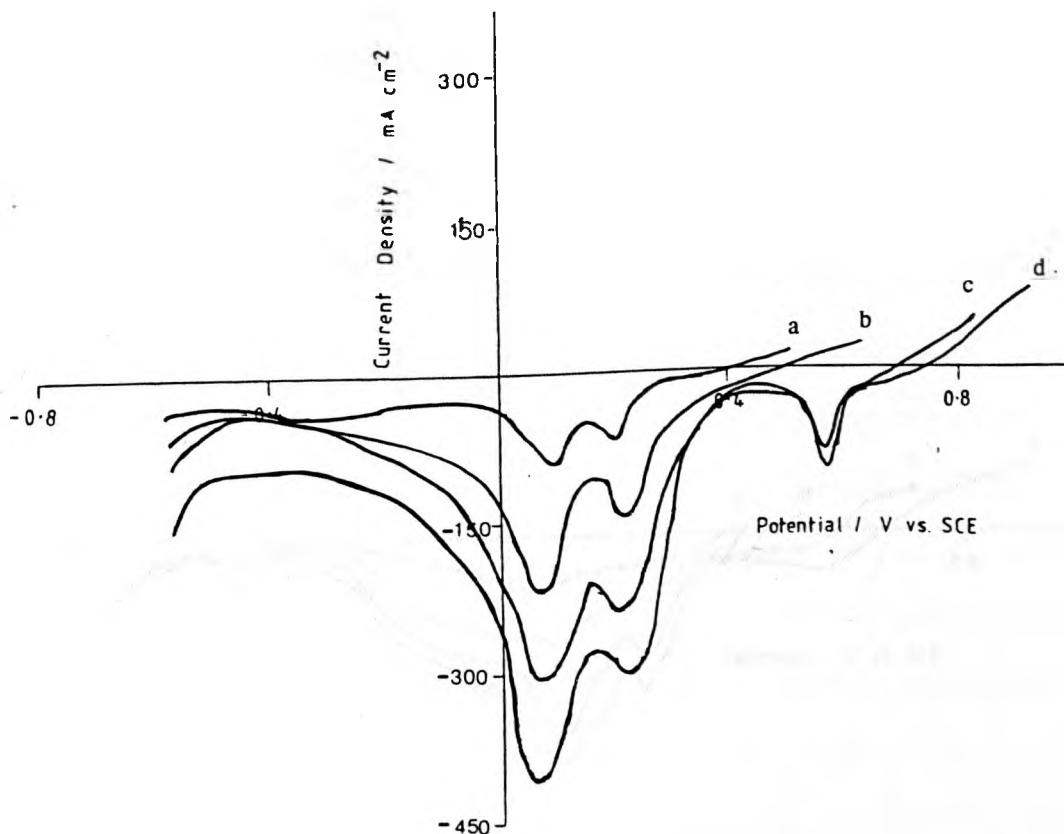


Figure 3.51 Stripping voltammograms for Ag_2Se in a stationary 1M HNO_3 solution at $325 \pm 0.5\text{K}$. Sweep rate : 0.01 Vs^{-1} . Previous anodic polarisation for 600s at applied potentials: (a) 0.5V (b) 0.6V (c) 0.8V (d) 0.9V.

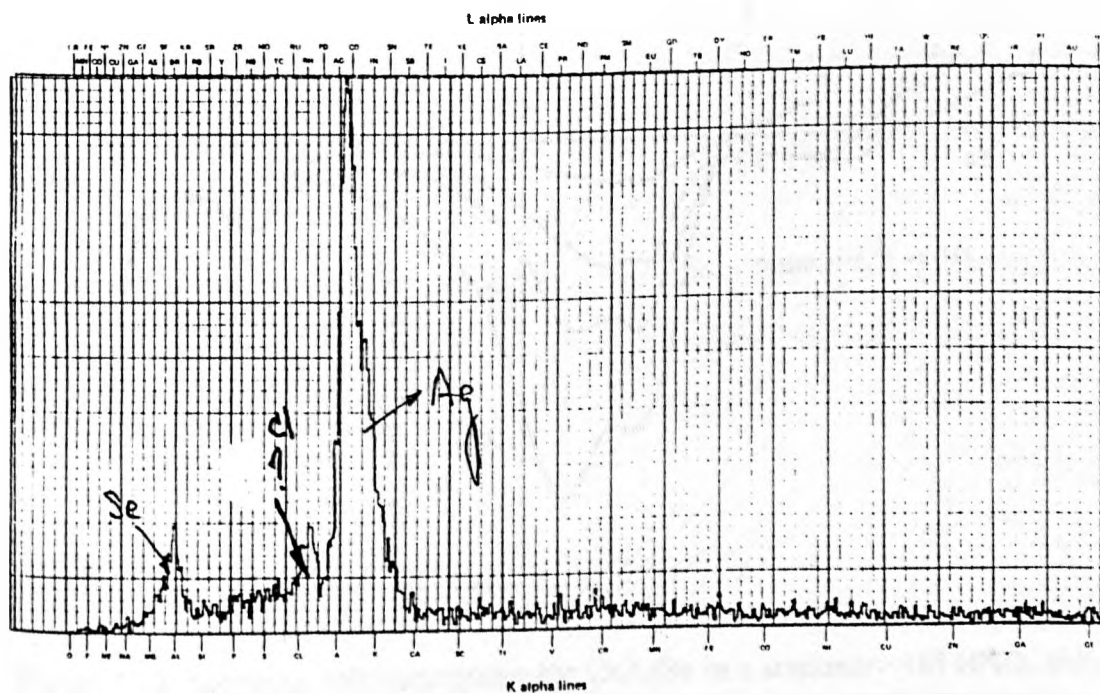


Figure 3.52 EDXA reveals the formation of silver on Ag_2Se electrodes after a cathodic excursion to -0.7V vs. SCE.

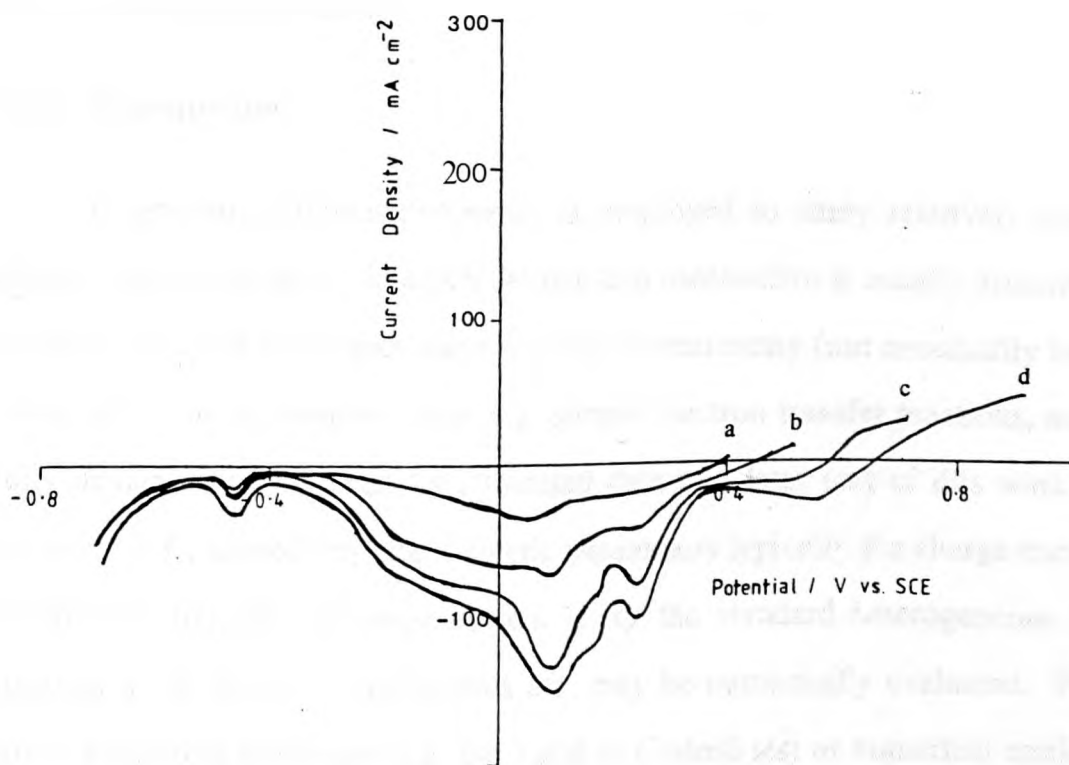


Figure 3.53 Stripping voltammograms for CuAgSe in a stationary 1M HNO_3 solution at $295 \pm 0.5\text{K}$. Sweep rate : 0.01 Vs^{-1} . Previous anodic polarisation for 600s at applied potentials: (a) 0.45V (b) 0.6V (c) 0.7V (d) 0.9V.

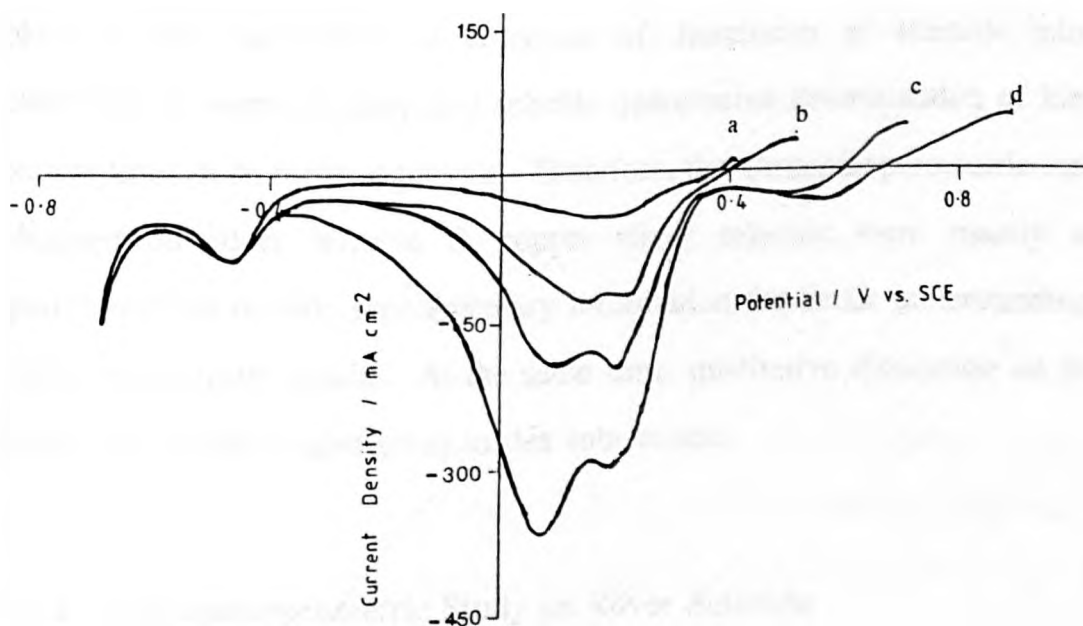


Figure 3.54 Stripping voltammograms for CuAgSe in a stationary 1M HNO_3 solution at $325 \pm 0.5\text{K}$. Sweep rate : 0.01 Vs^{-1} . Previous anodic polarisation for 600s at applied potentials: (a) 0.45V (b) 0.6V (c) 0.7V (d) 0.9V.

3.4 Chronoamperometry

3.4.1 Introduction

In general, chronoamperometry is employed to study relatively simple electrochemical systems for which the reaction mechanism is usually established via more versatile techniques namely cyclic voltammetry (not necessarily linear sweep CV). In the simplest cases e.g. simple electron transfer reactions, as are fully demonstrated via digitally simulated data in a later part of this work (*cf. Section 4.8.3*), several important kinetic parameters typically the charge transfer coefficients (α), the exchange current i_0 (or the standard heterogeneous rate constant k^0) & diffusion coefficients etc. may be numerically evaluated. Here either traditional techniques e.g. the Tafel or Cottrell test or numerical methods including convolution & allied techniques can be used. The latter can be well illustrated using results from the $\text{Fe}^{3+}/\text{Fe}^{2+}$ system (*cf. Section 3.7*).

However, due to the complexity arising from the involvement of a solid phase in the electrochemical processes of dissolution of selenide mineral electrodes, it seems unlikely that reliable quantitative determination of kinetic parameters can be made at present. Therefore, the chronoamperometric results obtained on silver selenide & copper silver selenide were mainly used qualitatively to provide supplementary information for better understanding of cyclic voltammetry results. At the same time, qualitative discussion on some kinetic parameters is also given in this sub-section.

3.4.2 Chronoamperometric Study on Silver Selenide

Chronoamperometric experiments on silver selenide electrodes were carried out in either nitric (1M) or perchloric acid (1M) solutions at temperatures ranging from 295K to 335K. As a precaution, the chronoamperometric (current-time)

responses resulting from the supporting (background) electrolytes (HNO_3 & HClO_4) were studied using a platinum electrode of similar geometry to the mineral electrodes. As can be seen from *Figure 3.55*, within the potential regions of practical interest (i.e. lower than 1.0V vs. SCE), the 'background' current is ultimately negligible as compared to the current resulting from the actual process of the oxidation of silver selenide & copper silver selenide (cf. *Figures 3.56-61 & 3.65-70*). The low current from the supporting electrolyte was also indicated in the cyclic voltammograms obtained earlier in this work (cf. *Figures 3.3 & 3.4*). Thus, the contribution of the supporting electrolyte to the OVERALL faradaic current resulting from the anodic dissolution of the mineral electrodes can be safely ignored.

Chronoamperograms for silver selenide in 1M HNO_3 & 1M HClO_4 solution at temperatures within the range 295 to 335K are illustrated in *Figures 3.56-61*. It can be seen that at lower temperatures reasonably large current densities ($>800\text{Am}^{-2}$) can ONLY be obtained at higher anodic potentials (0.8 to 1.1V vs. SCE) or more precisely at larger overpotentials (0.4 to 0.7V). To obtain an appreciable dissolution rate for silver selenide, a relatively strong oxidative environment is thus required. This helps to explain the phenomenon of low dissolution rate of selenide minerals observed during leaching with relatively weak oxidants e.g. solutions of FeCl_3 & CuCl_2 [4,25-9].

Furthermore, as can be seen from the chronoamperograms at relatively higher overpotentials, the current decays rapidly at the beginning of the application of external electric field, then the system gradually approaches a steady state & CONSTANT current is observed. Cottrell behaviour $i \cdot t^{1/2}$ constant has not been observed for ANY fragment of the response at overpotentials up to 0.7V, presumably due to the complexity of the electrode processes involving the diffusion within BOTH the aqueous & the solid phase. Nonetheless, an indication of slow heterogeneous electrode processes can be deduced from the

effect of potential on the chronoamperometric behaviour of silver selenide electrodes. Not surprisingly this is also indicated in the cyclic voltammetric results discussed earlier in this work (*cf. Section 3.2*). As can be seen from typical cyclic voltammograms (*Figures 3.5-3.12*, for example), the current peak on the anodic excursions is located at the potential region around 0.9V vs. SCE, which indicates substantial departure from the Nernstian type electron transfer reactions (*cf. Section 4.8.3* for more details).

Similarly, a general tendency for the increase in current (densities) with the increasing of temperature has also been observed. This is consistent with the temperature-dependent leaching behaviour of silver selenide.

In an effort to gain a better understanding of the mechanism of the anodic dissolution of silver selenide, a series of analytical techniques including AAS, SEM, EDXA & XRD have been employed to identify the products in BOTH the solid phase & the aqueous solution. AAS results confirmed that Ag^+ (aq) has been produced during the oxidation while ONLY traces of aqueous selenium species have been detected in the solution. XRD patterns (*cf. Figure 3.62*) of the product layer collected from several runs¹ under identical experimental conditions failed to provide positive evidence for the existence of an intermediate phase namely AgSe. The mechanism of formation of AgSe as an intermediate product was proposed by Zhou [14] during kinetic studies on the leaching of copper anode slimes though no analytical evidence was given. It was reported [14] that silver dissolves in HNO_3 in TWO stages & in the first stage half of the silver can be rapidly leached into solution with an activation energy of $58.6 \text{ kJ}\cdot\text{mol}^{-1}$. However, leaching experiments on synthetic Ag_2Se compounds did not show the TWO stage leaching behaviour of silver observed from leaching of

¹ As is also mentioned in section 2.2.1, the sample collected from a single electrode is insufficient for XRD analysis.

commercial anode slimes & SEM & EDXA analysis of the leaching residuals showed that amorphous (possibly with some metallic) selenium was the ONLY intermediate product [15]. This seems to be consistent with the present observations via electrochemical & analytical techniques. On the other hand, the TWO-stage leaching behaviour of silver from commercial anode slimes may be due to the fact^{that} several types of compounds of silver are present in the material (selenide, telluride & sulphide [14] for example). *Figure 3.63* shows SEM images of silver selenide electrode surface after polarization for 18 minutes at 1.2V vs. SCE in 1M HNO₃ solution at 315K. The electrode surface (silver selenide) was substantially etched & elemental selenium was observed (confirmed by EDXA, *cf. Figure 3.64*). Unlike the glassy nature of the amorphous elemental sulphur product layer observed during anodic polarisation of pentlandite [147], the elemental selenium seems to be porous & relatively randomly formed on the electrode surface rather than covering the entire electrode surface area. This may be due to the relatively short period of polarisation & the difference of physical & chemical properties between sulphur & selenium. In addition, for relatively longer periods of polarisation, a colour change of the electrode is observed from metallic 'shiny' state to brown (red?), which is similar to that of the product layer observed in the nitric acid leaching of silver selenide.

3.4.3 Chronoamperometric Study on Copper Silver Selenide

Similar to the silver selenide, synthetic copper silver selenide has also been subjected to chronoamperometric studies in 1M HNO₃ & 1M HClO₄ solution at temperatures ranging from 295K to 335K. As can be seen from the chronoamperograms (*cf. Figures 3.65-70*), unlike the silver selenide, which adopts a gradual approach towards 'steady state' currents, the 'steady state' current is established almost immediately at the beginning of the polarisation within the

potential range 0.35 to 1V vs. SCE. This indicates that an additional process akin to a catalytic reaction is also involved. A possible explanation for this observed behaviour is that the silver ions produced from oxidation of copper silver selenide instantaneously at the imposition of polarisation subsequently react with the solid phase.

In addition, copper was found to be preferentially "leached" into solution during the anodic polarisation of copper silver selenide (Cu:Ag \approx 25:1 to 50:1 at initial stages), forming a silver-rich product layer which was subsequently oxidised to elemental selenium. The large ratio of Cu:Ag in the aqueous solution at first sight seems easy to explain via deposition of silver ion on the counter electrode! However, this is ruled out by analysis of the "washing" solution (6M HNO₃) of the counter electrode.

Figures 3.71 (a) shows a back scattering electron image (BSE) of a copper silver selenide electrode initially polished, followed by polarisation at 1.0V vs. SCE in 1M HNO₃ solution for 8 minutes. As can be seen, the surface is substantially etched & the white 'spots' of product identified as Ag₂Se via X-ray mapping (*cf. Figures 3.71 (b) & 3.72*) & allied quantitative analysis. The etched areas especially the central 'ring' are identified as a silver rich intermediate product while the massive grey areas are copper silver selenide remaining un-attacked (*cf. Table 3.3* for more details).

The formation of Ag₂Se as a product of a possible catalytic reaction is very similar to a mechanism commonly proposed to explain the catalytic effect of Ag⁺ (aq) on sulphides e.g. chalcopyrite [166-7], heazlewoodite [168] & pyrite [169-170] though this is probably the first experiment to confirm the existence of Ag₂Se via quantitative analysis. In addition, during study of the leaching behaviour of Cu₂Se, CuSe, CuAgSe, Ag₂Se & mixtures of some of these synthetic anode slime components, Montoya-Jurado [15] reported that the leaching of copper from copper selenide was found to be apparently enhanced

in the mixture with silver selenide. This may also be attributed to the 'catalytic' effect of Ag^+ (aq) produced from decomposition of silver selenide in the mixture. Furthermore, preferential leaching of copper from commercial anode slimes (the main copper & silver compounds in the anode slimes are characterised as the corresponding selenides & tellurides) has also been reported [14].

Table 3.3 Results of EMPA analysis

Element	k i.x./i.std.	k. ratio	(Wt %) concen.	(mole fractions) atom. c
<i>Zone A :</i> (Ag:Se \approx 2:1)				
Cu :	0.0143	0.0143	1.330	2.03
Ag :	0.6700	0.6700	72.731	65.51
Se :	0.1519	0.1519	26.371	32.45
Total :		0.8362	100.432	
<i>Zone B :</i> (Cu:Ag:Se \approx 1:1:1)				
Cu :	0.2805	0.2805	26.332	34.68
Ag :	0.3448	0.3448	40.258	31.23
Se :	0.1606	0.1606	32.160	34.09
Total :		0.7859	98.750	
<i>Zone C :</i> (Cu:Ag:Se \approx 0.6:0.94:1)				
Cu :	0.1842	0.1842	17.769	23.636
Ag :	0.3924	0.3924	47.085	36.897
Se :	0.1817	0.1817	36.868	39.467
Total :		0.7583	101.722	

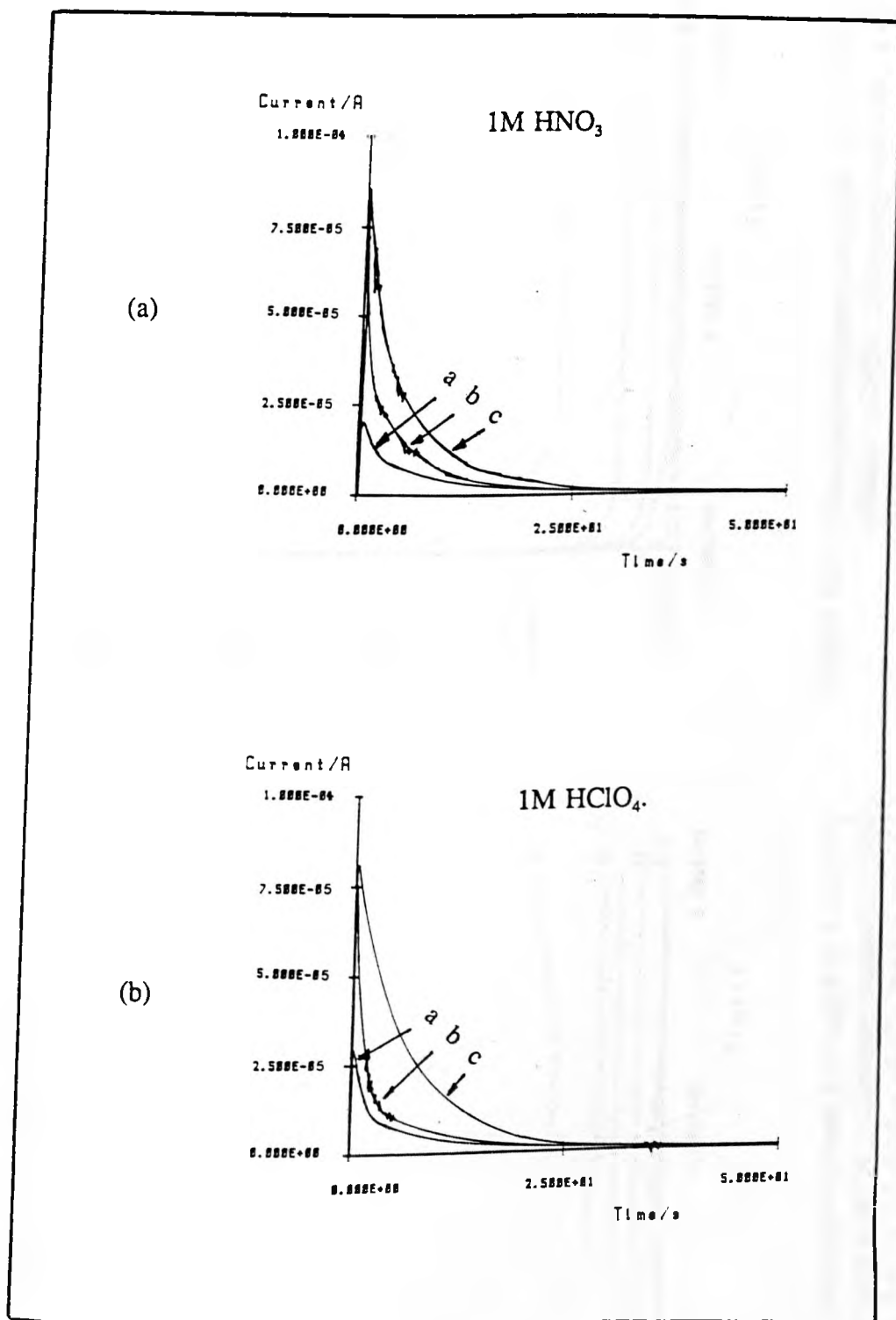


Figure 3.55 Chronoamperograms for 1M HNO₃ & 1M HClO₄ solutions (N₂ saturated) on stationary platinum electrodes at 305K. Overpotentials (V): (a) 0.2 (b) 0.5 (c) 0.9

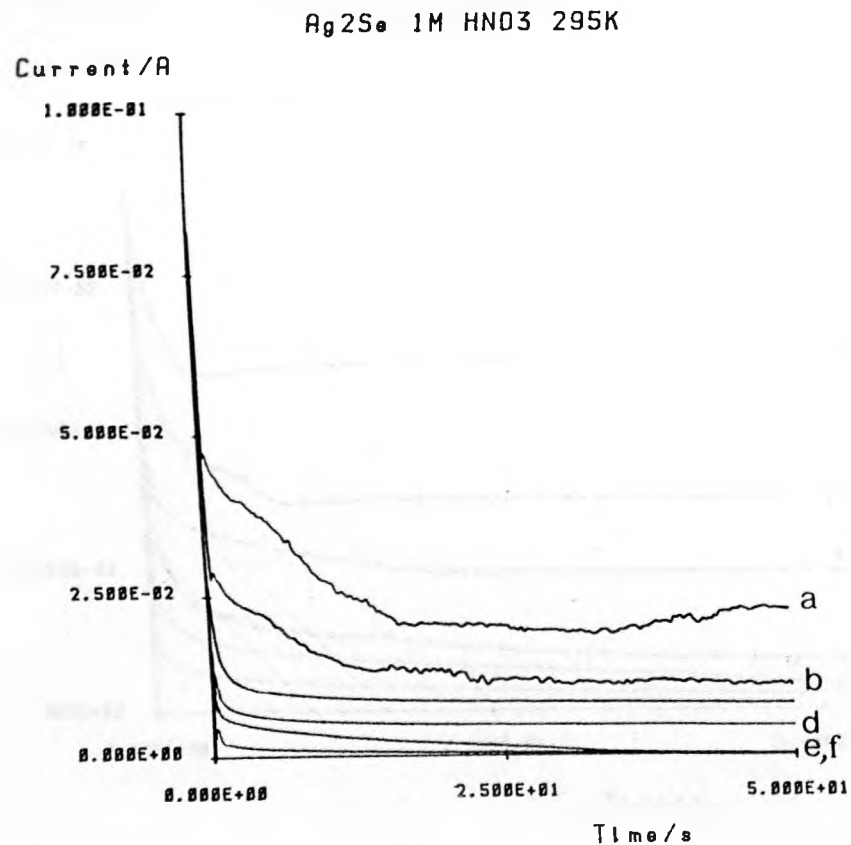


Figure 3.56 Chronoamperograms for Ag₂Se in 1M HNO₃ solution at 295K. Stationary electrode. η (V): (a) 0.6 (b) 0.5 (c) 0.4 (d) 0.3 (e) 0.2 (f) 0.1

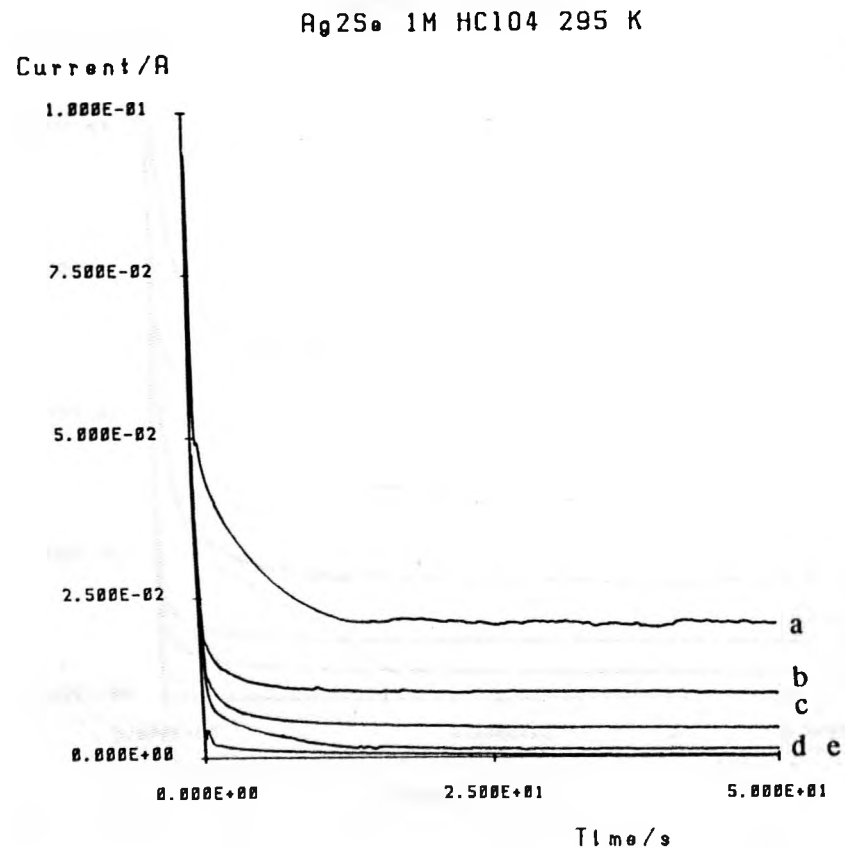


Figure 3.57 Chronoamperograms for Ag₂Se in 1M HClO₄ solution at 295K. Stationary electrode. η (V): (a) 0.6 (b) 0.5 (c) 0.4 (d) 0.3 (e) 0.1

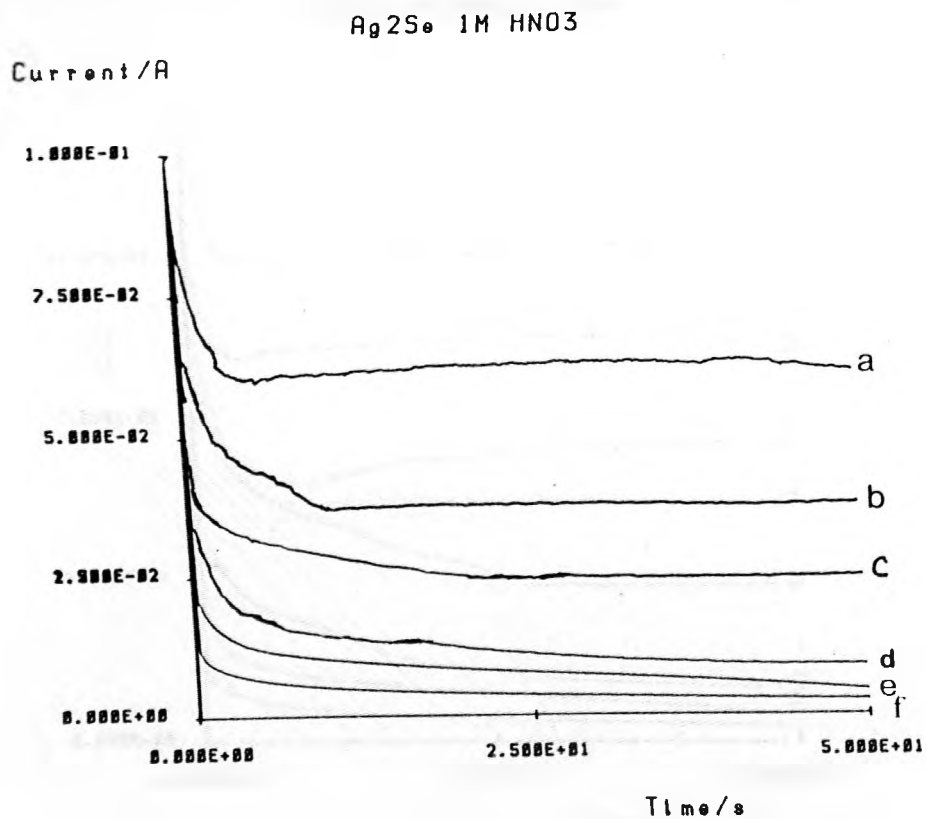


Figure 3.58 Chronoamperograms for Ag₂Se in 1M HNO₃ solution at 305K. Stationary electrode. η (V): (a) 0.8 (b) 0.7 (c) 0.6 (d) 0.4 (e) 0.3 (f) 0.2

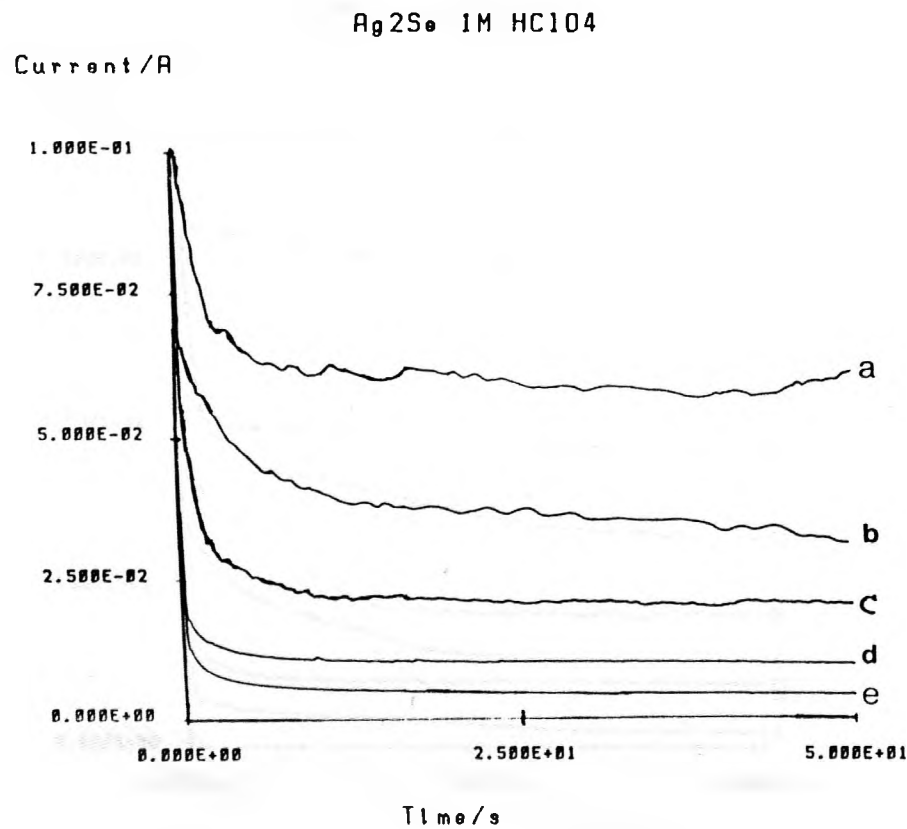


Figure 3.59 Chronoamperograms for Ag₂Se in 1M HClO₄ solution at 305K. Stationary electrode. η (V): (a) 0.8 (b) 0.7 (c) 0.6 (d) 0.4 (e) 0.3

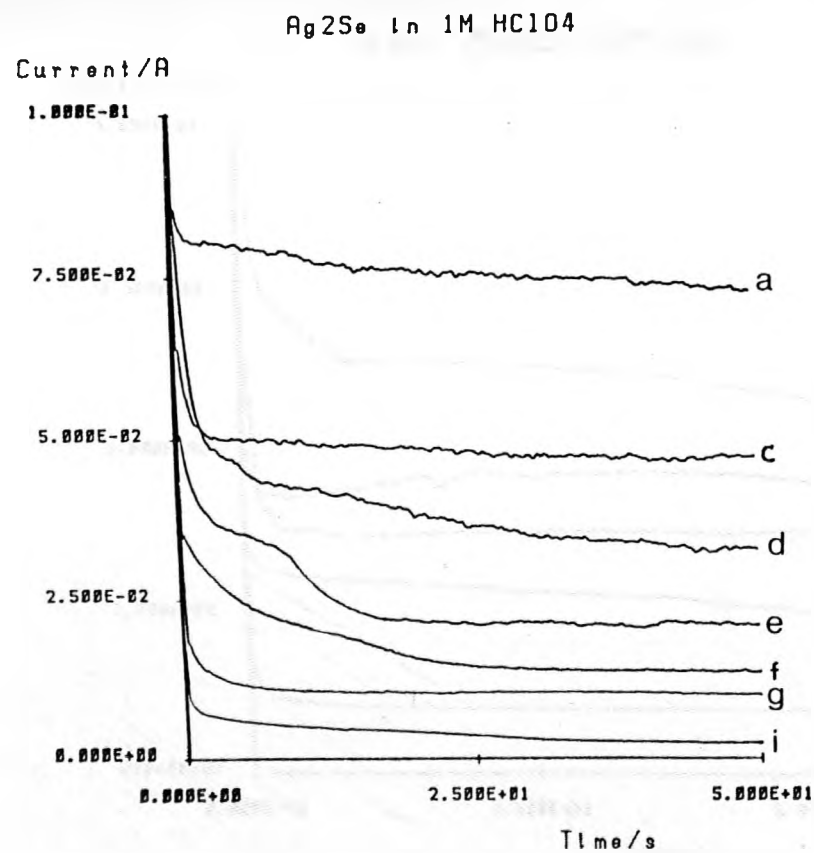
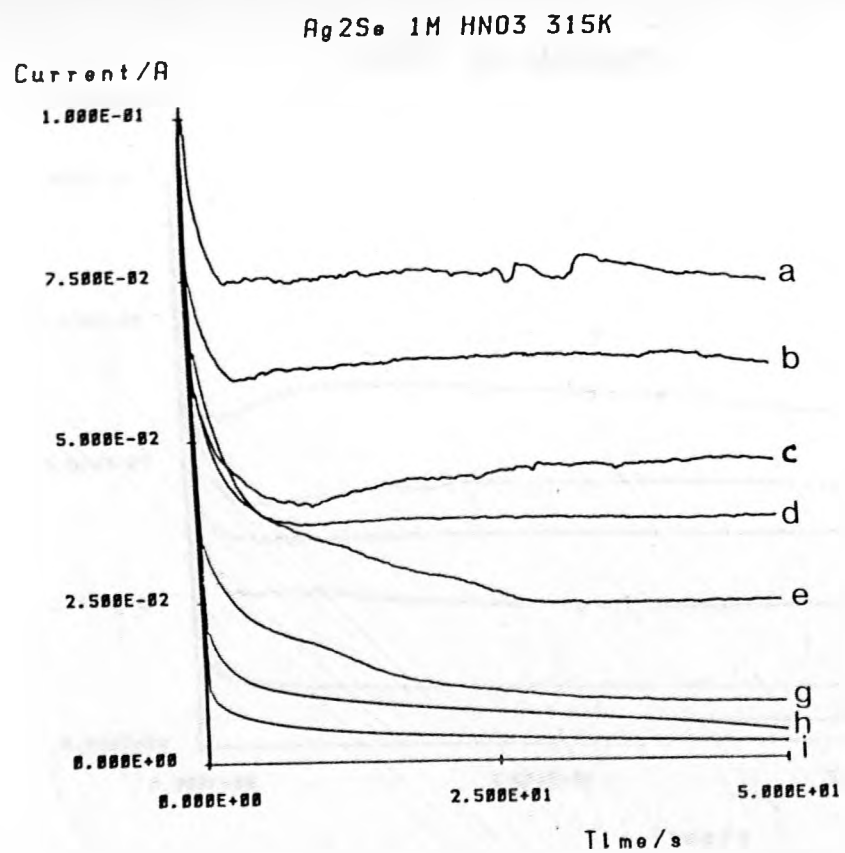


Figure 3.60 Chronoamperograms for Ag₂Se in 1M HNO₃ & 1M HClO₄ solutions at 315K.
 η (V): (a) 0.8 (b) 0.75 (c) 0.70 (d) 0.65 (e) 0.6 (f) 0.5 (g) 0.4 (h) 0.3 (i) 0.2

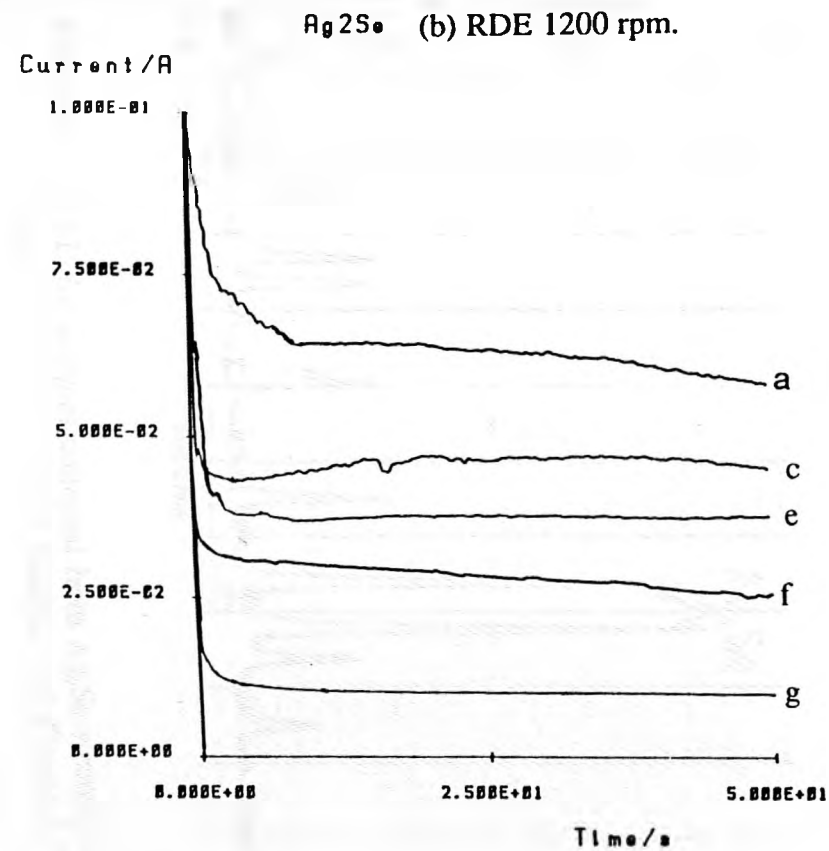
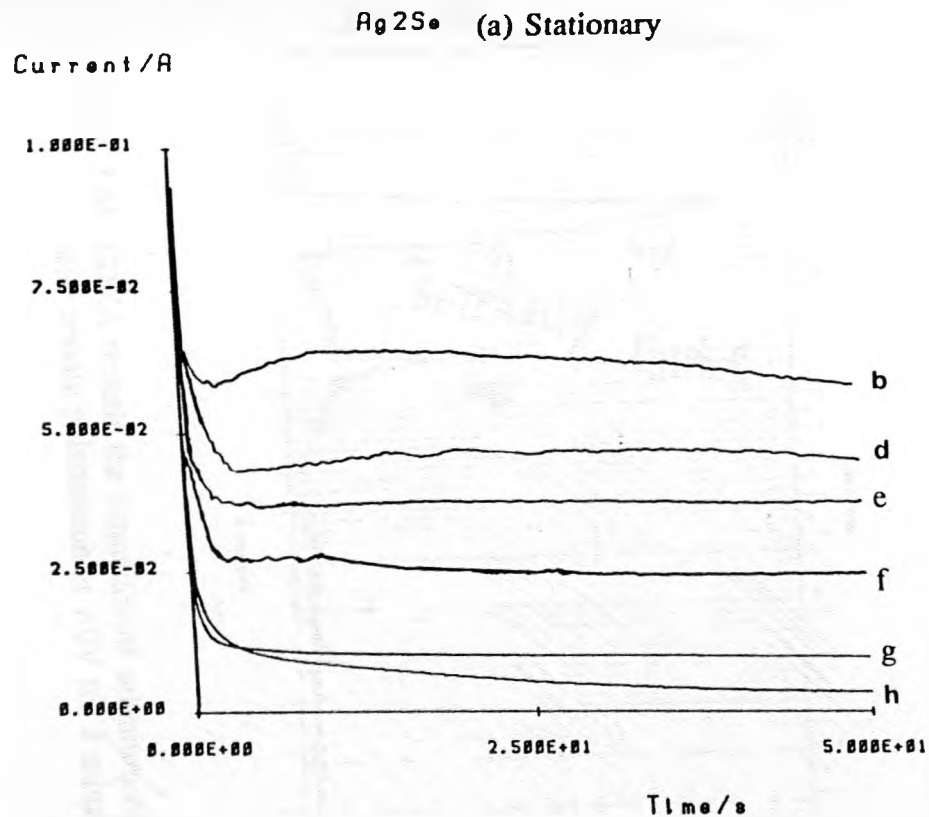


Figure 3.61 Chronoamperograms for Ag₂Se in 1M HNO₃ solution at 325K. (a) Stationary electrode (b) RDE 1200 rpm. η (V): (a) 0.75 (b) 0.70 (c) 0.65 (d) 0.6 (e) 0.55 (f) 0.5 (g) 0.4

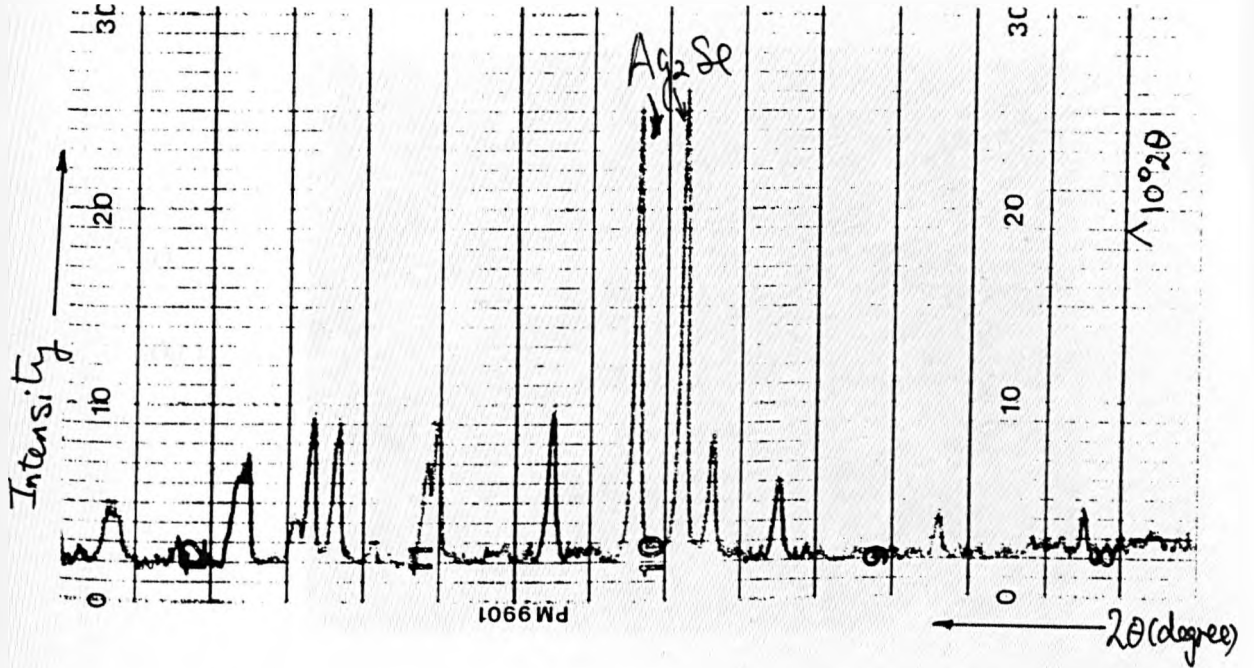


Figure 3.62 XRD for samples collected from Ag_2Se electrodes after anodic polarisation at 1.0V for 8 minutes. (cf. Figure 2.5).

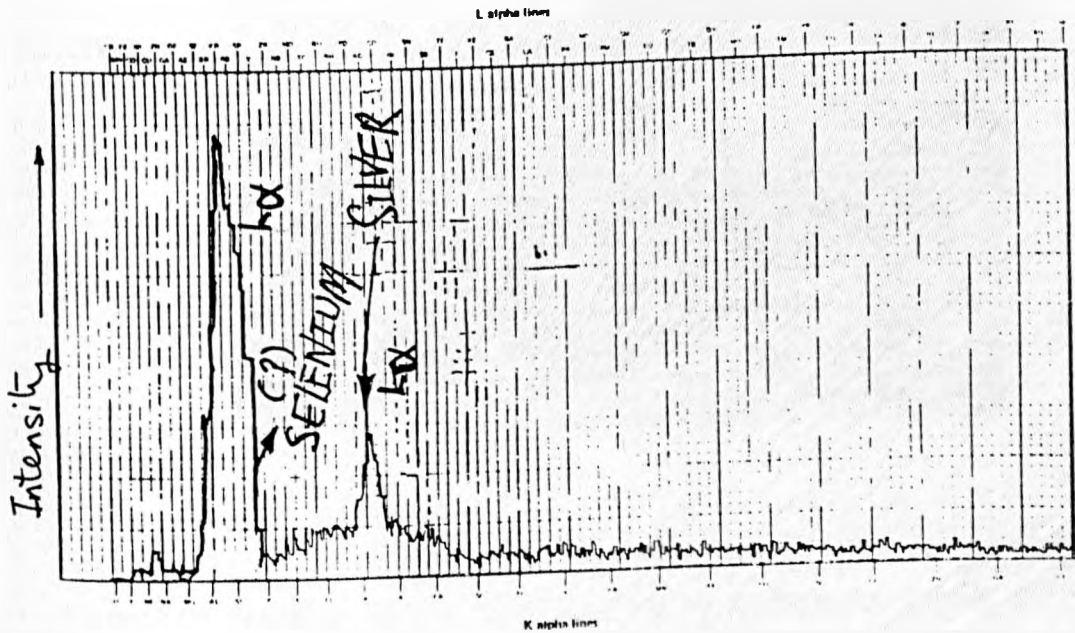
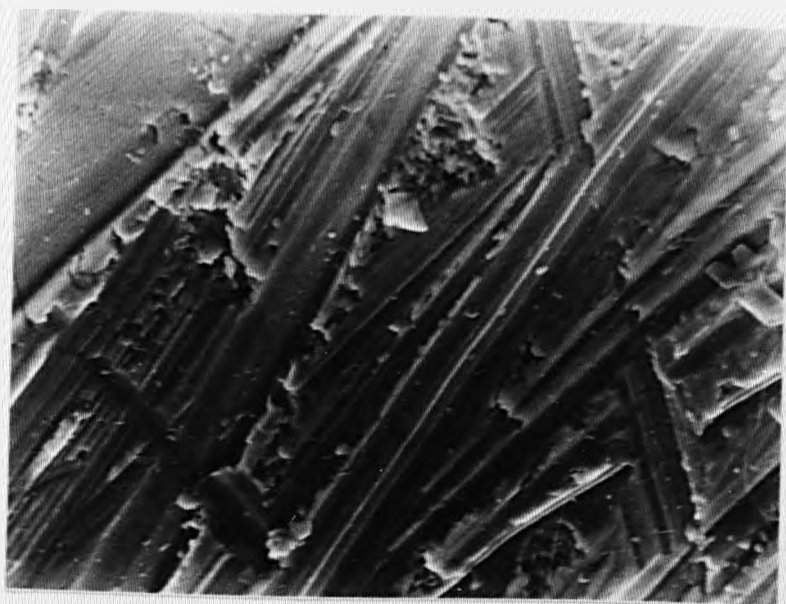


Figure 3.64 EDXA reveals the formation of selenium on Ag_2Se electrodes after anodic polarisation at 1.0V for 8 minutes.

(a)

100 x



(b)

2000 x

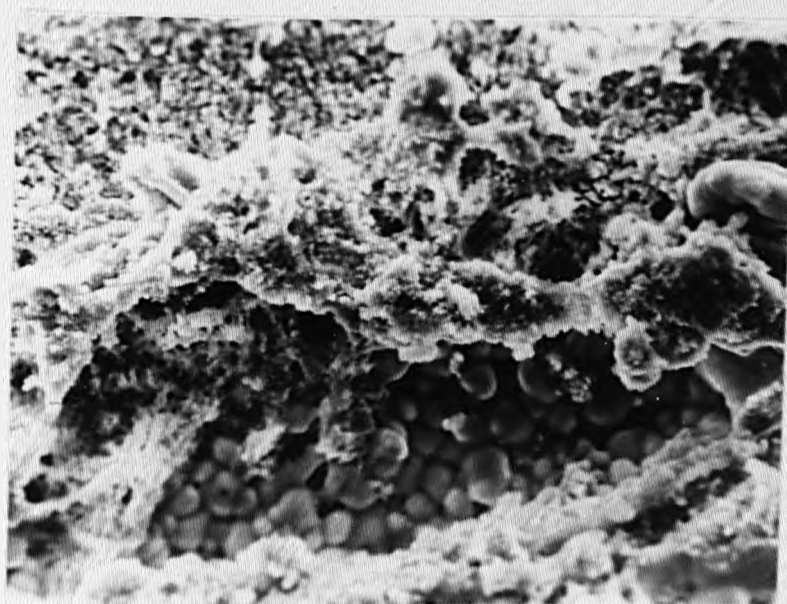


Figure 3.63 Scanning electron microscope (SEM) photographs of the silver selenide electrode surface after polarisation for 18 minutes at 1.2V vs SCE in 1M HNO₃ at 315K.

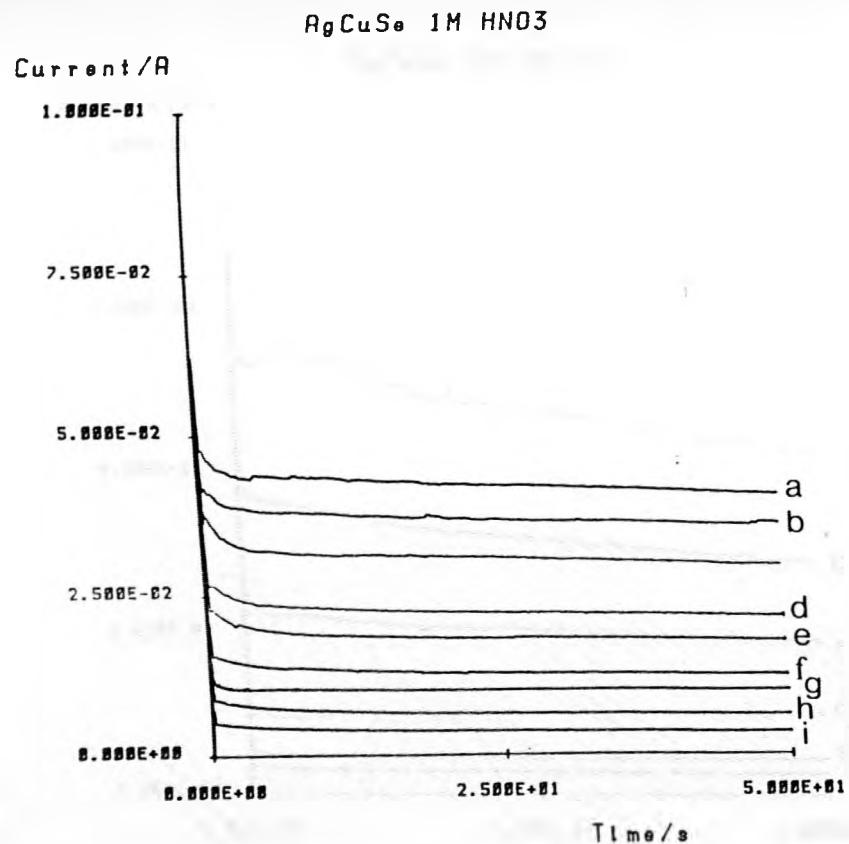


Figure 3.65 Chronoamperograms for CuAgSe in 1M HNO₃ solution at 295K. Stationary electrode. η (V): (a) 0.65 (b) 0.6 (c) 0.55 (d) 0.45 (e) 0.4 (f) 0.35 (g) 0.3 (h) 0.25 (i) 0.2

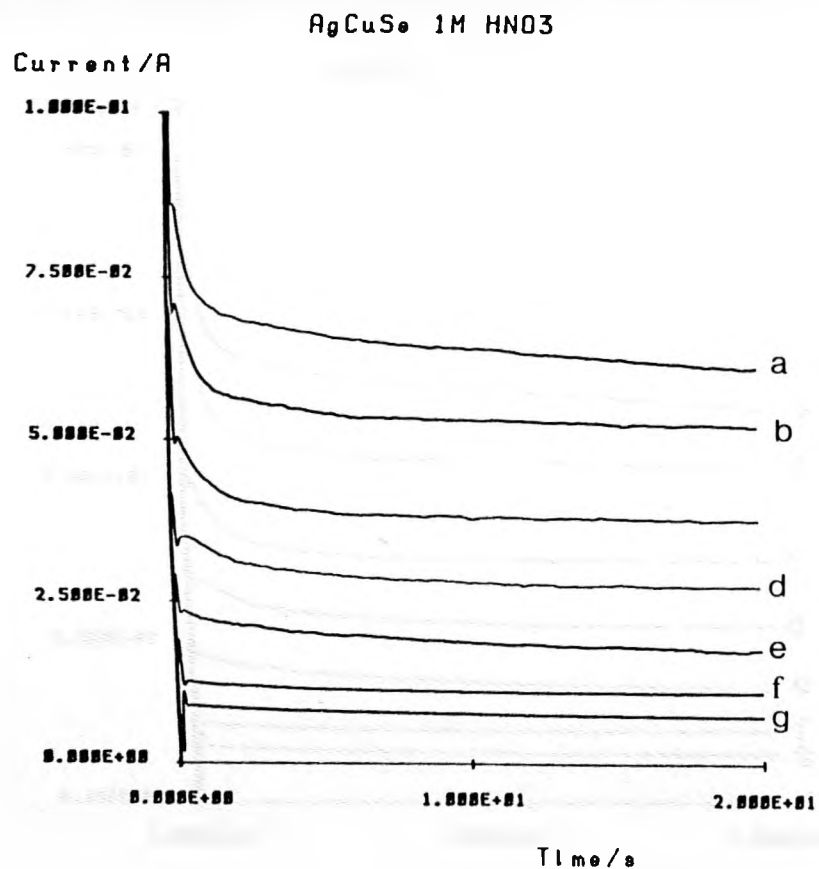


Figure 3.66 Chronoamperograms for CuAgSe in HNO₃ solution (1M) at 315K. Stationary electrode. η (V): (a) 0.75 (b) 0.7 (c) 0.6 (d) 0.5 (e) 0.4 (f) 0.3 (g) 0.2

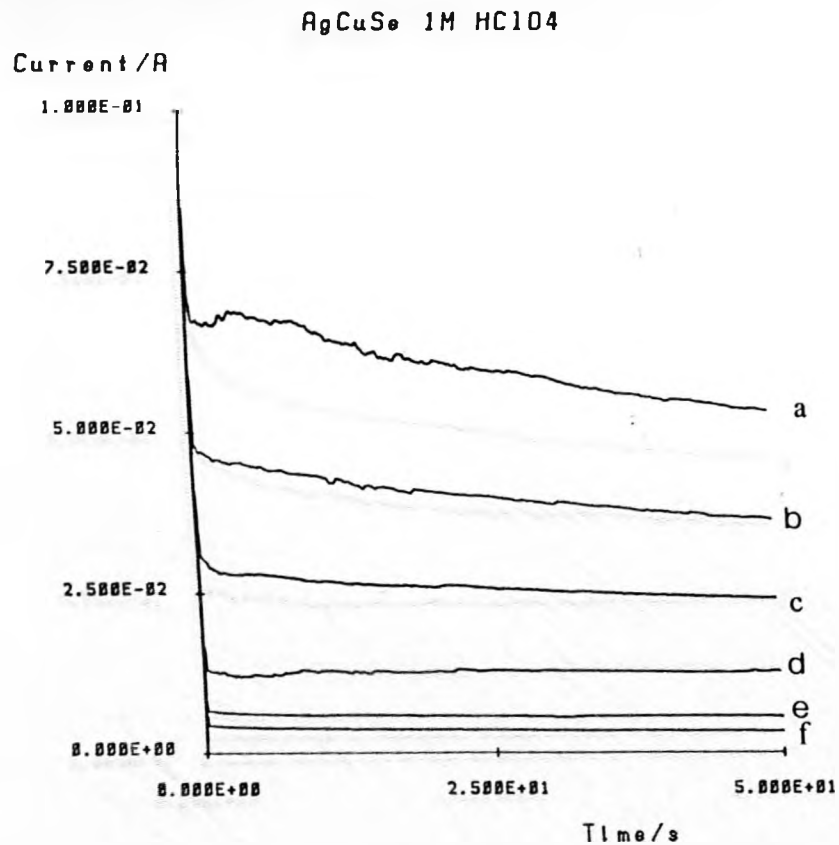


Figure 3.67 Chronoamperograms for CuAgSe in 1M HClO₄ solution at 305K. Stationary electrode. η (V): (a) 0.70 (b) 0.6 (c) 0.5 (d) 0.4 (e) 0.3 (f) 0.2

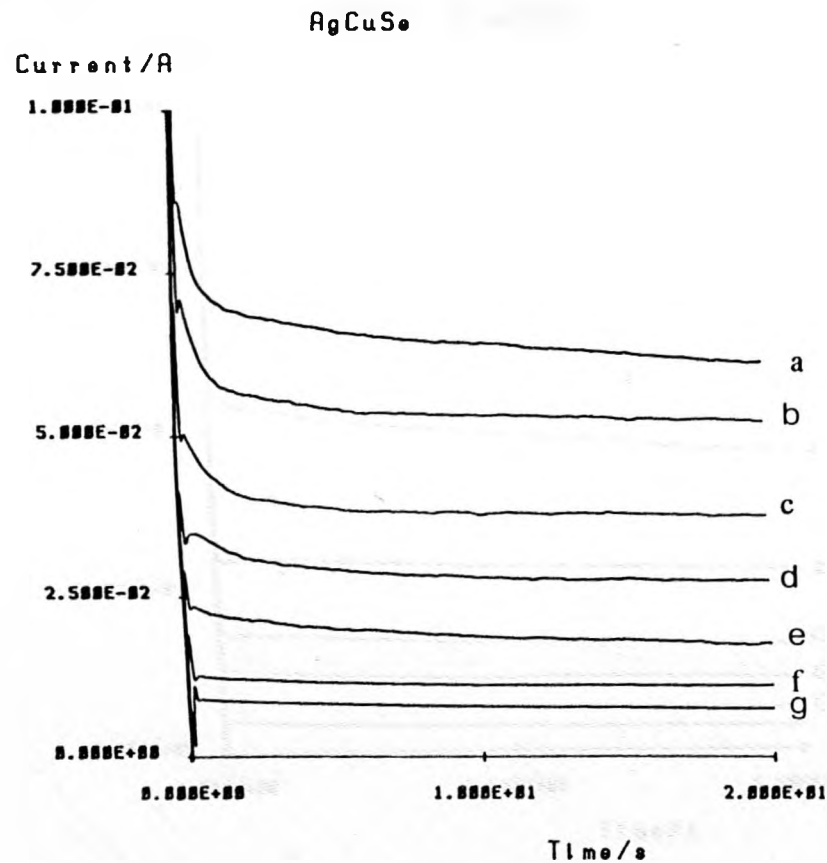


Figure 3.68 Chronoamperograms for CuAgSe in HClO₄ solution (1M) at 315K. Stationary electrode. η (V): (a) 0.70 (b) 0.6 (c) 0.55 (d) 0.5 (e) 0.4 (f) 0.3 (g) 0.2

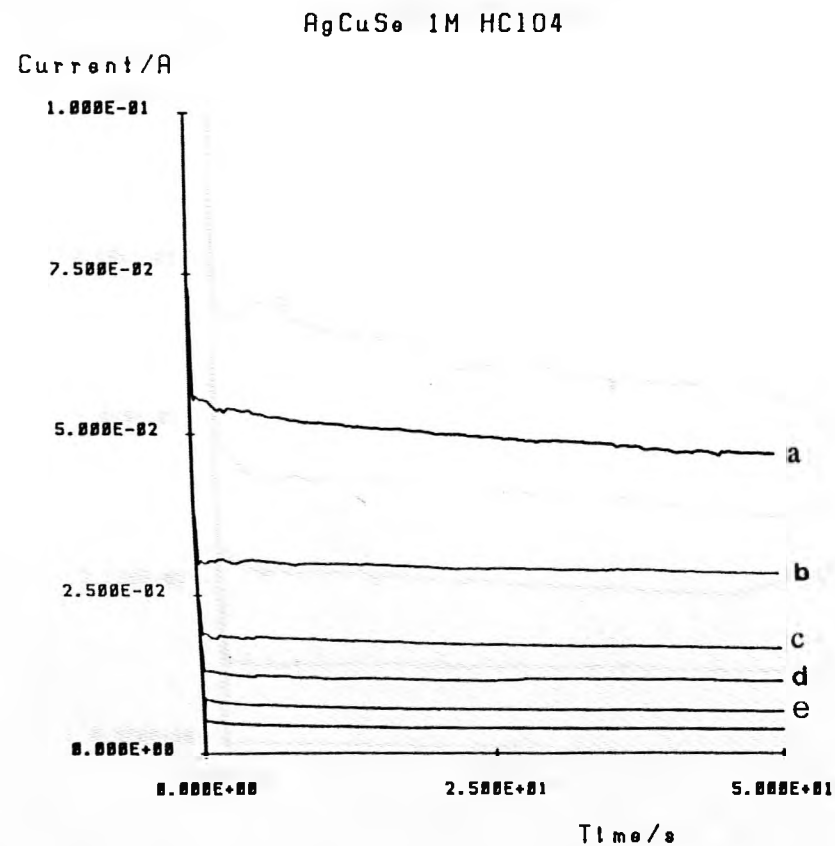
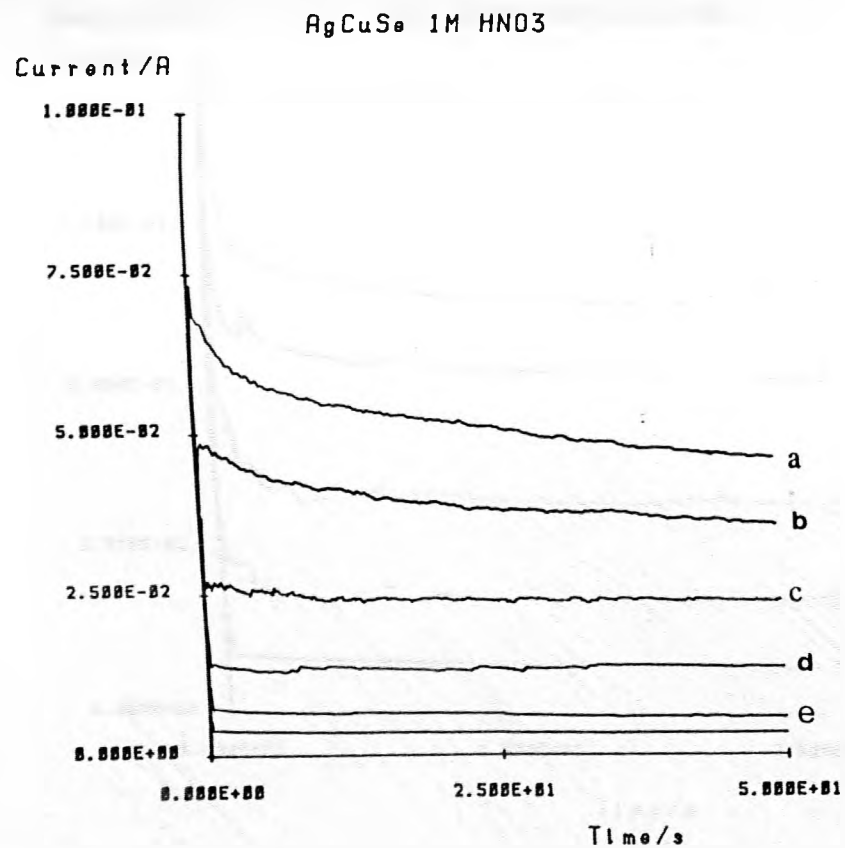


Figure 3.69 Chronoamperograms for CuAgSe in 1M HNO₃ & 1M HClO₄ solutions at 324K.
 η (V): (a) 0.65 (b) 0.6 (c) 0.55 (d) 0.5 (e) 0.4 (f) 0.3 (g) 0.2

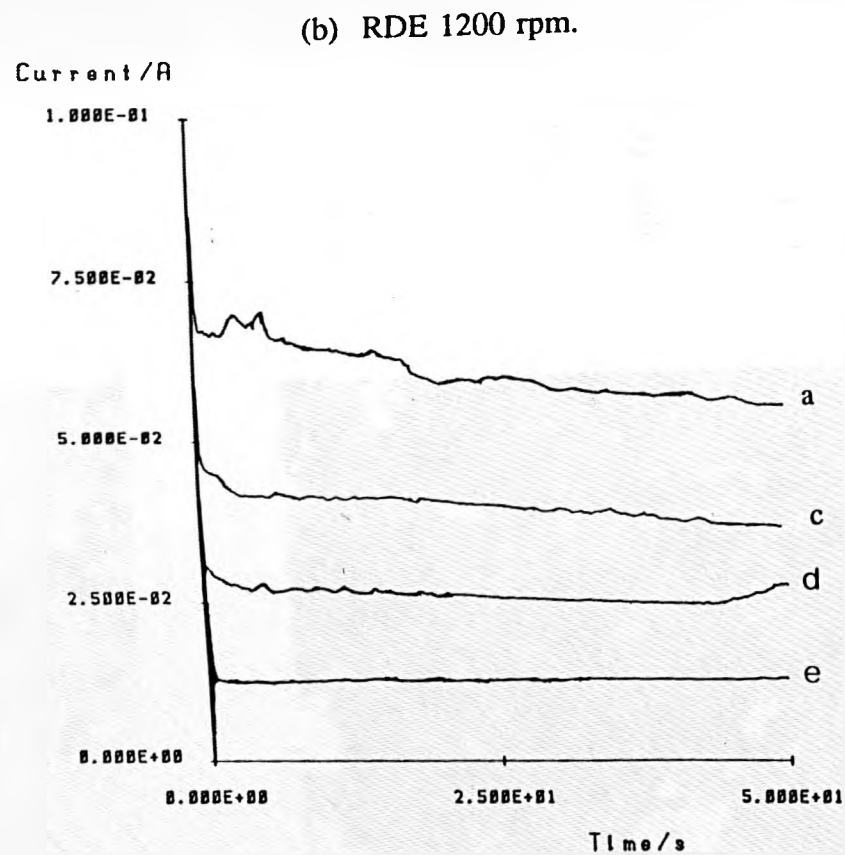
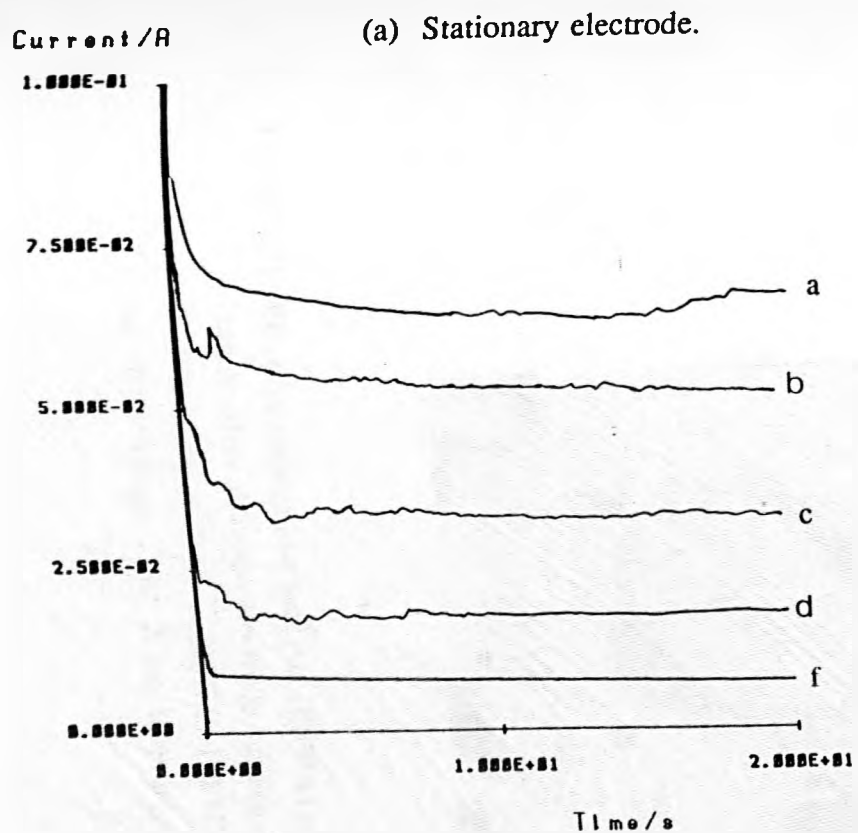
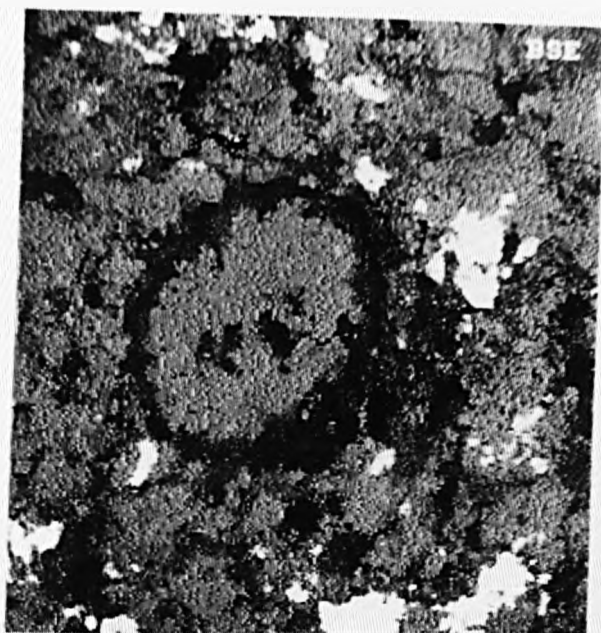


Figure 3.70 Chronoamperograms for CuAgSe in 1M HNO₃ solution at 328K. (a) Stationary electrode. (b) RDE 1200 rpm. η (V): (a) 0.70 (b) 0.65 (c) 0.6 (d) 0.5 (e) 0.4 (f) 0.3

(a) BSE

800 x



(b)

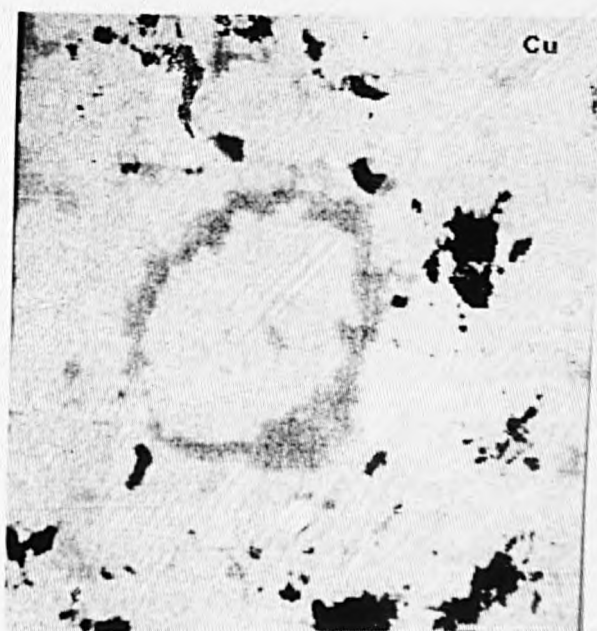


Figure 3.71 Electron microprobe analysis (EMPA) photographs of the copper silver selenide electrode surface after polarisation for 8 minutes at 1.0V vs SCE in 1M HNO₃ at 295K. (a) BSE image. (b) X ray mapping for copper.

(a)



(b)



Figure 3.72 Electron microprobe X-ray mapping for: (a) silver
(b) selenium. (cf. Figure 3.71 (a) for BSE image).

3.5 Chronopotentiometry

3.5.1 Introduction

Depending on the profiles of the polarisation currents, chronopotentiometry can be further categorised into several sub-groups of techniques. The most commonly used technique of this kind is constant current chronopotentiometry, in which the current flowing across the working & counter electrodes is maintained constant throughout the lifetime of the experiment.

Recently, the 'classical' stationary electrode theories have been directly employed for the quantitative analysis of chronopotentiometric results for the dissolution of several types of sulphide mineral electrodes [30,32,34,175-7]. Therefore, it is appropriate here to give a brief account on the original theoretical developments for planar stationary electrodes so that the applicability of these theories to the solid-state diffusion systems can be examined.

For a simple electron transfer reaction, the solution of the Fick's second law of diffusion yields the Sand equation at planar stationary electrodes:

$$i\tau^{1/2} = (\pi^{1/2}/2) nFA D^{1/2} C^{BULK} \quad (3.16)$$

where n is the number of electrons, D the diffusion coefficient, C^{BULK} the bulk concentration of the reactant. The quantity τ is defined as the transition time which spans the beginning of the polarisation to the moment where drastic change in potential occurs. The potential rise corresponds to the situation where the flux of electroactive material involved in the "present" electrode process is insufficient to sustain the current forced across the electrode/electrolyte interface.

If the system involves two independent ("parallel") electron transfer processes, the solution of the diffusional equations leads to [178]:

$$i\tau_1^{1/2} = (\pi^{1/2}/2) n_1 FA D_1^{1/2} C_1^{BULK} \quad (3.17)$$

for the first 'step' where the potential is not sufficiently positive (or negative) to allow the oxidation (or reduction) of the second species &

$$i(\tau_1 + \tau_2)^{1/2} = (\pi^{1/2}/2) FA (n_1 D_1^{1/2} C_1^{\text{BULK}} + n_2 D_2^{1/2} C_2^{\text{BULK}}) \quad (3.18)$$

for the second transitional state corresponding to the situation where the surface concentrations of BOTH reactants become zero.

Similarly, for a system involving consecutive electron transfer processes (i.e. the product of the first electron transfer process undergoes another electrochemical reaction to produce a final product which is 'non-electroactive' in that potential region), the transition time for the first τ_1 can be expressed exactly in the form of the Sand equation (*cf. eqns. 3.16 & 3.17*). The transition time for the second step τ_2 is proportional to τ_1 via [178]:

$$\tau_2/\tau_1 = 2n_2/n_1 + (n_2/n_1)^2 \quad (3.19)$$

As can be seen from *equations 3.16, 3.17, 3.18 & 3.19*, the determination of the *transition time* τ allows the numerical evaluation of the diffusion coefficient of the electroactive species, provided that the bulk concentration of the electroactive species & the number of electrons involved are known. However, practical problems arise in determining accurately the transition time. For example, at the beginning of the application of the current, the current contributes mostly to the charging of the electric double-layer capacitance rather than inducing a faradaic reaction. The above charging is especially significant in situations where the charge transfer reaction involves solid phase(s). In this case, a 'build up' of a transitional layer at the electrode/electrolyte interface may lead to a large double-layer capacitance. Furthermore, when the duration of electrolysis is sufficiently long, there are inevitable interferences by the natural convection process within the electrolyte. This in turn causes inaccuracy to the results obtained via the above simple model of semi-infinite diffusion. As a

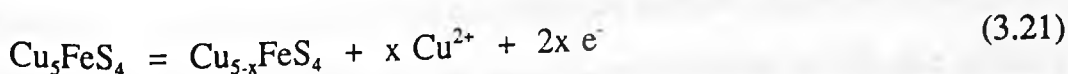
result, chronopotentiometry is not recommended for quantitative measurements in standard textbooks on electrochemistry [179,180].

Equations 4.17 & 4.18 were directly employed by Price & coworkers [32, 34,175-6] to the chronopotentiometric studies of several metal sulphide minerals e.g. chalcocite (Cu_2S), digenite (Cu_9S_5), chalcopyrite (CuFeS_2), bornite (Cu_5FeS_4) & Ni-S minerals. This was ultimately based on the simple assumption that the diffusion of electroactive species (the "free" copper ions) within the solid electrode (i.e. the mineral crystal lattice, as an "equivalent" to the "solution") is "analogous to the diffusional process within an unstirred, convection-free solution". Thus, the Sand equation etc. can be applied to the diffusion of the metal ions through the mineral crystal lattice during electrolysis. This leads to the following theoretical grounds for determination of stoichiometry etc.:

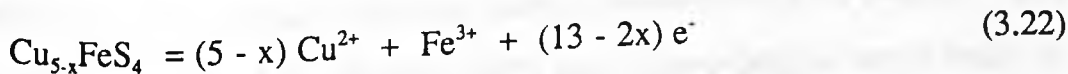
$$n_2/n_1 = [(\tau_1 + \tau_2)^{1/2} - \tau_1^{1/2}] / \tau_1^{1/2} \quad (3.20)$$

for a stepwise (or consecutive) process.

Note that the above equation (*eqn. 3.20*) is "mistakenly" derived from the classical theories for a PARALLEL process (*eqns. 3.17 & 3.18*) rather than a CONSECUTIVE process (*eqns. 3.17 & 3.19*). The latter is proposed for the dissolution mechanism of sulphide minerals by Price. For example, based on the experimental observation of preferential leaching of copper from bornite in the first stage during the chronopotentiometric studies on the bornite - H_2SO_4 system [32,176], the following mechanism was proposed:



&



for the first & second stages, respectively. In the case of bornite, x was determined as 2.5 via the treatment of chronopotentiometric data using *equation*

3.20, though experimental evidence showed that the stoichiometry of the intermediate stage was actually very close to Cu_3FeS_4 .

On the other hand, as has already been noticed by Aguayo-Salinas [177], equation 3.20 is ultimately based on further assumption (though Price did not point out) that the diffusion coefficient & concentration of the electroactive species ("free" copper ions) were the same for both stages of the reaction. This seems to difficult to explain because according to the above proposed model (eqns. 3.21 & 3.22) different solid phases were involved in the electrode processes of *stage 1* & *stage 2*. The concentration of "free" copper ions in Cu_5FeS_4 & $\text{Cu}_{5-x}\text{FeS}_4$ phases would be expected to be quite different. In addition, the nature of the electroactive species was not explicitly explained.

A different approach was made by Aguayo-Salinas [177] to study the same system using also the constant current chronopotentiometry technique. By using a model of "consecutive" electrode processes, he concluded that the intermediate copper deficient bornite phase produced during the first stage was idaite (Cu_3FeS_4), through which the solid state diffusion of cuprous ions was rate determining (during stage I of the reaction) with a diffusion coefficient $D_{\text{Cu}^+} = 1.5 \times 10^{-11} \text{m}^2 \text{s}^{-1}$. The above results were in good agreement with experimental evidence & results obtained by other investigators of the same group using other techniques.

However, referring to the complexity arising from the involvement of solid phases in the electrode processes & the fitness of different models ("parallel" & "consecutive") to the treatment of almost identical systems, Aguayo-Salinas [177] admitted that "this may indicate the uncertainty involved in the use of such simple models for complex reactions such as the dissolution of bornite". This was further confirmed by Warner [147] who systematically tested both the "parallel" & "consecutive" models, using pentlandite via conventional techniques & the more powerful numerical methods e.g. convolution & allied techniques.

The latter allows the numerical assessment of NOT ONLY the characteristic shown by the transition time (τ) BUT ALSO the shape of the potential - time responses.

3.5.2 Chronopotentiometric Study on Synthetic Silver Selenide & Copper Silver Selenide

The diffusion of metal ions in solid phases is far more complicated as compared to the aqueous diffusional systems. Therefore, one cannot use the models developed for semi-finite linear diffusion systems to fit the diffusional problems in solid phases, by simply assuming that the two types of systems are analogous. In this present work, chronopotentiometry is only used as a qualitative method to obtain useful information towards a better understanding of the sequence of anodic dissolution of silver selenide & copper silver selenide in 1M HNO₃ & 1M HClO₄ electrolyte media at temperatures of 295K & 325K.

Figures 3.73 & 3.74 show chronopotentiograms for stationary electrodes of silver selenide in 1M HNO₃ & 1M HClO₄ solutions at 295K for various polarisation currents. In both chronopotentiometric waves, a steep rise to approximately 1.0V vs. SCE is observed at the instance of the application of the polarisation current. This indicates that the charging effects are apparent at the start of the polarisation. On the other hand, the settling of the potential to a relatively high value also implies that a large overpotential is required to maintain the applied current. The potential then rises steadily until a sharp rise is evident again after a certain period of time (τ). This increase in potential corresponds to the situation where the surface concentration of the electroactive species Ag⁺ (?) falls to zero & thus the net flux of charge induced by the "present" charge transfer process is insufficient to sustain the polarisation current. The fluctuation of the potential - time responses at about 1.8V vs. SCE may

suggest that the evolution of gas (oxygen ?) probably sustains part of the current. The transition time seems to be less apparent for the chronopotentiometric behaviour of silver selenide at higher temperatures (*cf. Figure 3.76*), especially at large polarisation currents. This is comparable to the observations of increase in amount of selenium species in the electrolyte.

It seems that the composition of electrolyte does not significantly affect the chronopotentiometric behaviour of silver selenide. The effect of stirring or agitation was also studied. As can be seen from *Figures 3.73 & 3.75*, agitation of the solution also has no apparent effect on the potential - time responses for silver selenide in 1M HNO₃ at 295K. This suggests that mass transport within the aqueous electrolyte does not significantly influence the charge transfer processes for anodic dissolution of silver selenide. This is comparable with the observations in cyclic voltammetry & chronoamperometry experiments conducted earlier in this work (*cf. Section 3.2 & 3.4*).

The observed transition τ from chronopotentiometric experiments & analytical results of samples of the electrolyte at various durations of polarisation are listed in *Tables 3.4 & 3.5*, respectively. Though the quantities $i\tau^{1/2}$ under different polarisation are of similar magnitudes, there is no obvious constancy for $i\tau^{1/2}$, indicating that the anodic dissolution of silver selenide is far more complicated than the Sand equation can handle. On the other hand, the presence of selenium species in the electrolyte at large polarisation currents indicates the oxidation of either silver selenide or part of the elemental selenium to the higher valency state also participates in sustaining the current. Therefore, the use of a simple model to treat the above data is regarded as inappropriate here, irrespective of the uncertainties over the theoretical grounds of these models.

The chronopotentiometric study of copper silver selenide was carried in 1M HNO₃ & 1M HClO₄ solutions at 295K (*cf. Figures 3.77 & 3.78*). The potential - time responses are similar to those of silver selenide. The lack of

multi-stages may suggest that the observed "first stage" is a mixed behaviour of several processes. After a certain period of polarisation, the colour of the electrode changed to brown (red ?), indicating an appreciable amount of elemental selenium was produced. The "preferential" leaching of copper is again evident via AAS analysis (*cf. Table 3.6*).

Table 3.4 $i\tau^{1/2}$ data for Ag_2Se in 1M HNO_3 & 1M HClO_4 solutions

T/K	i/Am^{-2}	τ/s	$i\tau^{1/2}/\text{Am}^{-2}\text{s}^{1/2}$
1M HNO_3 solution :			
295	1250	451	26546
295	1000	674	25962
295	750	906	22575
295	500	1780	21095
295	425	2514	21562
Average $i\tau^{1/2}$			23548
$D/\text{m}^2\text{s}^{-1}$ (from Sand equation)			1.3115×10^{-11}
1M HClO_4 solution :			
295	1250	437	26131
295	1000	650	25495
295	750	926	22823
295	500	1721	20742
295	425	2544	21436
Average $i\tau^{1/2}$			23325
$D/\text{m}^2\text{s}^{-1}$ (from Sand equation)			1.2991×10^{-11}

Determination of D_A from the Sand equation, based on the following data:

$$n = 1 \quad \& \quad C_{\text{Ag}} = 26886.2 \text{ mol}\cdot\text{m}^{-3}$$

Note: C_{Ag} is Calculated from the cell parameters given by Early [128].

Self-diffusion coefficient of silver ions in Ag_2Se is of the order of 10^{-10} - $10^{-9}\text{m}^2\text{s}^{-1}$ at 298K [154]. The interdiffusion coefficient is usually about 2×10^3 times great than the self-diffusion coefficient.

Table 3.5 Aqueous analysis data for anodic polarisation of Ag_2Se .

(a) $i = 1000\text{Am}^{-2}$, Area = $7.85 \times 10^{-5}\text{m}^2$, 1M HNO_3 solution & T = 295K.			
<i>Sample 1:</i> $t = 300\text{s}$.			
Element	No. moles dissolved	Equivalent Charge/C	
Silver	2.316×10^{-4}	Ag(I)	22.36
Selenite	1.018×10^{-6}	Se(IV)	0.39
Q(applied)	= 23.55C	Q(equivalent) = 22.75C	
<i>Sample 2:</i> $t = 673\text{s}$, i.e. at the end of 1st wave.			
Element	No. moles dissolved	Equivalent Charge/C	
Silver	4.302×10^{-4}	Ag(I)	41.51
Selenite	1.796×10^{-5}	Se(IV)	6.93
Q(applied)	= 52.90C	Q(equivalent) = 48.44C	
(b) $i = 1600\text{Am}^{-2}$, Area = $7.85 \times 10^{-5}\text{m}^2$, 1M HNO_3 solution & T = 295K.			
<i>Sample 1:</i> $t = 200\text{s}$.			
Element	No. moles dissolved	Equivalent Charge/C	
Silver	1.986×10^{-4}	Ag(I)	19.16
Selenite	8.240×10^{-6}	Se(IV)	3.18
Q(applied)	= 25.12C	Q(equivalent) = 22.34C	
<i>Sample 2:</i> $t = 341\text{s}$, i.e. at the end of 1st wave.			
Element	No. moles dissolved	Equivalent Charge/C	
Silver	3.799×10^{-4}	Ag(I)	36.65
Selenite	2.360×10^{-5}	Se(IV)	9.11
Q(applied)	= 42.83C	Q(equivalent) = 45.76C	

Table 3.6 Aqueous analysis data for anodic polarisation of CuAgSe .

$i = 1600\text{Am}^{-2}$, Area = $7.85 \times 10^{-5}\text{m}^2$, 1M HNO_3 solution & T = 295K.
 $t = 461\text{s}$, i.e. at the end of 1st wave.

$i = 1600\text{Am}^{-2}$, Area = $7.85 \times 10^{-5}\text{m}^2$, 1M HNO_3 solution & T = 295K. $t = 461\text{s}$, i.e. at the end of 1st wave.			
Element	No. moles dissolved	Equivalent Charge/C	
Silver	1.701×10^{-5}	Ag(I)	1.64
Copper	3.199×10^{-4}	Cu(II)	61.73
Selenite	1.845×10^{-5}	Se(IV)	7.12
Q(applied)	= 57.90C	Q(equivalent) = 70.49C	

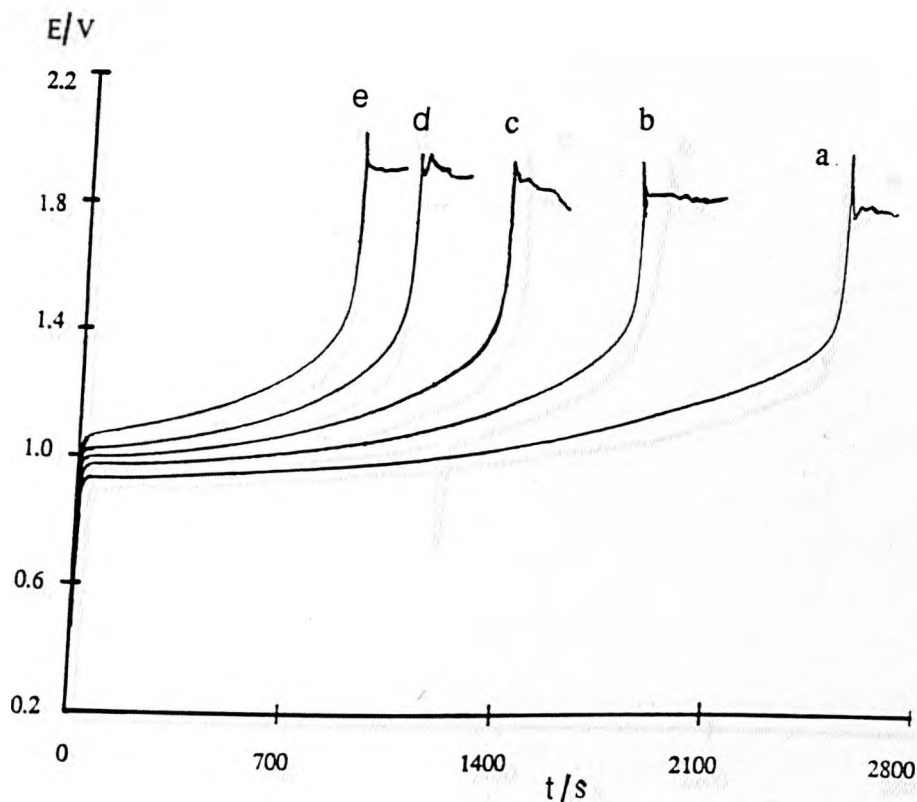


Figure 3.73 Chronopotentiograms for Ag_2Se in 1M HNO_3 solution at 295K. Stationary electrode. Current density (Am^{-2}): (a) 400 (b) 475 (c) 600 (d) 725 (e) 850

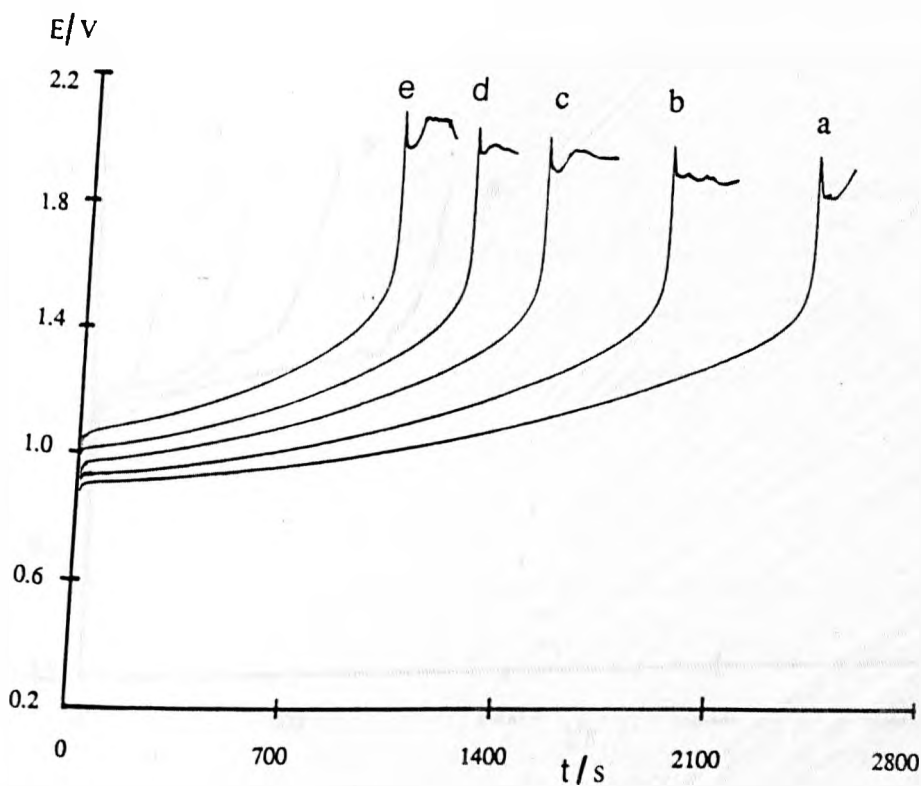


Figure 3.74 Chronopotentiograms for Ag_2Se in 1M HClO_4 solution at 295K. Stationary electrode. Current density (Am^{-2}): (a) 425 (b) 475 (c) 550 (d) 625 (e) 750

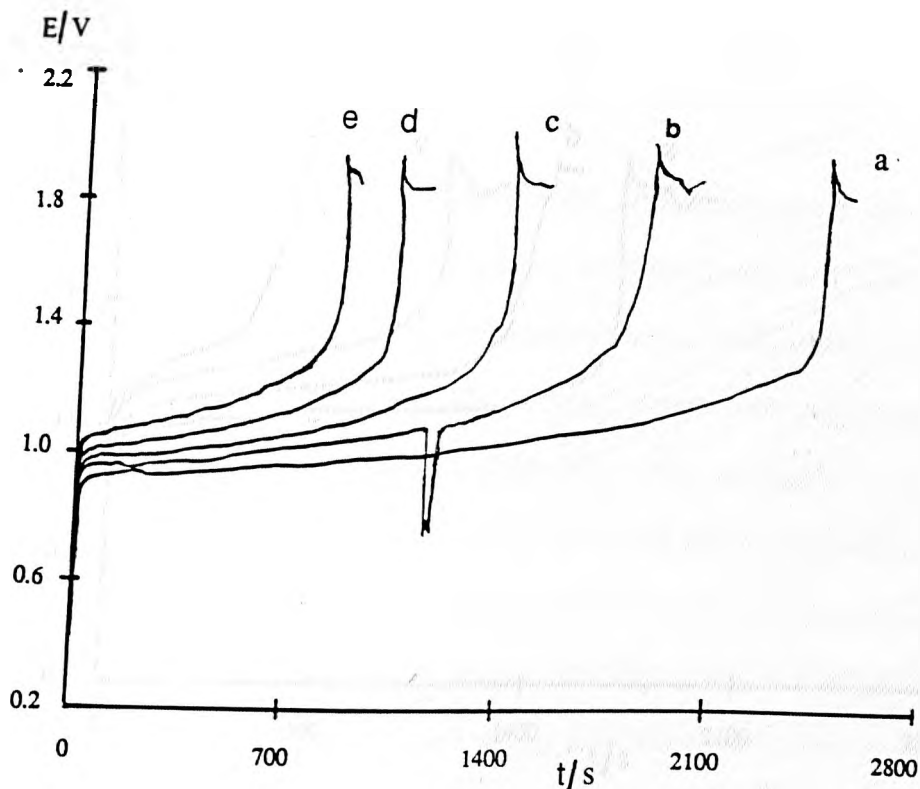


Figure 3.75 Chronopotentiograms for Ag_2Se in 1M HNO_3 solution at 295K . RDE 1200 rpm . Current density (Am^{-2}): (a) 400 (b) 475 (c) 600 (d) 725 (e) 850

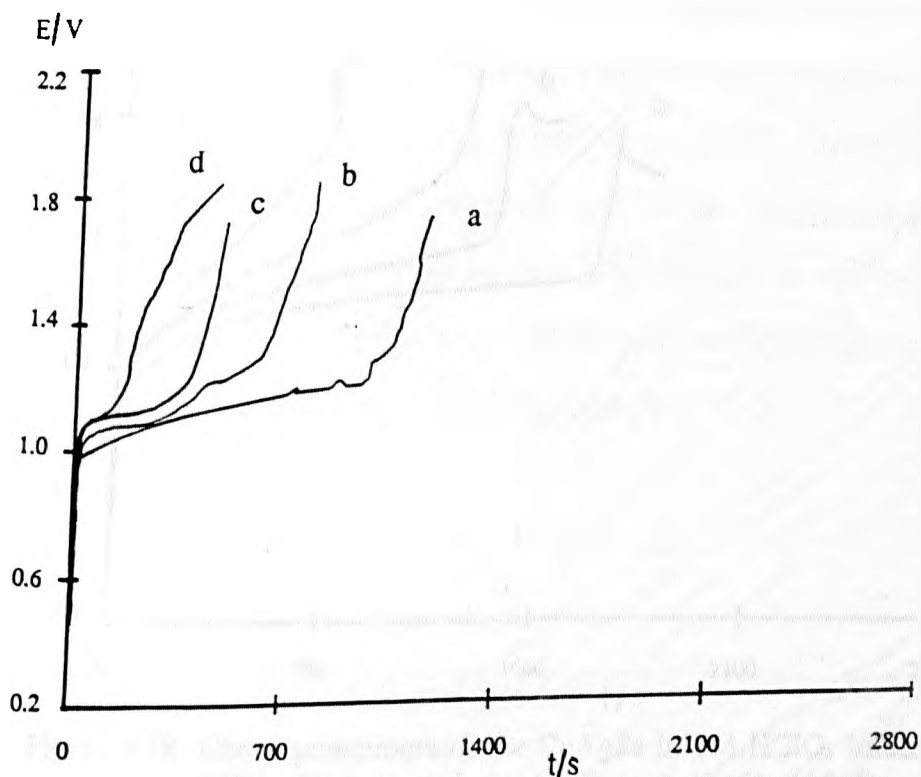


Figure 3.76 Chronopotentiograms for Ag_2Se in 1M HNO_3 solution at 325K . Stationary electrode. Current density (Am^{-2}): (a) 500 (b) 650 (c) 750 (d) 850

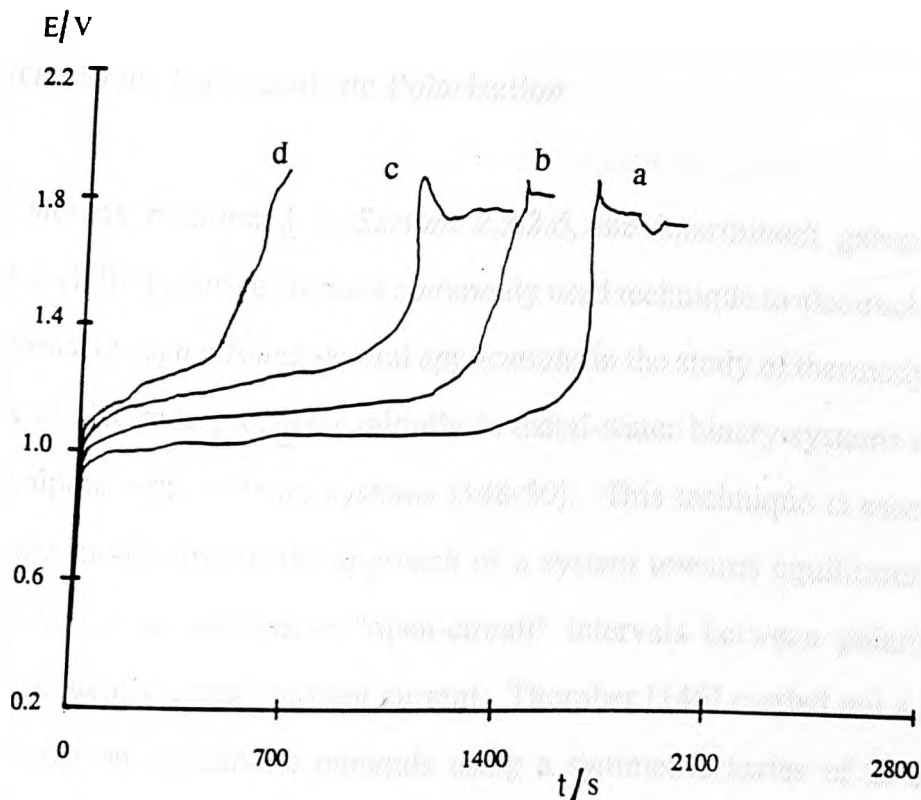


Figure 3.77 Chronopotentiograms for CuAgSe in 1M HNO_3 solution at 295K. Stationary electrode. Current density (Am^{-2}): (a) 500 (b) 600 (c) 725 (d) 800

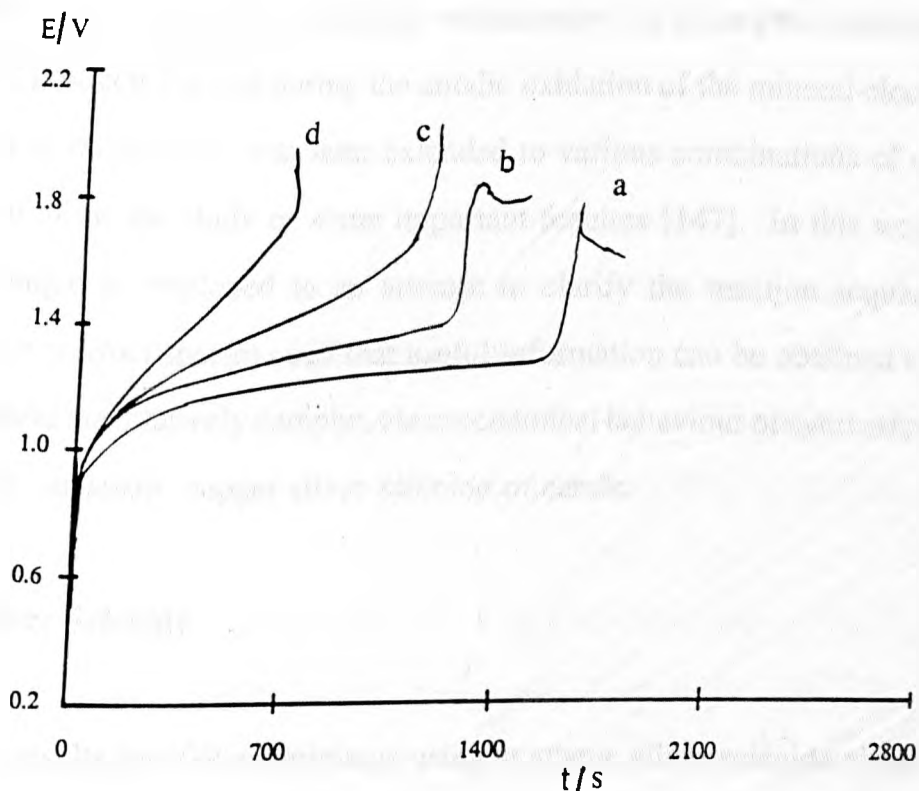


Figure 3.78 Chronopotentiograms for CuAgSe in 1M HClO_4 solution at 295K. Stationary electrode. Current density (Am^{-2}): (a) 500 (b) 600 (c) 725 (d) 800

3.6 Intermittent Galvanostatic Polarisation

As already mentioned in *Section 2.3.2.6*, the intermittent galvanostatic polarisation (IGP) technique is not a commonly used technique in electrochemical investigations, though it found several applications in the study of thermodynamic properties of electrode processes initially in metal-water binary systems & later in metal-sulphur-water ternary systems [148-50]. This technique is essentially based on the monitoring of the approach of a system towards equilibrium or a 'mixed' potential, at successive "open-circuit" intervals between polarisation treatment frequently under constant current. Thornber [146] carried out a series of experiments on pentlandite minerals using a symmetric series of 2s on/off anodic current pulses, followed by changing the polarity of the polarisation current after a certain period of anodic treatment. The following cathodic treatment is very similar to "stripping voltammetry" & allows the identification of several products formed during the anodic oxidation of the mineral electrodes. The form of polarisation was later extended to various combinations of current profiles to allow the study of some important features [147]. In this work, the IGP technique is employed in an attempt to clarify the reaction sequence & identify the product species such that useful information can be obtained to help to understand the relatively complex electrochemical behaviour of synthetic silver selenide & especially copper silver selenide minerals.

3.6.1 Silver Selenide

The results for IGP experiments using synthetic silver selenide electrodes in 1M HNO₃ & 1M HClO₄ solutions at 315K are shown in *Figures 3.79-81*. The polarisation current is essentially a "SQUARE" wave with two second "on", followed by two seconds "off" or "open-circuit". As can be seen from the above

figures, the IGP traces show a number of 'potential arrests'. The upper (or lower in the cases of cathodic polarisation) "curves" indicate the potential required for maintaining the applied polarisation current via a particular oxidation (or reduction) process at various stages, whilst the other side of the traces show the potentials of the corresponding approach to 'equilibrium' that the system makes during 'open-circuit'. However, due to the slow nature of the reactions involving solid phase(s), it is unlikely that these processes reach equilibrium at such a short period of "open-circuit". *Figure 3.82* shows the IGP traces for an experiment under similar conditions to those for *Figure 3.81*, except for the form of polarisation current. In *Figure 3.82*, the duration of a single polarisation operation is still two second but with a relatively longer time in open-circuit (40s) to allow the potential of the system to settle. As can be seen, the potential 'arrests' at "open-circuit" during anodic polarisation dropped from 0.75V vs. SCE to nearly 0.5V vs. SCE. As is illustrated in *Figure 3.83*, when the system is held at "open-circuit" for a sufficiently longer period, the potential settles gradually towards a well defined potential which corresponds to a thermodynamic equilibrium of a single process or the mixed potential for the dynamic equilibrium between two (or more) processes. In addition, the magnitudes of the polarisation currents also significantly influence the shape of IGP traces in a similar fashion to the situation of constant polarisation or chronopotentiometry. These are illustrated in *Figures 4.84-86*. Brief descriptions of IGP results is given below.

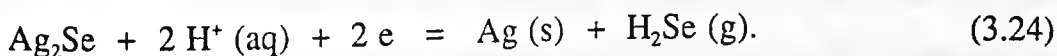
In practice, the IGP traces are frequently interpreted via mainly thermodynamic considerations. The results corresponding to the features in *Figures 3.79-86* are listed in *Table 3.7*.

As can be seen in *Figures 3.79 & 3.80*, during cathodic polarisation a relatively large negative potential of approximately -0.6V vs. SCE is required to maintain a cathodic current density of $178 \text{ A}\cdot\text{m}^{-2}$ after ONLY several current

pulses. This is consistent with the observations of low reactivity of freshly polished silver selenide in the first cathodic excursion in voltammetric studies (*cf. Section 3.2*). The electrode process in the above potential region can be ascribed as either the reduction of aqueous hydrogen ions or the reduction of the silver selenide electrode via the following reactions:



&



Gas evolution & colour change of the electrolyte were again observed at this stage. This suggests that at least an appreciable part of the current is sustained by the reduction of the silver selenide electrode via *equation 3.24*. The formation of elemental silver as a product of reduction of silver selenide is also confirmed via the subsequent anodic polarisation similar to the "anodic stripping" methods. The first "plateau" at a potential of 0.5V vs. SCE (*cf. Figures 3.79 & 3.80*) on subsequent anodic polarisation is probably caused by the dissolution of the elemental silver produced during the preceding cathodic treatment, via the following reaction:



The lack of this feature in the experiments without initial cathodic treatment (*cf. Figures 3.41 & 3.42*) also indicates the involvement of product(s) formed during the preceding cathodic polarisation rather than the oxidation of the silver selenide electrode itself. Most importantly, the formation of elemental silver is further confirmed by SEM & EDXA analysis. See *Figures 3.87-88* for more detail of the analytical results.

The closeness between the potentials during the corresponding polarisation & "open-circuit" periods at the first "plateau" indicates that the dissolution

process involves a relatively fast electron transfer process. Therefore, the oxidation of silver selenide at this stage is ruled out. As is expected from results of the cyclic voltammetric experiments (*cf. Section 3.2*), the slow nature of the anodic dissolution of silver selenide would require a much larger overpotential to sustain such a large anodic current.

Due to the limited amount of elemental silver produced during the cathodic polarisation, the dissolution of elemental silver is complete over a relatively short period of time. Immediately after the "complete" dissolution of the thin layer of elemental silver on the electrode surface, a sudden rise in the potential is observed while the system is "switched" to another electron transfer process i.e. the anodic dissolution of the silver selenide electrode via:

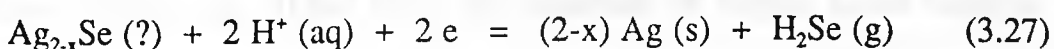


The above reaction subsequently becomes the dominant charge transfer process to sustain the current. At this stage, a much higher potential (about 0.9-1.1V vs. SCE) is required to support the polarisation current, which is consistent with the voltammetric results obtained earlier in this work. The "open-circuit" potentials at this stage are considered as a mixed-potential regime between Ag^+/Ag & the dissolution reaction of silver selenide. Note also the sharp increases in potential after a sufficiently longer period (i.e. number of cycles) of anodic polarisation. This is ultimately due to the fact that the anodic oxidation of silver selenide mineral to form silver ions & elemental selenium is gradually approaching the diffusion limited regime. The duration of polarisation before the dramatic increase in potential is somewhat proportional to the magnitudes of polarisation current. This is in good agreement with BOTH theoretical expectations (via the Sand equation as a rough guide for IGP experiments) & observations in the chronopotentiometry experiments (*cf. Section 3.5*).

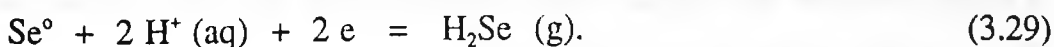
The "potential arrest" at 0.47V vs. SCE occurs immediately after the

change of polarity of the polarisation from anodic to cathodic. This corresponds to the reduction peak for silver deposition on a typical cyclic voltammogram (*cf. e.g. Figure 3.5*). This is also comparable to the potential arrests caused by the dissolution of elemental silver in *Figure 3.79* after a initial cathodic treatment. The observation of silver crystals, via SEM & EDXA analysis (*cf. Figures 3.87 & 3.89*), on the silver selenide electrode surface gives further evidence of the deposition at this stage. It should also be noted that the metallic silver formed via the cathodic reduction of silver selenide mineral seems to 'grow' within the mineral lattice along with the un-reacted mineral. The deposited silver, on the other hand, is in the form of well crystallised particles.

Immediately after the potential arrest "responsible" for silver deposition, two distinctive "potential arrests" occur successively until the reduction of the mineral electrode & possibly hydrogen ions in the electrolyte occurs. Comparing this behaviour with the results of voltammetric studies (*cf. Section 3.2*), the potential arrest after that of the reduction of silver ions seems to be likely caused by either of the following processes:



whilst that close to the main reduction domain is probably due to the reduction of elemental selenium:

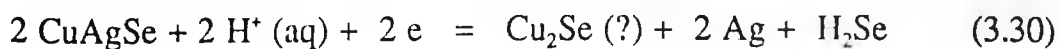


However, due to the insensitivity of XRD for identifying the possible presence of a thin transitional layer on the electrode surface, uncertainty remains over the above interpretations which are basically based on the grounds of experimental observations.

3.6.2 Copper Silver Selenide

The results of IGP experiments on copper silver selenide are shown in *Figures 3.90-92*. In general, the IGP traces for copper silver selenide are similar to those observed for silver selenide. However, due to the complexity caused by possible interaction between silver ions & the solid electrode, & the possible formation of more intermediate products, the interpretation of the "potential arrests" at interspersed "open-circuit" intervals is less clearly understood than those of silver selenide.

The results are very similar for 1M HNO₃ & 1M HClO₄ solutions, as is shown in *Figures 3.90 & 3.91*. As soon as the cathodic polarisation current is initiated, the potential of the working electrode (measured with respect to a SCE reference electrode) is after ONLY a few cycles driven to a large negative value in order to sustain the applied cathodic current. The evolution of gas & colour change of the electrolyte are again observed here, indicating the formation of hydrogen selenide gas (H₂Se) from the reduction of copper silver selenide. However, due to the difficulty in getting access to some more powerful surface/chemical analytical techniques (e.g. ESCA, XPS) at Leeds, the mechanism of the reduction of copper silver selenide remains unresolved. The narrow transitional region, during the subsequent anodic polarisation before the "plateau" where elemental silver dissolves, may suggest that metallic copper is not a major product of the preceding reduction process(es). Hence, the following reaction may be proposed:



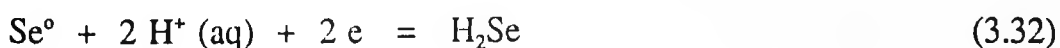
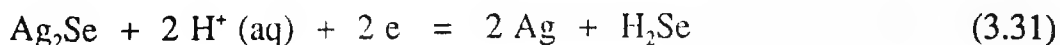
The proposal for formation of Cu²⁺ or Cu⁺ seems unrealistic in such a strong

reductive environment.

When the polarity of the polarisation current is changed from cathodic to anodic, the potential settles to around 0.5V vs. SCE after passing through a narrow transitional period. The apparent potential arrest in this potential is caused by the anodic dissolution of elemental silver produced during the previous cathodic polarisation. When the dissolution of silver is complete, anodic potentials of approximately 1.0V vs. SCE are observed. This is comparable to cyclic voltammetry results which suggest that a considerably large overpotential is required to obtain an appreciable anodic current for dissolution of copper silver selenide. The "open-circuit" potentials at this stage are probably a mixed-potential of several processes, including the interaction between silver ions (Ag^+) with the solid electrode.

Unlike the synthetic silver selenide, which displays several stages of potential arrests when the polarity of polarisation is reversed after a certain period of anodic treatment, the IGP features for copper silver selenide are less apparent. The "plateau" for deposition of silver ions almost disappears & this thus indicates a much lower concentration of Ag^+ (aq) at the electrode surface as compared to the case of silver selenide. This in turn may suggest that there exists some kind of interaction between Ag^+ (aq) & the solid phase.

The processes which sustain the cathodic current on the reversal of polarisation before the reduction of copper silver selenide & hydrogen ions at later stages probably involve the following reactions:





with the participation of possible intermediate products. The direct reduction of copper silver selenide is also thermodynamically favoured in the above potential region. As is mentioned in the previous section, the validity of the above deductions requires confirmation by additional experimental, especially to produce analytical, evidence via e.g. ESCA & XPS.

When the system is held at "open-circuit" for a sufficiently longer period, the electrode potential settles gradually towards the open circuit value prior to the the polarisation (*cf. Figures 3.93 & 3.94*).

Table 3.7

Processes denoted on the IGP traces

No.	Potential/reaction
1.	Mixed-potential $\text{Ag}_2\text{Se (s)} = 2 \text{Ag}^+ \text{(aq)} + \text{Se}^\circ + 2 \text{e}$ $2 \text{H}^+ \text{(aq)} + 2 \text{e} = \text{H}_2 \text{(g)}$
2.	Reduction $\text{Ag}_2\text{Se (s)} + 2 \text{H}^+ \text{(aq)} = 2 \text{Ag (s)} + \text{H}_2 \text{(g)}$ $2 \text{H}^+ \text{(aq)} + 2 \text{e} = \text{H}_2 \text{(g)}$
3.	Oxidation $\text{Ag (s)} = \text{Ag}^+ \text{(aq)} + \text{e}$
4.	Oxidation $\text{Ag}_2\text{Se (s)} = 2 \text{Ag}^+ \text{(aq)} + \text{Se}^\circ + 2 \text{e}$
5.	Mixed-potential $\text{Ag}_2\text{Se (s)} = 2 \text{Ag}^+ \text{(aq)} + \text{Se}^\circ + 2 \text{e}$ $\text{Ag}^+ \text{(aq)} + \text{e} = \text{Ag (s)}$
6.	Reduction $\text{Ag}^+ \text{(aq)} + \text{e} = \text{Ag (s)}$
7.	Reduction $\text{Ag}_2\text{Se} + 2 \text{H}^+ \text{(aq)} + 2 \text{e} = 2 \text{Ag (s)} + \text{H}_2\text{Se (g)}$ $\text{AgSe (s)} + 2 \text{H}^+ \text{(aq)} + 2 \text{e} = \text{Ag} + \text{H}_2\text{Se (g)} \quad (?)$
8.	Reduction $\text{Se}^\circ + 2 \text{H}^+ \text{(aq)} + 2 \text{e} = \text{H}_2\text{Se (g)}$
9.	Reduction $2 \text{CuAgSe} + 2 \text{H}^+ \text{(aq)} + 2 \text{e} = \text{Ag (s)} + \text{Cu}_2\text{Se} + \text{H}_2\text{Se} \quad (?)$ $2 \text{H}^+ \text{(aq)} + 2 \text{e} = \text{H}_2 \text{(g)}$
10.	Oxidation $\text{CuAgSe (s)} = \text{Cu}^{2+} \text{(aq)} + \text{Ag}^+ \text{(aq)} + \text{Se}^\circ + 3 \text{e} \quad (?)$

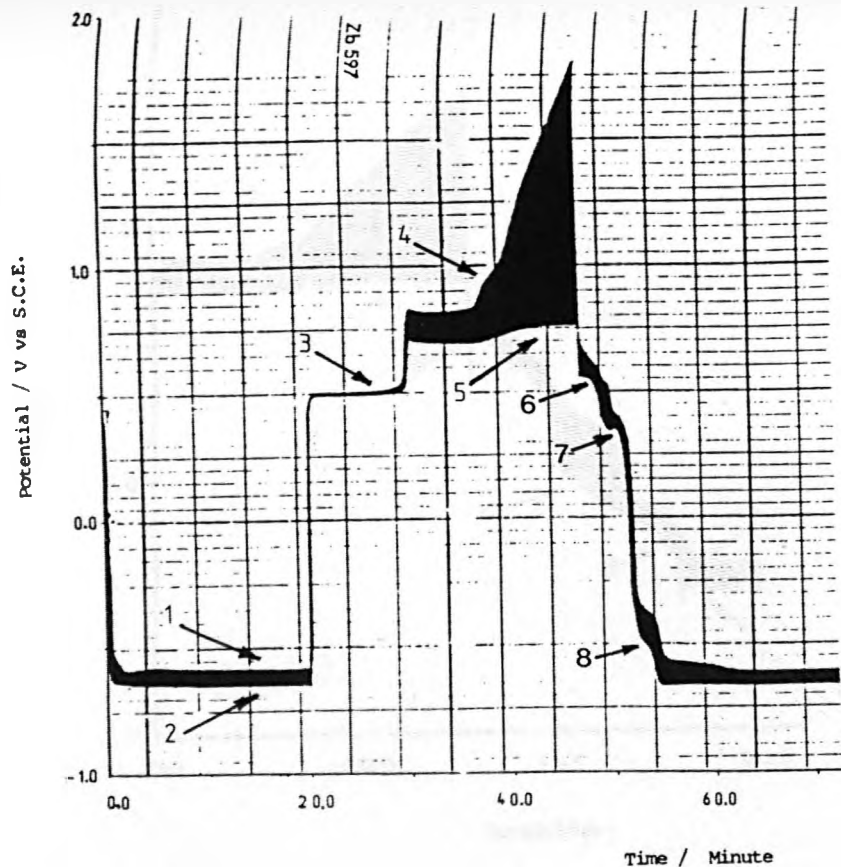


Figure 3.79 IGP traces for Ag_2Se in a stationary 1M HNO_3 solution at 315K using a rectangular pulse of 2s "on" & 2s "off". Current density: 178 Am^{-2} . Initially cathodic excursion.

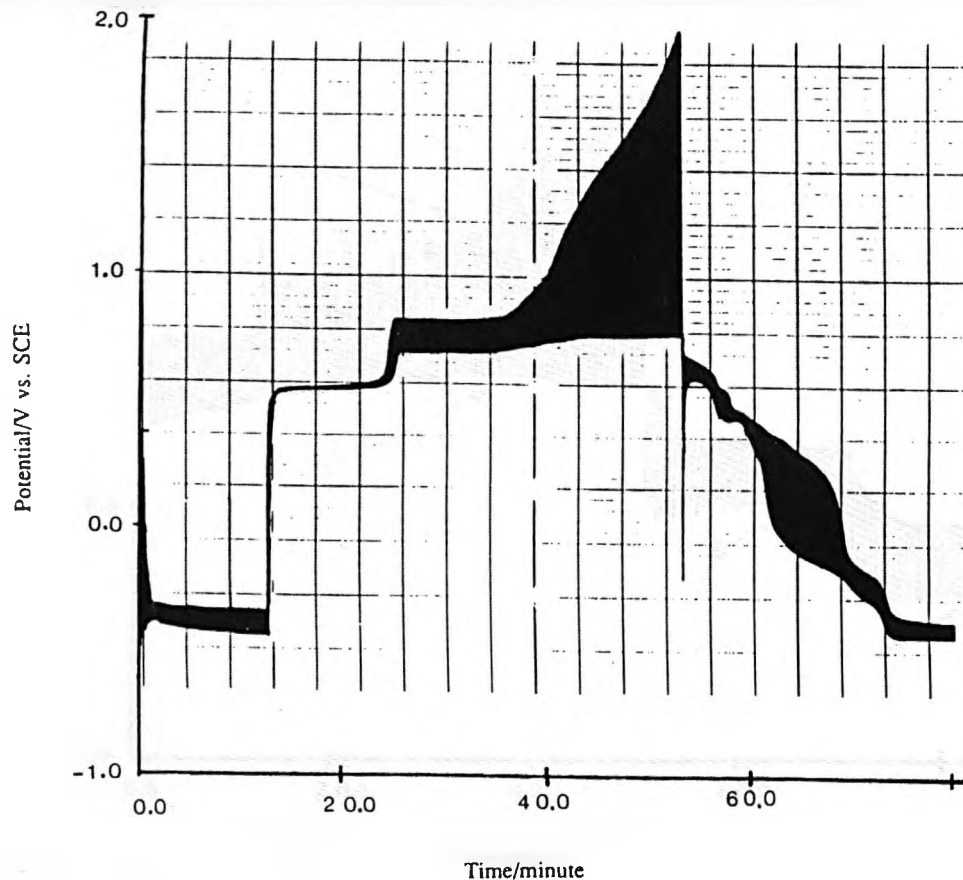


Figure 3.80 IGP traces for Ag_2Se in a stationary 1M HClO_4 solution at 315K using a rectangular pulse of 2s "on" & 2s "off". Current density: 178 Am^{-2} . Initially cathodic excursion.

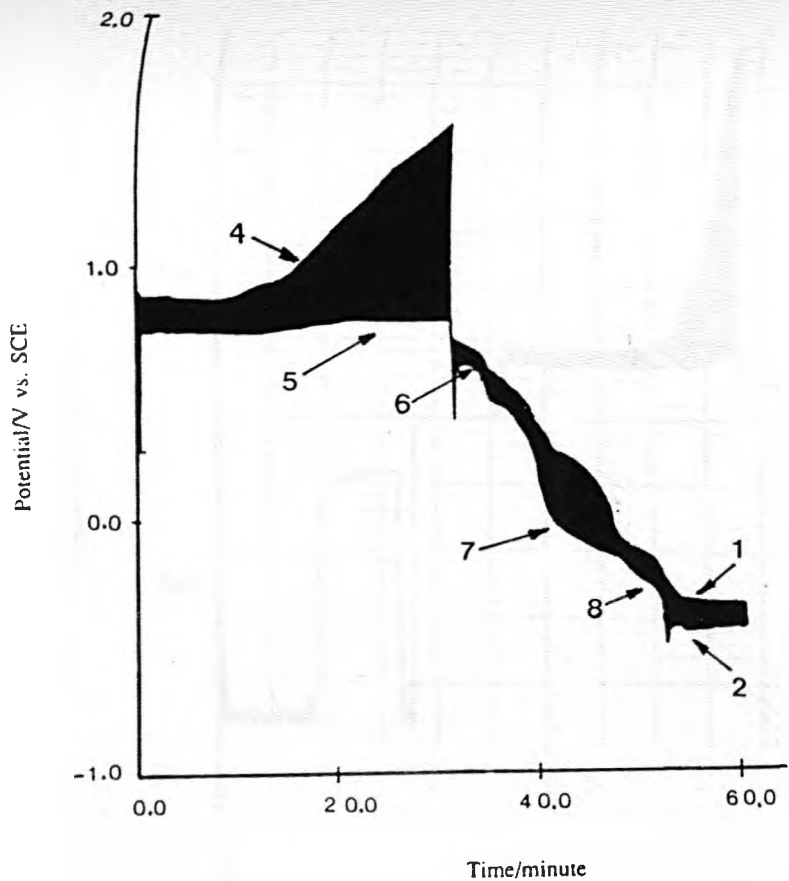


Figure 3.81 IGP traces for Ag_2Se in a stationary 1M HNO_3 solution at 315K using a rectangular pulse of 2s "on" & 2s "off". Current density: 178 Am^{-2} . Initially anodic excursion.

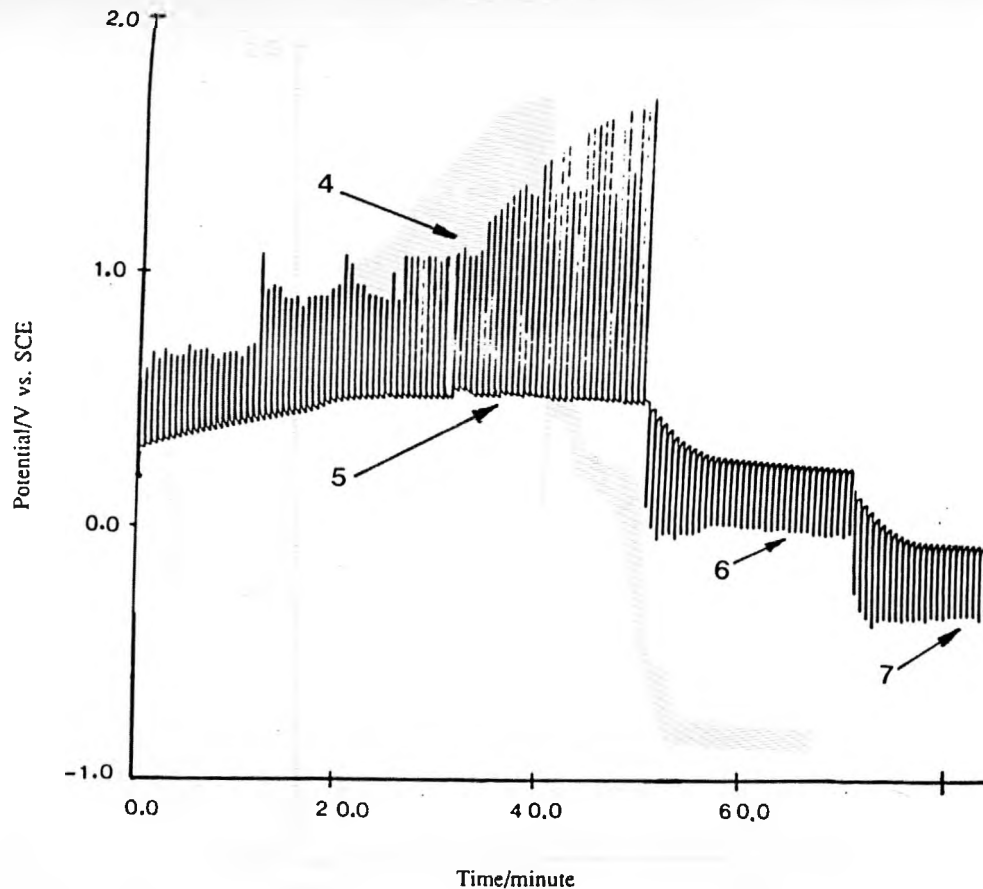


Figure 3.82 IGP traces for Ag_2Se in a stationary 1M HNO_3 solution at 315K using a rectangular pulse of 2s "on" & 40s "off". Current density: 178 Am^{-2} . Initially anodic excursion.

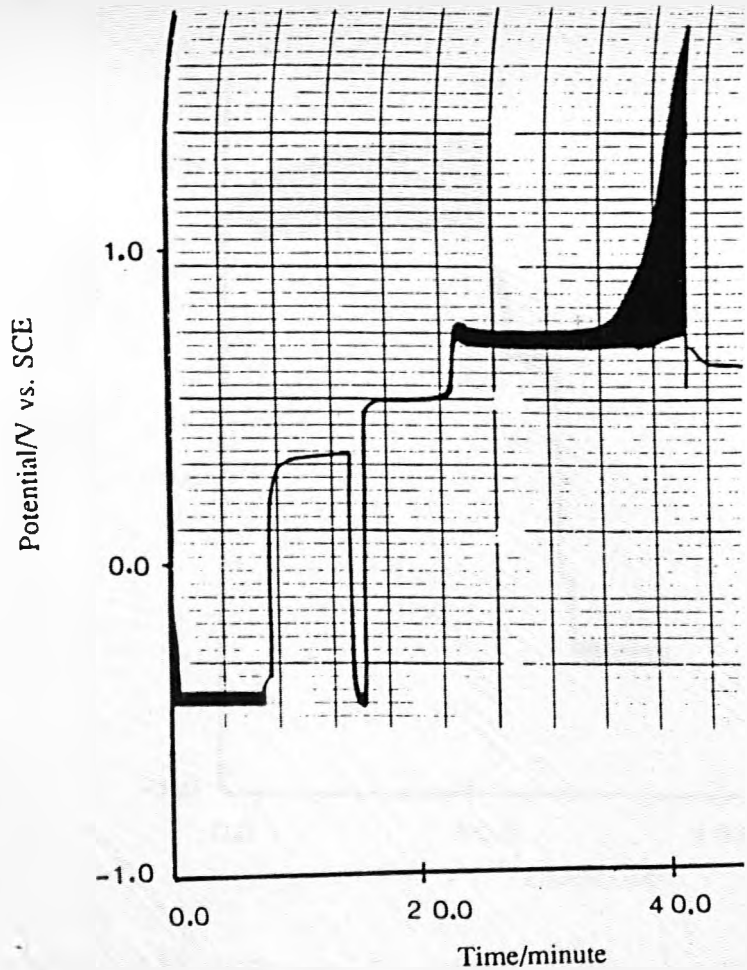


Figure 3.83 IGP traces for Ag_2Se in a stationary 1M HNO_3 solution at 315K using a rectangular pulse of 2s "on" & 2s "off". Current density: 178 Am^{-2} . Initially anodic excursion.

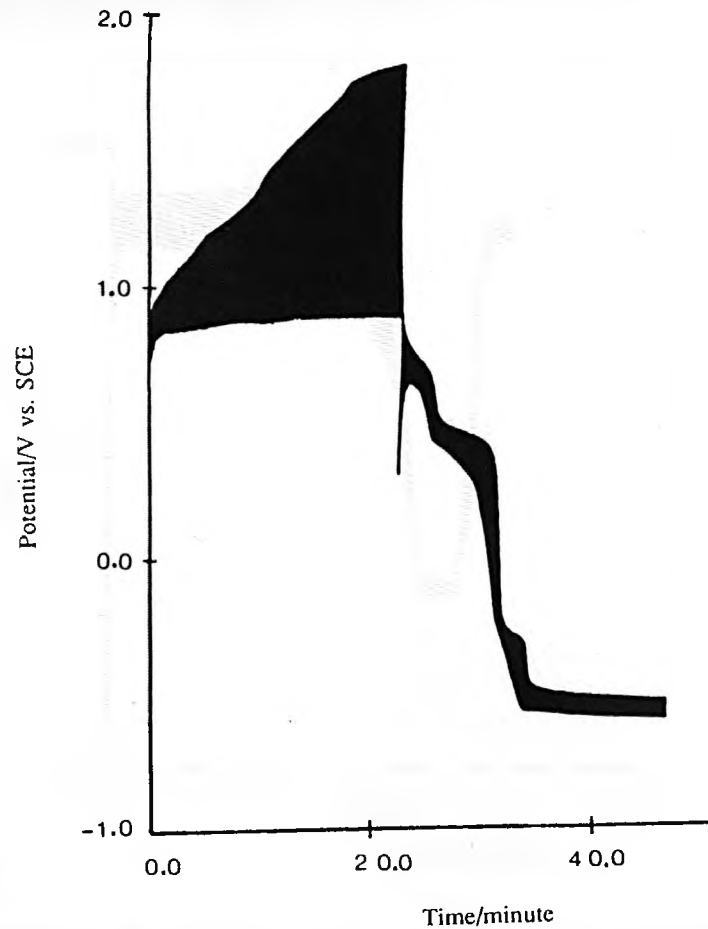


Figure 3.84 IGP traces for Ag_2Se in a stationary 1M HNO_3 solution at 315K using a rectangular pulse of 2s "on" & 2s "off". Current density: 250 Am^{-2} . Initially anodic excursion.

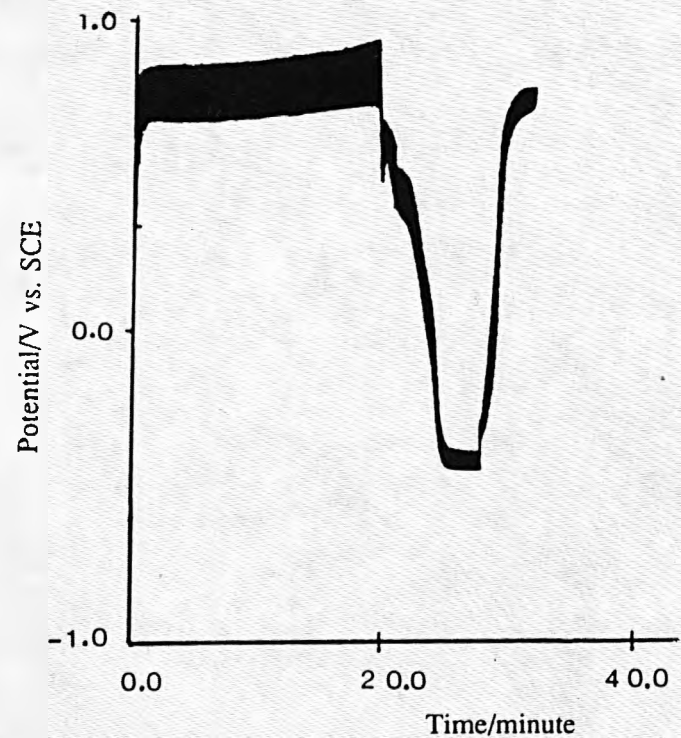
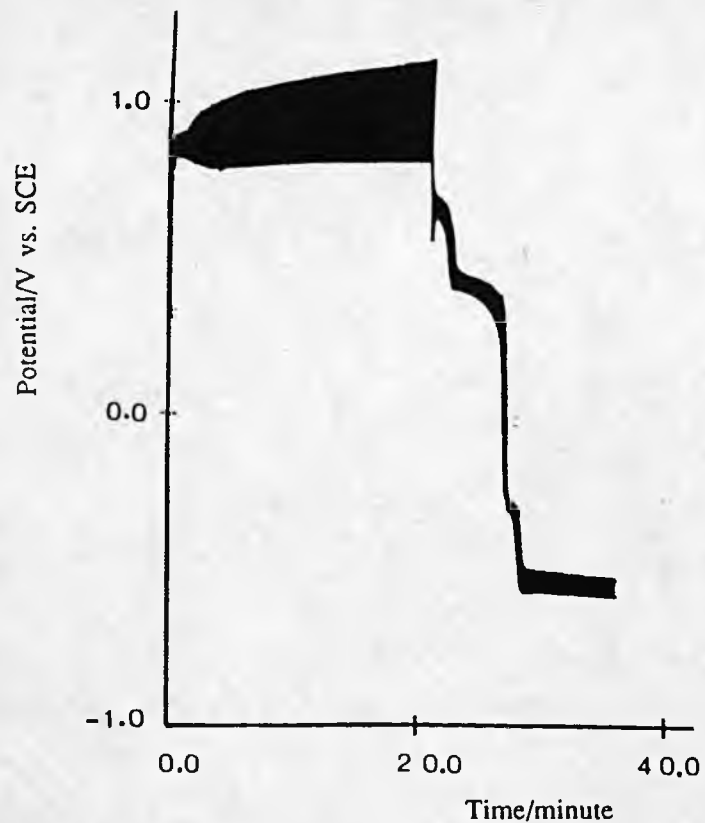
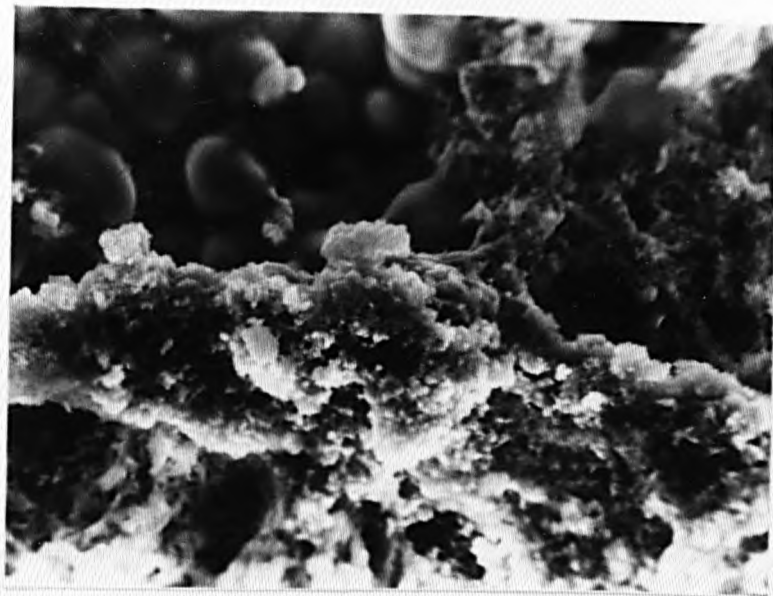


Figure 3.85 IGP traces for Ag_2Se in a stationary 1M HNO_3 solution at 315K using a rectangular pulse of 2s "on" & 2s "off". Current density: 150 Am^{-2} . Initially anodic excursion.

Figure 3.86 IGP traces for Ag_2Se in a stationary 1M HNO_3 solution at 315K using a rectangular pulse of 2s "on" & 2s "off". Current density: 100 Am^{-2} . Initially anodic excursion.

(a)

2000



(b)

1500

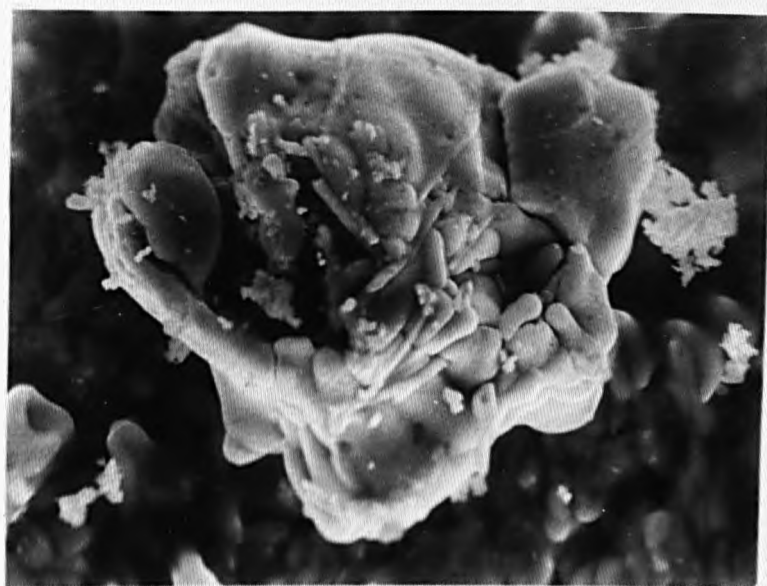


Figure 3.87 Scanning electron microscope (SEM) photographs of the silver selenide surface after initial anodic polarisation (17.8 A m^{-2}) for 720s followed by cathodic treatment for 120s in 1M HNO_3 at 295K. (a) Surface appears significantly etched. (b) Silver deposition.



Figure 3.88 EDXA analysis reveals the formation of silver on Ag_2Se electrodes after cathodic polarisation for 5 minutes.

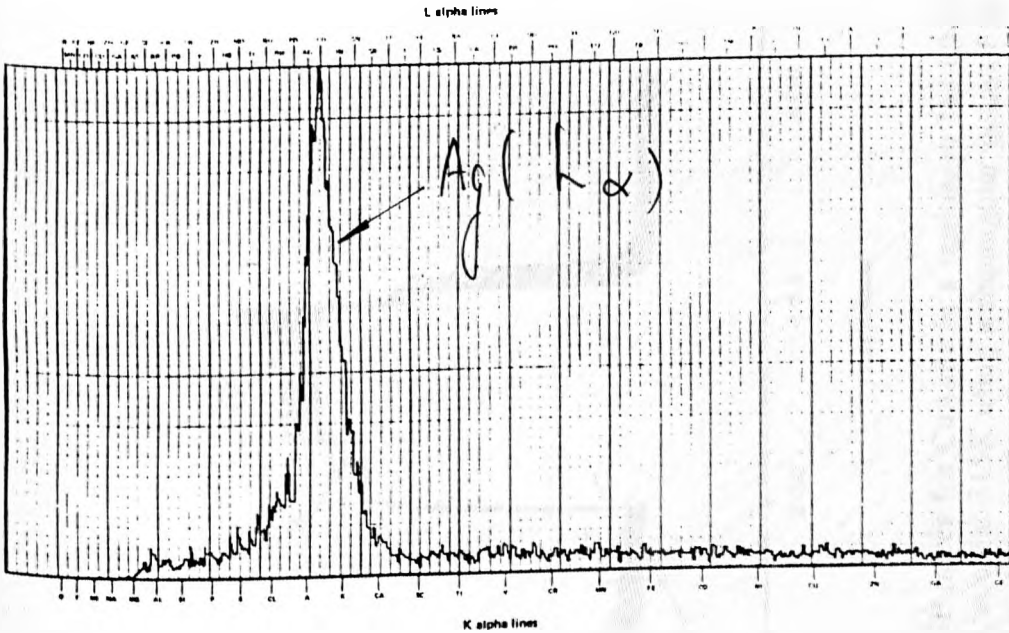


Figure 3.89 EDXA reveals that the crystals shown in *Figure 3.87(b)* are silver crystals.

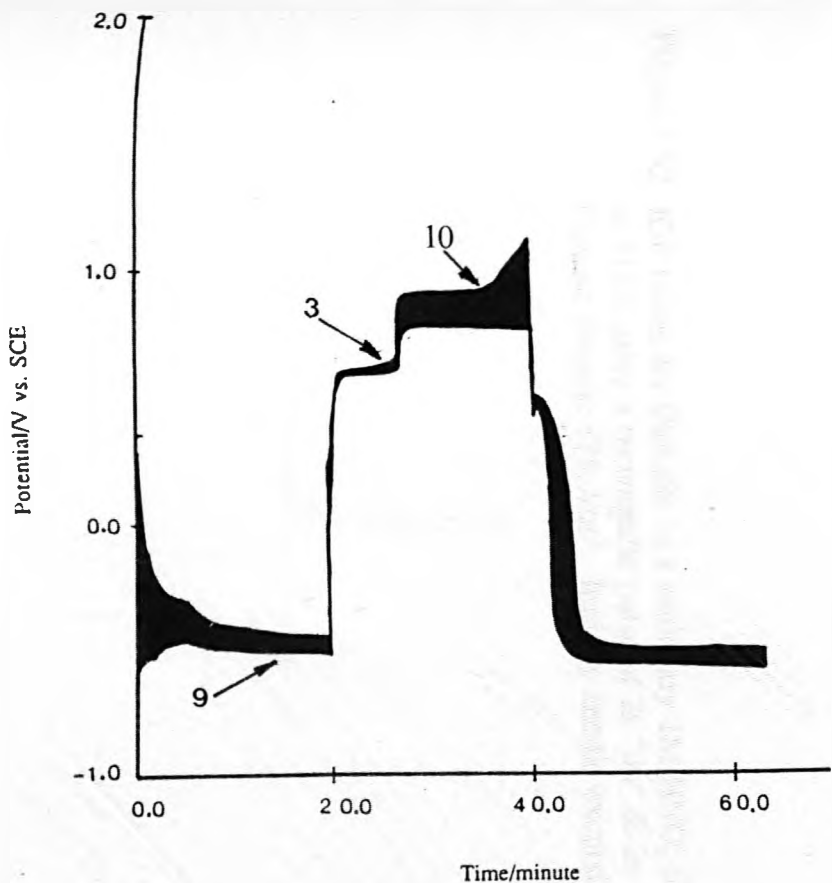


Figure 3.90 IGP traces for CuAgSe in a stationary 1M HNO₃ solution at 315K using a rectangular pulse of 2s "on" & 2s "off". Current density: 178 Am⁻². Initially cathodic excursion.

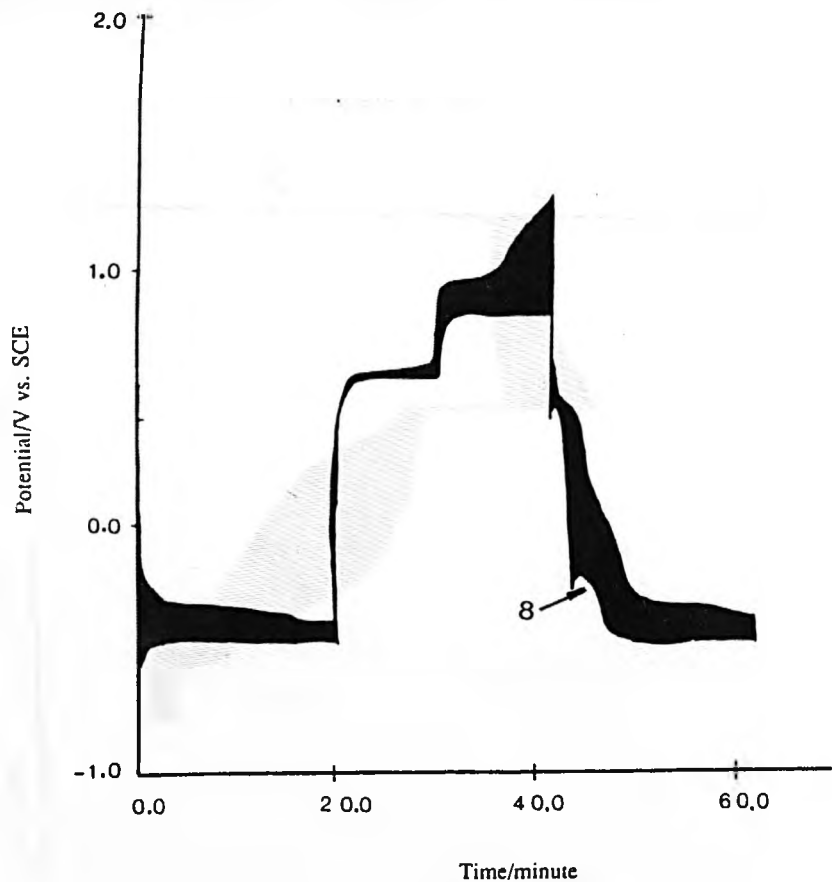


Figure 3.91 IGP traces for CuAgSe in a stationary 1M HClO₄ solution at 315K using a rectangular pulse of 2s "on" & 2s "off". Current density: 178 Am⁻². Initially cathodic excursion.

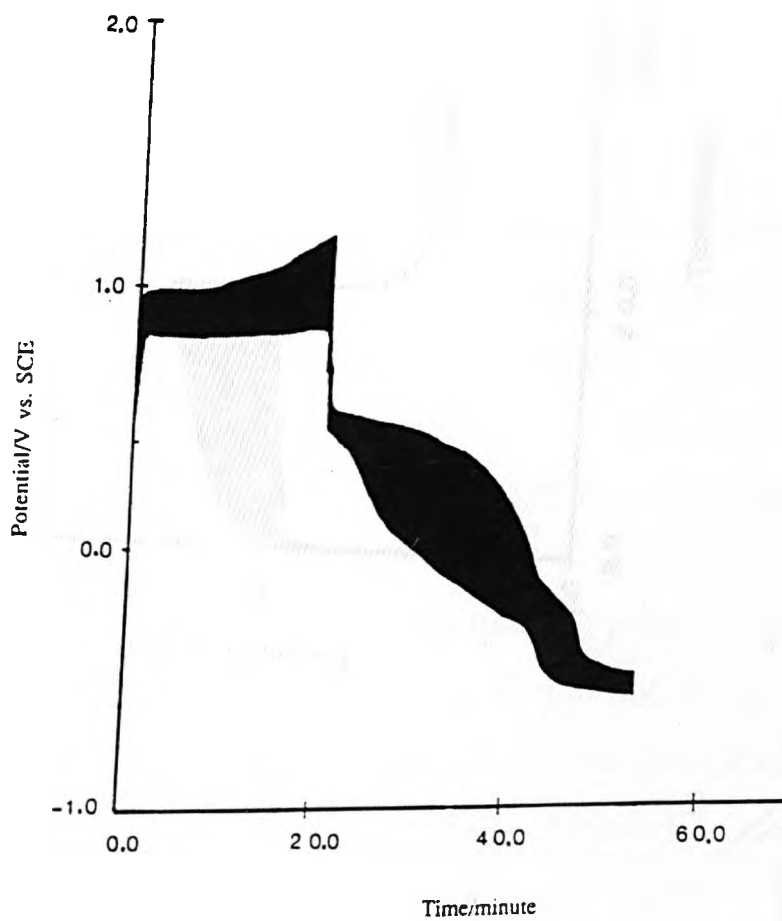


Figure 3.92 IGP traces for CuAgSe in a stationary 1M HNO₃ solution at 315K using a rectangular pulse of 2s "on" & 2s "off". Current density: 178 Am⁻². Initially anodic excursion.

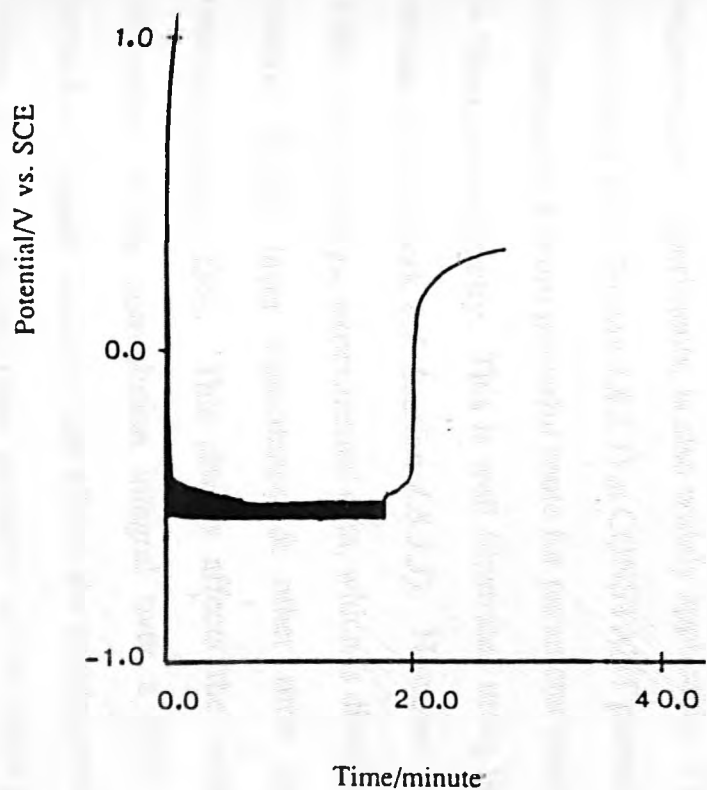


Figure 3.93 IGP traces for CuAgSe in a stationary 1M HNO₃ solution at 315K using a rectangular pulse of 2s "on" & 2s "off". Current density: 150 Am⁻². Initially cathodic excursion.

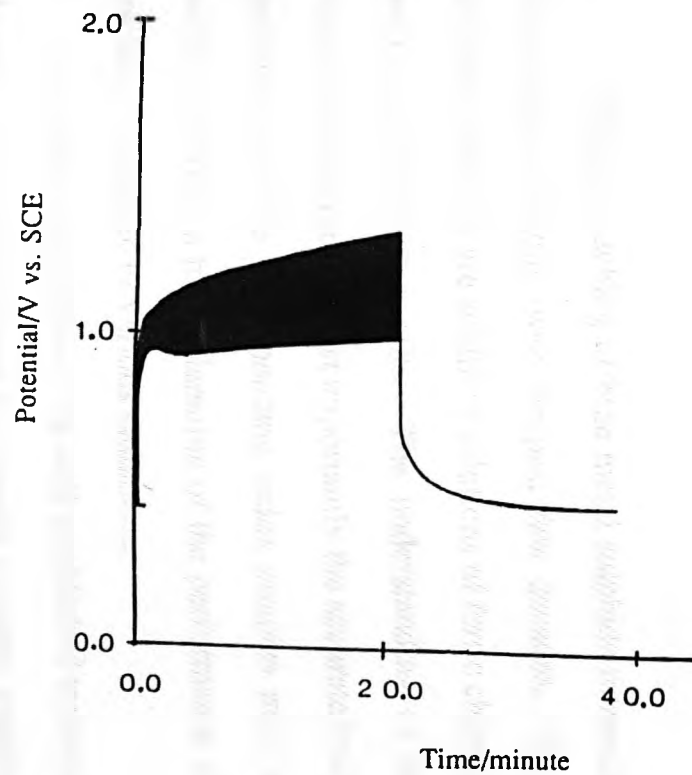


Figure 3.94 IGP traces for CuAgSe in a stationary 1M HNO₃ solution at 315K using a rectangular pulse of 2s "on" & 2s "off". Current density: 150 Am⁻². Initially anodic excursion.

3.7 Chronoamperometric Studies on the $\text{FeCl}_3/\text{FeCl}_2$ Couple in Acid Media

Chloride leaching of base metal sulphide minerals & mattes has attracted increasing attentions over the past few decades. The most commonly used chloride leachants are acidified solutions of ferric chloride, cupric chloride or the mixture of these two salts. The understanding of the fundamental electrochemical behaviour & most importantly the accurate evaluation of several kinetic parameters of the corresponding redox couples may be able to provide very useful information for explanation of the performance of these redox couples in leaching processes in various situations.

Potential step methods are well established techniques for determination of electrochemical parameters for simple electron transfer reactions (*cf. Section 4.8.3*). Tafel plots based on the Butler-Volmer equation (& variant) can be used to assess steady state currents at stationary electrodes. The Cottrell test, for treatment of the diffusion limited current-time responses obtained in chronoamperometric experiments, is also widely applicable. The linear relationship $i - I_1$ (*cf. eqn. 4.93 in Section 4.8.2.1*) at CONSTANT potential polarisation provides an alternative & more powerful route for parameter determination than the latter in chronoamperometry. This is well illustrated using theoretical data in a later section in this work (*cf. Section 4.8.3.3*). However, practical problems arise when used to analyse experimental data, which is distorted by the charging of the electric double layer capacitance & other time response factors of the instrumentation [236]. This always affects the accuracy of the numerical evaluation of the convolution integral over a time scale longer than the perturbation itself, which in turn affects the ensuing results from the $i - I_1$ plot. Below we shall discuss these problems of the extraction of electrochemical parameters, such as diffusion coefficients, heterogeneous rate constant k^0 & charge transfer (symmetry) coefficient (α) from the $\text{Fe}^{3+}/\text{Fe}^{2+}$ couple on a

platinum electrode. Brief accounts of the theoretical considerations of the technique & their application to the assessment of digitally simulated chronoamperometry data are presented in *section 4.8.3.4*. Treatment is based on the following EXACT linearized relationship in the form of 'interval' functions:

$$\frac{\Delta Q}{\Delta i} = \frac{2a}{\sqrt{\pi} b} \frac{\Delta t^{1/2}}{\Delta i} + \frac{1}{b^2} \quad (3.34)$$

where a & b are coefficients defined by:

$$a = (z_B - z_A)FAk^0e^{-\alpha p} \left[C_A^{\text{BULK}} - C_B^{\text{BULK}}e^p \right] \quad (3.35)$$

$$b = \frac{k^0e^{-\alpha p}}{\sqrt{D_A}} \left[1 + e^{(z_A - z_B)F(E - E_{1/2})/RT} \right] \quad (3.36)$$

$$\text{with } p = \frac{(z_A - z_B)F(E - E^0)}{RT}$$

The Δ symbol is the algebraic difference (final - initial) of the quantity at ANY two given time points of the data. The terms $\Delta Q/\Delta i$, $\Delta t^{1/2}/\Delta i$ are functions which DO NOT contain contributions from charging etc. once these have died away. Therefore, measurement of the data when the charging current etc. has diminished should reflect the real kinetic performance of the electrode process.

Experimentally, there is always risk of involvement of convection at longer durations. As a result, an alternative of *equation 3.34* can be used to give more emphasis to the data at the initial stage of the potential step:

$$\frac{\Delta i}{\Delta t^{1/2}} = b^2 \frac{\Delta Q}{\Delta t^{1/2}} + \frac{2ab}{\sqrt{\pi}} \quad (3.37)$$

In short time polarisation, either of the above equations (*eqns. 3.34 & 3.37*) can be used with more confidence than say the $i - I_1$ relationship.

Equation 3.34 can be rearranged into the following form:

$$y = mx + c \quad (3.38)$$

where $y = \Delta Q/\Delta i$, $x = \Delta t^{1/2}/\Delta i$, $c = b^{-2}$ & $m = 2a/(\sqrt{\pi} b)$. Therefore, by plotting $\Delta Q/\Delta i$ against $\Delta t^{1/2}/\Delta i$, two important parameters i.e. a & b can readily be evaluated from the slope (m) & intercept (c) of the graph:

$$b = c^{-1/2} \quad \& \quad a = \pi^{1/2} m c^{-1/2} / 2 \quad (3.38a)$$

Further development based on *equations 3.35 & 3.36* allow the determination of kinetic parameters (*cf. Section 4.8.3.4*).

In general, there are two major ways of extracting kinetic parameters from the two coefficients a & b . Note the relative magnitudes terms $e^{-\alpha p}$ & $e^{(1-\alpha)p}$ of the expressions for a & b (*cf. eqns. 3.35 & 3.36*). For example, for an oxidation process, when large overpotentials (but not large enough to force the system into the DIFFUSION control regimes) are applied, $p \rightarrow$ large negative values, the second term of BOTH *equations 3.35 & 3.36* becomes negligible as compared to the first one & the expressions for a & b reduce to:

$$a \rightarrow (z_B - z_A) F A C^{\text{BULK}} k^{\circ} e^{-\alpha p}$$

&

$$b \rightarrow k^{\circ} e^{-\alpha p} / \sqrt{D_A} \quad (\text{large anodic overpotentials})$$

As a consequence, the diffusion coefficient D_A & forward charge transfer rate k_{hf} ($= k^{\circ} e^{-\alpha p}$) can readily be calculated. The symmetry coefficient α (α_A) & the standard heterogeneous rate constant (k°) can subsequently be evaluated by plotting the logarithmic function $\text{Ln } k_{\text{hf}}$ against the overpotential ($E - E^{\circ}$) or its variant p . Similarly, D_B , α_B & k° can be obtained by treatment of the cathodic data. However, as discussed in *section 4.8.3.4*, if the heterogeneous rate constant k° is not sufficiently small (say $< 10^{-6} \text{ m}\cdot\text{s}^{-1}$), there is always the risk of inaccuracy in the estimation of heterogeneous parameters at higher overpotentials as diffusion control is emphasised.

Another approach, based on smaller electrochemical perturbations (< 100

mV, for example), is more capable of treating systems of relatively fast electron transfer kinetics. In this situation, the forward & backward charge transfer rate are comparable & hence the above approximation cannot be used. These types of experiments give more accurate information about the electrode kinetics, because at low overpotentials the faradaic current at zero time is more likely to be totally controlled by the electrode kinetics if k^0 is not too large. These complexities necessitate the use of the FULL expression for the two coefficients a & b for the accurate determination of kinetic parameters.

Combination of *equations 3.35, 3.36 & 3.38a* leads to the following linear relationship:

$$\left[C_A^{\text{BULK}} - C_B^{\text{BULK}} e^p \right] / m = s + s e^{(z_A - z_B)F(E - E_{1/2})/RT} \quad (3.39)$$

$$\text{or } y = s + qx$$

where $s = \sqrt{\pi} / [2(z_B - z_A)FA\sqrt{D_A}]$, $y = \Theta = [C_A^{\text{BULK}} - C_B^{\text{BULK}} e^p] / m$,

$$q' = s e^{(z_B - z_A)FE_{1/2}/RT} \quad \& \quad x' = e^{(z_A - z_B)FE/RT}$$

Note that the terms m & c are gradients & intercepts on the $\Delta Q/\Delta i$ vs. $\Delta t^{1/2}/\Delta i$ plots. For convenience of handling the exponential, q' & x' can be rearranged as:

$$q = s e^{(z_B - z_A)F(E_{1/2} - E^0)/RT} \quad \& \quad x = e^p$$

As a result, D_A & $E_{1/2}$ can be calculated from the intercept & slope of the plot & D_B can be obtained via similar treatment of the data from cathodic polarisation or from the definition of the half-wave potential $E_{1/2}$:

$$E_{1/2} = E^0 + \frac{RT}{2(z_B - z_A)F} \text{Ln}(D_A/D_B) \quad (3.40)$$

while the forward rate k_{hf} ($=k^0e^{-\alpha p}$) or the backward rate k_{hb} ($=k^0e^{(1-\alpha)p}$) can be calculated via *equation 3.35*. The standard heterogeneous rate constant of charge transfer k^0 & the charge coefficients α_A & α_B can finally be obtained by plotting $\text{Ln } k_{hf}$ (or k_{hb}) vs ΔE as discussed earlier.

Chronoamperometric experiments were performed on a stationary planar platinum electrode ($A = 1.96 \times 10^{-5} \text{m}^2$), in unstirred 1M HClO_4 & 1M HNO_3 solutions at 293K. The concentrations of the electroactive species in the electrolyte were: 0.01M FeCl_3 & 0.01M FeCl_2 . Data capture & subsequent treatment, was facilitated by the EG&G Condecon 300 software (*cf. Section 2.3.2.4*). The duration of polarisation was set to 2s to ensure that the influence of natural convection on the mass transport of electroactive species is negligible. As the time increases, the system gradually approaches the diffusion controlled regime & data in 'real time' becomes insensitive to the electron transfer process.

Figure 3.95 shows typical current-time responses for the 0.01M $\text{FeCl}_3/$ 0.01M FeCl_2 in 1M HNO_3 solution at overpotentials 0.08V & -0.08V. The slow rise in current at the initial stage is due to excess of damping. The characteristic linear relationship between the two 'step' functions $\Delta Q/\Delta i$ & $\Delta t^{1/2}/\Delta i$ is evident in *Figure 3.96*. The statistical results (slopes m & intercept c on the $\Delta Q/\Delta i$ axis) of those straight lines in *Figure 3.96* are listed in *Table 3.7*. The parameter $\Theta = [C_A^{\text{BULK}} - C_B^{\text{BULK}}e^p]/m$ at various overpotentials is then calculated & plotted against x values listed in the table (*cf. Figure 3.97*). As mentioned above, the slope (q) & intercept (c , on y axis) of plot leads to an immediate route to the knowledge of several kinetic parameters e.g. D_A , D_B & $E_{1/2}$ & the subsequential forward or backward heterogeneous rate k_{hf} or k_{hb} . The charge transfer coefficients α_A & α_B & the standard rate constant k^0 can finally be evaluated from the slope & intercept (on the $\text{Ln } k$ axis) of plot $\text{Ln } k$ (k_{hf} or k_{hb}) vs ΔE (*cf. Figure 3.98*).

The above results listed in *Table 3.8* are comparable with those obtained

by other workers [182-184]. Based on the above results, theoretical cyclic voltammograms were generated using the EG&G Condesim 300 software. These are in good agreement with experimental results obtained on $\text{FeCl}_3/\text{FeCl}_2$ couple in 1M HClO_4 using a platinum electrode (*cf. Figures 3.99 & 3.100*).

Similar results have also been obtained for the $\text{Fe}^{3+}/\text{Fe}^{2+}$ couple in unstirred 1M HNO_3 solution.

Table 3.8 Results from the plots $\Delta Q/\Delta i$ vs $\Delta t^{1/2}/\Delta i$ & $\ln k$ vs $\Delta E/V$

E-E°/V	c/s	m/As ^{1/2}	y (Θ)/y _u * x	Ln(k/ms ⁻¹)	
-0.100	0.0241±0.0004	-4.363x10 ⁻⁴	-22483	0.0191	- 8.9252±0.0041
-0.090	0.0321±0.0006	-4.258x10 ⁻⁴	-22820	0.0283	- 9.0766±0.0085
-0.080	0.0432±0.0007	-4.171x10 ⁻⁴	-22966	0.0421	- 9.2370±0.0080
-0.070	0.0496±0.0004	-3.983x10 ⁻⁴	-23537	0.0625	- 9.3235±0.0040
-0.060	0.0764±0.0006	-3.716x10 ⁻⁴	-24411	0.0929	- 9.5649±0.0039
-0.050	0.0975±0.0002	-3.425x10 ⁻⁴	-25166	0.1381	- 9.7233±0.0010
-0.040	0.1421±0.0008	-3.010x10 ⁻⁴	-26408	0.2051	- 9.9636±0.0028
-0.030	0.1885±0.0048	-2.435x10 ⁻⁴	-28550	0.3048	-10.1774±0.0126
-0.020	0.2342±0.0032	-1.776x10 ⁻⁴	-30805	0.4529	-10.3849±0.0068
-0.010	0.3281±0.0073	-1.018x10 ⁻⁴	-32123	0.6730	-10.6844±0.0110
0.010	0.1863±0.0051	7.872x10 ⁻⁵	41540	0.6730	-10.3792±0.0135
0.020	0.1649±0.0046	1.675x10 ⁻⁴	32662	0.4529	-10.1668±0.0138
0.030	0.1499±0.0026	2.501x10 ⁻⁴	27797	0.3048	-10.0025±0.0086
0.040	0.1242±0.0018	3.167x10 ⁻⁴	25099	0.2051	- 9.8215±0.0072
0.050	0.1024±0.0009	3.712x10 ⁻⁴	23221	0.1381	- 9.6620±0.0044
0.060	0.0769±0.0006	4.041x10 ⁻⁴	22447	0.0929	- 9.4738±0.0039
0.070	0.0599±0.0008	4.335x10 ⁻⁴	21626	0.0625	- 9.3178±0.0066
0.080	0.0490±0.0007	4.499x10 ⁻⁴	21292	0.0421	- 9.1958±0.0069
0.090	0.0414±0.0004	4.669x10 ⁻⁴	20811	0.0283	- 9.0967±0.0048
0.100	0.0310±0.0002	4.767x10 ⁻⁴	20578	0.0191	- 8.9419±0.0032

* $y_u = \text{mol m}^{-3} \text{A}^{-1/2}$ Results from statistical treatment on $y = s + qx$

CATHODIC BRANCH

$$s/y_u = -(22277.5 \pm 191.8), \quad q/y_u = -(19058.7 \pm 940.1)$$

$$D_{\text{Fe}^{3+}} = (4.4096 \pm 0.0761) \times 10^{-10} \text{ m}^2 \cdot \text{s}^{-1}, \quad E_{1/2} = 0.46094 \pm 0.00150 \text{ V}$$

ANODIC BRANCH

$$s/y_u = (19890.2 \pm 164.4), \quad q/y_u = (27138.0 \pm 805.6)$$

$$D_{\text{Fe}^{2+}} = (5.5314 \pm 0.0952) \times 10^{-10} \text{ m}^2 \cdot \text{s}^{-1}, \quad E_{1/2} = 0.46485 \pm 0.00136 \text{ V}$$

Average of $E_{1/2} = 0.4629 \text{ V}$. $E_{1/2}$ calculated from D values: 0.45986V.Results from statistical treatment on $\ln k$ vs $\Delta E/V$

CATHODIC BRANCH

$$\text{slope} = -(21.0651 \pm 0.6921), \quad \text{intercept} = -(10.8038 \pm 0.0360)$$

$$k^0 = (2.0322 \pm 0.0744) \times 10^{-5} \text{ m} \cdot \text{s}^{-1}, \quad \alpha_{\text{Fe}^{3+}} = (0.5319 \pm 0.0175)$$

ANODIC BRANCH

$$\text{slope} = (17.3739 \pm 0.6756), \quad \text{intercept} = -(10.5518 \pm 0.0185)$$

$$k^0 = (2.6146 \pm 0.0488) \times 10^{-5} \text{ m} \cdot \text{s}^{-1}, \quad \alpha_{\text{Fe}^{2+}} = (0.4386 \pm 0.0171)$$

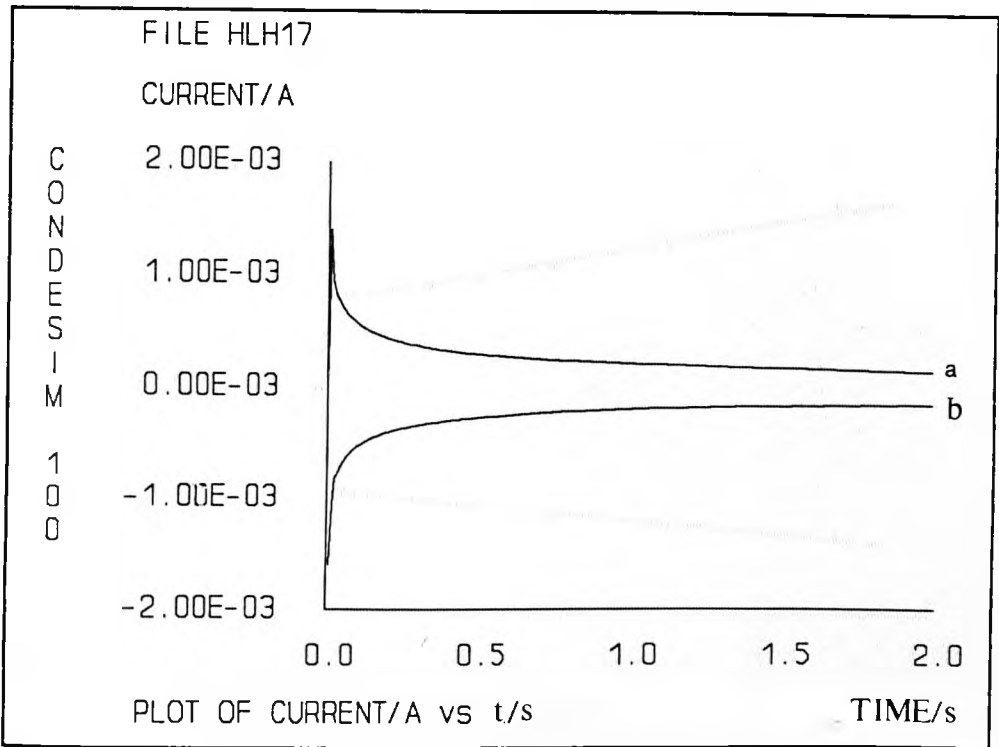


Figure 3.95 Chronoamperograms for the $\text{Fe}^{3+}/\text{Fe}^{2+}$ couple in unstirred 1M HClO_4 solution. $E-E_{\text{eq}}$ (mV) : (a) 60 (b) -60.

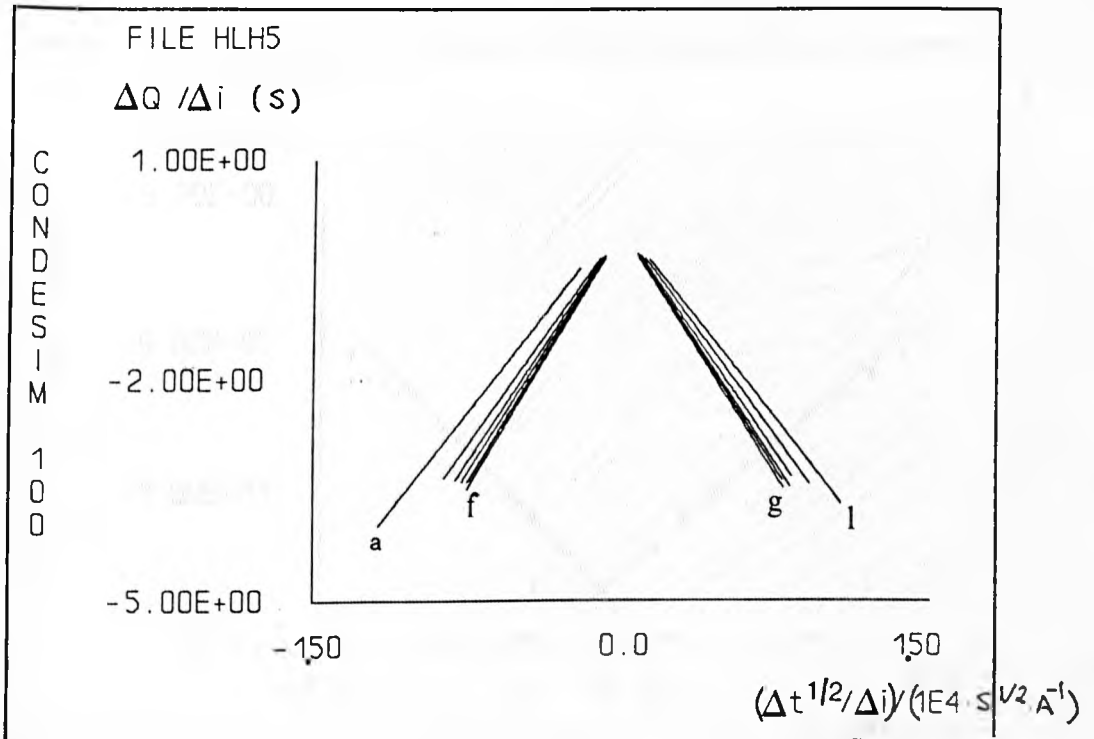


Figure 3.96 Plots of $\Delta Q/\Delta i$ vs $\Delta t^{1/2}/\Delta i$ at ΔE ($=E-E_{\text{eq}}$, mV): (a) 50 (b) 60 (c) 70 (d) 80 (e) 90 (f) 100 (g) -100 (h) -90 (i) -80 (j) -70 (k) -60 (l) -50.

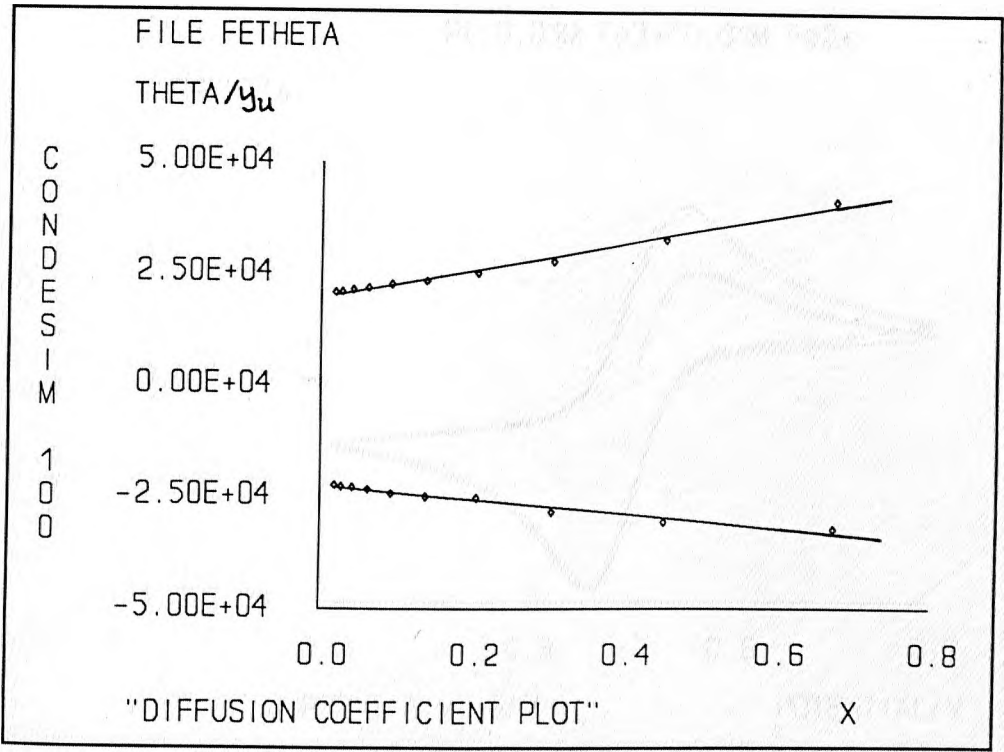


Figure 3.97 Plot of Θ versus e^p for the determination of diffusion coefficient $D_{Fe^{3+}}$ & $D_{Fe^{2+}}$ (data listed in Table 3.7).

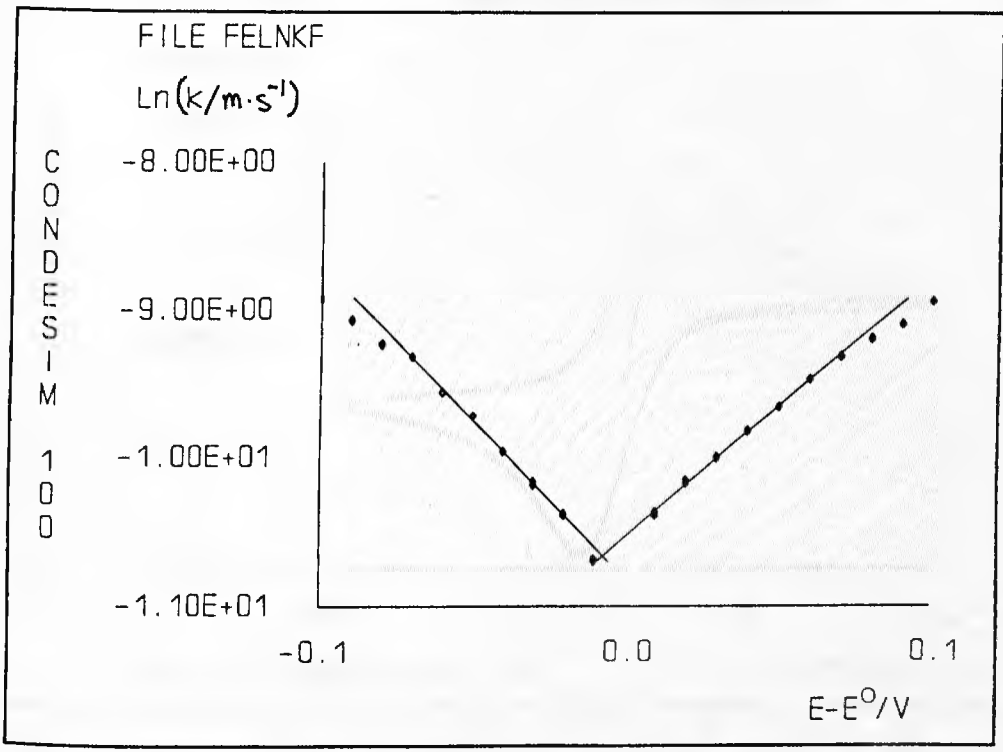


Figure 3.98 Plot of $\ln k$ vs $(E-E^0)$ for the determination of standard heterogeneous rate constant & symmetry coefficient.

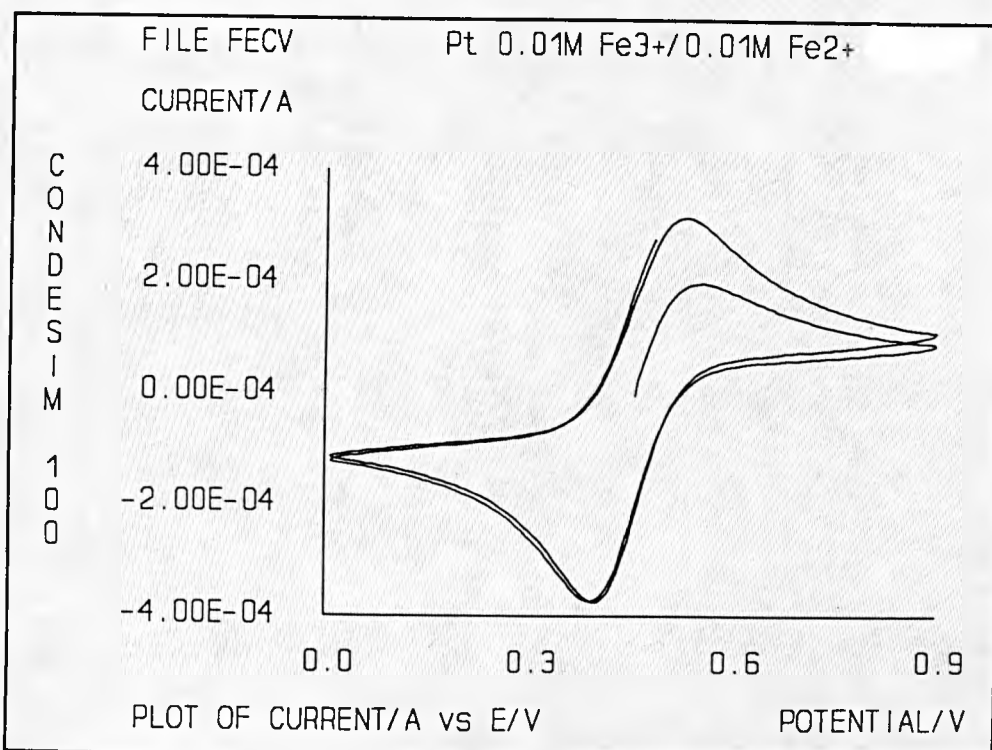


Figure 3.99 Cyclic voltammogram for the Fe³⁺/Fe²⁺ couple on a platinum electrode in 1M HClO₄ solution.

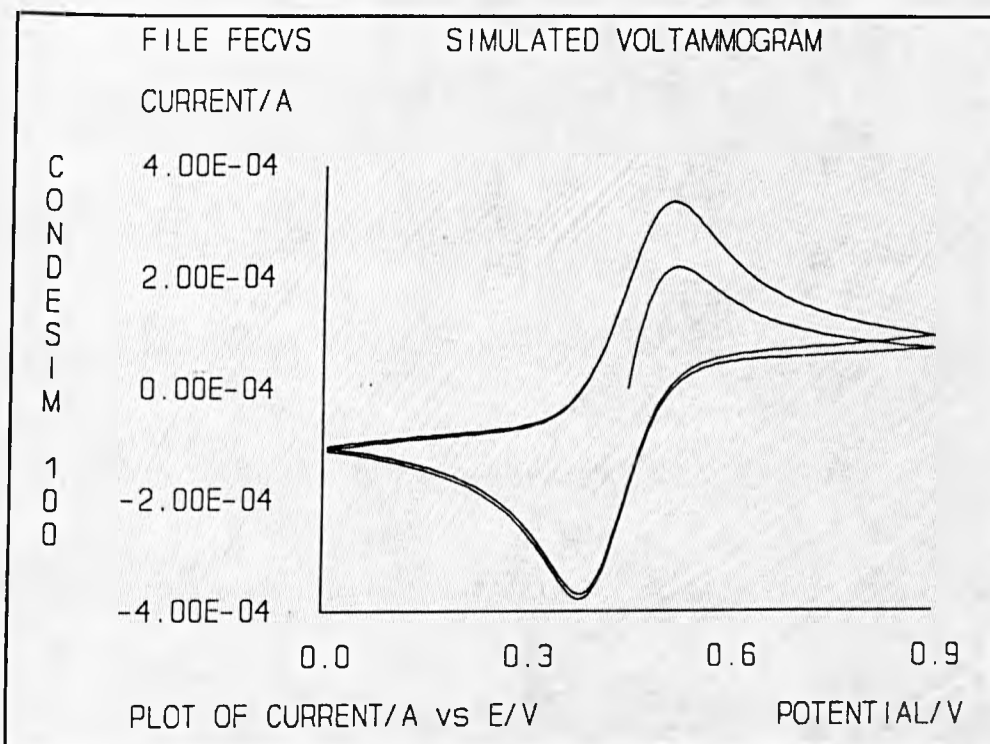


Figure 3.100 Simulated cyclic voltammogram using experimental determined parameters for the Fe³⁺/Fe²⁺ couple.

4. Digital Simulation in Electrochemistry

4.1 Introduction

The numerical solution of the diffusional problems in engineering (heat transfer, for example) & chemistry has fascinated scientists for decades. Generally, the basic diffusional problem which needs to be solved in electrochemistry is the Fick's second law (diffusion equation):

$$\frac{\partial C}{\partial t} = D_x \frac{\partial^2 C}{\partial x^2} + D_y \frac{\partial^2 C}{\partial y^2} + D_z \frac{\partial^2 C}{\partial z^2}$$

$$\text{or simply, } \partial C(x, t) / \partial t = D \nabla^2 C(x, t)$$

for the three dimensional semi-infinite diffusional process, where C is the concentration of the diffusing substance at any location in the solution or at the electrode surface, t is the time, x, y, z are the Cartesian coordinates with respect to the electrode surface & D_x, D_y, D_z are the space dependent diffusion coefficients (normally the trivial differences between D_x, D_y & D_z are ignored for simplicity). As we can see, the numerical or analytical solution to the above equation can be very complex. In practice, it is prudent to "simplify" the systems to be studied e.g. by controlling the experimental conditions where applicable such that the system can be treated by a relatively simple model. For example, in the case of a planar electrode of sufficiently large surface area in an appropriately sized un-stirred electrochemical cell, the diffusional process can be treated as a one dimensional semi-infinite linear diffusion, i.e. diffusion takes place only in the direction perpendicular to the electrode surface. Therefore, equation 4.1 can be simplified to:

$$\frac{\partial C}{\partial t} = D \frac{\partial^2 C}{\partial x^2}$$

In the case of the dropping mercury electrode (DME) the three dimensional diffusion problem reduces to one dimensional (planar) on time scales within which the radius of the mercury drop is greater than 1000δ (δ is the effective Nernstian diffusion layer thickness, cf. 4.2.1.2).

Technically, the above equations are partial second-order differential equations, of parabolic type. However, these two equations represent merely the two simplest cases of diffusional problems in electrochemistry (i.e. linear diffusion to a planar electrode of infinite dimensions). Such complications as convection, migration, electrode geometry (e.g. micro or ultramicro electrode system) & homogeneous chemical kinetics (proceeding or follow-up chemical reactions, for instance) will to a certain extent increase the difficulty of numerical solution & in some cases this could be critical.

Basically, there are three main numerical methods for the solution of the above diffusional problems (with coupled homogeneous chemical kinetics), i.e. transformation of these equations to 'continuous functions' by application of the Laplace transform techniques [206-8], conversion of the boundary problems to integral equations [209-214], & direct numerical solution using finite difference techniques [187,215-6]. One of the major advantages of the third method over the others is that the "real process" (e.g. viewed as instantaneous concentrations of all species at different positions in the solution as a function of time) can be followed via the construction of a three-dimensional graph in real time. Although more variables are required to represent various experimental parameters in this technique, we shall concentrate on direct numerical solution for its closeness to the "real world" though the others will be mentioned where necessary.

Although the employment of finite difference technique for the solution of differential equations dates back to the beginning of this century [187], it was not until the later 1940's that this technique was adopted by Randles [188] to simulate the current-potential response for linear sweep on a reversible simple

electron transfer (Nernstian case) system. This technique was later successfully extended to the polarographic study of stationary spherical & cylindrical electrode systems [206,211]. However, this technique did not gain much attention, mainly because of the considerable numerical tabulations & graphs involved, until the arrival of efficient computation tools - namely digital computers. Since S.W. Feldberg [189] first published on the digital simulation of current reversal chrono-potentiometry for the study of the uranium (VI) & uranium (V) systems in 1964, various numerical approaches have been made to obtain higher accuracy or more reliable results within a reasonable time for computation [190-201]. Meanwhile, complicated systems such as different electrode geometry (e.g. dropping mercury electrode, ultramicrodisk electrode & microdisk electrode) [202-5] & homogeneous chemical kinetics [194-6,199,205], have also been studied extensively. In the following sections we shall mainly discuss the development of methods for the digital simulation of various electrochemical problems & techniques for the assessment of the simulation results.

4.2 Mass Transport Phenomena in Cells

In general, in any electrochemical system, it is necessary to consider three types of mass transport; namely diffusion, migration & convection. However, the contributions of these processes to the concentration change of materials can differ considerably from one another, depending on the experimental conditions. Practically, in most electrochemical experiments (in aqueous or organic solvent system), one or two of the above mentioned processes may be negligible. For example, the addition of a certain amount of non electroactive electrolyte can significantly reduce the influence of migration on the transport of electroactive species (cf. section 4.2.2), while in situations where the rotating disk electrode

system (RDE) is used as the working electrode convection becomes, principally, the dominant mass transport process (cf. section 4.2.3). The nature of these three modes of mass transport processes is stated briefly below.

4.2.1 Diffusion

4.2.1.1 The Diffusional Process

In the presence of sufficient amount of supporting electrolyte, diffusion is the most significant form of mass transport process at stationary electrodes. Wherever there is a concentration difference for one species in the solution, caused e.g. by heterogeneous or homogeneous chemical reaction(s), there exists spontaneously a net flow of this substance down the concentration gradient. That is to say, the total flow of this species from the region of higher concentration to that of lower concentration is greater than the mass flow in the opposite direction. The net flow of substance (dn) crossing a small area (dA) on a plane at a given location x & parallel to the electrode surface, over the period from time t to $t + dt$, is defined by the classical Fick's first law of diffusion:

$$dn = - dA dt D \left(\frac{\partial C}{\partial x} \right)_{x, t} \quad (4.1)$$

where D is the diffusion coefficient & C is the concentration. Equation 4.1 can be rearranged to the more familiar form,

$$f_x = \frac{dn}{dA dt} = - D \left(\frac{\partial C}{\partial x} \right)_{x, t} \quad (4.2)$$

where f_x is known as the "flux" - the net mass transfer rate of a substance in units of amount per unit time per unit area (i.e. $\text{mol} \cdot \text{m}^{-2} \cdot \text{sec}^{-1}$). The numerical solution to the above equation remains as the essential problem of the so-called

"box method" simulation technique employed in the early stages of development of digital simulation when the Crank-Nicolson technique was not available.

In this linear case Fick's second law of diffusion describing the change of concentration with time, can be derived from the above equation (eqn. 4.2) using standard mathematical manipulations:

$$\frac{\partial C}{\partial t} = D \frac{\partial^2 C}{\partial x^2} \quad (4.3)$$

Similarly, a general form can be derived for the rectangular electrode geometry (cube-shaped electrode, for example),

$$\frac{\partial C}{\partial t} = D_x \frac{\partial^2 C}{\partial x^2} + D_y \frac{\partial^2 C}{\partial y^2} + D_z \frac{\partial^2 C}{\partial z^2} \quad (4.4)$$

where x, y & z are the cartesian coordinates. Obviously equation 4.3 is a limiting case of the three dimensional diffusional process (eqn. 4.4). For spherical & cylindrical geometries, coordinate transformations yield for example,

$$\frac{\partial C}{\partial t} = D \left[\frac{\partial^2 C}{\partial r^2} + \frac{2}{r} \frac{\partial C}{\partial r} \right] \quad (\text{spherical}) \quad (4.5)$$

and

$$\frac{\partial C}{\partial t} = D \left[\frac{\partial^2 C}{\partial r^2} + \frac{1}{r} \frac{\partial C}{\partial r} \right] \quad (\text{cylindrical}) \quad (4.6)$$

as alternatives to equation 4.4. In practice, the one-dimensional diffusional process (equation 4.3) is one of the most common diffusional problems in electrochemical investigations. The numerical solution (digital simulation) of this problem will be discussed in more detail in the following sections.

4.2.1.2 The Nernstian Diffusion Layer

Not to be confused with the diffuse double-layer¹, the Nernstian diffusion layer is an imaginary region in the solution adjacent to the electrode surface within which the electrochemical perturbation of concentrations at the electrode surface has an effect.

The concentration profile against distance of a diffusing substance within the Nernstian diffusion layer is well described by Fick's first law of diffusion (equation 4.2). In general, the concentration varies linearly over a relatively small distances from the electrode surface & then gradually approaches the bulk value (*Figure 4.1*).

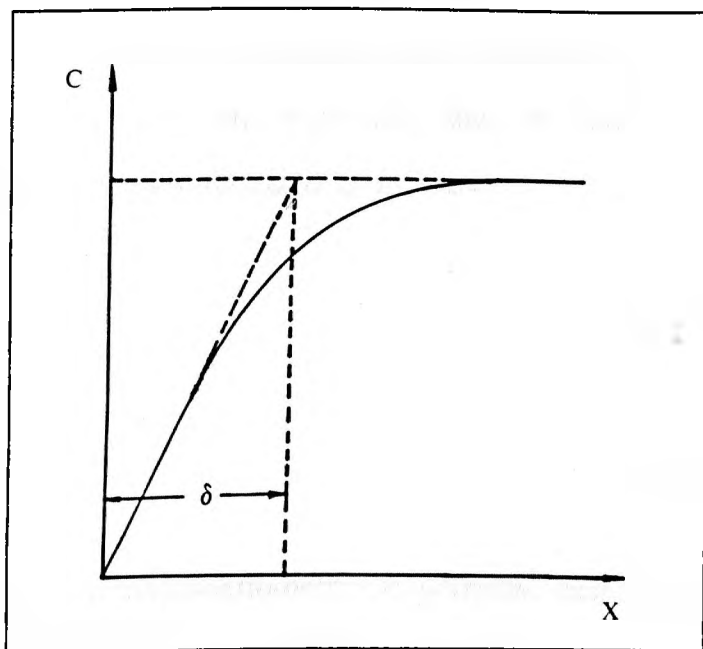


Figure 4.1 Concentration profile defined by semi-infinite linear diffusion (Fick's Law)

It can be seen from *Figure 4.1* & Fick's laws that the numerical evaluation of the actual thickness of the diffusion layer can be very arbitrary. A simple but very elegant approach was made by Nernst who suggested that the direct

¹ The modern theory divides the solution side of the electrical double-layer into two parts, i.e. the Helmholtz (or Stern) layer immediately adjacent to the electrode surface and the diffuse layer. The inner layer consists of solvent molecules and specifically absorbed molecules and ions which carry charges with opposite sign to those on the electrode surface. The diffuse layer contains an excess of ions of one particular charge up to the boundary with the bulk solution. The sum of the excess charges in both the Helmholtz and the diffuse layer balances the total charges on the electrode surface. Generally, for a given electrode and electrolyte, the thickness of the diffuse layer depends merely on the ionic strength of the solution. For example, the layer thickness is thinner than 300Å if the total ionic concentration is greater than 0.01 mol·dm⁻³.

extrapolation of the linear part of the curve could be used to determine the diffusion layer thickness. The distance between the interface & the point where the extrapolated line meets the bulk value of concentration was regarded as the effective diffusion layer thickness (*Figure 4.1*). If there is no forced convection, the effective thickness varies with time in the case of linear diffusion until interference by natural convection (cf. 4.2.3) becomes apparent.

Though it is very difficult to numerically determine the effective thickness of the Nernstian diffusion layer, it turns out empirically that the functional relationship between δ & time can be demonstrated as follows:

$$\delta = \frac{2}{\sqrt{\pi}} (Dt)^{1/2} \quad (4.7)$$

and

$$\delta = \sqrt{\pi}(Dt)^{1/2} \quad (4.8)$$

respectively for constant current (chronopotentiometry) & potential-step (cyclic voltammetry & chronoamperometry) experiments initiated at $t = 0$.

The above equations give us a rough guide to the effect of cell sizes on the concentration profile & the boundary conditions to be taken for the simulation of a diffusional process. As will be seen later in the numerical solution to the diffusional problems (e.g. equation 4.3) one always sets some boundaries such that these problems can be solved in a much simpler way. Theoretically, any perturbation at the electrode/electrolyte interface should cause changes across the entire solution though areas closest to the interface are most affected. In practice, the changes at a certain distance away from the interface can be safely ignored & it is assumed that the properties of solutions beyond this boundary remain the same as before the introduction of the perturbation (i.e. $C_b = C^{\text{Bulk}}$). In digital simulation, this boundary has to be carefully chosen so that an accurate results can be achieved with reasonable computation time (if the boundary is set

too close to the interface, computation time can be saved but at the expense of less accuracy, & *vice versa*). Normally, at least six Nernstian diffusion layer thickness from the interface have to be fully covered in the digital simulation so that satisfactory results can be obtained.

4.2.2 Migration

Unlike the diffusional process which is caused by the concentration differences of substances in the solution, migration is the movement of charged species through the electrolyte as a result of the potential gradient across the bulk of the electrolyte. In stationary electrode experiments, both the migrational & diffusional processes contribute to the transport of electroactive species, & thus to the faradaic current resulting from the changes at the electrode surface. Migration is purely caused by the gradient of the electric field in the electrolyte & therefore its influence on the transport of electroactive species can be substantially eliminated if there is a sufficiently large amount of inert (or non electroactive) electrolyte to carry most of the charges. Theoretically, the faradaic current resulting from a non-convective (stationary electrode & unstirred electrolyte) electrochemical system can be separated into two components, i.e. the diffusional (i_d) & migrational (i_m) currents. These fractional currents may be in the same or opposite directions.

Assuming the electroactive & inert cations have the same charge z_c with the two types of anions of charge z_a , & with the ratio of the concentrations of electrolyte/electroactive ions being r , the ratio of the pure migrational (i_m) & diffusive (i_d) component of the faradaic current in the absence of convection can therefore be expressed [217] as:

$$\frac{i_m}{i_d} = (1 + z_o) (1 + r) \left[1 - \left(\frac{r}{1 + r} \right)^{1/(1 + z_o)} \right] - 1 \quad (4.9)$$

where z_o is the ratio of the charges of cation & anion, i.e. $z_o = |z_C / z_A|$. If we take $z_o = 1$, then $i_m / i_d = 1$ for $r = 0$ (no supporting electrolyte), 0.17 for $r = 1$, 0.02 for $r = 10$ & 0.002 for $r = 100$. That is to say, if the ratio of the concentration of the inert electrolyte & the electroactive species is greater than 10 (which is not difficult to achieve), the migrational fraction of the faradaic current becomes, practically, negligible. This requirement is readily fulfilled under most experimental conditions & in the following this mass transport phenomenon will not be discussed in any detail.

4.2.3 Convection

Convection is the movement of reactants in the electrolyte due to mechanical forces e.g. by means of agitation. Typical examples are the rotating ring or cylinder disk electrodes, streaming mercury electrodes, dropping mercury electrodes, & situations where electrolyte is forced to flow past a stationary electrode e.g. bubbling electrodes, etc.. A rather special example is the natural convection which results from the concentration & the temperature difference in the electrolyte. Natural convection is thus a consequence of density differences of the electrolyte & the ensuing hydrostatic forces. A brief account is given below of the effect of the convection process on the transport of electroactive species in the electrolyte.

Figure 4.2 shows a one dimensional plot of concentration against the space coordinate x at a given time assuming there is no convection in the y & z directions. Assuming the solution is moving along the x direction with velocity V_x then after a time interval δt the solution previously at location x_2 (concentration C_2) will have moved to x_1 (previously at concentration of C_1). If δt & δx are small enough then the concentration distribution along PQ can be treated as a linear function, i.e.

$$\delta C = - \delta x \frac{dC}{dx} \quad (4.10)$$

Dividing both sides of the above equation by the factor δt , the rate of concentration change caused by convection can be obtained as:

$$\frac{\delta C}{\delta t} = - V_x \frac{\delta C}{\delta x} \quad (4.11)$$

where $V_x = \lim_{\delta t \rightarrow 0} (\delta x / \delta t)$ is

the instantaneous velocity on the x direction.

For more complicated convective systems the above equation can be expanded to the three dimensional form to take into account the convective effects in the other two directions,

$$\frac{\partial C}{\partial t} = - V_x \frac{\partial C}{\partial x} - V_y \frac{\partial C}{\partial y} - V_z \frac{\partial C}{\partial z} \quad (4.12)$$

where V_y & V_z are the other instantaneous velocity terms. It is not intended to discuss this problem further owing to complications in relation to numerical or analytical solutions.

4.2.4 Total Mass Transport Equation

Although the three types of mass transport processes are described individually in the above sections they are, strictly speaking, simultaneous processes. Therefore the mass transport terms relating to diffusional, convective

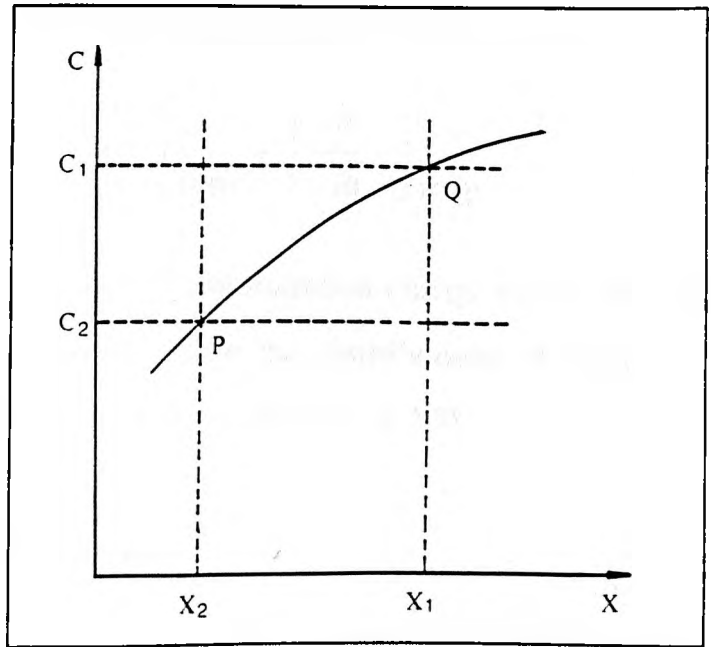


Figure 4.2 Plot of concentration against distance at a given time

& migrational processes are additive at any particular instant of time, i.e.

$$\frac{\partial C}{\partial t} = \left[\frac{\partial C}{\partial t} \right]_{\text{diff}} + \left[\frac{\partial C}{\partial t} \right]_{\text{conv}} + \left[\frac{\partial C}{\partial t} \right]_{\text{migr}} \quad (4.13)$$

where the left hand term is the "rate" of concentration change caused by mass transport, while the right hand terms denote the contributions of diffusional, convective & migrational processes (cf. 4.2.1, 4.2.2 & 4.2.3).

4.3. Homogeneous Chemical Kinetics

Leaving aside adsorption & electrode processes, the treatment of chemical kinetic processes in the development of digital simulation or analytical techniques is initially based on a simple model of homogeneous kinetic terms which are intrinsically additive to the simultaneous mass transport processes. Therefore, the rate of concentration changes of the reactants and/or products can be obtained by adding an extra kinetic term to the total mass transport equation (eqn. 4.13):

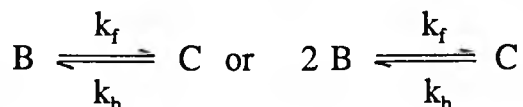
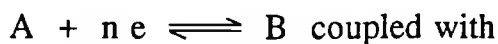
$$\frac{\partial C}{\partial t} = \left[\frac{\partial C}{\partial t} \right]_{\text{diff}} + \left[\frac{\partial C}{\partial t} \right]_{\text{conv}} + \left[\frac{\partial C}{\partial t} \right]_{\text{migr}} + \left[\frac{\partial C}{\partial t} \right]_{\text{chem}} \quad (4.14)$$

In most stationary experiments the migrational & convective terms are normally negligible, so that the above equation can be reduced to:

$$\frac{\partial C}{\partial t} = \left[\frac{\partial C}{\partial t} \right]_{\text{diff}} + \left[\frac{\partial C}{\partial t} \right]_{\text{chem}} \quad (4.15)$$

As discussed in Section 4.2.1, the diffusional processes are governed by Fick's diffusional laws while the "chemical terms" are strictly defined by the nature of the homogeneous chemical reactions coupled with the heterogeneous electron transfer process. For example, for an electrochemical reaction involving

a simple electron charge transfer process coupled with a first-order follow-up homogeneous chemical process or a second-order dimerisation process, i.e.



the kinetic terms for species B & C can be expressed as:

$$\frac{\partial C_B}{\partial t} = -k_f C_B + k_b C_C \quad \& \quad \frac{\partial C_C}{\partial t} = -\frac{\partial C_B}{\partial t} \quad \text{and}$$

$$\frac{\partial C_B}{\partial t} = -k_f C_B^2 + k_b C_C \quad \& \quad \frac{\partial C_C}{\partial t} = -\frac{1}{2} \frac{\partial C_B}{\partial t}$$

for the first-order & second-order chemical kinetics, respectively. Assuming the diffusional process is a one-dimensional semi-infinite linear diffusion & the convective & migrational factors are practically negligible, we have, for a simple electron transfer process followed by a first-order homogeneous chemical kinetics (EC reaction), the following three simultaneous differential equations:

$$\frac{\partial C_A}{\partial t} = D_A \frac{\partial^2 C_A}{\partial x^2}$$

$$\frac{\partial C_B}{\partial t} = D_B \frac{\partial^2 C_B}{\partial x^2} - k_f C_B + k_b C_C$$

$$\frac{\partial C_C}{\partial t} = D_C \frac{\partial^2 C_C}{\partial x^2} + k_f C_B - k_b C_C$$

The simultaneous solution to the above equations is already complicated, especially when the homogeneous kinetics are fast & reversible, & we shall see

later that numerical solution is feasible only if approximations are made.

The above examples are two of the most common mechanisms encountered in electrochemistry. In the following sections we shall see how implicit Crank-Nicolson techniques are implemented, & other rather complex strategies are employed for boundary conditions handling so as to develop powerful routines catering for the digital simulation of chronopotentiometric, chronoamperometric & cyclic voltammetric behaviour of a greater variety of electrochemical mechanisms. The full list includes simple electron transfer, successive electron transfers, proceeding and/or following up homogeneous chemical kinetics (including dimerisation & catalytic reactions), four-sided reactions (the "SQUARE" mechanism) & cross reactions, disproportionation reactions.

4.4 Digital Simulation of a Diffusional Process - the Implicit Crank-Nicolson Technique

As has been pointed out above, the essential task for the digital simulation of a diffusional process is to solve numerically *equations 4.2* ("box" method [188,190]) or *4.3* ("point" or the Crank-Nicolson method). Both the "box" & the Crank-Nicolson methods are based on the finite difference approximation technique. The former divides the space between a planar electrode & the boundary beyond which the solution is assumed to be unaffected throughout the experiment into small adjacent boxes of "homogeneity". The latter considers the concentration distribution as a *continuous function* of time & space and, by sampling at given time & space intervals (usually even spacing), allows the real process to be closely followed. In this section we shall mainly discuss the applications of the Crank-Nicolson method in the development of digital routines to the solution of simple diffusional problems & their implementation in some more complicated systems. This is probably owing to the fact that the Crank-Nicolson technique does have some advantages, e.g. stability¹, accuracy, over the traditional "box" method [197].

4.4.1 Digitisation of the Semi-finite Diffusional Equation

A brief description is now given on the essentials of the digitisation of the diffusional equation (*eqn. 4.3*) by the standard finite difference approximation technique. Suppose the electrochemical perturbation at the electrode/electrolyte

¹ The standard explicit technique ("box" method) becomes unworkable (i.e. results become oscillating) when the dimensionless quantity $[D\delta t/(\delta x)^2]$ (ascribed as the stability coefficient λ , where D is the diffusion coefficient, δt and δx are the time and space intervals respectively) is greater than 0.5, while there are no such restrictions to the implicit Crank-Nicolson method.

interface is only effective within a distance of x (at least six Nernstian diffusion layer thickness).

As shown in *Figure 4.3*, we divide the space (x) into m small intervals of length $\delta x (= x / m)$ & time into n small time steps of $\delta t (= t / n)$ to sample the concentration profile of the diffusing substances. Employing

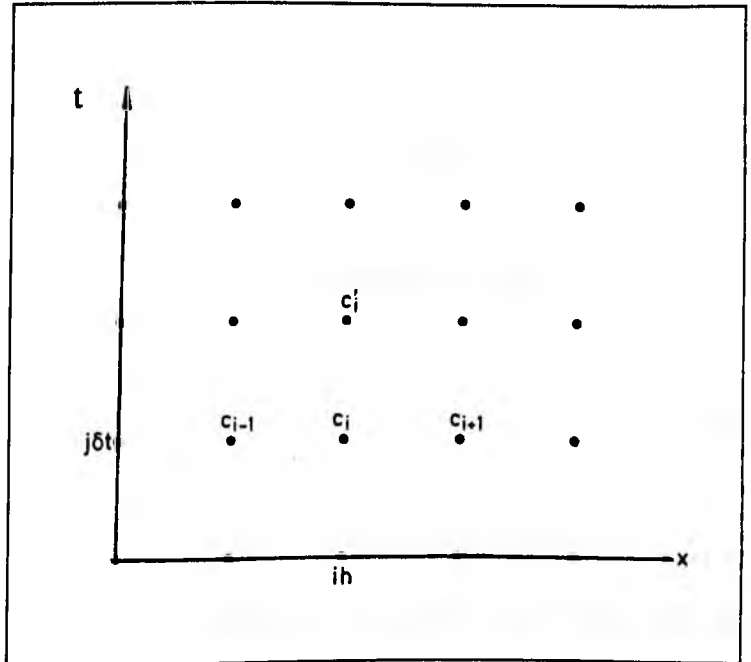


Figure 4.3 Principals for the sampling of the (x, t) plane - equal intervals

Taylor's theorem of expansion, the following expressions for three

adjacent points at locations centred at $x = i\delta x$ & at a given time $t = j\delta t$ are obtained:

$$C(x + \delta x) = C(x) + \delta x \left[\frac{\partial C(x, t)}{\partial x} \right]_x + \frac{(\delta x)^2}{2!} \left[\frac{\partial^2 C(x, t)}{\partial x^2} \right]_x + \frac{(\delta x)^3}{3!} \left[\frac{\partial^3 C(x, t)}{\partial x^3} \right]_x + O(\delta x^4) \quad (4.16)$$

and

$$C(x - \delta x) = C(x) - \delta x \left[\frac{\partial C(x, t)}{\partial x} \right]_x + \frac{(\delta x)^2}{2!} \left[\frac{\partial^2 C(x, t)}{\partial x^2} \right]_x - \frac{(\delta x)^3}{3!} \left[\frac{\partial^3 C(x, t)}{\partial x^3} \right]_x + O(\delta x^4) \quad (4.17)$$

Combining *equations 4.16 & 4.17* & ignoring the higher (4th) order

derivatives, we can isolate the second order difference of concentration at time $t(=j\delta t)$ & location $x(=i\delta x)$ as:

$$\frac{\partial^2 C(x, t)}{\partial x^2} = \frac{1}{(\delta x)^2} [C(i\delta x - \delta x) - 2 C(i\delta x) + C(i\delta x + \delta x)] \quad (4.18)$$

or in accordance with *Figure 4.3*, we can write *equation 4.18* as:

$$\frac{\partial^2 C(x, t)}{\partial x^2} = \frac{1}{(\delta x)^2} (C_{i-1} - 2 C_i + C_{i+1}) \quad (4.18a)$$

Looking back at *equation 4.3*, the discrete form of the right hand side of the equation can be readily generated by multiplying *equation set 4.18a* with the diffusion coefficient D . The left hand side, which describes the changes of concentration of diffusing species with time, can be replaced by the following approximate formula:

$$\frac{\partial C(x, t)}{\partial t} = \frac{C'_i - C_i}{\delta t} + O(\delta t^2) \quad (4.19)$$

Combining *equations 4.18a & 4.19* yields:

$$\frac{C'_i - C_i}{\delta t} = \frac{D}{(\delta x)^2} (C_{i-1} - 2 C_i + C_{i+1}) \quad (4.20)$$

By rearranging the above equation, C'_i for the next time interval can be obtained (as the concentrations at the previous time are known):

$$C'_i = C_i + \frac{D \delta t}{(\delta x)^2} (C_{i-1} - 2 C_i + C_{i+1}) \quad (i = 1 \text{ to } m) \quad (4.20a)$$

The term $D\delta t/(\delta x)^2$ (a dimensionless quantity) of the above equation is generally defined as the STABILITY coefficient (λ) because historically it

reflects the degree of stability of a simulation system (the "box" method. c.f. footnote on P 197.). It is worthwhile mentioning that the choice of this coefficient does not impose any restrictions on the implicit Crank-Nicolson technique (*cf. Section 4.4.2*).

4.4.2 The Implicit Crank-Nicolson Technique

The Crank-Nicolson technique was initially designed to solve numerically non-linear second-order partial differential equations (generally, there is at least one open boundary in one of the variables) in heat conduction. As the electrochemical diffusional processes are very similar to the heat transfer processes, the Crank-Nicolson (CN) technique can therefore be modified to solve most of the diffusional problems in electrochemistry by taking into account the specific nature of a heterogeneous electron transfer process, coupled homogeneous chemical kinetics & the corresponding boundary conditions.

As can be seen from the derivation of *equation 4.18 & Figures 4.4 & 4.5*, the time-derivative at time $j\delta t$ & location $i\delta x$ is used to evaluate the slope of the concentration profile at that particular occasion. This approximation is actually very accurate. However, a practical problem eg accumulation of error arises here when we intend to use this analytically estimated slope to calculate the concentration array for the next time step i.e. at time $(j+1)\delta t$. It is analysed [218] that a round-up error of the order 10^3 could be expected when the time interval δt is not short enough (which in turn restricts the magnitude of λ , i.e. $\lambda < 0.5$).

An innovative approach was made by Hartree [219] to solve the partial differential equations in heat transfer by taking finite steps in time & then integrating with respect to distance x by a differential analyser. Employing this

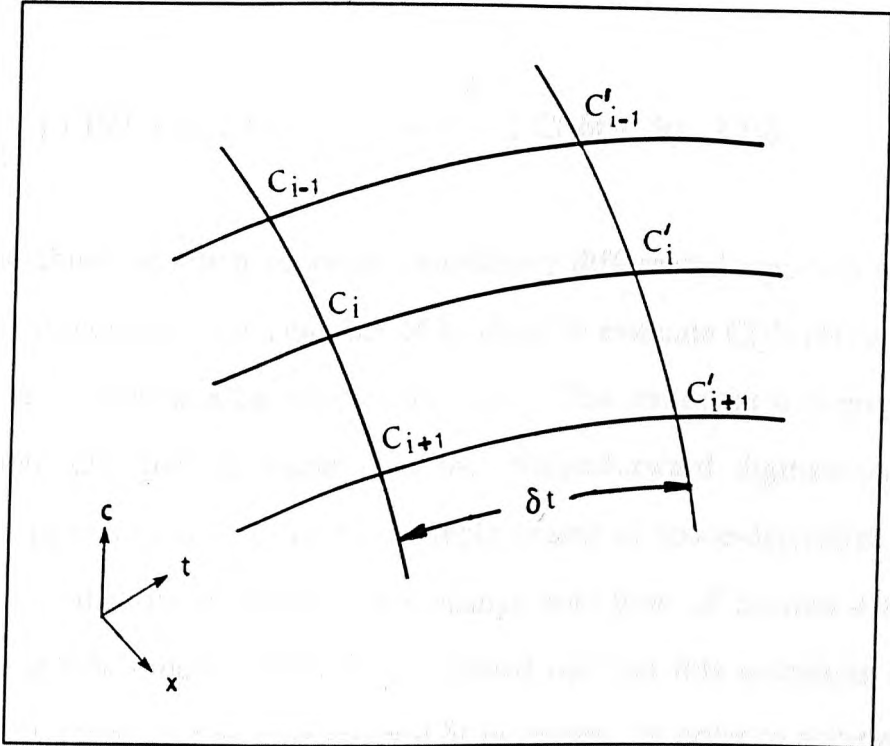


Figure 4.4 Sampling on the three dimensional concentration-space-time surface

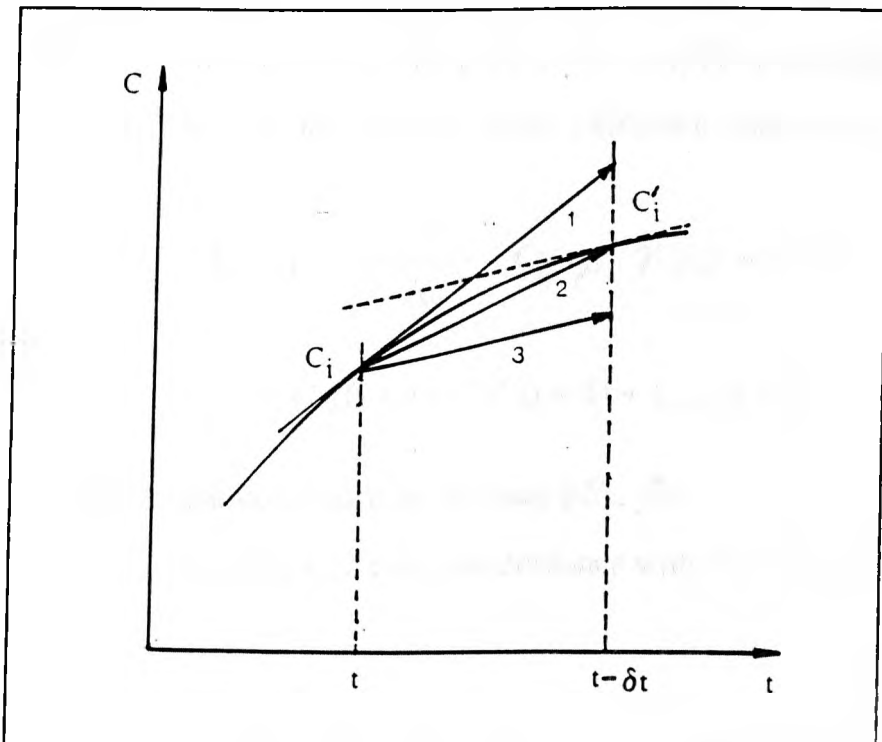


Figure 4.5 Cross-section of *Figure 4.4* on the plane $x = i\delta x$ showing the C - t relationship

technique, *equation 4.3* can be written:

$$\frac{1}{\delta t} [C(j\delta t + \delta t) - C(j\delta t)] = \frac{1}{2} \frac{\partial}{\partial x^2} [C(j\delta t + \delta t) - C(j\delta t)] \quad (4.21)$$

The above equation becomes an ordinary differential equation which can be solved numerically (by a number of δt steps) to evaluate $C(j\delta t + \delta t)$ as function of x because $C(j\delta t)$ is a known function of x . This treatment was proved to be much more effective & stable than the straightforward digitisation method discussed in *section 4.4.1*, due to the replacement of space-derivative (used to evaluate the rate of concentration change with time, *cf. Section 4.4.1*) at $j\delta t$ with that at $(j\delta t + \delta t/2)$. However, it turned out that this technique becomes increasingly inaccurate as time interval δt increases. In order to achieve certain accuracy, considerable iterations must be taken for each δt step.

Keeping in mind the inefficiency of Hartree's approach at large δt values, Crank & Nicolson modified *equation 4.21*, to obtain a set of finite difference formulae for *equation 4.3*, by replacing both the time & space derivatives at point $[i\delta x, (j + 1/2)\delta t]$ with the ordinary finite difference ratios (*eqn. 4.18*):

$$\begin{aligned} \frac{1}{\delta t} [C_i(j+1) - C_i(j)] &= \frac{1}{2} \frac{D}{(\delta x)^2} [C_{i-1}(j) - 2C_i(j) + C_{i+1}(j) \\ &+ C_{i-1}(j+1) - 2C_i(j+1) + C_{i+1}(j+1)] \end{aligned} \quad (4.22)$$

where $C_i(j)$ denotes the concentration at point $(i\delta x, j\delta t)$.

Alternatively, *equation 4.22* can, in accordance with *Figures 4.3, 4.4 & 4.5*, be written as:

$$\frac{1}{\delta t} (C'_i - C_i) = \frac{1}{2} \frac{D}{(\delta x)^2} (C'_{i-1} - 2C'_i + C'_{i+1} + C_{i-1} - 2C_i + C_{i+1}) \quad (4.22a)$$

where the prime represents the situation ($j\delta t + \delta t$), i.e. the next time step.

Let λ (the stability coefficient) = $D\delta t / (\delta x)^2$ & rearrange equation 4.22a:

$$C'_i - C_i = \frac{1}{2} \lambda [C'_{i-1} - 2C'_i + C'_{i+1} + C_{i-1} - 2C_i + C_{i+1}] \quad (4.22b)$$

The above discrete formula forms the base of the Crank-Nicolson technique for the solution of diffusional problems.

It seems that the Crank-Nicolson technique introduces a considerable complexity into the system because there is no easy way for the solution of *equation 4.22a* as there is for *equation 4.20a*. However, we should always keep in mind that the ordinary finite difference method is not suitable for larger λ values & the results obtained via this technique are not as accurate as those produced via the Crank-Nicolson methods, even though the λ values are in the lower range [218]. Besides, the solution (by the Gauss elimination method) of *equation 4.22b* is not as difficult as one might imagine.

On some occasions [203-5], the sampling of position along the x direction is deliberately shifted by $\delta x/2$ (*Figure 4.6*) such that the first point (indeed all the points!) becomes $\delta x/2$ closer to the electrode surface. This might

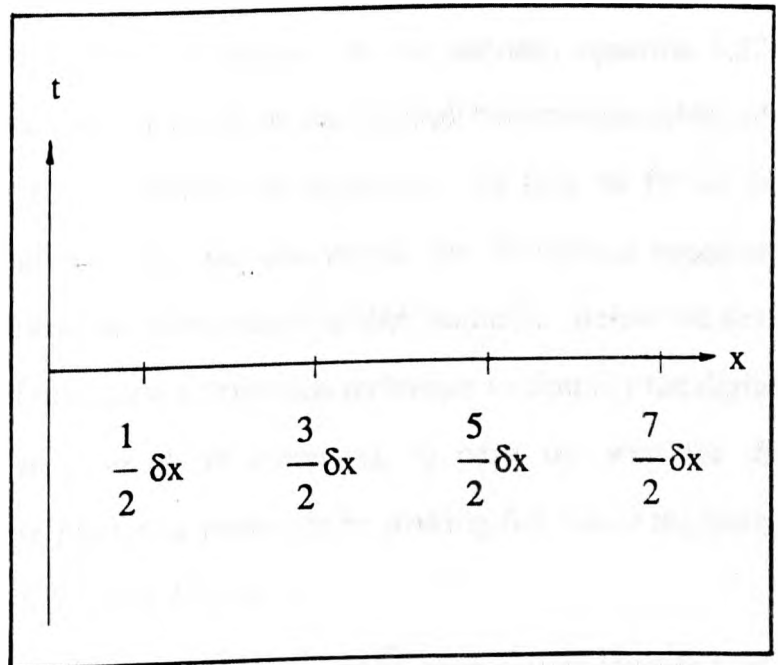


Figure 4.6 Sampling on the x axis with a $0.5\delta x$ shift towards the electrode surface

help increase the accuracy of the approximation for the concentration gradient at the electrode surface (and thus the faradaic current *cf. Section 4.5*), as its

provoker suggested [193]. The discrete form of the diffusion equation (4.3) is virtually the same as *equation 4.22b* except for the first point which is $\delta x/2$ distance away from the electrode surface where the concentration is governed by both the diffusional & the heterogeneous electron transfer processes. The digital form for this sampling point becomes:

$$C'_i - C_i = \frac{1}{2} \lambda [2C'_{i-1} - 3C'_i + C'_{i+1} + 2C_{i-1} - 3C_i + C_{i+1}] \quad (4.23)$$

This tactic is employed later in this work for the development of simulation techniques for solving some more complex problems.

4.4.3 Implementation of the Crank-Nicolson Technique

Unlike *equation 4.20a*, which can be readily handled (because each constituent equation contains only one unknown variable), the implementation of *equation 4.22b* seems to be very complicated. As we can see, *equation 4.22b* contains more than one unknown & therefore the solution becomes possible only if it is paired with an adequate number of equations. In fact, as far as the electrochemical diffusional problems are concerned, the diffusional equations ALONE cannot provide adequate information for their solution. Below we shall discuss the employment of the Gauss elimination technique to simplify the digital formula (matrices of m rows & m columns), to pave the way for the IMPLICIT solution of these particular problems by making full use of the initial & boundary conditions (*cf. Section 4.5, etc.*).

Rearranging equations 4.22b, we have the following simple equation set:

$$C'_{i-1} + a C'_i + C'_{i+1} = b_i \quad (i = 1, 2, \dots, m) \quad (4.24)$$

where $a = -2(\lambda + 1)/\lambda$, & $b_i = -C_{i-1} + 2(\lambda - 1) C_i/\lambda - C_{i+1}$ are known coefficients. Alternatively, writing equation 4.24 for all the sampling points at

time $j\delta t$, we have the following matrices:

$$\begin{aligned}
 C'_0 + a C'_1 + C'_2 &= b_1 \\
 C'_1 + a C'_2 + C'_3 &= b_2 \\
 \dots & \dots \dots \\
 C'_{i-1} + a C'_i + C'_{i+1} &= b_i \\
 \dots & \dots \dots \\
 C'_{m-1} + a C'_m + C'_{m+1} &= b_m
 \end{aligned} \tag{4.24a}$$

For the " $\delta x/2$ shift" method, the first equation of the above matrices takes the following form:

$$C'_0 + a_1 C'_1 + 0.5C'_2 = b_1$$

where $a_1 = (2\lambda + 1) / \lambda$, $b_1 = -C_0 + (2\lambda - 1)C_1/\lambda - 0.5C_{i+1}$ are similar coefficients as those for equation 4.24.

Using the Gauss elimination methods & considering the boundary condition $C_{m+1} = C^{\text{Bulk}}$ (cf. 4.5.1), we have for equations (4.24a) the following expressions:

$$C'_{i-1} + a'_i C'_i = b'_i \quad (i = 1, 2, \dots, m) \tag{4.25}$$

or

$$\begin{aligned}
 C'_0 + a'_1 C'_1 &= b'_1 \\
 C'_1 + a'_2 C'_2 &= b'_2 \\
 \dots & \dots \dots \\
 C'_{i-1} + a'_i C'_i &= b'_i \\
 \dots & \dots \dots \\
 C'_{m-1} + a'_m C'_m &= b'_m
 \end{aligned} \tag{4.25a}$$

where $a'_m = a$, $a'_i = a - 1/a'_{i+1}$, ($i = 1$ to $m-1$),

and $b'_m = b_m - C^{\text{Bulk}}$, $b'_i = b_i - b'_{i+1}/a'_{i+1}$ ($i = 1$ to $m-1$) are known coefficients.

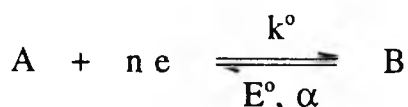
As far as the " $\delta x/2$ shift" method is concerned, ONLY the first pair of coefficients are slightly different, which are defined as follows:

$$a_1' = a_1 - 1/(2a_2'), \quad b_1' = b_1 - b_2'/(2a_2').$$

As can be seen from equation 4.25 or 4.25a, there are $(m + 1)$ unknown variables against m equations. Therefore we have to look for other routines to obtain at least one variable (C_0 , precisely) of the above unknowns. This is fulfilled by making use of the boundary conditions at the electrode/electrolyte interface, as we shall discuss next.

4.5 Simulation of A Simple Electron Transfer Process

Let us now consider as an example a simple electron transfer reaction mechanism (with n electrons), i.e.



where α is the charge transfer (or symmetry) coefficient, E° & k° are the standard potential & standard rate constant of charge transfer, respectively, & n ($n = z_A - z_B$, z_A & z_B are the valence of species A & B) is the number of electrons involved.

Equation 4.3 applies to both species A & B if the conditions for the derivation of this equation are satisfied, i.e. the transport to a planar electrode of both species A & B is entirely governed by diffusional processes. Therefore, *equation 4.25* (or 4.25a) also applies to both species. In this section, we shall be seeking for an effective path to the knowledge of the surface concentrations of both species, so that solution to equation set 4.25a becomes applicable (*cf. Section 4.4.2*).

4.5.1 Initial & Boundary Conditions

Generally, the partial differential equations which need to be solved always have some open boundaries. For example, the digital simulation of an electrochemical system with semi-infinite linear diffusion as the dominant form of mass transport requires the knowledge of an initial & two boundary conditions, i.e. those defining the electrode/electrolyte interface & the semi-infinite boundary in the bulk of the electrolyte.

Below we shall take as an example a system in which ONLY species A (concentration C_A^{BULK}) is initially present in the electrolyte, to demonstrate the basic principles of treatment for boundary conditions.

The initial conditions (values at $t = 0$) are relatively easy to define. Assuming both species are uniformly distributed, the following conditions should be satisfied:

$$C_A(x, 0) = C_A^{\text{Bulk}} \quad \& \quad C_B(x, 0) = 0 \quad (\text{for all } x)$$

For complicated processes where chemical reactions (*cf. Section 4.6*) proceed simultaneously with electron transfer process(es), the chemical equilibrium at $t=0$ should also be taken into account.

The semi-infinite boundary is artificially introduced to simplify the problems to be solved (*cf. Section 4.2.1.2*), i.e. at large distances from the electrode surface (source of electrochemical perturbation) the concentrations are assumed to remain the initial values:

$$\lim_{x \rightarrow \infty} C_A(x, 0) = C_A^{\text{Bulk}} \quad \& \quad \lim_{x \rightarrow \infty} C_B(x, 0) = 0 \quad (\text{for all } x).$$

It has become a general practice recently in digital simulation of diffusional problems etc. that solution beyond a distance of six Nernstian diffusion layer thickness from the electrode surface is treated as the "BULK"

solution - which remains un-disturbed throughout the lifetime of the experiment.

The boundary conditions at electrode/electrolyte interface, on the other hand, are usually defined by two principles, i.e. conservation of charge & mass:

$$f_A(0, t) = -D_A \left[\frac{\partial C_A(x, t)}{\partial x} \right]_{x=0} = \frac{i}{(z_A - z_B)FA} \quad (4.26)$$

and

$$D_A \left[\frac{\partial C_A(x, t)}{\partial x} \right]_{x=0} + D_B \left[\frac{\partial C_B(x, t)}{\partial x} \right]_{x=0} = 0 \quad (4.27)$$

Equation 4.26 shows the relationship between the flux of diffusing species at the electrode surface & the resulting faradaic current of the heterogeneous electrochemical processes. This serves as a bridge between the diffusional mass transport process & the electron transfer kinetics which defines the faradaic current via the universal current-overpotential equation (eqn. 4.31).

Normally, the terminology faradaic current in electrochemistry is referred to as the net resulting current² flowing in the system. It is, theoretically, the combination of both the forward & the backward current (i_f & i_b), defined by:

$$i_f = - (z_A - z_B)FA k_{hf} C_A \quad (4.28a)$$

and

$$i_b = (z_A - z_B)FA k_{hb} C_B \quad (4.28b)$$

where z_A & z_B are the valence of species A & B respectively, F (= 96484.6) is the faradaic constant, A the area of the electrode surface, C_A & C_B are the surface concentrations of species A & B. k_{hf} & k_{hb} are the forward & backward heterogeneous rate ^{constant}, defined by:

² Note the sign of the current. In this work the anodic (oxidation) current is defined as positive.

$$k_{hf} = k^{\circ} e^{-\alpha p} \quad (4.29a)$$

$$k_{hb} = k^{\circ} e^{(1-\alpha)p} \quad (4.29b)$$

where α & k° are the kinetic parameters i.e. the charge transfer coefficient & standard rate constant of charge transfer, respectively. The term p in the above equations is known as the "reduced" overpotential (deviation of potential from the standard value E°):

$$p = (z_A - z_B) F (E - E^{\circ}) / RT \quad (4.30)$$

Combination of equations 4.28a, 4.28b, 4.29a & 4.29b leads to the fundamental expression - "current-overpotential equation" - describing the relationship between the resulting faradaic current & the applied potential:

$$i = i_f + i_b = -(z_A - z_B) FA k^{\circ} [C_A e^{-\alpha p} - C_B e^{(1-\alpha)p}] \quad (4.31)$$

$$\text{or } i = -(z_A - z_B) FA [k_{hf} C_A - k_{hb} C_B] \quad (4.31a)$$

for short.

The above equation holds for any heterogeneous electron transfer process. For a Nernstian reaction where the charge transfer process is reversible (the process is diffusion-limited), for example, the above equation can be simplified to the same equation defining an electrochemical equilibrium:

$$E = E^{\circ} + \frac{RT}{(z_A - z_B) F} \text{Ln}(C_A / C_B) \quad (4.32)$$

This proves that the kinetic & thermodynamic treatments of an electrochemical system are evidently consistent. Therefore, we shall, for clarity of mathematical manipulation, deal with equation 4.31 as a general case in the rest of this section rather than following the traditional tracks to treat a process in a more specific way. For example, a simple electron transfer process can be

treated differently depending on whether it is reversible or quasi-reversible or irreversible. The classification of electron transfer processes into three groups is artificially made to fit some particular models depending on the rate of exchange of electrons at the electrode/electrolyte interface.

4.5.2 Digital Construction of E/t, i/t Profiles Generated by a Potentiostat in the Controlled Potential & Controlled Current Techniques

There are several DC techniques in electrochemistry for the investigation of particular problems. Below we shall discuss three types of the most commonly used techniques namely chronopotentiometry, cyclic voltammetry (e.g. linear sweep triangular wave) & chronoamperometry.

In chronopotentiometric (CP) experiments, a controlled current (via a galvanostat) is applied between the working & counter electrodes so that the potential of the working electrode becomes the dependent variable, which is normally determined as a function of time. These techniques are frequently referred to as the controlled current techniques. Generally, there are four main types of controlled current techniques depending on the ways in which the imposed current waves ($i = f(t)$) are generated. These include the constant current, current reversal, linear sweep & cyclic chronopotentiometry. The first two of the above techniques are generally of more practical importance & therefore they will be discussed in more detail. The generation of current-time relationship for these technique is readily completed by the definition of the magnitude of polarisation current(s) & time(s). It is worth mentioning here that the transient time calculated via the Sand equation should always be consulted during the choice of time scale of the polarisation. This is because beyond this time the depletion of one electroactive species occurs & therefore the electrode process falls into the diffusion controlled regime. One of its immediate

sequences is that the potential shoots dramatically unless another electrode process follows & sustains the current.

In both the cyclic voltammetric (CV) & chronoamperometric (CA) experiments (DC), the potential of the working electrode (w.r.p. reference electrode) is externally controlled such that the current resulting from the electrode process can be measured as a function either of time (CA) or of potential (CV). This family of techniques, especially the cyclic voltammetric ones, are the most useful tools for the solution of various electrochemical problems e.g. the elucidation of reaction mechanisms. Owing to the considerable variety of techniques being practised, we shall restrict our view to some of the most commonly used ones e.g. linear sweep cyclic voltammetry (triangular wave) & single & double potential step chronoamperometry. The construction of the potential wave for the single & double potential step chronoamperometric techniques are very simple. As far as the linear sweep cyclic voltammetric technique is concerned, the potential wave always starts at the equilibrium potential & then scans toward the first reversal potential where it turns around to scan toward the second reversal potential. The equilibrium potential is defined by the Nernstian equation (cf. 4.5.3). In situations where ONLY one electroactive species is initially present in the solution, the starting potential is set 0.5 volts off the wave which will force the concentration of the second electroactive species to be negligible. For example, for a one electron reaction, the ratio C_B/C_A is 3.5×10^{-9} at 298°C. Typical results of digital simulation of E-i-t responses from a Nerstian reaction under the CV, CA & CP techniques are illustrated in *Figure 4.7*.

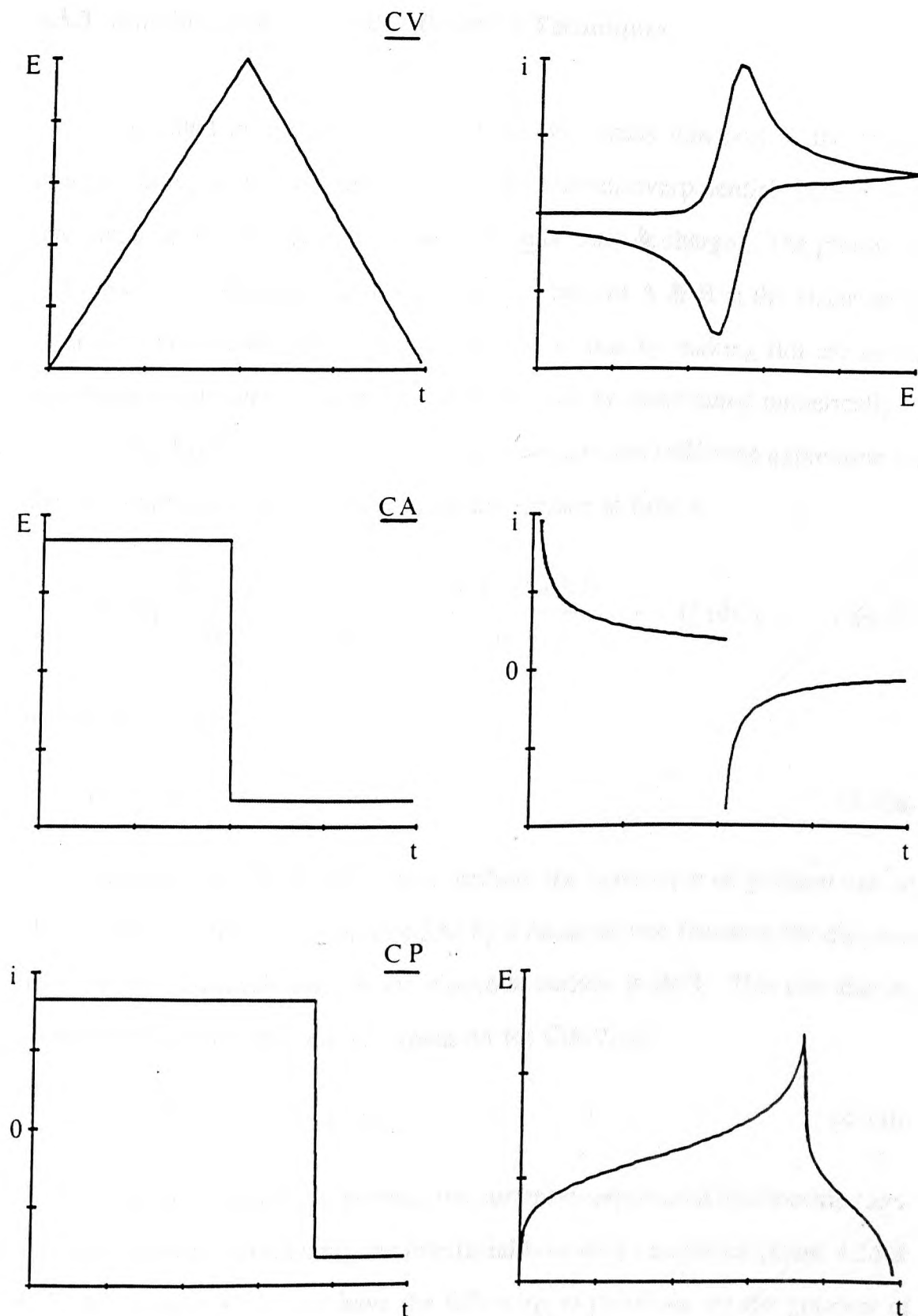


Figure 4.7 Simulated external signals and the responses from a Nerstian reaction under the CV, CA & CP techniques

4.5.3 Simulation of Controlled Potential Techniques

As stated in *section 4.5.1*, the diffusional mass transport & the charge transfer process can be bridged via the current-overpotential equation & interfacial boundary conditions (conservation of mass & charge). The prominent task now is to obtain the flux (or gradient) of species A & B at the electrode as a function of concentrations (at the interface) so that by making full use of the electrochemical kinetics these concentrations can be determined numerically.

Using Taylor's theorem of expansion, we have the following expression for the concentration gradient at the electrode surface at time t :

$$G = \left[\frac{\partial C(x, t)}{\partial x} \right]_{x=0} = \frac{C(\delta x, t) - C(0, t)}{\delta x} + O(\delta x) \quad (4.33)$$

or simply for both species:

$$G_I = [C_{I,1} - C_{I,0}] / \delta x \quad (4.33a)$$

Similarly, for " $\delta x/2$ shift" point method, the expression of gradient can be obtained by multiplying *equation 4.33a* by a factor of two (because the distance between the first mesh point & the electrode surface is $\delta x/2$). This can also be proved via Taylor's theorem of expansion for $C(\delta x/2, t)$:

$$G_I = 2 [C_{I,1} - C_{I,0}] / \delta x \quad (4.33b)$$

For an electrochemical process, the current-overpotential relationship (*eqn. 4.31*) also applies. Combining the interfacial boundary conditions (*eqns. 4.26 & 4.27*) & *equation 4.31a*, we have the following expressions for the gradient of species A & B at the electrode surface:

$$G_A = (k_{hf} C_{A,0} - k_{hb} C_{B,0}) / D_A \quad (4.34)$$

$$G_B = - G_A D_A / D_B \quad (4.35)$$

Traditionally, the surface concentrations of A & B are "indirectly" calculated via the evaluation of the concentration gradient (by combining equations 4.33a, 4.34 & 4.35):

$$G_A = \frac{D_B k^0 (C_{A,1} e^{-\alpha p} - C_{B,1} e^{(1-\alpha)p})}{D_A D_B + \delta x k^0 (D_B e^{-\alpha p} + D_A e^{(1-\alpha)p})} \quad (4.36)$$

where p is defined by *equation 4.30*. Therefore G_B & surface concentrations, $C_{A,0}$ & $C_{B,0}$, can be obtained via *equations 4.25a (or 4.25b) & 4.35*.

It is worthwhile pointing out that this method is not totally implicit because the values of $C_{A,1}$ & $C_{B,1}$ at the previous δt loop are used to calculate the concentration gradient at the new time step via *equation 4.36*. To obtain accurate results several iterations must be carried out at each time loop, which in turn increases the computation time dramatically. Furthermore, *equation 4.33* is only a rough estimation for the gradient. When large λ values (thus large δx) are used the remainder of this equation can be big enough to reduce the accuracy of the simulation system.

In attempt to improve the efficiency, Heinze [196] derived an extra equation showing the relationship between certain quantities at the electrode/electrolyte interface:

$$C'_{i,1} - C'_{i,0} = \lambda [(8 C'_{i,1} - 8 C'_{i,0} - 4 \delta x f'_{i,0}) + (8 C_{i,1} - 8 C_{i,0} - 4 \delta x f_{i,0})] \quad (4.37)$$

where $f_{i,0}$ & $f'_{i,0}$ are the fluxes at the electrode surface at time $j\delta t$ & $(j+1)\delta t$, which are defined by a parabolic fit treatment³ (3-point):

³ This is derived from Taylor's series at three points, i.e. $x = 0$, $x = \delta x/2$ & $x = 3 \delta x/2$ (" $\delta x/2$ shift"). There is an error in the original paper concerning the coefficient for $C_{i,2}$ (should be -1!).

$$C_{i,1} = b_{i,1}^i / a_{i,1}' - C_{i,0} / a_{i,1}' \quad (4.40)$$

Substituting the above equation for $C_{i,1}$ in *equation 4.33b* (" $\frac{1}{2}\delta x$ shift" method) the relationship between the gradient (flux) & concentration at the electrode surface can be written:

$$\begin{aligned} G_I &= 2(b_{i,1}' / a_{i,1}' - C_{i,0} / a_{i,1}' - C_{i,0}) / \delta x \\ &= u_I + v_I C_{i,0} \end{aligned} \quad (4.41)$$

where $u_I = 2b_{i,1}' / (a_{i,1}' \delta x)$, $v_I = -2(1 + 1/a_{i,1}') / \delta x$.

Combining *equation 4.41* & the boundary conditions (*eqns. 4.34 & 4.35*) yields the desired surface concentrations of both species for the new time loop ($t = [j + 1] \delta t$):

$$C_{A,0} = \frac{D_A u_A D_B v_B - k_{hb} (D_A u_A + D_B u_B)}{-D_A v_A D_B v_B + D_A v_A k_{hb} + D_B v_B k_{hf}} \quad (4.42)$$

$$C_{B,0} = - \frac{D_A * u_A + D_B * u_B}{D_B v_B - D_A v_A C_{A,0} / (D_B v_B)} \quad (4.43)$$

The rest of the concentration arrays at the new time loop ($j\delta t + \delta t$) can subsequently be obtained by substituting the above calculated values for $C_{A,0}$ & $C_{B,0}$ in *equation 4.34*. Therefore, the concentration gradients of species A & B can be calculated via *equation 4.36*, & finally the current can be obtained via:

$$i = (z_A - z_B) FA f_{A,0} = -(z_A - z_B) FA D_A G_A \quad (4.44)$$

From the concentration arrays of both species at time $(j+1)\delta t$, we can easily obtain arrays for the next δt step, i.e. time $(j+2)\delta t$. This iterative (according to time-step) operation continues until $j = m$, i.e. $t =$ time for "experiment". It is later found out that slightly more accurate results can be achieved if the parabolic

$$f_{I,0} = D_I (- C_{I,2} + 9C_{I,1} - 8C_{I,0}) / (3\delta x) \quad (4.38)$$

The flux at the new δt -loop is an unknown quantity which needs to be evaluated such that the combination of *equation 4.37, 4.25a & 4.25b* (" $\frac{1}{2}\delta x$ shift") can yield the concentration arrays of A & B at the new time-step, i.e. $(j+1)\delta t$. Combining *equation 4.38* with the boundary conditions yields an improved expression for the flux of A & B at the electrode surface:

$$f_{A,0} = \frac{k_f (9C_{A,1} - C_{A,2}) - k_b (9C_{B,1} - C_{B,2})}{8 + 3k_f \delta x / D_A + 3k_b \delta x / D_B} \quad (4.39)$$

A very good accuracy (error $<0.01\%$ when $0.1 < \lambda < 100$) is obtained via this technique. It must be mentioned again that concentrations of the previous time step are used in *equation 4.39* to evaluate the flux at the NEW δt -loop.

As can be seen, both *equations 4.36 & 4.39* are, theoretically, implicit forms for the evaluation of flux for the new δt -loop. However, in practice, it is "impossible" to implement these equations implicitly because one has always to utilise the concentrations at the previous time step as a "substitute" for the corresponding new values for the estimation of the new flux.

Below we present briefly an entire implicit method⁴ for handling the boundary problems in the implementation of the Crank-Nicolson (CN) scheme. Although we cannot evaluate any concentration arrays via *equations 4.25(or 4.25a)*, we can easily obtain the functional relationship between the concentration at the first space grid ($C_{I,1}$) & the concentration at the electrode surface ($C_{I,0}$) & therefore that between the flux & the surface concentration:

⁴ Acknowledgment is due to Dr. T. Boddington for discussions we have had e.g. regarding the Heinze method [10] and its implication in the development of entirely implicit techniques.

fit treatment for the gradient (eqn. 4.38) is used because this treatment presents a more accurate approximation (numerically) to the gradient at the interface.

A more general method (n-points for estimation of gradient) has been developed by Britz [197-200] - one of the pioneering workers on electrochemical digital simulation - to estimate the gradient by modifying the parabolic fit treatment (3-point " $\delta x/2$ shift") employed by Heinze [196]. This is proved later to be very efficient & accurate in this work. Similar to the earlier approach made in this work, Britz attempts to calculate the concentration arrays by fully implicit methods. Below is a brief account on the strategy he has employed.

As can be seen from equation 4.25a, there is no immediate path to the knowledge of the concentration arrays (2m equations with $[2m + 2]$ unknown variables). However, it is quite convenient to derive the concentrations as functions of $C_{l,0}$ - concentration at the electrode surface - which can be obtained through the use of boundary conditions:

$$C_{l,i} = u_{l,i} + v_{l,i} C_{l,0} \quad (4.45)$$

where $u_{l,0} = 0$, $u_{l,i} = (b'_{l,i} - u_{l,i-1}) / a'_{l,i}$,

$$v_{l,0} = 1, \quad v_{l,i} = -v_{l,i-1} / a'_{l,i} \quad (I = A, B, i = 1, 2, \dots, m).$$

Therefore, employing Taylor's theorem of expansion, the gradient at the electrode surface can be obtained as a function of concentrations at several space points (2 to 7 points are analysed) close to the interface:

$$g_{l,0}(n) \approx (1 / a_n \delta x) \sum_{i=0}^{n-1} b_{n,i} C_{l,i} \quad (4.46)$$

where a_n & $b_{n,i}$ are coefficients (optimum values are recommended [197]), while n indicates the number of points used for the evaluation of the gradient.

Combining equations 4.45 & 4.46 yields the gradient as a function of the

surface concentration:

$$g_{i,0}(n) = P_I + Q_I C_{i,0} \quad (4.47)$$

$$\text{where } P_I = (1 / a_n \delta x) \sum_{i=0}^{n-1} b_{n,i} u_{i,i}, \quad Q_I = (1 / a_n \delta x) \sum_{i=0}^{n-1} b_{n,i} v_{i,i}$$

It is obvious that *equation 4.41* is merely the simplest case of this technique ($n=2$). Therefore *equation 4.47* can be treated in a very similar fashion to obtain the surface concentrations & subsequently the gradients (fluxes) & the resulting faradaic current.

Generally, the more points that are used for the approximation of the gradient the more accurate the results obtained although this will increase the difficulty of derivation of proper expressions for the evaluation of the gradient. It is recommended [197] that 5-7 points are good enough in most circumstances. Having done a variety of experiments, we are certain that the 7-points " $\frac{1}{2}\delta x$ shift" method is most suitable for the development of digital routines for the simulation of various electrochemical mechanisms, although it was earlier suggested by Britz [197] that the " $\delta x/2$ shift" method becomes inapplicable when n (number of points used for estimation of the gradient) is beyond 5.

The recommended values for coefficients of the gradient expression (*equation 4.46*) by a 7-points approximation (for the " $\delta x/2$ shift" method) are as follows: $b_{7,0} = -200$, $b_{7,1} = 315$, $b_{7,2} = -174$, $b_{7,3} = 75$,

$$b_{7,4} = -36, \quad b_{7,5} = 32, \quad b_{7,6} = -12 \quad \& \quad a_7 = 36.$$

Therefore, the gradient at the electrode surface can be written:

$$G_I = (-200C_{i,0} + 315C_{i,1} - 174C_{i,2} + 75C_{i,3} - 36C_{i,4} + 32C_{i,5} - 12C_{i,6}) / (36 \delta x) \quad (4.48)$$

4.5.4 Controlled Current (Chronopotentiometry) Technique

Although the electrochemical digital simulation technique was initially developed for chronopotentiometric studies of certain redox couples [189,190], much of the recent development in this technique has focused on the controlled-potential systems (cyclic voltammetry & chronoamperometry). Below we shall discuss the application of the above implicit technique (*cf. Section 4.5.2*) to the digital simulation of the chronopotentiometric behaviour for various electrochemical mechanisms. We shall again use the universal current-overpotential relationship for the development of a general simulation package which caters for both the Nernstian (reversible electron transfer), the quasi-reversible, & the irreversible processes. The simulation of the last two processes has virtually not been studied so far mainly due to the complexity of numerical solutions.

In chronopotentiometry (CP) experiments, we normally pass a constant current to the cell (for multiple step CP several constant currents are passed to the system at certain time intervals). Thus, the concentration gradients (or fluxes) of the reacting species at the electrode surface are forced to remain constant throughout the lifetime of experiment:

$$G_{A,0} = \frac{-i}{(z_A - z_B) FAD_A} \quad (4.49)$$

In other words, the electrode process (reduction or oxidation) is forced to proceed at a CONSTANT rate.

Combining the above equation (*eqn. 4.49*) with *equation 4.47*, the surface concentrations of both species, $C_{A,0}$ & $C_{B,0}$, for the new time step can be obtained. Therefore, the rest of the concentration arrays at the new time loop ($[j+1]\delta t$) can be calculated without any practical difficulty. The real problem arises here regarding how we can evaluate the potential of the working electrode

(measured with respect to a reference electrode) because the standard Nernstian equation (eqn. 4.32) ONLY applies to the extremely fast electron transfer kinetics, which strongly forces the system to retain equilibrium status at the electrode/electrolyte interface. This in turns forces us to adopt some more complicated treatment.

Rearranging equation 4.31 yields:

$$M = \frac{-i}{(z_A - z_B) FA} = C_A e^{-\alpha p} - C_B e^{(1-\alpha)p} \quad (4.50)$$

where all the symbols have the same physical meaning as described above (cf. Section 4.5.1). Obviously the above equation falls into the category of non-linear equations which can ONLY be solved numerically in most cases.

It is quite clear that two exceptional cases can be "isolated" from the above equation. Firstly, when $k^0 \rightarrow \infty$, the above equation can be treated via the standard Nernstian equation (eqn. 4.32). The second exceptional case arises when the charge transfer (symmetrical) coefficient α becomes 0.5. In this case, equation 4.50 can be simplified to an ordinary quadratic problem:

$$C_B e^p + M e^{p/2} - C_A = 0 \quad (4.51)$$

Therefore, there is no difficulty in assessing the values of p (via the evaluation of $e^{p/2}$) & subsequently the potential values. If these extreme situations are not qualified, equation 4.50 can only be solved numerically.

Below we shall discuss briefly the general practice in the solution of non-linear equations by the iterative techniques & the implementation of these techniques to the solution of our particular problem (eqn. 4.50).

Generally, there are two major iterative methods [220], e.g. first-order (the method of false position) & second-order (Newton's method) processes, for the solution of non-linear equation $f(x) = 0$. Both the above mentioned iterative

processes are of the basic form:

$$x_{n+1} = x_n - f(x_n) / m$$

where m is the slope of the line joining two approximations in the first-order process (Figure 4.8) i.e.

$$m = (f_n - f_0) / (x_n - x_0).$$

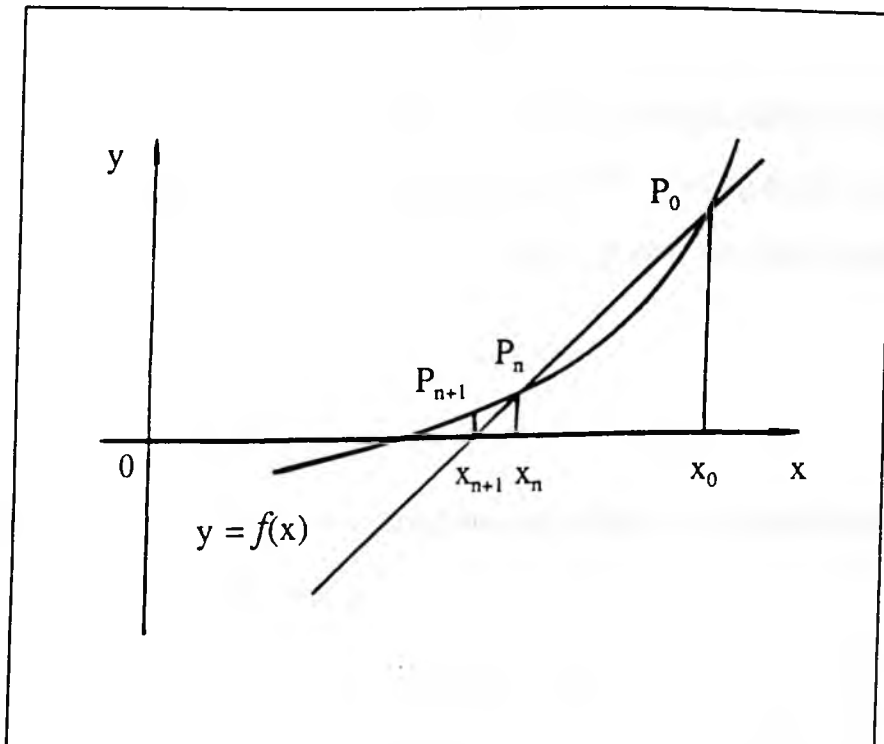


Figure 4.8 Geometrical illustration of a first-order process - *the Method of False Position*

In the second-order process (Newton's method), on the other hand, m is the slope (tangent, Figure 4.9) at point (x_n, f_n) i.e.

$$m = f'(x_n)$$

In practice, the second-order process converges much faster than the first-order treatment but it is not applicable in the situation when $f'(x) = 0$. In addition, the

choice of initial value for the iterative treatment in the second-order process is not as crucial as in the first-order process.

Below we shall mainly concentrate on the employment of Newton's methods for the development of a universal digital method for the assessment of the potential or, for simplicity, the "reduced overpotential" p ($p=(z_A-z_B)(E-E^\circ)/RT$, cf. equation 4.30 in Section 4.5.1).

From equation 4.50, we can define our target function as:

$$F(p) = C_A e^{-\alpha p} - C_B e^{(1-\alpha)p} - M \quad (4.52)$$

As can be seen from equation 4.52, $F(p)$ is a single-valued function of p (Figure 4.10). Therefore, there exists at most ONE crossing point on the p axis for the function $F(p)$. In other words, if there is a root for the equation:

$$F(p) = 0, \quad (4.52a)$$

it will be the unique one.

Differentiation of the above equation with respect to p yields the first-order derivative, i.e. slope (tangent):

$$F'(p) = -\alpha C_A e^{-\alpha p} + (1-\alpha) C_B e^{(1-\alpha)p} \quad (4.53)$$

In the potential region of practical interest, $F'(p) \neq 0$. Therefore, Newton's method is applicable (otherwise the first-order process e.g. method of false position has to be used):

$$p_{n+1} = p_n - F(p_n) / F'(p_n) \quad (4.54)$$

Given an initial value of p_0 ($n=0$), the above iterative process proceeds until a certain pre-defined criterion is satisfied. In the case of solving equation 4.50, it is very safe to set this criterion as $[ABS(1 - p_{n+1} / p_n) \leq 1e-6]$. As far as the choice of initial value of p_0 is concerned, the potential defined by the Nernstian

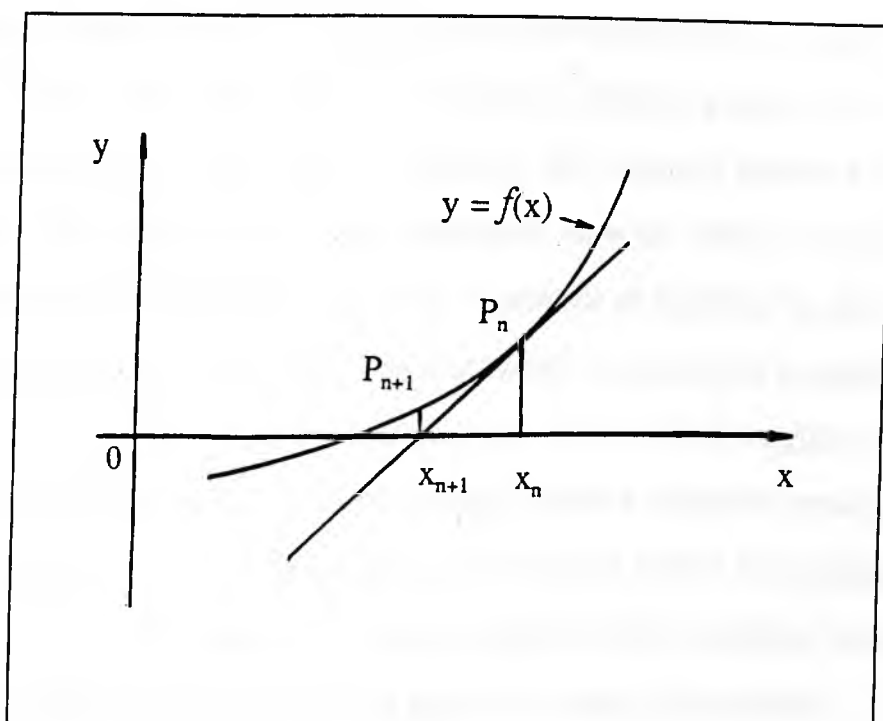


Figure 4.9 Geometrical illustration of a second-order process e.g. *Newton's Method*

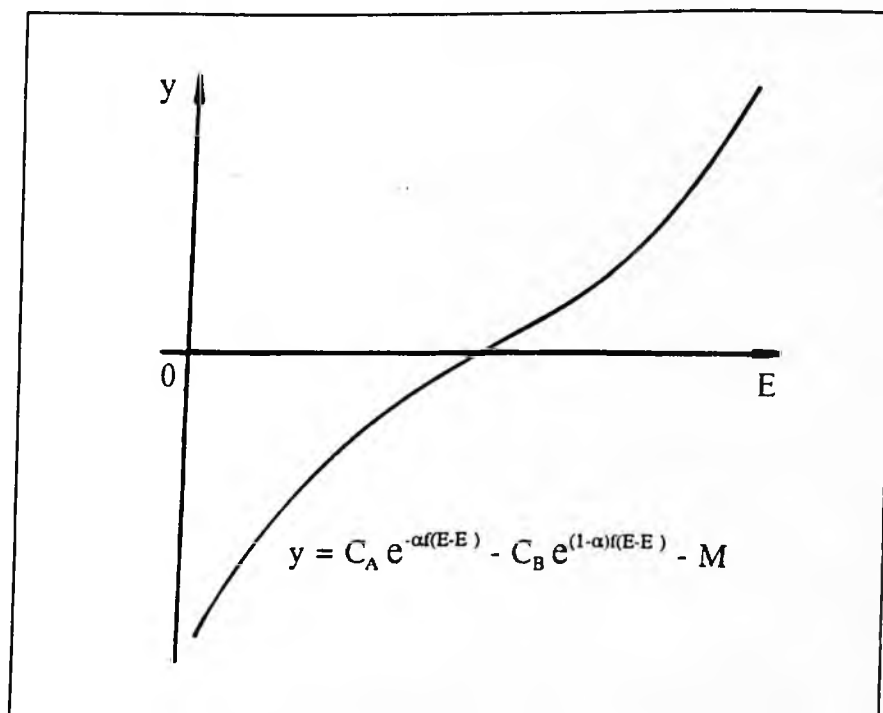


Figure 4.10 Graphic illustration of the function
 $F(p) = C_A e^{-\alpha p} - C_B e^{(1-\alpha)p} - M$

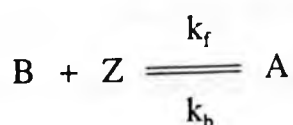
equation of equilibrium (cf. eqn. 4.32) is proved to be very satisfactory in this work. In the case where ONLY one species^{is} initially present, the Nernstian equilibrium E_{eq} is unobtainable & therefore the standard potential E° is used instead. Furthermore, certain tough measures must be taken to ensure that the simulation system is not interrupted by overshoot of potential in the diffusion-limiting regime e.g. when time for electrolysis exceeds the transition time τ defined e.g. by the Sand equation (cf. Section 4.8.4). In this regime, a dramatic increase of the potential is expected unless another electrode process follows instantaneously. This is because the depletion of either the oxidised or the reduced species would occur at the electrode/electrolyte interface, which in turn requires a huge electric field in this region to sustain the current.

4.6 Digital Simulation of Electrochemical Mechanisms with Homogeneous Chemical Kinetics e.g. Following-up or/and Proceeding Chemical Reactions

Having discussed the development of entirely implicit digital routines for the simulation of a simple electron transfer process - the fundamental process in any electrochemical reactions we shall now move to the solution of some more exciting reaction mechanisms to explore the application of the combination of these routines and auxiliary techniques catering for homogeneous chemical kinetics. In this section we shall discuss in brief the basic strategies for tackling the following reaction mechanisms:

- (1) Electron transfer with following-up chemical (first-order) reaction (EC);
- (2) Electron transfer with following-up dimerisation (second-order) reaction (ECdimer);
- (3) Electron transfer with following-up catalytic (first-order) reaction ¹ (ECcat);
- (4) electron transfer with proceeding chemical (first-order) reaction (CE);
- (5) electron transfer with proceeding and following-up chemical (first-order) reactions (CEC).

¹ The catalytic reaction is sometimes expressed as:



The above reaction is, strictly speaking, a second-order reaction. However, in most circumstances, species Z is always present in large excess. Therefore the concentration of Z can always be regarded as a CONSTANT and it can be incorporated into the rate constant. This in turn makes the OVERALL reaction look like an apparent (pseudo) first-order reaction.

As mentioned earlier (*cf. Section 4.4.1*), the model for building digital solutions to homogeneous kinetic problems is ultimately based on a simple assumption which states that homogeneous kinetics and mass transport processes proceed simultaneously, and they are intrinsically additive in terms of individual importance. Therefore, by adding these homogeneous kinetic terms to the fundamental mass transport equations, various required sets of simultaneous equations can be obtained. These differential equations & corresponding initial & boundary conditions for the EC, ECdimer, ECcat, CE and CEC mechanisms are shown in *Table 4.1* & *Table 4.2*, respectively.

The linear terms (chemical kinetics) of the simultaneous equations in *Table 4.1* introduce considerable practical difficulties to the implementation of the implicit Crank-Nicolson technique. Therefore, the kinetic and mass transport terms of those simultaneous equations are traditionally treated in separate step to make the process of digital simulation simpler and more straightforward [189, 190, 193]. We can, for example, use the concentration arrays at the previous time steps to evaluate the kinetic terms. Doing this, the simultaneous differential equations with kinetic complications can be arranged into a format similar to the pure diffusional ones which can be readily handled by the implicit Crank-Nicolson technique. Alternatively, we can solve initially the mass transport problem (equivalent to simple electron transfer) by "forgetting" the chemical kinetics and subsequently utilise those estimated results to correct the kinetic influence, by subtraction or addition of the corresponding kinetic terms where appropriate. These approximation treatments have proved to be satisfactory for processes such as the one way chemical reaction - irreversible chemical kinetics. However, significant problems, e.g. accuracy and stability, stem from this rough approximation in situations such as fast chemical kinetics. For example, when the forward and backward chemical rate constants are of the same order of magnitude, especially when they are sufficiently large, the entire system is forced

Table 4.1 Differential Equations for Simple Electron Transfer Process with Coupled Homogeneous Chemical Kinetics

Reaction	Differential Equations
EC $A + ne \xrightleftharpoons{k^o} B$ $B \xrightleftharpoons[k_b]{k_f} C$	$\frac{\partial C_A}{\partial t} = D_A \frac{\partial^2 C_A}{\partial x^2}$ $\frac{\partial C_B}{\partial t} = D_B \frac{\partial^2 C_B}{\partial x^2} - k_f C_B + k_b C_C$ $\frac{\partial C_C}{\partial t} = D_C \frac{\partial^2 C_C}{\partial x^2} + k_f C_B - k_b C_C$
ECdimer $A + ne \xrightleftharpoons{k^o} B$ $2B \xrightleftharpoons[k_b]{k_f} C$	$\frac{\partial C_A}{\partial t} = D_A \frac{\partial^2 C_A}{\partial x^2}$ $\frac{\partial C_B}{\partial t} = D_B \frac{\partial^2 C_B}{\partial x^2} - k_f C_B^2 + k_b C_C$ $\frac{\partial C_C}{\partial t} = D_C \frac{\partial^2 C_C}{\partial x^2} + \frac{1}{2} k_f C_B^2 - \frac{1}{2} k_b C_C$
ECcat $A + ne \xrightleftharpoons{k^o} B$ $B \xrightleftharpoons[k_b]{k_f} A$	$\frac{\partial C_A}{\partial t} = D_A \frac{\partial^2 C_A}{\partial x^2} - k_b C_A + k_f C_B$ $\frac{\partial C_B}{\partial t} = D_B \frac{\partial^2 C_B}{\partial x^2} + k_b C_A - k_f C_B$
CE $A \xrightleftharpoons[k_b]{k_f} B$ $B + ne \xrightleftharpoons{k^o} C$	$\frac{\partial C_A}{\partial t} = D_A \frac{\partial^2 C_A}{\partial x^2} - k_f C_A + k_b C_B$ $\frac{\partial C_B}{\partial t} = D_B \frac{\partial^2 C_B}{\partial x^2} + k_f C_A - k_b C_B$ $\frac{\partial C_C}{\partial t} = D_C \frac{\partial^2 C_C}{\partial x^2}$
CEC $A \xrightleftharpoons[k_b]{k_f} B$ $B + ne \xrightleftharpoons{k^o} C$ $C \xrightleftharpoons[k_{b2}]{k_{r2}} D$	$\frac{\partial C_A}{\partial t} = D_A \frac{\partial^2 C_A}{\partial x^2} - k_f C_A + k_b C_B$ $\frac{\partial C_B}{\partial t} = D_B \frac{\partial^2 C_B}{\partial x^2} + k_f C_A - k_b C_B$ $\frac{\partial C_C}{\partial t} = D_C \frac{\partial^2 C_C}{\partial x^2} - k_{r2} C_C + k_{b2} C_D$ $\frac{\partial C_D}{\partial t} = D_D \frac{\partial^2 C_D}{\partial x^2} + k_{r2} C_C - k_{b2} C_D$

Table 4.2 Initial and Boundary Conditions for the EC, ECdimer, ECcat, CE and CEC Mechanisms

Reaction	Initial Conditions	Boundary Conditions	
	$t = 0, x \geq 0$	$t > 0, x \rightarrow \infty$	$t > 0, x = 0$
EC	$C_A = C_A^{BULK}$ $C_B = C_B^{BULK}$ $k_f C_B = k_b C_C$	$C_A = C_A^{BULK}$ $C_B = C_B^{BULK}$ $k_f C_B = k_b C_C$	$D_A \frac{\partial C_A}{\partial x} = - D_B \frac{\partial C_B}{\partial x}$ $D_C \frac{\partial C_C}{\partial x} = 0$
ECdimer	$C_A = C_A^{BULK}$ $C_B = C_B^{BULK}$ $k_f C_B^2 = k_b C_C$	$C_A = C_A^{BULK}$ $C_B = C_B^{BULK}$ $k_f C_B^2 = k_b C_C$	$D_A \frac{\partial C_A}{\partial x} = - D_B \frac{\partial C_B}{\partial x}$ $D_C \frac{\partial C_C}{\partial x} = 0$
ECcat	$C_A = C_A^{BULK}$ $k_b C_A = k_f C_B$	$C_A = C_A^{BULK}$ $k_b C_A = k_f C_B$	$D_A \frac{\partial C_A}{\partial x} = - D_B \frac{\partial C_B}{\partial x}$
CE	$C_A = C_A^{BULK}$ $k_f C_A = k_b C_B$ $C_C = C_C^{BULK}$	$C_A = C_A^{BULK}$ $k_f C_A = k_b C_B$ $C_C = C_C^{BULK}$	$D_B \frac{\partial C_B}{\partial x} = - D_C \frac{\partial C_C}{\partial x}$ $D_A \frac{\partial C_A}{\partial x} = 0$
CEC	$C_A = C_A^{BULK}$ $k_f C_A = k_b C_B$ $C_C = C_C^{BULK}$ $k_{r2} C_C = k_{b2} C_D$	$C_A = C_A^{BULK}$ $k_f C_A = k_b C_B$ $C_C = C_C^{BULK}$ $k_{r2} C_C = k_{b2} C_D$	$D_B \frac{\partial C_B}{\partial x} = - D_C \frac{\partial C_C}{\partial x}$ $D_A \frac{\partial C_A}{\partial x} = 0$ $D_D \frac{\partial C_D}{\partial x} = 0$

throughout the lifetime of experiment to retain chemical equilibrium status in the solution. In this case, the chemical kinetics are at least of the same importance as the heterogeneous electron transfer process (the driving force for mass transport process) and therefore the differential equations listed in *Table 4.1* MUST be solved simultaneously to make the digital simulation system stable, efficient and reasonably accurate.

Although there exist considerable differences in these coupled homogeneous chemical kinetics, the digital treatment of these problems can be made more or less in a similar fashion. Below, the EC mechanism is taken as an example to illustrate how the implicit Crank-Nicolson technique is implemented in these complicated reaction schemes.

Applying the Crank-Nicolson technique to the differential equations for the EC reaction (cf. *Table 4.1*) yields the following digital formula for species A:

$$C'_{A,i} - C_{A,i} = \frac{1}{2} \lambda (C'_{A,i-1} - 2C'_{A,i} + C'_{A,i+1} + C_{A,i-1} - 2C_{A,i} + C_{A,i+1}) \quad (4.55)$$

and for species B & C (adding the kinetic terms to *eqn. 4.55*):

$$C_{B,i} - C_{B,i} = \frac{1}{2} \lambda (C'_{B,i-1} - 2C'_{B,i} + C'_{B,i+1} + C_{B,i-1} - 2C_{B,i} + C_{B,i+1}) - \frac{1}{2} k_f \delta t (C'_{B,i} + C_{B,i}) + \frac{1}{2} k_b \delta t (C'_{C,i} + C_{C,i}) \quad (4.56)$$

$$C_{C,i} - C_{C,i} = \frac{1}{2} \lambda (C'_{C,i-1} - 2C'_{C,i} + C'_{C,i+1} + C_{C,i-1} - 2C_{C,i} + C_{C,i+1}) + \frac{1}{2} k_f \delta t (C'_{B,i} + C_{B,i}) - \frac{1}{2} k_b \delta t (C'_{C,i} + C_{C,i}) \quad (4.57)$$

where the prime denotes the concentrations at the new time loop (i.e. unknown quantities) and *i* indicates the space mesh where the point is located (*i* = 1 to *m*, cf. *Figure 4.3*). As for the " $\delta x/2$ shift" method, the ONLY alteration which needs to be made is the digital formula for the diffusional terms at the first mesh point (*i*=1), which are defined by *equation 4.25* because the chemical kinetics is un-affected by the changes of sampling.

As can be seen, *equation 4.55* is identical with *equation 4.22b* (because the differential equation of species A consists of diffusional terms ONLY. cf. *Table 4.1*) and therefore it can be readily manipulated by methods discussed in *section 4.4.3*. The solution of *equations 4.56 & 4.57*, on the other hand, requires much more mathematical manipulation . Rearrangement of these equations yields:

$$C'_{B,i-1} + a_B C'_{B,i} + C'_{B,i+1} = b_{B,i} + p_B C'_{C,i} \quad (i=1,2,\dots,m) \quad (4.58)$$

$$C'_{C,i-1} + a_C C'_{C,i} + C'_{C,i+1} = b_{C,i} + p_C C'_{B,i} \quad (i=1,2,\dots,m) \quad (4.59)$$

where $a_B = - (2 \lambda_B + 2 + k_f \delta t) / \lambda_B$, $p_B = - k_b \delta t / \lambda_B$ &

$$b_{B,i} = - C_{B,i-1} + (2 \lambda_B - 2 + k_f \delta t) C_{B,i} / \lambda_B - C_{B,i+1} - k_b \delta t C_{C,i} / \lambda_B$$

and $a_C = - (2 \lambda_C + 2 + k_b \delta t) / \lambda_C$, $p_C = - k_f \delta t / \lambda_C$ &

$$b_{C,i} = - C_{C,i-1} + (2 \lambda_C - 2 + k_b \delta t) C_{C,i} / \lambda_C - C_{C,i+1} - k_f \delta t C_{B,i} / \lambda_C$$

are known coefficients. Alternatively, expressing *equations 4.58 & 4.59* for all the sampling points at time $j\delta t$, the following matrices can be obtained:

$$\begin{aligned} C'_{B,0} + a_B C'_{B,1} + C'_{B,2} &= b_{B,1} + p_B C'_{C,1} \\ C'_{B,1} + a_B C'_{B,2} + C'_{B,3} &= b_{B,2} + p_B C'_{C,2} \\ \dots & \dots \dots \end{aligned} \quad (4.58a)$$

$$\begin{aligned} C'_{B,i-1} + a_B C'_{B,i} + C'_{B,i+1} &= b_{B,i} + p_B C'_{C,i} \\ \dots & \dots \dots \\ C'_{B,m-1} + a_B C'_{B,m} + C'_{B,m+1} &= b_{B,m} + p_B C'_{C,m} \end{aligned}$$

&

$$\begin{aligned} C'_{C,0} + a_C C'_{C,1} + C'_{C,2} &= b_{C,1} + p_C C'_{B,1} \\ C'_{C,1} + a_C C'_{C,2} + C'_{C,3} &= b_{C,2} + p_C C'_{B,2} \\ \dots & \dots \dots \end{aligned} \quad (4.59a)$$

$$\begin{aligned} C'_{C,i-1} + a_C C'_{C,i} + C'_{C,i+1} &= b_{C,i} + p_C C'_{B,i} \\ \dots & \dots \dots \\ C'_{C,m-1} + a_C C'_{C,m} + C'_{C,m+1} &= b_{C,m} + p_C C'_{B,m} \end{aligned}$$

for species B and C respectively.

The above equations (4.58a & 4.59a) are very similar to those describing the unique diffusional process (eqn. 4.24a). The ONLY difference is the extra linear terms (UNKNOWN QUANTITIES) on the right hand side which partly show the influence of the homogeneous kinetics (because the chemical kinetics is also incorporated into the coefficients a_B , a_C , b_B & a_C). Exact solutions of these equations are impossible and therefore we have to search for methods to solve them with reasonable precision, analytically or approximately. The easiest way is to use the corresponding concentrations at the previous time step ($j\delta t$) to replace the unknown quantities (concentrations) on the right hand side. Thus these equations can be arranged into similar formula as equation 4.24a and can be readily solved by the Gauss elimination method.

It can be seen clearly why the conventional treatment of the homogeneous chemical kinetics by SIMPLY substituting the unknown concentrations on the right hand side with those at the previous time causes inaccuracy and even instability. For example, in cyclic voltammetric experiments with the potential gradually stepping into the "half-wave" potential ($E_{1/2}$) region, the changes in concentrations of BOTH species increase rapidly and therefore considerably large errors will be brought into the simulation system by replacing the concentrations at the new time loop with the corresponding values at the previous time. These deviations accumulate gradually and produce substantial round-up errors and instability in the system. It is analysed in this work that up to 15% of error would be expected for a fast charge transfer process ($k^0=10 \text{ ms}^{-1}$) with a fast reversible chemical reaction ($k_f = k_b = 10 \text{ s}^{-1}$). If k_f and k_b are great than 30 s^{-1} , the simulation system oscillates.

To meet this challenge, two iterative methods have been proposed in this work and have been proved later to be much more efficient and accurate than the conventional treatment. Brief descriptions of these numerical approaches are

given below.

In the first approach the concentrations at the previous δt -loop ($j\delta t$) are used as the first approximation of the unknown concentrations on the right hand sides of equations 4.60a and 4.61a. The "TRUE" concentration arrays of both species B & C can be subsequently obtained by the implicit method discussed in section 4.4.3, with the specific initial & boundary conditions being fully taken into account. These calculated concentration arrays then serve as the second approximation for the corresponding terms on the right hand sides of equations 4.60a & 4.61a to obtain yet another set of "TRUE" concentration arrays for species B & C. This iterative treatment continues until the "ESTIMATED" concentrations and the "TRUE" ones are close enough. For example the iteration process can be set to terminate automatically if the percentage differences of concentrations at all the sampling points are less than 0.0001%.

In the second approach, on the other hand, a 5-point polynomial fit treatment is developed² to extrapolate the concentrations at the "present" time using the concentrations at the five time loops immediately before the "present" time. These extrapolated values of concentrations are subsequently used as the initial approximation to "trigger" the above iterative process. This has proved to be much more efficient than the first approach mainly owing to the fact that the first approximation of concentrations takes into account the shape (trend) of the concentration profile and therefore it should be much closer to the TRUE values. Several other treatments e.g. two-point linear extrapolation method have also been practised here. Although this gives reasonably satisfactory results, it always requires much longer computation time because the linear extrapolation does not take into account the shape of the concentration profile. This is particular severe

² Acknowledgment is due to Dr. T. Boddington for his constructive suggestions.

in potential regions just beyond the half-wave potential ($E_{1/2}$) where drastic changes in the concentrations are expected to occur.

Both the above approaches have been proved via convolution technique (*c.f. section 4.8*) to be very accurate if both the chemical rate constants, k_f & k_b , are less than 400 s^{-1} . The error when $k_f (= k_b) \leq 1000 \text{ s}^{-1}$ is less than 6%. Furthermore, the simulation system is stable in situations where very fast chemical kinetics (e.g. $k_f = k_b \geq 10^5 \text{ s}^{-1}$) are involved.

Although the above numerical treatment is developed for the digital simulation of the EC reactions, it also applies to the ECcat, ECdimer, CE and CEC mechanisms by making some specific modifications on e.g. the initial & boundary conditions treatment. For example, in the CE reaction, the differential equation and boundary conditions for species C are very similar to those of species A in the EC mechanism (*cf. Tables 4.1 & 4.2*), therefore the concentration arrays of species C can be readily evaluated in a similar fashion by the implicit Crank-Nicolson technique. As far as species A and B are concerned, their concentration profiles can ONLY be obtained by approximation due to the complexity caused by the homogeneous chemical kinetics. The CEC mechanism, on the other hand, can be regarded as a CE reaction followed by a homogeneous chemical reaction e.g. decomposition of the electroactive species C. Therefore, the digital treatment is very similar to that of the CE case although further complications, e.g. the simultaneous evaluation of the concentration array for the final product (species D) are encountered in the former.

4.7 Digital Simulation of Multistep Charge Transfer Processes

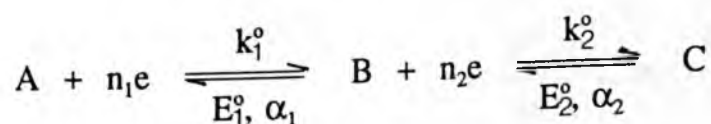
Frequently the product of an electron transfer process or the substance chemically converted from this product is also electroactive. Therefore, this new electroactive species may, in a given potential region, undergo an electrochemical reaction to produce a final substance which is electrochemically inactive. In the following sections, examples of the reaction schemes listed below will be used to demonstrate the application of the implicit Crank-Nicolson technique to the numerical solutions of processes involving multistep charge transfers:—

- (1) Simple multistep charge transfer reaction (EE);
- (2) Parallel chemically coupled electron transfer reactions (ECE2);
- (3) Successive electron transfers with coupled chemical reaction (ECE);
- (4) Successive electron transfers with coupled chemical reactions (ECEC);
- (5) The "SQUARE" mechanism - four sided reaction.

The simultaneous differential diffusional equations and corresponding initial & boundary conditions for the above reaction schemes are shown in *Table 4.3* & *Table 4.4* respectively.

4.7.1 Simple Multistep Charge Transfers - the EE Mechanism

A multistep electron transfer reaction can be schematically represented by



where A, B are electroactive species, n_1 & n_2 the number of electrons involved in the successive charge transfer steps, k_1° & k_2° the corresponding standard rate constants of charge transfer and E_1° & E_2° the corresponding standard potentials.

Table 4.3 Differential Equations for Multistep Electron Transfer Process with/without Coupled Homogeneous Chemical Kinetics

Reaction	Differential Equations
EE	$A + n_1 e \xrightleftharpoons{k^o} B$ $B + n_2 e \xrightleftharpoons{k^o} C$ $\frac{\partial C_A}{\partial t} = D_A \frac{\partial^2 C_A}{\partial x^2}$ $\frac{\partial C_B}{\partial t} = D_B \frac{\partial^2 C_B}{\partial x^2}$ $\frac{\partial C_C}{\partial t} = D_C \frac{\partial^2 C_C}{\partial x^2}$
ECE	$A + n_1 e \xrightleftharpoons{k^o} B$ $B \xrightleftharpoons[k_b]{k_f} C$ $C + n_2 e \xrightleftharpoons{k^o} D$ $\frac{\partial C_A}{\partial t} = D_A \frac{\partial^2 C_A}{\partial x^2}$ $\frac{\partial C_B}{\partial t} = D_B \frac{\partial^2 C_B}{\partial x^2} - k_f C_B + k_b C_C$ $\frac{\partial C_C}{\partial t} = D_C \frac{\partial^2 C_C}{\partial x^2} + k_f C_B - k_b C_C$ $\frac{\partial C_D}{\partial t} = D_D \frac{\partial^2 C_D}{\partial x^2}$
ECEC	$A + n_1 e \xrightleftharpoons{k^o} B$ $B \xrightleftharpoons[k_b]{k_f} C$ $C + n_2 e \xrightleftharpoons{k^o} B$ $D \xrightleftharpoons[k_{b2}]{k_{f2}} E$ <p>Differential equations for species A, B & C are the same as the ECE mechanism.</p> $\frac{\partial C_D}{\partial t} = D_D \frac{\partial^2 C_D}{\partial x^2} - k_{f2} C_D + k_{b2} C_E$ $\frac{\partial C_E}{\partial t} = D_E \frac{\partial^2 C_E}{\partial x^2} + k_{f2} C_D - k_{b2} C_E$
SQUARE	$A + n_1 e \xrightleftharpoons{k^o} B$ $B \xrightleftharpoons[k_b]{k_f} C$ $C + n_2 e \xrightleftharpoons{k^o} B$ $D \xrightleftharpoons[k_{b2}]{k_{f2}} A$ $\frac{\partial C_A}{\partial t} = D_A \frac{\partial^2 C_A}{\partial x^2} + k_{f2} C_D - k_{b2} C_A$ $\frac{\partial C_B}{\partial t} = D_B \frac{\partial^2 C_B}{\partial x^2} - k_f C_B + k_b C_C$ $\frac{\partial C_C}{\partial t} = D_C \frac{\partial^2 C_C}{\partial x^2} + k_f C_B - k_b C_C$ $\frac{\partial C_D}{\partial t} = D_D \frac{\partial^2 C_D}{\partial x^2} - k_{f2} C_D + k_{b2} C_A$

Table 4.4 Initial and Boundary Conditions for the EE, ECE, ECEC
and SQUARE (4-sided) Mechanisms

Reaction	Initial Conditions	Boundary Conditions	
	$t = 0, x \geq 0$	$t > 0, x \rightarrow \infty$	$t > 0, x = 0$
EE	$C_A = C_A^{\text{BULK}}$ $C_B = C_B^{\text{BULK}}$ $C_C = C_C^{\text{BULK}}$	$C_A = C_A^{\text{BULK}}$ $C_B = C_B^{\text{BULK}}$ $C_C = C_C^{\text{BULK}}$	$D_A \frac{\partial C_A}{\partial x} + D_B \frac{\partial C_B}{\partial x} + D_C \frac{\partial C_C}{\partial x} = 0$
ECE	$C_A = C_A^{\text{BULK}}$ $C_B = C_B^{\text{BULK}}$ $k_f C_B = k_b C_C$ $C_D = C_D^{\text{BULK}}$	$C_A = C_A^{\text{BULK}}$ $C_B = C_B^{\text{BULK}}$ $k_f C_B = k_b C_C$ $C_D = C_D^{\text{BULK}}$	$D_A \frac{\partial C_A}{\partial x} = - D_B \frac{\partial C_B}{\partial x}$ $D_C \frac{\partial C_C}{\partial x} = - D_D \frac{\partial C_D}{\partial x}$
ECEC	$C_A = C_A^{\text{BULK}}$ $C_B = C_B^{\text{BULK}}$ $k_f C_B = k_b C_C$ $C_D = C_D^{\text{BULK}}$ $k_{r2} C_D = k_{b2} C_E$	$C_A = C_A^{\text{BULK}}$ $C_B = C_B^{\text{BULK}}$ $k_f C_B = k_b C_C$ $C_D = C_D^{\text{BULK}}$ $k_{r2} C_D = k_{b2} C_E$	$D_A \frac{\partial C_A}{\partial x} = - D_B \frac{\partial C_B}{\partial x}$ $D_C \frac{\partial C_C}{\partial x} = - D_D \frac{\partial C_D}{\partial x}$ $D_E \frac{\partial C_E}{\partial x} = 0$
SQUARE	$C_A = C_A^{\text{BULK}}$ $C_B = C_B^{\text{BULK}}$ $k_f C_B = k_b C_C$ $k_{r2} C_C = k_{b2} C_A$	$C_A = C_A^{\text{BULK}}$ $C_B = C_B^{\text{BULK}}$ $k_f C_B = k_b C_C$ $k_{r2} C_D = k_{b2} C_A$	$D_A \frac{\partial C_A}{\partial x} = - D_B \frac{\partial C_B}{\partial x}$ $D_C \frac{\partial C_C}{\partial x} = - D_D \frac{\partial C_D}{\partial x}$

Employing the standard Crank-Nicolson technique to the differential equations describing the EE reaction (cf. *Table 4.3*) yields the following digital formula for species A, B & C

$$C'_{I,i} - C_{I,i} = \frac{1}{2} \lambda [C'_{I,i-1} - 2C'_{I,i} + C'_{I,i+1} + C_{I,i-1} - 2C_{I,i} + C_{I,i+1}] \quad (4.60)$$

where I = A, B & C, the prime denotes the concentrations at the new time loop (i.e. unknown quantities) and i indicates the space mesh where the point is located (i = 1 to m, cf. *Figure 4.3*). As for the " $\delta x/2$ shift" method, the ONLY alteration which needs to be made is the digital formula at the first mesh point (i = 1) which is defined by *equation 4.23*.

As can be seen, *equation 4.60* is identical with *equation 4.22b* which represents the digital formula for the differential equations describing the simple charge transfer process (no chemical kinetics). Therefore it can readily be manipulated by the Gauss elimination methods, and the implicit techniques developed earlier in this work and in references [196-200], to obtain the expressions of gradient of species A, B & C as functions of related surface concentrations:

$$G_I = u_I + v_I C_{I,0} \quad (4.61)$$

where u_I and v_I are coefficients similar to those defined for *equation 4.47* (cf. *sections 4.4.3 & 4.5.2*).

The prominent problem at present is to make full use of the boundary conditions shown in *Table 4.4* and the heterogeneous kinetics (via the current-overpotential relationship) so that the surface concentrations of species A, B & C can be obtained. This in turn leads to the knowledge of all the concentrations at the new time step ($[j + 1] \delta t$).

Generally, the following equations hold at the electrode/electrolyte interface:

$$D_A \left[\frac{\partial C_A}{\partial x} \right]_{x=0} + D_B \left[\frac{\partial C_B}{\partial x} \right]_{x=0} + D_C \left[\frac{\partial C_C}{\partial x} \right]_{x=0} = 0 \quad (4.62)$$

$$\text{or } f_A(0, t) + f_B(0, t) + f_C(0, t) = 0 \quad (4.62a)$$

$$- f_A(0, t) = k_1^o [C_{A,0} e^{-\alpha_1 p_1} - C_{B,0} e^{(1-\alpha_1)p_1}] \quad (4.63)$$

$$f_C(0, t) = k_2^o [C_{B,0} e^{-\alpha_2 p_2} - C_{C,0} e^{(1-\alpha_2)p_2}] \quad (4.64)$$

where p_1 & p_2 are the "reduced overpotentials" which are defined by equation 4.30 (*cf. Section 4.5.1*) and all other symbols have their usual meanings as defined previously.

In practice, there is no easy route for the numerical solution of controlled-current experiments owing to the fact that the faradaic current resulting from a multistep charge transfer reaction is the combination of two individual steps. Therefore, development of digital solutions is confined to the controlled-potential systems in this work. Another important feature of the EE reactions lies in the fact that there is no simple equality between the fluxes of the reduced & oxidised species involved in each individual charge transfer step. This is because the flux of species B is governed by both charge transfer steps of the OVERALL reaction. Therefore, the UNIVERSAL law of conservation of mass (*eqn. 4.62*) must be used.

Combining *equations 4.61, 4.62, 4.63 & 4.64*, the surface concentrations for species A, B & C can be obtained after detailed standard mathematical manipulations:

$$C_{A,0} = - \frac{s_1 + s_2 D_B v_B + s_4 D_C v_C}{D_A v_A + s_3 D_B v_B + s_5 D_C v_C} \quad (4.65)$$

$$C_{B,0} = s_2 + s_3 C_{A,0} \quad (4.66)$$

$$C_{C,0} = s_4 + s_5 C_{A,0} \quad (4.67)$$

where s_1, s_2, s_3, s_4, s_5 are coefficients defined by

$$s_1 = D_A u_A + D_B u_B + D_C u_C \quad (4.68)$$

$$s_2 = -D_A u_A / (k_1^0 e^{(1-\alpha_1) p_1}) \quad (4.69)$$

$$s_3 = (k^0 e^{-\alpha_1 p_1} - D_A v_A) / (k_1^0 e^{(1-\alpha_1) p_1}) \quad (4.70)$$

$$s_4 = (D_C u_C + s_2 k_2^0 e^{-\alpha_2 p_2}) / (k_2^0 e^{(1-\alpha_2) p_2} - D_C v_C) \quad (4.71)$$

$$s_5 = (s_3 k_2^0 e^{-\alpha_2 p_2}) / (k_2^0 e^{(1-\alpha_2) p_2} - D_C v_C) \quad (4.72)$$

Having acquired the knowledge of the corresponding surface concentrations i.e. $C_{A,0}, C_{B,0}$ & $C_{C,0}$, the concentration arrays of species A, B and C at the new time step can be subsequently calculated. Therefore the fluxes of these species and the contribution of the two individual charge transfer process to the OVERALL faradaic current can also be readily evaluated:

$$i_{AB} = (z_A - z_B) FA f_A(0, t) \quad \& \quad i_{BC} = - (z_B - z_C) FA f_C(0, t)$$

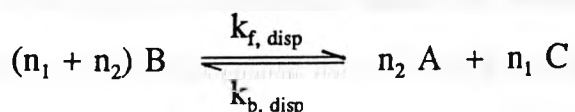
The resulting faradaic current from the entire process can be finally calculated via:

$$i = i_{AB} + i_{BC} = (z_A - z_B) FA f_A(0, t) - (z_B - z_C) FA f_C(0, t) \quad (4.73)$$

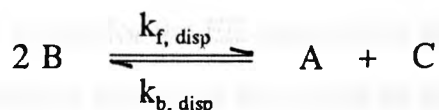
Frequently a homogeneous redox reaction (disproportionation reaction) is also considerably sluggish under certain experimental conditions [221-2]. Therefore this homogeneous chemical kinetics must be fully considered in the development of any analytical or numerical techniques for the treatment of a multistep consecutive electron transfer process. For example, in the study of the electrochemical reduction of benzil in the presence of alkaline earth ions e.g. $Ba(ClO_4)_2$ in dimethylformamide (DMF), the forward rate constant of the disproportionation reaction was found to be as fast as $4 \times 10^4 \text{ mol}^{-1} \text{ s}^{-1} \text{ dm}^3$ [221]. This

will in certain conditions, e.g. relatively slow scan rates, compete vigorously with the charge transfer reactions, especially when the charge transfer processes are not fast enough to overrule the homogeneous reaction.

A general illustration of this homogeneous redox (disproportionation) reaction can be given by:



Obviously there are several variations of the above reaction scheme depending on the thermodynamic parameters of the two charge transfer steps. Below we shall discuss in brief a special case in which the number of electrons for the two consecutive charge transfer steps are identical, i.e. $n_1 = n_2$. In this case the disproportionation reaction becomes a second order reaction and can be written as:



The free energy change of the above reaction can readily be evaluated from those of the two charge transfer steps, i.e.

$$\Delta G^\circ = \Delta G_{BC} - \Delta G_{AB} = -n_2 F E_2^\circ - (-n_1 F E_1^\circ) = -n_2 F (E_2^\circ - E_1^\circ) \quad (4.74)$$

Therefore, the equilibrium constant for the disproportionation reaction can subsequently be obtained via:

$$K_{\text{disp}} = \frac{k_{f, \text{disp}}}{k_{b, \text{disp}}} = e^{[-\Delta G^\circ / RT]} = e^{[n_2 F (E_2^\circ - E_1^\circ) / RT]} \quad (4.75)$$

As can be seen from equations 4.74 & 4.75, the relative magnitudes of the standard potentials of the two charge transfer steps e.g. E_1° & E_2° play a

determining role in the kinetics of the homogeneous redox reaction. Once again, we shall focus on one of the most common cases in which consecutive charge transfers are involved. In other words, E_2° is more positive than E_1° if both electrode processes are oxidation and *vice versa*.

Taking into account the effect of the above homogeneous redox reaction, the simultaneous differential equations describing a basic EE reaction can be modified by incorporating the following terms into the corresponding equations listed in *Table 4.3*:

$$k_{f, \text{disp}} C_B - k_{b, \text{disp}} C_A C_C, \quad -2(k_{f, \text{disp}} C_B + k_{b, \text{disp}} C_A C_C) \quad \& \quad k_{f, \text{disp}} C_B - k_{b, \text{disp}} C_A C_C$$

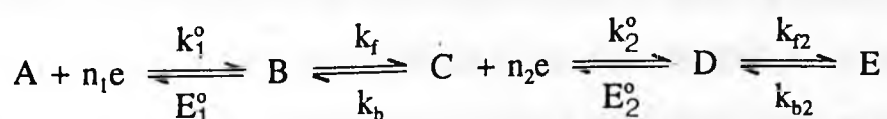
for species A, B & C respectively.

This will apparently cause some practical difficulties to the numerical solutions. However, after some operations by approximation, the numerical treatment for the modified differential equations can be arranged into similar style to that for the EE mechanism described previously. For example, the above mentioned additional terms can be estimated with the concentration arrays at the previous time step and then incorporated into various coefficients of *equation 4.61*. As a result, the expressions of gradients at the electrode surface end up with the same structures as those for the EE reaction (e.g. *equation 4.61*). Therefore, the surface concentrations and the rest of the concentration arrays as their consequences can be readily assessed. The ONLY difference is that several iterations are necessary if the disproportionation reaction is very fast and high precision is required.

4.7.2 Successive Electron Transfer Processes with Coupled Chemical Reaction(s) e.g. the ECE, ECE2 & ECEC Mechanisms

The EE mechanism is the simplest example of multistep charge transfer reactions. Frequently these involve such complications as homogeneous chemical reaction(s) between the two charge transfer steps. For example, there is a coupled chemical reaction between the two successive charge transfer steps in the ECE mechanism, while in the ECEC scheme each charge transfer step is followed by a homogeneous chemical reaction. Furthermore, homogeneous charge transfer reactions - i.e. disproportionation reaction - will bring further complexity to the development of numerical solutions. The ECEC mechanism will be taken as an example to illustrate the numerical solutions of these particularly complex reactions.

Details of the differential equations and initial & boundary conditions for the ECEC reaction are shown in *Tables 4.3 & 4.4*. A schematic illustration of an ECEC reaction can be given by:



where A, C are electroactive species, n_1 & n_2 the number of electrons involved in the successive charge transfer steps, k_1° & k_2° the corresponding standard rate constants of charge transfer, E_1° & E_2° the corresponding standard potentials. In addition, k_f , k_b , k_{f2} and k_{b2} are the forward and backward chemical rate constants of the two coupled homogeneous chemical reactions respectively. This full reaction scheme, rather than the simple case where ONLY irreversible chemical reactions are involved (i.e. k_b & k_{b2} are very small compared with k_f & k_{f2}), will be discussed in this section.

The digitisation of the differential equations describing an ECEC reaction

(cf. *Table 4.3*) can be achieved by the introduction of the standard Crank-Nicolson techniques:

$$C'_{A,i} - C_{A,i} = \frac{1}{2} \lambda (C'_{A,i-1} - 2C'_{A,i} + C'_{A,i+1} + C_{A,i-1} - 2C_{A,i} + C_{A,i+1}) \quad (4.76)$$

$$C'_{B,i} - C_{B,i} = \frac{1}{2} \lambda (C'_{B,i-1} - 2C'_{B,i} + C'_{B,i+1} + C_{B,i-1} - 2C_{B,i} + C_{B,i+1}) \\ - \frac{1}{2} k_f \delta t (C'_{B,i} + C_{B,i}) + \frac{1}{2} k_b \delta t (C'_{C,i} + C_{C,i}) \quad (4.77)$$

$$C'_{C,i} - C_{C,i} = \frac{1}{2} \lambda (C'_{C,i-1} - 2C'_{C,i} + C'_{C,i+1} + C_{C,i-1} - 2C_{C,i} + C_{C,i+1}) \\ + \frac{1}{2} k_f \delta t (C'_{B,i} + C_{B,i}) - \frac{1}{2} k_b \delta t (C'_{C,i} + C_{C,i}) \quad (4.78)$$

$$C'_{D,i} - C_{D,i} = \frac{1}{2} \lambda (C'_{D,i-1} - 2C'_{D,i} + C'_{D,i+1} + C_{D,i-1} - 2C_{D,i} + C_{D,i+1}) \\ - \frac{1}{2} k_{r2} \delta t (C'_{D,i} + C_{D,i}) + \frac{1}{2} k_{b2} \delta t (C'_{E,i} + C_{E,i}) \quad (4.79)$$

$$C'_{E,i} - C_{E,i} = \frac{1}{2} \lambda (C'_{E,i-1} - 2C'_{E,i} + C'_{E,i+1} + C_{E,i-1} - 2C_{E,i} + C_{E,i+1}) \\ + \frac{1}{2} k_{r2} \delta t (C'_{D,i} + C_{D,i}) - \frac{1}{2} k_{b2} \delta t (C'_{E,i} + C_{E,i}) \quad (4.80)$$

where the prime denotes the concentrations at the new time loop (i.e. unknown quantities) and i indicates the space mesh where the point is located ($i = 1$ to m , cf. *Figure 4.3*). As for the " $\delta x/2$ shift" method, the ONLY alteration which needs to be made is the digital formula for the diffusional terms at the first mesh point, which are defined by *equation 4.25* because the chemical kinetics is unaffected by the changes of sampling. Rearrangement of *equations 4.76-80* yields:

$$C'_{A,i-1} + a_A C'_{A,i} + C'_{A,i+1} = b_{A,i} \quad (i = 1, 2, \dots, m) \quad (4.76a)$$

$$C'_{B,i-1} + a_B C'_{B,i} + C'_{B,i+1} = b_{B,i} + p_B C'_{C,i} \quad (i = 1, 2, \dots, m) \quad (4.77a)$$

$$C'_{C,i-1} + a_C C'_{C,i} + C'_{C,i+1} = b_{C,i} + p_C C'_{B,i} \quad (i = 1, 2, \dots, m) \quad (4.78a)$$

$$C'_{D,i-1} + a_D C'_{D,i} + C'_{D,i+1} = b_{D,i} + p_D C'_{E,i} \quad (i = 1, 2, \dots, m) \quad (4.79a)$$

$$C'_{E,i-1} + a_E C'_{E,i} + C'_{E,i+1} = b_{E,i} + p_E C'_{D,i} \quad (i = 1, 2, \dots, m) \quad (4.80a)$$

where $a_A, a_B, a_C, a_D, a_E, b_A, b_B, b_C, b_D, b_E, p_B, p_C, p_D$ & p_E are known coefficients

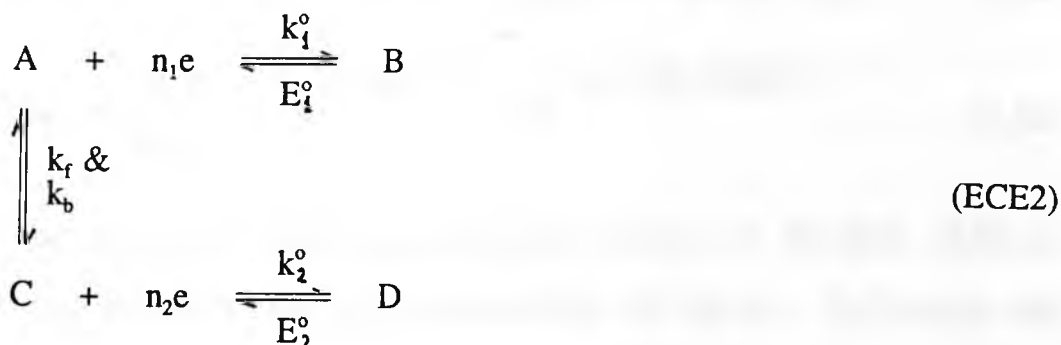
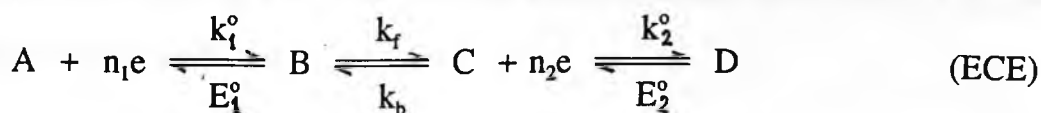
defined by:

$$\begin{aligned}
 a_A &= -2(\lambda_A + 1)/\lambda_B, \quad b_{A,i} = -C_{A,i-1} + 2(\lambda_A - 1)C_{A,i}/\lambda_A - C_{A,i+1} \\
 a_B &= -(2\lambda_B + 2 + k_f \delta t)/\lambda_B, \quad p_B = -k_b \delta t/\lambda_B \quad \& \\
 b_{B,i} &= -C_{B,i-1} + (2\lambda_B - 2 + k_f \delta t)C_{B,i}/\lambda_B - C_{B,i+1} - k_b \delta t C_{C,i}/\lambda_B \\
 a_C &= -(2\lambda_C + 2 + k_b \delta t)/\lambda_C, \quad p_C = -k_f \delta t/\lambda_C \quad \& \\
 b_{C,i} &= -C_{C,i-1} + (2\lambda_C - 2 + k_b \delta t)C_{C,i}/\lambda_C - C_{C,i+1} - k_f \delta t C_{B,i}/\lambda_C \\
 a_D &= -(2\lambda_D + 2 + k_{f2} \delta t)/\lambda_D, \quad p_D = -k_{b2} \delta t/\lambda_D \quad \& \\
 b_{D,i} &= -C_{D,i-1} + (2\lambda_D - 2 + k_{f2} \delta t)C_{D,i}/\lambda_D - C_{D,i+1} - k_{b2} \delta t C_{E,i}/\lambda_D \\
 a_E &= -(2\lambda_E + 2 + k_{b2} \delta t)/\lambda_E, \quad p_E = -k_{f2} \delta t/\lambda_E \quad \& \\
 b_{E,i} &= -C_{E,i-1} + (2\lambda_E - 2 + k_{b2} \delta t)C_{E,i}/\lambda_E - C_{E,i+1} - k_{f2} \delta t C_{D,i}/\lambda_E
 \end{aligned}$$

Generally, the numerical treatment of *equations 4.76a-80a* is very similar to that for the EC mechanism (*eqns. 4.55, 4.58 & 4.59*) discussed in *section 4.6*. It is worth mentioning that special care must be taken in handling the boundary conditions because in both the ECEC & the ECE mechanism there are two charge transfer steps involved in the OVERALL reaction scheme, and each charge transfer step has its particular boundary conditions (*cf. Table 4.4*) which need to be satisfied. Similar to the EE reaction, the faradaic current resulting from an ECEC or ECE reaction also consists of two fractions reflecting the two individual charge transfer steps.

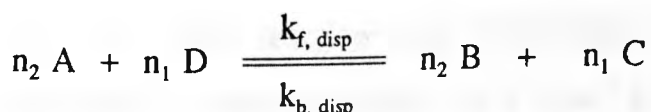
The above treatment also applies to the ECE & ECE2 mechanisms by making some particular modifications. In fact, if we set both the forward and backward rate constants of the second homogeneous chemical reactions, i.e. k_{f2} & k_{b2} , to zero, the ECEC scheme reduces exactly to the ECE mechanism. The two charge transfer steps are successive processes in the ECE & ECEC mechanisms. The ECE2 reaction, on the other hand, consists of two separate electron transfer steps, with the initial electroactive species of both charge transfer steps being chemically coupled. Due to the differences in reaction

routes, the electrochemical performance of the ECE and ECE2 mechanisms is considerably different. However, from the point of view of digital simulation, the ECE2 reaction scheme can be considered as a special case of the ECE mechanism:

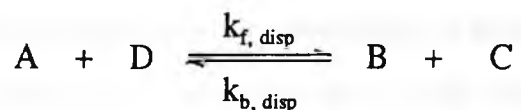


In digital simulation, the main difference between the ECE & ECE2 mechanisms in handling the initial & boundary conditions is that there is usually ONE starting species (A) in the former while there are TWO chemically interacting electroactive species (A & C) initially present in solution in the latter.

Similar to the EE mechanism, the ECE, ECEC & ECE2 mechanisms are also frequently accompanied by a homogeneous redox (disproportionation) reaction. The reduction of the uranyl cation at a mercury electrode in strongly acidified perchlorate media [223] and 4-methylcatechol [224] are examples. The homogeneous redox reaction can generally be described as follows:



It is quite useful to simplify the problem by making some assumptions e.g. $n_1 = n_2$. In this case the disproportionation reaction becomes a second-order reaction and has the pathway:



The free energy change and thus the equilibrium constant of the above reaction can readily be evaluated from the thermodynamic parameters of the two charge transfer steps, i.e.

$$\Delta G^\circ = \Delta G_{CD} - \Delta G_{AB} = -n_2 F E_2^\circ - (-n_1 F E_1^\circ) = -n_2 F (E_2^\circ - E_1^\circ) \quad (4.81)$$

$$K_{\text{disp}} = \frac{k_{f, \text{disp}}}{k_{b, \text{disp}}} = e^{[-\Delta G^\circ/RT]} = e^{[n_2 F (E_2^\circ - E_1^\circ)/RT]} \quad (4.82)$$

The treatment of the disproportionation reaction in the ECE, ECE2 & ECEC mechanisms is very similar to that for the EE reaction. For example, the following kinetic term

$$k_{f, \text{disp}} C_A C_D - k_{b, \text{disp}} C_B C_C,$$

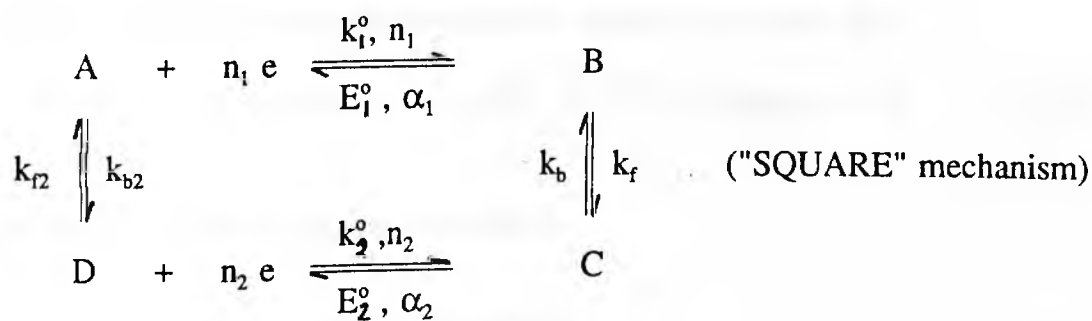
is accordingly added on or subtracted from the basic simultaneous differential diffusional equations listed in *Table 4.3*, and subsequently incorporated into the corresponding digital formula by approximation.

4.7.3 The "SQUARE" Mechanism - Four Sided Reaction

The four-sided reaction (the "SQUARE" mechanism) is a complex electrochemical process, especially as a cross reaction (homogeneous redox reaction) is thermodynamically favoured. Generally, most examples of this type of reaction scheme are associated with the electrochemical study of certain organic & organometallic complex compounds. One of the main chemical

characteristics of these compounds is that they or the product electrochemically or chemically converted from them are able to undergo isomerisation or protonation reactions. Typical examples are group VI carbonyl complexes [225-7] of the general formula $cis-[M(CO)_2(DPM)_2]^{0,+2+}$, $cis-[M(CO)_2(DPE)_2]^{0,+2+}$ ($M = Cr, Mo, W$; $DPM = 1,2$ -bis(diphenylphosphino)methane; $DPE = 1,2$ -bis(diphenylphosphino) ethane) & $fac-[M(CO)_3P_3]$ ($M = Cr, Mo$; $P = P(OPh)_3, P(OMe)_2Ph, PMe_2Ph, P(OMe)_3$), and quinone Q [228]. The isomers of the *cis*-series complexes are the corresponding *trans*- complexes while those of the *fac*-complexes are the *mer*- ones. As far as quinone (Q) is concerned, it can readily combine a proton (H^+) from a proton-donor (e.g. acid media) in the solution to form hydroquinone ions HQ^+ .

Generally, by incorporating all the kinetic parameters describing the heterogeneous & homogeneous processes, the "SQUARE" mechanism can be packed as a closed cycle:



where n_1 & n_2 are the number of electrons involved in the successive charge transfer steps, k_1° & k_2° the corresponding standard rate constants of charge transfer, E_1° & E_2° the corresponding standard potentials, and α_1 & α_2 the charge transfer (symmetrical) coefficients. In addition, k_f , k_b , k_{f2} and k_{b2} are the forward and backward chemical rate constants of the two coupled homogeneous chemical reactions respectively.

Obviously, the above model is simplified for clarity of describing the reaction pathways and the ease of numerical treatment in digital simulation. In

practice, it encompasses many variations depending on the thermodynamic properties, e.g. chemical rate constants and standard potentials, of the corresponding chemical or charge transfer steps.

The above reaction pathway is thermodynamically favoured ONLY if the following *provisos* are satisfied:

$$(1) \quad n_1 = n_2;$$

(2) The standard free energy change of the ENTIRE reaction pathways is ZERO, i.e. the SUM of the standard free energy changes of the four constituent reactions MUST be zero.

The standard free energy change of the reaction cycle can be obtained by summing up the free energy changes of the four constituent reactions, i.e.

$$\begin{aligned} \Delta G^\circ &= \Delta G_1^\circ + \Delta G_2^\circ + \Delta G_3^\circ + \Delta G_4^\circ \\ &= -n_1 FE_1^\circ - RT \ln(k_f/k_b) - n_2 FE_2^\circ - RT \ln(k_{f2}/k_{b2}) \end{aligned}$$

Implementation of the second requirement stated above leads to:

$$n_1 FE_1^\circ + RT \ln(k_f/k_b) + n_2 FE_2^\circ + RT \ln(k_{f2}/k_{b2}) = 0 \quad (4.83)$$

Rearranging the above equation, we have:

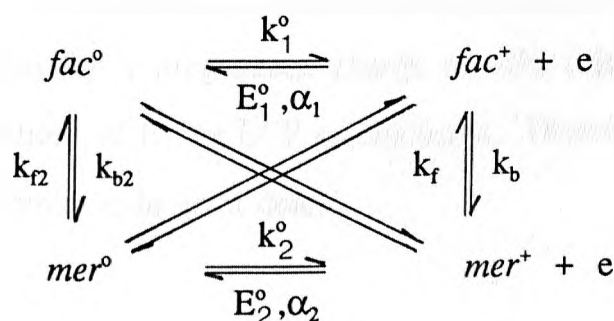
$$\frac{k_{f2}}{k_{b2}} = \frac{k_b}{k_f} e^{[n_2 F(E_2^\circ - E_1^\circ)/RT]} \quad (4.84)$$

This implies that ONE of the thermodynamic or kinetic parameters of the "SQUARE" mechanism is always determined by the rest via equation 4.84. That is to say, in digital simulation, ONE of the parameters MUST be adjusted automatically via equation 4.84 when any of the rest of the related parameters is altered by manual entry.

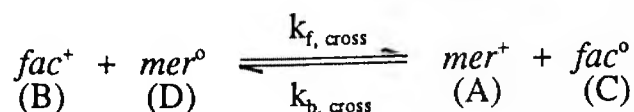
As can be seen from *Tables 4.3 & 4.4*, the simultaneous differential

equations describing the four sided reactions are very similar to that for ECE & ECEC schemes. They can, therefore, be treated in a similar fashion, provided the particular initial & boundary conditions associated with the "SQUARE" reaction are taken into account during numerical treatment.

As already mentioned, a cross reaction (homogeneous redox reaction) is frequently thermodynamically favoured if the "SQUARE" mechanism is feasible. For example, in the electrochemical reduction of *fac*-[M(CO)₃P₃] (M=Cr, Mo; P=P(OPh)₃, P(OMe)₂Ph, PMe₂Ph, P(OMe)₃), the following scheme is proposed to explain reasonably the rather complex electrochemical behaviour [227]:



where *fac* & *mer* represent the corresponding facial & meridional isomers, and the cross represents the following redox reaction:



with $k_{f, \text{cross}}$ & $k_{b, \text{cross}}$ being the forward and backward second order homogeneous rate constants.

Detailed analysis, e.g. electrochemical measurements, thermodynamic calculations and NMR (¹³P & ¹³C) and ESR spectroscopic determination of intermediates, gives strong support to the above proposal.

The equilibrium constant of the above cross redox reaction can be evaluated either by assessing the free energy change or simply by making use of the kinetics of the two homogeneous chemical kinetics of the "SQUARE":

$$K_{\text{cross}} = \frac{k_{f, \text{cross}}}{k_{b, \text{cross}}} = \frac{[A][C]}{[B][D]} = \frac{[A]}{[D]} \frac{[C]}{[B]} = K_{\text{AD}} K_{\text{BC}}$$

Substituting K_{AB} by *equation 4.84* and rearranging the above equation leads to the expression of K_{AB} as a function of the standard potentials of the two charge transfer steps:

$$K_{\text{cross}} = \frac{k_{f, \text{cross}}}{k_{b, \text{cross}}} = e^{[n_2 F(E_2^\circ - E_1^\circ)/RT]} \quad (4.85)$$

The numerical treatment of the above cross redox reaction is very similar to that for homogeneous charge transfer (disproportionation) reaction in the variations of EE or ECE mechanisms. Therefore, it is not intended to discuss this problem in great detail.

4.8 Assessment of Results

Based on the above described theoretical development, software has been composed for digital simulation of electrochemical data e.g. the current/potential/time responses. This includes provision for a large variety of electrochemical mechanisms & for the techniques of linear sweep cyclic voltammetry, chronoamperometry & chronopotentiometry (single or double steps). The accuracy of simulations has been checked wherever possible using literature tabulations. Below we shall firstly discuss the quantitative & qualitative analysis of the simulated data using existing theories¹, analytical & numerical techniques e.g. convolution (available from EG&G). At the same time, considerable attention will be directed towards the development of techniques for the assessment of complex systems e.g. the EC catalytic reaction (unequal diffusion coefficients for the oxidised & reduced species).

4.8.1 Convolution Transform of Current

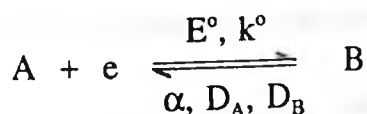
Over the past several decades, convolution techniques have found wide applications in assessing electrochemical data [229-235]. Amongst various electrochemical techniques, cyclic voltammetry is probably the most favourable method for studying the electrochemical properties of complex systems e.g. coupled homogeneous chemical kinetics & successive electron transfers. Therefore, discussions in this section are generally confined to cyclic voltammetry though in certain degrees they also apply to other techniques e.g.

¹ These will be mentioned briefly wherever used. For more detail three standard text books are recommended for consultation. These include 1) A.J. Bard & L.R. Faulkner, "Electrochemical Methods", John Wiley & Sons; 2) Southampton Electrochemistry Group, "Instrumental Methods in Electrochemistry", John Wiley & Sons; 3) J.O'M Bockris & A.K.N. Reddy, "Modern Electrochemistry", Plenum Press.

chronoamperometry.

Traditionally, the interpretation (mechanistic or estimation of parameters) of cyclic voltammograms is ultimately based on the analysis of several particular features e.g. the magnitude & position of various current peaks & their variations with sweep rate & concentrations etc.. In some simple circumstances (Nernstian case, for example), the above treatment might be able to provide satisfactory explanations. However, this fails to analyze effectively the electrochemical behaviour of complex systems mainly because of the fact that information of much greater importance, e.g. the shapes of the voltammograms has, not been used. As an alternative, a proper mathematical treatment, namely the convolution or semi-integral technique, has been proposed to transform the current to simpler functional forms which are frequently much more convenient for data analysis [229-235]. The basic principles of the convolution technique is stated below.

Considering a simple electron transfer reaction e.g.



under the conditions of semi-infinite linear diffusion (e.g. planar electrode), the solution (via Laplace transformation, back Laplace transformation followed by convolution theorem) of the diffusion equations (eqn. 4.3) yields for any electrochemical technique the following expression for the surface concentrations of species A & B [213]:

$$C_A(t) = C_A^{\text{BULK}} - \frac{1}{(z_B - z_A)FA\sqrt{D_A}} \left[\frac{1}{\sqrt{\pi}} \int_0^t \frac{i(u)}{\sqrt{(t-u)}} du \right] \quad (4.86)$$

$$C_B(t) = C_B^{\text{BULK}} + \frac{1}{(z_B - z_A)FA\sqrt{D_B}} \left[\frac{1}{\sqrt{\pi}} \int_0^t \frac{i(u)}{\sqrt{(t-u)}} du \right] \quad (4.87)$$

is
If ONLY species A initially present in the solution, equation 4.87 reduces to:

$$C_B(t) = \frac{1}{(z_B - z_A)FA\sqrt{D_A}} \left[\frac{1}{\sqrt{\pi}} \int_0^t \frac{i(u)}{\sqrt{(t-u)}} du \right] \quad (4.87a)$$

The common term (inside the square brackets) of the above expressions is generally defined as the *convoluted current* $I_1(t)$:

$$I_1(t) = \frac{1}{\sqrt{\pi}} \int_0^t \frac{i(u)}{\sqrt{(t-u)}} du \quad (4.88)$$

Substituting the above expression into *equations 4.86 & 4.87*, the surface concentrations can be written in terms of the convoluted current $I_1(t)$:

$$C_A^{\circ}(t) = C_A^{\text{BULK}} - I_1(t) / [(z_B - z_A) FA\sqrt{D_A}] \quad (4.86a)$$

$$C_B^{\circ}(t) = C_B^{\text{BULK}} + I_1(t) / [(z_B - z_A) FA\sqrt{D_B}] \quad (4.87b)$$

Obviously, the convoluted current reaches its limiting values I_A^{lim} & I_B^{lim} when the surface concentration of species A or B becomes zero:

$$I_A^{\text{lim}} = (z_B - z_A) FA\sqrt{D_A} C_A^{\text{BULK}} \quad \& \quad I_B^{\text{lim}} = (z_A - z_B) FA\sqrt{D_B} C_B^{\text{BULK}} \quad (4.89)$$

This implies that the diffusion coefficient of both species can be readily obtained by evaluation of the limiting values of the convoluted current (corresponding to plateaux on the I_1 - potential curve).

Substituting the surface concentrations of the electroactive species into the *current-overpotential* relationship (*eqn. 4.31, cf. Section 4.5.1*), the resulting faradaic current can be expressed as a function of the I_1 convolution:

$$i = (z_B - z_A)FAk^{\circ} \left[C_A^{\text{BULK}} e^{-\alpha p} - \frac{I_1 e^{-\alpha p}}{(z_B - z_A)FA\sqrt{D_A}} - C_B^{\text{BULK}} e^{(1-\alpha)p} - \frac{I_1 e^{(1-\alpha)p}}{(z_B - z_A)FA\sqrt{D_B}} \right] \quad (4.90)$$

or in terms of the limiting values of convolution:

$$i = (I_A^{\text{lim}} - I_1) \frac{k^0 e^{-\alpha p}}{\sqrt{D_A}} + (I_B^{\text{lim}} - I_1) \frac{k^0 e^{(1-\alpha)p}}{\sqrt{D_B}} \quad (4.90a)$$

It is worth mentioning that no assumptions have been made for derivation of *equations 4.86-90a*. Therefore, these equations hold for any electron transfer rate & any forms of perturbation so far as the experiments are carried out under the above stated conditions i.e. semi-finite linear diffusion. We shall see later that variations of these equations under some particular circumstances can be used extensively for the determination of various electrochemical parameters.

In practice, it is impossible to calculate the exact values of $I_1(t)$ from *equation 4.88*. Instead, the function $I_1(t)$ is evaluated numerically using e.g. the closed Newton-Cotes formulas (the Trapezoidal & Simpson's rules) for equally-spaced abscissas (the time axes is divided into N equal intervals of Δt , cf. *Figure 4.11*). This can be done by direct numerical solution of *equation 4.88* or by using special algorithms e.g. the Gamma function ($\Gamma(x)$):

$$I_1(k\Delta t) = \frac{1}{\sqrt{\pi}} \sum_{j=1}^{j=k} \frac{i(j\Delta t - 1/2\Delta t) \sqrt{\Delta t}}{\sqrt{k - j + 1/2}} \quad (4.91)$$

$$I_1(k\Delta t) = \frac{1}{\sqrt{\pi}} \sum_{j=1}^{j=k} \frac{\Gamma(k - j + 1/2)}{(k - j)!} \sqrt{\Delta t} \cdot i(j\Delta t) \quad (4.92)$$

where j represents the integration index i.e. $j=u/\Delta t$. The above equations give the approximate value of I_1 at time $t=k\Delta t$ (k ranges from 0 to N).

Generally, as far as computational speed is concerned, the second algorithm is relatively faster than the first one. However, it is found that the second algorithm converges much slower in situations where the current data at the beginning is very important (e.g. CA data). For example, in the first method the convolution of the Cottrell behaviour $f(t) = at^{-1/2}$ in chronoamperometry reaches a "plateau" much faster than the Gamma function method (cf. *Figure 4.12*). In

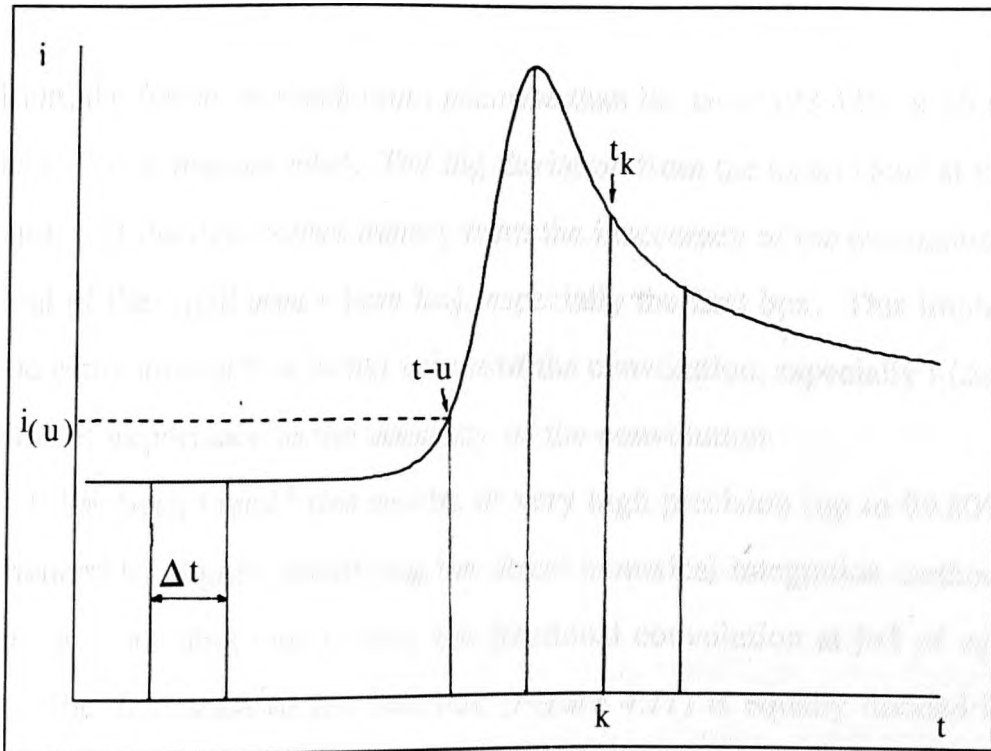


Figure 4.11 Schematic illustration for the numerical calculation of the convolution integral I_1

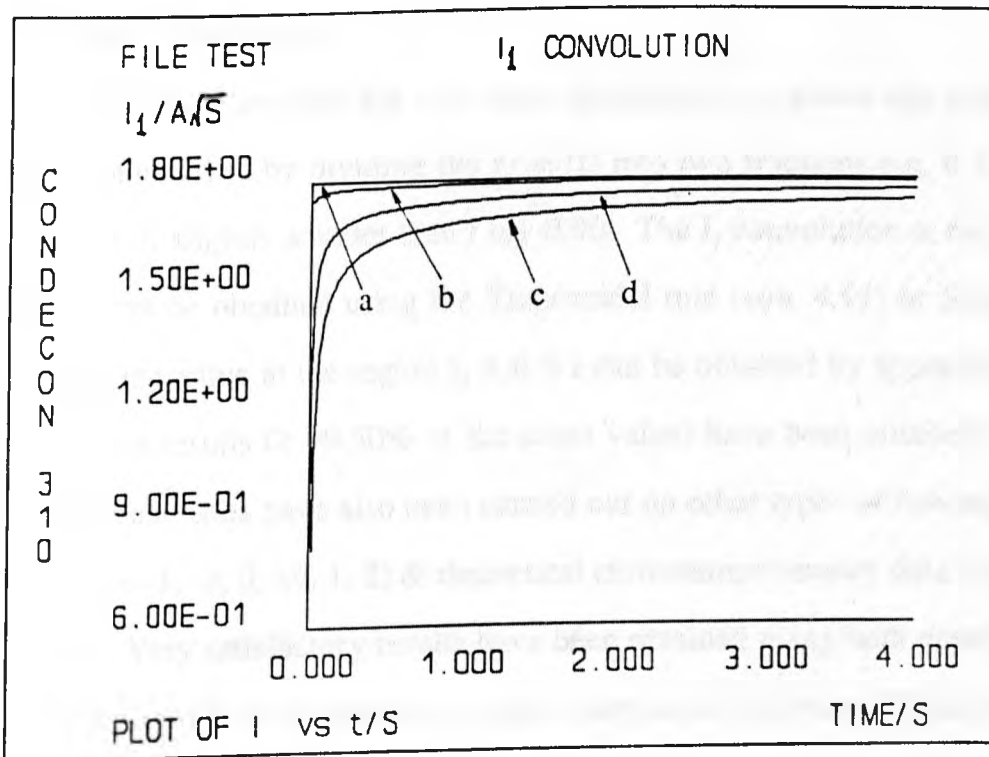


Figure 4.12 Comparison of values of the I_1 convolution obtained using various numerical methods with theoretical values (exact)
 (a) true value (b) eqn 4.92 (modified) (c) Γ -function
 (d) eqn 4.92

addition, the former is much more accurate than the latter (98.42% & 96.80% of the exact value respectively). The big deviation from the exact value at the very beginning of the data comes mainly from the inaccuracy of the evaluation of the integral of the small area where $k=j$, especially the first box. This implies that a good estimation of few initial values of the convolution, especially $I_1(\Delta t)$, is of significant importance to the accuracy of the convolution.

It has been found² that results of very high precision (up to 99.80%) can be obtained by slightly modifying the direct numerical integration method (*eqn. 4.91*) e.g. evaluating individually the fractional convolution at $j=1$ of *equation 4.91*. The time scale of the first box (*Figure 4.11*) is equally divided into M ($=100$) small intervals $\Delta t_1 = \Delta t/M$ & the current (i) corresponding to each small time interval is estimated by a polynomial extrapolation method based on the current of the first 11 points on the "macro" scale. The fractional convolution at $j=1$ is subsequently evaluated (similar to *equation 4.91*) using the above data on the "micro" time scale.

An analytical method has also been developed to improve the evaluation of the I_1 convolution by dividing the time (t) into two fractions e.g. $0 \leq u \leq t_1$ & $t_1 \leq u \leq t$ (t_1 slightly smaller than t say $0.9t$). The I_1 convolution at the region $0 \leq u \leq t_1$ can be obtained using the Trapezoidal rule (*eqn. 4.91*) or Simpson's rule, whilst the value at the region $t_1 \leq u \leq t$ can be obtained by approximation. Very accurate results ($\geq 99.50\%$ of the exact value) have been obtained.

The above tests have also been carried out on other types of functions e.g. $f(t) = at^n$ ($n = -1, -2, 0, 1/2, 1, 2$) & theoretical chronoamperometry data (digitally simulated). Very satisfactory results have been obtained using both approaches.

Generally, the first approach is more convenient for computation & more

² Acknowledgement is due to Dr. T. Boddington for discussions and help with some of the mathematical development.

accurate. However, it is common in CA experiments that the data at the very beginning are always distorted by the charging of the double layer capacitance. In this situation, there is considerable limitation to the accuracy of the first approach (though still more accurate than the conventional methods e.g. eqns. 4.91 & 4.92), because the correction of the I_1 fraction at the first box is limited. The accuracy of the second approach is not severely affected, however.

4.8.2 Analysis of Simulated Data for Cyclic Voltammetry

Cyclic voltammetry is probably the most commonly used technique in studying electrode process especially complex reaction mechanisms. It is obvious that electrochemical responses resulting from different systems may differ considerably from each other depending on the nature of both the electron transfer & the homogeneous chemical kinetics. This in turns requires different techniques to be used for the quantitative and/or qualitative analysis of various electrochemical systems. In this section, we shall mainly discuss the analysis of cyclic voltammograms simulated for several electrochemical mechanisms e.g. E, EC, CE, CEC, EC catalytic, EE, ECE & the "SQUARE" reactions, using the convolution & allied techniques.

4.8.2.1 Simple Electron Transfer Reactions

As already discussed, the faradaic current resulting from a simple charge transfer reaction can be expressed as a function of the I_1 convolution by rearranging the *current-overpotential* relationship (eqn. 4.31):

$$i = (I_A^{\text{lim}} - I_1) \frac{k^0 e^{-\alpha p}}{D_A^{1/2}} + (I_B^{\text{lim}} - I_1) \frac{k^0 e^{(1-\alpha)p}}{D_B^{1/2}} \quad (4.90a)$$

Rearrangement of the above equation yields:

$$i = I_A^{\text{lim}} \frac{k^\circ e^{-\alpha p}}{D_A^{1/2}} + I_B^{\text{lim}} \frac{k^\circ e^{(1-\alpha)p}}{D_B^{1/2}} - I_1 k^\circ \left[\frac{e^{-\alpha p}}{D_A^{1/2}} + \frac{e^{(1-\alpha)p}}{D_B^{1/2}} \right] \quad (4.93)$$

The above equation serves as an alternative for the current-overpotential equation which applies to systems of any electron transfer rate.

As mentioned previously, heterogeneous charge transfer reactions can be categorised into three sub-groups e.g. the Nernstian (reversible, k° large), quasi-reversible (ET moderate fast, $k^\circ \geq 5 \times 10^{-6} \text{ m} \cdot \text{s}^{-1}$) & irreversible (slow ET, k° small) electron transfer reaction, depending on the standard heterogeneous rate constant k° . Below we shall discuss the ramifications of the above equation (eqn. 4.93) under these various specific circumstances.

4.8.2.1.1 The Nernstian i.e. Reversible Electron Transfer Reactions

One of the major characteristics of a Nernstian reaction is that the heterogeneous charge transfer step is so fast ($k^\circ \longrightarrow \infty$) that the system is forced to maintain equilibrium at the electrode & the pace of the entire process is virtually controlled by the transport of electroactive species to & from the electrode/electrolyte interface.

Traditionally, the analysis of cyclic voltammograms is ultimately based on the positions & heights of the current peaks & their variations with the sweep rate. *Figure 4.13* shows the simulated cyclic voltammograms of a Nernstian reaction under sweep rates (v) 0.1, 1.0, 5.0 & 10.0 V/s. As can be seen, the peak positions do not change with the sweep rate, & the linearity of dependence of peak current on square root of the sweep rate $v^{1/2}$ is well illustrated in *Figure 4.14*. Therefore, the two important diagnoses of the Nernstian type reactions are

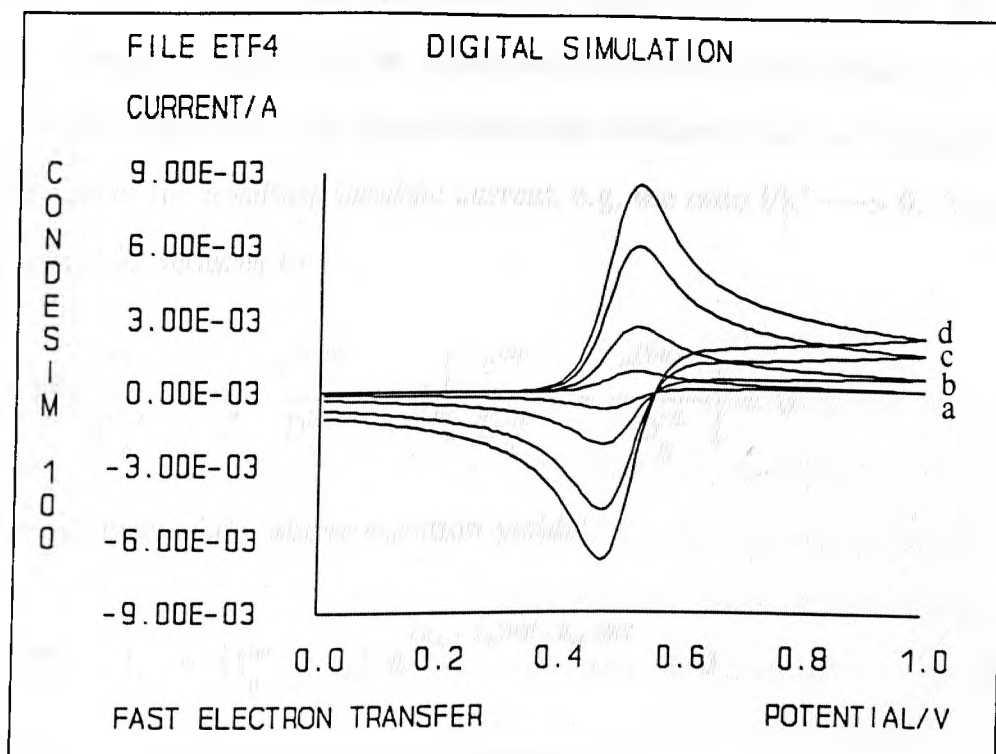


Figure 4.13 Cyclic voltammograms for a Nernstian reaction under the sweep rates (Vs^{-1}) of: (a) 0.1 (b) 1 (c) 5 (d) 10

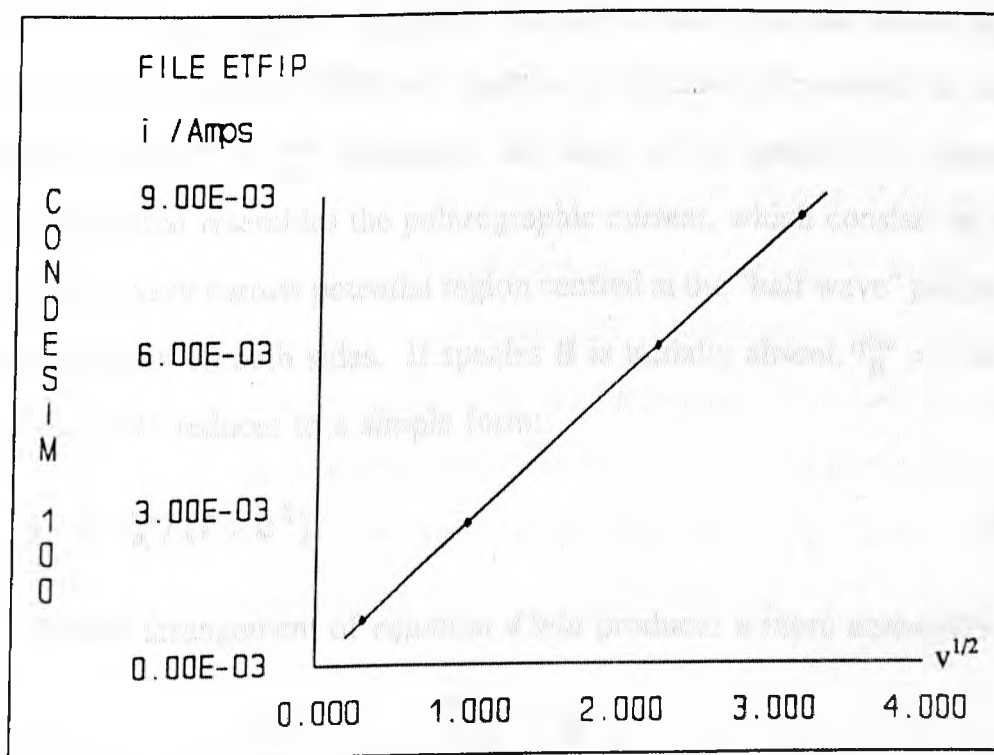


Figure 4.14 A plot of the dependence of the peak current i_p on the square root of the sweep rate $v^{1/2}$

satisfied. However, this does not provide a TEST for the entire data. Below we shall discuss the analysis of the simulated data via the convolution technique.

In the Nernstian case, the standard rate constant k° is much larger than the magnitude of the resulting faradaic current, e.g. the ratio $i/k^\circ \rightarrow 0$. Therefore, *equation 4.93* reduces to:

$$I_A^{\text{lim}} \frac{e^{-\alpha p}}{D_A^{1/2}} + I_B^{\text{lim}} \frac{e^{(1-\alpha)p}}{D_B^{1/2}} - I_1 \left[\frac{e^{-\alpha p}}{D_A^{1/2}} + \frac{e^{(1-\alpha)p}}{D_B^{1/2}} \right] = 0 \quad (4.94)$$

Rearrangement of the above equation yields:

$$I_A^{\text{lim}} - I_1 + (I_B^{\text{lim}} - I_1) e^{(z_A - z_B)F(E - E_{1/2})/RT} = 0 \quad (4.94a)$$

Isolate I_1 from the above equation, we have:

$$I_1 = \frac{I_A^{\text{lim}} + I_B^{\text{lim}} e^\xi}{1 + e^\xi} \quad (4.94b)$$

where $\xi = (z_A - z_B)F(E - E_{1/2})/RT$. As can be seen from the above equation, I_1 convolution should OVERLAY itself as a function of potential & take the values between I_A^{lim} & I_B^{lim} . Basically, the shape of the graph of I_1 convolution against potential resembles the polarographic current, which consists of a sharp rise within a very narrow potential region centred at the "half wave" potential $E_{1/2}$ & two plateaux on both sides. If species B is initially absent, $I_B^{\text{lim}} = 0$ & hence *equation 4.94b* reduces to a simple form:

$$I_1 = I_A^{\text{lim}} / (1 + e^\xi) \quad (4.94c)$$

Further arrangement of *equation 4.94a* produces a more convenient form

$$E = E_{1/2} + \frac{RT}{(z_A - z_B)F} \text{Ln} \left[\frac{I_A^{\text{lim}} - I_1}{I_1 - I_B^{\text{lim}}} \right] \quad (4.95)$$

If species B is initially absent in the electrolyte e.g. $I_B^{\text{lim}} \rightarrow 0$, the above equation (eqn. 4.95) reduces to the classic POLAROGRAPHIC RELATIONSHIP type of expression, with I_1 substituted for the polarographic current:

$$E = E_{1/2} + \frac{RT}{(z_A - z_B)F} \text{Ln} \left[\frac{I_A^{\text{lim}} - I_1}{I_1} \right] \quad (4.95a)$$

The above relationship presents a critical test for the Nernstian reaction, & parameters e.g. the "half-wave" potential $E_{1/2}$ & number of electrons ($z_A - z_B$) can be immediately evaluated by plotting $\text{Ln} [(I_A^{\text{lim}} - I_1)/I_1]$ against the potential.

Differentiation of equation 4.94b against time t & subsequential rearrangement yields dI_1/dt or the deconvolution of the current:

$$\frac{dI_1}{dt} = \frac{(z_B - z_A)F}{RT} \frac{dE}{dt} \left(I_A^{\text{lim}} - I_B^{\text{lim}} \right) \frac{e^\xi}{(1 + e^\xi)^2} \quad (4.96)$$

If species B initially absent, $I_B^{\text{lim}} = 0$ & hence equations 4.96 reduces to

$$\frac{dI_1}{dt} = \frac{(z_B - z_A)F}{RT} \frac{dE}{dt} I_A^{\text{lim}} \frac{e^\xi}{(1 + e^\xi)^2} \quad (4.96a)$$

The above relationship shows another important feature of the Nernstian type electron transfer process. By plotting dI_1/dt versus the potential E for a triangular waveform, the plot should be strictly symmetrical about the E axis & the peaks should be centred at precisely the "half wave" potential $E_{1/2}$ (i.e. $\xi = 0$). The width of the peaks is related to the number of electrons (*see later developments for use of the function dI_1/dE*), whilst the peak height is proportional to the sweep rate & limiting convolution via:

$$\left[\frac{dI_1}{dt} \right]_{\text{max}} = \frac{(z_B - z_A)F}{4 RT} \frac{dE}{dt} I_A^{\text{lim}} \quad (4.96b)$$

An alternative of the dI_1/dt vs E plot is frequently used by introducing the term dI_1/dE via $E = E_{\text{initial}} + v t$ to yield:

$$\frac{dI_1}{dE} = \frac{(z_B - z_A)F}{RT} I_A^{\text{lim}} \frac{e^{\xi}}{(1 + e^{\xi})^2} \quad (4.97)$$

This plot overlays itself as a function of potential but without the symmetry about the E axis as observed in the dI_1/dt vs E plot. In practice, it is more useful to introduce an intermediate or rationalised term (for convenience, this term is also referred to as dI_1/dE) by dividing *equation 4.96a* with the sweep rate ($v = |dE/dt|$) such that the results of any sweep rate overlay while the characteristic doubly symmetrical peaks are preserved. Similarly, the peak height is proportional to the limiting convolution via:

$$\left[\frac{dI_1}{dE} \right]_{\text{max}} = \frac{(z_B - z_A)F}{4 RT} I_A^{\text{lim}} \quad (4.97a)$$

As mentioned previously, in a Nernstian reaction, the width of the peaks of either dI_1/dt vs. E or dI_1/dE vs. E plot is related to the number of electrons involved in the electrode process. Below the peak shaped function dI_1/dE is taken as an example to demonstrate the development of an EXACT expression for the 'HALF WIDTH'³ of the peak. Combination of *equations 4.97a & 4.97* & noting that $dI_1/dE = [dI_1/dE]_{\text{max}}/2$ in this particular situation, we have:

$$\frac{e^{\xi}}{(1 + e^{\xi})^2} = 1/8 \quad (4.98)$$

Solution of the above gives:

³ This term is traditionally linked to the *differential pulse & normal pulse polarography* techniques & AC voltammetry. It is the difference between potentials, which correspond to HALF of the peak height, on EACH side of the peak.

$$e^{\xi} = 3 \pm 2\sqrt{2} = (\sqrt{2} \pm 1)^2 \quad (4.98a)$$

or

$$\xi = 2 \operatorname{Ln}(\sqrt{2} \pm 1) \quad (4.98b)$$

Thus the 'HALF WIDTH' can be finally obtained:

$$|\Delta E| = \frac{RT}{|(z_A - z_B)| F} |\Delta \xi| = \frac{RT}{|(z_A - z_B)| F} \left[2 \operatorname{Ln} \frac{\sqrt{2} + 1}{\sqrt{2} - 1} \right] \quad (4.98c)$$

At 298.15K, $|\Delta E| = 90.58/|(z_A - z_B)|$ mV for a Nernstian reaction.

Figures 4.15, 4.16 & 4.17 illustrate various tests, using the above analytical developments, for the simulated cyclic voltammograms for a Nernstian reaction with ONLY species A initially present. In Figure 4.15 the characteristic "polarographic" behaviour of the I_1 convolution as a function of potential is evident. The diffusion coefficient of species A (D_A) calculated from the limiting value of the convolution is $1.0001 \times 10^{-8} \text{ m}^2 \text{ s}^{-1}$ as compared with $1.0000 \times 10^{-8} \text{ m}^2 \text{ s}^{-1}$ in the entry for the simulation. The differentiated (dI_1/dE , cf. eqn. 4.98) & logarithmic forms (eqn. 4.95a) are shown in Figures 4.16 & 4.17, respectively. The symmetrical behaviour of the dI_1/dE vs E plot is evident & the centre of the peaks gives a "half wave" potential $E_{1/2}$ of 0.5002 V which is very close to the theoretical value of 0.5V. On the other hand, the overlay of the logarithmic plot gives further solid evidence of the accuracy of the simulation. The slope of the 'log' plot for 298.15K using the unweighed least square method is -38.9299 compared with a calculated value of -38.9217 for $n = 1$. While the intercept on the E axis gives $E_{1/2}$ as 0.49973V. Additionally, the overlay of results of different sweep rate provides a comprehensive test of the simulation technique.

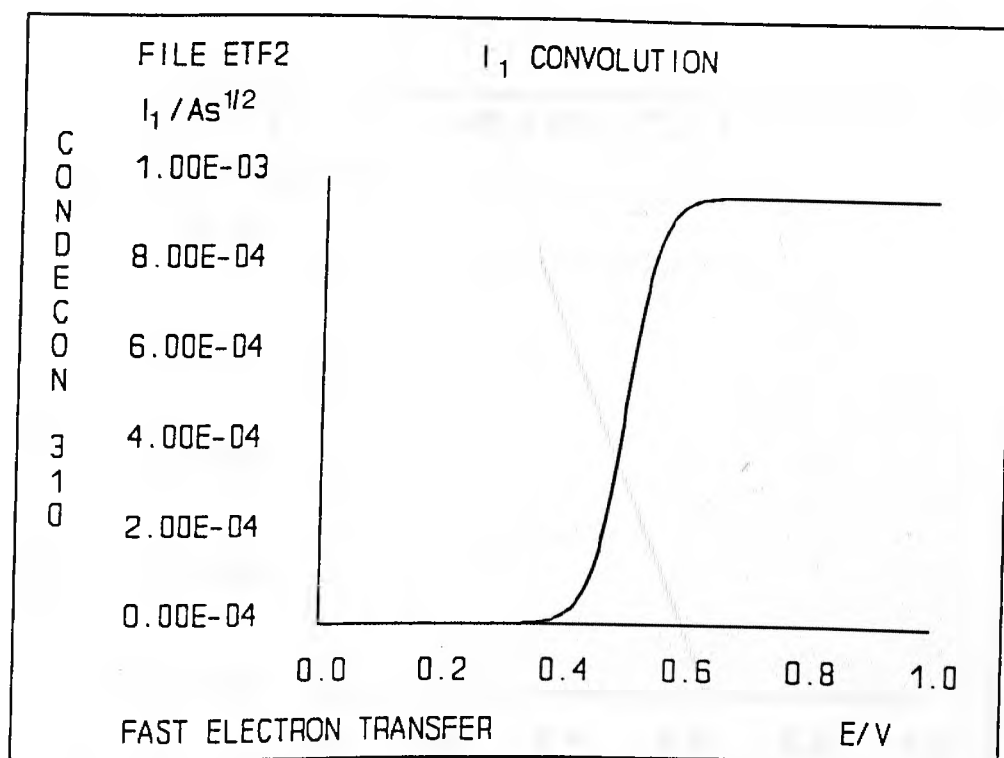


Figure 4.15 The plot of the I_1 convolution vs potential E displays clearly the characteristic polarographic wave

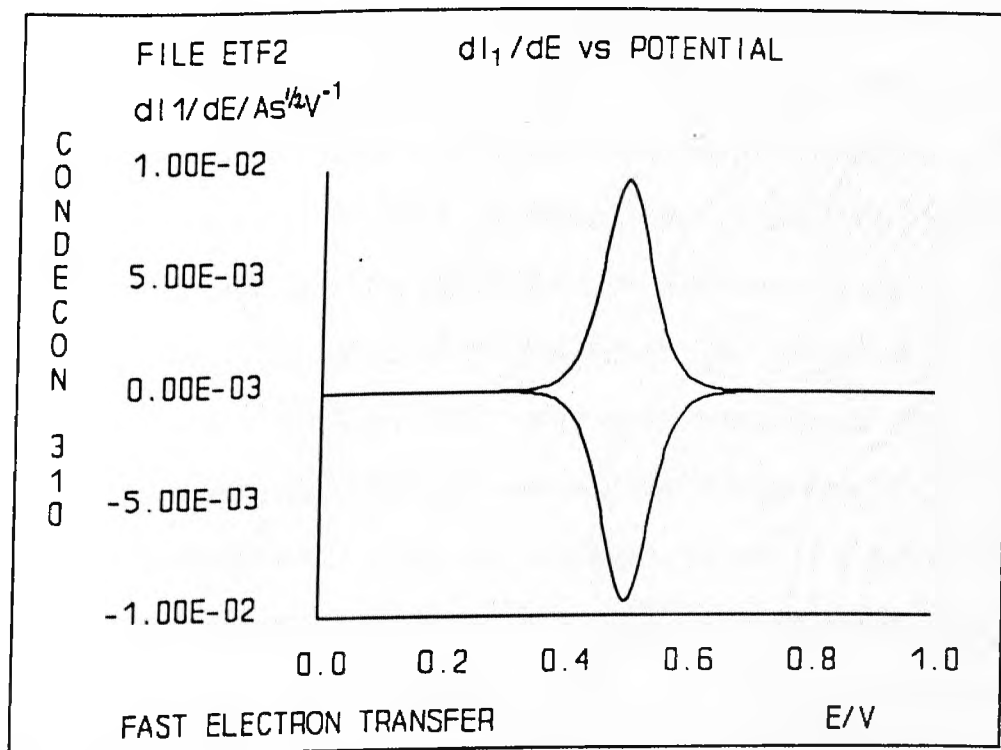


Figure 4.16 The dI_1/dE vs E plot displays two strictly symmetrical peaks centred on the "half wave" potential $E_{1/2}$

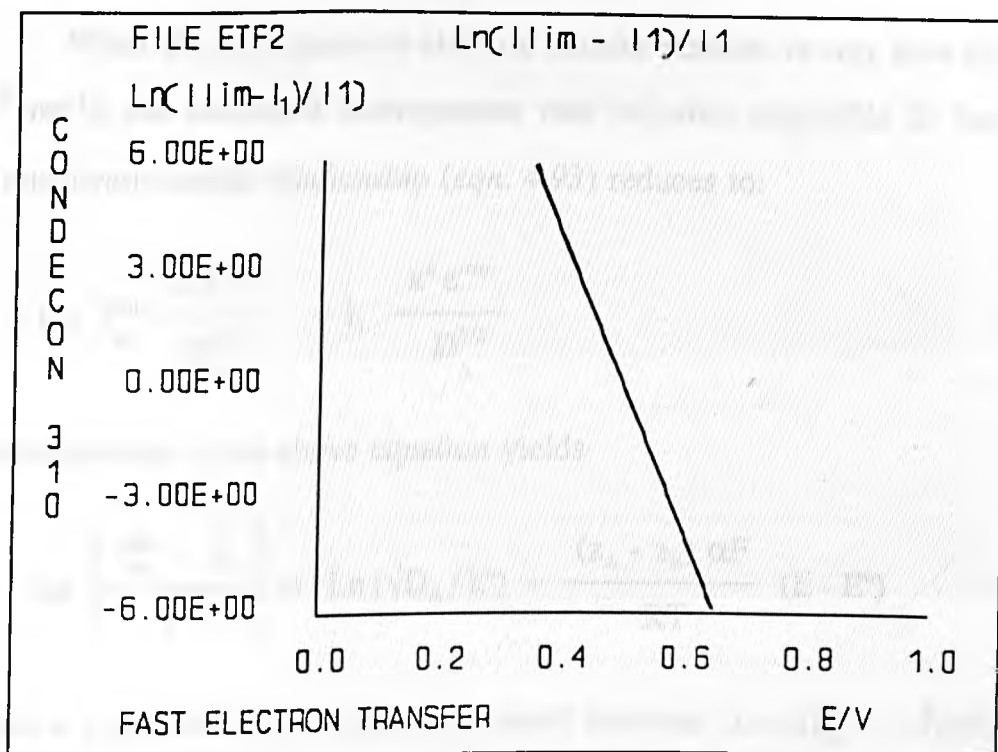


Figure 4.17 Plot of $\text{Ln}[(I_{\text{A}}^{\text{lim}} - I_1)/I_1]$ vs potential for fast ET - a test of polarographic behaviour of the I_1 convolution

4.8.2.1.2 The Irreversible Electron Transfer Reactions

When the heterogeneous electron transfer reaction is very slow (e.g. $k^0 < 10^{-6} \text{ ms}^{-1}$), the backward heterogenous rate becomes negligible & hence the current-overpotential relationship (eqn. 4.93) reduces to:

$$i = I_A^{\text{lim}} \frac{k^0 e^{-\alpha p}}{D_A^{1/2}} - I_1 \frac{k^0 e^{-\alpha p}}{D_A^{1/2}} \quad (4.99)$$

Rearrangement of the above equation yields

$$\text{Ln} \left[\frac{I_A^{\text{lim}} - I_1}{i} \right] = \text{Ln} (\sqrt{D_A}/k^0) + \frac{(z_A - z_B) \alpha F}{RT} (E - E^0) \quad (4.99a)$$

Again a linearized relationship is obtained between $\text{Ln} [(I_A^{\text{lim}} - I_1)/i]$ & the potential. The slope leads to an immediate route to the knowledge of the charge transfer coefficient α , provided the number of electrons is known. *Figures 4.19, 4.20 & 4.21* show a test of the digital simulated voltammogram (*Figure 4.18*) for an irreversible system ($k^0 = 10^{-8} \text{ ms}^{-1}$). As can be seen, the I_1 convolution does not display the polarographic wave & the peaks of the dI_1/dE vs E plot are considerably separated. However, the linear shape & the OVERLAY of the forward & backward scan of the logarithmic type plot shows clearly the accuracy of the simulation. The slope of the logarithmic plot evaluated via built-in statistical facilities is 19.4604. This value is subsequently divided by F/RT ($T=298.15 \text{ K}$) to give the value of α because the involvement of ONLY one electron in the charge transfer step can readily be proved. The estimated value for α is 0.49999 compared with the EXACT value of 0.5 for parameter entry for the digital simulation. The diffusion coefficient calculated from the limiting value of the I_1 convolution is $1.00000 \times 10^{-8} \text{ m}^2 \text{ s}^{-1}$, which is exactly the same as the entry for simulation.

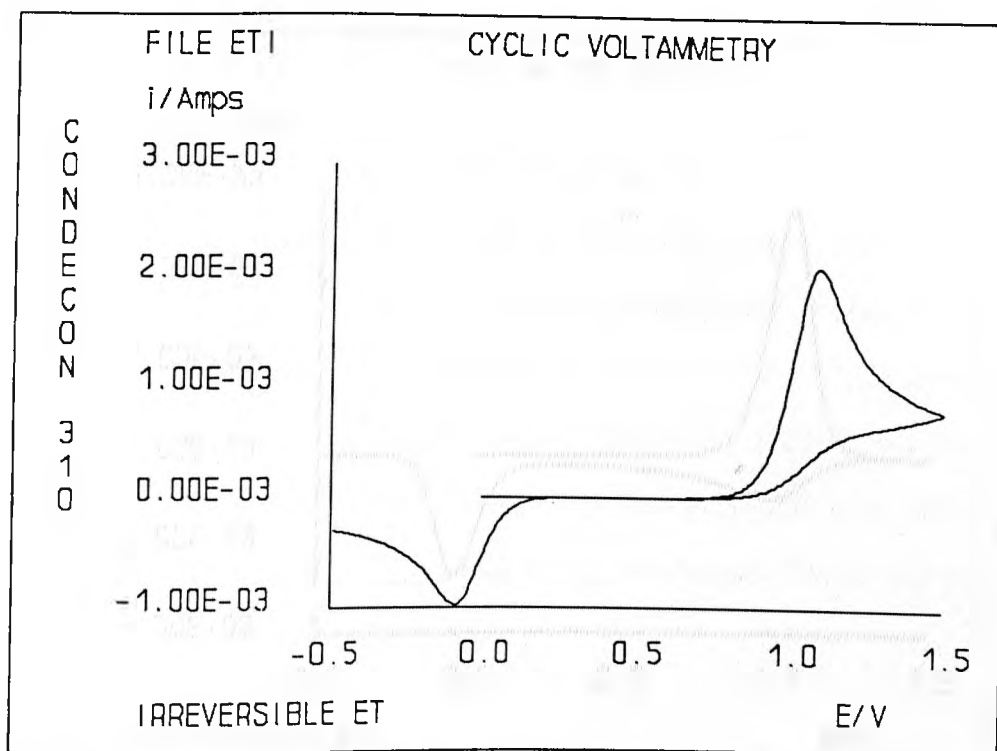


Figure 4.18 Cyclic voltammograms for an irreversible ET reaction with $\alpha = 0.5$, $k^0 = 10^{-8}$ m/s, $D = 10^{-8}$ m/s & $v = 1$ V/s

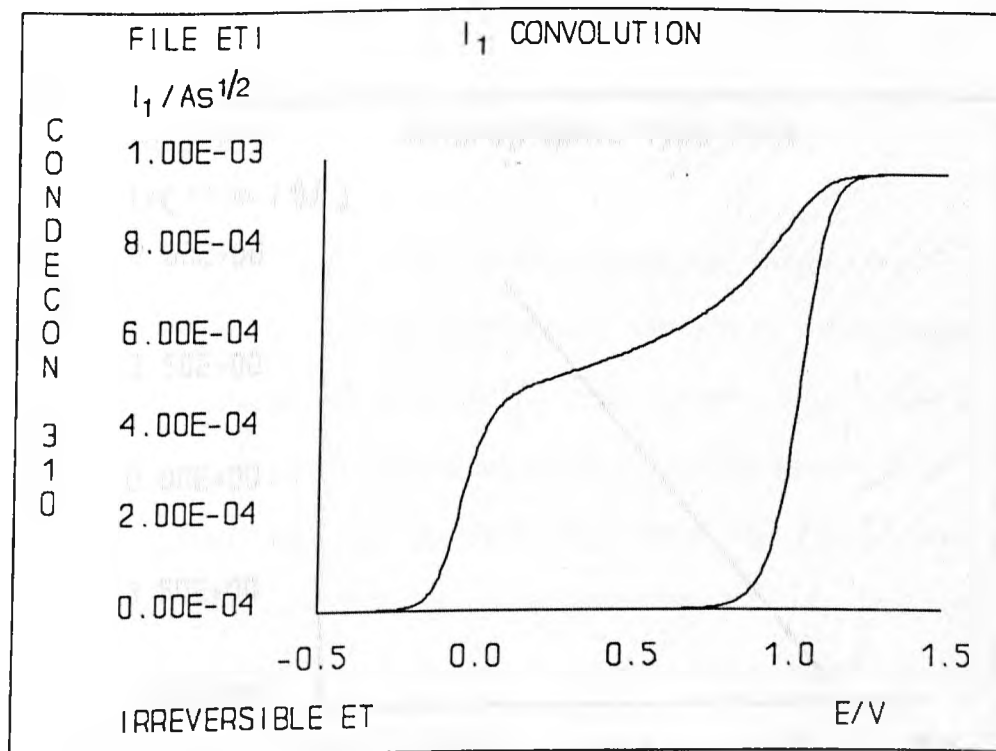


Figure 4.19 The plot of the I_1 convolution vs potential E does not adhere to the characteristic polarographic wave.

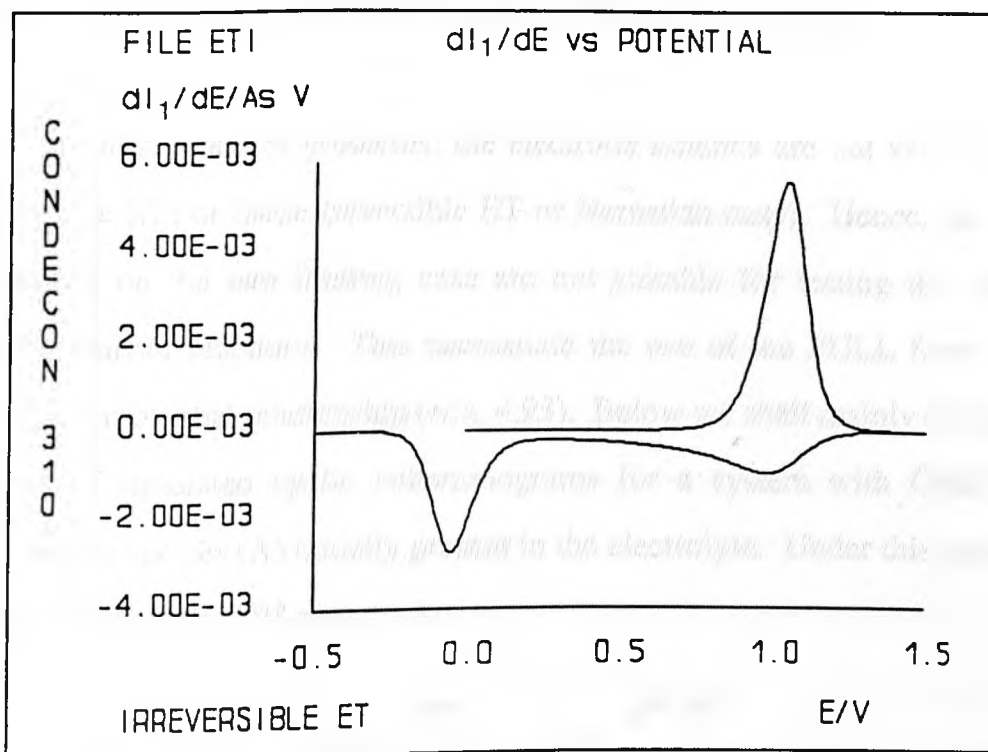


Figure 4.20 The dI_1/dE vs E plot for an irreversible ET reaction shows two well separated peaks similar to those of isomerisation (ECE) reactions

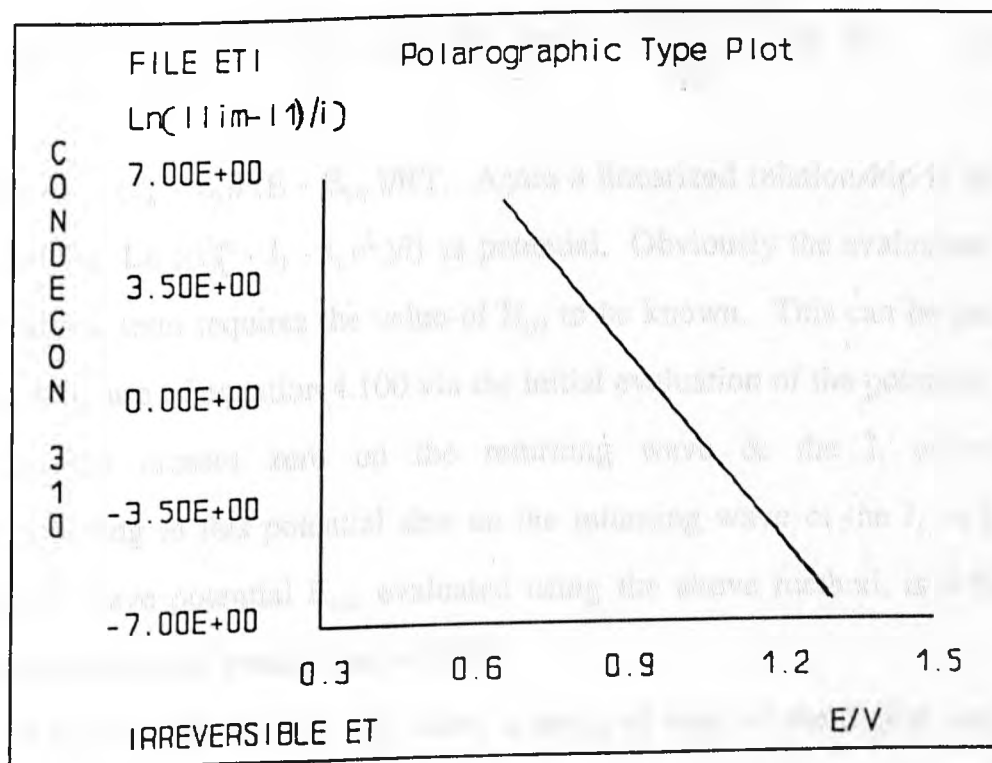


Figure 4.21 Plot of $\ln [(I_A^{lim} - I_1)/i]$ vs potential E - linearity & overlay of the forward & return waves are evident

4.8.2.1.3 The Quasi-reversible Electron Transfer Reactions

In most practical problems, the electrode kinetics are not very sluggish (irreversible ET) or facile (reversible ET or Nernstian case). Hence, the above discussions on the two limiting case are not suitable for testing this type of electron transfer reactions. This necessitate the use of the FULL form of the current-overpotential relationship (eqn. 4.93). Below we shall mainly discuss the analysis of simulated cyclic voltammograms for a system with ONLY one electroactive species (A) initially present in the electrolyte. Under this particular condition, equation 4.93 reduces to:

$$i = I_A^{\text{lim}} \frac{k^{\circ} e^{-\alpha p}}{D_A^{1/2}} - I_1 k^{\circ} \frac{e^{-\alpha p}}{D_A^{1/2}} - I_1 k^{\circ} \frac{e^{(1-\alpha)p}}{D_B^{1/2}} \quad (4.100)$$

Rearrangement of the above equation yields:

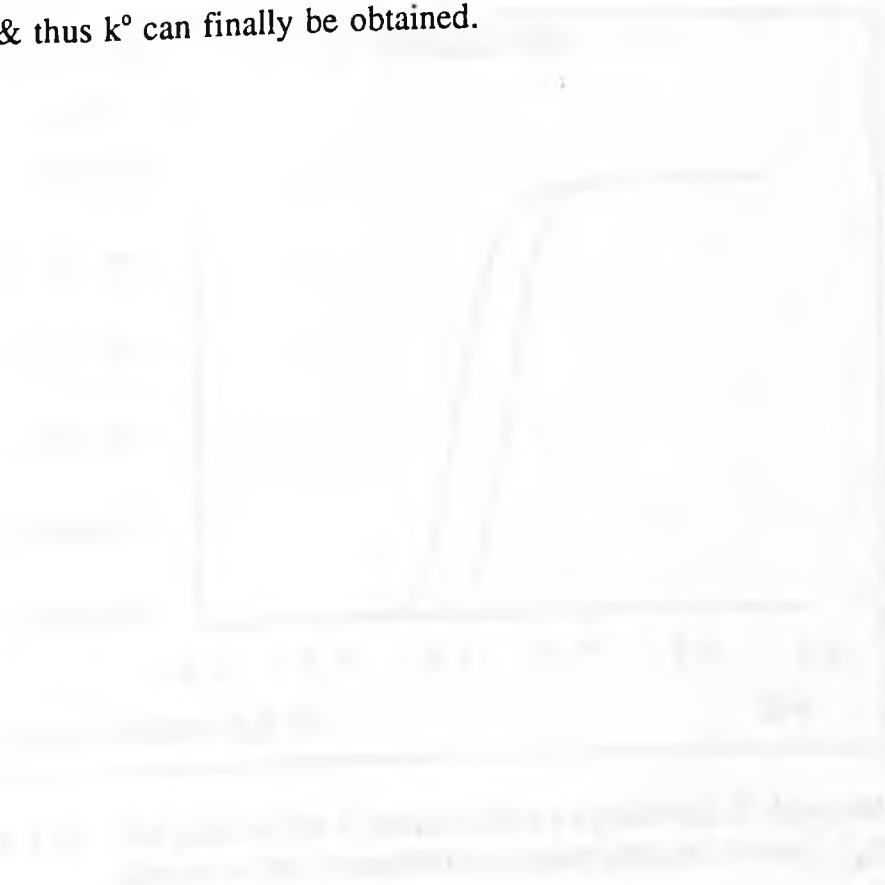
$$\text{Ln} \left[\frac{I_A^{\text{lim}} - I_1 - I_1 e^{\xi}}{i} \right] = \text{Ln} (\sqrt{D_A} / k^{\circ}) + \frac{(z_A - z_B) \alpha F}{RT} (E - E^{\circ}) \quad (4.100a)$$

where $\xi = (z_A - z_B)F(E - E_{1/2})/RT$. Again a linearized relationship is obtained by plotting $\text{Ln} [(I_A^{\text{lim}} - I_1 - I_1 e^{\xi})/i]$ vs potential. Obviously the evaluation of the logarithmic term requires the value of $E_{1/2}$ to be known. This can be done e.g. by making use of equation 4.100 via the initial evaluation of the potential where the current crosses zero on the returning wave & the I_1 convolution corresponding to this potential also on the returning wave of the I_1 vs E plot. The half wave potential $E_{1/2}$, evaluated using the above method, is 0.50012V compared with the exact value of 0.5V.

Figures 4.23, 4.24 & 4.25 show a series of tests of the digital simulated voltammogram (Figure 4.22) for a typical quasi-reversible system ($k^{\circ} = 10^{-4} \text{ms}^{-1}$).

As can be seen from *Figure 4.23*, unlike the Nernstian reactions, the I_1 convolution for a quasi-reversible process does not display the polarographic wave. Similar to the irreversible case, the I_1 convolution maintains at a certain value over a considerable wide potential region until the backward heterogeneous rate is sufficiently large to cause the depletion of species B at the electrode. This in turn causes the I_1 convolution to drop to zero because the surface concentration of species B is proportional to I_1 (cf. eqn. 4.87b & note that $C_B^{\text{BULK}} = 0$). Another departure from the Nernstian behaviour lies in the fact that appreciable peak displacement on dI_1/dE vs E plot is evident.

However, the linear shape & the OVERLAY of the forward & backward scan of the logarithmic type plot shows clearly the accuracy of the simulation. The calculated slope of the logarithmic plot is -19.4733 from which the value of α is determined to be 0.50032 (the exact value is 0.5). If D_B is known (in practice it is usually evaluated in a similar fashion as described above, from another simulation or experiment with ONLY species B initially present), the value of E° & thus k° can finally be obtained.



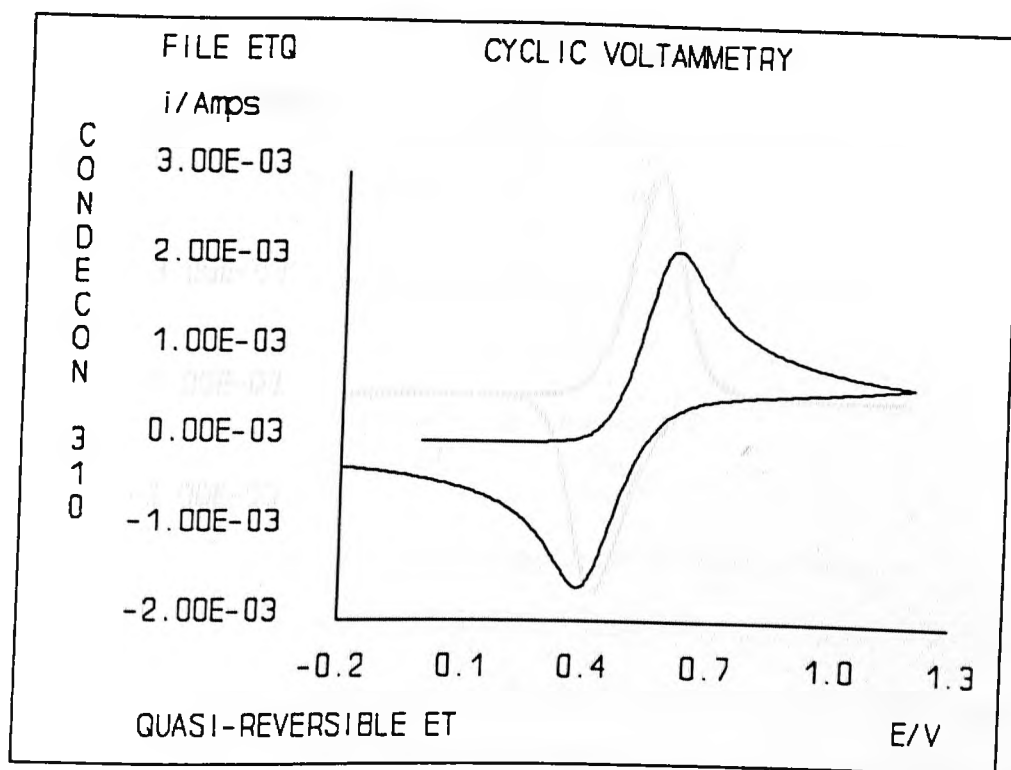


Figure 4.22 Cyclic voltammogram for a quasi-reversible ET reaction with $\alpha = 0.5$, $k^0 = 10^{-3} m/s$, $D = 10^{-8} m^2/s$ & $v = 1 V/s$

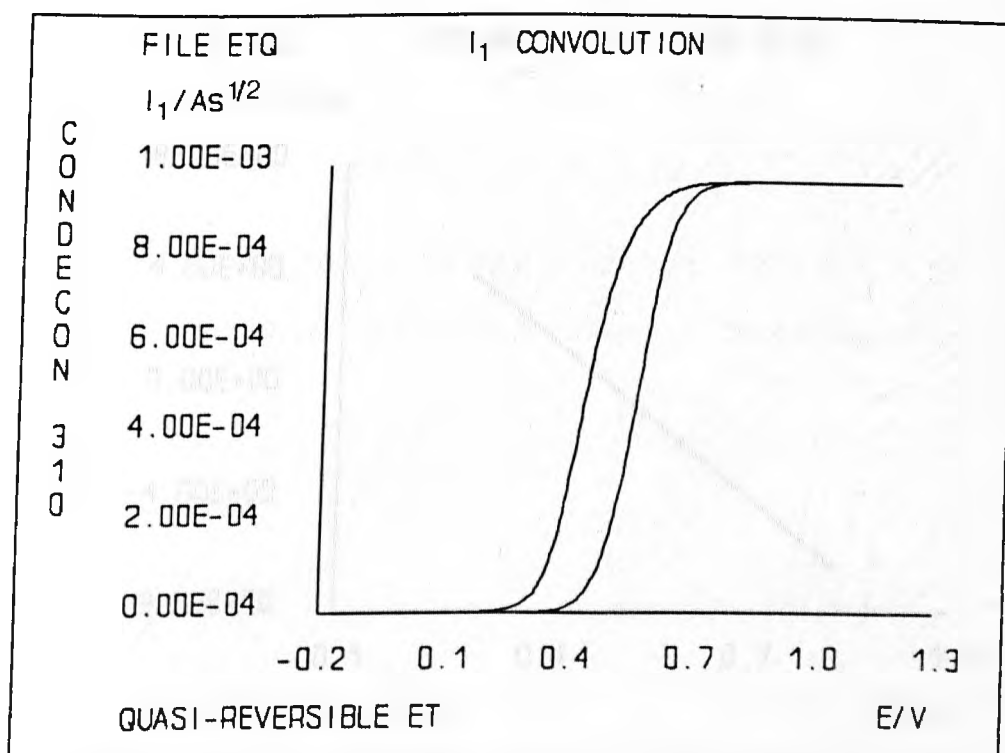


Figure 4.23 The plot of the I_1 convolution vs potential E does not adhere to the characteristic polarographic wave

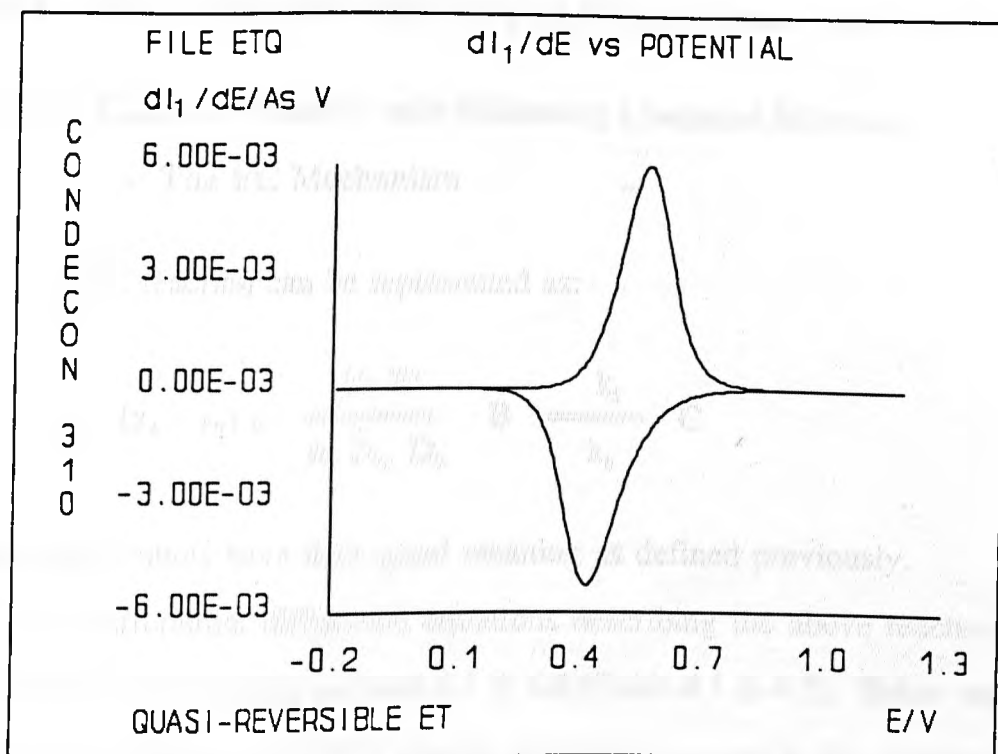


Figure 4.24 The dI_1/dE vs E plot shows appreciable departure from the symmetrical behaviour for Nernstian reactions

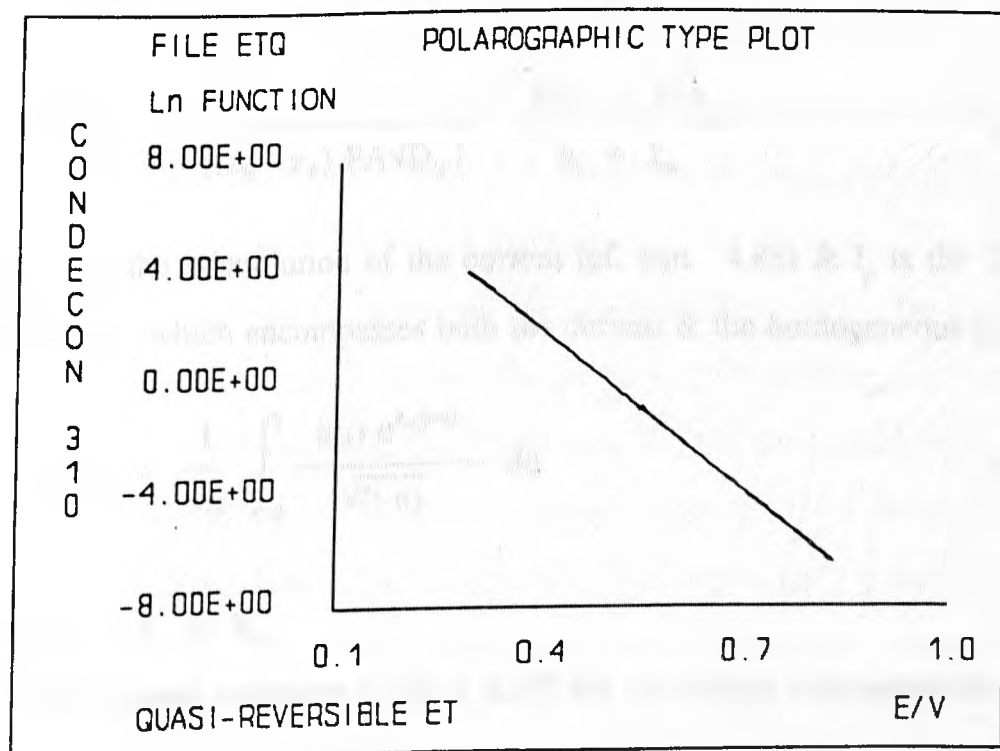


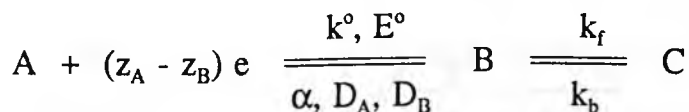
Figure 4.25 Plot of $\ln[(I_A^{\text{lim}} - I_1 - I_1 e^{\xi})/i]$ vs potential E - linearity & overlay of the forward & return wave are evident

4.8.2.2 Electron Transfer with Coupled Homogeneous Chemical Reaction

4.8.2.2.1 Electron Transfer with Following Chemical Kinetics

- The EC Mechanism

An EC reaction can be represented as:



where the symbols have their usual meaning as defined previously.

The differential diffusional equations describing the above reaction have already been discussed in *sections 4.3 & 4.6 (Table 4.1 & 4.2)*. Below we shall discuss the system with ONLY species A initially present in the solution. The solution of these partial differential equations via the Laplace transforms gives the surface concentrations of species A & B ⁴:

$$C_A^o(t) = C_A^{BULK} - I_1(t)/[(z_B - z_A) FAD_A^{1/2}] \quad (4.101)$$

$$C_B^o(t) = \frac{1}{[(z_B - z_A) FA\sqrt{D_B}]} \frac{k_b I_1 + k_f I_2}{k_f + k_b} \quad (4.102)$$

where I_1 is the convolution of the current (cf. eqn. 4.88) & I_2 is the "kinetic convolution" which encompasses both the current & the homogeneous kinetics:

$$I_2(t) = \frac{1}{\sqrt{\pi}} \int_0^t \frac{i(u) e^{k_c(t-u)}}{\sqrt{(t-u)}} du \quad (4.103)$$

where $k_c = k_f + k_b$.

Substituting *equations 4.101 & 4.102* for the surface concentrations in the

⁴ Note: For EC_{rev} reaction, at present, solution is applicable ONLY if $D_A = D_B = D_C$.

current-overpotential relationship (eqn. 4.31), we have:

$$i = (I_A^{\text{lim}} - I_1) \frac{k^o e^{-\alpha p}}{D_A^{1/2}} - \frac{k^o e^{(1-\alpha)p}}{D_B^{1/2}} \frac{k_b I_1 + k_f I_2}{k_f + k_b} \quad (4.104)$$

Rearrangement of the above equation yields:

$$\frac{i \sqrt{D_A}}{k^o e^{-\alpha p}} = I_A^{\text{lim}} - I_1 - e^{\xi} \frac{k_b I_1 + k_f I_2}{k_f + k_b} \quad (4.104a)$$

where $p = (z_A - z_B)F(E - E^o)/RT$ & $\xi = (z_A - z_B)F(E - E_{1/2})/RT$. The above equation is the basic tool for the analysis of the EC mechanism. Below we shall take as an example the case when $(z_A - z_B) < 0$ to demonstrate the extraction of several important kinetic parameters e.g. D_A , $E_{1/2}$, k_f , k_b etc..

For an oxidative process, when the potential is scanning well "past" the wave eg p (or ξ) \rightarrow large negative values, we have: $e^{\xi} \rightarrow 0$ & $e^{-\alpha p} \rightarrow \infty$. Hence the I_1 convolution approaches its limiting value I_A^{lim} irrespective of the electrode & homogeneous kinetics. This ultimately leads to the knowledge of the diffusion coefficient of species A i.e. D_A . On the other hand, on the return of the wave to potential region well "past" the cathodic wave (e.g. back to the initial potential) $e^{\xi} \rightarrow \infty$ & $e^{-\alpha p} \rightarrow 0$ & therefore $I_1 \rightarrow -k_f I_2 / k_b$. Thus the constant $K (= k_f/k_b)$ can be calculated for that particular "test" value of k_c used for evaluation of the I_2 convolution. Therefore, a series of K can be calculated by altering the "test" values of k_c . By plotting K vs k_c for several sweep rates, these curves should meet at the EXACT point where the TRUE values of k_c & K are located. Thus, k_f & k_b can be obtained. The "half wave" potential $E_{1/2}$ can be obtained in a similar fashion as the quasi-reversible ET case. By evaluating I^{lim} & the values of I_1 & I_2 corresponding to the potential where the returning current wave crosses zero, $E_{1/2}$ can readily be calculated via equation 4.104.

Figures 4.26, 4.27, 4.28 & 4.29 show plots of various data sets obtained for an EC_{rev} system with fast ET ($k^{\circ} = 10\text{ms}^{-1}$), $k_f = k_b = 1.0\text{ s}^{-1}$ & $E_{1/2} = 0.5\text{V}$ & at a sweep rate of 1 Vs^{-1} . Note the alignment of the peaks on the plot dI_1/dE vs. E - an indication of fast ET. The decrease of the height of the reductive peak is due to the decomposition of species B. Similar data for an EC_{rev} reaction with slow ET ($k^{\circ} = 10^{-6}\text{ ms}^{-1}$) is shown in *Figures 4.30-33*. In *Figures 4.34 & 4.35* the calculated values of K are displayed against the corresponding test values of k_c for three different sweep rates. The intersections yield the TRUE values of K & k_c , which are exactly the same as those entered for the simulation.

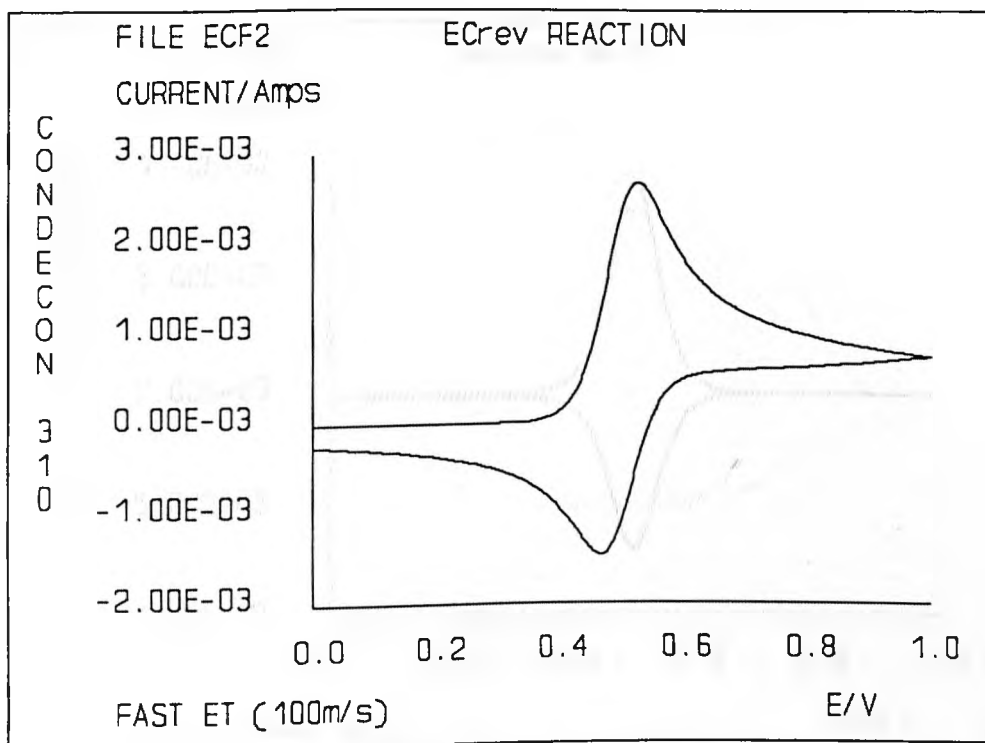


Figure 4.26 Cyclic voltammogram for an EC_{rev} reaction with fast ET, $k^0 = 10\text{ms}^{-1}$, $D = 10^{-8}\text{m}^2\text{s}^{-1}$, $\alpha = 0.5$, $k_f = k_b = 1\text{s}^{-1}$

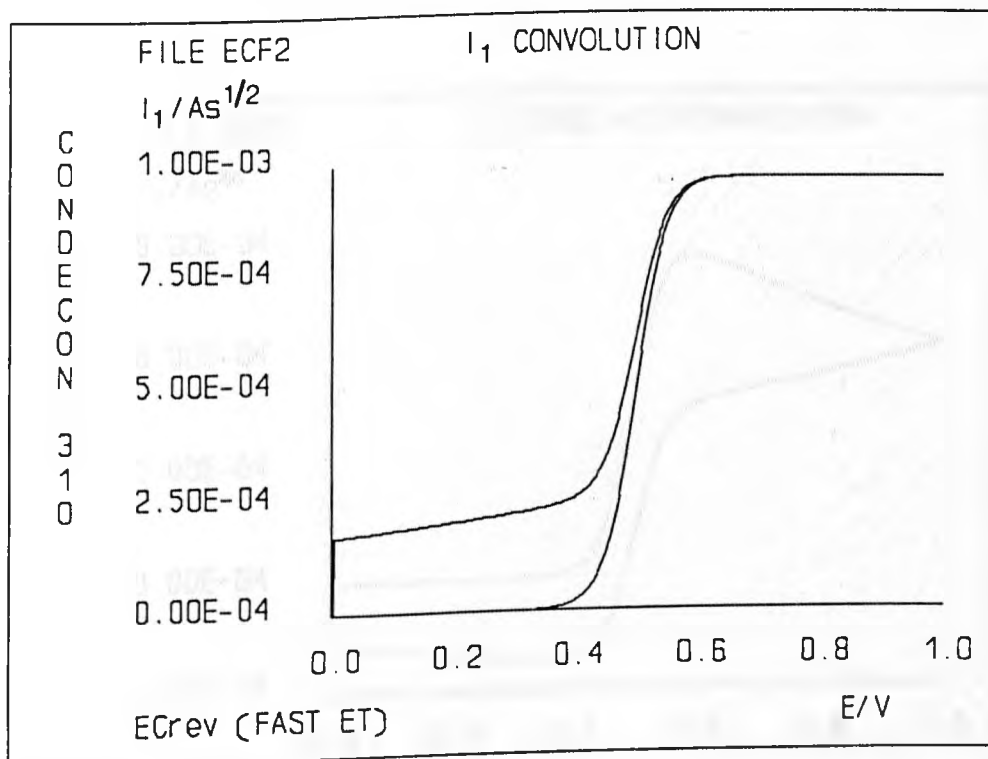


Figure 4.27 Unlike the simple ET reaction the I₁ convolution of an EC system does not fall to zero on the returning wave.

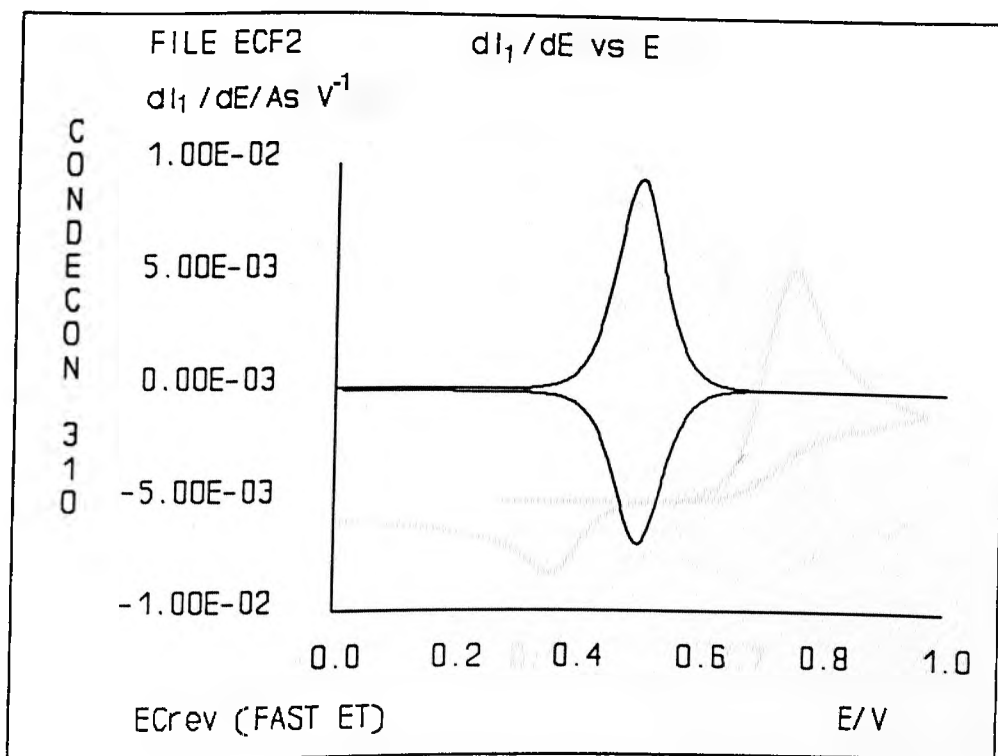


Figure 4.28 Though the peaks of the dI_1/dE vs E plot are aligned the peak heights are different due to decomposition of species B via the following homogeneous reaction

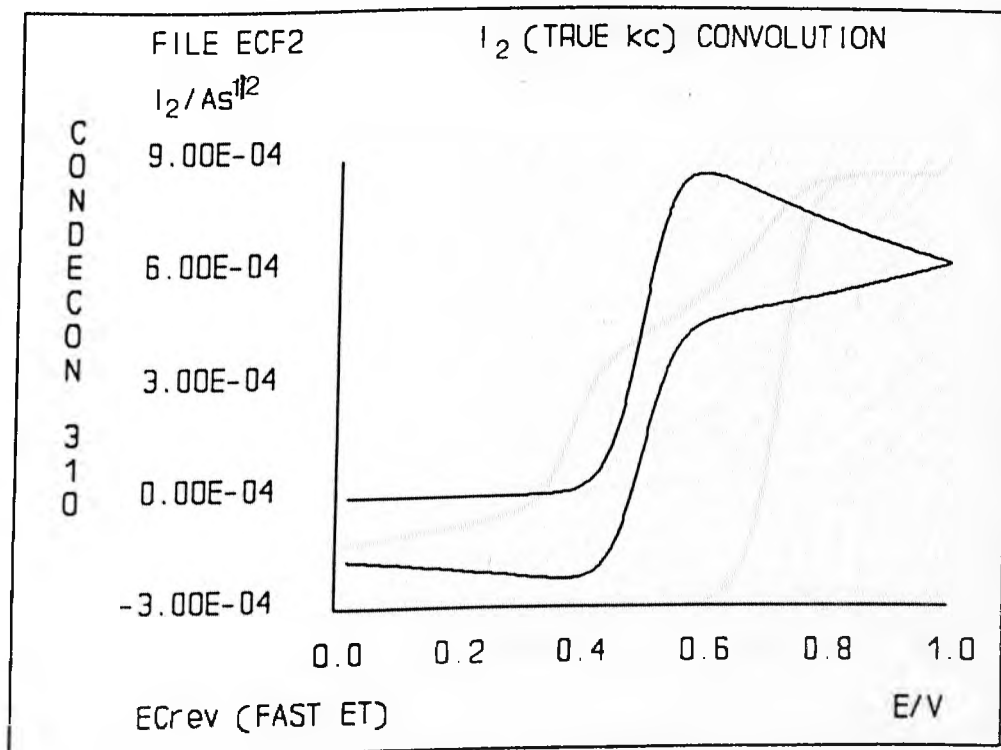


Figure 4.29 Plot of I_2 convolution (calculated with true k_c) versus potential. Note the equality of $-I_2$ & I_1 at end of sweep

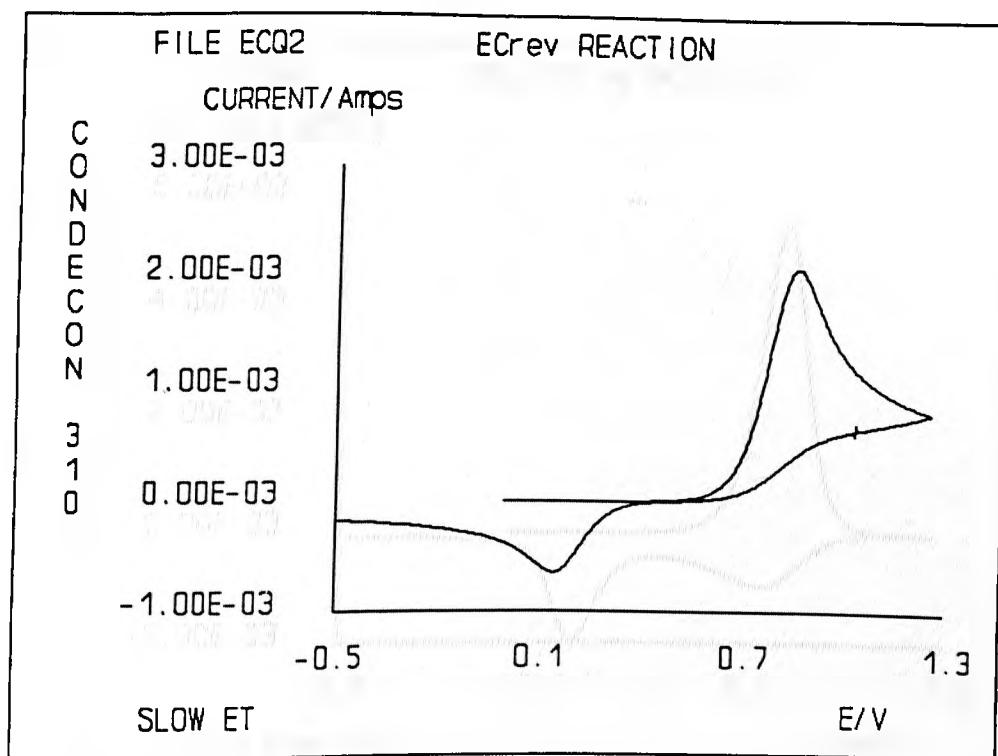


Figure 4.30 Cyclic voltammogram for an EC_{rev} reaction with slow ET, $k^0 = 10^{-8} \text{ms}^{-1}$, $D = 10^{-8} \text{m}^2 \text{s}^{-1}$, $\alpha = 0.5$, $k_f = k_b = 1 \text{s}^{-1}$

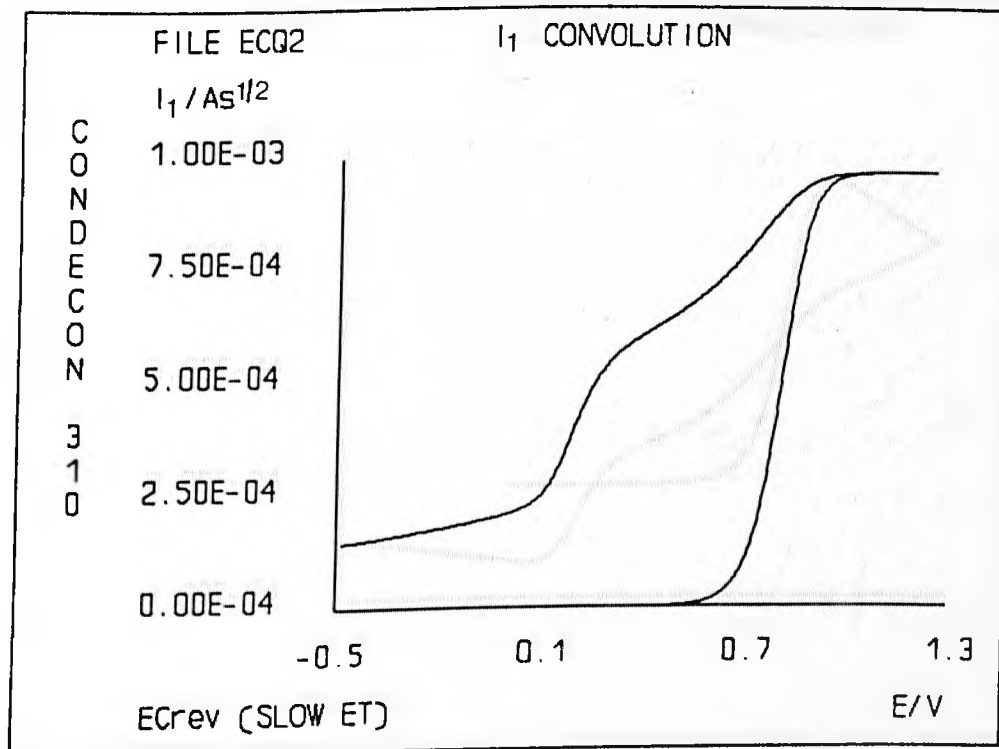


Figure 4.31 Unlike simple ET reactions the I_1 convolution for an EC system does not return to zero at end of sweep

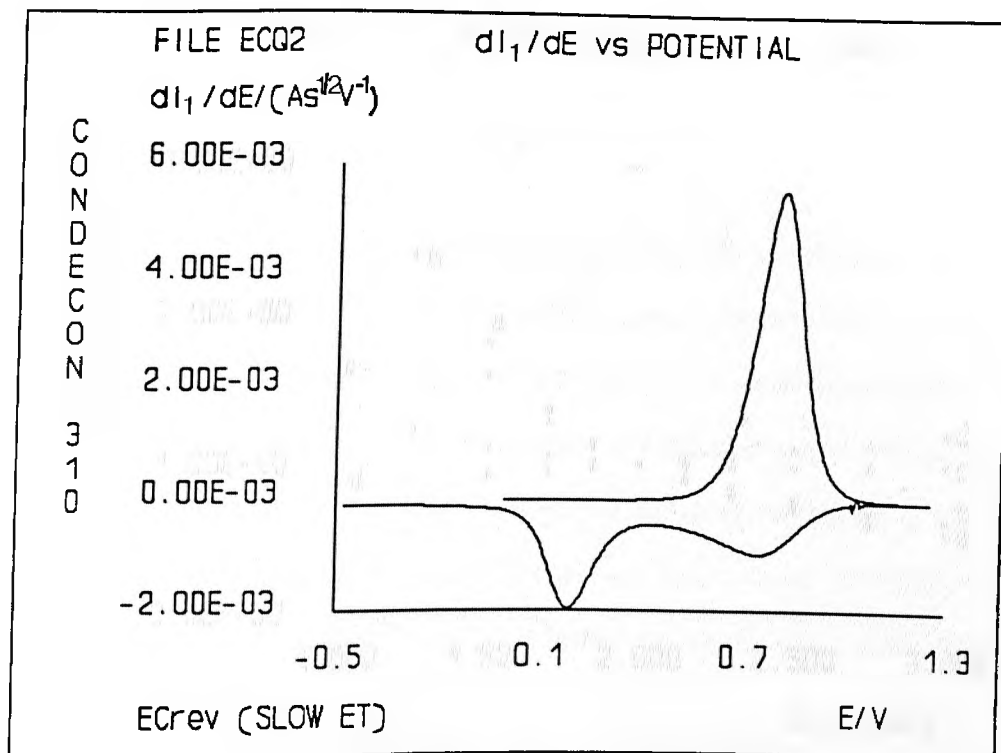


Figure 4.32 Plot of dI_1/dE vs E for an EC_{rev} reaction with slow ET. The peaks are separated & peak heights different

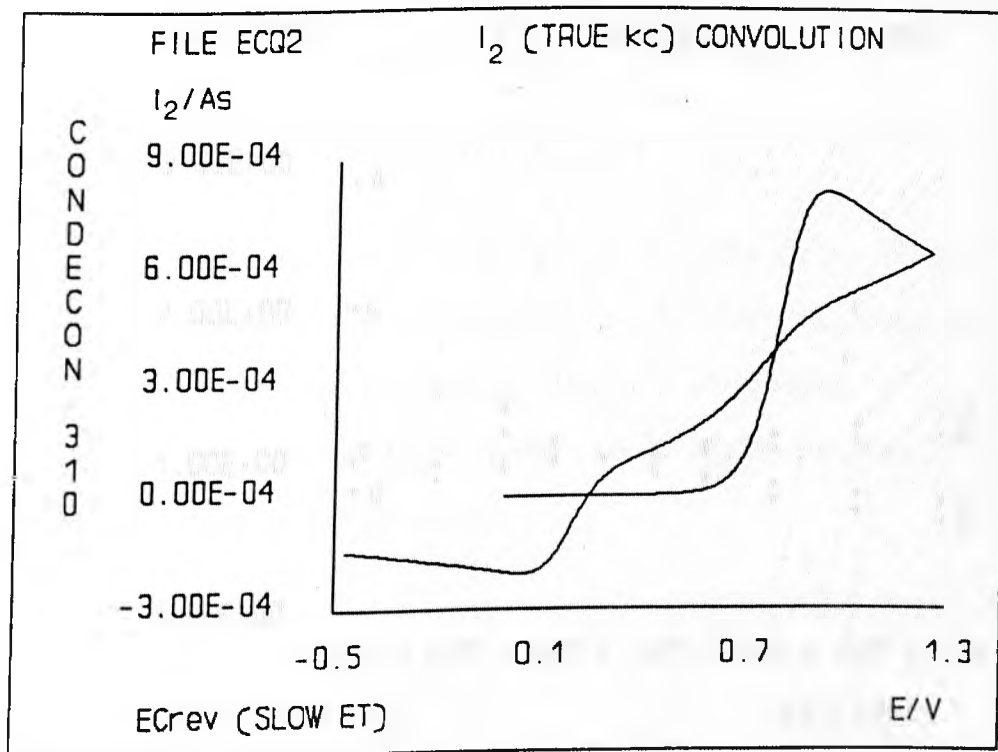


Figure 4.33 Plot of I_2 convolution (calculated with true k_c) versus potential. Note the equality of $-I_2$ & I_1 at end of sweep

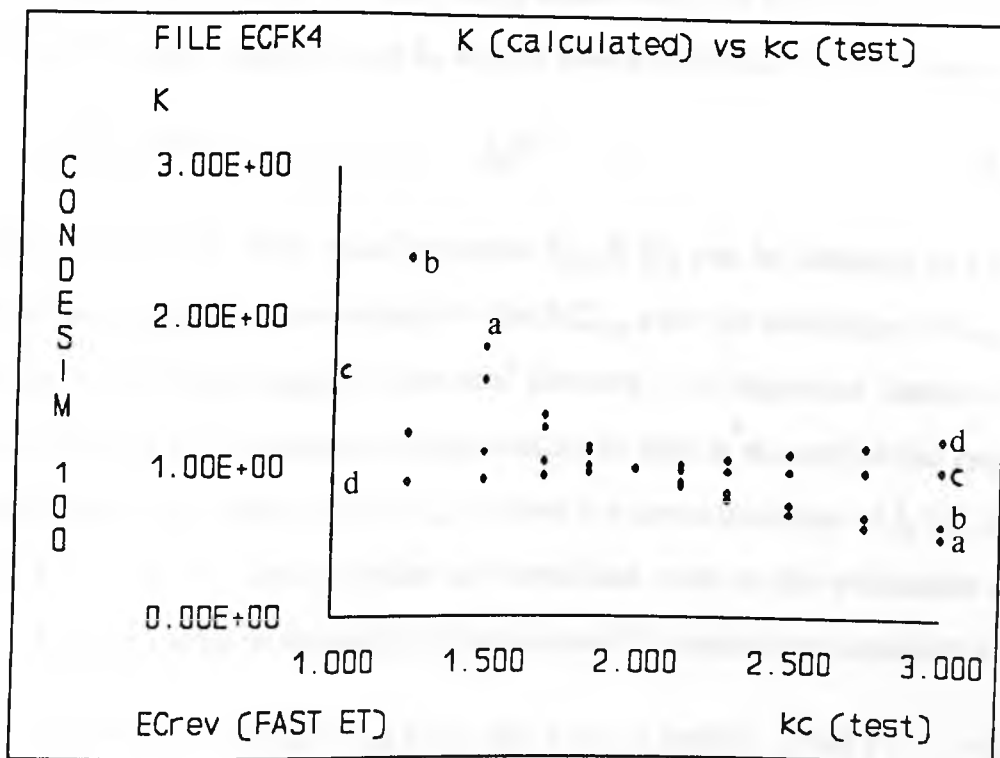


Figure 4.34 Plots of K vs k_c (test) for simulated data for an EC process with fast ET at sweep rates (V/s) of (a) 10 (b) 4 (c) 1 (d) 0.5. Note the well defined intersection.

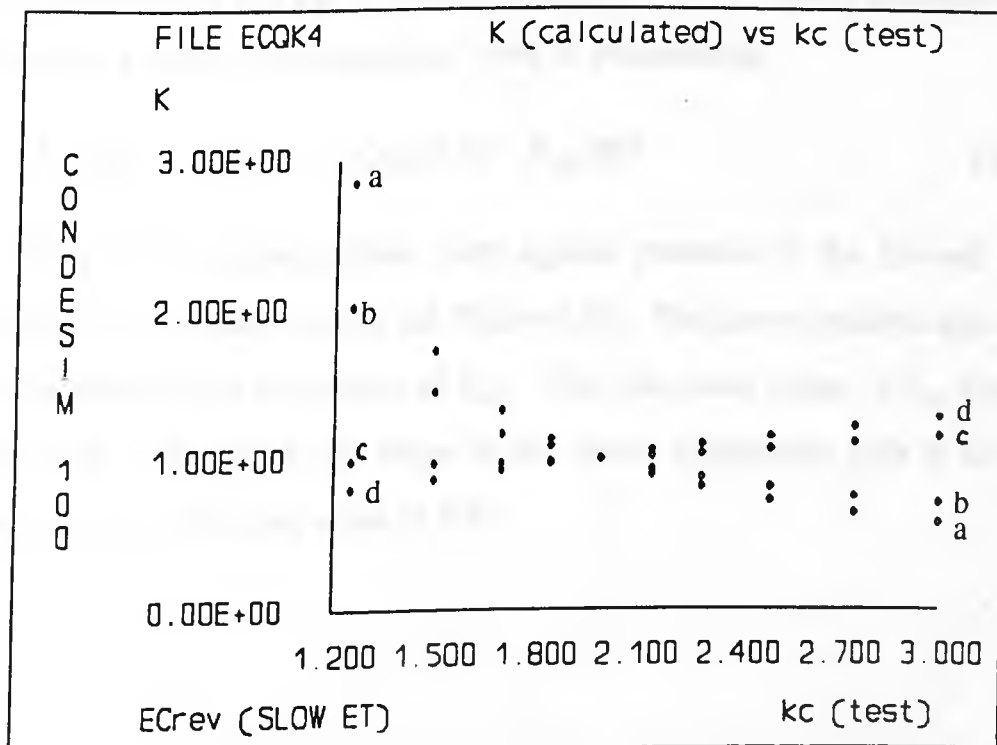


Figure 4.35 Plots of K vs k_c (test) for simulated data for an EC process with slow ET at sweep rates (V/s) of (a) 10 (b) 4 (c) 1 (d) 0.5. Note the well defined intersection.

A special case eg that of the EC_{irrev} arises when the backward chemical rate constant becomes negligible eg $k_b \ll k_f$ & hence equation 4.104a reduces to:

$$i \sqrt{D_A} e^{\alpha p} / k^{\circ} = I_A^{\text{lim}} - I_1 - I_2 e^{\xi} \quad (4.104b)$$

As can be seen, the "half wave" potential $E_{1/2}$ & D_A can be obtained in a similar manner as discussed above though in the EC_{irrev} case the evaluation of $E_{1/2}$ does not rely on the knowledge of chemical kinetics. An important feature of this case is that the I_2 convolution returns exactly to zero at the end of the returning scan if the correct value of $k_c (= k_f)$ is used for the calculation of I_2 (cf. *Figure 4.36, 4.37 & 4.38*). This provides an immediate route to the evaluation of k_c .

Another useful relationship can be obtained by rearranging equation 4.104b:

$$\text{Ln} \left[(I_A^{\text{lim}} - I_1 - I_2 e^{\xi}) / i \right] = \text{Ln} (\sqrt{D_A} / k^{\circ}) + (z_A - z_B) \alpha F (E - E^{\circ}) / RT \quad (4.105)$$

which is very similar equation 4.100a for a quasi-reversible simple ET system. The slope of the above linear relationship gives rise the evaluation of α . When the electron is very fast e.g. Nernstian case, $(i/k^{\circ}) \rightarrow 0$. Hence, equation 4.100b reduces to a simple "polarographic" type of relationship:

$$\text{Ln} \left[(I_A^{\text{lim}} - I_1) / I_2 \right] = (z_A - z_B) F (E - E_{1/2}) / RT \quad (4.105a)$$

By plotting the logarithmic term against potential E , the forward & the returning waves should overlay (cf. *Figure 4.39*). The above equation also serves as an alternative for evaluation of $E_{1/2}$. The calculated value of $E_{1/2}$ from the ratio of the intercept & the slope of the above logarithmic plot is 0.5004V compared with the exact value of 0.5V.

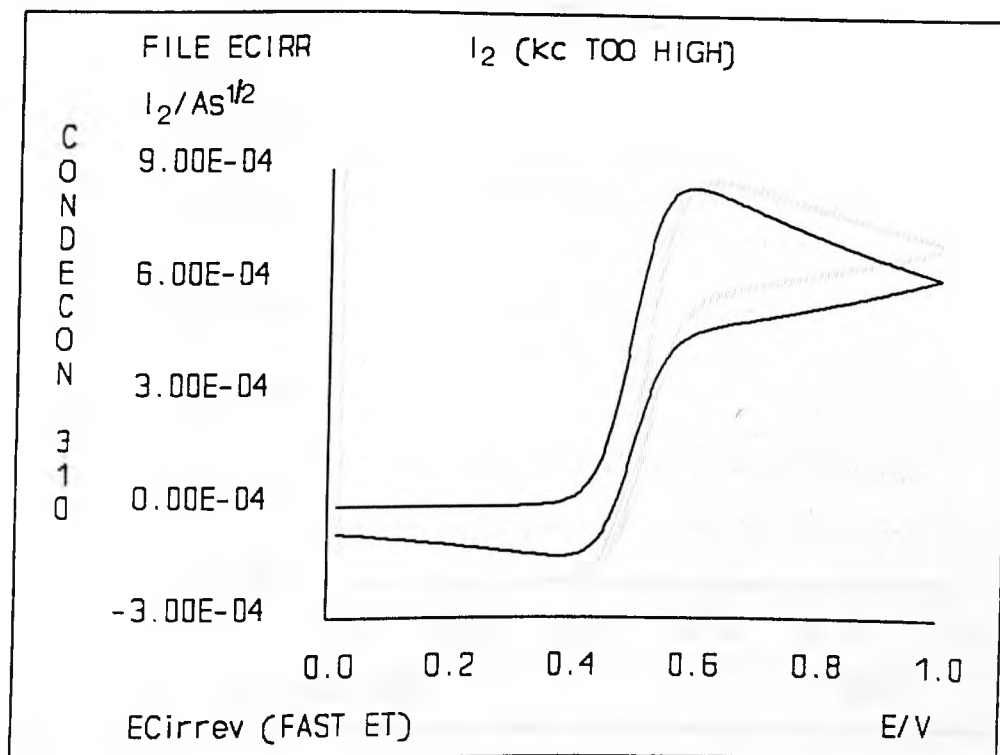


Figure 4.36 Plot of I_2 convolution versus potential. I_2 is calculated with a test value much higher than TRUE k_c .

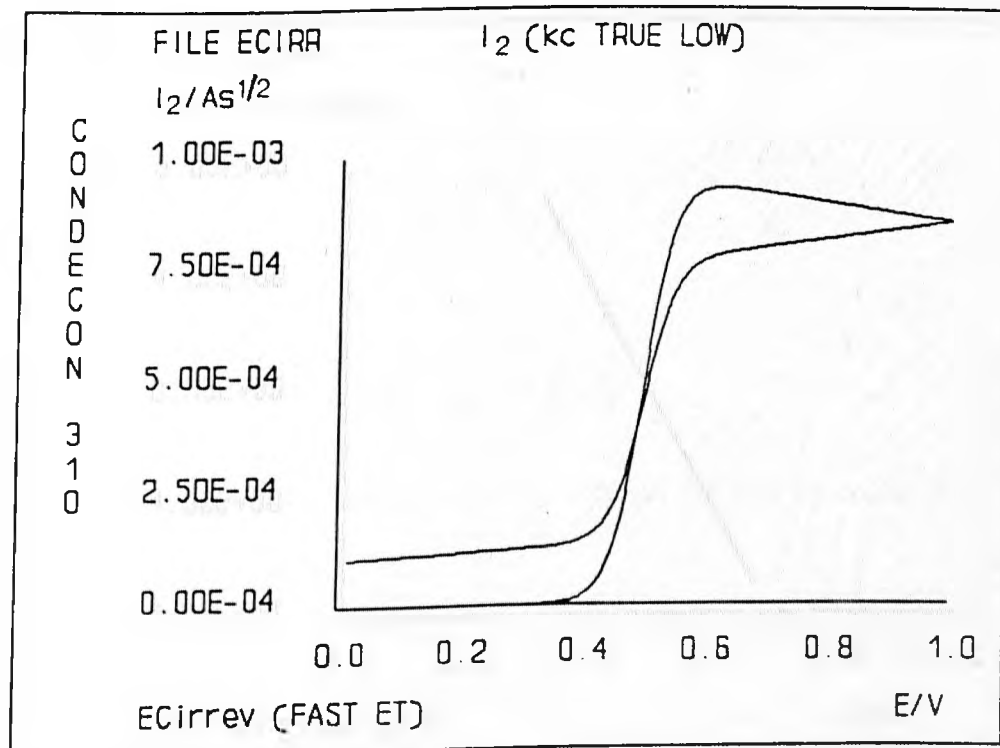


Figure 4.37 Plot of I_2 convolution versus potential. I_2 is calculated with a test value much lower than TRUE k_c .

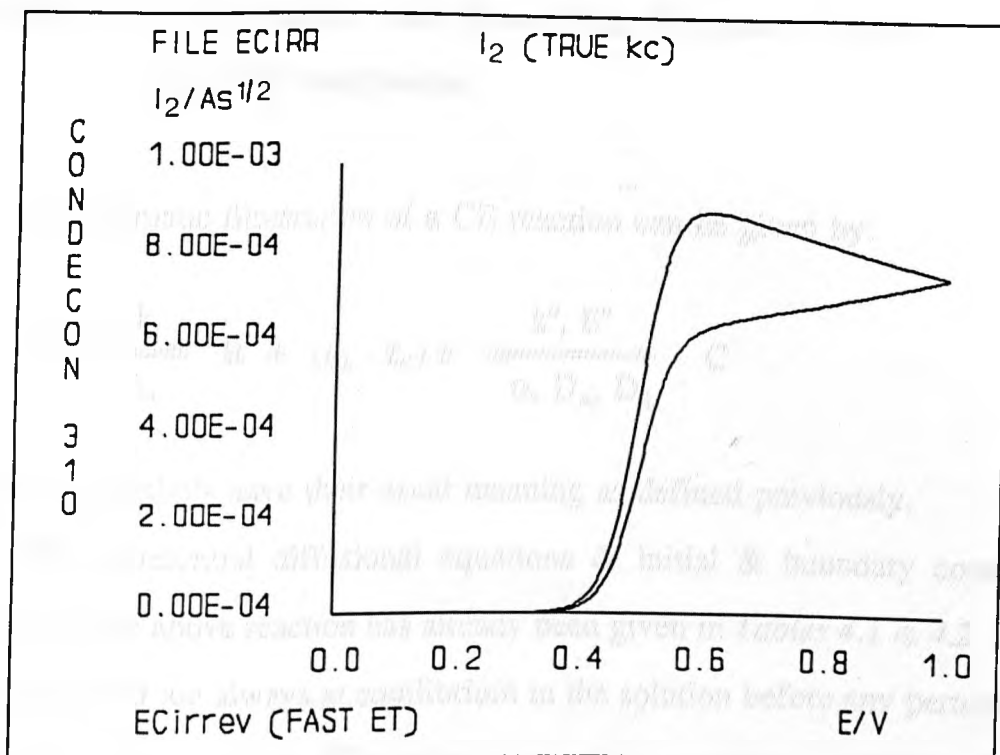


Figure 4.38 Plot of I_2 convolution (calculated with true k_c) versus potential. I_2 maintains at zero at end of sweep.

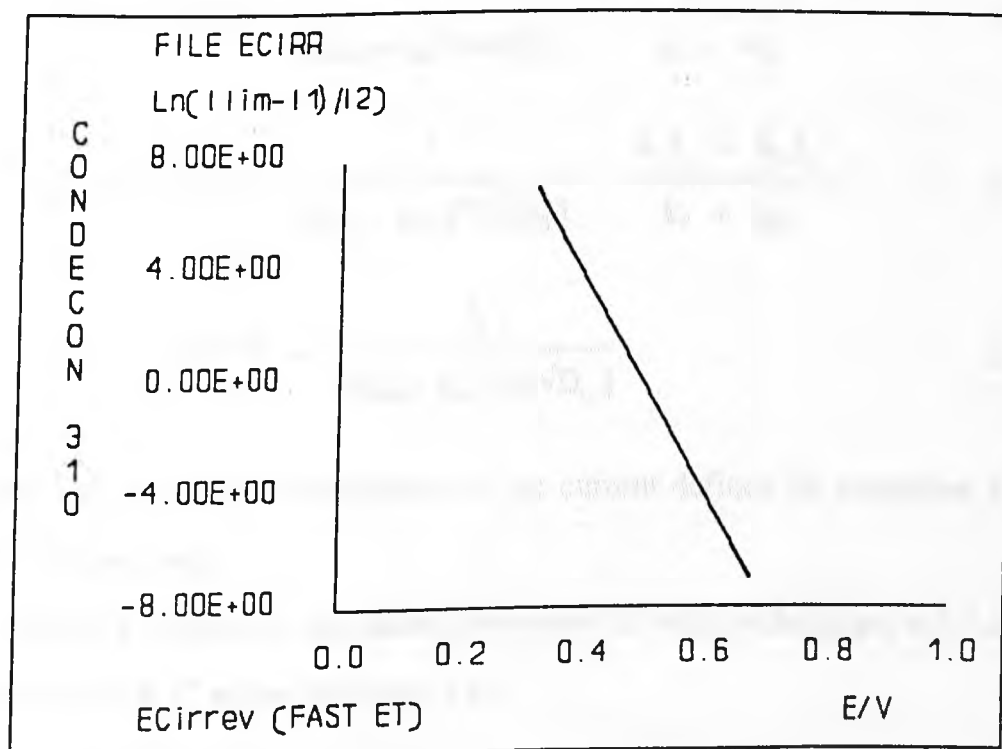
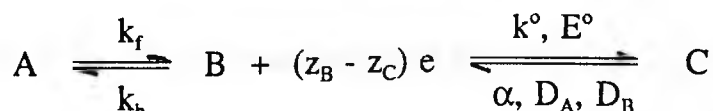


Figure 4.39 Polarographic type plot for an EC_{irrev} reaction with fast ET. Linearity & overlay of forward & return waves are evident.

4.8.2.2.2 Electron Transfer with Preceding Chemical Kinetics

- The CE Mechanism

A schematic illustration of a CE reaction can be given by:



where the symbols have their usual meaning as defined previously.

The differential diffusional equations & initial & boundary conditions describing the above reaction has already been given in *Tables 4.1 & 4.2*. Here, species A & B are always at equilibrium in the solution before any perturbation is applied. Similar to the EC reaction, the surface concentrations of species A, B & C can be obtained by solving the corresponding diffusion equations using the Laplace transforms, in terms of the I_1 & I_2 convolutions of the current:

$$C_A^\circ(t) = C_A^{\text{BULK}} - \frac{1}{[(z_C - z_B) FA\sqrt{D_A}]} \frac{k_b(I_1 - I_2)}{k_f + k_b} \quad (4.106)$$

$$C_B^\circ(t) = C_B^{\text{BULK}} - \frac{1}{[(z_C - z_B) FA\sqrt{D_B}]} \frac{k_f I_1 + k_b I_2}{k_f + k_b} \quad (4.107)$$

$$C_C^\circ(t) = C_C^{\text{BULK}} + \frac{I_1}{[(z_C - z_B) FA\sqrt{D_C}]} \quad (4.109)$$

where I_1 & I_2 are the convolutions of the current defined by *equations 4.88 & 4.103*, respectively.

In the CE reaction, the current-overpotential relationship (*eqn. 4.31*) applies to species B & C at the electrode, i.e.

$$i = (z_C - z_B) FA [k_{hf} C_B - k_{hb} C_C] \quad (4.110)$$

Hence, substituting *equations 4.107 & 4.108* for the surface concentrations of B & C in the above equation, we have:

$$i = \frac{k_{hf}}{\sqrt{D_B}} \left[I_B^{BULK} - \frac{k_f I_1 + k_b I_2}{k_f + k_b} \right] + \frac{k_{hb}}{\sqrt{D_C}} (I_C^{lim} - I_1) \quad (4.111)$$

where I_B^{lim} & I_C^{lim} are constants given by:

$$I_B^{lim} = (z_C - z_B) FA \sqrt{D_B} C_B^{BULK} \quad \& \quad I_C^{lim} = (z_B - z_C) FA \sqrt{D_C} C_C^{BULK}$$

Rearrangement of the above equation yields:

$$\frac{i \sqrt{D_A}}{k_{hf}} = I_B^{lim} - \frac{k_f I_1 + k_b I_2}{k_f + k_b} + e^\xi (I_C^{lim} - I_1) \quad (4.111a)$$

where $\xi = (z_A - z_B)F(E - E_{1/2})/RT$. The above equation forms the base for the analysis of the CE mechanism. Below we shall take as an example an oxidative process e.g. $(z_A - z_B) < 0$ to demonstrate the extraction of several important kinetic parameters e.g. $E_{1/2}$, k_f , k_b etc..

When the potential is scanning well "past" the wave e.g. p (or ξ) \rightarrow large negative values, $e^\xi \rightarrow 0$ & $e^{-\alpha p}$ (or k_{hf}) $\rightarrow \infty$. Hence *equation 4.110a* reduces to the following simple form:

$$I^{lim} = \frac{k_f I_1 + k_b I_2}{k_f + k_b} = \frac{K I_1 + I_2}{K + 1} \quad (4.112)$$

where $K = k_f/k_b$ is the equilibrium constant. *Equation 4.111* as it stands does not provide immediate route to the evaluation of any kinetic parameters because unlike the EC reaction the "limiting" convolution I_B^{lim} for an CE process cannot be readily obtained (*cf. Figure 4.41*). Considering two sets of data under different sweep rates, the above relationship applies to both data. If we use the

same test value of k_c to evaluate the I_2 convolution, the value of K should also be the same. As I_B^{lim} is a CONSTANT, the value of K corresponding to this particular test value k_c can be obtained via:

$$K = [I_2^a - I_2^b] / [I_1^b - I_1^a] \quad (4.112a)$$

Thus, by varying the test value of k_c , a series of K can be calculated. Similar treatment can be made on another pair of data under different sweep rates. It is proved that the plots of K vs k_c should cross at exactly the point where the TRUE values of K & k_c are located. Thus, k_f & k_b can be obtained. This in turn leads to the knowledge of I_B^{lim} via *equation 4.112a* & subsequently the diffusion coefficients of species B. The evaluation of I_C^{lim} is relatively simple. By scanning well past the cathodic wave (for slow ET, potential MUST be scanned about 1.0V more negative than E° or $E_{1/2}$), *equation 4.111* reduces simply to $I_1 = I_C^{\text{lim}}$. As a consequence, the diffusion coefficient of species C e.g. D_C can be obtained without any difficulty. If species C is initially absent, then $I_C^{\text{lim}} = 0$ & D_C is unobtainable. Hence, by evaluating the values of I_1 & I_2 corresponding to the potential where the returning current wave crosses zero ($i = 0$), $E_{1/2}$ can readily be calculated via *equation 4.111 or 4.111a*.

Figures 4.40-43 show plots of various data sets of obtained for a CE system with fast ET ($k^\circ = 10\text{ms}^{-1}$), $k_f = k_b = 1.0 \text{ s}^{-1}$ & $E_{1/2} = 0.5\text{V}$ & at a sweep rate of 1 Vs^{-1} . Note the alignment of the peaks on the plot dI_1/dE vs E - an indication of fast ET. Again, the peak heights are not equal which is a strong indication of the involvement of homogeneous kinetics apart from the electrode kinetics. Results for a CE system with slow ET ($k^\circ = 10^{-6} \text{ ms}^{-1}$) are shown in *Figures 4.44, 4.55, 4.46 & 4.47*. In *Figures 4.48 & 4.49* the calculated values of K are displayed against the corresponding test values of k_c for two different pairs of simulated data. The intersections yield the TRUE values of K & k_c , which are exactly the same as those entered for the simulation.

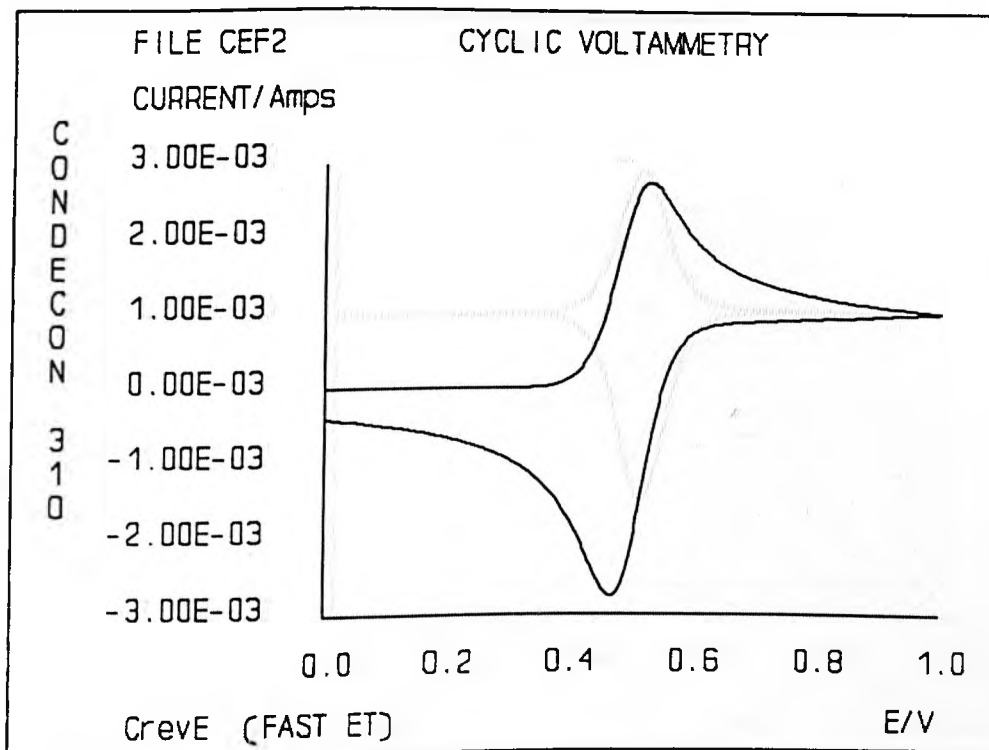


Figure 4.40 Cyclic voltammogram for a $C_{rev}E$ reaction with fast ET, $k^0 = 100\text{ms}^{-1}$, $D = 10^{-8}\text{m}^2\text{s}^{-1}$, $\alpha = 0.5$, $k_f = k_b = 1\text{s}^{-1}$

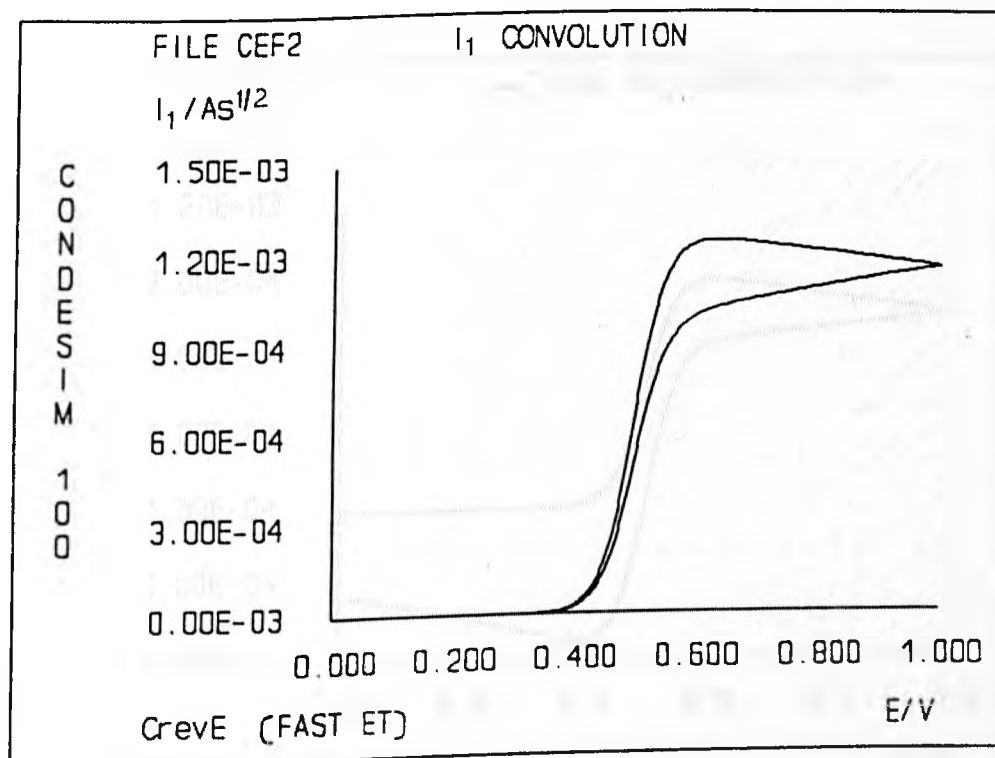


Figure 4.41 The I_1 convolution of a CE reaction does not maintain constant at potentials "past" the wave but returns to zero on the returning journey as $C_c \propto I_1$

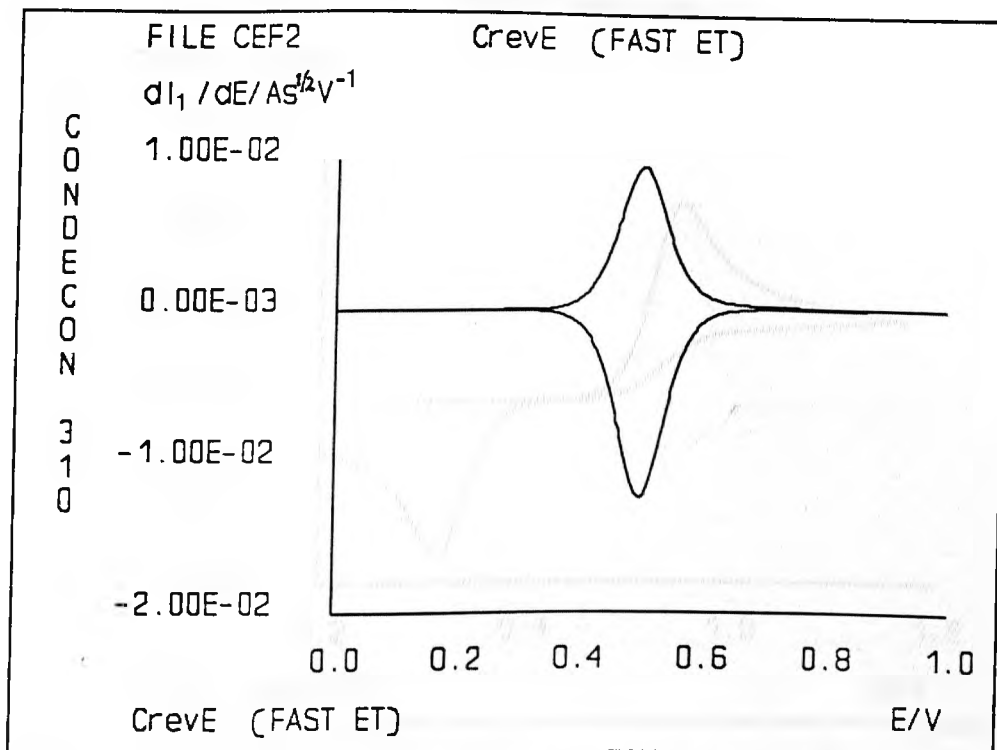


Figure 4.42 Though the peaks of the dI_1/dE vs E plot are aligned the peak heights are considerably different due to the preceding homogeneous kinetics

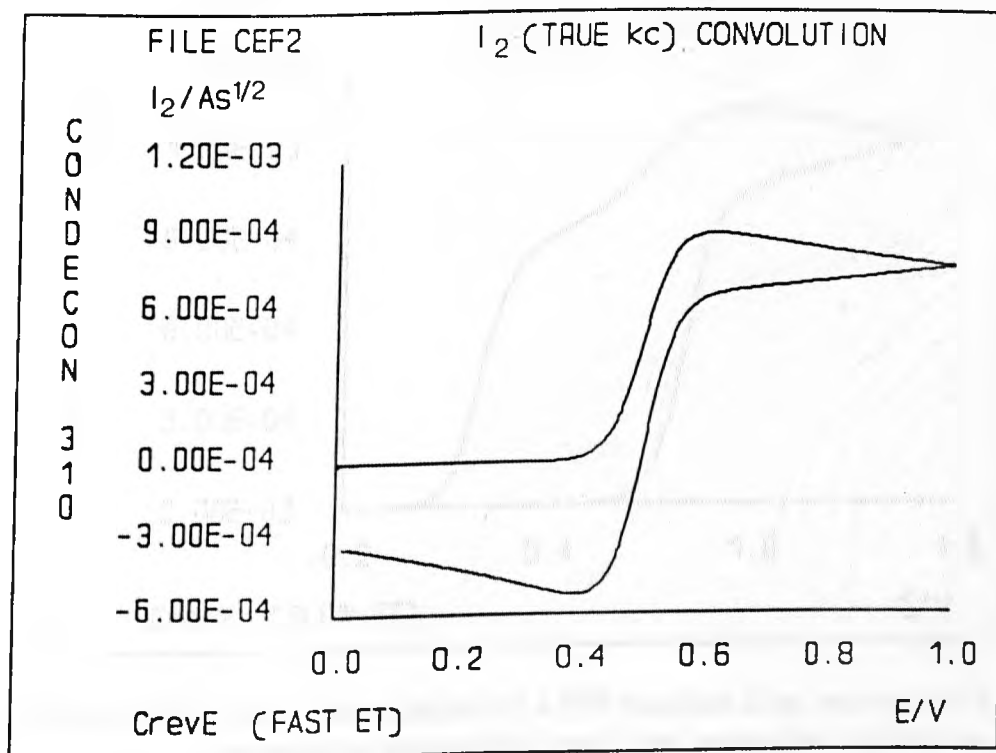


Figure 4.43 Plot of I_2 convolution (k_c TRUE) vs potential E .

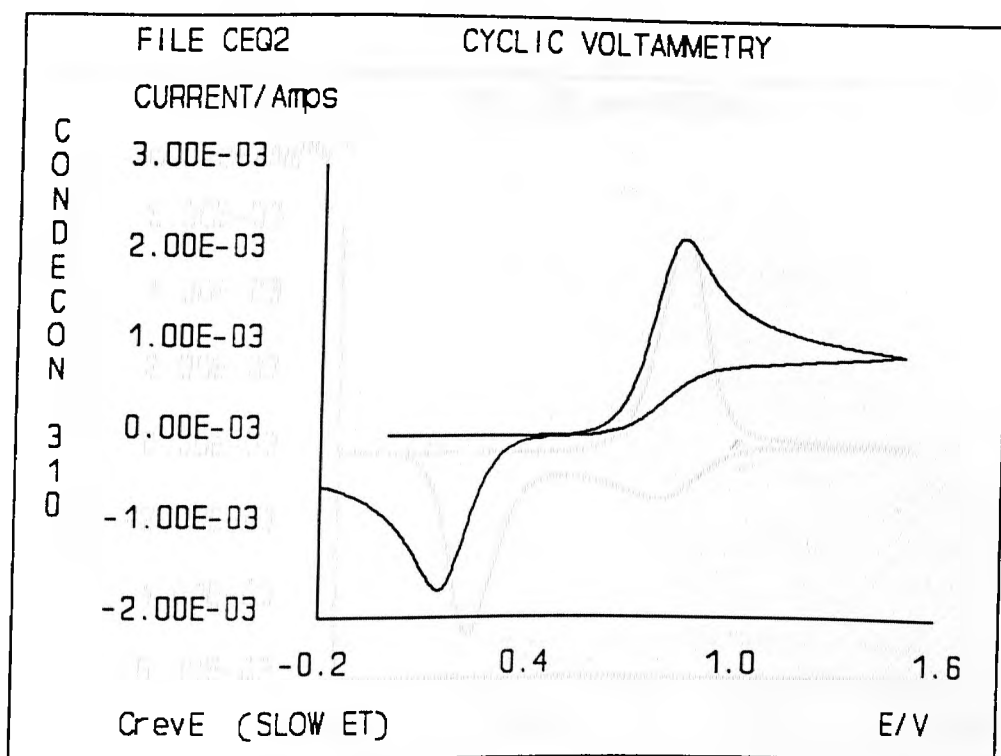


Figure 4.44 Cyclic voltammogram for a $C_{rev}E$ reaction with slow ET, $k^0 = 10\text{ms}^{-1}$, $D = 10^{-8}\text{m}^2\text{s}^{-1}$, $\alpha = 0.5$, $k_f = k_b = 1\text{s}^{-1}$

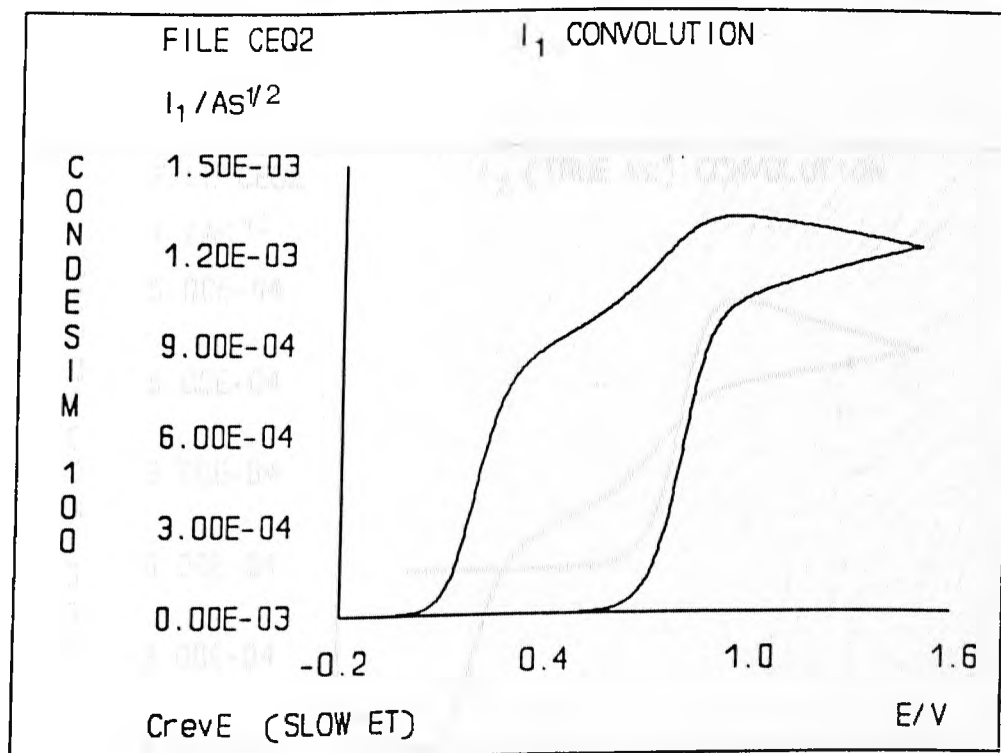


Figure 4.45 The I_1 convolution of a CE reaction does not maintain constant at potentials "past" the wave but returns to zero on the returning journey because $I_1 \propto C_c \rightarrow 0$

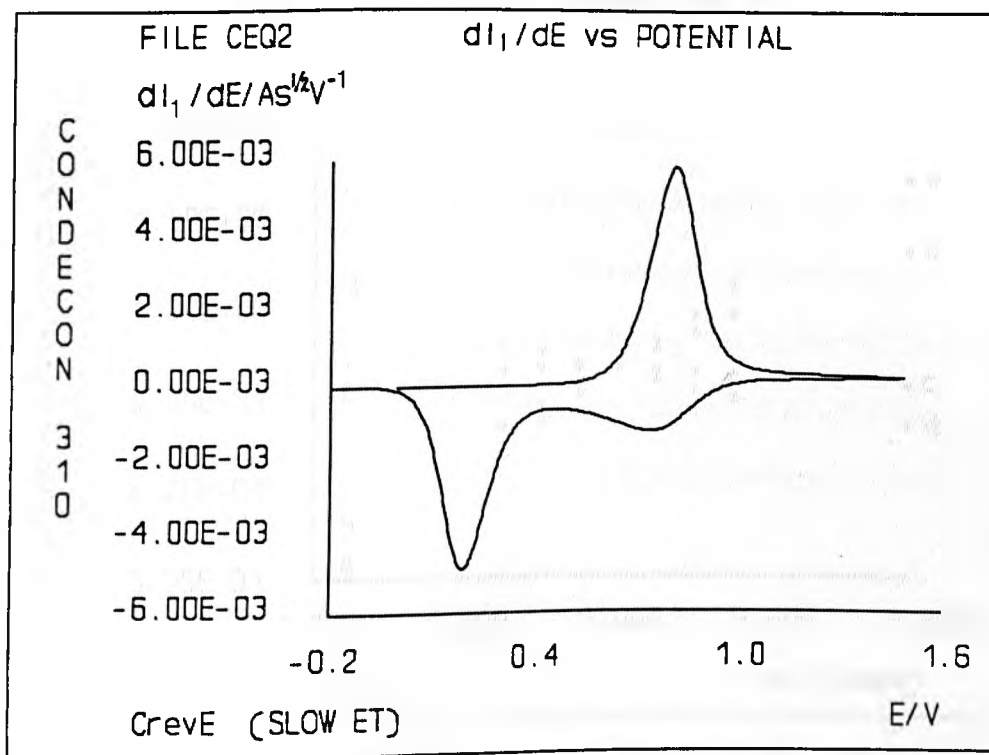


Figure 4.46 Plot of dI_1/dE vs E for a $C_{rev}E$ process with slow ET. The peaks are separated & peak heights are different.

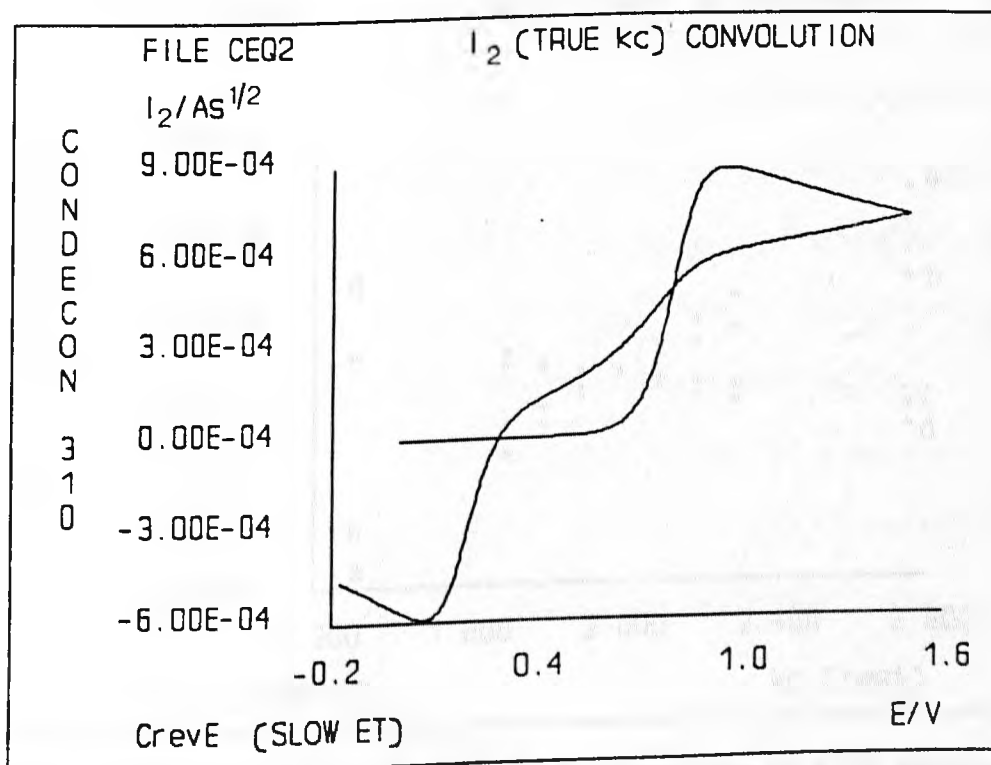


Figure 4.47 Plot of I_2 convolution (k_c TRUE) vs potential E .

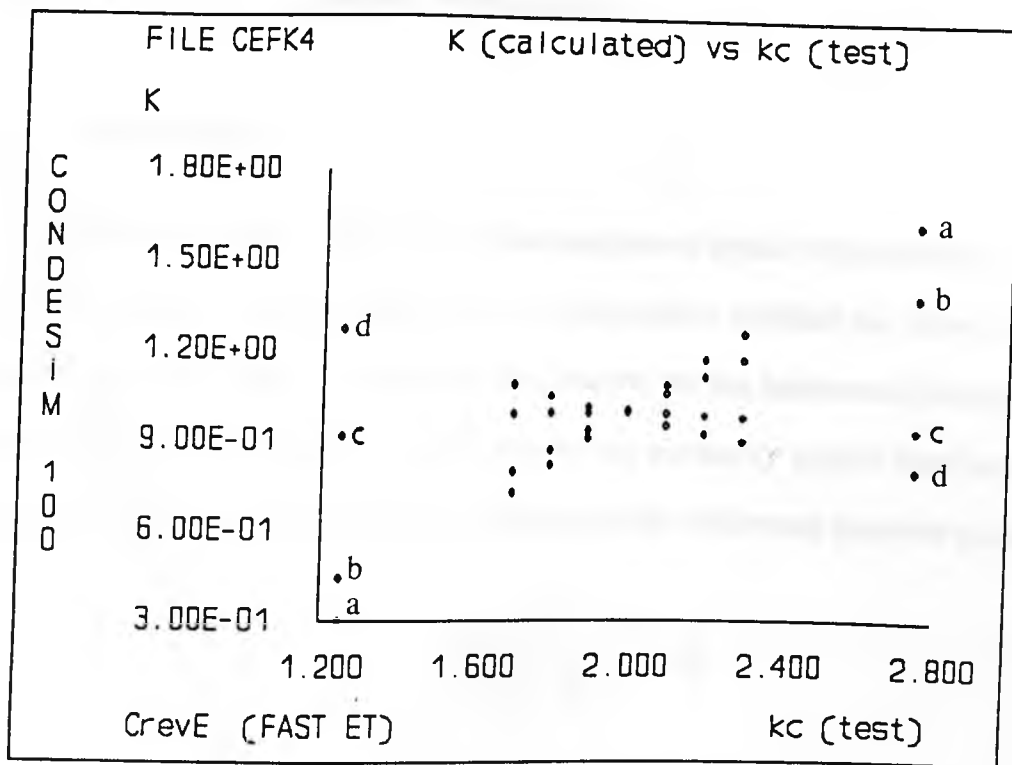


Figure 4.48 Plots of K vs k_c (test) for simulated data for a CE reaction with fast ET. K is calculated at sweep rates (V/s) of (a) 10 & 5 (b) 5 & 1 (c) 1 & 0.2 (d) 0.2 & 0.1.

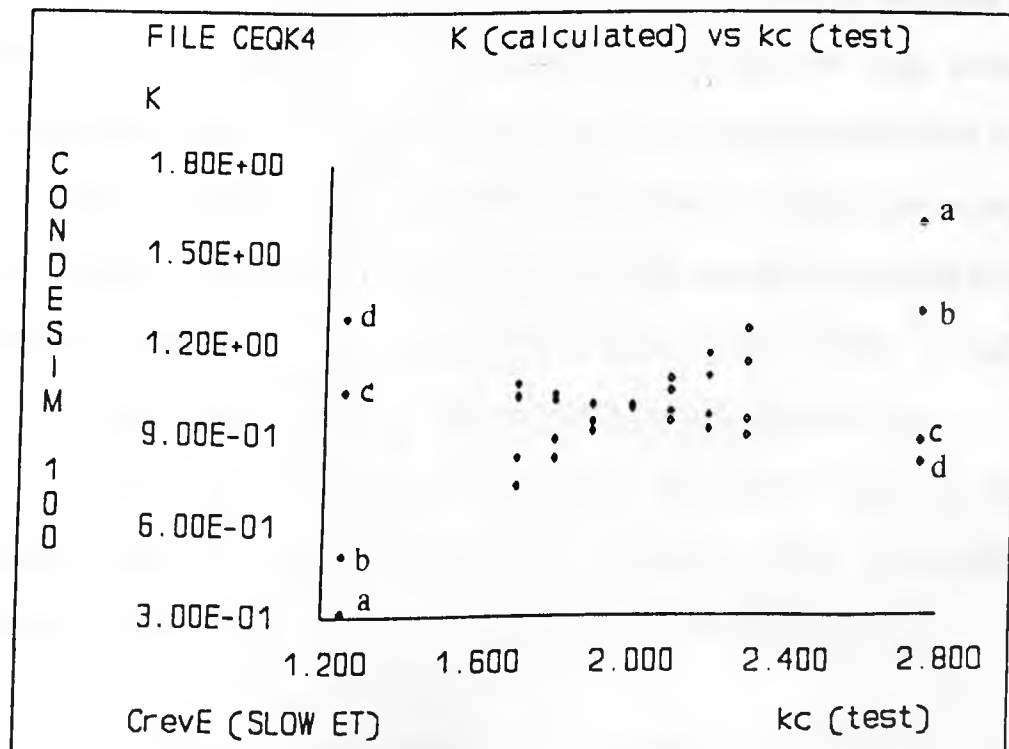
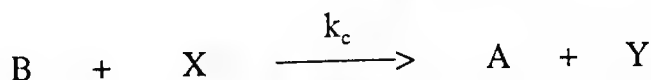
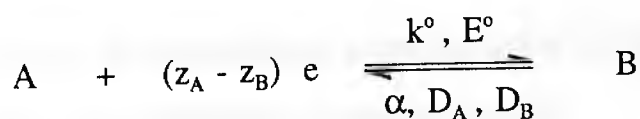


Figure 4.49 Plots of K vs k_c (test) for simulated data for a CE reaction with slow ET. K is calculated at sweep rates (V/s) of (a) 10 & 5 (b) 5 & 1 (c) 1 & 0.2 (d) 0.2 & 0.1.

4.8.2.2.3 The EC Catalytic Mechanism

A. Introduction

In this section we shall discuss the analysis of cyclic voltammetric data for the EC catalytic reaction using a new convolution method we have recently developed [238]. Due to the complexity caused by the backward homogeneous reaction, we shall confine our discussion to the relatively simple case involving irreversible homogeneous kinetics undergoing the following reaction pathways:



where the oxidising or reducing species X, present in large excess, reverses (in the solution) via a homogeneous "one-way" reaction the net electron transfer process at the electrode. As species X is present in large excess, the homogeneous reaction is a pseudo first-order reaction with an effective chemical rate constant of k_c (by incorporating the concentration of X into the second-order rate constant). The differential diffusion equations, initial & boundary conditions underlying the above system are listed in *Table 4.1 & 4.2*. Below we shall focus on the system when species B is initially absent from the solution.

A solution to these second-order partial differential equations using the Laplace transforms leads to the following expressions for the concentrations of species A & B at the electrode in terms of the convolutions:

$$C_A = C_A^{\text{BULK}} - \frac{I_1 - I_3}{(z_B - z_A)FA\sqrt{D_A}} \quad (4.113)$$

$$C_B = \frac{I_2}{(z_B - z_A)FA\sqrt{D_E}} \quad (4.114)$$

where I_1 is the "semi-integral" of current (eqn. 4.88) as described in section 4.8.1, I_2 the "kinetic convolution" (cf. eqn. 4.103) which encompasses both the current & the homogeneous chemical kinetics $k_c (= k_f + k_b)$, whilst the term I_3 is a new type of convolution defined as follows:

$$I_3(t) = \int_0^t i(u) \phi(t-u) du \quad (4.115)$$

Here the term $\phi(t)$ has different expressions depending on the relative magnitude of the diffusion coefficients of species A & B:

$$D_A = D_B : \quad \phi(t) = \frac{1 - e^{-k_c t}}{\sqrt{\pi t}} \quad (4.116)$$

$$D_A > D_B : \quad \phi(t) = \frac{2a}{\sqrt{\pi}} \left[F(a\sqrt{t}) - e^{-k_c t} F(b\sqrt{t}) \right] \quad (4.117)$$

$$D_A < D_B : \quad \phi(t) = -\frac{2a}{\sqrt{\pi}} \left[G(a\sqrt{t}) - e^{-k_c t} G(b\sqrt{t}) \right] \quad (4.118)$$

where a & b are the positive quantities:

$$a = \sqrt{D_A k_c / |D_B - D_A|} \quad \& \quad b = a\sqrt{d} \quad \text{with} \quad d = D_B / D_A \quad (4.119)$$

and the functions F & G are defined by:

$$F(x) = e^{-x^2} \int_0^x e^{\lambda^2} d\lambda \quad \text{i.e. 'Dawson's integral'} \quad (4.120)$$

$$G(x) = e^{x^2} \int_0^x e^{-\lambda^2} d\lambda = \frac{\sqrt{\pi}}{2} e^{x^2} \text{erf}(x) \quad (4.121)$$

In the important limiting case where $|D_A - D_B| \rightarrow 0$ (i.e. the frequently encountered situation in which the diffusion coefficients of A & B are nearly the same), it becomes very difficult to evaluate numerically *equations 4.117 & 4.118*. As a consequence, an approximate form is proposed here:

$$\phi(t) \approx \frac{1 - e^{-k_d t}}{\sqrt{\pi t}} - \frac{d - 1}{2k_c} \frac{1 - e^{-k_d t}}{\sqrt{\pi} t^{3/2}} \quad (4.122)$$

Obviously, in the special case where $D_A = D_B$ i.e. $d=1$, the above equation reduces exactly to *equation 4.116*. This demonstrates the consistency of the above approximate form with the exact treatment described earlier.

B. Numerical Evaluation of the I_3 Convolution

In general, the numerical integration of *equation 4.115* (I_3) can be accomplished in a similar fashion to I_1 & I_2 convolution via the use of the Trapezoidal or Simpson's rule (*cf. Section 4.8.1*). In the special case where the diffusion coefficients of species A & B are equal i.e. $D_A = D_B$, the calculation of the I_3 convolution is very simple since by comparing *equation 4.117* with the definition of the I_1 & I_2 convolutions (*cf. eqns. 4.88 & 4.103*), one finds that $I_3 = I_1 - I_2$! On the other hand, as is demonstrated by *equations 4.117-122*, the evaluation of the I_3 convolution at unequal diffusion coefficients, especially when $|D_A - D_B|$ is sufficiently large, is relatively complex & necessitates the initial evaluation of the function $\phi(t)$ under various circumstances. Below we shall briefly discuss the strategies for the evaluation of *equations 4.117 & 4.118*.

B.1 $D_A > D_B$ ($d < 1$)

Substituting *equations 4.119 & 4.120* into *equation 4.117* & subsequent

rearrangement yields the following expression for the function $\phi(t)$:

$$\phi(t) = 2 (r/\pi)^{1/2} [F((rt)^{1/2}) - F((dr)^{1/2})] \quad (4.117a)$$

where $r = k_c/(1-d)$.

A brief description of the numerical evaluation of Dawson's integral $F(x)$ is given below. When the x is either small or very large, Dawson's integral can be evaluated via the following simple series [239]:

$$F(x) = x(1 - 2x^2/3 + 4x^4/15 - 8x^6/105 + 16x^8/945 - \dots) \quad \text{for } x \leq 1 \quad (4.123)$$

$$F(x) = 1/(2x) + 1/(4x^3) + 3/(8x^5) + 15/(16x^7) + 105/(32x^9) + \dots$$

(semi-convergent) (x ≥ 6) (4.124)

In the region $1 \leq x \leq 6$, a more complex series form is employed:

$$F(x) = (\sqrt{\pi}/2) e^{-x^2} \tan\left[\frac{\pi}{2\sqrt{s}}\right] - 2\sqrt{s/\pi} \sum e^{-m^2 s x^2} / (m^2 s - 1) \quad (4.125)$$

where $m (= 1,3,5,7 \dots)$ is an odd number, & s is a x -dependent coefficient chosen to enable the error of the approximation to be less than an accuracy criterion. For example, in each computation if s is given the value $0.1/x^2$, the error of the approximation is always less than 5×10^{-12} .

It is worth mentioning that there exist certain regions where $(m^2 s - 1) \rightarrow 0$, which make the above numerical process unworkable. As a result, a special treatment is developed to overcome the inefficiency of *equation 4.125*.

B.2 $D_A < D_B$ ($d > 1$)

Substituting *equations 4.119 & 4.121* into *equation 4.118* & further rearrangement yields the following expression for the function $\phi(t)$:

$$\phi(t) = - r^{1/2} e^{\pi} [\operatorname{erf}(\pi t)^{1/2} - \operatorname{erf}(d\pi t)^{1/2}] \quad (4.118a)$$

where $r = k/(d-1)$.

The numerical evaluation of *equation 4.118a* requires the knowledge of the two terms containing the error function $\operatorname{erf}(x)$. This can readily be achieved via the initial evaluation of the error function complement $\operatorname{erfc}(x)$ using standard digital routines (such as those based on the 'continued fraction' algorithm) listed in standard numerical handbooks [240-1].

C. Current-overpotential Characteristic in Terms of Convolution

As mentioned earlier, the current-overpotential relationship (*cf. eqn. 4.31 in Section 4.5.1*) applies to ANY type of electrode process (with/without coupled homogeneous reaction & multiple electron transfers, for example). On the other hand, the solution of the differential diffusional equation for an EC catalytic reaction via the Laplace transforms yields the surface concentrations of species A & B in terms of various types of convolution (*cf. eqns. 4.113 & 4.114*). Thus, substituting *equations 4.113 & 4.114* for the surface concentrations in *equation 4.31* followed by standard mathematical manipulations, we have, for an EC catalytic reaction, the following expression for the resulting faradaic current:

$$i = I_A^{\lim} \frac{k^{\circ} e^{-\alpha p}}{D_A^{1/2}} - (I_1 - I_3) \frac{k^{\circ} e^{-\alpha p}}{D_A^{1/2}} - I_2 \frac{k^{\circ} e^{(1-\alpha)p}}{D_B^{1/2}} \quad (4.126)$$

where $I_A^{\lim} = (z_B - z_A) F A \sqrt{D_A} C_A^{\text{BULK}}$, $p = (z_A - z_B) F (E - E^{\circ}) / RT$.

Further rearrangement yields:

$$\frac{\sqrt{D_A}}{k^{\circ}} e^{\alpha p} i = I_A^{\lim} - (I_1 - I_3) - I_2 e^{\xi} \quad (4.126a)$$

where $\xi = (z_A - z_B)F(E - E_{1/2})/RT$.

The above equation (eqn. 4.126 & 4.126a) is the general portrayal of the current-potential relationship & applies to ANY rate of electron transfer, homogeneous chemical ('catalytic') kinetics & ANY variations of diffusion coefficients for species A & B. Below we shall discuss briefly the application of these equations to various particular situations. To simplify the problem we are dealing with, discussions will be confined to the FAST electron transfer (Nernstian case) system ONLY.

D. Analysis of Cyclic Voltammetric Data for EC_{cat} Reactions

D.1 Equal Diffusion Coefficients eg $D_A = D_B$

In the simplest case where the diffusion coefficients of the two species are equal, $I_3 = I_1 - I_2$. Taking into account the FAST nature of the electron transfer e.g. $i/k^0 \rightarrow 0$, equation 4.126a reduces to:

$$I_A^{\text{lim}} - I_2 - I_2 e^{\xi} = 0 \quad (4.127)$$

Thus a very important feature for the EC catalytic (FAST ET) mechanism can be obtained:

$$I_2 = \frac{I_A^{\text{lim}}}{1 + e^{\xi}} \quad (4.127a)$$

As can be seen above, when calculated using the TRUE value of k_c , I_2 SHOULD display a shape of the typical POLAROGRAPHIC current wave in a similar fashion to the I_1 convolution for a Nernstian simple electron transfer process (cf. Section 4.8.2.1.1). In short, the I_2 convolution (k_c TRUE) should OVERLAY itself as a function of potential & approach I_A^{lim} at potentials well 'PAST' the

current wave. The 'HALF WIDTH' of the derivatives of I_2 e.g. dI_2/dE is exactly the same as that for I_1 of a Nernstian simple electron transfer reaction. For an EC_{cat} (FAST ET) reaction, the 'half width' (ΔE) of dI_2/dE is $90.579/n$ mV (n is the number of electrons involved in the electrode process) at 298.15K. This behaviour can be more conveniently TESTED via further rearrangement of the above equation to produce the logarithmic type relationship:

$$\text{Ln} \left[\frac{I_A^{\text{lim}} - I_2}{I_2} \right] = \frac{(z_A - z_B) F}{RT} (E - E_{1/2}) \quad (4.128)$$

or

$$E = E_{1/2} + \frac{RT}{(z_A - z_B)F} \text{Ln} \left[\frac{I_A^{\text{lim}} - I_2}{I_2} \right] \quad (4.128a)$$

The above 'polarographic' or Heyrovsky-Ilkovich type relationship presents a critical test for the EC catalytic (FAST ET & equal diffusion coefficients) & parameters e.g. homogeneous chemical rate constant k_c , 'half wave' potential $E_{1/2}$ (here equal to E°) & the number of electrons can be immediately evaluated by plotting the logarithmic function $\text{Ln} \left[(I_A^{\text{lim}} - I_2)/I_2 \right]$ against the potential.

Similarly, the symmetrical behaviour of dI_1/dt (or dI_1/dE) vs E plot observed in the Nernstian type simple electron transfer reaction should also be anticipated for I_2 (k_c TRUE) in EC catalytic reactions with FAST ET & equal diffusion coefficients.

Figure 4.50 shows the original i - E responses of EC catalytic reactions with different rates of homogeneous kinetics in comparison with the Nernstian type simple electron transfer reaction, while a series of tests for the simulated data based on the above numerical (analytical) development are illustrated in *Figures 4.51-4.55*. As can be seen, the plot of I_1 convolution vs potential does not show any sign of the typical polarographic behaviour for a Nernstian type simple

electron transfer process, obviously due to the interference of the homogeneous chemical kinetics with the diffusion fields of the TWO electroactive species as is also the case in the EC & CE mechanisms. Again, similar to the EC & CE reaction (with FAST ET), the perfect alignment of the two peaks of the dI_1/dE vs E plot gives an strong indication of fast electron transfer. As is expected from equation 4.127a, for an EC_{cat} reaction with fast ET & equal diffusion coefficients, the I_2 calculated from the appropriate value of k_c should display the shape of a polarographic wave. This suggests an immediate route to the evaluation of k_c via the plateau behaviour 'after' the wave. An alternative test, based on Heyrovsky-Ilkovich relationship (eqn. 4.128), of the polarographic behaviour is shown in *Figure 4.55*. The crossing of the E axis at zero value of the logarithmic function gives immediately the value of the "half wave" potential $E_{1/2}$ – here 0.4987V as compared with the EXACT value of 0.5V. On the other hand, the slope gives accurately the charge transfer coefficient α as 0.5007 which is once again very close to the true value of 0.5. Another test of the polarographic behaviour of I_2 for equal D is accomplished by the plot of dI_2/dE vs E , which is ultimately based on the differentiation & further development of *equation 4.127a*. As is indicated in *Figure 4.54*, the symmetrical behaviour of dI_2/dE as a function of E is also clearly evident. The centre of the peaks also gives accurately the value of the "half wave" potential.

To summarize, the agreement of the above tests with theoretical expectations reveals the high accuracy of the DIGITAL simulation techniques developed earlier in this work.

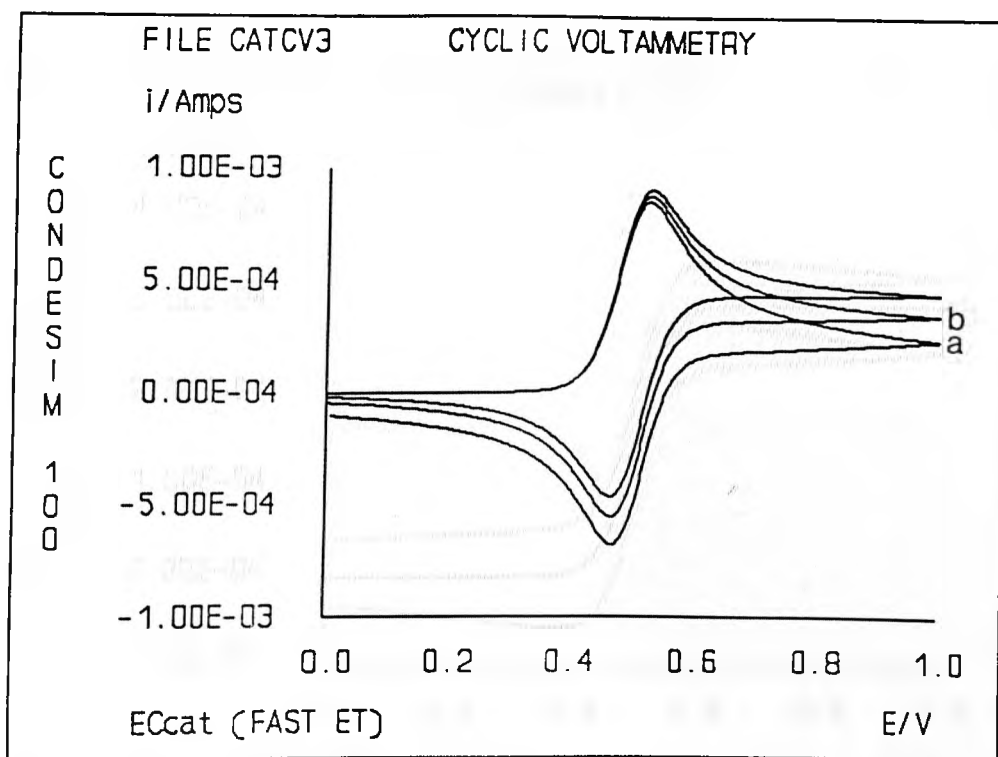


Figure 4.50 Cyclic voltammograms for EC_{cat} & E processes with FAST ET. $v = 1Vs^{-1}$. k_f (s^{-1}): (a) 0 (b) 1.0 (c) 2.0

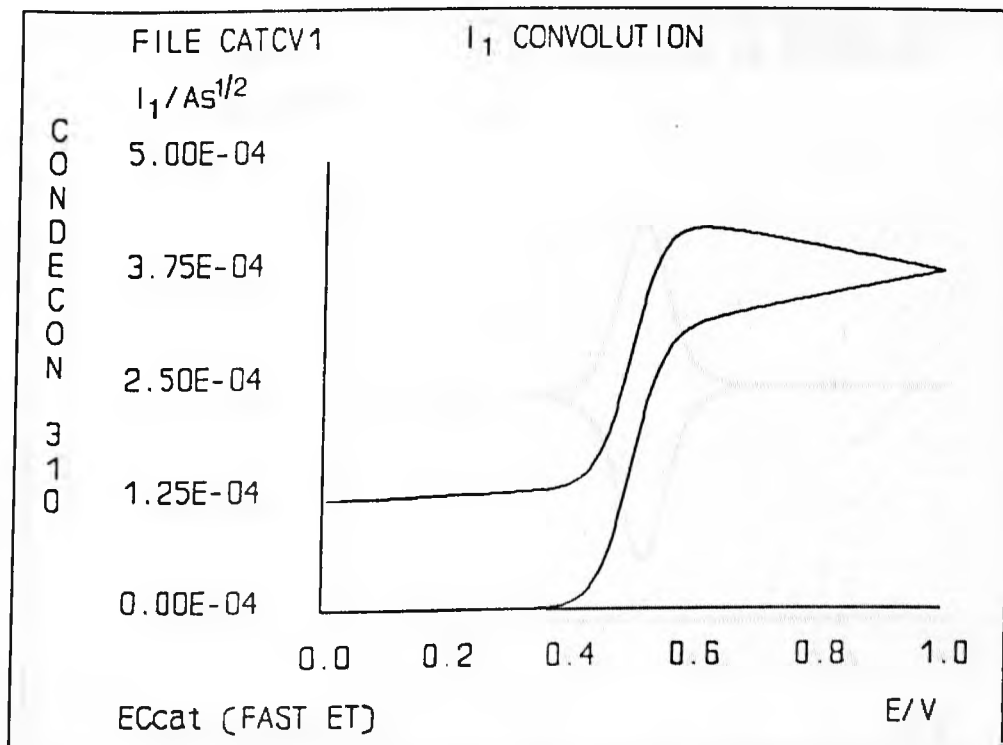


Figure 4.51 The plot of I_1 convolution vs E for an EC_{cat} process is significantly different from the polarographic wave

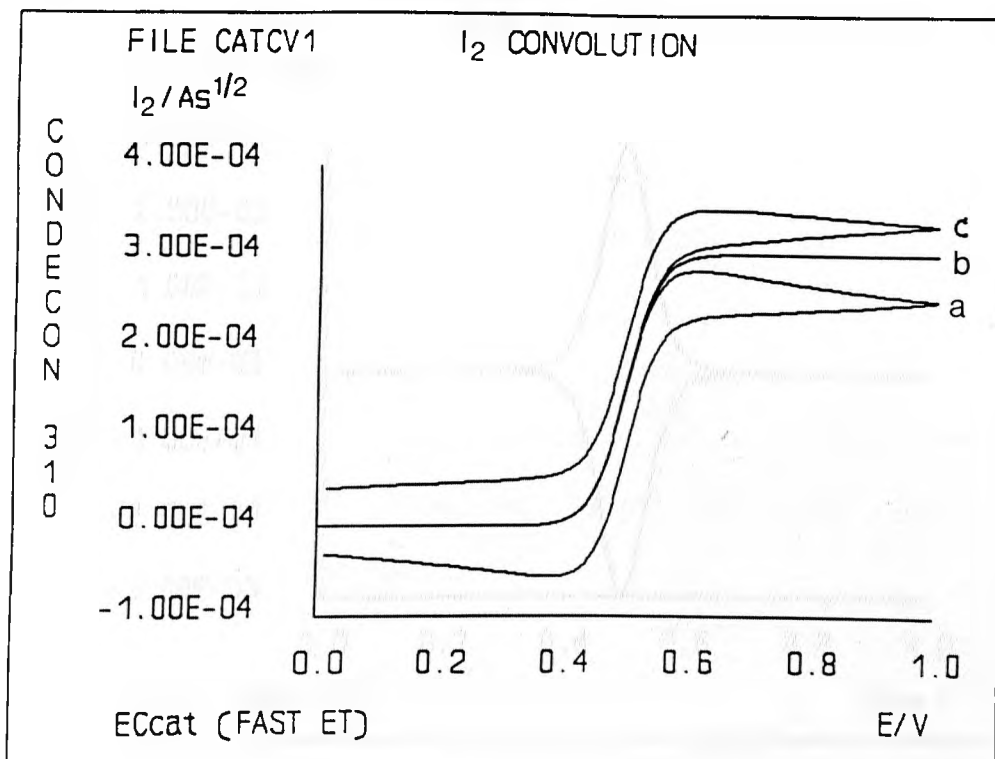


Figure 4.52 Plots of I_2 vs E . Test values of k_c (s^{-1}) are (a) 2.0 (b) 1.0 (TRUE k_c) & (c) 0.5. Note the polarographic behaviour of I_2 for true k_c .

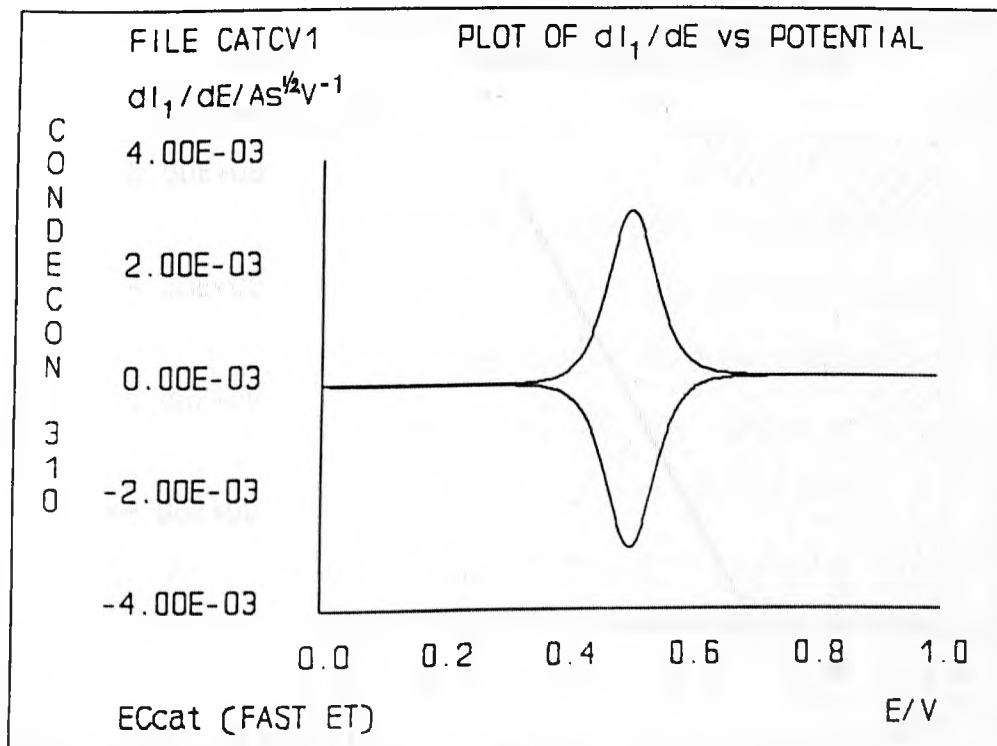


Figure 4.53 The dI_1/dE vs E displays TWO strictly aligned peaks centred on the "half wave" potential $E_{1/2}$ - a strong indication of FAST electron transfer.

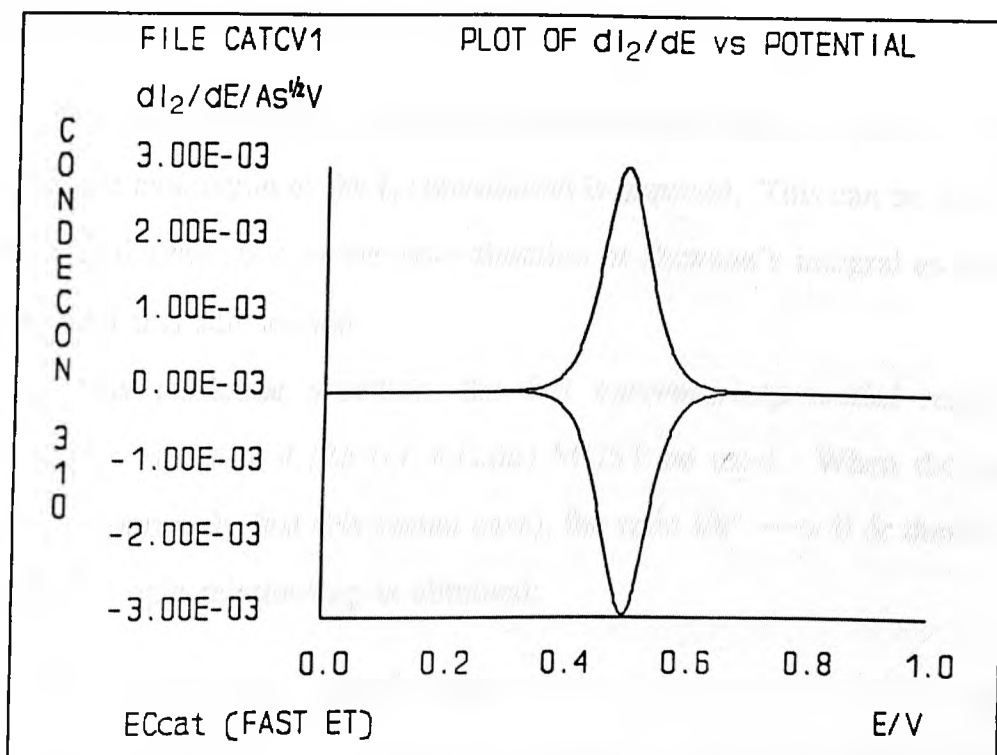


Figure 4.54 The dI_2/dE vs E plot displays two strictly symmetrical peaks centred on the "half wave" potential $E_{1/2}$. A critical test for the polarographic behaviour of I_2 .

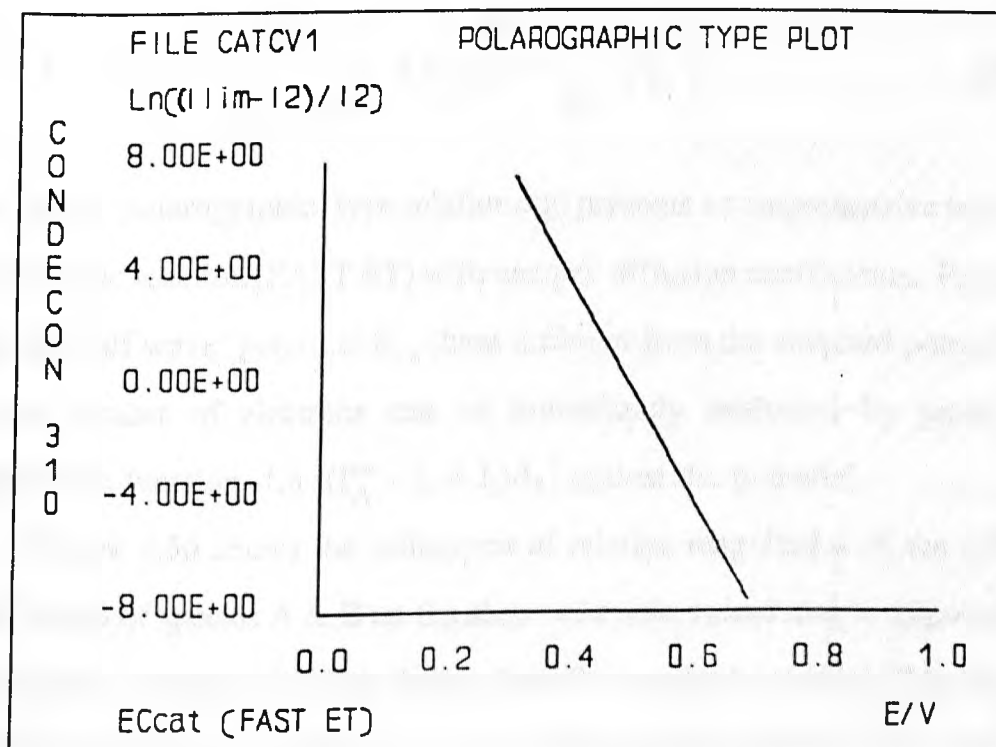


Figure 4.55 Plot of $\ln[(I_A^{lim} - I_2)/I_2]$ vs potential for EC_{cat} with fast ET - an alternative test of polarographic behaviour of the I_2 convolution

D.2 Unequal Diffusion Coefficients

As mentioned earlier, when the diffusion coefficients of species A & B are unequal, the evaluation of the I_3 convolution is required. This can be done either by the initial evaluation of the error function or Dawson's integral as discussed in part B of this sub-section.

In this particular situation, the full *current-overpotential* relationship described in *equation 4.126 (or 4.126a)* MUST be used. When the electron transfer is extremely fast (Nernstian case), the ratio $i/k^\circ \rightarrow 0$ & therefore the following simple relationship is obtained:

$$I_A^{\text{lim}} - (I_1 - I_3) - I_2 e^\xi = 0 \quad (4.129)$$

Rearrangement of the above produces the logarithmic type relationship:

$$\text{Ln} \left[\frac{I_A^{\text{lim}} - (I_1 - I_3)}{I_2} \right] = \frac{(z_A - z_B) F}{RT} (E - E_{1/2}) \quad (4.130)$$

or

$$E = E_{1/2} + \frac{RT}{(z_A - z_B)F} \text{Ln} \left[\frac{I_A^{\text{lim}} - (I_1 - I_3)}{I_2} \right] \quad (4.131a)$$

The above 'polarographic' type relationship presents a comprehensive test for the EC catalytic reaction (FAST ET) with unequal diffusion coefficients. Parameters e.g. the 'half wave' potential $E_{1/2}$ (here different from the standard potential E°) & the number of electrons can be immediately evaluated by plotting the logarithmic function $\text{Ln} \left[(I_A^{\text{lim}} - I_1 + I_3)/I_2 \right]$ against the potential.

Figure 4.56 shows the influences of relative magnitudes of the diffusion coefficients of species A & B on the shape of cyclic voltammetric responses. As can be seen, the peak positions depart from the standard potential E° in the cases of unequal diffusion coefficients. The shifts of peak positions are 29.61 mV before E° & 29.51 mV after E° for D_A/D_B of 0.1 & 10, respectively. Here, they

are very close to the theoretical values of ± 29.58 mV at 298.15K for $n = 1$. A series of tests on the simulated cyclic voltammetry data is presented in *Figures 4.57-62 & Figures 4.63-68* for $D_A/D_B = 0.1$ & 10, respectively.

The evaluation of homogeneous chemical rate constant k_c for an EC_{cat} reaction with UNEQUAL diffusion coefficients is very similar to that for an EC_{irrev} reaction. By varying the test values of k_c for the evaluation of the I_2 convolution, one can readily find out the TRUE k_c . The criterion is ultimately based on the returning to zero of the I_2 convolution at potential region just 'before' the wave on the return potential scan. This is because, the I_2 convolution is directly proportional to the surface concentration of species B via equation 4.114 & in the Nernstian case this concentration should fall rapidly to zero due to the dramatic increase of the backward heterogeneous rate at potentials before the wave (*cf. Figures 4.57 & 63*). On the other hand, as the term $(I_1 - I_3)$ reflects the 'departure' of the surface concentration of species A from the corresponding BULK value, a plateau (limiting value) of the plot of $(I_1 - I_3)$ vs E should be anticipated at potential regions well pass the wave on the forward scan (*cf. Figures 4.60 & 4.66*). Therefore, the diffusion coefficient of species A & the ensuing value of D_B can be numerically evaluated.

Figures 4.62 & 4.68 illustrate the polarographic type plots (*cf. eqn. 4.130*) for D_A/D_B values of 0.1 & 10, respectively. Note that in BOTH plots, the I_2 convolutions are evaluated with the appropriate k_c values & the I_3 convolutions with the proper value of D_B/D_A (d). As is shown in both plots, the linearity & overlay of the forward & backward potential scan are evident. The crossing of the E axis at zero value of the logarithmic function gives immediately the "half wave" potential $E_{1/2}$ — here 0.47067V & 0.52849V as compared with the theoretical values of 0.47042V & 0.52958V for $D_A/D_B = 0.1$ & 10, respectively. The slopes of these linear lines give accurately the charge transfer coefficients (α) as 0.50002 & 0.50004 which are very close to the true values of 0.5.

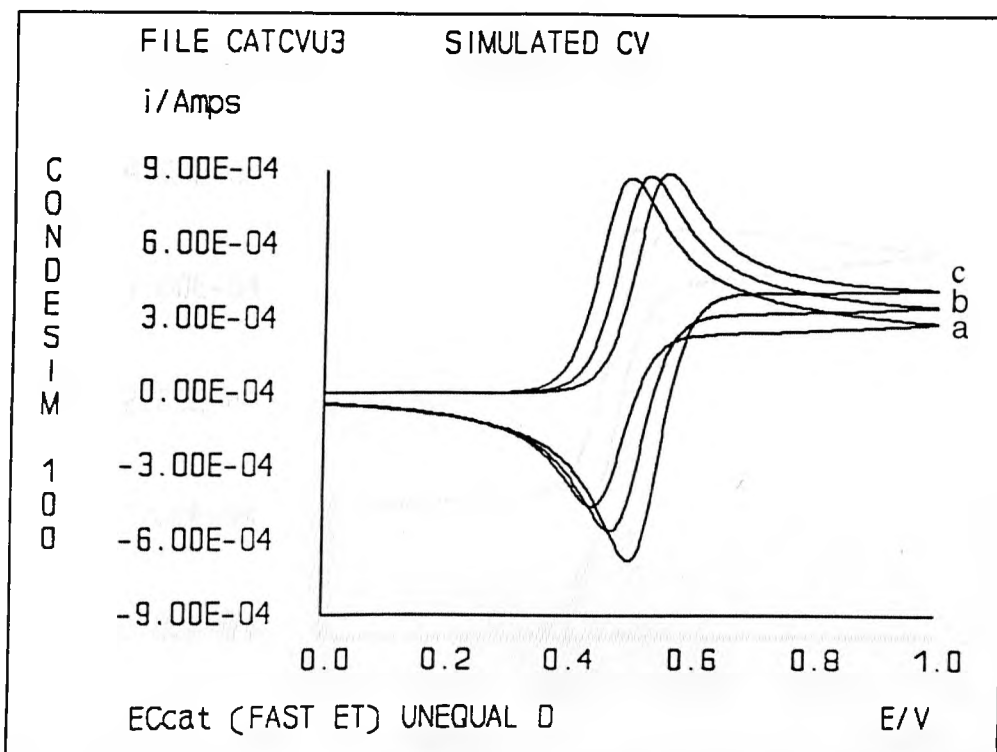


Figure 4.56 Cyclic voltammograms for an EC_{cat} process with fast ET. D_A is fixed at 10^{-9} m/s with D_B varying from (a) 10^{-8} (b) 10^{-9} to (c) 10^{-10} m/s. $v = 1$ V/s.

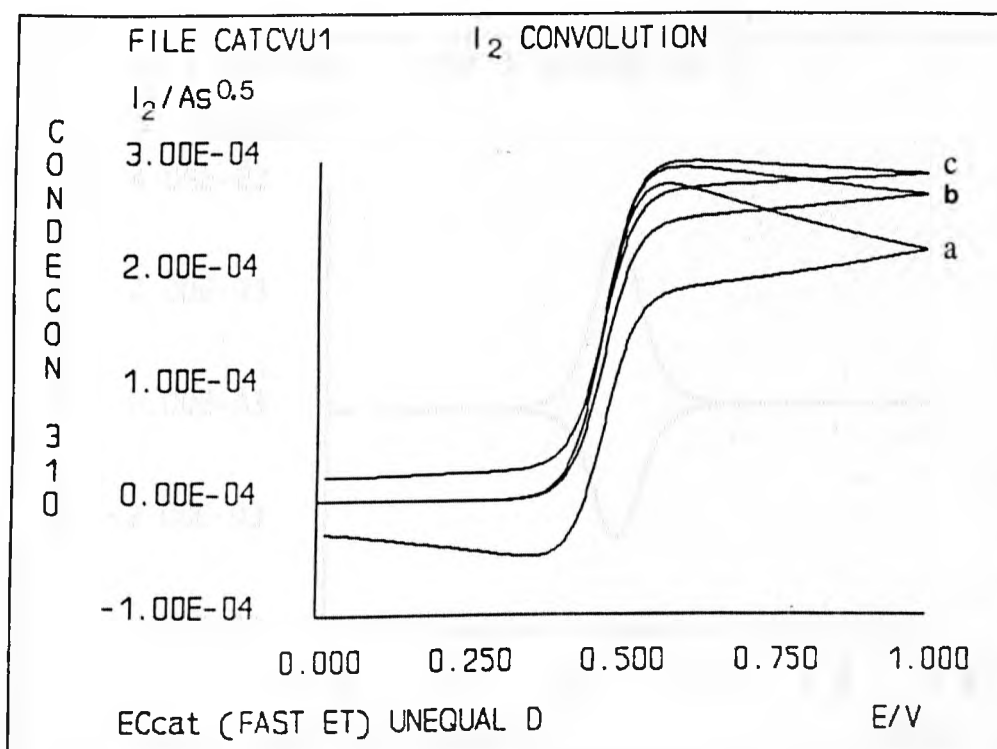


Figure 4.57 Plot of I_2 vs E for (a) of Figure 4.56. Note that when calculated with true k_c , I_2 falls to zero on the returning sweep. k_c 'test' (s^{-1}) are: (a) 2 (b) 1 (true) & (c) 0.5

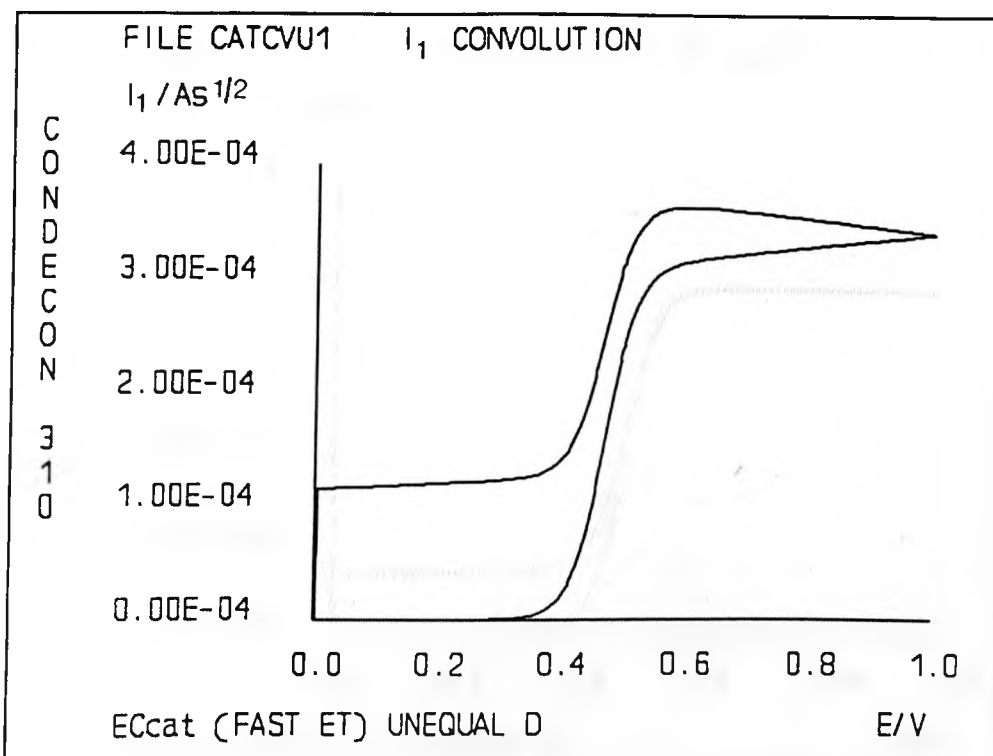


Figure 4.58 The plot of I_1 convolution vs E for an EC_{cat} process is significantly different from the polarographic wave

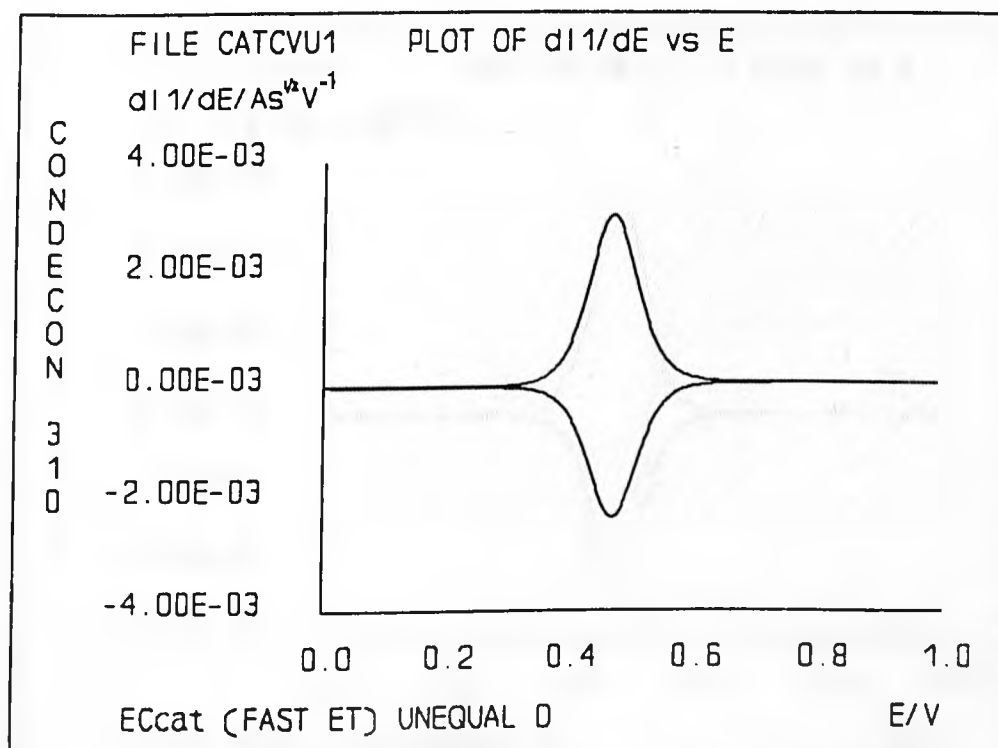


Figure 4.59 The dI_1/dE vs E displays TWO aligned peaks centred on $E_{1/2}$ - a strong indication of FAST ET. However, the peak height differs due to different D values.

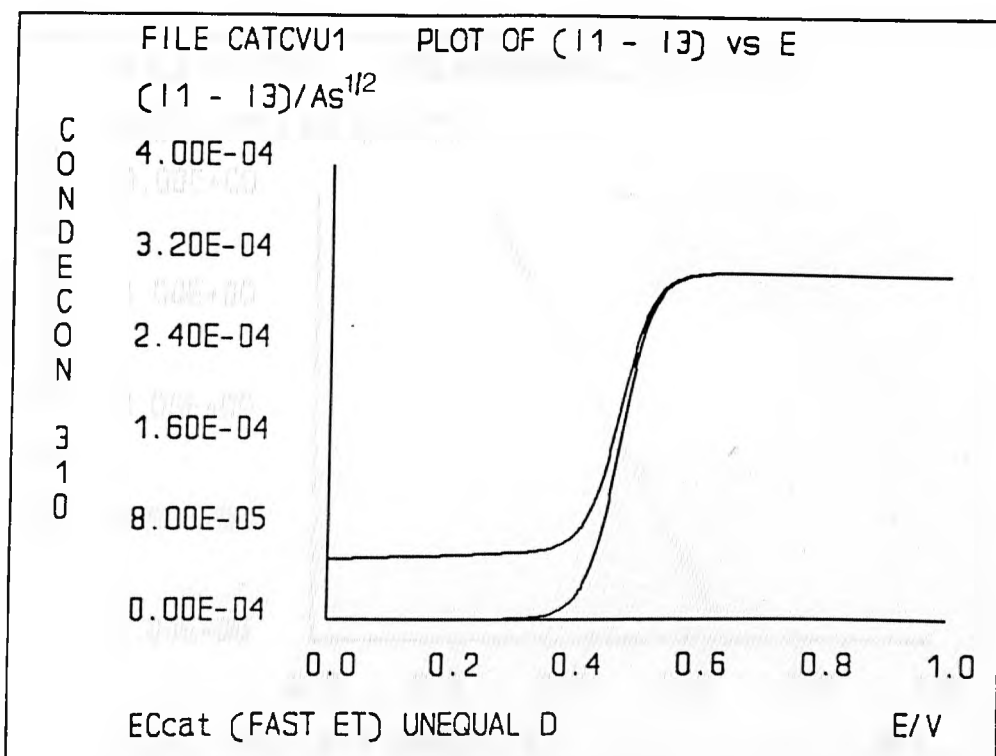


Figure 4.60 The plot of $(I_1 - I_3)$ vs E for an EC_{cat} process with $D_B > D_A$ has similar shape to I_1 vs E for an EC_{irrev} reaction.

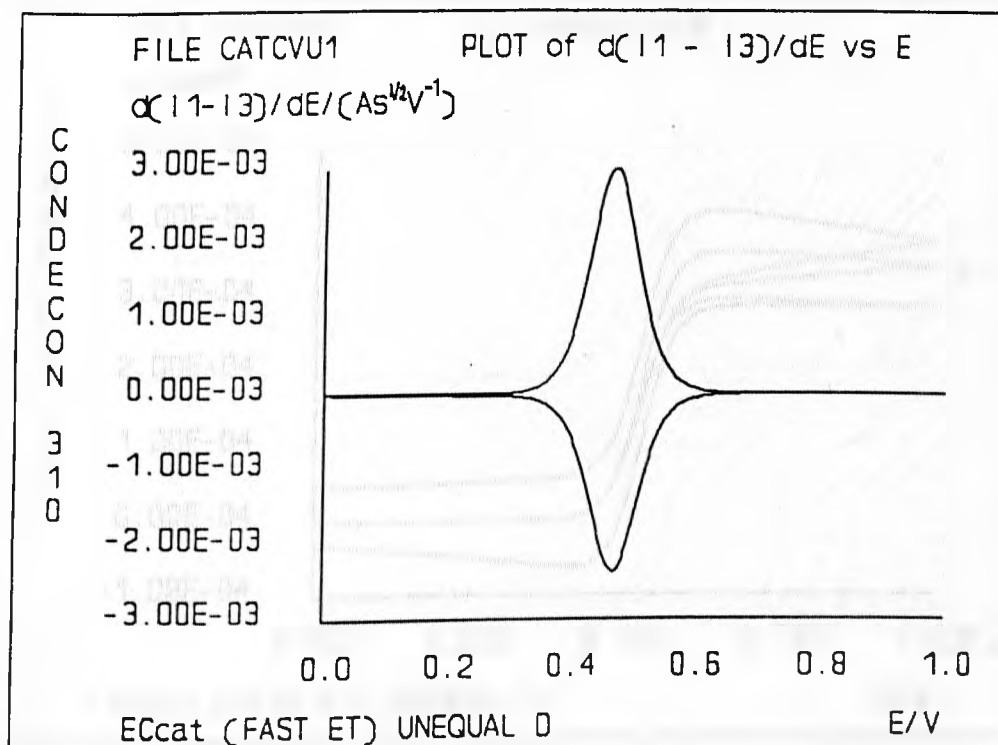


Figure 4.61 The $d(I_1 - I_3)/dE$ vs E displays two aligned peaks centred on $E_{1/2}$. The peak heights differ due to different D values.

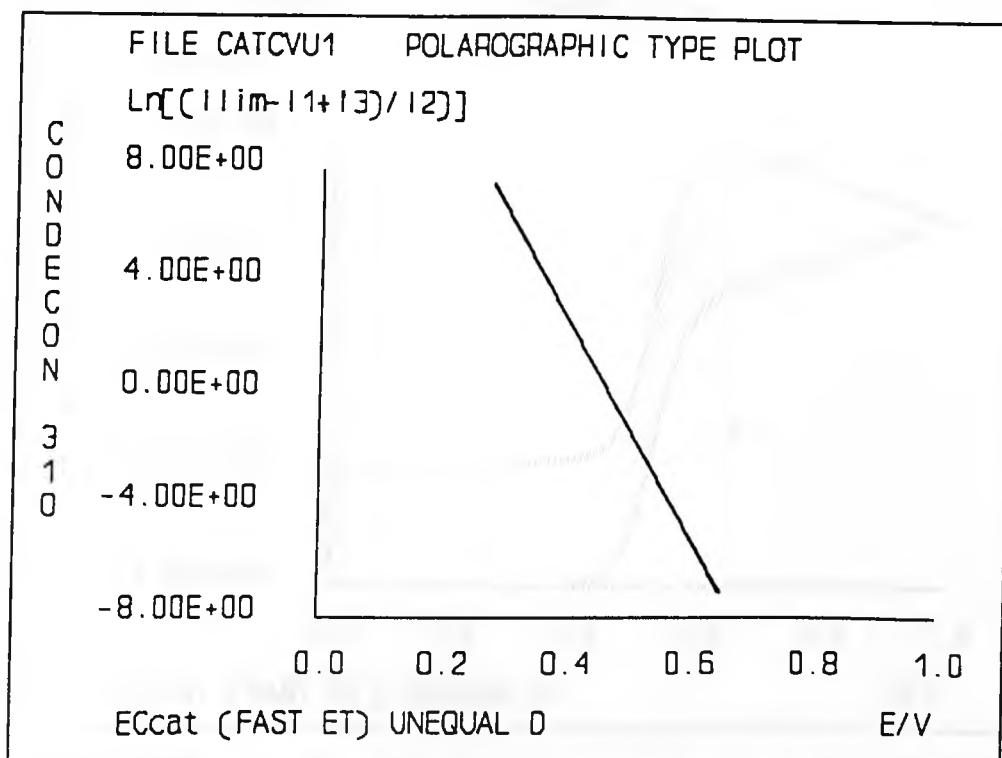


Figure 4.62 Plot of $\text{Ln} [(I_{\text{A}}^{\text{lim}} - I_1 + I_3)/I_2]$ vs potential E - linearity & overlay of the forward & return waves are evident.

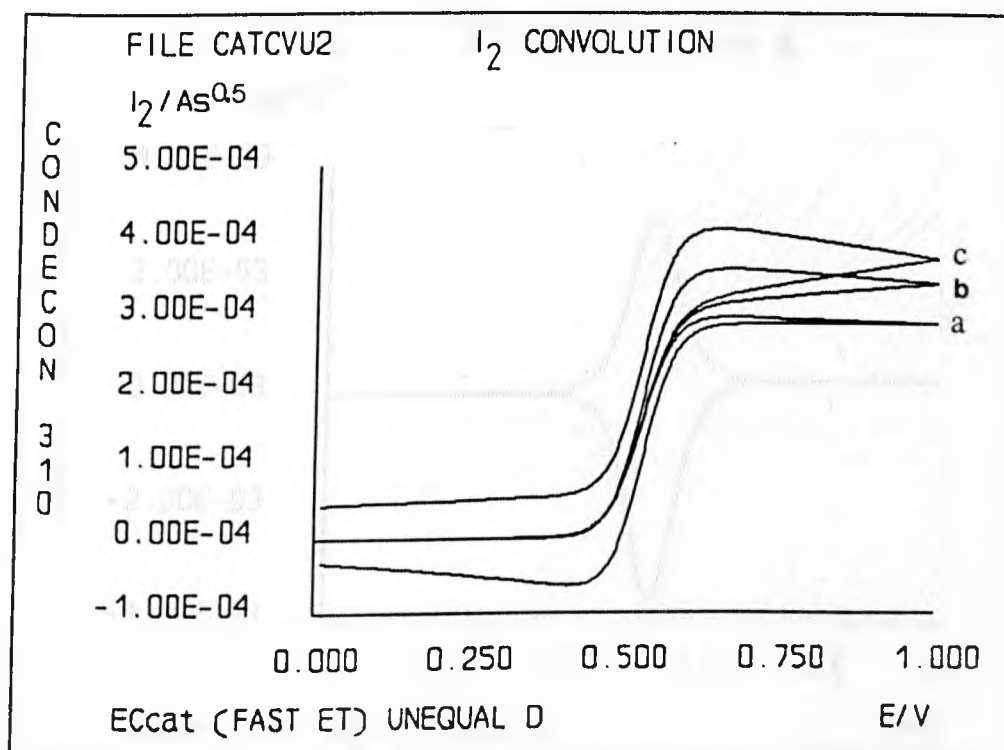


Figure 4.63 Plot of I_2 vs E for (c) of Figure 4.56. Note that when calculated with true k_c , I_2 falls to zero on the returning sweep. k_c 'test' (s^{-1}) are: (a) 2 (b) 1 (true) & (c) 0.5

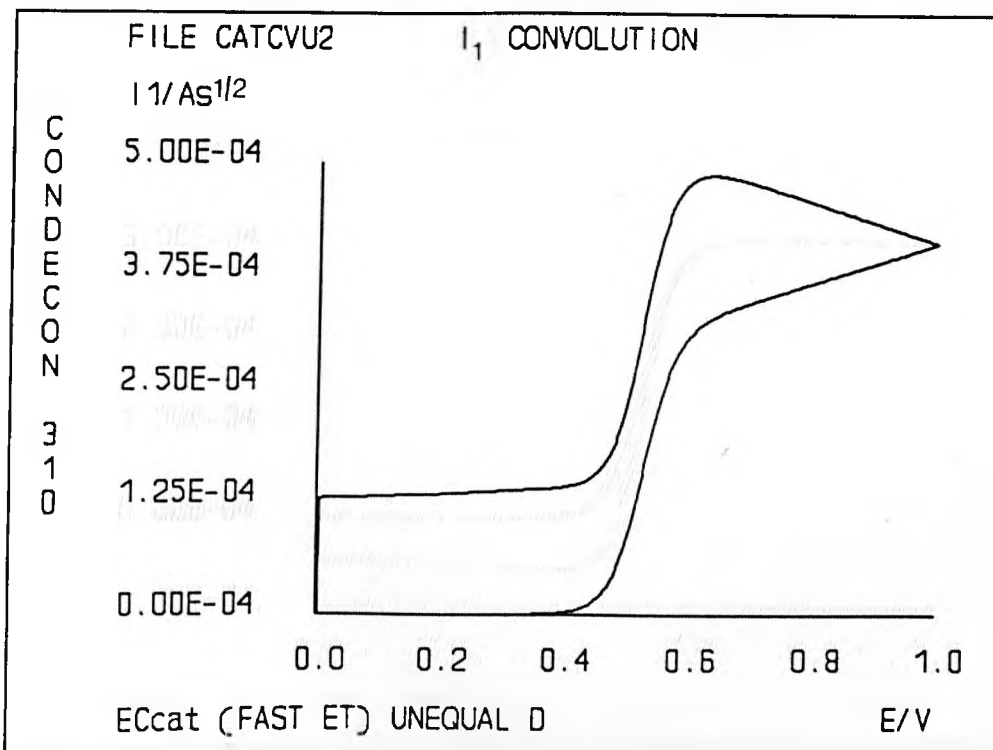


Figure 4.64 The plot of I_1 convolution vs E for an EC_{cat} process is significantly different from the polarographic wave

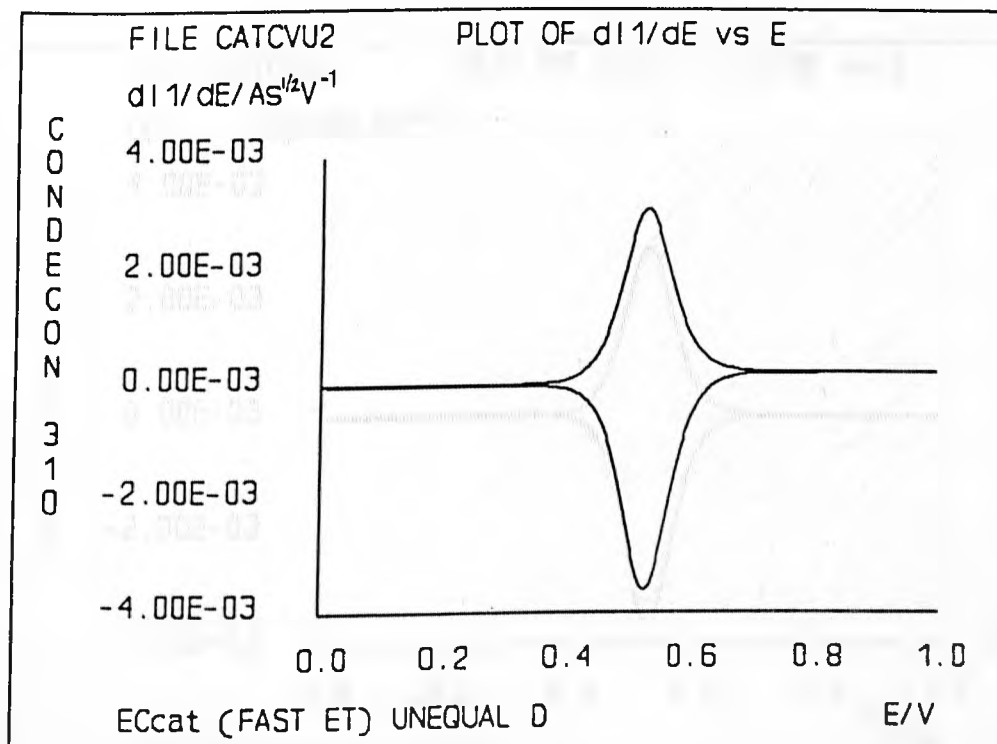


Figure 4.65 The dI_1/dE vs E displays TWO aligned peaks centred on $E_{1/2}$ - a strong indication of FAST ET. However, the peak height differs due to different D values.

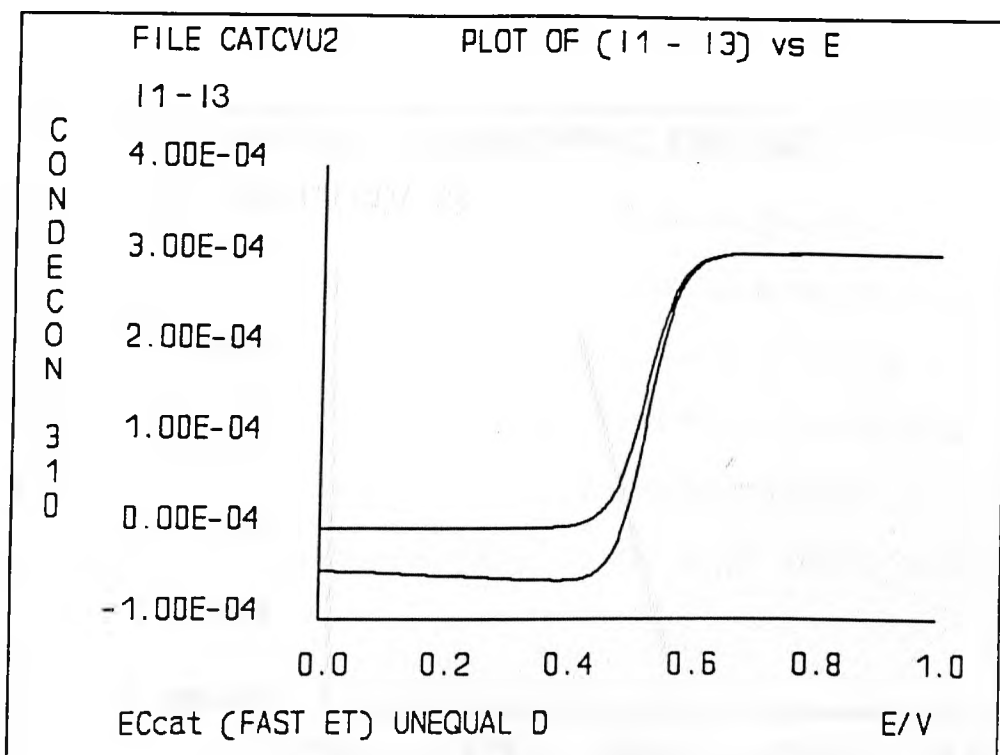


Figure 4.66 The plot of $(I_1 - I_3)$ vs E for an EC_{cat} process with $D_A > D_B$ has similar shape to I_2 vs E for an EC_{rev} (TRUE k_c) reaction.

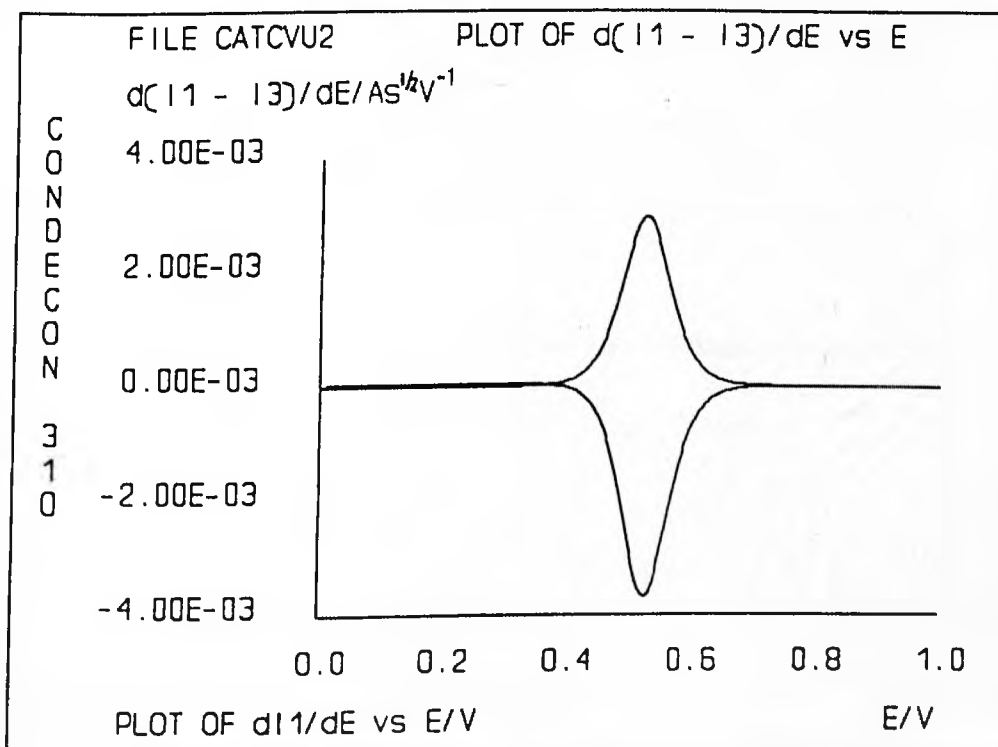


Figure 4.67 The $d(I_1 - I_3)/dE$ vs E displays two aligned peaks centred on $E_{1/2}$. The peak heights differ due to different D values.

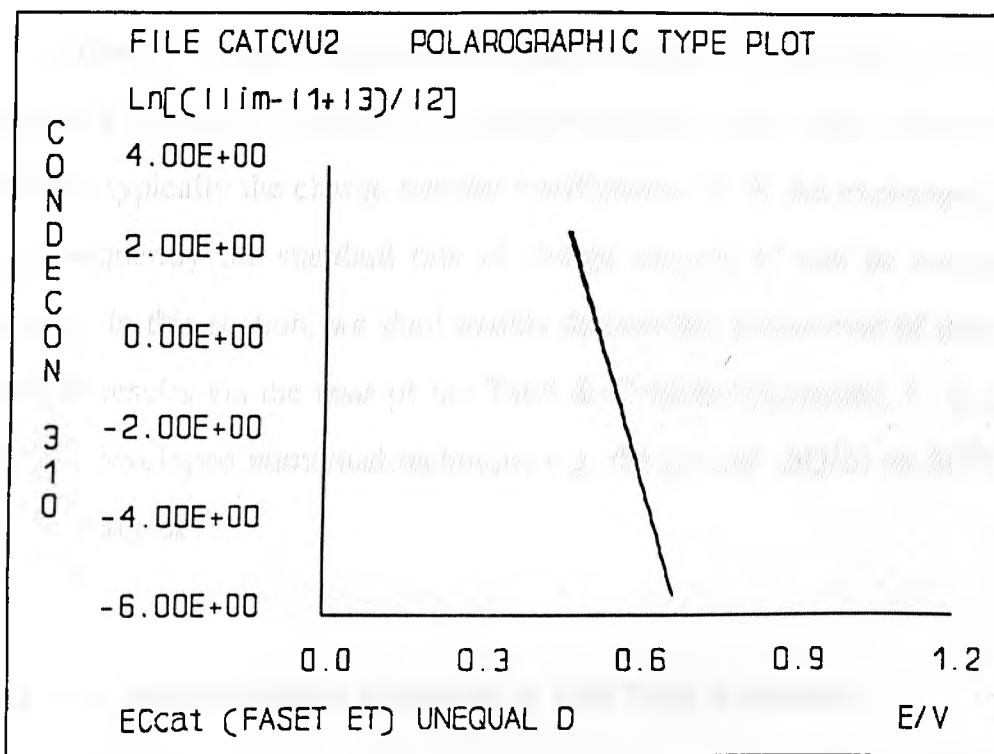


Figure 4.68 Plot of $\text{Ln} [(I_A^{\text{lim}} - I_1 + I_3)/I_2]$ vs E for (c) of Figure 4.56 - linearity & overlay of the forward and return waves are evident.

4.8.3 Analysis of Simulated Data for Chronoamperometry

In most of its applications, chronoamperometry is employed to study the simple electron transfer process. For example, under steady state, several kinetic parameters typically the charge transfer coefficients (α) & the exchange current i_0 & subsequently the standard rate of charge transfer k^0 can be numerically evaluated. In this section, we shall mainly discuss the assessment of the digital simulation results via the tests of the Tafel & Cottrell behaviours, $i - I_1$ plot & a recently developed numerical technique e.g. the plot of $\Delta Q/\Delta i$ vs $\Delta t^{1/2}/\Delta i$ & $\Delta i/\Delta t^{1/2}$ vs $\Delta Q/\Delta t^{1/2}$.

4.8.3.1 The Butler-Volmer Equation & The Tafel Behaviour

For a simple electron transfer process, the resulting faradaic current can be expressed as a function of the potential (current-overpotential relationship, see also equation 4.31 in *Section 4.5.1*):

$$i = z_1 i_0 \left[\frac{C_A^o}{C_A^{BULK}} e^{-\alpha p_1} - \frac{C_B^o}{C_B^{BULK}} e^{(1-\alpha)p_1} \right] \quad (4.131)$$

where p_1 & i_0 are reduced overpotential & the exchange current respectively, which are defined by:

$$p_1 = (z_A - z_B) F(E - E_{eq})/RT \quad (4.132)$$

$$i_0 = |z_A - z_B| F A k^0 C_A^{o(1-\alpha)} C_B^{o\alpha} \quad (4.133)$$

While z_1 is a "sign" symbol which is defined by $z_1 = -(z_A - z_B)/|z_A - z_B|$.

A special case arises when the solution is properly stirred (usually in the steady state) or the electrochemical perturbation is insufficient ($k^0 \leq 10^{-5} \text{ m s}^{-1}$ &

E not far from E_{eq}) to cause any appreciable change. The latter situation falls into the kinetic control regime ("Tafel region"). At this state, the difference between the surface concentrations & the corresponding bulk values can be neglected & therefore equation 4.131 reduces to the Butler-Volmer relationship:

$$i = z_1 i_o [e^{-\alpha p_1} - e^{(1-\alpha)p_1}] \quad (4.134)$$

The above equation is usually rearranged into the Tafel type relationship:

$$\text{Ln} \frac{z_1 i}{1 - e^{p_1}} = \text{Ln} i_o - \alpha p_1 \quad (4.134a)$$

As can be seen, two important kinetic parameters e.g. transfer coefficient α & exchange current (i_o) can readily be extracted by plotting $\text{Ln}[z_1 i/(1 - e^{p_1})]$ versus the potential term p_1 or usually the overpotential ($E - E_{eq}$).

Obviously two limiting cases can be isolated from equation 4.134a when the magnitude of the potential term $p_1 [= (z_A - z_B)F(E - E_{eq})/RT]$ is sufficiently large (e.g. $p_1 \geq 4.59$ or $p_1 \leq -4.59$):

$$\text{Ln} i = \text{Ln} i_o - \alpha p_1 \quad (\text{large anodic overpotential})$$

$$\text{Ln} (-i) = \text{Ln} i_o + (1 - \alpha)p_1 \quad (\text{large cathodic overpotential})$$

The above equations are usually called the Tafel relationship.

Figure 4.69 shows a set of current-time responses simulated for a simple electron transfer reaction (irreversible, $k^0 = 10^{-6} \text{ m}\cdot\text{s}^{-1}$, $\alpha = 0.5$). Due to the low overpotentials & the slow nature of the charge transfer, the currents are generally insufficiently large to cause appreciable changes in the concentrations of both species. Therefore, the Tafel relationship is suitable to treat the data. *Figure 4.70* shows the Tafel plots based on the current data on *Figure 4.69*. The slopes of the anodic & cathodic branches give the transfer coefficients α_A & α_B as 0.4947

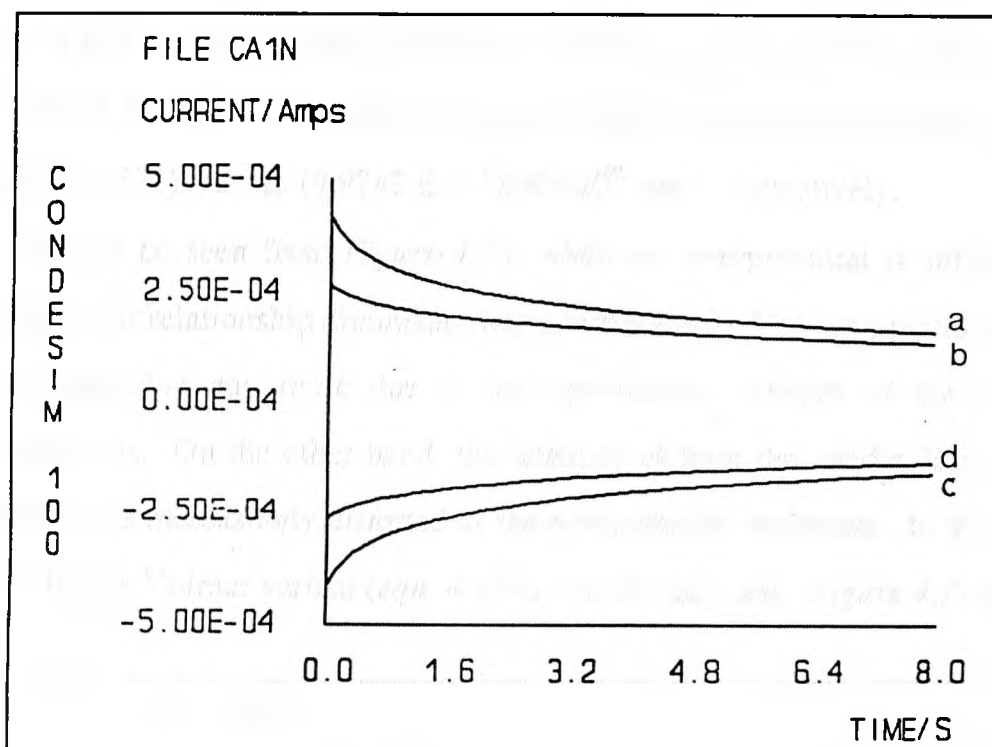


Figure 4.69 Simulated current-time responses for a simple ET process with $n=1$, $\alpha=0.5$, $k^0=10^{-6}\text{ms}^{-1}$ & $D=10^{-8}\text{m}^2\text{s}^{-1}$. ΔE (mV) are: (a) 75 (b) 50 (c) -75 (d) -50.

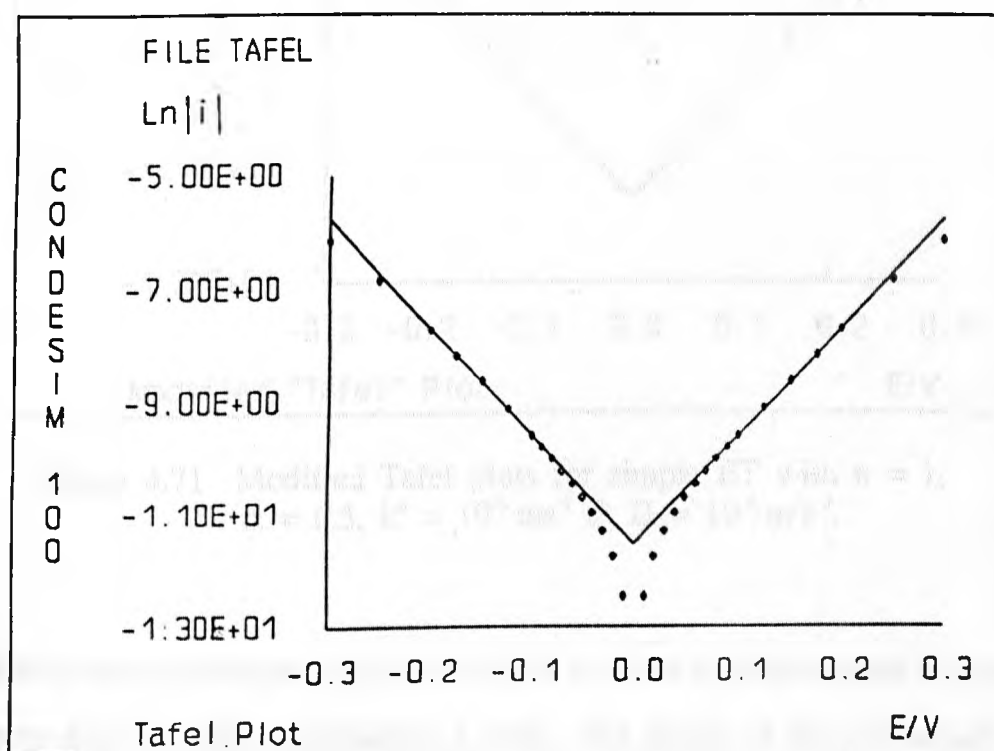


Figure 4.70 Tafel plots for a simple ET process with $n = 1$, $\alpha = 0.5$, $k^0 = 10^{-6}\text{ms}^{-1}$ & $D = 10^{-8}\text{m}^2\text{s}^{-1}$. $t = 50\text{ms}$.

± 0.0058 & 0.4941 ± 0.0032 . The intercepts of the cathodic & anodic branches on the $\text{Ln}|i|$ axis give the exchange current i_0 as $(9.6317 \pm 0.3205) \times 10^{-6}$ & $(9.6276 \pm 0.1741) \times 10^{-6} \text{ A}$ & thus the standard heterogeneous rate constant (k^0) as $(9.9835 \pm 0.3321) \times 10^{-7}$ & $(9.9782 \pm 0.1804) \times 10^{-7} \text{ ms}^{-1}$, respectively.

As can be seen from *Figure 4.70*, when the overpotential is sufficiently high the linear relationship diminishes because the Butler-Volmer equation (4.96) is not applicable any more due to the appreciable changes of the surface concentrations. On the other hand, the linearity of both the anodic & cathodic sides becomes increasingly distorted as the overpotential decreases. In this case, the full Butler-Volmer variant (*eqn. 4.134a*) MUST be used. *Figure 4.71* shows

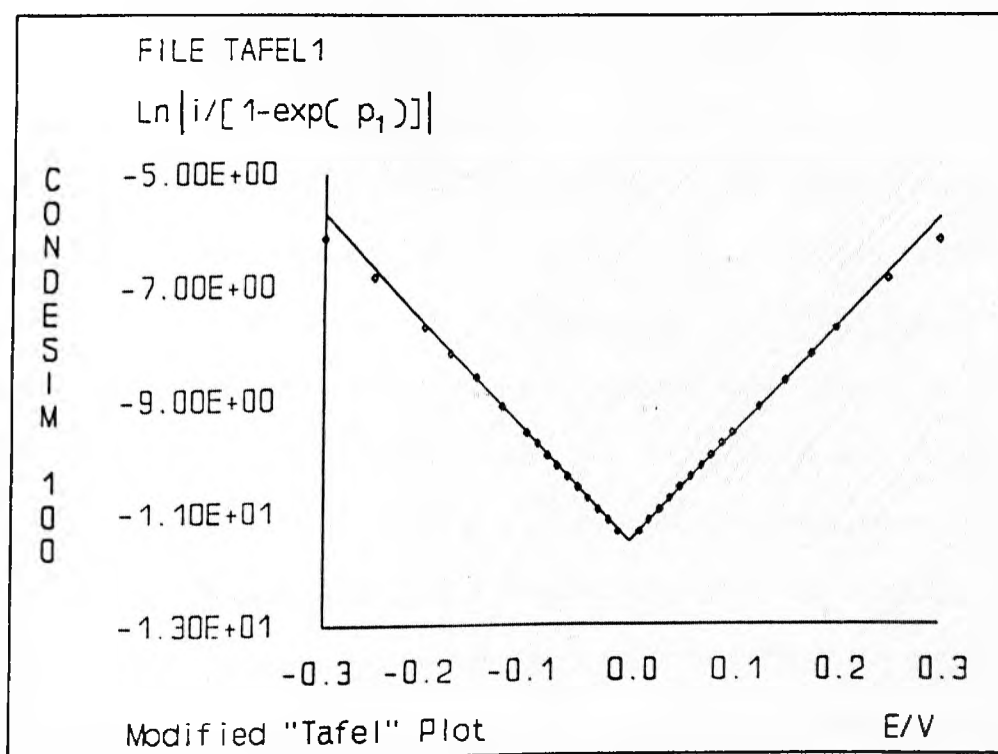


Figure 4.71 Modified Tafel plots for simple ET with $n = 1$, $\alpha = 0.5$, $k^0 = 10^{-6} \text{ ms}^{-1}$ & $D = 10^{-8} \text{ m}^2 \text{ s}^{-1}$.

that the linearity of the plot can be recovered at lower over-potentials by treating the same data according to equation 4.134a. The slopes of the two branches & intercepts on the "Ln" axis give the following kinetic information, $\alpha_A = 0.4957$

± 0.0008 , $\alpha_B = 0.4974 \pm 0.0013$, & $k^0 = (1.0033 \pm 0.0046) \times 10^{-6} \text{ m}\cdot\text{s}^{-1}$ & $(1.0064 \pm 0.0028) \times 10^{-6} \text{ m}\cdot\text{s}^{-1}$ for the cathodic & anodic branches, respectively.

It is worthwhile mentioning that the 'Tafel plot' is an approximate form of the universal current-overpotential relationship (*eqns. 4.31 & 4.131*). It is based ultimately on the assumption that the surface concentration does not differ considerably from the bulk values. This is hopefully achieved by stirring the solution or applying small electrochemical perturbations. This also implies that the accuracy of the measurements always depends on closeness between the experimental conditions & those on which the Tafel relationship is based, which in turn restricts the flexibility of this technique.

4.8.3.2 The Cottrell Behaviour - A Test for Diffusion-Control

Generally, an electrode reaction involves three major steps, namely the transport of reactant to the electrode, the exchange of electrons (charge transfer) at the electrode & the transport of the product to the bulk of the solution. The first & the last steps are usually referred to as the mass transport process. The relative magnitude of these steps determines the characteristics of the resulting faradaic current.

When the electron transfer process is very fast (e.g. Nernstian case, fully reversible) or the overpotential ($E - E_{eq}$) is sufficiently large, the kinetics of this step has no significant influence on the pace of the entire process. Instead, it is the transportation of the electroactive species to & from the electrode surface that plays a dominant role in determining the rate. This situation is usually referred to as the "mass transport (or DIFFUSION if other forms of mass transport are negligible) controlled regime". In other words, the resulting faradaic current from this system has ONLY one component i.e. the diffusional current i_d . Generally, when the standard rate constant is greater than $100\text{m}\cdot\text{s}^{-1}$ or ($E - E^\circ$) is greater than 0.5V (1.0V or higher in the case of slow electron transfer), the system can be approximately treated as mass transport controlled regime.

A typical characteristic of this regime lies in the fact that the surface concentration of species A approaches zero instantaneously at the imposition of the external electric field. Therefore, an extra boundary condition emerges besides those discussed in *section 4.5.1* (eg the initial & semi-finite conditions):

$$C_A(0,t) = 0 \quad \text{for } t > 0$$

Under these conditions, the solution of Fick's second (diffusion) law (*eqn. 4.3*) becomes much simpler & leads to the following current-time relationship excluding the potential & kinetic parameters:

$$i = \frac{-(z_A - z_B) FA \sqrt{D_A} C_A^{\text{BULK}}}{\sqrt{\pi t}} \quad (4.135)$$

The above equation is generally referred to as the Cottrell behaviour. In this regime, the current i is independent of E & the electrode kinetics e.g. k° .

As can be seen from *equation 4.135*, the product $i\sqrt{t}$ is constant in the diffusion-controlled region. This criterion can thus serve as a characteristic test for the Cottrell behaviour. By plotting $i\sqrt{t}$ versus t (or \sqrt{t}), a straight line parallel to the t axis should be observed. The diffusion coefficient D_A can be calculated from the intercept on the $i\sqrt{t}$ axis. *Figures 4.72 & 4.73* show the simulated i - t response & test of Cottrell behaviour for a typical 'diffusion control' regime: $k^\circ = 100 \text{ ms}^{-1}$, $D_A = D_B = 10^{-8} \text{ m}^2\text{s}^{-1}$, $C_A^{\text{BULK}} = 1.0 \text{ mol}\cdot\text{m}^{-3}$, $\Delta E = 1.0\text{V}$. The diffusion coefficient calculated from the intercept on the $i\sqrt{t}$ axis (the value corresponding to this axis of the plateau on *Figure 4.73*) is $1.0009 \times 10^{-8} \text{ m}^2\text{s}^{-1}$. Similar results have also been obtained from the quasi-reversible & irreversible systems (with relatively larger overpotentials). Note the small deviation at the beginning of the graph. This is mainly due to the fact that the assumption that the surface concentration of electroactive species reaches zero instantaneously at the imposition of perturbation is not, in practice, true. Instead, it always takes a short period of time for a system to reach the totally "diffusion-control" regime.

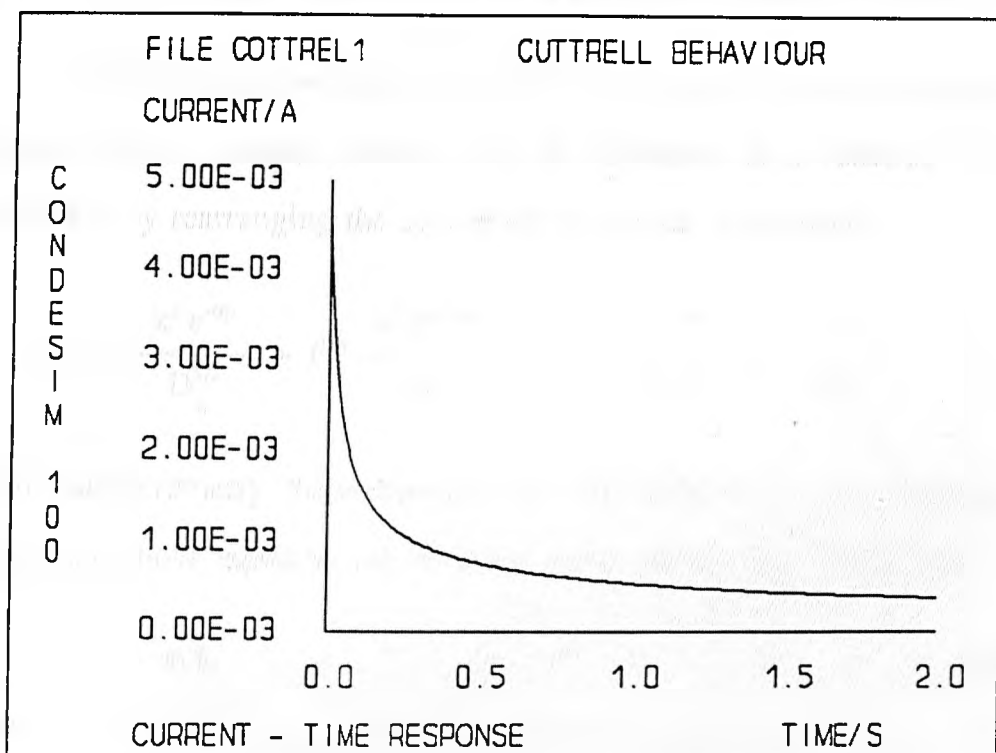


Figure 4.72 Current-time response for a simple ET process under 'diffusion control' - the $t^{-1/2}$ transient behaviour

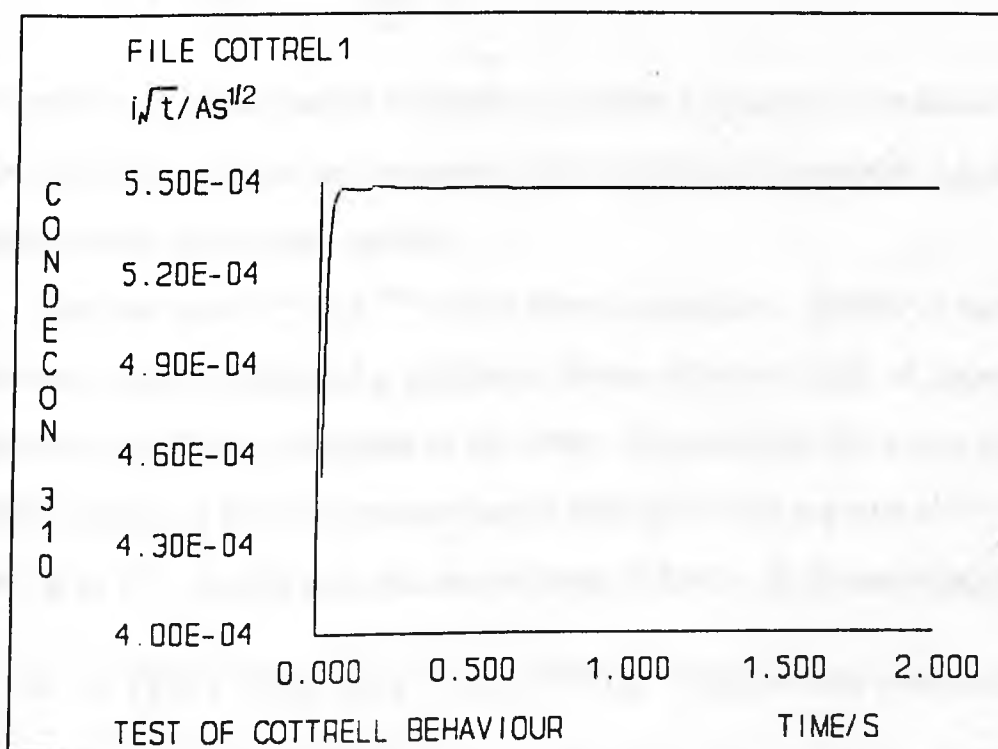


Figure 4.73 Test of Cottrell behaviour via plot of $i\sqrt{t}$ versus t - a characteristic "horizontal" line observed

4.8.3.3 Test of Digital Simulation Using the Convolution Technique

As already discussed in *section 4.8.2.1*, the faradaic current resulting from a simple electron transfer reaction can be expressed as a function of the I_1 convolution by rearranging the current-overpotential relationship:

$$i = I_A^{\text{lim}} \frac{k^o e^{-\alpha p}}{D_A^{1/2}} + I_B^{\text{lim}} \frac{k^o e^{(1-\alpha)p}}{D_B^{1/2}} - I_1 k^o \left[\frac{e^{-\alpha p}}{D_A^{1/2}} + \frac{e^{(1-\alpha)p}}{D_B^{1/2}} \right] \quad (4.136)$$

In chronoamperometry, the potential is kept CONSTANT, i.e. p is constant. As a result, the above equation can be rewritten in the familiar linear form:

$$i = a - b I_1 \quad (4.136a)$$

where

$$a = I_A^{\text{lim}} \frac{k^o e^{-\alpha p}}{D_A^{1/2}} + I_B^{\text{lim}} \frac{k^o e^{(1-\alpha)p}}{D_B^{1/2}} \quad (4.136b)$$

$$b = k^o \left[\frac{e^{-\alpha p}}{D_A^{1/2}} + \frac{e^{(1-\alpha)p}}{D_B^{1/2}} \right] \quad (4.136c)$$

are coefficients which can be obtained by plotting i against I_1 & measuring the slope ($-b$) & intercept (a) on the current axis via statistical treatment, e.g. the unweighed mean least square method.

Note the terms $e^{-\alpha p}$ & $e^{(1-\alpha)p}$ of the above expression. Similar to the Tafel treatment, when the value of p satisfies a certain criterion, ONE of these terms becomes negligible as compared to the other. For example, for a one electron transfer process, if $(E-E^o)$ is greater than 118mv ($p \leq -4.59$), the term $e^{(1-\alpha)p}$ is less than 1% of $e^{-\alpha p}$. In this case, the second term of both a & b can be ignored:

$$a \longrightarrow I_A^{\text{lim}} k^o e^{-\alpha p} / \sqrt{D_A} \quad \& \quad b \longrightarrow k^o e^{-\alpha p} / \sqrt{D_A} \quad (\text{large anodic overpotentials})$$

The limiting convolution I_A^{lim} & therefore the diffusion coefficient D_A can be

obtained from the ratio a/b . On the other hand, the charge transfer coefficient α (α_A) & the standard rate constant of charge transfer (k°) can be evaluated by plotting the term $\text{Ln } k_{\text{hf}}$ ($= k^\circ e^{-\alpha p}$, the forward charge transfer rate) against the overpotential ($E-E^\circ$) or its variant p . Similarly, D_B , α_B & k° can be obtained by treatment of the cathodic data.

Figure 4.74 & 4.75 illustrate the original digitally simulated chronoamperometric data & the convoluted current (I_1 convolution) at overpotentials 0.15V & -0.15V for a slow electron transfer system with $k^\circ = 5.0 \times 10^{-6} \text{ m} \cdot \text{s}^{-1}$, $D_A = D_B = 10^{-8} \text{ m}^2 \cdot \text{s}^{-1}$. *Figure 4.76* shows the $i - I_1$ relationship at various overpotentials. The slopes (-b) & intercepts (a) from the $i - I_1$ plots & the ensuing results from further data treatment are listed in *Table 4.5*. At high overpotentials ($|\Delta E| \geq 0.16\text{V}$), the diffusion coefficients D_A & D_B can be obtained in relative high accuracy ($9.976 \times 10^{-9} \text{ m}^2 \cdot \text{s}^{-1}$ for both D_A & D_B). The kinetic parameters α_A (or α_B) & k° are obtained by plotting (cf. *Figure 4.77*) the term $\text{Ln } k_{\text{hf}}$ ($k^\circ e^{-\alpha p}$, $= b\sqrt{D_A}$) or $\text{Ln } k_{\text{hb}}$ ($k^\circ e^{(1-\alpha)p}$, $= b\sqrt{D_B}$) against the overpotential ($E-E^\circ$). These parameters determined are: $\alpha_A = \alpha_B = 0.5003 \pm 0.0007$ & $k^\circ = (5.0164 \pm 0.0228) \times 10^{-6} \text{ m} \cdot \text{s}^{-1}$ & $(5.0152 \pm 0.0221) \times 10^{-6} \text{ m} \cdot \text{s}^{-1}$ by extrapolation of the anodic & cathodic branches to $E=E^\circ$, respectively.

For relatively fast electron transfer process (quasi-reversible, $k^\circ = 10^{-3} \sim 10^{-5} \text{ m} \cdot \text{s}^{-1}$), the slope of the i vs I_1 plots may not be accurately evaluated due to approaching the mixed or even DIFFUSION control regimes in which case the plots tends to be perpendicular to the I_1 axis. In this case, the overpotentials must be kept at low levels ($|\Delta E| \leq 0.10\text{V}$) & the full expression of the slope (a) & intercept (-b) of equation 4.136a must be used for data analysis. To simply the problem, diffusion coefficients are obtained independently by forcing the system into the diffusion-control regime to allow accurate evaluation of the limiting values of the I_1 convolution.

The major advantage of this technique over the classical Tafel method lies

in that in the former the majority of the data is used & no assumption is made regarding the surface concentrations (in the Tafel method these are supposed to be very close to the BULK values). Therefore, the results obtained in this method appear to be slightly better than those from the Tafel plots. In addition, this technique can theoretically be used to test any rate of electron transfer rather than being restricted to the irreversible case. However, in practice, it is not easy to extract kinetic parameters, except for diffusion coefficients, from chronoamperometric data for relatively fast electron transfer systems ($k^{\circ} \geq 1e^{-4}m^2/s$, which approaches to the diffusion-control regime at relative low overpotentials say $\pm 0.3V$) via the $i - I_1$ plots. This is mainly due to the fact that the $i - I_1$ plots become almost perpendicular to the I_1 axis, which in turn causes great difficulty in measuring accurately the slope of the plot.

Table 4.5 Results from the plots i vs I_1 (eqn. 4.136a) & $\ln k$ vs ΔE

$E-E^{\circ}/V$	a/A	$b/s^{-1/2}$	I_{lim}	$\ln k$
-0.300	-1.2787×10^{-2}	13.2508	-9.6503×10^{-4}	-6.6275
-0.200	-2.3798×10^{-3}	2.4695	-9.6367×10^{-4}	-8.3075
-0.180	-1.6077×10^{-3}	1.6701	-9.6275×10^{-4}	-8.6987
-0.160	-1.0867×10^{-3}	1.1314	-9.6047×10^{-4}	-9.0881
-0.140	-7.3384×10^{-3}	0.7676	-9.5600×10^{-4}	-9.4760
-0.120	-4.9442×10^{-4}	0.5225	-9.4621×10^{-4}	-9.8606
-0.100	-3.3113×10^{-4}	0.3578	-9.2559×10^{-4}	-10.2395
0.100	3.3115×10^{-4}	0.3578	9.2548×10^{-4}	-10.2393
0.120	4.9442×10^{-4}	0.5225	9.4619×10^{-4}	-9.8606
0.140	7.3387×10^{-3}	0.7677	9.5592×10^{-4}	-9.4759
0.160	1.0867×10^{-3}	1.1315	9.6045×10^{-4}	-9.0880
0.180	1.6077×10^{-3}	1.6700	9.6269×10^{-4}	-8.6987
0.200	2.3799×10^{-3}	2.4696	9.6366×10^{-4}	-8.3075
0.300	1.2781×10^{-2}	13.2436	9.6506×10^{-4}	-6.6280

$$D_A = D_B = 9.9756 \times 10^{-9} \text{ m}^2 \cdot \text{s}^{-1}, \quad \alpha_A = \alpha_B = 0.5003 \pm 0.0007$$

$$k^{\circ} = (5.0164 \pm 0.0228) \times 10^{-6} \quad \& \quad (5.0152 \pm 0.0221) \times 10^{-6} \text{ m} \cdot \text{s}^{-1}$$

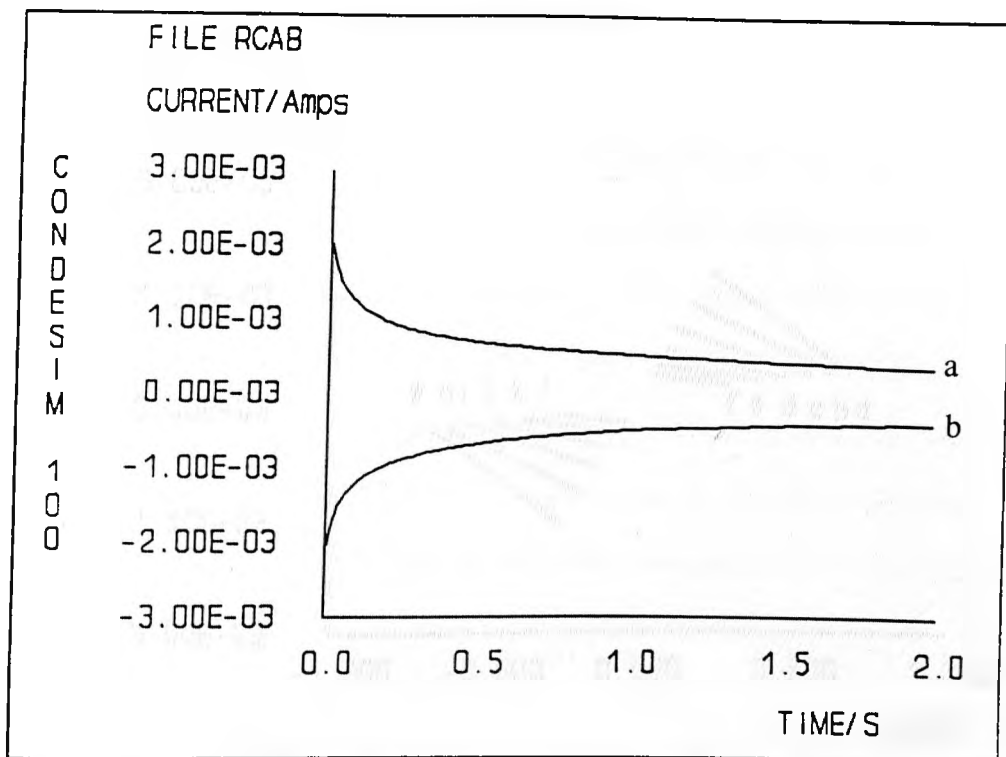


Figure 4.74 Simulated chronoamperometry data for simple ET with $n=1$, $\alpha=0.5$, $k^0=5 \times 10^{-6} \text{ms}^{-1}$ & $D=10^{-8} \text{m}^2 \text{s}^{-1}$

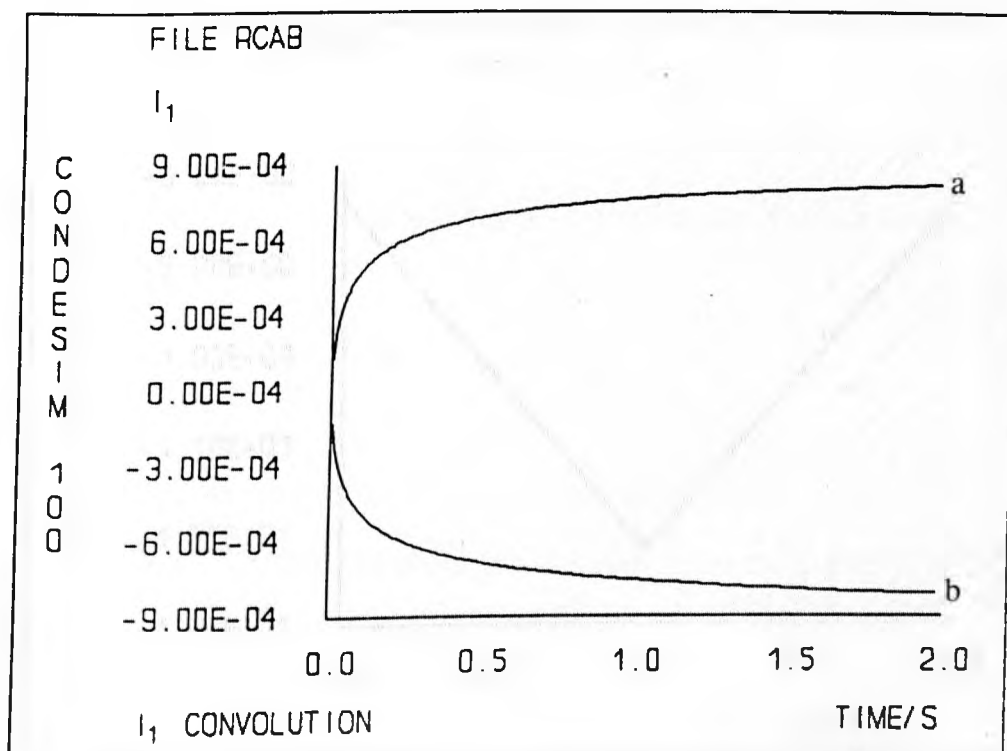


Figure 4.75 I_1 convolution of the simulated chronoamperometry data displayed in Figure 4.17.

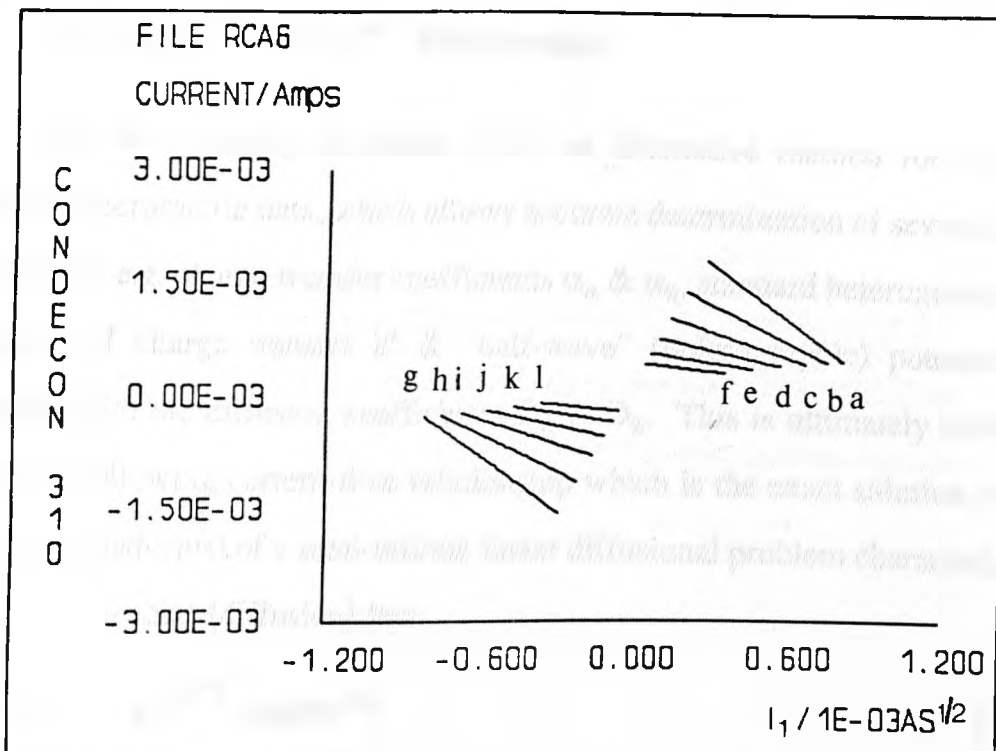


Figure 4.76 Plots of i vs I_1 for simulated data at $(E-E^0)$ (V):
 (a) 0.20 (b) 0.18 (c) 0.16 (d) 0.14 (e) 0.12 (f) 0.10
 (g) -0.20 (h) -0.18 (i) -0.16 (j) -0.14 (k) -0.12 (l) -0.10

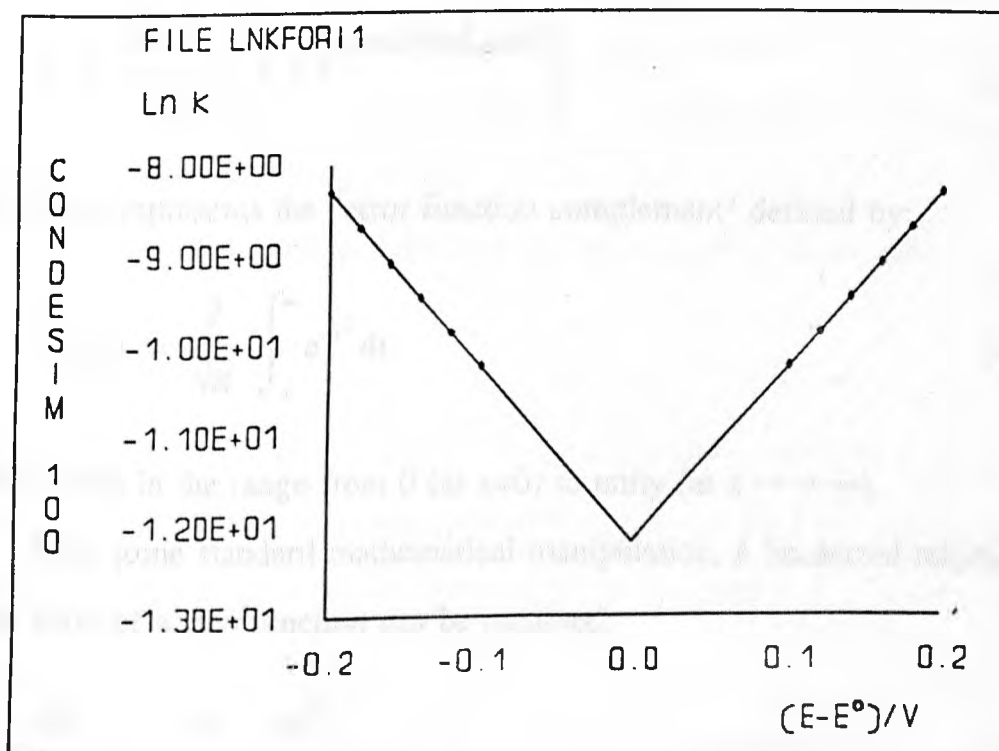


Figure 4.77 Plot of $\text{Ln } k$ vs $(E-E^0)$ for the determination of αk^0 . Data are based on those in *Figure 4.76*.

4.8.3.4 Analysis of Digital Simulation Results Using e.g. the $\Delta Q/\Delta i$ vs $\Delta t^{-1/2}/\Delta i$ & $\Delta i/\Delta t^{1/2}$ vs $\Delta Q/\Delta t^{1/2}$ Relationship

We have recently described [236] an alternative method for analyzing chronoamperometric data, which allows accurate determination of several kinetic parameters e.g. charge transfer coefficients α_A & α_B , standard heterogeneous rate constant of charge transfer k^0 & "half-wave" (polarographic) potential $E_{1/2}$, together with the diffusion coefficients D_A & D_B . This is ultimately developed from the following current-time relationship which is the exact solution (via the Laplace transforms) of a semi-infinite linear diffusional problem characterised by the Fick's second (diffusion) law:

$$i(t) = a e^{-b^2 t} \operatorname{erfc}(bt^{1/2}) \quad (4.137)$$

where a & b are known quantities in constant potential techniques & have the same meaning as in *equation 4.136a*. Rearrangement of these expression yields:

$$a = (z_B - z_A)FAk^0 e^{-\alpha p} [C_A^{\text{BULK}} - C_B^{\text{BULK}} e^p] \quad (4.138)$$

$$b = \frac{k^0 e^{-\alpha p}}{\sqrt{D_A}} \left[1 + e^{\frac{(z_A - z_B)F(E - E_{1/2})}{RT}} \right] \quad (4.139)$$

and $\operatorname{erfc}(x)$ represents the "error function complement" defined by:

$$\operatorname{erfc}(x) = \frac{2}{\sqrt{\pi}} \int_x^\infty e^{-t^2} dt \quad (4.140)$$

which varies in the range from 0 (at $x=0$) to unity (at $x \rightarrow \infty$).

After some standard mathematical manipulation, a linearized relationship in the form of a 'step' function can be obtained:

$$\frac{\Delta Q}{\Delta i} = \frac{2a}{\sqrt{\pi} b} \frac{\Delta t^{1/2}}{\Delta i} + \frac{1}{b^2} \quad (4.141)$$

or alternatively, to give more emphasis to the data at the initial stage of the potential step (as there is risk of involvement of convection at longer durations):

$$\frac{\Delta i}{\Delta t^{1/2}} = b^2 \frac{\Delta Q}{\Delta t^{1/2}} + \frac{2ab}{\sqrt{\pi}} \quad (4.142)$$

where the Δ symbol is the algebraic difference of the quantity at ANY two time points at t_1 & t_2 . The evaluation of Δt & Δi is very obvious, whilst ΔQ (charge difference) must be obtained via integration of the current over the time interval from t_1 to t_2 :

$$\Delta Q = Q_2 - Q_1 = \int_0^{t_2} i(t) dt - \int_0^{t_1} i(t) dt = \int_{t_1}^{t_2} i(t) dt \quad (4.143)$$

The numerical evaluation of the above integral is readily done using known method e.g. the Trapezoidal rule or Simpson's rule.

Both *equation 4.141 & 4.142* show a linear relationship between the step functions of various quantities therein indicated. Graphic & subsequential statistical treatment of these relationships allow evaluation of various kinetic parameters. Below we shall take *equation 4.141* as an example to demonstrate how these parameters are extracted.

Equation 4.141 can be written in the more familiar linear equation:

$$y = mx + c \quad (4.141a)$$

where $y = \Delta Q/\Delta i$, $x = \Delta t^{1/2}/\Delta i$, $c = b^{-2}$ & $m = 2a/(\sqrt{\pi} b)$. Therefore, by plotting $\Delta Q/\Delta i$ against $\Delta t^{1/2}/\Delta i$, two important parameters i.e. **a** & **b** can readily be evaluated from the slope (**m**) & intercept (**c**) of the graph:

$$b = c^{-1/2} \quad \& \quad a = \pi^{1/2} m c^{-1/2} / 2 \quad (4.141b)$$

As already discussed in *section 4.8.3.3*, at relatively higher anodic overpotentials

(but insufficient to force the system into diffusion controlled regime), the second term (corresponding to $e^{(1-\alpha)p}$ with $p \rightarrow$ large negative value) of both a & b becomes negligible. Hence a & b reduce to:

$$a \rightarrow I_A^{\text{lim}} k^{\circ} e^{-\alpha p} / \sqrt{D_A} \quad \& \quad b \rightarrow k^{\circ} e^{-\alpha p} / \sqrt{D_A} \quad (\text{large anodic overpotentials})$$

As a result, the diffusion coefficient D_A can be calculated. The above argument also applies to the treatment of the case of reduction & leads to the evaluation of the diffusion coefficient for species B (D_B). Similar to the treatment of plots of i vs I_1 , the forward heterogeneous rate k_{hf} ($=k^{\circ}e^{-\alpha p}$) or the backward heterogeneous rate k_{hb} ($=k^{\circ}e^{(1-\alpha)p}$) can be obtained which in turns leads to the evaluation of α_A , α_B & k° via the plot of $\text{Ln } k_{\text{hf}}$ (or k_{hb}) vs ΔE .

However, the above treatment is not suitable for chronoamperometric data at relatively lower overpotentials ($|\Delta E| \leq 0.10\text{V}$) because in these situations the forward & backward charge transfer rate are comparable. These types of experiments usually give more accurate information about the electrode kinetics, because at low over-potentials the faradaic current at time zero is more likely to be totally controlled by the electrode kinetics if k° is not too large. On the other hand, at relatively higher overpotentials mass transport also plays a significant role in determining the rate. In this case, inaccuracy arises during the statistical treatment because the data is concentrated in a small area. A route to the determination of kinetic parameters at very low overpotentials is stated below.

Combination of *equations 4.138, 4.139 & 4.141b* leads to the following linear relationship:

$$\left[C_A^{\text{BULK}} - C_B^{\text{BULK}} e^p \right] / m = s + s e^{(z_A - z_B)F(E - E_{1/2})/RT} \quad (4.144)$$

or $y = s + qx$ for short

where $s = \sqrt{\pi} / [2(z_B - z_A)FA\sqrt{D_A}]$, $y = \Theta = \left[C_A^{\text{BULK}} - C_B^{\text{BULK}} e^p \right] / m$,

$$q = s e^{(z_B - z_A)FE_{1/2}/RT} \quad \& \quad x = e^{(z_A - z_B)FE/RT}$$

or for convenience of handling the exponential, q & x can be rearranged as:

$$q = s e^{(z_B - z_A)F(E_{1/2} - E^{\circ})/RT} \quad \& \quad x = e^p$$

As a result, D_A & $E_{1/2}$ can be calculated from the intercept & slope of the plot & D_B can be obtained via similar treatment of the data from cathodic excursions or simply from the definition of the half-wave potential $E_{1/2}$:

$$E_{1/2} = E^{\circ} + \frac{RT}{2(z_B - z_A)F} \text{Ln}(D_A/D_B) \quad (4.145)$$

while the forward rate k_{hf} ($=k^{\circ}e^{-\alpha p}$) or the backward rate k_{hb} ($=k^{\circ}e^{(1-\alpha)p}$) can be calculated via *equation 4.142*. The standard heterogeneous rate constant of charge transfer k° & the charge coefficients α_A & α_B can finally be obtained by plotting $\text{Ln } k_{hf}$ (or k_{hb}) vs ΔE as discussed earlier.

Below we shall take as an example simulated data of a system with parameters comparable to those for the $\text{Fe}^{3+}/\text{Fe}^{2+}$ couples to demonstrate the application of the above theoretical development to the analysis of chronoamperometric data (see also *section 3.6* for practical applications). These conditions are as follows: $\alpha_A = 0.4000$, $\alpha_B = 0.6000$, $D_A = 5.000 \times 10^{-10} \text{ m}^2 \text{ s}^{-1}$, $D_B = 2.500 \times 10^{-10} \text{ m}^2 \text{ s}^{-1}$, $k^{\circ} = 5.000 \times 10^{-6} \text{ ms}^{-1}$, $C_A^{\text{BULK}} = 10.00 \text{ mol m}^{-3}$, $C_B^{\text{BULK}} = 2.000 \text{ mol m}^{-3}$, $E^{\circ} = 0.5000 \text{ V}$ & $T = 293.00 \text{ K}$. The starting potential is always set to the equilibrium potentials ($E_{eq} = 0.4594 \text{ V}$) defined by the Nernst equation (*eqn. 4.32*). The magnitude of the overpotentials are kept below 100mv such that more accurate results for the kinetic parameters might be obtained.

The simulated current-time responses are very similar to those illustrated in *Figure 4.74*. Linearity of the plots of $\Delta Q/\Delta i$ vs $\Delta t^{1/2}/\Delta i$ or $\Delta i/\Delta t^{1/2}$ vs $\Delta Q/\Delta t^{1/2}$

(calculated from original data using the EG&G Condecon 310 software) is evident in *Figures 4.78 & 4.79*. The statistical results (slopes m & intercept c on the $\Delta Q/\Delta i$ axis) of those straight lines in *Figure 4.78* are listed in *Table 4.6*. The parameter $\Theta = [C_A^{\text{BULK}} - C_B^{\text{BULK}}e^p]/m$ at various overpotentials is then calculated & plotted against x values listed in the table (cf. *Figure 4.80*). As mentioned above, the slope (q) & intercept (c , on y axis) of plot leads to an immediate route to the knowledge of several kinetic parameters e.g. D_A , D_B & $E_{1/2}$ & the subsequential forward or backward heterogeneous rate k_{hf} or k_{hb} . The charge transfer coefficients α_A & α_B & the standard rate constant k° can finally be evaluated from the slope & intercept (on the $\text{Ln } k$ axis) of plot $\text{Ln } k$ (k_{hf} or k_{hb}) vs ΔE (cf. *Figure 4.81*). As can be seen from *Table 4.6*, the results are very close (error $\leq 0.5\%$) to the corresponding values entered for the simulation.

Similar results have been obtained for moderately fast electron transfer processes (k° up to $10^2 \text{ m}^2\text{s}^{-1}$). However, appreciable discrepancy has been observed (not surprisingly) as the rate constant increases. This may be attributed to the "interference" of mass transfer (diffusion) step because at large k° values the pace of the entire heterogeneous reaction is not monitored by the electrode kinetics alone. As indicated in the $\Delta Q/\Delta i$ vs $\Delta t^{1/2}/\Delta i$ or $\Delta i/\Delta t^{1/2}$ vs $\Delta Q/\Delta t^{1/2}$ plots (*Figures 4.78 & 4.79*), at larger overpotentials (thus the forward or backward charge transfer rate), the plots become increasingly perpendicular to the x axes. This inevitably brings appreciable error to the statistical treatment & therefore the final results.

Similar to the convolution technique (cf. *Section 4.8.3.3*), the above linearized step functions can be used to evaluate several kinetic parameters e.g. the diffusion coefficients, charge transfer coefficients & standard heterogeneous rate constant for relatively slow electron transfer systems. Generally, the latter has several advantages over the former (i - I_1 plot) e.g. higher upper limits of k° (10^2 & $10^4 \text{ m}^2\text{s}^{-1}$, respectively) & simplicity for treatment of data at low

overpotentials. In addition, as discussed in *section 3.6*, the latter possesses a convincing advantage in analyzing experimental data, which is frequently distorted by the charging of the double layer capacitance. This always affects the accuracy of the numerical evaluation of the convolution integral, which in turn affects the ensuing results from the $i - I_1$ plot. However, the terms $\Delta Q/\Delta i$, $\Delta t^{1/2}/\Delta i$, $\Delta i/\Delta t^{1/2}$ & $\Delta Q/\Delta t^{1/2}$ are step functions, which are able to "forget" the charging current etc. when they have died away. Therefore, measurement of the data when the charging current has diminished should reflect the real kinetic performance of the electrode process.

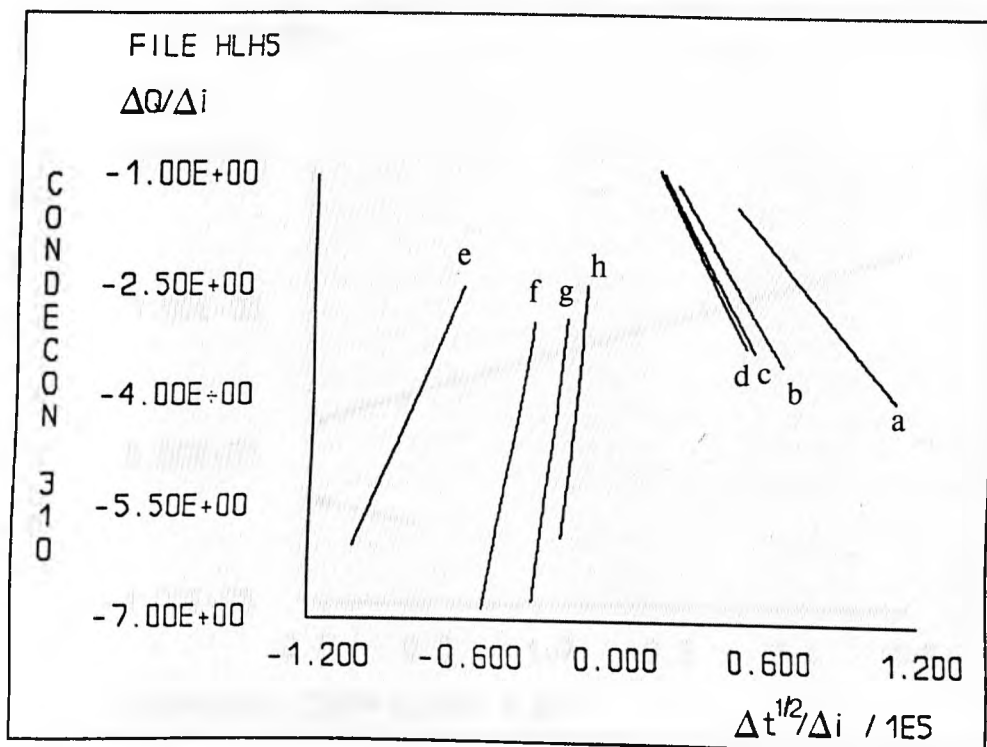


Figure 4.78 Plots of $\Delta Q/\Delta i$ vs $\Delta t^{1/2}/\Delta i$ at $\Delta E (=E-E_{eq}, \text{mV})$: (a)-10 (b)-30 (c)-50 (d)-75 (e) 10 (f) 30 (g) 50 (h) 75

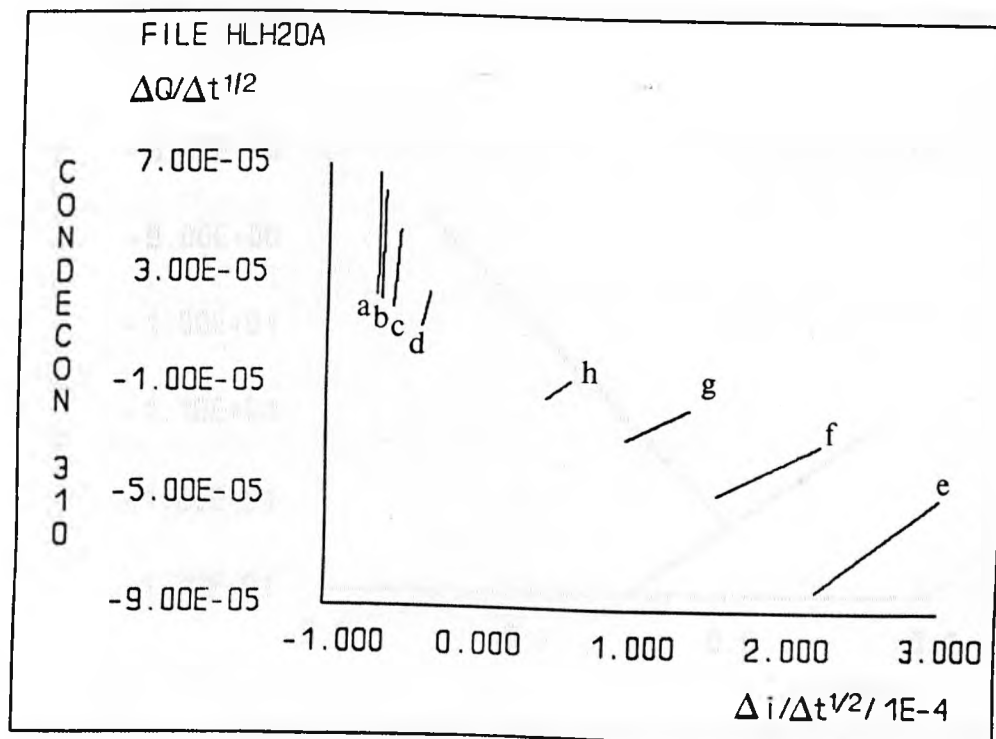


Figure 4.79 Plots of $\Delta i/\Delta t^{1/2}$ vs $\Delta Q/\Delta t^{1/2}$ at $\Delta E (E-E_{eq}, \text{mV})$: (a)-10 (b)-30 (c)-50 (d)-75 (e) 10 (f) 30 (g) 50 (h) 75

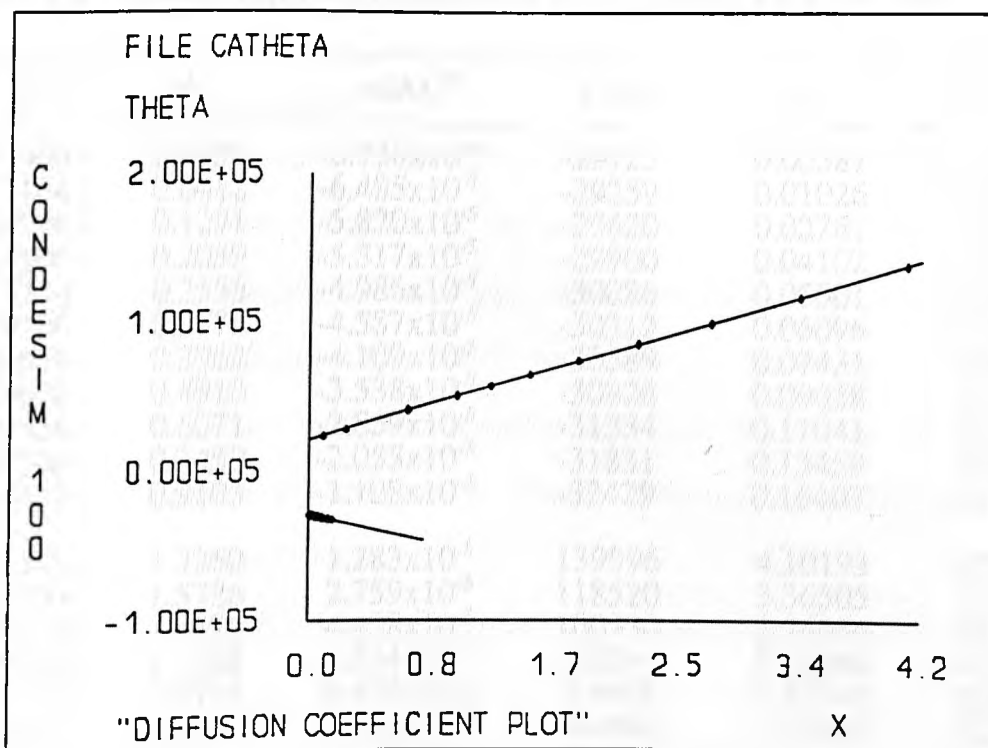


Figure 4.80 Plot of Θ versus e^p for the determination of diffusion coefficients D_A & D_B (data listed in Table 4.6)

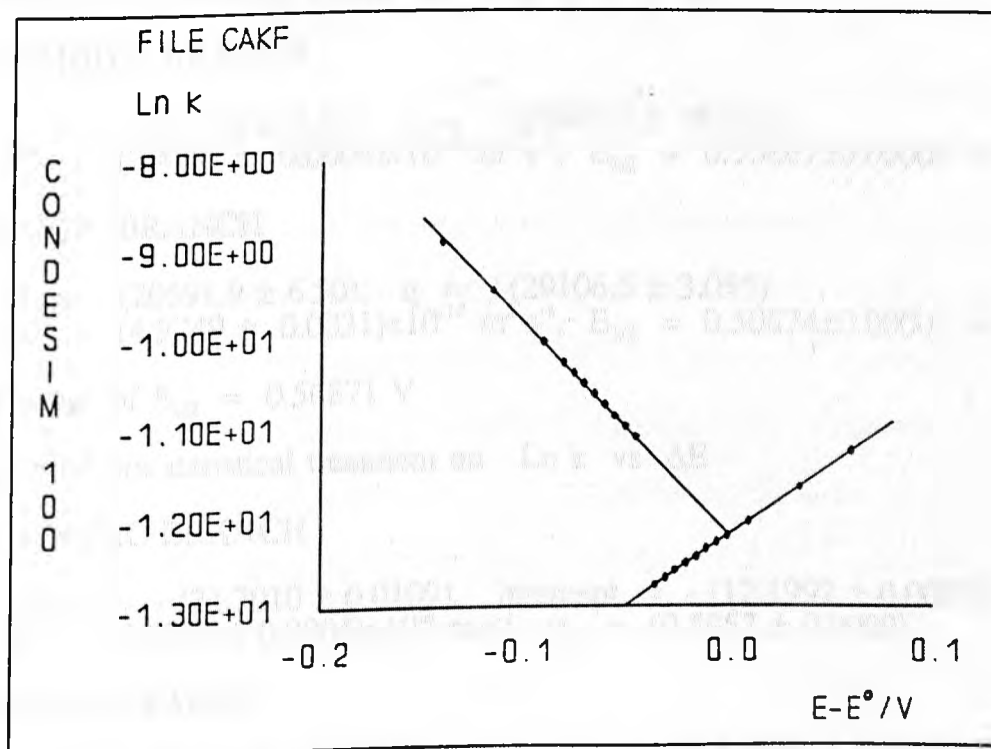


Figure 4.81 Plot of $\ln k$ vs $(E-E^\circ)$ for the determination of standard heterogeneous rate constant & symmetry coefficient

Table 4.6 Results from the plots $\Delta Q/\Delta i$ vs $\Delta t^{1/2}/\Delta i$ & $\ln k$ vs ΔE

E-E°/V	c/s	m/As ^{1/2}	y (Θ)	x	Ln k
-0.1406	0.0136	-6.736x10 ⁻⁵	-29125	0.00381	- 8.910
-0.1156	0.0412	-6.485x10 ⁻⁵	-29259	0.01026	- 9.468
-0.0906	0.1291	-5.820x10 ⁻⁵	-29620	0.02761	-10.052
-0.0806	0.2039	-5.317x10 ⁻⁵	-29900	0.04102	-10.288
-0.0756	0.2556	-4.986x10 ⁻⁵	-30086	0.05001	-10.406
-0.0706	0.3178	-4.587x10 ⁻⁵	-30312	0.06096	-10.525
-0.0656	0.3962	-4.109x10 ⁻⁵	-30589	0.07431	-10.643
-0.0606	0.4910	-3.538x10 ⁻⁵	-30926	0.09058	-10.761
-0.0556	0.6071	-2.859x10 ⁻⁵	-31334	0.11041	-10.881
-0.0506	0.7459	-2.055x10 ⁻⁵	-31831	0.13459	-10.999
-0.0456	0.9103	-1.108x10 ⁻⁵	-32429	0.16407	-11.118
-0.0356	1.3260	1.283x10 ⁻⁵	139996	4.10193	-12.767
-0.0306	1.5786	2.759x10 ⁻⁵	118520	3.36505	-12.688
-0.0256	1.8575	4.438x10 ⁻⁵	100930	2.76054	-12.609
-0.0206	2.1588	6.324x10 ⁻⁵	86504	2.26462	-12.530
-0.0156	2.4741	8.416x10 ⁻⁵	74668	1.85780	-12.451
-0.0106	2.7902	1.070x10 ⁻⁴	64960	1.52406	-12.371
-0.0056	3.0944	1.316x10 ⁻⁴	56995	1.25027	-12.239
-0.0006	3.3797	1.575x10 ⁻⁴	50457	1.02567	-12.213
0.0094	3.7753	2.118x10 ⁻⁴	40693	0.69026	-12.551
0.0344	3.5969	3.382x10 ⁻⁴	28053	0.25657	-11.660
0.0594	2.3512	4.202x10 ⁻⁴	23347	0.09529	-11.264

Results from statistical treatment on $y = s + qx$

CATHODIC BRANCH

$$s = -(29051.4 \pm 3.39), \quad q = -(20642.0 \pm 28.096)$$

$$D_B = (2.4991 \pm 0.0004) \times 10^{-10} \text{ m}^2 \cdot \text{s}^{-1}, \quad E_{1/2} = 0.50867 \pm 0.00004 \text{ V}$$

ANODIC BRANCH

$$s = (20591.9 \pm 6.50), \quad q = (29106.5 \pm 3.055)$$

$$D_A = (4.9749 \pm 0.0031) \times 10^{-10} \text{ m}^2 \cdot \text{s}^{-1}, \quad E_{1/2} = 0.50874 \pm 0.00002 \text{ V}$$

$$\text{Average of } E_{1/2} = 0.50871 \text{ V}$$

Results from statistical treatment on $\ln k$ vs ΔE

CATHODIC BRANCH

$$\text{slope} = -(23.7010 \pm 0.0109), \quad \text{intercept} = -(12.1992 \pm 0.00074)$$

$$k^\circ = (5.0344 \pm 0.0004) \times 10^{-6} \text{ m} \cdot \text{s}^{-1}, \quad \alpha_B = (0.5957 \pm 0.0009)$$

ANODIC BRANCH

$$\text{slope} = (15.8198 \pm 0.0015), \quad \text{intercept} = -(12.2032 \pm 0.00004)$$

$$k^\circ = (5.0141 \pm 0.0002) \times 10^{-6} \text{ m} \cdot \text{s}^{-1}, \quad \alpha_R = (0.3995 \pm 0.00004)$$

4.8.3.5 Analysis of Digital Simulation of Coupled Homogeneous Reactions

In the previous sections we have discussed the assessment of digitally simulated chronoamperometry data for the fundamental electrochemical process e.g. simple electron transfer reaction, using a variety of techniques. In a large number of practical situations, the charge transfer reaction is frequently coupled with homogeneous chemical reaction(s) or followed by a successive electron transfer reaction. The chronoamperometric responses from these systems are, generally speaking, very complex & hence there are no simple analytical techniques for data treatment.

Traditionally, to simplify the problem, the experiments are usually carried out under conditions such that the electrode reaction falls ultimately into the diffusion controlled regime. Under this extreme, ONLY the diffusion coefficient can be obtained. However, parameter evaluation is frequently still carried out by perhaps comparing experimental results with simulated data. For example, double step chronoamperometry is used for the study of the reduction of azobenzene (an EC reaction) [237]. The basic procedures involve the construction of "working curves" (theoretical) &, subsequently, consulting these curves for extraction of kinetic information.

Below we shall discuss the analysis of chronoamperometric data for the EC catalytic reaction using a new convolution method which we have recently developed [238]. As discussed in *section 4.4.2.2.3*, for an EC catalytic reaction with irreversible homogeneous chemical kinetics, the following current-overpotential relationship holds for ANY diffusion coefficients of A & B, in terms of three different types of convolution i.e. I_1 , I_2 & I_3 (*cf. eqns. 4.88, 4.103 & 4.115*) of the original current function:

$$\frac{\sqrt{D_A}}{k^0} e^{\alpha \eta} i = I_A^{\text{lim}} - (I_1 - I_3) - I_2 e^{\frac{\eta}{E_0}} \quad (4.146)$$

where the parameters have the same meaning as those for equation 4.126.

Due to the complexity caused by inequality between the diffusion coefficients of species A & B (*cf.* 4.8.2.2.3), we shall confine our discussion to the situation where the diffusion coefficients of species A & B are equal. In this case, I_3 becomes $(I_1 - I_2)$ & $p = \xi$. Hence, the above equation reduces to:

$$\frac{\sqrt{D_A}}{k^o} e^{\alpha p} i = I_A^{\text{lim}} - I_2 (1 + e^p) \quad (4.146a)$$

In chronoamperometry experiments, the potential & thus also the 'reduced overpotential' term p are CONSTANT. As a consequence, the above equation shows a linear relationship between the current i & I_2 convolution (for TRUE k_c). The intercept of the plot of i vs I_2 on the I_2 axis at $i = 0$ is $I_A^{\text{lim}} / (1 + e^p)$. This suggests an immediate route to finding the homogeneous chemical rate constant k_c & diffusion coefficient.

By applying a large overpotential (say 0.2V past the wave), one can readily find out k_c , independently of all other parameters, via the criterion that the linear relationship between i & I_2 can be observed ONLY if the appropriate value of k_c is used for the evaluation of I_2 (*cf.* Figure 4.82). In addition, in this situation $e^p \rightarrow 0$ & I_2 takes effectively a CONSTANT value i.e. I_A^{lim} . In other words, the $i - I_2$ plot becomes perpendicular to the I_2 axis. The diffusion coefficient can therefore be readily obtained if the BULK concentration & number of electrons are known.

Other parameters can also be obtained via application of small voltage pulses. Again, in the case of a Nernstian reaction, I_2 retains a CONSTANT value, here $I_A^{\text{lim}} / (1 + e^p)$, if the appropriate k_c value is used. In this case, the standard potential can readily be evaluated because I_A^{lim} is already known. If the electrode process is not extremely fast, a linearity between i & I_2 (*cf.* Figure 4.84, which is based on the $i - t$ data shown in Figure 4.83) can be obtained &

the crossing of the I_2 axis at $i = 0$ gives $I^{\text{lim}}/(1 + e^p)$ from which E° can also be evaluated. On the other hand, the intercept on the i axis at $I_2 = 0$ determines $i(t=0) = (z_B - z_A)F k_{\text{hf}} C^{\text{BULK}}$ & thus k_{hf} . By varying the 'polarisation' potentials, a series of values for k_{hf} can thus be obtained. This in turn leads to the numerical evaluation of the standard heterogeneous rate constant k° & charge transfer coefficient α via the plot of $\text{Ln } k$ vs E as discussed earlier.

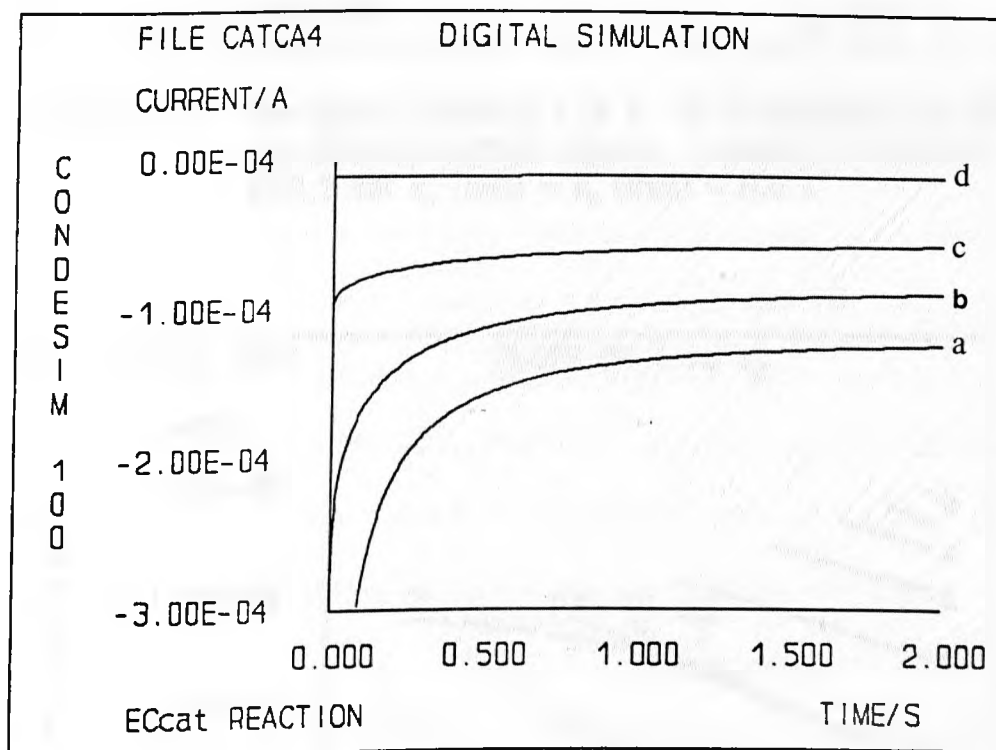


Figure 4.82 i - t responses for EC_{cat} reactions with $D=10^{-9}\text{m}^2/\text{s}$, $n=1$, $\alpha=0.5$, $k_c=0.6\text{ s}^{-1}$, $\Delta E=-0.3\text{V}$ & k° (m/s): (a) 100 (b) 3×10^{-5} (c) 10^{-5} (d) 10^{-6}

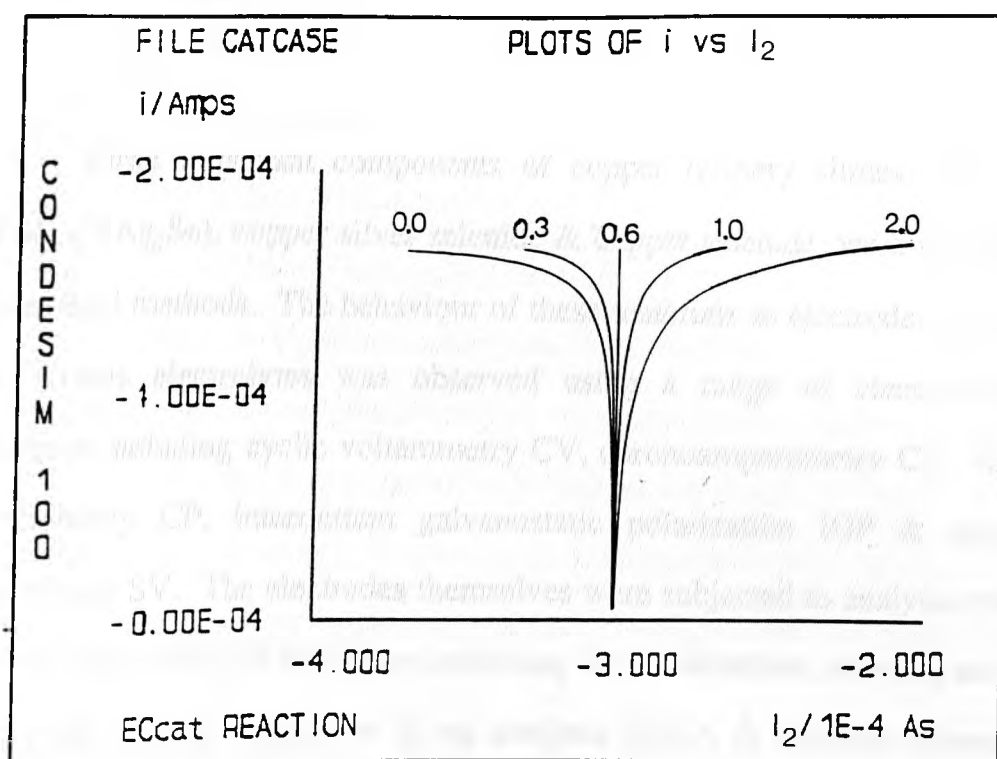


Figure 4.83 The current response i vs I_2 for a potential step into the diffusion limited regime. Linearity is observed ONLY for k_c (test) = k_c (true) = 0.6 s^{-1}

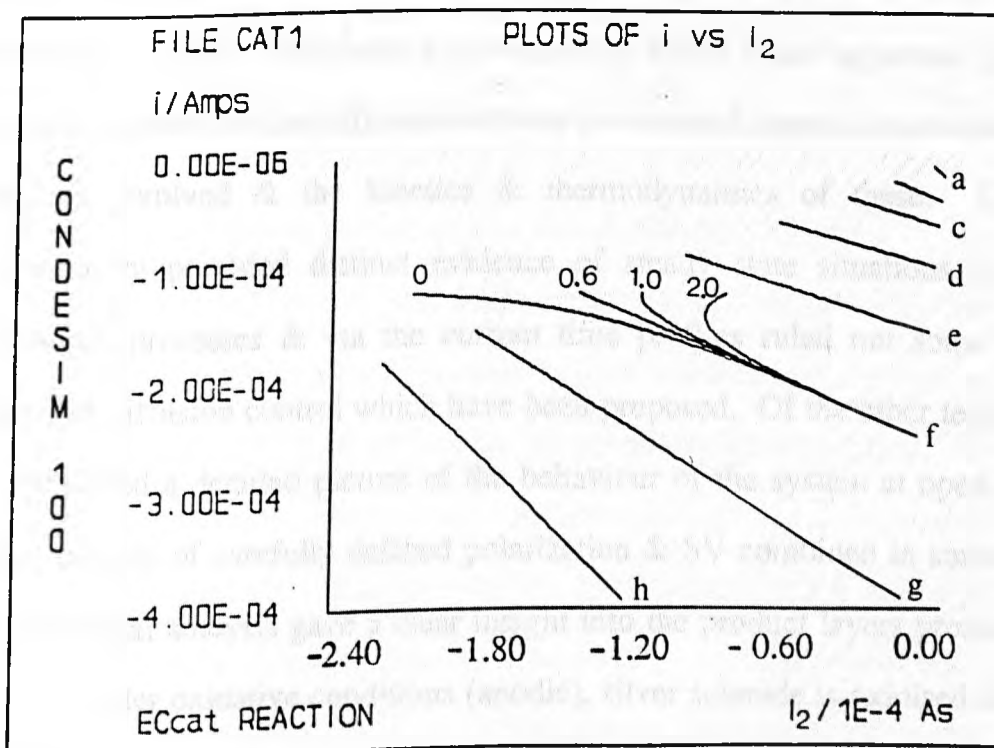


Figure 4.84 Plots of i vs I_2 for an EC_{cat} reaction. $k^0 = 10^{-5} \text{ m/s}$.
At overpotentials (V) of: (a) -0.200 (b) -0.250 (c) -0.275
(d) -0.300 (e) -0.325 (f) -0.350 (g) -0.375 (h) -0.400

5. Conclusions

Three important components of copper refinery slimes, e.g. silver selenide (β -Ag₂Se), copper silver selenide & copper selenide, were synthesised via chemical methods. The behaviour of these materials as electrodes in contact with various electrolytes was observed using a range of electrochemical techniques including cyclic voltammetry CV, chronoamperometry CA, chronopotentiometry CP, intermittent galvanostatic polarization IGP & stripping voltammetry SV. The electrodes themselves were subjected to analysis prior & after use via a variety of techniques including X ray diffraction, scanning electron microscopy, energy dispersive X ray analysis EDXA & electron microprobe analysis EMPA to characterise the chemical & physical nature of the surfaces & sub-surfaces & hence directly elucidate changes which occur.

The electrochemical techniques each provided a range of information & results which together formed the basis of a description of behaviour for anodic dissolution. Cyclic voltammetry provided the broad brush approach yielding potential regimes for the different electrode processes & hence some ideas of the reactions involved & the kinetics & thermodynamics of these. Chronoamperometry provided distinct evidence of steady state situations in some dissolution processes & via the current time profiles ruled out some of the models of diffusion control which have been proposed. Of the other techniques IGP provided a detailed picture of the behaviour of the system at open circuit within periods of carefully defined polarization & SV combined in some cases with chemical analysis gave a clear insight into the product layers produced.

Under oxidative conditions (anodic), silver selenide is oxidised directly to elemental selenium via the reaction $\text{Ag}_2\text{Se} = 2\text{Ag}^+ + \text{Se} + 2\text{e}$. No evidence

for the formation of any intermediate phases, e.g. AgSe, was found by surface analysis, though CV & IGP experiments may suggest the possible presence of an intermediate. The formation of a metastable elemental selenium product was proved by both EDXA & electrochemical techniques e.g. cathodic stripping (including cathodic excursions in CV & IGP) in which the reduction of the elemental selenium to H_2Se was observed. The elemental selenium product is porous & does not impose considerable restrictions to the diffusion of product or reactant across the silver selenide/electrolyte interface. Instead, the slow heterogeneous charge transfer process plays an important role in determining the rate. Silver selenide was reduced at potentials around 0.2V to elemental silver & released H_2Se gas.

Copper was found to be preferentially "leached" into solution during the anodic polarization of copper silver selenide (Cu:Ag \approx 30:1 in the solution at initial stages), forming a silver-rich product layer which was subsequently oxidised to elemental selenium. This is probably due to the catalytic effect of silver ions released instantaneously at the imposition of polarization. EMPA reveals positive evidence for formation of Ag_2Se on the electrode surface, which is similar to a mechanism commonly proposed to explain the catalytic effect of Ag^+ (aq) on sulphides e.g. chalcopyrite, heazlewoodite & pyrite.

The Fe^{3+}/Fe^{2+} couple was studied extensively because of its importance generally in hydrometallurgy & because it provided an excellent opportunity to test out in depth a range of techniques for parameter determination. The work in progress at Leeds on treatment of voltammetric data is wide ranging but was considerably extended in this study by the development of a unique & accurate simulation package covering initially a wide range of mechanisms encountered in solution electrochemistry & by considerable theoretical development for systems exhibiting chemically reversible reactions of species of different

diffusion coefficients. Because of the general nature of the current potential time relationships for the variety of mechanisms all voltammetric methods could be encompassed via the convolution techniques & this leads to a considerable clarification of the experimental conditions & constraints necessary to determine adequately given parameters. The digital simulation work represented a very considerable extension of this area & via the convolution techniques etc was able to be tested for accuracy & also supplied unique data for exemplifying the parameter determination methods themselves.

Furthermore simulations could be carried out for mechanisms outside those treatable by theoretical methods & thus provided via direct comparison of simulated with for example experimental voltammograms a means of parameter validation. The latter includes for example second order chemical reactions, the ECE system & where diffusion coefficients differed for interacting species. In the latter context a complete solution for any range of diffusion coefficients was obtained for the important EC_{CAT} system & the resolution of a suitable technique for parameter determination involved considerable mathematical & computational work to estimate the complex convolutions involving "Dawsons Integral".

Returning to the Fe^{3+}/Fe^{2+} system a unique complete determination of parameters was carried out which represents in depth & accuracy a considerable step forward in this area & can now be extended to other redox systems of hydrometallurgical importance. The heterogeneous rate parameters were particularly interesting in view of the wide variation of magnitudes which have been reported in the literature.

The work described in this thesis encompassed a wide range of theoretical areas & techniques & thus generates a somewhat disparate range of suggestions for future developments. The synthetic methods described are now well

established & can be readily extended to other materials of hydrometallurgical interest. Likewise much experience was gained in the encapsulation & production of electrodes from a range of stock materials. In the area of digital simulation the techniques developed can be extended to model systems including the dissolution of the solid phase & the chemical & diffusional aspects arising from this. This would allow clearer & more positive interpretation of voltammetric results & would provide an adequate bridge to the more direct picture available from *in situ* & other methods of analysis. The latter methods also require refining & extending & in some important areas were used somewhat spasmodically due to breakdowns & over utilisation. The area of electron spectroscopy ESCA for identification of surface species could provide important additional information to complement the other techniques.

Bibliography

Extractive Hydrometallurgy: Leaching

- Burkin, A.R., "The Chemistry of Hydrometallurgical Processes", E. & F.N. Spon Ltd., London, 1966.
- Burkin, A.R., (Editor) "Leaching and Reduction in Hydrometallurgy", The Institution of Mining & Metallurgy, London, 1975.
- Burkin, A.R., "Extractive Metallurgy of Nickel" (Editor), Critical Reports on Applied Chemistry Vol.17 (1987) Society of Chemical Industry, John Wiley & Sons.
- Wadsworth, M.E., (ed.) "Rate Processes of Extractive Metallurgy", Plenum Press, 1979.

Mineralogy

- Vaughan, D.J, and Craig, J.C., "Mineral Chemistry of Metal Sulphides", Cambridge University Press, 1978.

Electrochemistry

- Bard, A.J. & Faulkner, L.R.; "Electrochemical methods"; John Wiley & Sons, New York, 1980.
- Bockris, J.O'M. & Reddy, A.K.N., "Modern Electrochemistry", Plenum Press, 1973.
- Britz, D.; " Digital Simulation in Electrochemistry", Springer-Verlag, Berlin, 1981.
- Southampton Electrochemistry Group; "Instrumental methods in electrochemistry", Ellis Horwood Ltd., Chichester, 1985.
- Vetter, K.J., "Electrochemical Kinetics- Theoretical and Experimental Aspects", Academic Press, 1967.

Thermodynamic Data

- Bard, A.J. & Parsons, R.; Standard potentials in aqueous solutions; IUPAC, Marcel Deker, New York, 1985.
- Wangman, D.D.; Selected values of chemical thermodynamic properties; National Bureau of Standards, U.S. Government Office, Technical note 270-4, 1969.
- Mills, K.C.; Thermodynamic data for inorganic sulphides, selenides & tellurides; Butterworths, London, 1974.

References

1. Eichrodt, C.W. & Schloen, J.H.; Electrolytic copper refining; In "Copper", Butts, A.(Ed.), Reinhold Pub. Co., New York, 1954, 165-222.
2. Schoen, J.H. & Elkin, E.M.; Treatment of copper refining slimes; In "Copper", Butts, A. (ed), Reinhold Pub. Co., New York, 1954, 265-289.
3. Biswas, A.K.& Davenport, W.G.; Extractive metallurgy of copper; Pergaman Press, Oxford, 1980, 295-321.
4. Bandmann, F. & Kniprath, E.; Decomposition of anodic slime; Ger. Offen. 2,304,498 (Cl. B01j, C01b), 08 Aug 1974; from CA 81:173496s.
5. Habashi, F.; Recent methods for the treatment of anodic slimes of copper electrolysis; Metallurgia, 12 (1965) 257-263.
6. Kudryavstev, A.; The chemistry and technology of selenium and tellurium; Collect's (Pubs.) Ltd. London, 1974.
7. Hoh, Y.C. et al; Iner process for recovering precious metals from copper refining anode slimes; In "Hydrometallurgy: Research, development, plant practice. Proc. Int. Symp.", 3rd, Atlanta, 1983.
8. Yannopoulos, J.C.; Treatment of copper refining slimes; US Pat. 4,094,668 (1978).
9. Morrison, B.H.; Recovery of Ag and gold from refinery slimes at the Canadian copper Refiners; In "Extraction Metallurgy'85", IMM, London, 1985, 249-261.
10. Gendolla, T. & Charewicz, W.; Selenium and tellurium in anode slimes processing; Rudy Met. Niezelaz, 19 (1974) 524-527.
11. Morrison, B.H.; The recovery and separation of Se and tellurium by pressure leaching of copper anode slimes; in "Unit processes in hydrometallurgy", Wadsworth, M.E. & Davis, F.T. (eds), Met. Soc. 24 (1963) 227-249.
12. Buketov, E.A. et al; Consolidated testing of the autoclave of tellurium and selenium from copper electrolyte slimes; Tr. Khim. Inst. Akad. Nauk Kaz. SSR., 16 (1970) 3-12; CA 74:116430p.
13. Subramanian, K.N.; Recovery of metals from anode slimes; US Pat. 4,229,270 (Cl.204-109; C25C1/00), 21 Oct 1980; CA 94:9288y.
14. Zhou, Taili; Hydrometallurgical treatment of copper Anode Slimes; Ph.D. Thesis, University of Leeds, 1984.
15. Montoya-Jurado, J.L.; Leaching of synthetic components of Copper Anode Slimes; M.Sc. Thesis, University of Leeds, 1984.
16. Yanagida, T.; Flotation of anode slimes in copper electrolysis; Nippon Kogyo Kaishi, 91 (1975) 308-310.
17. Subramanian, K.N. & Themelis, N.J.; Copper recovery by flotation; J. Metals, 24 (1950) 33-38.

18. Nagumanov, P.N., Semina, O.I.; Formation of Se (VI) during electrochem. leaching of selenium-containing intermediate products, *Tsvetn. Met.*, 3 (1986) 26-28.
19. Kubicki, J. et al; Electrolytic separation of silver in the hydrometallurgical process for anode slime treatment; *Rudy Met. Niezelz.*, 25 (1980) 190-192.
20. Ugorets, M.Z., Semina, O.I. & Buketov, E.A.; Potential - pH diagram for the silver selenide - water system; *Vestn. Akad. Nauk Kaz. SSR*, 29 (1973) 58-60.
21. Ugorets, M.Z., Sagindykova, Z.B. & Buketov, E.A.; Oxidation of copper chalcogenide by atmospheric oxygen in a H_2SO_4 medium; *Tsetn. Met.*, 6 (1977) 8-9.
22. Ugorets, M.Z., Buketov, E.A. & Baikenov, Kh.I.; Oxidation of chalcogenides in alkaline solutions, *Zh. Prikl. Khim.*, 45 (1972) 1207-1210; CA 77:118778c.
23. Sagindykova, Z.B. & Akhmetov, K.M.; Oxidation of copper chalcogenides with atmospheric oxygen in soda solutions; *Tr. Khim.-Metallurg. In-ta. AN Kaz SSR*, 28 (1978) 101-104; CA 90:44435h.
24. Sagindykova, Z.B., Semina, O.I. & Ugorets, M.Z.; Sulphuric acid decoppering of copper electrolyte anodic slimes with oxygen; *Tsvetn. Met.*, 8 (1986) 35-38.
25. Azerbaeva, R. G. & Tseft, A. L.; Thermodynamic analysis of solubility of some selenides and tellurides in a solution of iron chloride; *Tr. Inst. Met. i Obogashch.*, Akad. Nauk Kaz. SSR, 8 (1963) 50-56; CA 60:13935a.
26. Azerbaeva, R. G. & Tseft, A. L.; Behaviour of selenide and telluride of certain metals during saline leaching; *Met. i Khim. Prom. Kazakhstana, Nauchn.- Tekhn. Sb.*, 6 (1962) 92-95; CA 60:233g.
27. Azerbaeva, R.G. & Tseft, A.L.; Behavior of telluride and selenide of bismuth during leaching out with salts; *Tr. Inst. Met. i Obogashch.*, *Nauk Kaz. SSR* 8 (1963) 65-71; CA 60:12722h.
28. Azerbaeva, R.G. & Tseft, A.L.; Behavior of silver sulphide, selenide and telluride in salt leaching; *Zh. Prikl. Khim.*; 37 (1964) 2367-2371.
29. Azerbaeva, R.G. & Tseft, A.L.; Behavior of iron and lead selenide and lead telluride in leaching with salts; *Tr. Khim.- Met.Inst.*, Akad. Nauk Kaz. SSR, 1 (1963) 232-239; CA 60:15483d.
30. Biegler, T. & Swift, D.A.; Dissolution kinetics of copper sulphide anodes; *Hydrometallurgy*, 2 (1976/1977) 335-349.
31. Parker, A.J., Paul, R.L. & Power, G.P.; Electrochemistry of oxidative leaching of copper from chalcopyrite; *J. Electroanal. Chem.*, 118 (1981) 305-316.
32. Price, D.C. & Chilton, J.P.; The anodic reactions of bornite in sulphuric acid solution; *Hydrometallurgy*, 7 (1981) 117-133.
33. Ammou-Chokroum, M. et al; In Laskonski, J. (ed), "Mineral Processing (Proc. of the 13th Int. Mineral Congress)", Vol. 2, Elsevier, New York, 1981, 759-807.
34. Price, D.C. & Davenport, W.G.; Anodic reactions of heazlewoodite, millerite and nickel matte; *J. Appl. Electrochem.*, 12 (1982) 281-290.

35. Parker, A.J., Paul, R.L. & Power, P.; Electrochemical aspects of leaching copper from CuFeS_2 in Fe^{3+} & Cu^{2+} salt solutions; Austral. J. Chem., 34 (1981) 13-34.
36. McMillan, R.S., MacKinnon, D.J. & Dutrizac, J.E.; Anodic dissolution of n- & p-type chalcopyrite; J. Appl. Electrochem., 12 (1982) 743-757.
37. Jackson, E.; Hydrometallurgical extraction and reclamation, Ellis Horwood Ltd., Chichester, 1986.
38. Chizhikov, D.M.S.; Selenium & selenides; Collect's (Publishers), London, 1968.
39. Takahashi, M. & Honda, S.; Electrolytic refining of copper; Jpn.Kokai 74 36,522 (Cl.10L123), 04 Apr 1974.
40. Semina, O.I. & Pivovarova, L.S.; Cathodic leaching of electrolytic copper sludges in sulphite-alkaline solutions for extraction of selenium and tellurium; Deposited Document 1984, VINITI 2379-84, 11pp.
41. Ugorets, M.Z., Ugorets, V.M., & Semina, O.I.; Potentiodynamic study of electrochemical reduction of powdered tellurium & silver telluride in sodium hydroxide solutions; Zh. Prikl. Khim., 59 (1986) 1115-1117; CA 105:124211p.
42. Laikin, V.K.; Hydrochlorination of anodic sludge, Tr. Inst. Met. Obogashch. Akad. Nauk Kaz. SSR., 42 (1971) 37-47; CA 76:79944m
43. Makarov, G.V. et al; Electrochemical behavior of copper (I) chalcogenides in acid media; Zh. Prikl. Khim. (Leningrad), 53 (1980) 1542-1546.
44. Amsden, M.P., Sweetin, R.M. & Treilhard, D.M.; Selection and design of Texasgulf Canada's copper smelter and refinery; J. Met., 30 (1978) 16-31.
45. Schloen, J.H. & Elkin, E.M.; Treat. of electrolytic copper refinery slimes; Trans. Amer. Inst. Min. Met. Engineers, 188 (1950) 764-777.
46. Jennings, P.H. & Yannopoulos, J.C.; Recovery and refining of selenium; in "Selenium", R.A. Zingaro, & W.C. Cooper (eds); Van Nostrand Reinhold Comp., London, 1974, 31-77.
47. Gromakova, Z.I., Buketov, E.A.; Phase analysis of copper electrolytic sludges for selenium compounds; Tr. Khim.- Met. Inst., Akad. Nauk Kaz SSR., 3 (1967) 40-51; CA 69:48552b.
48. Sheveleva, L.D.; Lead phase in copper electrolysis slimes; Izv. Vyssh. Vchebn. Zaved., Tsvetn. Metall., 4 (1985) 33-37; CA 104:133430c.
49. Bayraktar, I. & Garner, F.A.; Hydrometallurgical processing of secondary copper anode slimes for metals recovery; in "Recycle and secondary recovery of metals"; P.R. Taylor et al (eds); The Met. Soc., Warrendale, 1985, 547-562.
50. Hukki, R.T.; Separation of precious metals from copper anode slimes by flotation; Trans. AIME, 187 (1950) 1131-1132.
51. Greiver, T.N.; Some feature of slime formation during electrolytic refining of copper and nickel; Tsvetn. Met. 33 (1965) 28-33.
52. Dancheva, N.; Phase chemical determination of forms of Se and Te in copper

- electrolyte sludges from the G. Damyanov metallurgical plants; *Metallurgia (Sofia)*; 3 (1972) 42-43; also CA 80:86409b.
53. Gromokova, Z.I., Gorokhova, L.G.; Phase analysis of tellurium compounds in copper electrolytic slimes; *Tr. Khim.- Met. Inst., Akad. Nauk Kaz.SSR*, 7 (1969) 150-154; also CA 73:49147z.
 54. Young, R.S.; The analysis of copper refinery slime; *Analytica Chimica Acta*, 4 (1950) 366-385.
 55. Erdenbaeva, M.I.; Phase analysis of selenium in anode slimes; *Izv. Akad. Nauk Kaz.SSR, Ser. Khim.*, 3 (1962) 42-45; also CA 57:3190g.
 56. G.Zarate, C.; Alternative processes for copper electrolyte purification; in "Recycle and secondary recovery metals", P.R. Teylor, H.Y. Sohn & N. Jarrett (eds); *The Met. Soc., AIME, Warrendale*, 1985, 589-607.
 57. Braun, T.B. et al; Factors affecting the quality of electrorefined cathode Cu; in "Extractive metallurgy of copper", Vol.2, Yannopoulos, J.C. and Agarwal, J.C. (eds), *The Met. Soc., AIME, New York*, 1976, 511-524.
 58. Barker, J.L.; Slimes treatment and silver refining operations by the Cerro de Pasco Co., Peru, in "Silver", Butts, A. & Cox, C.D.(eds); *D. Van Nostrand Comp., Princeton*, 1967, 95-102.
 59. Titarenko, A.G.; Feature of the behavior of nickel in the electrolytic refining of copper; *Tsvetn. Met.*, 3 (1981) 37-39.
 60. Vanorden, N.; State and concentration of selenium in copper refining electrolyte; *Metl. Trans.*, 11B (1980) 639-640.
 61. Makarov, G.V., Songina, O.A. & Buketov, E.A.; Role of Cu(I) in the electrolytic refining of copper; *Zh. Prikl. Khim.*, 45 (1972), 310-314; CA 96:120669r.
 62. Leigh, A.H.; Precious Metals Refining Practice; in "Int. Sym. Hydrometall."; Evans, D.J.I. & Shoemaker, R.S. (eds) *AIME*, 1973, 95-110.
 63. Lin, C.C. et al; Recovery of selenium from copper refining anodic slimes; *KungYeh ChiShu (Taipei)* 73 (1982) 1-7.
 64. Kukleva, T.V.; Low temperature oxidation of Cu(I) selenide; *Zhurnal Neorg. Khim.*, 27 (1982) 2191-2193.
 65. Lange, H.J. et al; Studies on anodic reactions of selenium in electrolytic copper refining; *Freiberg. Forschungsh.*, B228 (1981) 123-142; CA 96:171059n.
 66. Morrison, B.H.; Treatment of anode slimes in a top-blown rotary converter; U.S. US 4,581,064 (Cl.75-72; C22B15/00), 08 Apr 1986; CA 104:210610r.
 67. Ugorets, M.Z., Sagindykova, Z.B.; Rate of copper oxidation in a sulphuric acid media; *Tsvetn. Met.*, 8 (1972) 7-9.
 68. Nippon Mining Co.; Treatment of anode slime from copper electrolysis; *Japan Tokkyo Koho* 80/27,138 (Cl. C22B7/00), 18 July 1980; CA 94:107170y.
 69. Chang, C.C. et al; INER process for recovering precious metals from copper

- refinery anodic slimes; K'uang Yeh, 28 (1984) 71-79.
70. Pivovarova, L.S.; Electrochemical leaching of selenium from flue dust from roasting copper electrolyte slurry; Kompleksn. Ispol'Z. Miner. Syr'ya, 11 (1986) 59-63; CA 106:52596a.
 71. Tamura, T.; Treatment of anodic slimes produced by electrolytic refining of copper; Japan. 7052 ('55), 05 Oct 1955, CA 51:17532h.
 72. Heimala, S.O. & Hyvarinen, O.V.J.; Process for recovering useful elements from the anodic residues produced during the electrorefining copper; Belg. 834,488 (Cl.C22B), 02 Feb 1976.
 73. Ctyan, G.S., Vartanyants, S.A.; Processing copper electrolyte sludges by the action of ozone-air mixtures; Prom.-st. Arm., 12 (1975) 27-9; CA 85:51300.
 74. Bilson, E.A.; Recovery of metals from copper refining slimes; CA 88:179405c.
 75. Baeshov, A.; Effect of the electrode material on the reduction of hexavalent tellurate in alkaline solutions; Tsvetn. Met., pp.28-29 (1985).
 76. Naboichenko, S.S.; Autoclave leaching of copper electrolytic sludges; Tsvetn. Met., 1 (1981) 35-36.
 77. Snow, G.N.; Separation selenium and tellurium from each other; U.S. US 4,299,810 (Cl. C01B19/02) 10 Nov 1981; CA 96:127028c.
 78. Kunda, W.; Hydrometallurgical process for the recovery of silver from bearing materials; Hydrometallurgy, 17 (1981) 77-97.
 79. Subramanian, K.N. et al; Recovering selenium from copper anode slime; Mining Engineering, 30 (1978) 1538-1542.
 80. Tanaka, H. & Shimizu, F.; Recovery of tellurium from extract of copper electrorefining; Nippon Kogyo Kaishi, 101, pp.267-270
 81. Jennings, P.H; Extractive Metallurgy of tellurium; in "Tellurium", Copper, W.C.(ed), Van Nostrand Reinhold Comp., New York, 1971, 15-54.
 92. Golgstein, J. et al; Extraction of selenium and tellurium from the by-product of non-ferrous metallurgy; Rev. Chim., 14 (1963) 164-7; CA 59:12425g.
 83. Hyvarinen, O.; Selenium & precious metals recovery from anode slimes at Outokumpu Pori Refinery; in "Precious metals, mining, extraction & processing"; Kudryk, V. et al (eds), AIME, 1984, 537-548.
 84. Wang, W.K.; Hydrometallurgical process for recovering precious metals from anode slimes; Eur. Pat. Appl. 20826 (Cl. C22 B11/04), from CA 94:143163g.
 85. Baeshova, A.K. & Baeshov, A.; Anodic behavior of selenite ion in alkaline solutions; Deposited Document, 1982, VINITI 5362-82, 12pp.
 86. Semina, O.I., Ugorets, M.Z. & Buketov, E.A.; Using oxygen for autoclave oxidation of silver selenide; Tsvetn. Met., 45 (1972) 23-5.
 87. Buketov, E.A.; Autoclave extraction of selenium from copper electrolysis slimes;

- Tsvetn. Met., 41 (1968) 72-74.
88. Ugorets, M.Z., Semina, O.I. & Buketov, E.A.; Kinetics of sodium selenite oxidation by oxygen in an alkaline solution; CA 81:41950a.
 89. Ugorets, M.Z. & Semina, O.I.; Reaction of chalcogens with alkaline solutions; Tr. Khim.-Met. Inst., Akad. Nauk Kaz. SSR, 22 (1973) 21-31; CA 81:69003t.
 90. Semina, O.I. & Ugorets, M.Z.; Selenium & sulphur reaction with CuO in NaOH solution; CA 79:129626u.
 91. Dutton, W.A.; Inorganic chemistry of tellurium; in "Tellurium"; Cooper, W.C.(ed); Van Nostrand Reinhold Comp., New York, 1971, 110-184.
 92. Bagnall, K.W.; The Chemistry of selenium, tellurium & polonium, Elsevier Pub. Comp., Amsterdam (1961).
 93. Baeshova, E.A.; Cathodic behavior of Te(VI) on solid electrodes in H₂SO₄ solution; Izv. Vyssh.Uchebn. Zaved., Tsvetn. Metall., 4 (1986) 117-119; CA 106:92391m.
 94. Grieg, J.A.; Oxidative chloride leaching of sulphidic concentrates; Proc. Int. Sym. on Hydrometall., The Soc. Chem. Ind., Manchester, 1987, pp.35-48.
 95. McDonald, G.W.; Equilibria associated with chloride leaching of chalcopyrite; Hydrometallurgy, 13 (1984) 125-135.
 96. Bonan, M.; Chalcopyrite leaching by Cu(I) chloride in strong NaCl solutions; Met. Trans., 12B (1981) 269-274.
 97. Kunda, W.; Treatment of sulphidic concentrate in chloride system; in "Extractive metallurgy of Copper"; Yannopoulos, J.C. (eds); AIME, 1976, 793-811.
 98. Buketov, E.A. & Ugorets, M.Z.; CA 59:211d .
 99. Whitney, J.H.; Recovery of silver & gold; S. Afr. ZA 85/07,833 (Cl. C22B), 1986.
 100. James, E. & Ernst, R.G.; Silver recovery from sludges of electrolytic copper refining; Ger. Offen. 2,117,513 (Cl. C 22b); CA 76:27327t.
 101. Belenkii, A.M.; Leaching of lead antimonate from decoppered copper-electrolysis slimes; Tsvetn. Met., 6 (1986) 24-26.
 102. Ilic, I., Bugarski, P.; Chlorination of mud from copper electrolysis; Chem. Ind.; 26 (1972) 449-452.
 103. Gladyshev, S.V.; Study of the reaction of copper selenide with (NH₄)₂SO₄ in vacuo; Metallurgiya i Metalloved., 6 (1977) 85-88; CA 89:114516r.
 104. Gendolla, T. & Charewicz, W.; Selenium & tellurium in anode slime processing; Rudy Met. Niezelaz., 19 (1974) 524-527.
 105. Charewicz, W., Gendolla, T., Klapa, R. & Zagora, Z.; Recovery of silver and gold from anode slimes; Pol. 88,165 (Cl. C22B11/04), 15 Mar 1977.
 106. Koperski, S. & Herod, M.; Extraction of selenium from slag by leaching nitric acid containing thiourea; Rudy Met. Niezelaz., 21 (1976) 178-180.

107. Gluszek, J.; Electrolytic isolation of silver from acid solutions obtained in treatment of anodic slimes by HNO_3 ; Rudy Met. Niezelaz., 26 (1981) 28-30.
108. Charewick, W. & Gendolla, T.; Recovery of selenium and tellurium from anode slime; Pol. 84, 725 (Cl. C01B19/00), 15Dec1978, 2pp.; CA 91:11367e.
109. Segawa, T. et al; Concentration of noble metals in slag from chlorinated anode slimes; Jpn.Kokai Tokkyo Koho JP 61/217,536 (Cl. C22B7/00), 27 Sep 1986.
110. Kniprath, E., Repenhagen, C.; Recovery of selenium; CA 86:92567s.
111. Murayama, K.; Recovery of silver by solvent extraction; Jpn. Kokai Tokkyo Koho JP 60[85],228,626 (Cl.C22B11/04), 13 Nov 1985; CA 104:113594f.
112. Koperski, S; Recovery of silver and gold from anode slimes obtained in electro-refining of copper; Pol. 74,033 (Cl. C22b11/02), 306-76, 1976.
113. Bandmann, F. & Kniprath, E.; Dissolution of tellurium in acid solution; Ger. Offen. 2,244,829 (Cl. C01b), 21 Mar 1974.
114. Chang, C.C.; Recovery of copper from copper refining anode slime by liquid extraction; J. Chin. Inst. Chem. Eng. (Taipei), 10 (1979) 125-34.
115. Chang, C.C., Shaw, I.S., Hoh, Y.C. & Wang, W.K.; Denitration & acid recovery by solvent extraction; J. Chin. Inst. Chem. Eng., 11 (1980) 41-47.
116. Hoh, Y.C., Chang, C.C. & Wang, W.K.; Anode slime treatment; Eur. Pat. Appl. EP 59,806 (Cl.C22B3/00), 15Sep1982; Jpn.Kokai Tokkyo Koho, JP 57,149,437 (Cl. B14/04), 16 Sep 1982.
117. Hoh, Y.C.; Treatment of copper refining anode slime; U.S. US 4,352,786 (Cl.423-98,C01G21/02), 05 Oct 1982.
118. Hoh, Y.C., Shaw, I.S. & Wang, W.K.; Kinetic characteristics on silver leaching from copper refinery anode slime; Paper presented at 72th AIChE Annual meeting, San Francisco (1979).
119. Wang, W.C., Hoh, Y.C.; Hydrometallurgical process recovering precious metals from anode slimes; U.S. US 4,293,332 (Cl.75-99,C2B11/04), 06 Oct 1981.
120. Hoh, Y.C., Chang, C.C., Cheng, W.L. & Shaw, I.S.; The separation of selenium from tellurium in hydrochloric acid media by solvent extraction with tri-butyl phosphate (TBP); Hydrometallurgy, 9 (1983) 381-392.
121. Takei, M. & Ohto, S.; Denuding anode slime during electrolytic refining of copper, Jpn. Kokai Tokkyo Koho 78 10,325 (Cl.C25C1/12), 30 Jan 1978.
122. Erdenbaeva, M.I.; Kinetics and mechanism of the interaction of suspensions of selenium and tellurium compounds of varying valence with a sodium amalgam; Tr. Inst. Khim. Nauk, Akad. Nauk Kaz. SSR, 54 (1981) 100-116.
123. Erdenbaeva, M.I. et al; Behavior of copper telluride suspension on a mercury electrode and a sodium amalgam in various electrolytes; Deposited Document, 1981, 4467-81, 12pp. (VINITI).
124. Ugorets, M.Z., Pivovarova, L.S. & Semina, O.I.; Studies of extraction of selenium

- from copper electrolyte slurries by cathodic treatment in alkaline solution; Tr. Khim.- Metallurg. In-ta. AN Kaz. SSR., 1978, 73-90.
125. Shalaeva, T.S., Buketov, E.A. & Makarov, G.V.; Study of the electrochemical behavior of Cu(I) sulphide, selenide & telluride by the rotating disk electrode method; Tr. Khim.-Metallurg. In-ta. AN Kaz. SSR, 28 (1978) 94-100.
 126. Zlomanov, V.P.; Preparation of lead selenides; Russ. J. Inorg. Chem., 6, 882-883.
 127. Early, J.W.; Study of natural and artificial selenides. I-Klockmannite, CuSe; The American Mineralogist ; 34 (1949) 435-440.
 128. Early, J.W.; Description and synthesis of the selenide minerals; The American Mineralogist; 35 (1950) 337-364.
 129. Mikolaichuk, A.G. et al; Synthesis conditions and structure of some copper and silver chalcogenides, Deposited Documents, VINITI, 19pp. (1981)
 130. Shafizade, R.B. et al; Electron diffraction study of the phase transformation of the compound copper selenide; Thin solid films, 55 (1978) 211-220.
 131. Pinsker, Z.G. et al; Determination of the crystal structure of the low temperature phase α -Ag₂Se; Sov. Phys. Crystallogr. 10 (1965) 225-231.
 132. Wieggers, G.A.; The crystal structure of the low-temperature form of silver selenide; The Amer. Mineralogist, 26 (1971) 1882-1888.
 133. Fonzes-diacon; Bull. Soc. Chim. France; 3 (1900) 366-372.
 134. Borchet, W; Solid state reaction of copper and silver with selenium; Heidelberger Beitr. Mineral. u.u. Petrog. Mitt.; 4 (1955) 434-442; from CA 49:15394e.
 135. Hocart, R.; Synthesis of two copper selenides by compression powdered crystals of copper and selenium, Comptes Rendus, 233 (1951) 661-662; CA 46:2947d.
 136. Benzing, W.C. et al; Synthesis of selenides and tellurides: I. The reduction of selenites by hydrazine; J. Amer. Chem. Soc., 80 (1958) 2657-2659.
 137. Kulifay, S.M.; A low temperature synthesis for powder form intermetallics and other compounds; J. Amer. Chem. Soc., 80 (1958) 4916-4919.
 138. Kulifay, S.M.; A low temperature synthesis for powder-form intermetallics and other compounds-(II). Selenides; J. Inorg. Nucl. Chem., 25 (1963) 75-78.
 139. Ugorets, M.Z.; Study of the formation of Ag₂Se under hydrothermal conditions; Tr. Khim.-Met. Inst., Akad. Nauk Kaz, SSR, 22 (1974) 37-47; CA 83:36981y.
 140. Meshkova, M.; Ion-selective electrodes with sensors of electrochemically plated chalcogenide coatings. Part I. Copper ion-selective electrode based on plated copper selenide; J. Electroanal. Chem., 102 (1979) 189-198.
 141. Michele, D et al; Electrodeposition & electrodisolution of metal-semiconductor composite mixture - I. silver selenide, Elektrokhim. Acta, 31 (1986) 851-857.
 142. Bhattacharya, R.; Electrodeposited CdSe_{0.5}Te_{0.5}: Photoelectrochemical solar cells; J. Appl. Electrochem., 16 (1986) 168-174.

143. Korezyski, A.; Preparation of heavy metal selenides in solution; *Chem. Sosow.*, 25 (1981) 391-399.
144. Alekperov, A.I. et al; Electroprecipitation and dissolution of copper selenide from a formic electrolyte, *Azerb. Khim. Zh.*, 5 (1981) 104-106; CA 96:151266z.
145. Vaughan, D.J. & Craig J.R.; "Mineral chemistry of metal sulphides", Cambridge University Press, 1978.
146. Thornber, M.R.; Mineralogical & electrochemical stability of the nickel-iron sulphides - pentlandite & violarite, *J. Appl. Electrochem.* 13 (1983) 253-267.
147. Warner, T.E.; An electrochemical study of the oxidative dissolution of synthetic nickel-iron-sulphide minerals in aqueous media; Ph.D. thesis, University of Leeds, 1989.
148. Horváth, J. & Hackl, L.; Check of the potential/pH equilibrium diagrams of different metal-sulphur-water ternary systems by intermittent galvanostatic polarisation method; *Corrosion Science*, 5 (1965) 525-538.
149. Horváth, J. & Novák, M.; Electrochemical studies on the corrosion of copper in H₂S (aq) environments, *Acta Chim. Hung. Tomus.* 34 (1962) 455-467.
150. Hackl, Von L.; *Acta Univ. Szeged (Hung.) Acta Phys. Chem.* 11 (1965) 89-97.
151. Hansen, M.; *Constitution of Binary Alloys*; McGraw Hill (1958).
152. Conn, J.B. & Taylor, R.C.; Thermoelectric & crystallographic properties of Ag₂Se, *J. Electrochem. Soc.*, 107 (1960) 977-982.
153. Rahlfs, P.; Über die kubischen hochtemperaturmodifikationen der sulfide, selenide und telluride des silbers und des einwertigen kupfers; *Z. Phys. Chem. B31* (1936) 157-194.
154. Okazaki, H.; Deviation from the Einstein relation in average crystals: self-diffusion of Ag⁺ in α -Ag₂S & α -Ag₂Se; *J. Phys. Soc. Japan*, 23 (1969) 355-360.
155. Pourbaix, M.; *Atlas of electrochemical equilibria in aqueous solutions*; Pergamon Press, 1960.
156. Wangman, D.D.; Selected values of chemical thermodynamic properties; National Bureau of Standards, U.S. Government Office, Technical note 270-4, 1969.
157. Bard, A.J. & Parsons, R.; *Standard potentials in aqueous solutions*; IUPAC, Marcel DeKer, New York, 1985.
158. Mills, K.C.; *Thermodynamic data for inorganic sulphides, selenides & tellurides*; Butterworths, London, 1974.
159. Barin, I. & Knacke, O.; *Thermodynamic properties of inorganic substances*; Springer-Verlog, Berlin, 1973.
160. Ferreira, R.C.H.; High-temperature E-pH diagrams for the systems S-H₂O, Cu-S-H₂O and Fe-S-H₂O; In "Leaching & reduction in hydrometallurgy", Burkin, A.R. (ed); IMM, 1975, 67-83.

161. Warren, G.W.; Relationships between the pourbaix diagram for Ag-S-H₂O & electrochem. oxidation & reduction of Ag₂S; *Met. Trans.*, 15B (1984) 235-242
162. Peters, E.; The electrochemistry of sulphide minerals; In "Trends in electrochemistry", Bockris, J. O'M. (ed); Plenum Pub., New York, 1977, 267-290.
163. Sagindykova, Z.B.; Potential-pH diagrams of the copper-selenium-water & copper selenide-water systems; Deposited Document 4446-81, 1981 .
164. Criss, C.M. & Cobble, J.W.; The thermodynamic properties of high temperature aqueous solutions, *J. Am. Chem. Soc.* 86 (1964) 5385-5401.
165. Taylor, D.; Thermodynamic properties of metal-water systems at elevated temperatures, *J. Electrochem. Soc.* 125 (1978) 808-812.
166. Miller, J.D. & Portillo, H.Q.; Silver catalysis in ferric sulphate leaching of chalcopyrite; *Dev. Miner. Process.* 2 (1981) 851-897.
167. Price, D.W. & Warren, G.W.; The influence of silver ion on the electrochemical response of chalcopyrite & other mineral sulphide electrodes in sulphuric acid; *Hydrometallurgy* 15 (1986) 303-324.
168. Mulak, W.; Silver ion catalysis in nitric acid dissolution of Ni₃S₂; *Hydrometallurgy* 18 (1987) 195-205.
169. Buckley, A.N., Wouterlood, H.J. & Woods, R.; The interaction of pyrite with solutions containing silver ions; *J. App. Electrochem.* 19 (1989) 744-751.
170. Hamilton, I.C. & Woods, R.; *J. Electroanal. Chem.*, 118 (1981) 327.
171. Sato, M.; Oxidation of sulphide ore bodies. II. Oxidation Mechanisms of sulphide minerals at 25°C; *Economic Geology* 55 (1960) 1202-1231.
172. Price, D.W., Warren, G.W. & Drouven, B.; The electrochemical behaviour of silver sulphide in sulphuric acid solutions; *J. App. Electrochem.* 16 (1986) 719-731.
173. MacDonald, D.D.; *Transient techniques in electrochemistry*; Plenum Press, New York, 1977.
174. Hirato, T., Majima, H. & Awakura, Y.; The leaching of chalcopyrite with cupric chloride; *Metall. Trans. B*, 18B (1987) 31-39.
175. Price, D.C.; Application of chronopotentiometric analysis to the treatment of copper sulphides; *Met. Trans.* 12B (1981) 231-239.
176. Price, D.C.; The electroleaching of bornite & chalcopyrite; *Hydrometallurgy*, 5 (1980) 381-394.
177. Aguayo-Salinas, S.; "A study of the leaching of bornite by electrochemical techniques", Ph.D. Thesis, University of London, 1985.
178. Berzins, T. & Delahay, P.; Theory of electrolysis at constant current in unstirred solution; *J. Am. Chem. Soc.*, 75 (1953) 4205-4213.
179. Southampton Electrochemistry Group; "Instrumental methods in electrochemistry", Ellis Horwood Ltd., Chichester, 1985.

180. Bard, A.J. & Faulkner, L.R.; "Electrochemical methods"; John Wiley & Sons, New York, 1980.
181. Kholmanskikh Yu.B. et al; "Kinetics of dissolution of copper & its compounds in aqueous solutions; Tr. Ural. Nauch.-Issled. Proekt. Inst. Mednoi Prom., 9 (1966) 289-293.
182. Cooke, A.V., Chilton, J.P. & Fray, D.J.; Trans. Inst. Min. Met., 98C (1989) 123-131.
183. Sharma, L.R. & Dutt, J.; Indian J. Chem., 8 (1970) 170.
184. Suzuki, J.; Bull. Chem. Soc. Japan, 43 (1970) 755.
185. Sheridan, M.J.; "Leaching of sulphide minerals containing copper & silver", Ph.D. Thesis, University of London, 1975.
186. Potashnikov, Yu.M. et al; Kinetics of stromgyerite dissolution in aqueous nitric acid solutions, Izv. Vyssh. Ucheb. Zaved., Tsvet. Met., 12 (1969) 22-51.
187. Richardson, L.F.; Phil. Trans. A210 (1911) 307.
188. Randles, J.E.B.; Trans. Farady Soc. 44 (1948) 327.
189. Feldberg, S.W. & Auerbach, C.; Anal. Chem. 36 (1964) 505.
190. Feldberg, S.W.; in Electroanal. Chem. (ed A.J. Bard), 3 (1969) 199.
191. Hanafey, M.K.; Scott, R.L.; Ridgway, T.H. & Reilley, C.N.; Anal. Chem. 50 (1978) 116.
192. Britz, D.; Anal. Chim. Act. 122 (1980) 331.
193. Britz, D.; "Digital simulation in Electrochemistry", Springer-Verlag, Berlin, 1981.
194. Magno, F.; Bontempelli, G. & Sedeia, M.A.; Anal. Chim. Act. 140 (1982) 65.
195. Lasia, A.; J. Electroanal. Chem. 146 (1983) 397.
196. Heinze, J.; Storzbach, M. & Mortensen, J.; J. Electroanal. Chem. 165 (1984) 61.
197. Britz, D.; Anal. Chim. Act. 193 (1987) 277.
198. Britz, D. & Thomsen, K.; Anal. Chim. Act. 194 (1987) 317.
199. Britz, D.; J. Electroanal. Chem. 240 (1988) 17.
200. Britz, D.; Heinze, J.; Mortensen, J. & Storzbach, M.; J. Electroanal. Chem. 240 (1988) 27.
201. Friedrichs, M.S.; Friesner, R.A. & Bard, A.J.; J. Electroanal. Chem. 256 (1988) 239.
202. Ruzic, I. & Feldberg, S.W.; J. Electroanal. Chem. 63 (1975) 1
203. Heinze, J.; J. electroanal. Chem. 124 (1981) 73.
204. Heinze, J.; Ber. Bunsenges. phys. Chem. 85 (1981) 1096.

205. Heinze, J.; *Ber. Bunsenges. phys. Chem.* 90 (1986) 1043.
206. Berzins, T. & Delahay, P.; *J. Am. Chem. Soc.* 75 (1953) 555.
207. Koutecky, J.; *Collect. Cze. Chem. Commun.*, 21(1956) 433.
208. Reinmuth, W.H.; *J. Am. Chem. Soc.* 79 (1957) 6358.
209. Gokhshtein, Y.P.; *Doklady Akad.Nauk SSSR* 126 (1959) 598.
210. Matsuda, H.; *Z. Elektrochem.* 61 (1957) 489.
211. Nicholson, M.M.; *J. Am. Chem. Soc.* 79 (1957) 7.
212. Saveant, J.M. & Vianello, E.; in "Progress in Polarography", I.S. Longmuir (ed.), Vol I, p. 367, Pergamon Press, New York, 1960.
213. Nicholson, R.S. & Shain, I.; *Anal. Chem.* 36 (1964) 706.
214. Nicholson, R.S. & Shain, I.; *Anal. Chem.* 37 (1965) 178.
215. Nicholson, M.M.; *J. Am. Chem. Soc.* 76 (1954) 2539.
216. Frankkental, R.P. & Shain, I.; *J. Am. Chem. Soc.* 78 (1956) 2969.
217. Vetter, K.J.; "Electrochemical Kinetics", Academic Press, New York, 1967.
218. Crank, J. & Nicolson, P.; *Proc. Camb. Phil. Soc.* 43 (1947) 50.
219. Hartree, D.R. & Womersley, J.R.; *Proc. Roy. Soc. A*, 161 (1937) 353.
220. Redish, K.A.; *An Introduction to Computational Methods*, Chapter 3, The English Universities Press Ltd., London, 1961.
221. Ryan, M.D.; *J. Electrochem. Soc.*, 125 (1978) 547.
222. Hinkelmann, K. & Heinze, J.; *Ber. Bunsenges. phys. Chem.* 91 (1987) 243.
223. Mastragostino, M. & Saveant, J.M.; *Electrochimica Acta*, 13 (1968) 751.
224. Hawley, M.D. & Feldberg, S.W.; *J. Phys. Chem.*, 70 (1966) 3459.
225. Wimmer, F.L.; Snow, M.R. & Bond, A.M.; *Inorg. Chem.*, 13 (1974) 1617.
226. Bond, A.M.; Colton, R. & Jackowski, J.J.; *Inorg. Chem.*, 14(1975) 274, 2526.
227. Carr, S.W.; *Studies in Platinum Group and Group VI Carbonyl Chemistry*, PhD Thesis, University of Melbourne, 1983.
228. Vetter, V.K.J.; *Z. Elektrochem.*, 56 (1952) 797.
229. Imbeaux, J.C. & Savéant, J.M.; *J. Electroanal. Chem.*, 44 (1973) 169.
230. Savéant, J.M. & Tessier, D.; *J. Electroanal. Chem.*, 61 (1975) 251.
231. Oldham, K. B.; *Anal. Chem.*, 44 (1972) 196.

232. Oldham, K.B.; *J. Chem. Soc., Faraday Trans. 1*, 82 (1986) 1099.
233. Savéant, J.M. & Tessier, D.; *J. Electroanal. Chem.*, 65 (1975) 57.
234. Dobson, I.D., Taylor, N. & Tipping, L.R.H.; In "Electrochemistry, Sensors & Analysis", pp. 61-75, Elsevier, Amsterdam, 1986
235. Barnard, G.M., Boddington, T., Gregor, J.E., Pettit, L.D. & Taylor, N.; *J. Chem. Soc. Talanta*, 37 (1990) 219.
236. Boddington, T., Luo, R., Rice, N.M., Taylor, N. & Warner, T.E.; to be published.
237. Schwarz, W.M. & Shain, I.; *J. Phys. Chem.*, 69 (1965) 30.
238. Boddington, T., Luo, R. & Taylor, N.; to be published.
239. Miler, W.L. & Gordon, A.R.; *J. Phys. Chem.* 35 (1931) 2787-2884.
240. Abramowitz, M. & Stegun, I.A.; *Handbook of mathematical functions*; Dover Publications, Inc., New York, 1965.
241. Press, W.H., Flannery, B.P., Teukolsky, S.A. & Vetterling, W.T.; *Numerical Recipes*; Cambridge University Press, Cambridge, 1986.

101
102
103
104
105
106
107
108
109
110
111
112
113
114
115
116
117
118
119
120
121
122
123
124
125
126
127
128
129
130
131
132
133
134
135
136
137
138
139
140
141
142
143
144
145
146
147
148
149
150
151
152
153
154
155
156
157
158
159
160
161
162
163
164
165
166
167
168
169
170
171
172
173
174
175
176
177
178
179
180
181
182
183
184
185
186
187
188
189
190
191
192
193
194
195
196
197
198
199
200

Appendix

A-1 Thermodynamic Data and Equilibria Equations for Construction of Eh-pH Diagrams

A-1.1 Thermodynamic data for copper, silver & selenium species at 298.15K

Substance	State	$\Delta H_f^\circ / \text{kJ} \cdot \text{mol}^{-1}$	$\Delta G_f^\circ / \text{kJ} \cdot \text{mol}^{-1}$	S/J mol ⁻¹	Ref.
H ₂	g	0.0	0.0	130.68	156
H ⁺	aq	0.0	0.0	0.0	156
O ₂	g	0.0	0.0	205.03	156
OH ⁻	aq	-229.99	-157.29	-10.75	156
H ₂ O	l	-285.83	-237.18	-69.91	156
S	c	0.0	0.0	31.80	156
Se	c	0.0	0.0	42.26	158
Se ²⁻	aq		-129.29		156
HSe ⁻	aq	15.90	43.93	79.50	156
H ₂ Se	aq	19.25	22.18	163.59	156
	g	29.71	15.90	218.91	156
SeO ₃ ²⁻	aq	-509.19	-369.87	12.55	156
HSeO ₃ ⁻	aq	-514.55	-411.54	135.14	156
H ₂ SeO ₃	aq	-507.48	-426.22	207.95	156
SeO ₄ ²⁻	aq	-599.15	-441.41	53.97	156
HSeO ₄ ⁻	aq	-581.58	-452.29	149.37	156
H ₂ SeO ₄	aq	-599.1	-441.40	54.10	156
Ag	c	0.0	0.0	42.57	156
Ag ⁺	aq	105.63	77.16	72.71	156
Ag ²⁺	aq	268.74	269.16	-87.91	156
AgO ⁺	aq	225.63			157
AgO ⁻	aq		-22.98		157
Ag ₂ O	c	-31.06	-11.22	121.39	156
AgO	c	-12.14	14.65	57.35	156
Ag ₂ O ₃	c	33.91	121.39	100.46	156
Ag ₂ S	c ^{**}	-32.61	-40.69	144.08	157
Ag ₂ S	c	-29.43	-39.47	150.70	157
Ag ₂ S	c	-31.59		143.51	158
Ag ₂ SO ₃	c	-491.02	-441.48	158.23	157
Ag ₂ SO ₄	c	-716.22	-618.77	200.51	157
Ag ₂ Se	c	-43.514	-50.313 [*]	150.164	158
Ag ₂ Se	c	-37.67	-44.37	150.78	157
Ag ₂ SeO ₃	c	-365.44	-304.32	230.23	157

Substance	State	$\Delta H_f^\circ / \text{kJ} \cdot \text{mol}^{-1}$	$\Delta G_f^\circ / \text{kJ} \cdot \text{mol}^{-1}$	$S / \text{J} \cdot \text{mol}^{-1}$	Ref.
Ag_2SeO_3	aq	-298.04	-215.58	159.07	157
Ag_2SeO_4	c	-420.69	-334.46	248.65	157
Ag_2SeO_4	aq	-388.04	-287.16	199.67	157
AgTe	c	-37.26	-43.12	154.88	157
Ag_2Te	c	-35.982	-41.621*	153.55	157
Ag_2CO_3	c	-506.09	-437.02	167.44	156
Cu	c	0.0	0.0	33.35	156
Cu^+	aq	71.67	50.0	40.58	156
Cu^{2+}	aq	64.77	65.52	-99.58	156
Cu_2O	c	-168.62	-146.02	93.14	156
CuO	c	-157.32	-129.70	42.63	156
$\text{Cu}(\text{OH})_2$	c	-443.7	-359.5	87.2	157
HCuO_2^-	aq		-258.57		156
CuO_2	aq		-183.68		156
Cu_2S	c	-81.3	-87.6	118.8	157
	c	-79.50		120.92	158
CuS	c	-52.8	-53.2	66.96	157
	c	-52.30		66.53	158
Cu_2Se	c	-65.27	-71.58*	129.70	158
Cu_3Se_2	c	-62.76	-69.66*	207.11	158
CuSe	c	-41.84	-42.69*	78.241	158
CuSe_2	c	-48.12	-45.10*	107.53	158
CuSeO_3	c		-348.11		?
CuSeO_4	c	-478.48			?
Cu_2Te	c	-41.84	-47.48	134.73	158
CuTe	c	-25.10	-26.29	86.61	158

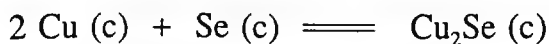
* Calculated from known thermodynamic data listed in reference 158. These calculated data are quite different from Barin's values (Ref. 159) which were also derived from Mills' data (Ref. 158). The latter are incorrect because the Third Law entropies of the selenides & tellurides were considered as entropy changes of the reactions of formation of the related substances (cf. A-3.2).

** With an orthorhombic crystal structure.

A-1.2 Evaluation of Free Energy Change of Formation for Various Selenides, & Tellurides

Standard free energies of formation for selenides & tellurides of copper & silver e.g. Ag₂Se, CuSe, Cu₂Se, Cu₃Se₂, CuSe₂, Ag₂Te, Cu₂Te and CuTe are evaluated from entropy and enthalpy values of the corresponding substances involved in the formation reaction. Below is an example illustrating procedures for the evaluation the free energy of formation of Cu₂Se at 298.15K.

Copper selenide is formed via the following reaction involving Cu & Se



As the standard enthalpy change of formation of Cu₂Se is known (Ref. 3) & those for the elements are zero, the enthalpy change of the above reaction can be readily obtained

$$\begin{aligned} \Delta H_{298}^{\circ} &= \Delta H_{f,298}^{\circ}(\text{Cu}_2\text{Se}) - \Delta H_{f,298}^{\circ}(\text{Se}) - 2.0 \times \Delta H_{f,298}^{\circ}(\text{Cu}) \\ &= - 65.27 \text{ (kJ}\cdot\text{mol}^{-1}) - 0.0 - 2.0 \times 0.0 \\ &= - 65.27 \text{ (kJ}\cdot\text{mol}^{-1}) \end{aligned}$$

Similarly, the entropy change can be evaluated via

$$\begin{aligned} \Delta S_{298}^{\circ} &= S_{298}^{\circ}(\text{Cu}_2\text{Se}) - S_{298}^{\circ}(\text{Se}) - 2.0 * S_{298}^{\circ}(\text{Cu}) \\ &= 129.70 - 42.26 - 2.0 * 33.15 \\ &= 21.14 \text{ (J}\cdot\text{mol}^{-1}\cdot\text{K}^{-1}) \end{aligned}$$

Therefore, the free energy change of the above reaction and subsequently the free energy of formation of Cu₂Se can be obtained

$$\begin{aligned} \Delta G_{298}^{\circ} &= \Delta H_{298}^{\circ} - T \times \Delta S_{298}^{\circ} \\ &= - 65.27 - 298.15 \times 21.14 \times 10^{-3} \\ &= - 71.58 \text{ (kJ}\cdot\text{mol}^{-1}) \end{aligned}$$

$$\begin{aligned} \Delta G_{f,298}^{\circ}(\text{Cu}_2\text{Se}) &= \Delta G_{298}^{\circ} + \Delta G_{f,298}^{\circ}(\text{Se}) + 2.0 \times \Delta G_{f,298}^{\circ}(\text{Cu}) \\ &= - 71.58 + 0.0 + 2.0 \times 0.0 \\ &= - 71.58 \text{ (kJ}\cdot\text{mol}^{-1}) \end{aligned}$$

A-1.3 Equilibria equations for construction of Eh-pH diagrams

Here $[B] = C_B / (\text{mol} \cdot \text{dm}^{-3})$, $E = E(\text{electrode}) / \text{Volt}$.

Cu - H₂O System Eh - pH equilibrium equations

A. Relative Stability of Dissolved Species

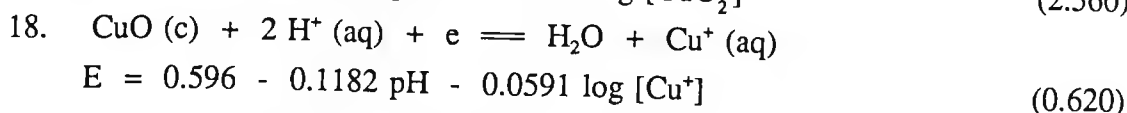
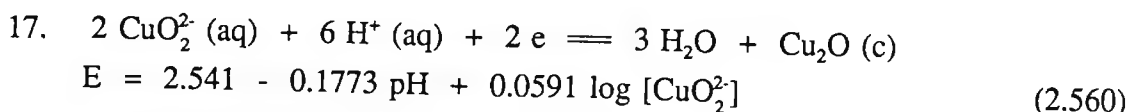
1. $\text{Cu}^{2+}(\text{aq}) + 2 \text{H}_2\text{O} \rightleftharpoons 3 \text{H}^+(\text{aq}) + \text{HCuO}_2^-(\text{aq})$
 $\text{pH} = 8.777 + 0.333 \log [\text{HCuO}_2^-] - 0.333 \log [\text{Cu}^{2+}]$
2. $\text{Cu}^{2+}(\text{aq}) + 2 \text{H}_2\text{O} \rightleftharpoons 4 \text{H}^+(\text{aq}) + \text{CuO}_2^{2-}(\text{aq})$
 $\text{pH} = 9.864 + 0.250 \log [\text{CuO}_2^{2-}] - 0.250 \log [\text{Cu}^{2+}]$
3. $\text{HCuO}_2^-(\text{aq}) \rightleftharpoons \text{H}^+(\text{aq}) + \text{CuO}_2^{2-}(\text{aq})$
 $\text{pH} = 13.122 + \log [\text{CuO}_2^{2-}] - \log [\text{HCuO}_2^-]$
4. $\text{Cu}^{2+}(\text{aq}) + e \rightleftharpoons \text{Cu}^+(\text{aq})$
 $E = 0.160 - 0.0591 \log [\text{Cu}^+] + 0.0591 \log [\text{Cu}^{2+}]$ (**)
5. $\text{HCuO}_2^-(\text{aq}) + 3 \text{H}^+(\text{aq}) + e \rightleftharpoons \text{Cu}^+(\text{aq}) + 2 \text{H}_2\text{O}$
 $E = 1.733 - 0.1773 \text{pH} - 0.0591 \log ([\text{Cu}^+]/[\text{HCuO}_2^-])$ (**)
6. $\text{CuO}_2^{2-}(\text{aq}) + 4 \text{H}^+(\text{aq}) + e \rightleftharpoons \text{Cu}^+(\text{aq}) + 2 \text{H}_2\text{O}$
 $E = 2.510 - 0.2364 \text{pH} - 0.0591 \log ([\text{Cu}^+]/[\text{CuO}_2^{2-}])$ (*)

B. Solubility of Copper

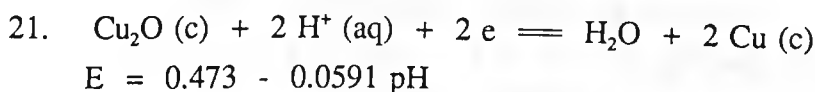
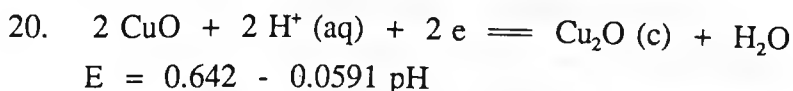
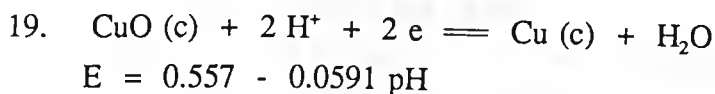
7. $\text{Cu}^+(\text{aq}) + e \rightleftharpoons \text{Cu}(\text{s})$
 $E = 0.520 + 0.0591 \log [\text{Cu}^+]$ (**)
8. $\text{Cu}^{2+}(\text{aq}) + 2e \rightleftharpoons \text{Cu}(\text{s})$
 $E = 0.337 + 0.0296 \log [\text{Cu}^{2+}]$ (**)
9. $\text{CuO}_2^{2-}(\text{aq}) + 4 \text{H}^+(\text{aq}) + 2e \rightleftharpoons 2 \text{H}_2\text{O} + \text{Cu}(\text{s})$
 $E = 1.515 - 0.1182 \text{pH} + 0.0296 \log [\text{CuO}_2^{2-}]$ (*)
10. $\text{HCuO}_2^-(\text{aq}) + 3 \text{H}^+(\text{aq}) + 2e \rightleftharpoons 2 \text{H}_2\text{O} + \text{Cu}(\text{s})$
 $E = 1.118 - 0.0887 \text{pH} + 0.0296 \log [\text{HCuO}_2^-]$ (1.127)

C. Solubility of Copper Oxides

11. $\text{CuO}(\text{s}) + 2 \text{H}^+(\text{aq}) \rightleftharpoons \text{Cu}^{2+}(\text{aq}) + \text{H}_2\text{O}$
 $\text{pH} = 3.6764 - 0.5000 \log [\text{Cu}^{2+}]$
12. $\text{CuO}(\text{s}) + \text{H}_2\text{O} \rightleftharpoons \text{HCuO}_2^-(\text{aq}) + \text{H}^+(\text{aq})$
 $\text{pH} = 18.979 + \log [\text{HCuO}_2^-]$
13. $\text{CuO}(\text{s}) + \text{H}_2\text{O} \rightleftharpoons \text{CuO}_2^{2-}(\text{aq}) + 2 \text{H}^+(\text{aq})$
 $\text{pH} = 16.032 + 0.500 \log [\text{CuO}_2^{2-}]$
14. $\text{Cu}_2\text{O}(\text{s}) + 2 \text{H}^+(\text{aq}) \rightleftharpoons 2 \text{Cu}^+(\text{aq}) + \text{H}_2\text{O}$
 $\text{pH} = 0.773 - \log [\text{Cu}^+]$
15. $2 \text{Cu}^{2+}(\text{aq}) + \text{H}_2\text{O} + 2e \rightleftharpoons \text{Cu}_2\text{O}(\text{s}) + 2 \text{H}^+(\text{aq})$
 $E = 0.207 + 0.0591 \log [\text{Cu}^{2+}] + 0.0591 \text{pH}$ (0.203)
16. $2 \text{HCuO}_2^-(\text{aq}) + 4 \text{H}^+(\text{aq}) + 2e \rightleftharpoons 3 \text{H}_2\text{O} + \text{Cu}_2\text{O}(\text{s})$
 $E = 1.764 - 0.1182 \text{pH} + 0.0591 \log [\text{HCuO}_2^-]$ (1.783)

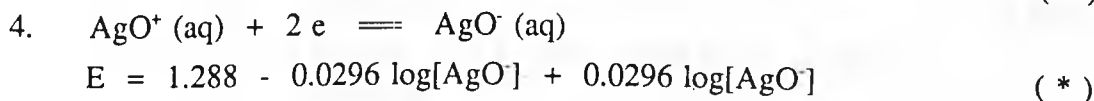
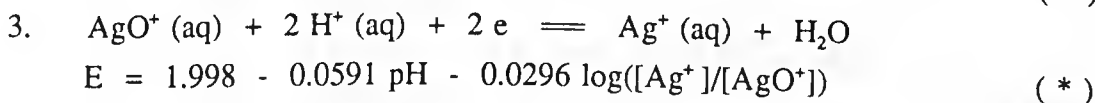
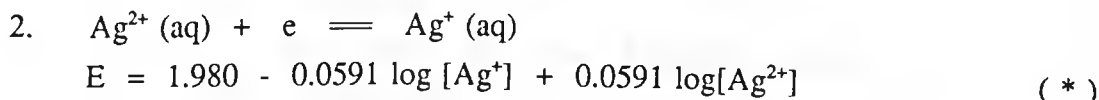
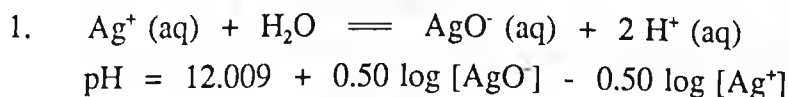


C. Equilibria involving two Solid Phases

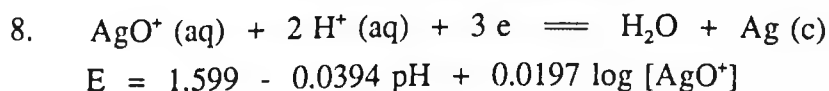
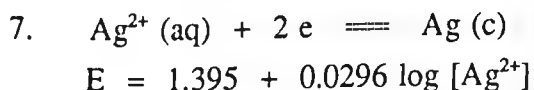
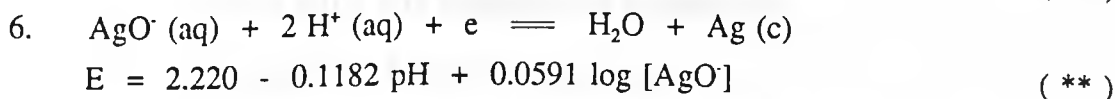
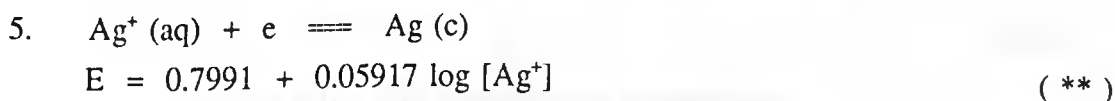


Ag - H₂O System Eh - pH Equilibrium equations

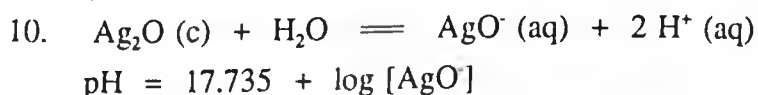
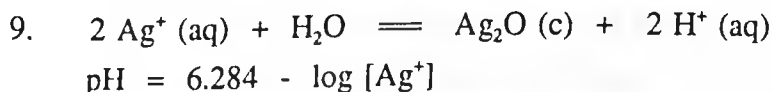
A. Stability of dissolved species



B. Solubility of Silver



C. Solubility of silver oxides



11. $2 \text{AgO}^+(\text{aq}) + \text{H}_2\text{O} \rightleftharpoons \text{Ag}_2\text{O}(\text{c}) + 2 \text{H}^+(\text{aq})$
 $\text{pH} = -8.119 - \log [\text{AgO}^+]$
12. $\text{AgO}(\text{c}) + 2 \text{H}^+(\text{aq}) + \text{e} \rightleftharpoons \text{Ag}^+(\text{aq}) + \text{H}_2\text{O}$
 $E = 1.811 - 0.1182 \text{pH} - 0.0591 \log [\text{Ag}^+]$ (1.772)
13. $\text{AgO}(\text{c}) + \text{e} \rightleftharpoons \text{AgO}^-(\text{aq})$
 $E = 0.390 - 0.0591 \log [\text{AgO}^-]$ (0.351)
14. $\text{Ag}_2\text{O}_3(\text{c}) + 6 \text{H}^+(\text{aq}) + 4 \text{e} \rightleftharpoons 2 \text{Ag}^+(\text{aq}) + 3 \text{H}_2\text{O}$
 $E = 1.759 - 0.0887 \text{pH} - 0.0296 \log [\text{Ag}^+]$ (1.670)
15. $\text{Ag}_2\text{O}_3(\text{c}) + 2 \text{H}^+(\text{aq}) + 4 \text{e} \rightleftharpoons 2 \text{AgO}^-(\text{aq}) + \text{H}_2\text{O}$
 $E = 1.048 - 0.0296 \text{pH} - 0.0296 \log [\text{AgO}^-]$ (0.960)
16. $\text{Ag}_2\text{O}_3(\text{c}) + 6 \text{H}^+(\text{aq}) + 2 \text{e} \rightleftharpoons 2 \text{Ag}^+(\text{aq}) + 3 \text{H}_2\text{O}$
 $E = 1.527 - 0.1773 \text{pH} - 0.0591 \log [\text{Ag}^+]$ (1.360)

D. Equilibria involving two solid phases

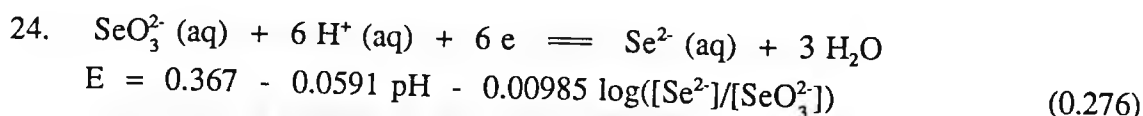
17. $\text{Ag}_2\text{O}(\text{c}) + 2 \text{H}^+(\text{aq}) + 2 \text{e} \rightleftharpoons 2 \text{Ag}(\text{c}) + \text{H}_2\text{O}$
 $E = 1.173 - 0.0591 \text{pH}$ (*)
18. $\text{Ag}_2\text{O}(\text{c}) + 2 \text{H}^+(\text{aq}) + 2 \text{e} \rightleftharpoons \text{Ag}(\text{c}) + \text{H}_2\text{O}$
 $E = 1.305 - 0.0591 \text{pH}$
19. $\text{Ag}_2\text{O}_3(\text{c}) + 6 \text{H}^+(\text{aq}) + 6 \text{e} \rightleftharpoons 2 \text{Ag}(\text{c}) + \text{H}_2\text{O}$
 $E = 1.4389 - 0.0591 \text{pH}$
20. $2 \text{AgO}(\text{c}) + 2 \text{H}^+(\text{aq}) + 2 \text{e} \rightleftharpoons \text{Ag}_2\text{O}(\text{c}) + \text{H}_2\text{O}$
 $E = 1.4392 - 0.0591 \text{pH}$ (1.398)
21. $\text{Ag}_2\text{O}_3(\text{c}) + 4 \text{H}^+(\text{aq}) + 4 \text{e} \rightleftharpoons \text{Ag}_2\text{O}(\text{c}) + 2 \text{H}_2\text{O}$
 $E = 1.573 - 0.0591 \text{pH}$
22. $\text{Ag}_2\text{O}_3(\text{c}) + 2 \text{H}^+(\text{aq}) + 2 \text{e} \rightleftharpoons 2 \text{AgO}(\text{c}) + \text{H}_2\text{O}$
 $E = 1.707 - 0.0591 \text{pH}$ (1.569)

Se - H₂O System Eh - pH equilibrium equations

A. Relative stability of dissolved species

1. $\text{H}_2\text{Se}(\text{aq}) \rightleftharpoons \text{HSe}^-(\text{aq}) + \text{H}^+(\text{aq})$ $K_1 = 1.88 \times 10^{-4}$
 $\text{pH} = 3.726 + \log [\text{HSe}^-] - \log [\text{H}_2\text{Se}]$
2. $\text{HSe}^-(\text{aq}) \rightleftharpoons \text{Se}^{2-}(\text{aq}) + \text{H}^+(\text{aq})$ $K_2 = 1.0 \times 10^{-14}$
 $\text{pH} = 14.000 + \log [\text{Se}^{2-}] - \log [\text{HSe}^-]$
3. $\text{H}_2\text{SeO}_3(\text{aq}) \rightleftharpoons \text{HSeO}_3^-(\text{aq}) + \text{H}^+(\text{aq})$ $K_1 = 2.7 \times 10^{-3}$
 $\text{pH} = 2.569 + \log [\text{HSeO}_3^-] - \log [\text{H}_2\text{SeO}_3]$
4. $\text{HSeO}_3^-(\text{aq}) \rightleftharpoons \text{SeO}_3^{2-}(\text{aq}) + \text{H}^+(\text{aq})$ $K_2 = 2.63 \times 10^{-7}$
 $\text{pH} = 6.580 + \log [\text{SeO}_3^{2-}] - \log [\text{HSeO}_3^-]$
5. $\text{H}_2\text{SeO}_4(\text{aq}) \rightleftharpoons \text{HSeO}_4^-(\text{aq}) + \text{H}^+(\text{aq})$

- $\text{pH} = -1.906 + \log[\text{HSeO}_4^-] - \log[\text{H}_2\text{SeO}_4]$
6. $\text{HSeO}_4^- (\text{aq}) \rightleftharpoons \text{SeO}_4^{2-} (\text{aq}) + \text{H}^+ (\text{aq}) \quad K_2 = 8.9 \times 10^{-3}$
 $\text{pH} = 2.051 + \log[\text{SeO}_4^{2-}] - \log[\text{HSeO}_4^-]$
 7. $\text{H}_2\text{SeO}_4 (\text{aq}) + 2 \text{H}^+ (\text{aq}) + 2 \text{e} \rightleftharpoons \text{H}_2\text{SeO}_3 (\text{aq}) + \text{H}_2\text{O}$
 $E = 1.151 - 0.0591 \text{pH} - 0.0296 \log([\text{H}_2\text{SeO}_3]/[\text{H}_2\text{SeO}_4])$
 8. $\text{H}_2\text{SeO}_4 (\text{aq}) + 3 \text{H}^+ (\text{aq}) + 2 \text{e} \rightleftharpoons \text{HSeO}_3^- (\text{aq}) + \text{H}_2\text{O}$
 $E = 1.074 - 0.0296 \text{pH} - 0.0296 \log([\text{HSeO}_3^-]/[\text{H}_2\text{SeO}_4])$
 9. $\text{H}_2\text{SeO}_4 (\text{aq}) + 2 \text{e} \rightleftharpoons \text{H}_2\text{O} + \text{SeO}_3^{2-} (\text{aq})$
 $E = 0.859 - 0.0296 \log([\text{SeO}_3^{2-}]/[\text{H}_2\text{SeO}_4])$
 10. $\text{HSeO}_4^- (\text{aq}) + 3 \text{H}^+ (\text{aq}) + 2 \text{e} \rightleftharpoons \text{H}_2\text{SeO}_3 (\text{aq}) + \text{H}_2\text{O}$
 $E = 1.094 - 0.0887\text{pH} - 0.0296 \log([\text{H}_2\text{SeO}_3]/[\text{HSeO}_4^-]) \quad (**)$
 11. $\text{HSeO}_4^- (\text{aq}) + 2 \text{H}^+ (\text{aq}) + 2 \text{e} \rightleftharpoons \text{HSeO}_3^- (\text{aq}) + \text{H}_2\text{O}$
 $E = 1.018 - 0.0591 \text{pH} - 0.0296 \log([\text{HSeO}_3^-]/[\text{HSeO}_4^-])$
 12. $\text{HSeO}_4^- (\text{aq}) + \text{H}^+ (\text{aq}) + 2 \text{e} \rightleftharpoons \text{SeO}_3^{2-} (\text{aq}) + \text{H}_2\text{O}$
 $E = 0.802 - 0.0296 \text{pH} - 0.0296 \log([\text{SeO}_3^{2-}]/[\text{HSeO}_4^-])$
 13. $\text{SeO}_4^{2-} (\text{aq}) + 4 \text{H}^+ (\text{aq}) + 2 \text{e} \rightleftharpoons \text{H}_2\text{SeO}_3 (\text{aq}) + \text{H}_2\text{O}$
 $E = 1.151 - 0.1182\text{pH} - 0.0296 \log([\text{H}_2\text{SeO}_3]/[\text{SeO}_4^{2-}]) \quad (**)$
 14. $\text{SeO}_4^{2-} (\text{aq}) + 3 \text{H}^+ (\text{aq}) + 2 \text{e} \rightleftharpoons \text{HSeO}_4^- (\text{aq}) + \text{H}_2\text{O}$
 $E = 1.074 - 0.0887\text{pH} - 0.0296 \log([\text{HSeO}_3^-]/[\text{SeO}_4^{2-}]) \quad (**)$
 15. $\text{SeO}_4^{2-} (\text{aq}) + 2 \text{H}^+ (\text{aq}) + 2 \text{e} \rightleftharpoons \text{SeO}_3^{2-} (\text{aq}) + \text{H}_2\text{O}$
 $E = 0.859 - 0.0591\text{pH} - 0.0296 \log([\text{SeO}_3^{2-}]/[\text{SeO}_4^{2-}]) \quad (**)$
 16. $\text{H}_2\text{SeO}_3 (\text{aq}) + 6 \text{H}^+ (\text{aq}) + 6 \text{e} \rightleftharpoons \text{H}_2\text{Se} (\text{aq}) + 3 \text{H}_2\text{O}$
 $E = 0.454 - 0.0591\text{pH} - 0.00985 \log([\text{H}_2\text{Se}]/[\text{H}_2\text{SeO}_3]) \quad (0.360)$
 17. $\text{H}_2\text{SeO}_3 (\text{aq}) + 5 \text{H}^+ (\text{aq}) + 6 \text{e} \rightleftharpoons \text{HSe}^- (\text{aq}) + 3 \text{H}_2\text{O}$
 $E = 0.417 - 0.0493 \text{pH} - 0.00985 \log([\text{HSe}^-]/[\text{H}_2\text{SeO}_3])$
 18. $\text{H}_2\text{SeO}_3 (\text{aq}) + 4 \text{H}^+ (\text{aq}) + 6 \text{e} \rightleftharpoons \text{Se}^{2-} (\text{aq}) + 3 \text{H}_2\text{O}$
 $E = 0.270 - 0.0394 \text{pH} - 0.00985 \log([\text{Se}^{2-}]/[\text{H}_2\text{SeO}_3])$
 19. $\text{HSeO}_3^- (\text{aq}) + 7 \text{H}^+ (\text{aq}) + 6 \text{e} \rightleftharpoons \text{H}_2\text{Se} (\text{aq}) + 3 \text{H}_2\text{O}$
 $E = 0.480 - 0.0690\text{pH} - 0.00985 \log([\text{H}_2\text{Se}]/[\text{HSeO}_3^-]) \quad (0.386)$
 20. $\text{HSeO}_3^- (\text{aq}) + 6 \text{H}^+ (\text{aq}) + 6 \text{e} \rightleftharpoons \text{HSe}^- (\text{aq}) + 3 \text{H}_2\text{O}$
 $E = 0.442 - 0.0591\text{pH} - 0.00985 \log([\text{HSe}^-]/[\text{HSeO}_3^-]) \quad (0.349)$
 21. $\text{HSeO}_3^- (\text{aq}) + 5 \text{H}^+ (\text{aq}) + 6 \text{e} \rightleftharpoons \text{Se}^{2-} (\text{aq}) + 3 \text{H}_2\text{O}$
 $E = 0.295 - 0.0493 \text{pH} - 0.00985 \log([\text{Se}^{2-}]/[\text{HSeO}_3^-])$
 22. $\text{SeO}_3^{2-} (\text{aq}) + 8 \text{H}^+ (\text{aq}) + 6 \text{e} \rightleftharpoons \text{H}_2\text{Se} (\text{aq}) + 3 \text{H}_2\text{O}$
 $E = 0.552 - 0.0788 \text{pH} - 0.00985 \log([\text{H}_2\text{Se}]/[\text{SeO}_3^{2-}])$
 23. $\text{SeO}_3^{2-} (\text{aq}) + 7 \text{H}^+ (\text{aq}) + 6 \text{e} \rightleftharpoons \text{HSe}^- (\text{aq}) + 3 \text{H}_2\text{O}$
 $E = 0.514 - 0.0690 \text{pH} - 0.0098 \log([\text{HSe}^-]/[\text{SeO}_3^{2-}]) \quad (0.414)$



C Solubility of Selenium

- $$25. \quad \text{Se}(\text{c}) + 2 \text{H}^+(\text{aq}) + 2 \text{e} \rightleftharpoons \text{H}_2\text{Se}(\text{aq})$$
- $$E = -0.115 - 0.0591 \text{ pH} - 0.0296 \log [\text{H}_2\text{Se}] \quad (**)$$
- $$26. \quad \text{Se}(\text{c}) + \text{H}^+(\text{aq}) + 2 \text{e} \rightleftharpoons \text{HSe}^-(\text{aq})$$
- $$E = -0.228 - 0.0296 \text{ pH} - 0.0296 \log [\text{HSe}^-] \quad (**)$$
- $$27. \quad \text{Se}(\text{c}) + 2 \text{e} \rightleftharpoons \text{Se}^{2-}(\text{aq})$$
- $$E = -0.670 - 0.0296 \log [\text{Se}^{2-}] \quad (**)$$
- $$28. \quad \text{Se}(\text{c}) + 2 \text{H}^+(\text{aq}) + 2 \text{e} \rightleftharpoons \text{H}_2\text{Se}(\text{g})$$
- $$E = -0.082 - 0.0591 \text{ pH} - 0.0296 \log P_{\text{H}_2\text{Se}} \quad (**)$$
- $$29. \quad \text{H}_2\text{SeO}_3(\text{aq}) + 4 \text{H}^+(\text{aq}) + 4 \text{e} \rightleftharpoons \text{Se}(\text{c}) + 3 \text{H}_2\text{O}$$
- $$E = 0.739 - 0.0591 \text{ pH} + 0.0148 \log [\text{H}_2\text{SeO}_3] \quad (**)$$
- $$30. \quad \text{HSeO}_3^-(\text{aq}) + 5 \text{H}^+(\text{aq}) + 4 \text{e} \rightleftharpoons \text{Se}(\text{c}) + 3 \text{H}_2\text{O}$$
- $$E = 0.777 - 0.0739 \text{ pH} + 0.0148 \log [\text{HSeO}_3^-] \quad (**)$$
- $$31. \quad \text{SeO}_3^{2-}(\text{aq}) + 6 \text{H}^+(\text{aq}) + 4 \text{e} \rightleftharpoons \text{Se}(\text{c}) + 3 \text{H}_2\text{O}$$
- $$E = 0.885 - 0.0887 \text{ pH} + 0.0148 \log [\text{SeO}_3^{2-}] \quad (**)$$
- $$32. \quad \text{H}_2\text{SeO}_4(\text{aq}) + 6 \text{H}^+(\text{aq}) + 6 \text{e} \rightleftharpoons \text{Se}(\text{c}) + 4 \text{H}_2\text{O}$$
- $$E = 0.876 - 0.0591 \text{ pH} + 0.00985 \log [\text{H}_2\text{SeO}_4] \quad (**)$$
- $$33. \quad \text{HSeO}_4^-(\text{aq}) + 7 \text{H}^+(\text{aq}) + 6 \text{e} \rightleftharpoons \text{Se}(\text{c}) + 4 \text{H}_2\text{O}$$
- $$E = 0.858 - 0.0690 \text{ pH} + 0.00985 \log [\text{HSeO}_4^-] \quad (**)$$
- $$34. \quad \text{SeO}_4^{2-}(\text{aq}) + 8 \text{H}^+(\text{aq}) + 6 \text{e} \rightleftharpoons \text{Se}(\text{c}) + 4 \text{H}_2\text{O}$$
- $$E = 0.876 - 0.0788 \text{ pH} + 0.00985 \log [\text{SeO}_4^{2-}]$$

D Solubility of H₂Se (g)

- $$35. \quad \text{H}_2\text{Se}(\text{g}) \rightleftharpoons \text{H}_2\text{Se}(\text{aq}) \quad K = 7.88 \times 10^{-2}$$
- $$\log\left(\frac{[\text{H}_2\text{Se}]}{P_{\text{H}_2\text{Se}}}\right) \rightleftharpoons -1.099$$
- $$36. \quad \text{H}_2\text{Se}(\text{g}) \rightleftharpoons \text{H}^+(\text{aq}) + \text{HSe}^-(\text{aq})$$
- $$\text{pH} = 4.905 + \log [\text{HSe}^-] - \log P_{\text{H}_2\text{Se}}$$
- $$37. \quad \text{H}_2\text{Se}(\text{g}) \rightleftharpoons 2 \text{H}^+(\text{aq}) + \text{HSe}^-(\text{aq})$$
- $$\text{pH} = 9.933 + 0.500 \log [\text{Se}^{2-}] - 0.500 \log P_{\text{H}_2\text{Se}}$$
- $$38. \quad 2 \text{H}^+(\text{aq}) + 2 \text{e} \rightleftharpoons \text{H}_2(\text{g})$$
- $$E = -0.0591 \text{ pH} \quad (P = 1 \text{ atm})$$
- $$39. \quad \text{O}_2(\text{g}) + 4 \text{H}^+(\text{aq}) + 4 \text{e} \rightleftharpoons 2 \text{H}_2\text{O}$$
- $$E = 1.229 - 0.0591 \text{ pH} \quad (P = 1 \text{ atm})$$

Cu - Se - H₂O system Eh-pH equilibrium equations

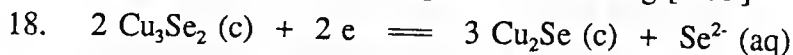
A. Stability of copper in Se²⁻ environment

1. $\text{Cu}_2\text{Se (c)} + 2 \text{H}^+ \text{(aq)} + 2 \text{e} \rightleftharpoons 2 \text{Cu (c)} + \text{H}_2\text{Se (aq)}$
 $E = -0.486 - 0.0591 \text{ pH} - 0.0296 \log [\text{H}_2\text{Se}]$
2. $\text{Cu}_2\text{Se (c)} + \text{H}^+ \text{(aq)} + 2 \text{e} \rightleftharpoons 2 \text{Cu (c)} + \text{HSe}^- \text{(aq)}$
 $E = -0.599 - 0.0296 \text{ pH} - 0.0296 \log [\text{HSe}^-]$
3. $\text{Cu}_2\text{Se (c)} + 2 \text{e} \rightleftharpoons \text{Cu (c)} + \text{Se}^{2-} \text{(aq)}$
 $E = -1.041 - 0.0296 \log [\text{Se}^{2-}]$
4. $\text{Cu}_3\text{Se}_2 \text{(c)} + 4 \text{H}^+ \text{(aq)} + 4 \text{e} \rightleftharpoons 2 \text{H}_2\text{Se (aq)} + 3 \text{Cu (c)}$
 $E = -0.404 - 0.0591 \text{ pH} - 0.0296 \log [\text{H}_2\text{Se}]$
5. $\text{Cu}_3\text{Se}_2 \text{(c)} + 2 \text{H}^+ \text{(aq)} + 4 \text{e} \rightleftharpoons 2 \text{HSe}^- \text{(aq)} + 3 \text{Cu (c)}$
 $E = -0.517 - 0.0296 \text{ pH} - 0.0296 \log [\text{HSe}^-]$
6. $\text{Cu}_3\text{Se}_2 \text{(c)} + 4 \text{e} \rightleftharpoons 2 \text{Se}^{2-} \text{(aq)} + 3 \text{Cu (c)}$
 $E = -0.959 - 0.0296 \log [\text{Se}^{2-}]$
7. $\text{CuSe (c)} + 2 \text{H}^+ \text{(aq)} + 2 \text{e} \rightleftharpoons \text{Cu (c)} + \text{H}_2\text{Se (aq)}$
 $E = -0.336 - 0.0591 \text{ pH} - 0.0296 \log [\text{H}_2\text{Se}]$
8. $\text{CuSe (c)} + \text{H}^+ \text{(aq)} + 2 \text{e} \rightleftharpoons \text{Cu (c)} + \text{HSe}^- \text{(aq)}$
 $E = -0.449 - 0.0296 \text{ pH} - 0.0296 \log [\text{HSe}^-]$
9. $\text{CuSe (c)} + 2 \text{e} \rightleftharpoons \text{Cu (c)} + \text{Se}^{2-} \text{(aq)}$
 $E = -0.891 - 0.0296 \log [\text{Se}^{2-}]$

B. Phase transfer of selenides in Se²⁻ environment

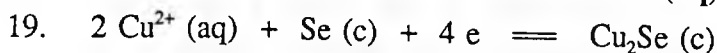
10. $3 \text{CuSe (c)} + 2 \text{H}^+ \text{(aq)} + 2 \text{e} \rightleftharpoons \text{Cu}_3\text{Se}_2 \text{(c)} + \text{H}_2\text{Se (aq)}$
 $E = -0.201 - 0.0591 \text{ pH} - 0.0296 \log [\text{H}_2\text{Se}]$
11. $3 \text{CuSe (c)} + \text{H}^+ \text{(aq)} + 2 \text{e} \rightleftharpoons \text{Cu}_3\text{Se}_2 \text{(c)} + \text{HSe}^- \text{(aq)}$
 $E = -0.3135 - 0.0296 \text{ pH} - 0.0296 \log [\text{HSe}^-]$
12. $3 \text{CuSe (c)} + 2 \text{e} \rightleftharpoons \text{Cu}_3\text{Se}_2 \text{(c)} + \text{Se}^{2-} \text{(aq)}$
 $E = -0.756 - 0.0296 \log [\text{Se}^{2-}]$
13. $2 \text{CuSe (c)} + 2 \text{H}^+ \text{(aq)} + 2 \text{e} \rightleftharpoons \text{Cu}_2\text{Se (c)} + \text{H}_2\text{Se (aq)}$
 $E = -0.186 - 0.0591 \text{ pH} - 0.0296 \log [\text{H}_2\text{Se}]$
14. $2 \text{CuSe (c)} + \text{H}^+ \text{(aq)} + 2 \text{e} \rightleftharpoons \text{Cu}_2\text{Se (c)} + \text{HSe}^- \text{(aq)}$
 $E = -0.299 - 0.0296 \text{ pH} - 0.0296 \log [\text{HSe}^-]$
15. $2 \text{CuSe (c)} + 2 \text{e} \rightleftharpoons \text{Cu}_2\text{Se (c)} + \text{Se}^{2-} \text{(aq)}$
 $E = -0.742 - 0.296 \log [\text{Se}^{2-}]$
16. $2 \text{Cu}_3\text{Se}_2 \text{(c)} + 2 \text{H}^+ \text{(aq)} + 2 \text{e} \rightleftharpoons 3 \text{Cu}_2\text{Se (c)} + \text{H}_2\text{Se (aq)}$
 $E = -0.158 - 0.0591 \text{ pH} - 0.0296 \log [\text{H}_2\text{Se}]$
17. $2 \text{Cu}_3\text{Se}_2 \text{(c)} + \text{H}^+ \text{(aq)} + 2 \text{e} \rightleftharpoons 3 \text{Cu}_2\text{Se (c)} + \text{HSe}^- \text{(aq)}$

$$E = -0.270 - 0.0296 \text{ pH} - 0.0296 \log [\text{HSe}^-]$$

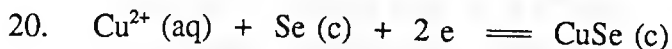


$$E = -0.713 - 0.0296 \log [\text{Se}^{2-}]$$

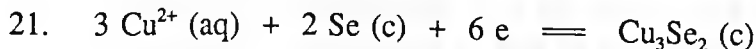
C. Oxidation of selenides to Se(c) and Cu²⁺ (aq)



$$E = 0.525 + 0.0296 \log [\text{Cu}^{2+}]$$

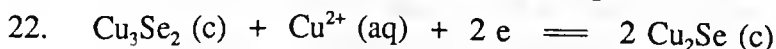


$$E = 0.561 + 0.0296 \log [\text{Cu}^{2+}]$$

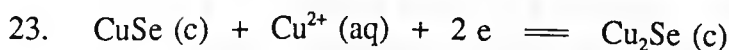


$$E = 0.532 + 0.0296 \log [\text{Cu}^{2+}]$$

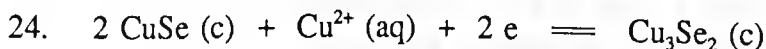
D. Phase transfer of selenides involving release of Cu²⁺(aq) ion



$$E = 0.5037 + 0.0296 \log [\text{Cu}^{2+}]$$

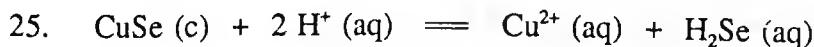


$$E = 0.489 + 0.0296 \log [\text{Cu}^{2+}]$$

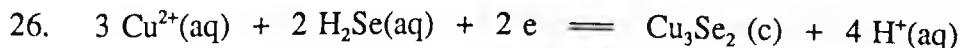


$$E = 0.475 + 0.0296 \log [\text{Cu}^{2+}]$$

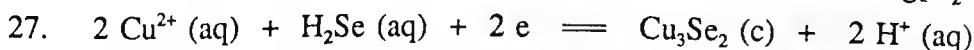
E. Oxidative Dissolution of selenides in acidic medium



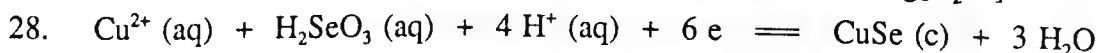
$$\text{pH} = -11.422 - 0.500 \log [\text{Cu}^{2+}] - 0.500 \log [\text{H}_2\text{Se}]$$



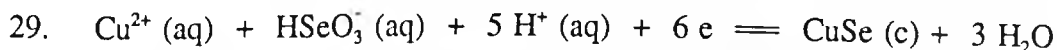
$$E = 1.826 + 0.118 \text{ pH} + 0.0887 \log [\text{Cu}^{2+}] + 0.0591 \log [\text{H}_2\text{Se}]$$



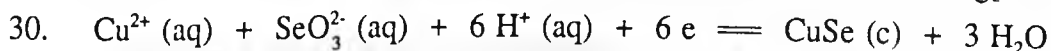
$$E = 1.17 + 0.0591 \text{ pH} + 0.0591 \log [\text{Cu}^{2+}] + 0.0296 \log [\text{H}_2\text{Se}]$$



$$E = 0.680 - 0.0394 \text{ pH} + 0.00985 \log [\text{H}_2\text{SeO}_3]$$

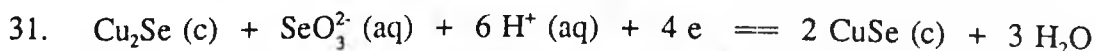


$$E = 0.705 - 0.0493 \text{ pH} + 0.00985 \log [\text{HSeO}_3^-] + 0.00985 \log [\text{Cu}^{2+}]$$

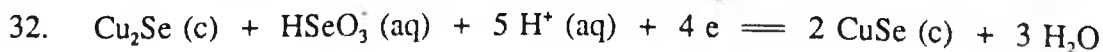


$$E = 0.777 - 0.0591 \text{ pH} + 0.00985 \log [\text{SeO}_3^{2-}] + 0.00985 \log [\text{Cu}^{2+}]$$

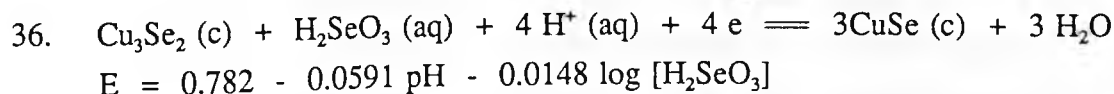
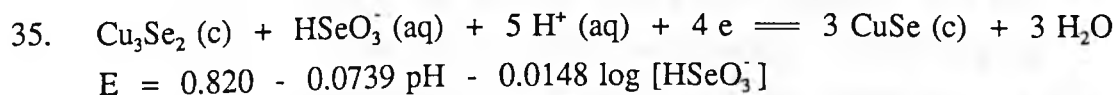
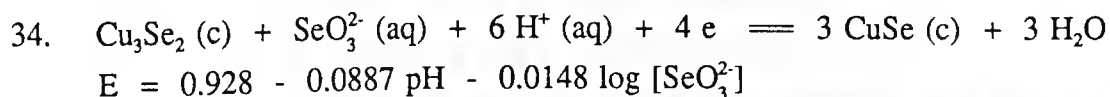
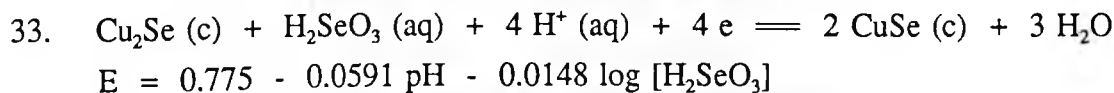
F. Phase transfer between selenides with the formation of high valence species of selenium



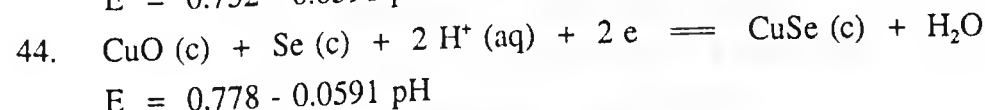
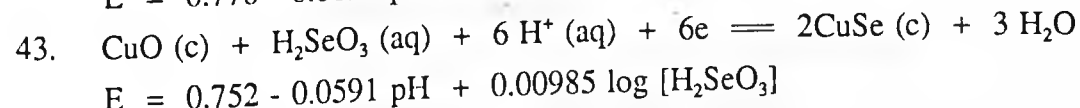
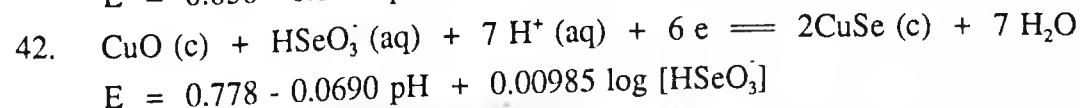
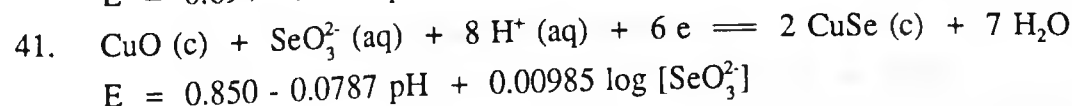
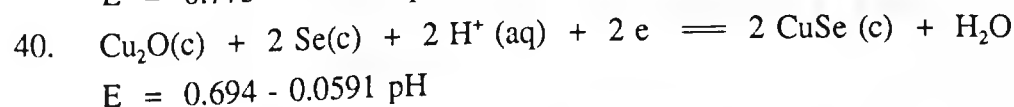
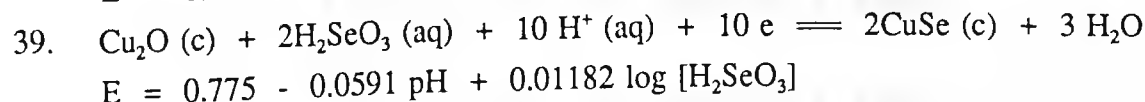
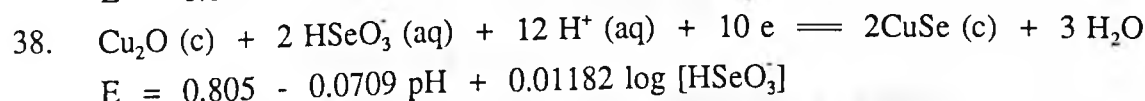
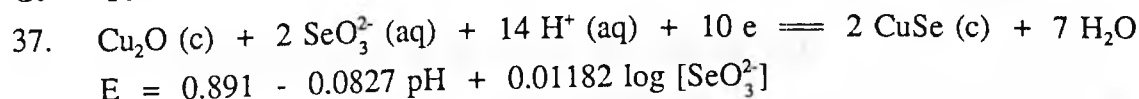
$$E = 0.921 - 0.0887 \text{ pH} - 0.0148 \log [\text{SeO}_3^{2-}]$$



$$E = 0.813 - 0.07396 \text{ pH} - 0.0148 \log [\text{HSeO}_3^-]$$

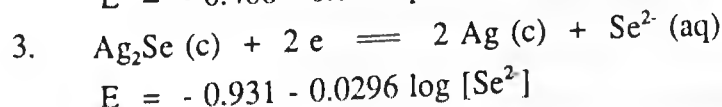
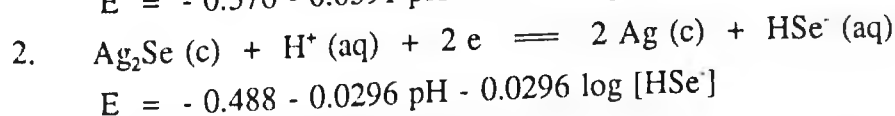
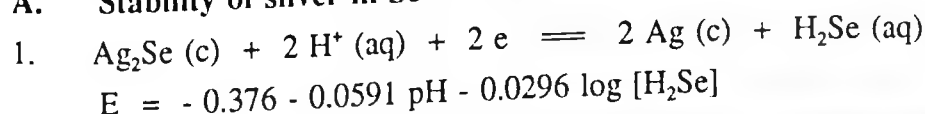


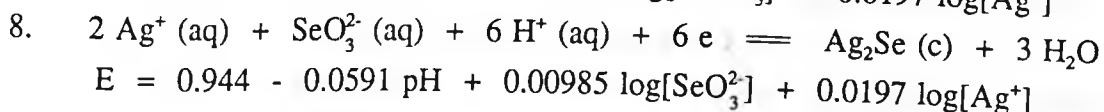
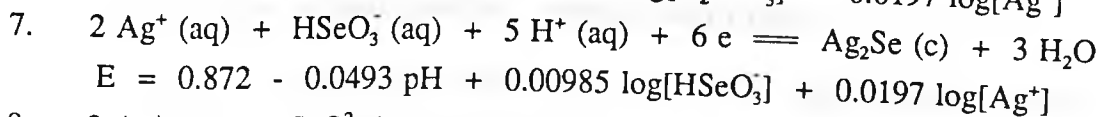
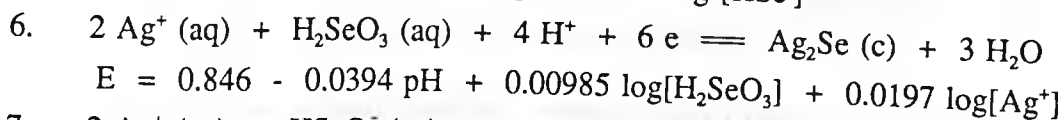
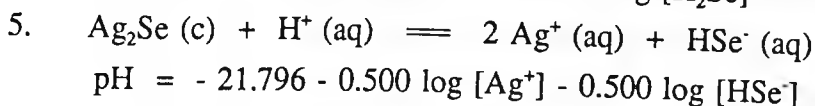
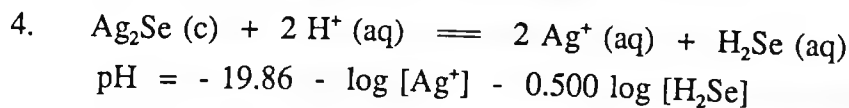
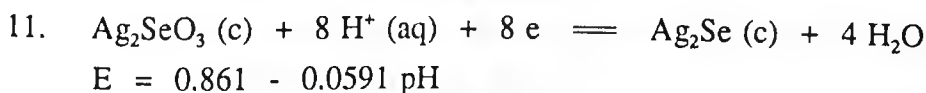
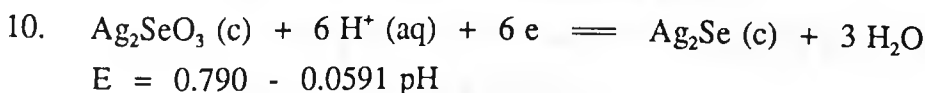
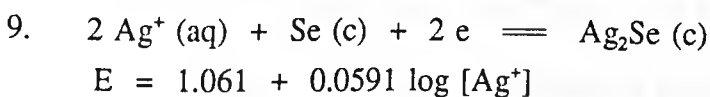
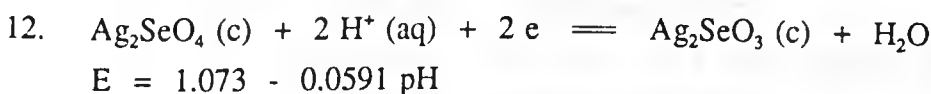
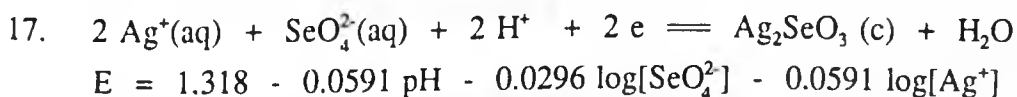
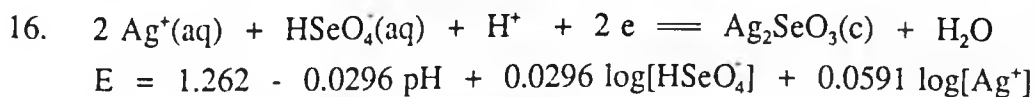
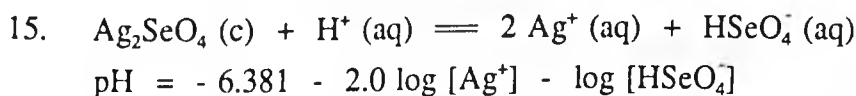
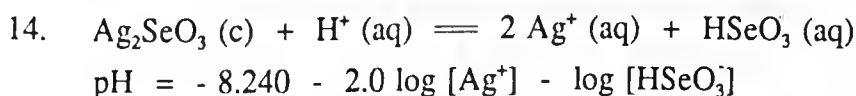
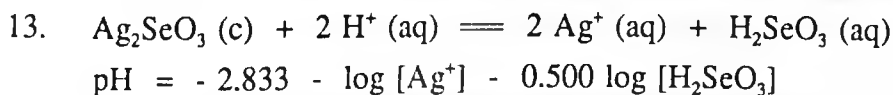
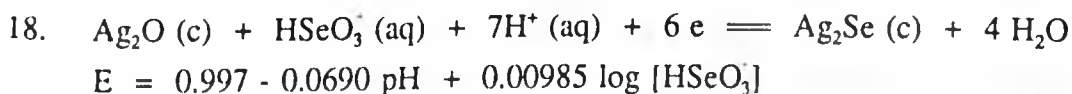
G. Oxidation of selenides to oxides



Ag - Se - H₂O System Eh-pH equilibrium equations

A. Stability of silver in Se²⁻ environment



B. Dissolution of selenides**C. Oxidation of selenide to Se (c), Se (IV) and Se (VI)****D. Equilibrium between selenite and selenate****E. Dissolution of selenite and selenate****F. Equilibrium between selenide and oxides**

19. $\text{Ag}_2\text{O}(\text{c}) + \text{SeO}_3^{2-}(\text{aq}) + 8\text{H}^+(\text{aq}) + 6\text{e} \rightleftharpoons \text{Ag}_2\text{Se}(\text{c}) + 4\text{H}_2\text{O}$
 $E = 1.068 - 0.0788 \text{ pH} + 0.00985 \log [\text{SeO}_3^{2-}]$
20. $2\text{AgO}(\text{c}) + \text{HSeO}_3^-(\text{aq}) + 9\text{H}^+(\text{aq}) + 6\text{e} \rightleftharpoons \text{Ag}_2\text{Se}(\text{c}) + 5\text{H}_2\text{O}$
 $E = 1.475 - 0.0887 \text{ pH} + 0.00985 \log [\text{HSeO}_3^-]$
21. $2\text{AgO}(\text{c}) + \text{SeO}_3^{2-}(\text{aq}) + 10\text{H}^+(\text{aq}) + 6\text{e} \rightleftharpoons \text{Ag}_2\text{Se}(\text{c}) + 5\text{H}_2\text{O}$
 $E = 1.547 - 0.0986 \text{ pH} + 0.00985 \log [\text{SeO}_3^{2-}]$

G. Equilibrium between selenite / selenate and oxides

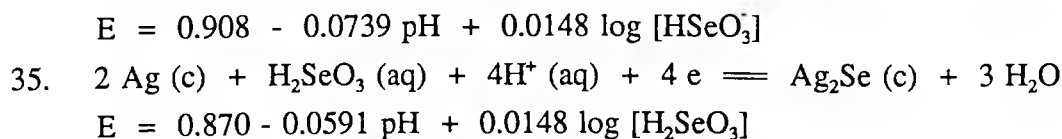
22. $\text{Ag}_2\text{O}_3(\text{c}) + \text{SeO}_4^{2-}(\text{aq}) + 6\text{H}^+(\text{aq}) + 2\text{e} \rightleftharpoons \text{Ag}_2\text{SeO}_3(\text{c}) + 3\text{H}_2\text{O}$
 $E = 1.881 - 0.0887 \text{ pH} + 0.0148 \log [\text{SeO}_4^{2-}]$
23. $\text{Ag}_2\text{O}_3(\text{c}) + \text{HSeO}_4^-(\text{aq}) + 5\text{H}^+(\text{aq}) + 2\text{e} \rightleftharpoons \text{Ag}_2\text{SeO}_3(\text{c}) + 3\text{H}_2\text{O}$
 $E = 1.854 - 0.0739 \text{ pH} + 0.0148 \log [\text{HSeO}_4^-]$
24. $2\text{AgO}(\text{c}) + \text{SeO}_4^{2-}(\text{aq}) + 4\text{H}^+(\text{aq}) + 2\text{e} \rightleftharpoons \text{Ag}_2\text{SeO}_4(\text{c}) + 2\text{H}_2\text{O}$
 $E = 2.056 - 0.1182 \text{ pH} + 0.0296 \log [\text{SeO}_4^{2-}]$
25. $\text{Ag}_2\text{O}(\text{c}) + \text{SeO}_4^{2-}(\text{aq}) + 2\text{H}^+(\text{aq}) \rightleftharpoons \text{Ag}_2\text{SeO}_4(\text{c}) + \text{H}_2\text{O}$
 $\text{pH} = 10.427 + 0.500 \log [\text{SeO}_4^{2-}]$
26. $\text{Ag}_2\text{O}(\text{c}) + \text{SeO}_3^{2-}(\text{aq}) + 2\text{H}^+(\text{aq}) \rightleftharpoons \text{Ag}_2\text{SeO}_3(\text{c}) + \text{H}_2\text{O}$
 $\text{pH} = 14.054 + 0.500 \log [\text{SeO}_3^{2-}]$
27. $\text{Ag}_2\text{O}(\text{c}) + \text{SeO}_4^{2-}(\text{aq}) + 4\text{H}^+(\text{aq}) + 2\text{e} \rightleftharpoons \text{Ag}_2\text{SeO}_3(\text{c}) + 2\text{H}_2\text{O}$
 $E = 1.690 - 0.1182 \text{ pH} + 0.0296 \log [\text{SeO}_4^{2-}]$
28. $2\text{AgO}(\text{c}) + \text{SeO}_3^{2-}(\text{aq}) + 4\text{H}^+(\text{aq}) + 2\text{e} \rightleftharpoons \text{Ag}_2\text{SeO}_3(\text{c}) + 2\text{H}_2\text{O}$
 $E = 2.271 - 0.1182 \text{ pH} + 0.0296 \log [\text{SeO}_4^{2-}]$
29. $2\text{AgO}(\text{c}) + \text{SeO}_4^{2-}(\text{aq}) + 6\text{H}^+(\text{aq}) + 4\text{e} \rightleftharpoons \text{Ag}_2\text{SeO}_3(\text{c}) + 3\text{H}_2\text{O}$
 $E = 1.564 - 0.0887 \text{ pH} + 0.0148 \log [\text{SeO}_4^{2-}]$

H. Equilibrium between selenite / selenate and silver

30. $\text{Ag}_2\text{SeO}_4(\text{c}) + 2\text{e} \rightleftharpoons 2\text{Ag}(\text{c}) + \text{SeO}_4^{2-}(\text{aq})$
 $E = 0.554 - 0.0296 \log [\text{SeO}_4^{2-}]$
31. $\text{Ag}_2\text{SeO}_3(\text{c}) + 2\text{e} \rightleftharpoons 2\text{Ag}(\text{c}) + \text{SeO}_3^{2-}(\text{aq})$
 $E = 0.340 - 0.0296 \log [\text{SeO}_3^{2-}]$
32. $\text{Ag}_2\text{SeO}_3(\text{c}) + \text{H}_2\text{O} \rightleftharpoons 2\text{Ag}(\text{c}) + \text{SeO}_4^{2-}(\text{aq}) + 2\text{H}^+(\text{aq})$
 $\text{pH} = 8.769 + 0.500 \log [\text{SeO}_4^{2-}]$

I. Oxidation of selenide to Ag /Se (IV) or Se (VI)

33. $2\text{Ag}(\text{c}) + \text{SeO}_3^{2-}(\text{aq}) + 6\text{H}^+(\text{aq}) + 4\text{e} \rightleftharpoons \text{Ag}_2\text{Se}(\text{c}) + 3\text{H}_2\text{O}$
 $E = 1.016 - 0.0887 \text{ pH} + 0.0148 \log [\text{SeO}_3^{2-}]$
34. $2\text{Ag}(\text{c}) + \text{HSeO}_3^-(\text{aq}) + 5\text{H}^+(\text{aq}) + 4\text{e} \rightleftharpoons \text{Ag}_2\text{Se}(\text{c}) + 3\text{H}_2\text{O}$



Cu - Ag - Se - H₂O System Eh-pH Equilibrium Equations

A. Stability of metals in Se²⁻ medium

1. $\text{Ag}_2\text{Se (c)} + 2 \text{ H}^+ \text{ (aq)} + 2 \text{ e} \rightleftharpoons 2 \text{ Ag (c)} + \text{H}_2\text{Se (aq)}$
 $E = -0.376 - 0.0591 \text{ pH} - 0.0296 \log [\text{H}_2\text{Se}]$
2. $\text{Ag}_2\text{Se (c)} + \text{H}^+ \text{ (aq)} + 2 \text{ e} \rightleftharpoons 2 \text{ Ag (c)} + \text{HSe}^- \text{ (aq)}$
 $E = -0.488 - 0.0296 \text{ pH} - 0.0296 \log [\text{HSe}^-]$
3. $\text{Ag}_2\text{Se (c)} + 2 \text{ e} \rightleftharpoons 2 \text{ Ag (c)} + \text{Se}^{2-} \text{ (aq)}$
 $E = -0.931 - 0.0296 \log [\text{Se}^{2-}]$
4. $\text{Cu}_2\text{Se (c)} + 2 \text{ H}^+ \text{ (aq)} + 2 \text{ e} \rightleftharpoons 2 \text{ Cu (c)} + \text{H}_2\text{Se (aq)}$
 $E = -0.486 - 0.0591 \text{ pH} - 0.0296 \log [\text{H}_2\text{Se}]$
5. $\text{Cu}_2\text{Se (c)} + \text{H}^+ \text{ (aq)} + 2 \text{ e} \rightleftharpoons 2 \text{ Cu (c)} + \text{HSe}^- \text{ (aq)}$
 $E = -0.599 - 0.0296 \text{ pH} - 0.0296 \log [\text{HSe}^-]$
6. $\text{Cu}_2\text{Se (c)} + 2 \text{ e} \rightleftharpoons 2 \text{ Cu (c)} + \text{Se}^{2-} \text{ (aq)}$
 $E = -1.041 - 0.0296 \log [\text{Se}^{2-}]$
7. $\text{AgCuSe (c)} + 2 \text{ H}^+ \text{ (aq)} + 2 \text{ e} \rightleftharpoons \text{Ag (c)} + \text{Cu (c)} + \text{H}_2\text{Se (aq)}$
 $E = -0.392 - 0.0591 \text{ pH} - 0.0296 \log [\text{H}_2\text{Se}]$
8. $\text{AgCuSe (c)} + \text{H}^+ \text{ (aq)} + 2 \text{ e} \rightleftharpoons \text{Ag (c)} + \text{Cu (c)} + \text{HSe}^- \text{ (aq)}$
 $E = -0.505 - 0.0296 \text{ pH} - 0.0296 \log [\text{HSe}^-]$
9. $\text{AgCuSe (c)} + 2 \text{ e} \rightleftharpoons \text{Ag (c)} + \text{Cu (c)} + \text{Se}^{2-} \text{ (aq)}$
 $E = -0.948 - 0.0296 \log [\text{Se}^{2-}]$
10. $2 \text{ AgCuSe (c)} + 2 \text{ H}^+ \text{ (aq)} + 2 \text{ e} \rightleftharpoons 2\text{Ag (c)} + \text{Cu}_2\text{Se (c)} + \text{H}_2\text{Se (aq)}$
 $E = -0.299 - 0.0591 \text{ pH} - 0.0296 \log [\text{H}_2\text{Se}]$
11. $2 \text{ AgCuSe (c)} + \text{H}^+ \text{ (aq)} + 2 \text{ e} \rightleftharpoons 2\text{Ag (c)} + \text{Cu}_2\text{Se (c)} + \text{HSe}^- \text{ (aq)}$
 $E = -0.412 - 0.0296 \text{ pH} - 0.0296 \log [\text{HSe}^-]$
12. $2 \text{ AgCuSe (c)} + 2 \text{ e} \rightleftharpoons 2 \text{ Ag (c)} + \text{Cu}_2\text{Se (c)} + \text{Se}^{2-} \text{ (aq)}$
 $E = -0.854 - 0.0296 \log [\text{Se}^{2-}]$
13. $2 \text{ CuSe (c)} + 2 \text{ H}^+ \text{ (aq)} + 2 \text{ e} \rightleftharpoons \text{Cu}_2\text{Se (c)} + \text{H}_2\text{Se (aq)}$
 $E = -0.186 - 0.0591 \text{ pH} - 0.0296 \log [\text{H}_2\text{Se}]$
14. $2 \text{ CuSe (c)} + \text{H}^+ \text{ (aq)} + 2 \text{ e} \rightleftharpoons \text{Cu}_2\text{Se (c)} + \text{HSe}^- \text{ (aq)}$
 $E = -0.299 - 0.0296 \text{ pH} - 0.0296 \log [\text{HSe}^-]$
15. $2 \text{ CuSe (c)} + 2 \text{ e} \rightleftharpoons \text{Cu}_2\text{Se (c)} + \text{Se}^{2-} \text{ (aq)}$
 $E = -0.742 - 0.0296 \log [\text{Se}^{2-}]$

16. $\text{Ag}_2\text{Se}(\text{c}) + 2\text{CuSe}(\text{c}) + 2\text{H}^+ + 2\text{e} \rightleftharpoons 2\text{AgCuSe}(\text{c}) + \text{H}_2\text{Se}(\text{aq})$
 $E = -0.263 - 0.0591 \text{ pH} - 0.0296 \log [\text{H}_2\text{Se}]$
17. $\text{Ag}_2\text{Se}(\text{c}) + 2\text{CuSe}(\text{c}) + \text{H}^+(\text{aq}) + 2\text{e} \rightleftharpoons 2\text{AgCuSe}(\text{c}) + \text{HSe}^-(\text{aq})$
 $E = -0.376 - 0.0296 \text{ pH} - 0.0296 \log [\text{HSe}^-]$
18. $\text{Ag}_2\text{Se}(\text{c}) + 2\text{CuSe}(\text{c}) + 2\text{e} \rightleftharpoons 2\text{AgCuSe}(\text{c}) + \text{Se}^{2-}(\text{aq})$
 $E = -0.818 - 0.0296 \log [\text{Se}^{2-}]$
19. $\text{Cu}^{2+}(\text{aq}) + \text{Se}(\text{c}) + 2\text{e} \rightleftharpoons \text{CuSe}(\text{c})$
 $E = 0.5618 + 0.0296 \log [\text{Cu}^{2+}]$
19. $2\text{Cu}^{2+}(\text{aq}) + \text{Ag}_2\text{Se}(\text{c}) + \text{Se}(\text{c}) + 4\text{e} \rightleftharpoons 2\text{AgCuSe}(\text{c})$
 $E = 0.487 + 0.0296 \log [\text{Cu}^{2+}]$
20. $2\text{Cu}^{2+}(\text{aq}) + \text{Ag}_2\text{Se}(\text{c}) + \text{Se}(\text{c}) + 2\text{e} \rightleftharpoons 2\text{AgCuSe}(\text{c})$
 $E = 0.813 + 0.0591 \log [\text{Cu}^{2+}]$
21. $\text{Cu}^{2+}(\text{aq}) + \text{Ag}^+(\text{aq}) + \text{Se}(\text{c}) + 3\text{e} \rightleftharpoons \text{AgCuSe}(\text{c})$
 $E = 0.678 + 0.0197 \log [\text{Cu}^{2+}] - 0.0197 \log [\text{Ag}^+]$
22. $\text{Cu}^{2+}(\text{aq}) + \text{Ag}^+(\text{aq}) + \text{Se}(\text{c}) + 2\text{e} \rightleftharpoons \text{AgCuSe}(\text{c})$
 $E = 0.936 + 0.0296 \log [\text{Cu}^{2+}] + 0.0296 \log [\text{Ag}^+]$
23. $\text{AgCuSe}(\text{c}) + 2\text{H}^+(\text{aq}) \rightleftharpoons \text{Ag}^+(\text{aq}) + \text{Cu}^+(\text{aq}) + \text{H}_2\text{Se}(\text{aq})$
 $\text{pH} = -43.62 - 0.5 \log [\text{Cu}^+] - 0.5 \log [\text{Ag}^+] - 0.5 \log [\text{H}_2\text{Se}]$
24. $\text{Ag}_2\text{Se}(\text{c}) + 2\text{Cu}^{2+}(\text{aq}) + \text{Se}(\text{c}) + 4\text{e} \rightleftharpoons 2\text{AgCuSe}(\text{c})$
 $E = 0.566 + 0.0296 \log [\text{Cu}^{2+}]$
25. $\text{Ag}_2\text{Se}(\text{c}) + 2\text{Cu}^{2+}(\text{aq}) + \text{H}_2\text{Se}(\text{aq}) + 2\text{e} \rightleftharpoons 2\text{AgCuSe}(\text{c}) + 2\text{H}^+(\text{aq})$
 $E = 1.230 - 0.0591 \text{ pH} - 0.0591 \log [\text{Cu}^{2+}] - 0.0591 \log [\text{H}_2\text{Se}]$

Note : Thermodynamic data for related calculation are based on National standards values (Ref. 156). "***" denotes that the data are extracted from A.J. Bard's values (Ref. 157). Data enclosed in parentheses are taken from Pourbaix's values (Ref. 155).